Analysis of squamous cell carcinoma invasion identifies a role for TRAF6

Shahid Iqbal Chaudhry

BDS MBBS FDSRCS MRCP(UK)

Tumour Cell Biology Laboratory

Cancer Research UK London Research Institute

44 Lincoln's Inn Fields

London

WC2A 3PX

Thesis submitted for the degree of Doctor of Philosophy

University College London 2010

Declaration

I, Shahid Iqbal Chaudhry, declare that the contents of this dissertation are my own and that this work has not previously been submitted, in part or in full, for a degree or diploma to this or any other University or Examining Board.

Work performed in collaboration with other individuals and laboratories or obtained from other sources is clearly stated in the appropriate place.

Word count ~ 58, 100

……

Shahid Iqbal Chaudhry

Abstract

The principal objectives of the work in this thesis were: (a) to investigate cancer cell invasion in squamous cell carcinoma (SCC) by examining the role of ubiquitin-linked pathways in the regulation of the actin cytoskeleton and (b) to establish a human tissue bank of SCCHN specimens matched to adjacent non-cancerous tissue.

An siRNA screen was performed with the premise that genes that regulate the actin cytoskeleton would be involved in the invasion of cancer cells. 289 E3 ubiquitin ligases and 137 de-ubiquitinating enzymes (DUBs) were screened yielding 3 gene hits (RKHD2, TRAF6 and ZA20d1) capable of regulating both the F-actin cytoskeleton of SCC cells as well as their collective invasion in a three-dimensional organotypic invasion system. A secondary morphological and functional screen of 20 E3 ligases and 9 DUBs in carcinoma-associated fibroblasts demonstrated that 5 genes (MKRN2, RKHD2, TRAF6, ZA20d1 and USP6) influenced the ability of stromal fibroblasts to promote SCC invasion. Following transcriptional analysis using qPCR, the E3 ligase TRAF6 and its complementary DUB ZA20d1 emerged as candidate genes for detailed study.

TRAF6 was shown to influence NF-κB signalling in SCC cells by modulating the levels of IκBα. Given the importance of NF-κB activation in the pathogenesis of SCC, I investigated its significance in our organotypic system. Using TNFα, IL-1α and several IKK inhibitors, I demonstrated that SCC invasion was dose-responsive and NF-κB dependent. Furthermore, infliximab (a monoclonal antibody to TNFα in clinical use) inhibited carcinoma invasion at a therapeutic dose.

Ethical and R&D approval for the establishment of a human tissue bank was obtained and SCCHN tumour samples with patient matched control tissue are now being banked. Analysis of these specimens and commercial tissue microarrays indicates that TRAF6 is overexpressed in a subset of SCC.

Acknowledgements

I would like to thank my three supervisors, Dr Erik Sahai, Professor Julian Downward and Dr Nic Tapon, as well as Dr Sally Leevers (Academic Director, Cancer Research UK London Research Institute) for their guidance and advice throughout the duration of my PhD. A very big thank you to Cancer Research UK for supporting this work by a Clinical Research Training Fellowship and to the many fundraisers without whom such sponsorship would not exist.

My utmost gratitude goes to Emma Nye (Operational Head of the Experimental Histopathology Laboratory) for her help in preparing my histology samples. Without Emma's hard work I would not have been able to complete my bench work within three years!

Thank you to Dr Kevin Harrington (Senior Lecturer / Honorary Consultant in Clinical Oncology, The Royal Marsden Hospital, London) and Mr Peter Williamson (Consultant ENT / Head & Neck Surgeon, St George's Hospital, London) for their help in establishing a tissue bank for the Tumour Cell Biology Laboratory. Their efforts have been greatly appreciated and the tissue bank is already proving to be an invaluable research resource.

Thanks also to my brother, Dr Afzal Chaudhry (Consultant in Renal Medicine, Addenbrooke's Hospital, Cambridge) for advice regarding the statistical analysis of my data and to Dr Selvam Thavaraj (Lecturer / Honorary Consultant in Oral & Pathology, KCL Dental Institute, London) for his informative discussions regarding head and neck pathology.

Finally, I would like to thank my wife, Kokila, for her patience over the last three years and my parents for their considerable support and encouragement throughout my career to date. They, of course, are the ones that have made this all possible.

Contents

CHAPTER 5: VALIDATION OF GENE HITS & CANDIDATE GENES

CHAPTER 6: NF-κB SIGNALLING IN SCC INVASION

List of Figures

Chapter 1

Chapter 3

Chapter 4

Chapter 5

Chapter 6

Chapter 7

Chapter 8

Chapter 9

List of Tables

Chapter 1

Chapter 3

Chapter 8

Chapter 9

Abbreviations

ABC	Aneurysmal bone cyst
AML	Acute myeloid leukaemia
ANOVA	Analysis of variance
AOM	Azaxymethane
AP1	Activator protein 1
αMEM	Alpha minimum essential medium
αSMA	Alpha smooth muscle actin
Arp2/3	Actin related 2/3 complex
ATP	Adenosine triphosphate
BAFF	B cell activating factor
BCL-3	B cell lymphoma 3
BCR	B-cell receptor
BDT	Big Dye® Terminator
BSA	Bovine serum albumin
CAF	Carcinoma associated fibroblasts
CAS	Crk associated substrate
Cdc42	Cell division control protein 42
CIS	Carcinoma in situ
CLL	Chronic lymphocytic leukaemia
CML	Chronic myeloid leukaemia
COREC	Central Office for Research Ethics Committees
CSCC	Cutaneous squamous cell carcinoma
CTP	Cytosine triphosphate
CXCR4	CXC chemokine receptor 4
Cy5	Cyanine 5 fluorescent dye
CYLD	Ubiquitin carboxyl-terminal hydrolase
cDNA	Complimentary deoxyribonucleic acid
DAPI	4,6-diamidino-2-phenylindole
DD	Death domain
DIRA	Deficiency of the IL-1 receptor antagonist
DMBA	7,12-dimethylbenzanthracene
DMEM	Dulbecco's Modified Eagle Medium
DNA	Deoxyribonucleic acid

dNTP	Deoxyribonucleotide mixture
DSS	Dextran sodium sulphate
DTT	Dithiothreitol
DUB	De-ubiquitinating enzyme
EBV	Epstein Barr virus
ECM	Extra-cellular matrix
EDTA	Ethylene diamine tetra-acetic acid
EGF	Epidermal growth factor
EGFR	Epidermal growth factor receptor
EKO	Epidermal knockout
EMT	Epithelial to mesenchymal transition
ENDPB	Executive Non-Department Public Body
ERK	Extra-cellular signal-regulated kinase
EtOH	Ethanol
EUTCD	European Union Tissue and Cells Directive
F-actin	Filamentous actin
FAD	DMEM with Ham's F12 medium
FADD	Fas-associated-DD
FAK	Focal adhesion kinase
FCS	Foetal calf serum
FH	Formin-homology
FLIP	FLICE-like inhibitory protein
FSP1	Fibroblast-specific protein 1
G-actin	Globular actin
GFP	Green fluorescent protein
GRO-1	Growth-related oncogene 1
GST	Glutathione-S-transferase
GTP	Guanosine triphosphate
GVHD	Graft versus host disease
H&E	Haematoxylin and eosin
HCl	Hydrochloric acid
HECT	Homologous to the E6-associated protein C terminus
HED	Hypohidrotic ectodermal dysplasia
HEK293	Human embryonic kidney 293
HPV	Human papilloma virus

HTA	Human Tissue Authority
HT Act	Human Tissue Act
IAP	Inhibitor of apoptosis
IBD	Inflammatory bowel disease
ICAM-1	Inter-cellular adhesion molecule 1
ICE	Interleukin-1 converting enzyme
ic	Intracellular
IFNγ	Interferon gamma
IGF	Insulin-like growth factor
IHC	Immunohistochemistry
IκB	Inhibitor of NF-κB family
IκBαM	IκBα phosphorylation mutant
IκB-DR	Degradation resistant IκB
IKK	IκB kinase
IL-1	Interleukin-1
IL-1F	Interleukin-1 family member
IL-1NTP	N-terminal cleavage product of IL-1
IL-1R	Interleukin-1 receptor
IL-1RA	Interleukin-1 antagonist
IL-1RAcP	IL-1R acceptor protein
ILP	Isolated limb perfusion
IMF	Immunofluoresence
IP	Incontinentia pigmenti
IRAK	IL-1 receptor-associated kinase
IRAS	Integrated Research Application System
JAMM	JAB1/MPN/Mov34 motif
JNK	c-Jun N-terminal kinase
kD	KiloDaltons
KO	Knockout
LB	Luria-Bertani medium
LPS	Lipopolysaccharide
LTβ	Lymphotoxin beta
M	Molar
MAPK	Mitogen activated protein kinase
mDia	Mammalian homologue of *Drosophilia diaphanous*

Mdm	Murine double minute
MEF	Mouse embryonic fibroblast
MeOH	Methanol
µg	Microgram(s)
mg	Milligram(s)
MJD	Machado-Joseph disease
µl	Microlitre(s)
ml	Millilitre(s)
µm	Micrometre(s)
mm	Millimetres(s)
mM	MilliMolar
min	Minute
MLC	Myosin light chain
MLCK	Myosin light chain kinase
MMP	Matrix metalloproteinase
MSC	Mesenchymal stem cells
MTA	Material Transfer Agreement
ng	Nanogram(s)
NaCl	Sodium chloride
NBF	Normal buffered formalin
NEMO	NF-κB essential modulator
NF-κB	Nuclear factor kappa-light-chain-enhancer of activated B cells
NHS	National Health Service
NHS REC	National Health Service Research Ethics Committee
NIH	National Institute of Health
NIHR CSP	National Institute for Health Research Co-ordinated System for gaining NHS Permissions
NIK	NF-κB inducing kinase
NLS	Nuclear localisation sequence
NP-40	Nonyl phenoxylpolyethoxylethanol
NPSA	National Patient Safety Agency
NRES	National Research Ethics Service
OCL	Osteoclast-like multinucleated cell
OSCC	Oral squamous cell carcinoma
OUT	Ovarian tumour-like protease

PAGE	Polyacrylamide gel electrophoresis
PAK1	p21-activated kinase 1
PAMP	Pathogen-associated molecular pattern
PBS	Phosphate buffered saline
PC3	Prostate cancer 3
PCR	Polymerase chain reaction
PDK1	3-phosphoinositide dependent protein kinase 1
PFA	Paraformaldehyde
pg	Picogram(s)
p53	Protein 53
PGE_2	Prostaglandin E_2
PI3K	Phosphatidylinositol 3-kinase
PKCζ	Atypical protein kinase C
pOC	Prefusion osteoclast
PTEN	Protein phosphatase and tensin homologue
R&D	Research and Development
RHD	Rel-homology domain
Rho	Ras-homologue family
RIP1	Receptor interacting protein
RING	Really interesting new gene
RNA	Ribonucleic acid
ROCK	Rho-kinase
RTK	Receptor tyrosine kinase
S	Svedberg sedimentation coefficient
SCC	Squamous cell carcinoma
SCCHN	Squamous cell carcinoma of the head and neck
SDF1	Stromal cell derived factor 1
SDS	Sodium dodecyl sulphate
siRNA	Small interference ribonucleic acid
SLE	Systemic lupus erythematosus
Smurf1	SMAD specific E3 ubiquitin ligase 1
Src	Sarcoma
SSA	Site Specific Assessment
STS	Soft tissue sarcoma
TAB	TAK1-binding proteins

TACE	TNFα converting enzyme
TAK1	Transforming growth factor-β-activated kinase
TAM	Tumour associated macrophages
TB	Terrific broth
TBE	Tris / Borate / EDTA
TBS	Tris buffered saline
TEMED	Tetramethylethylenediamine
TFB	Transformation buffer
TGF	Transforming growth factor
TIMP	Tissue inhibitor of MMP
TIR	Toll-IL-1 receptor
TLR	Toll-like receptor
TNFα	Tumour necrosis factor alpha
TNFR	TNF-receptor
TPA	12-*O*-tetradecanoylphorbol-13-acetate
TRAF	TNFR-associated factor
TRAIL	TNF-related apoptosis-inducing ligand
TRAPS	TNF receptor-associated periodic syndrome
TRIKA	TRAF6-regulated IKK activator
TRITC	Tetramethyl rhodamine iso-thiocyanate
UBA	Ubiquitin-associated
UBD	Ubiquitin-binding domain
UC	Ulcerative colitis
UCH	Ubiquitin C-terminal hydrolase
uPA	Urokinase plasminogen activator
USP	Ubiquitin-specific protease
UTP	Uridine triphosphate
UV	Ultraviolet
VEGF	Vascular endothelial growth factor
VIN	Vulval intraepithelial neoplasia
WAVE	WASP-family verprolin-homologous protein 1
WASP	Wiskott-Aldrich syndrome protein
ZA20d1	Zinc finger A20 domain containing 1
ZIPK	Zipper-interacting protein kinase

Chapter 1

Introduction

1.1 Squamous cell carcinoma (SCC)

1.1.1 Squamous cell carcinoma of the head and neck (SCCHN)

Squamous cell carcinoma of the head and neck (SCCHN) is the sixth most common cancer worldwide and represents greater than 90% of all head and neck cancers [1]. It constitutes a heterogeneous group of malignancies each of which have distinct pathophysiology, biological behaviour and varying degrees of sensitivity to therapeutic intervention [2].

Every year in the UK more than 5,000 people develop oral cancer of which six out of ten patients present with late-stage disease. Patient mortality rates exceed 50% in 5 years and treatment often results in significant problems with eating, swallowing, speech and appearance [1]. The burden of mouth cancer is therefore greater than that of other cancers with approximately 13,000 people in the UK currently being left disabled by the disease.

SCC is an epithelial derived cancer of variable clinical presentation and histological appearance (Figure 1.1). Important tumour-related factors associated with patient prognosis include the tumour type, size and grade, the depth of carcinoma invasion, infiltration of neighbouring structures such as nerves and bone, evidence of extra-capsular spread, and the presence or absence of metastases [3, 4].

The management of the neck is central to the treatment strategy of SCCHN [5]. In the absence of neck disease, the pathological and local features of the primary tumour described above determine the need for a neck dissection. A selective neck dissection directed to the regions at risk for lymphatic spread is generally used in this instance [2]. Conversely, palpable neck metastases necessitate comprehensive clearance of the cervical lymph nodes and related structures - the 'radical' neck dissection [4].

a

b

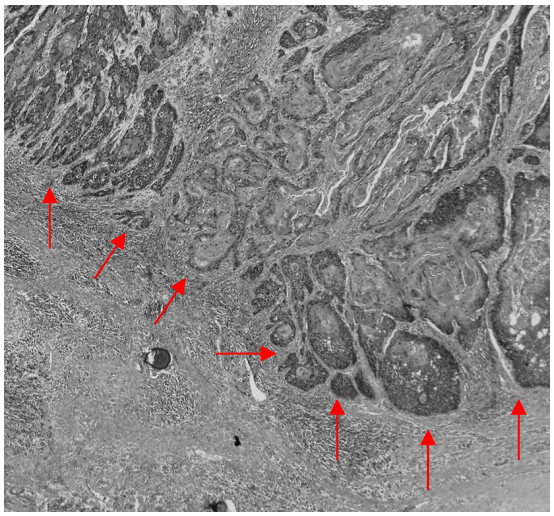

Figure 1.1 Squamous cell carcinoma of the head and neck (SCCHN)

(**a**) Photograph of an extensive SCC involving the right lateral border of the tongue. Image courtesy of Professor Stephen Porter, Honorary Consultant in Oral Medicine, UCL Eastman Dental Institute, London. (**b**) Photomicrograph of an H&E section of a SCCHN. Red arrows indicate the invasive front. Image magnification 10x.

With an improved understanding of cancer cell biology, an increasing knowledge of the factors influencing cancer cell invasion, and enhanced surgical techniques the 'functional' neck dissection has evolved. This in turn has led to improved patient survival and outcome [6].

In principle, early-stage SCCHN can be adequately treated with surgery alone. Patients with late-stage disease, however, require adjuvant therapy which traditionally has been either radiotherapy or chemotherapy; both have been shown to improve patient 5 year survival rates [7]. More recently cancer scientists have focused their attention on the tumour micro-environment. This has led to a greater appreciation of the interactions a cancer cell has with its surrounding stroma and an increasing awareness of the influence the host's immune system and inflammatory response has on cancer progression. Targeted therapy, immune therapy and gene therapy have thus emerged as additional treatment modalities for the management of SCCHN [8, 9].

1.1.2 Cutaneous squamous cell carcinoma (CSCC)

Cutaneous squamous cell carcinoma (CSCC) represents approximately 20% of non-melanotic skin cancers [10]. Exposure to ultraviolet (UV) light is the most common cause of this cancer and therefore the majority of lesions arise in the sun-exposed areas of the head and neck [11].

Carcinoma in situ (CIS) is defined histologically by cellular atypia involving the full thickness of the epidermis without invasion into the dermis. The most common forms are Bowen's disease and erythroplasia of Queyrat. Left untreated, CIS may progress to invasive disease [12].

Primary CSCC typically presents as a raised, firm papule or plaque on the background of photodamaged skin (Figure 1.2). Surface changes may include ulceration, scaling and crusting. Several variants of CSCC are recognised but in some cases these may be difficult to distinguish with routine histology alone. Immunohistochemical staining with antibodies to cytokeratins and epithelial membrane antigens is therefore used to determine the epithelial origin of the tumour in such circumstances.

a

b

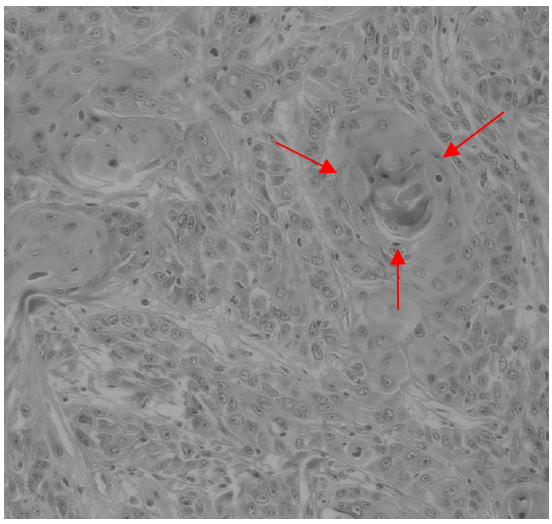

Figure 1.2 Cutaneous squamous cell carcinoma (CSSC)

(**a**) Photograph of a CSCC involving the vermillion border of the lower lip. (**b**) Photomicrograph of an H&E section of a CSSC. Red arrows indicate an epithelial nest (keratin or squamous pearl). Image magnification 20x.

Patients diagnosed with CSCC and regional lymphadenopathy should undergo nodal biopsy to allow adequate staging. Subsequent complete lymphadenectomy of the draining nodal basin in these individuals along with adjuvant radiotherapy improves 5 year survival rates to as high as 73% [13]. In addition, sentinel lymph node biopsy (SLNB) has been shown to identify micrometastasis in 21% of patients with high-grade SCC and clinically negative nodes [14]. These observations taken together imply that early detection of nodal metastases is likely to be beneficial to patient outcome. Unfortunately prognostic models that accurately predict which tumours give rise to nodal micrometastasis and therefore which patients should undergo nodal staging do not exist. Identifying cancer cell molecular markers and genetic signatures which correlate with metastatic risk would therefore be of significant clinical benefit.

The majority of people with primary CSCC have an excellent prognosis [15]. For those with metastatic disease, however, the long-term prognosis is poor with 10 year survival rates being less than 20% and 10% for regional and distant metastases respectively [11]. Most metastatic nodes from head and neck CSSC occur in the parotid gland and the upper cervical nodes within the first 2 years; the reported rate ranging from 0.3% to 20.7% [10].

As with SCCHN, treatment of metastatic CSCC may include adjuvant radiotherapy, chemotherapy and immune response modifiers [16, 17]. Although the efficacy of 'biologics' in this setting has not been fully established they offer exciting new opportunities in cancer therapy and are likely to become increasingly important as our understanding of cancer cell biology advances in forthcoming years [18].

1.1.3 Vulval squamous cell carcinoma

Vulval SCC (Figure 1.3) is relatively uncommon with approximately 1,000 cases diagnosed annually in the UK [19]. Aetiologically vulval SCC can be classified into two forms. The first is associated with human papillomavirus (HPV) infection and smoking. The second is related to chronic vulval dermatoses, in particular lichen sclerosus. Both forms are preceded by vulval intraepithelial neoplasia (VIN) [20, 21].

a

b

Figure 1.3 Vulval squamous cell carcinoma

Photographs of (**a**) early and (**b**) late vulval SCC. Images courtesy of Dr Sallie Neill, Consultant Dermatologist, St John's Institute of Dermatology, St Thomas' Hospital, London.

Vulval SCC arises on the labia of the vulva in the majority of cases and has many different growth characteristics. Early lymphatic spread to inguinal lymphatics is common being directly related to both the size of the primary lesion and the depth of stromal invasion.

Primary lesions less than 2cm in diameter, with superficial invasion less than 1mm from the epithelial stromal junction, can be treated with wide local surgical excision. Lesions with stromal invasion greater than 1mm dictate ipsilateral inguinal lymphadenectomy as part of the primary resection [22]. If the nodes are negative on frozen section a modified vulvectomy is performed; if positive the contralateral lymphatic basin is removed [23]. Total or complete vulvectomy is reserved for bilateral disease but is now largely a redundant procedure.

1.1.4 Verrucous carcinoma

Verrucous carcinoma is a variant of well differentiated SCC that was first described by Lauren Ackerman in 1947 [24]. It occurs most frequently on the mucous membranes of the oral cavity, larynx and vulva but may also involve any cutaneous site [25, 26]. Chewing tobacco is the primary aetiological factor for oro-pharyngeal lesions and cigarette smoking correlates with laryngeal disease. HPV 16 related DNA sequences have been regularly extracted from lesions prompting the suggestion of viral initiated oncogenesis [27].

The diagnosis of verrucous carcinoma is made from its characteristic exophytic, papillomatous appearance (Figure 1.4), its indolent clinical behaviour and the histological findings of an expansive but locally invasive tumour [28]. Microscopically broad based, blunted rete ridges composed of well differentiated squamous cells are evident. The associated basement membrane appears intact and invariably the underlying stroma is mildly inflamed with a lymphocyte predominant infiltrate (Figure 1.5).

Although locally aggressive, verrucous carcinoma is less likely to metastasise. Consequently, surgery is the treatment of choice [29]. Primary radiotherapy has previously been advocated but concern that this may promote a transition to a more aggressive variant has limited its use [30].

a

b

Figure 1.4 Verrucous carcinoma: (a) oral and (b) vulval

Photographs of (**a**) oral and (**b**) vulval verrucous carcinoma showing the exophytic and papillomatous nature of this variant of SCC. Images courtesy of (**a**) Dr Mehri Eghtessad, Honorary Lecturer in Oral Surgery, UCL Eastman Dental Institute, London and (**b**) Dr Sallie Neill, Consultant Dermatologist, St John's Institute of Dermatology, St Thomas' Hospital, London.

a

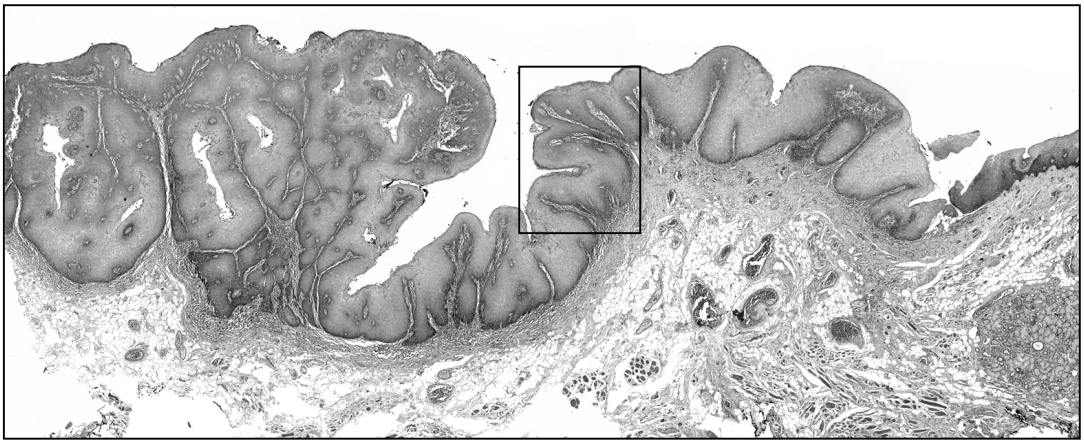

b

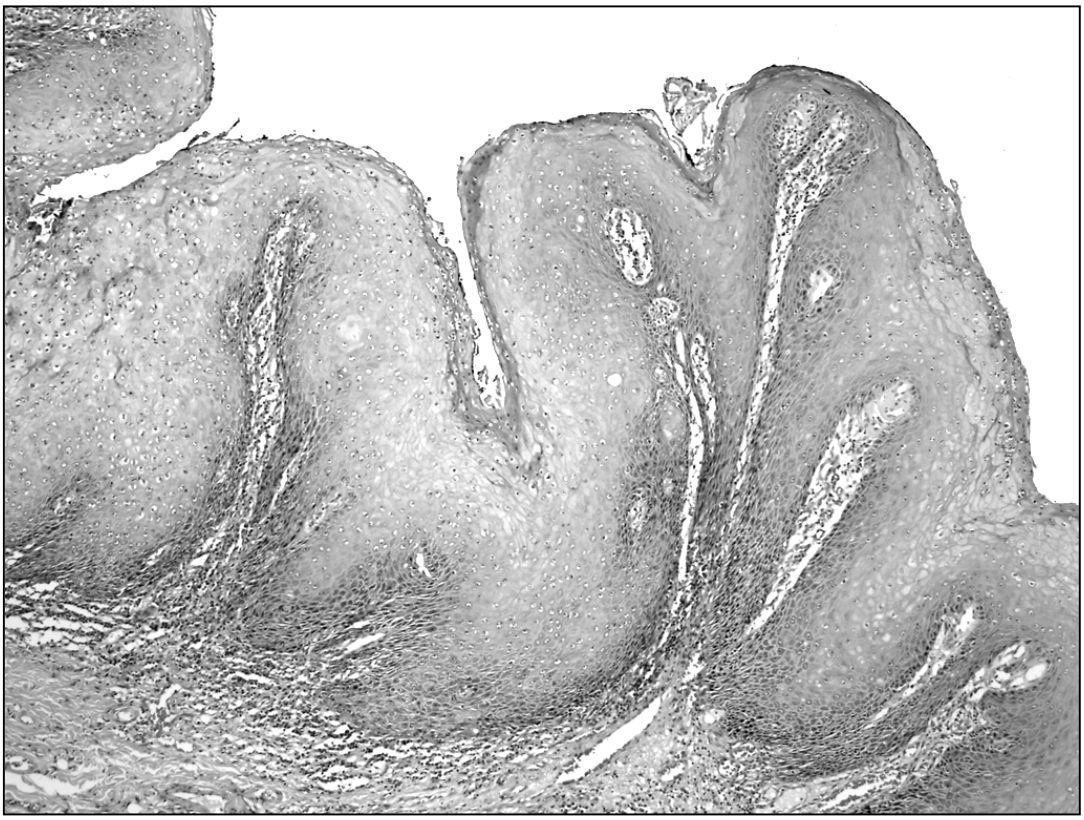

Figure 1.5 Histopathology of verrucous carcinoma

Photomicrographs of verrucous carcinoma of the tongue. (**a**) Low power view. Magnification 10x. (**b**) High power view of inset showing broad based, blunted rete ridges composed of well differentiated squamous cells. The associated basement membrane appears intact. Image magnification 40x. Images courtesy of Dr Selvam Thavaraj, Honorary Consultant in Oral Pathology, KCL Dental Institute, London.

Understanding the signalling mechanisms involved in the regulation of cancer cell morphology, motility and invasion has provided new insights into the clinical behaviour of tumours and their pattern of spread. Many questions still remain unanswered however. In the case of verrucous carcinoma, for example, an obvious one is why is it characterised by a collective pushing invasive front with a reduced propensity for metastasis compared to typical SCC? In time, as our knowledge of the process of cancer cell invasion improves, such issues will hopefully be resolved.

1.2 The tumour micro-environment

1.2.1 Tumourigenesis

'Carcinoma' is the term used to describe a malignancy derived from epithelial tissue which until relatively recently was often regarded as being merely a mass of individual cancer cells. Similarly, carcinoma cells had been considered to be transformed immortalized keratinocytes with their greater proliferative, invasive and survival capacities being attributed solely to genetic or epigenetic changes [31].

Tumours are now recognised as being composed of not only carcinoma cells, but of several other cell types capable of interacting with each other within a highly ordered extra-cellular matrix (ECM). This surrounding stroma has been the focus of considerable research in recent years and has given rise to the concept of the tumour micro-environment. Tumourigenesis is dependent upon contextual signals between cancer cells and their associated stroma [32]. Both the epithelial and mesenchymal components evolve together and it is now appropriate to consider this micro-environment of cancer as a single functional unit [33, 34].

Tissue homeostasis is fundamental for the preservation of normal tissue morphology and the identification of multipotent mesenchymal stem cells (MSC) in adult connective tissue has provided new insights into this process [35]. MSC have the potential to differentiate into endothelial cells, fibroblasts, myofibroblasts, smooth muscle cells and inflammatory immune cells; all of which are now considered to be key players in tumourigenesis [36].

Epithelial cells can become dysfunctional if tissue homeostasis becomes perturbed but the crucial question of which comes first remains unanswered [37, 38]. There is no intrinsic reason to assume that tumour development begins with epithelial aberrations. Epithelial differentiation during embryogenesis, for example, is determined by molecular cues from the underlying mesenchyme and recent evidence indicates that genetic changes occur in the stroma during the early stages of carcinogenesis [39, 40]. This has led to the suggestion that a genetically unstable stroma may facilitate tumourigenesis in the overlying epithelium [41].

CIS is characterised by connective tissue which bears a close resemblance to that of granulation tissue typical of wound healing. This is often referred to as 'reactive stroma' and its relationship with dysplastic epithelium continues to be an area of considerable interest. The sequence of events resulting in the progression of CIS to invasive carcinoma is not fully understood [42]. Reactive stroma, compared to 'normal' tissue, contains an enhanced capillary network and increased levels of vascular endothelial growth factor (VEGF) [43, 44]. VEGF induces micro-vascular changes which favour the recruitment of fibroblasts, endothelial cells and inflammatory cells [45]. These cells secrete ECM rich in type I collagen, fibrin and fibronectin and there by create the perfect environment for tumour angiogenesis [43].

Carcinoma is defined by the invasion of cancer cells beyond the 'constraints' of the epithelial basement membrane into the underlying connective tissue. Expansion of the stroma occurs in order to actively support tumour growth and is of vital importance to the further progression of the carcinoma [46]. Increased deposition of ECM may result in a desmoplastic stroma composed of a dense network of fibrillar collagens, fibronectin, proteoglycans and tenascin C [47]. The latter's expression correlates with a poor prognosis for both breast and bladder cancer and has led to the suggestion that tenascin C may be a surrogate marker of cancer cell invasiveness [48, 49].

The regulatory pathways that orchestrate tumour development, growth and spread are intricate. It is now clear, however, that stromal cells are not just innocent bystanders but assume a very central and active role in tumourigenesis [50].

1.2.2 Carcinoma associated fibroblasts (CAF)

Normal fibroblasts constitutively express vimentin and fibroblast-specific protein 1 (FSP1) [51]. When 'activated' they express α-smooth muscle actin (αSMA) and are referred to as myofibroblasts [52]. Fibroblast to myofibroblast differentiation is a central event in the physiological response to tissue injury and the actions of myofibroblasts during wound healing have been extensively studied [53, 54].

To synthesise abundant ECM proteins, a myofibroblast typically has a large oval euchromatic nucleus with several nucleoli, extensive endoplasmic recticulum and a prominent Golgi apparatus [42]. In addition to ECM proteins, myofibroblasts secrete matrix metalloproteinases (MMPs), in particular MMP2, MMP3 and MMP9, which facilitate ECM turnover [55]. Increased synthesis of growth factors such as epidermal-growth factor (EGF) and insulin-like growth factor (IGF) induce adjacent epithelial cells to proliferate [56]. Cytokines, such as interleukin-1 (IL-1), which modulate the immune response are also released by myofibroblasts [57].

Under normal circumstances the myofibroblast to fibroblast ratio is reflective of the degree of connective tissue remodelling [53, 54]. In disorders characterised by excessive fibrosis, fibroblasts remain in an activated state being sustained by a self-perpetuating autocrine loop [58]. Myofibroblasts derived from such tissues are capable of promoting tumourigenesis when co-cultured with carcinoma cells compared to control fibroblasts from normal tissues [59]. This observation supports emerging data that tumour derived myofibroblasts are genetically and functionally similar to those found in these chronic fibrosing conditions and granulation tissue [60].

Carcinoma associated fibroblasts (CAF) have been extracted from a variety of human tumours including breast, colon, oesophageal, and pancreatic carcinoma [36, 42]. Different CAF isolates have different gene expression profiles encoding for a variety of cytokines, enzymes, growth factors and ECM-related proteins [61, 62]. The origin of these differences and their functional significance remain indeterminate with studies investigating genetic and epigenetic alterations in CAF being inconclusive [50].

The factors governing the transformation of normal fibroblasts to CAF are not fully understood. Epithelial to mesenchymal transition (EMT), in which epithelial cells acquire mesenchymal properties, probably accounts for a small proportion of the CAF

present in tumours [63, 64]. For the origin of tumour myofibroblasts (ie: activated CAF) several hypotheses have been proposed (Figure 1.6) [65]. The obvious is the differentiation of CAF to myofibroblast without the acquisition of any genetic alterations, mirroring the situation observed in wound healing [66]. The next most plausible explanation is that MSC, recruited into the developing tumour, serve as a source for a number of stromal cells including the myofibroblast [67]. Other explanations include clonal expansion of pre-existing tissue myofibroblasts and, as mentioned above, possible genetic or epigenetic changes in CAF such as p53 loss [50, 68].

1.2.3 Carcinoma associated fibroblasts and tumour spread

Intra-vital imaging of experimental tumours has revealed that only 1-5% of tumour cells are motile [69]. These moving cells are not uniformly distributed but are observed in localized areas of the tumour [70].

Several studies have demonstrated the invasive promoting role of activated CAF and tumour associated macrophages (TAM) [36, 70, 71]. Both cell types are a source of MMPs which facilitate cancer cell motility by degrading the ECM [72]. CAF also secrete high levels of the cytokine stromal cell derived factor 1 (SDF1) which increases carcinoma cell proliferation *in vivo*, via its action on CXCR4, a CXC chemokine receptor [73, 74]. Furthermore, CXCR4 expression is up-regulated on the surface of cancer cells by high levels of transforming growth factor-β (TGFβ) secreted by CAF, there by completing a paracrine loop [74, 75, 76]. Stromal fibroblasts have also been shown to lead collective chains of invading carcinoma cells (which retain their epithelial markers) through a collagen-Matrigel® ECM by a combination of force-mediated and protease-mediated matrix remodelling [77].

Tumour cell motility requires both intrinsic changes that confer motile competence and extrinsic factors that promote invasion. The detection of motility signatures by global analyses of primary tumours before the clinical appearance of secondary lesions suggests that metastatic potential is determined early in carcinogenesis [78]. This contradicts the previously held view that invasive cell behaviour is a late acquisition in tumour progression. It is, however, not a complete explanation. Desmoplastic tumours (which have a high proportion of myofibroblasts), for example, are associated with increased invasion and secondary spread and consequently have an unfavourable

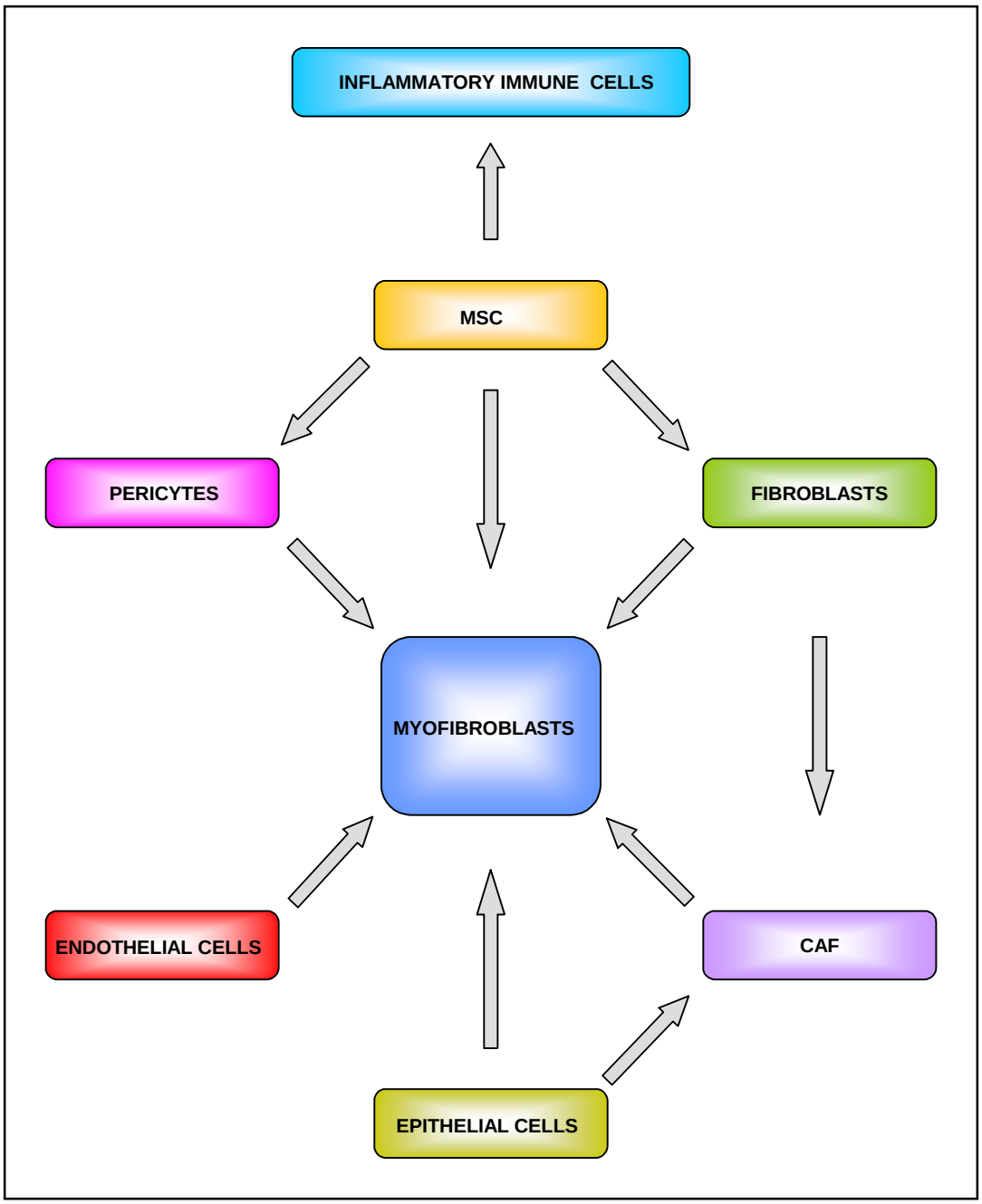

Figure 1.6 The multiple origins of tumour myofibroblasts / activated carcinoma associated fibroblasts (CAF)

Schematic to illustrate the various hypotheses proposed for the origin of tumour myofibroblasts (activated CAF). Multipotent mesenchymal stem cells (MSC) have the potential to differentiate into endothelial cells, fibroblasts, myofibroblasts, pericytes and inflammatory immune cells; all of which are now considered to be key players in tumourigenesis.

clinical prognosis [79, 80, 81]. It is therefore likely that CAF paracrine signalling also facilitates metastasis [73, 74, 82].

Further research is required in order to clarify the molecular mechanisms underlying the potential role of CAF in promoting invasion and metastasis. Subsequently, new opportunities for therapeutic approaches which target the tumour stroma are likely to arise.

1.3 Cancer cell motility

1.3.1 The mechanics of cancer cell motility

Cell migration (Figure 1.7) is a dynamic, cyclical process where by a protrusion is formed at the front of the cell (extension) which then attaches to the substrate on which the cell is moving (adhesion). This is followed by a contraction which moves the cell body in the direction of its leading edge (translocation). Finally, surface attachments at the rear of the cell are lost (de-adhesion), the tail retracts and the cell continues forwards. Motility is driven by the polymerization of actin monomers into polarized filaments (F-actin). F-actin associates with myosin II filaments to form a protein complex which when phosphorylated powers actin-myosin contraction [83]. The contractile force generated leads to cytoskeletal reorganization, ECM remodelling and cell movement. Optimal cell migration requires the correct synchronization of protrusive, adhesive and contractile events [84].

1.3.2 Actin polymerization

Actin polymerization is central to the formation of cell protrusions and cancer cell motility. Monomeric globular actin molecules (G-actin) are assembled asymmetrically; being added at the barbed end of the filament and subtracted from the pointed end [85]. Simultaneously, actin-binding proteins regulate a number of processes including: capping, nucleating, cross-linking, bundling, severing and depolymerising of filaments.

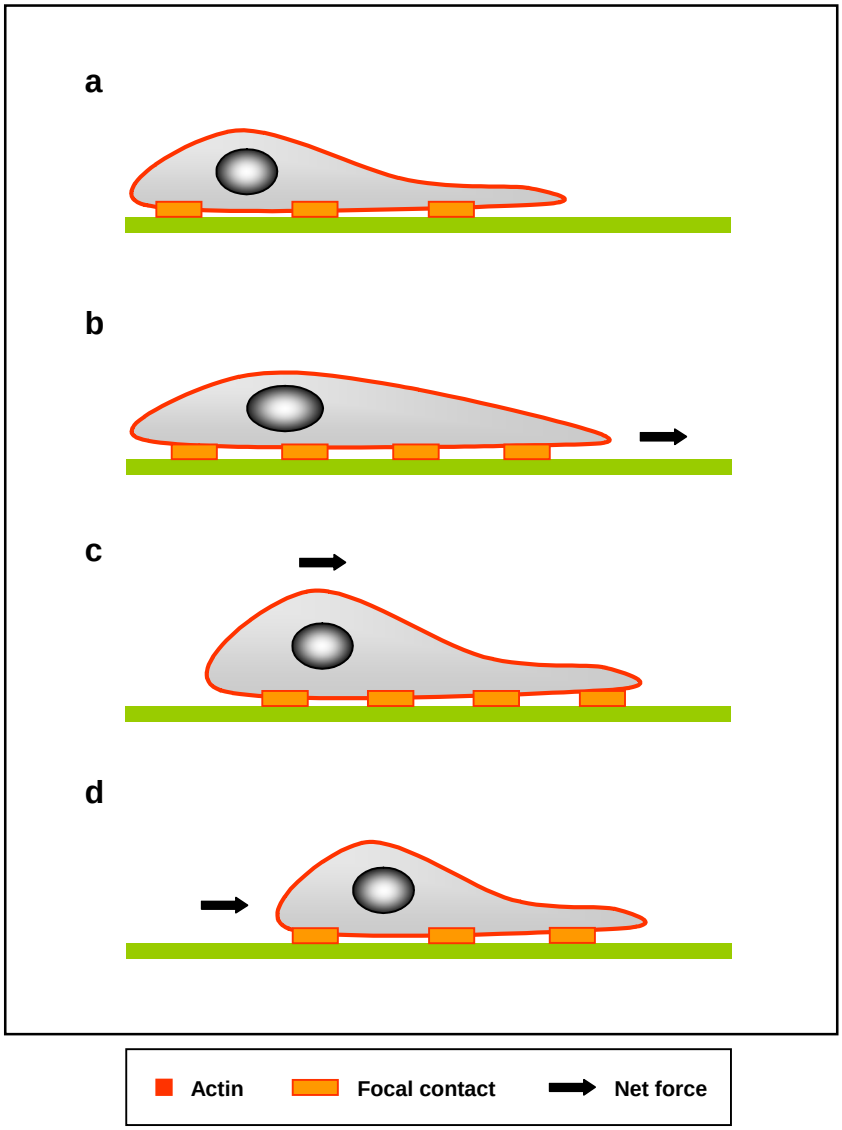

Figure 1.7 The mechanics of cell motility

(**a**) Extension. A protrusion is formed at the front of the cell. (**b**) Adhesion. New focal contacts are established between the cell and the substratum. (**c**) Translocation. Actin-myosin contraction moves the cell body in the direction of the leading edge. (**d**) De-adhesion. Surface attachments at the rear of the cell are lost, the tail retracts and the cell moves forwards.

Figure adapted from http://www.cytochemistry.net/Cell-Biology.

Several protein groups and signalling pathways are recognised to be involved in cancer cell motility and invasion; notably receptor and non-receptor tyrosine kinases, integrin-associated proteins and the Rho family of small GTPases. The activation of the Rho family GTPases Cdc42 and Rac results in protrusive events by initiating the nucleation of new actin filaments. Cdc42 bound to GTP interacts with Wiskott-Aldrich syndrome protein (WASP), attenuating WASP auto-inhibition and promoting WASP interaction with F-actin [86]. WASP also binds with the actin related 2/3 complex (Arp2/3) causing branching of actin filaments at a 70º angle [87]. WASP-family verprolin-homologous protein 1 (WAVE) is another nucleation promoting protein, which when activated by GTP-bound Rac, also recruits Arp2/3 to the cell membrane [88]. The resulting actin polymerization by Arp2/3 initiated at the inner leaflet of the plasma membrane provides the internal force to push the membrane forwards and begin cell movement [85, 89].

1.3.3 Cell protrusions

Several types of cell protrusion have been described, including filopodia, lamellipodia, podosomes, invadopodia and membrane blebs. The generation and cycling of these structures is dependent either directly or indirectly upon the co-ordinate activity of actin-binding and modifying proteins [90].

Filopodia are long, thin cell projections driven by Cdc42 actin bundling at the leading edge [91]. Straight actin filaments are produced by formins binding to their barbed ends promoting lengthening without branching [92]. Ena/VASP proteins also assist in this process [91].

Lamellipodia are broad membrane protrusions observed at the front of cells migrating across two-dimensional (2D) substrates. Actin polymerization occurs downstream of Rac activation [93]. They require the nucleation activity of Arp2/3 which sustains the propagation of a broad, branching actin network.

The distinction between podosomes and invadopodia is obscure; the former having been observed in monocyte-derived cells and the latter noted in carcinoma cells [94, 95, 96]. Podosomes are actin-rich cell-substrate adhesion sites which are activated by the tyrosine kinase Src [97]. They correlate with a cancer cell's ability to cross a basement membrane [98].

Membrane blebbing is thought to be generated by contractile forces which squeeze the cell membrane and cause parts of it to detach from the underlying actin cytoskeleton [99]. It has been observed in carcinoma cells moving in an amoeboid manner *in vivo* but overall, this mechanism of cell protrusion is poorly understood [100, 101, 102].

1.3.4 Focal adhesion dynamics

Tumour cell migration requires the cell to establish stable contacts with the ECM. These focal contacts enable contractile forces to be generated which ultimately result in translocation of the cell body [103]. Focal contacts are composed of integrins coupled to the actin cytoskeleton via linker proteins such as paxillin, talin, and vinculin. They are dynamic structures, with their assembly and composition being dependent upon the rigidity of the substrate [104]. The majority of work studying focal adhesion dynamics has been performed using cell cultures on either glass or plastic [104]. Extrapolating these *in vitro* findings to the tumour micro-environment may therefore be difficult [105].

Integrins exist as transmembrane heterodimers, consisting of α and β subunits. Different integrins regulate focal contact assembly depending on the cell type and the nature of the substrate [106]. Integrin α5β6, for example, functions as a receptor for fibronectin, vitronectin, tenascin and TGFβ. Its distribution is restricted to epithelial cells and it is overexpressed in a variety of carcinomas, including SCCHN [107]. Signalling downstream of the integrins also confers specificity [108]. α2β1 integrin binding to collagen is known to activate Rho A, where as α3β1 integrin binding to laminin inhibits Rho A but stimulates p21-activated kinase 1 (PAK1) [109]. The engagement of different integrins with the ECM and the cycling of focal contacts are key events in cancer cell motility and carcinoma invasion [110].

Focal adhesion kinase (FAK) is an intracellular non-receptor tyrosine kinase that is recruited to focal contacts during cell migration [111]. Integrin-mediated cell adhesion to the ECM results in the phosphorylation and activation of FAK at tyrosine 397 [112]. This creates a docking site for the SH2 phosphotyrosine binding domain of the Src family kinases [113]. The activated Src-FAK complex induces the downstream phosphorylation of paxillin and p130 Crk Associated Substrate (CAS) which in turn stimulates cell migration [114].

Non-integrin cell surface receptors, such as CD44 and CD26 also interact with ECM components and affect cell motility. Their precise role in force generation, however, is poorly defined [115].

1.3.5 Degradation of the ECM

The degradation of ECM is an integral aspect of tumour cell invasion and metastasis. Surface proteases are recruited in a integrin-dependent manner at the leading edge of motile cells, resulting in localized proteolysis of matrix components such as collagen, fibronectin, and laminin [116]. ECM degradation occurs as the advancing cell body gains volume, creating space required for further cell expansion and directional movement. Consequently, cell migration tracks are generated within the tumour stroma [117].

MMPs are a family of zinc-dependent endopeptidases which are secreted as inactive proenzymes and cleaved to their active forms. They are capable of degrading basement membrane and ECM components, including fibrillar collagen [118]. Over 20 MMPs have been characterised, each being classified according to their substrate specificity and numbered according to the order of discovery [107]. Increased expression and activity of MMPs has been demonstrated in a variety of carcinomas. In SCCHN, MMP2 and MMP9 has been correlated with invasion, metastasis and poor patient prognosis [119, 120].

Matrix proteases generate chemotactic ECM fragments and promotility neoepitopes that engage specific integrins [121]. Many of these factors, besides enhancing cell migration, influence other cell functions such as cell survival and proliferation.

1.3.6 Cortical actin, stress fibres and actin-myosin contraction

Cross-linked actin networks below the inner leaflet of the cell membrane are termed cortical actin (Figure 1.8) [108]. Stress fibres, in contrast, consist of elongated cytoplasmic bundles of 10-30 actin filaments held together by crosslinking proteins such as α-actinin and fascin [104]. They are prominent structures in cells cultured on glass and plastic but are less evident in cells plated on 3D matrices [101].

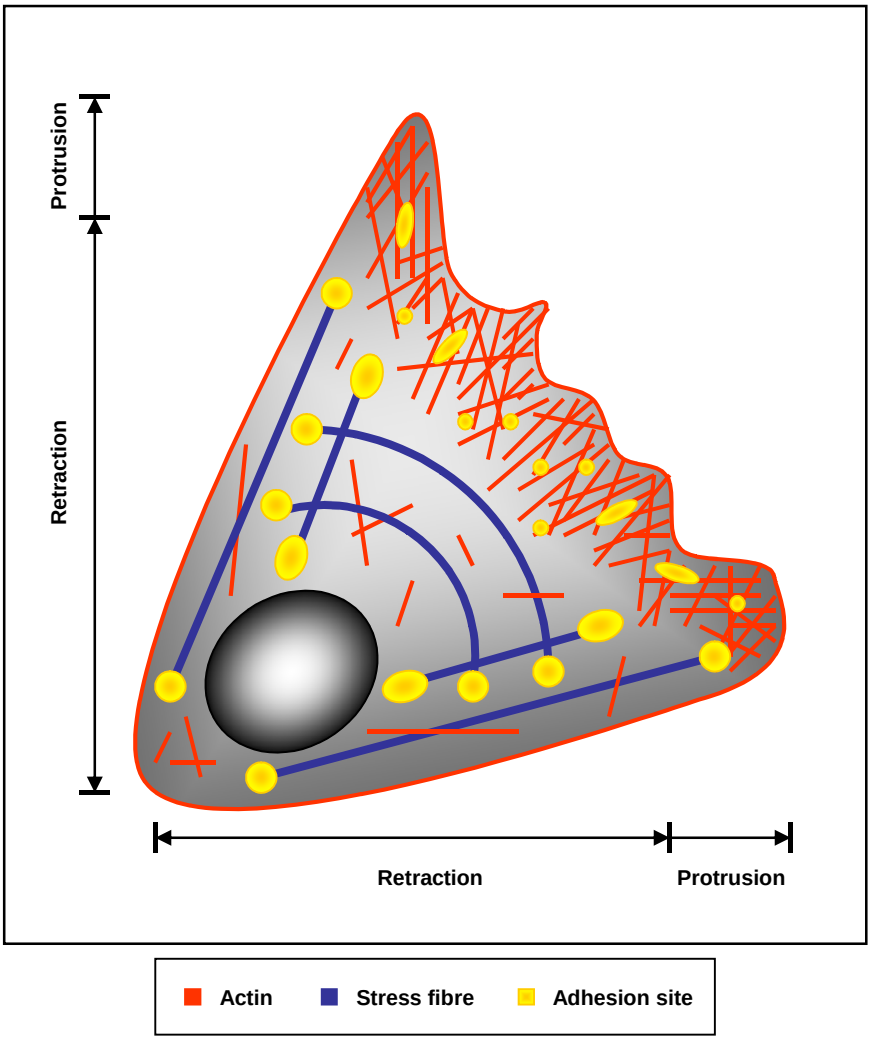

Figure 1.8 Cortical actin, stress fibres and cell motility

Cortical actin is comprised of cross-linked actin networks below the inner leaflet of the cell membrane. Stress fibres, in contrast, consist of elongated cytoplasmic bundles of 10-30 actin filaments. Cell motility is dependent on the co-ordinated assembly and disassembly of F-actin as well as the generation of contractile forces. The dissociation of cortical actin and stress fibre dynamics confers plasticity to cell migration.

Figure adapted from http://www.cellix.imba.oeaw.ac.at.

Myosin II binding to actin is facilitated by the action of tropomyosin and when phosphorylated, induces actin contraction via an increase in ATPase activity. Myosin light chain (MLC) can be phosphorylated at two sites, T18 and S19, and the regulation of this process is critical to the control of cell contractility [122]. Cell motility is dependent on the co-ordinated assembly and disassembly of F-actin as well as the generation of contractile forces. Inhibition of either actin polymerization with cytochalasin D or myosin II ATPase activity with blebbistatin can thus block cell migration [83].

Stress fibre assembly and contraction are governed by the small G-protein Rho through its downstream effectors ROCK1 and ROCK2 (generically termed ROCK). ROCK1 and ROCK2 are serine threonine kinases that increase the availability of phosphorylated MLC via several methods. They (a) phosphorylate and inhibit MLC phosphatase, (b) potentiate the phosphorylation of MLC through the action of zipper-interacting protein kinase (ZIPK) and (c) directly phosphorylate MLC at S19 [123, 124].

Many other downstream effectors of Rho have now been identified. mDia is one such protein and is the mammalian homologue of *Drosophilia diaphanous*. It is a member of the formin-homology (FH) family and, by extending the polymerization of actin filaments, is associated with the formation of thick stress fibres orientated parallel to each other [125, 126].

In contrast to stress fibres, the turnover of cortical actin is regulated by the action of myosin light chain kinase (MLCK) [108]. This enables the cell to disassociate cortical actin and stress fibre dynamics from one another and in doing so confers plasticity to cell migration [100].

1.3.7 The plasticity of cancer cell motility

Several types of tumour cell motility have been identified, the tumour micro-environment being a key determinant of the mode of cell motility adopted [100]. Such diversity of movement is a reflection of the molecular repertoire used by cancer cells to migrate.

Mesenchymal cell motility is typical of cells derived from connective tissue tumours such as fibrosarcomas, but is also observed in carcinomas which have undergone EMT.

EMT is estimated to occur in 10-40% of epithelial derived tumours with cells exhibiting a fibroblast-like spindle shaped morphology [63]. These phenotypic changes are accompanied by an alteration in protein expression profiles, which include the loss of epithelial cytokeratins and the *de novo* expression of vimentin [127, 128]. Mesenchymal motility is dependent on integrin-mediated adhesion dynamics, pericellular proteolysis and actin-myosin contraction [108]. Cells move at relatively slow speeds (0.1-1μm/min) but overall this type of motility represents an efficient mechanism for cancer cell dissemination and metastasis [129].

High resolution intra-vital imaging has demonstrated that a small proportion of carcinoma cells move at very high speeds (4-20μm/min) with an amoeboid morphology. This pattern of 'amoeboid' movement is driven by the rapid remodelling of cortical actin by Rho and ROCK signalling [100, 108]. It does not require the formation of focal contacts or ECM degradation and as a result these cells are highly deformable [130]. This type of cell motility is also used by leucocytes [131].

Collective cell motility, in contrast to both mesenchymal and amoeboid motility, involves the movement of clusters or sheets of cells with the maintenance of adherens junctions [132]. Mechanistically, this is equivalent to a collective form of mesenchymal motility [108, 116]. Signalling through Cdc42 and MRCK is thought to control the *en masse* movement of cells by regulating the contraction of actin-myosin bundles that are continuous around the perimeter of the group rather than within individual cells [77].

In vivo studies have shown that the tumour micro-environment is very heterogeneous with regions of motile and non-motile cells [133, 134]. The reasons why one cell, or group of cells, should be motile and its neighbours not are poorly understood. Cancer cells have also been observed switching their mode of motility; indicating that these categories of movement are not completely distinct [135]. This plasticity in cancer cell motility represents a significant obstacle to the development of successful anti-invasive drug strategies [33, 108, 115]. Small cell lung carcinoma cells, for example, acquire increased resistance to cytostatic drugs and irradiation by switching from amoeboid single cell motility to collective cell invasion [136, 137].

1.3.8 The E3 ubiquitin ligase Smurf1 regulates tumour cell plasticity

As previously mentioned the Rho GTPases (Rho A, Rac and Cdc42) are key regulators of cell migration. Rho A has been shown to be targeted for degradation at the leading edge of motile cells by a HECT domain E3 ubiquitin ligase, Smurf1 [138, 139, 140]. Consequently Rho A activity, which controls actin-myosin contractility, is high at the back of the cell where it is involved in tail retraction. At the front of the cell, Rho A levels are reduced, and Rac along with Cdc42 drive actin polymerization. This localized inhibition of contractile forces permits the formation of lamellipodia and the establishment of cell polarity necessary for movement [141].

Three dimensional invasion assays and intra-vital imaging indicate that silencing Smurf1 increases tumour cell motility by inducing a mesenchymal to amoeboid-like transition in cell phenotype [142]. This observation, which suggests that ubiquitin type modifications are regulators of the actin cytoskeleton and cell movement, formed the starting point of my research. A review of the published literature to date reveals that current knowledge in this area is limited.

1.4 The ubiquitin-proteasome system

1.4.1 Ubiquitination enzymes

Ubiquitin is a 76 amino acid (8kDa) polypeptide that can be attached to other proteins through a process known as ubiquitination [143, 144]. This requires the sequential action of three enzymes: ubiquitin-activating enzyme (E1), ubiquitin-conjugating enzyme (E2) and ubiquitin ligase (E3) (Figure 1.9).

Initially, ubiquitin is activated by E1 in an ATP-dependent reaction. In the second step, the activated ubiquitin is transferred to a ubiquitin-conjugating enzyme forming an E2-ubiquitin thioester. Finally, an E3 ubiquitin ligase mediates the attachment of ubiquitin to the ε-amino group of a lysine residue in the target protein via an isopeptide bond. Ubiquitin contains seven lysine residues, each of which can be covalently bound to another ubiquitin, resulting in the formation of a polyubiquitin chain. The types of ubiquitin modifications are diverse, as are their functions [145, 146]. Ubiquitin chains linked through lysine-48 (K48) target their substrates for proteasomal degradation where

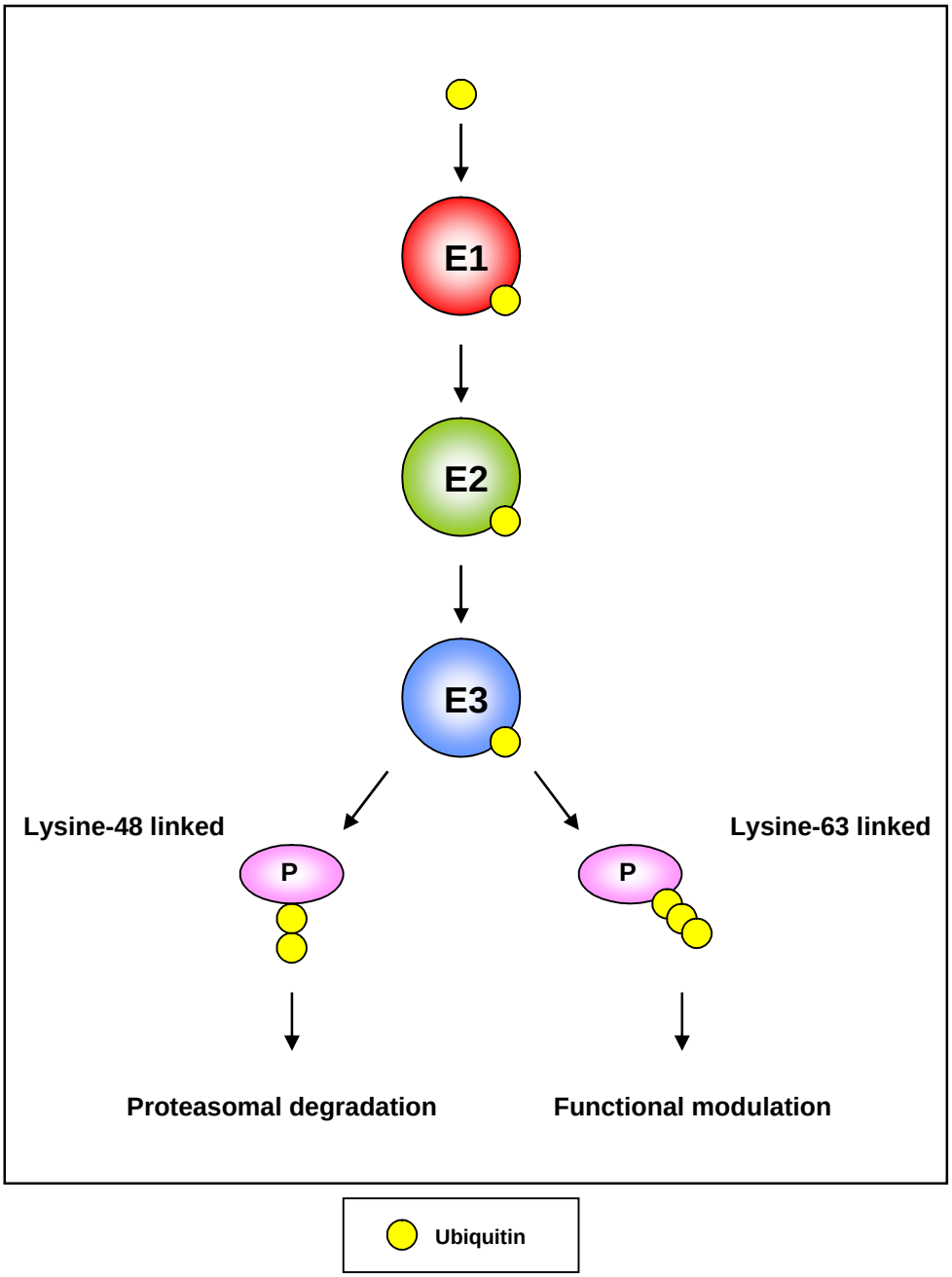

Figure 1.9 The ubiquitin-proteasome system

Ubiquitin is a 8kDa polypeptide that can be attached to other proteins (P) by a process known as ubiquitination. This typically requires the action of three enzymes: ubiquitin-activating enzyme (E1), ubiquitin-conjugating enzyme (E2) and ubiquitin ligase (E3). Ubiquitin modifications linked through lysine-48 target their substrates for proteasomal degradation. Those attached through lysine-63 result in functional modulation of their tagged proteins.

Figure adapted from Jesenberger V, Jentsch S. Deadly encounter: ubiquitin meets apoptosis. *Nat Rev Mol Cell Biol* 2002; **32**: 112-121.

as those attached through lysine-63 (K63) typically result in functional modulation of their tagged proteins [147].

E3 ligases are primarily responsible for substrate recognition and may be divided into two families [148, 149, 150]. The RING (really interesting new gene) type contains a series of histidine and cysteine residues and can be further classified according to the spatial relationship of their RING and substrate binding domains. The HECT (homologous to the E6-associated protein C terminus) E3 ligases contain a conserved cysteine residue within the HECT domain which allows ubiquitin to be transferred directly to its target protein.

1.4.2 Ubiquitin-binding domains

Biochemical and bioinformatic modelling has identified at least 20 different ubiquitin-binding domains (UBDs). These domains are diverse in both structure and function being composed of 50-150 amino acid residues [151]. UBDs bind polyubiquitin chains in addition to monoubiquitin with relatively low binding affinities [152]. When mutated, UBDs are unable to correctly handle ubiquitin and consequently protein function *in vivo* is impaired. This emphasises the physiological significance of these low-affinity interactions and illustrates the important role UBDs have in signal transduction [146].

1.4.3 The proteasome

The proteasome is a large, hollow, cylindrical protein complex which uses ATP to degrade ubiquitin-tagged proteins. Its components are referred to by their Svedberg sedimentation coefficient (denoted S) [153]. The 26S proteasome contains a 20S core particle and two 19S regulatory caps [151]. The core particle is itself composed of two α and two β heptameric rings. The α subunits are structural in nature where as the β subunits, which form the inner structure of the core, are predominantly catalytic [154].

A target protein must be labelled with at least four ubiquitin molecules for efficient binding to the proteasome. Once recognised by the 19S regulatory cap, the substrate protein is partially unfolded and de-ubiquitinated prior to being translocated into the central channel of the 20S core particle [155]. Within the core particle, peptide bonds are

hydrolysed and the protein is digested into short fragments of 3-23 amino acid residues in length [156].

1.4.4 De-ubiquitinating enzymes

Ubiquitination is a reversible process and the human genome encodes for greater than 100 de-ubiquitinating enzymes (DUBs) [157]. DUBs can be classified into cysteine proteases and metalloproteases which contain the JAB1/MPN/Mov34 (JAMM) motif. The cysteine proteases can be further divided on the basis of their protease domains into: (a) ubiquitin-specific proteases (USP), (b) ubiquitin C-terminal hydrolases (UCH), (c) ovarian tumour-like proteases (OUT) and (d) Machado-Joseph disease proteases (MJD) [151].

Genetic and biochemical evidence suggests that de-ubiquitination is fundamental to mammalian physiology [158]. DUBs are involved in ubiquitin recycling by the processing of ubiquitin precursors, the editing of protein ubiquitination, and the disassembly of inhibitory ubiquitin chains. Depending on the cellular circumstances DUBs may act as both positive and negative regulators of ubiquitin-linked pathways [159, 160].

1.4.5 Ubiquitin and cancer

Experimental and clinical data implicates the deregulation of ubiquitin-linked pathways in oncogenesis (Table 1.1) [146]. This is not surprising given the integral role ubiquitination has in cell biology. Knowledge of the temporal and spatial dynamics of ubiquitin-dependent processes is essential for the understanding of the physiological and pathological consequences of ubiquitin signalling in cancer. This, however, is complicated by the finding that E3 ligases and DUBs often interact with each other, and that both E3 and DUB activity can reside in the same protein [161]. Furthermore, cross-talk between the ubiquitin-proteasome system and several cellular pathways, such as p53 and NF-κB signalling, is likely to occur simultaneously [162, 163]. Key molecules from multiple signalling pathways are also subject to a wide array of ubiquitin editing, including monoubiquitination, polyubiquitination, neddylation and sumoylation [133]. Current research is focusing on successfully mapping these complex interactions.

Pathway	Deregulated protein	Substrate	Modification	Tumour type
NF-κB signalling	CYLD	IKKγ	De-ubiquitination	Cylindromatosis
	IAP2	BCL10	Polyubiquitination	MALT lymphomas
RTK signalling	CBL	RTKs	Monoubiquitination	Gastric carcinoma
DNA repair	FANCL	FANCD2	Monoubiquitination	Fanconi anaemia related cancers
Cell cycle	Mdm2	p53	Polyubiquitination	Colorectal carcinoma

Table 1.1 Examples of deregulated ubiquitin-linked pathways implicated in oncogenesis

Table adapted from Hoeller D, Hecker CM, Dikic I. Ubiquitin and ubiquitin-like proteins in cancer pathogenesis. *Nature Rev Cancer* 2006; **6**: 776-88.

1.5 NF-κB signalling: an overview

1.5.1 NF-κB and related proteins

NF-κB was first identified in B lymphocytes in 1986 as a regulator of the genes encoding for the synthesis of immunoglobulin kappa (κ) light chains [164]. It was originally implicated in oncogenesis through the v-Rel protein of the avian Rev-T retrovirus. The latter was shown to induce cell proliferation and confer resistance to apoptosis in transformed chicken tumour cells [165]. Several NF-κB (Rel) transcription factors have now been characterised and the family, as a whole, has been linked to the expression of over 150 target genes [166].

The NF-κB family consists of five members: p65 (RelA), RelB, c-Rel, p50 and p52. All individuals can form homo- or heterodimers and each contain an N-terminal Rel-homology domain (RHD) [167]. This motif is approximately 300 amino acid residues in length and mediates dimerization, nuclear translocation, DNA binding and interaction with the inhibitor of NF-κB family (IκB proteins) [163].

IκB proteins are classified as: IκBα, IκBβ, IκBγ, IκBε, as well as the p105 and p100 precursors of p50 and p52 respectively. Atypical members function as NF-κB co-activators and include: IκBζ, IκBδ (IκBNS) and B cell lymphoma 3 (BCL-3). All individuals contain ankyrin repeat domains which bind to NF-κB dimers and retain the latter in the cytoplasm under basal conditions [168].

Activation of NF-κB occurs through canonical (classical) and non-canonical (alternative) pathways. Both involve initiation of all or part of the IκB kinase (IKK) complex. This is composed of: IKKα (IKK1), IKKβ (IKK2) and the regulatory subunit NEMO (NF-κB essential modulator; also known as IKKγ) [151, 163, 169, 170].

1.5.2 The canonical NF-κB pathway

The canonical or classical NF-κB pathway (Figure 1.10) is activated by a variety of stimuli, such as the inflammatory cytokines TNFα and interleukin-1 (IL-1) [169]. These agonists induce the IKK complex to phosphorylate IκBα at serines 32 and 36. Consequently, IκBα is ubiquitinated and rapidly degraded through the 26S proteasome.

Now free of their IκB binding partners, NF-κB p50-p65 dimers translocate to the nucleus and mediate gene transcription [151]. NF-κB p65 also requires phosphorylation, a process which appears to involve both IKKα and IKKβ [171].

One of the many genes up-regulated by NF-κB is IκBα itself [151]. IκBα also enters the nucleus where it subsequently displaces DNA-bound NF-κB; thus establishing a negative feedback loop. In the absence of further upstream signalling, NF-κB is rapidly sequestered by IκBα and returned back to the cytoplasm. The IκB proteins, (IκBα, IκBβ and IκBε) display temporal differences in their rate of degradation and re-synthesis indicating that they do not have entirely overlapping functions [172].

1.5.3 The non-canonical NF-κB pathway

The non-canonical or alternative NF-κB pathway (Figure 1.11) predominates in B lymphocytes in response to stimulation of a subset of TNF-receptor (TNFR) superfamily members. These include the receptors for B cell activating factor (BAFF), lymphotoxin-β (LTβ) and the CD40 ligand. Activation of this pathway requires IKKα but is independent of IKKβ and NEMO [173].

Following cell stimulation, activated NF-κB inducing kinase (NIK) leads to IKKα dependent processing of RelB-p100 to RelB-p52 [174]. Nuclear accumulation of RelB-p52 promotes the expression of several genes important in lymphoid organ development and adaptive B-cell mediated immunity [173, 174].

1.5.4 NF-κB signalling and tissue homeostasis

NF-κB is an important regulator of several cellular processes [169]. On one hand, it promotes the transcription of key genes involved in the initiation and maintenance of inflammatory and immune responses. On the other hand, it is cytoprotective and induces the production of a number of anti-apoptotic proteins, including Bcl-X_L[175], FLIP (FLICE-like inhibitory protein)[176] and members of the IAP (inhibitor of apoptosis) family [177]. This dual role has led to paradoxical observations and provocative theories regarding the function of NF-κB in normal and diseased tissue.

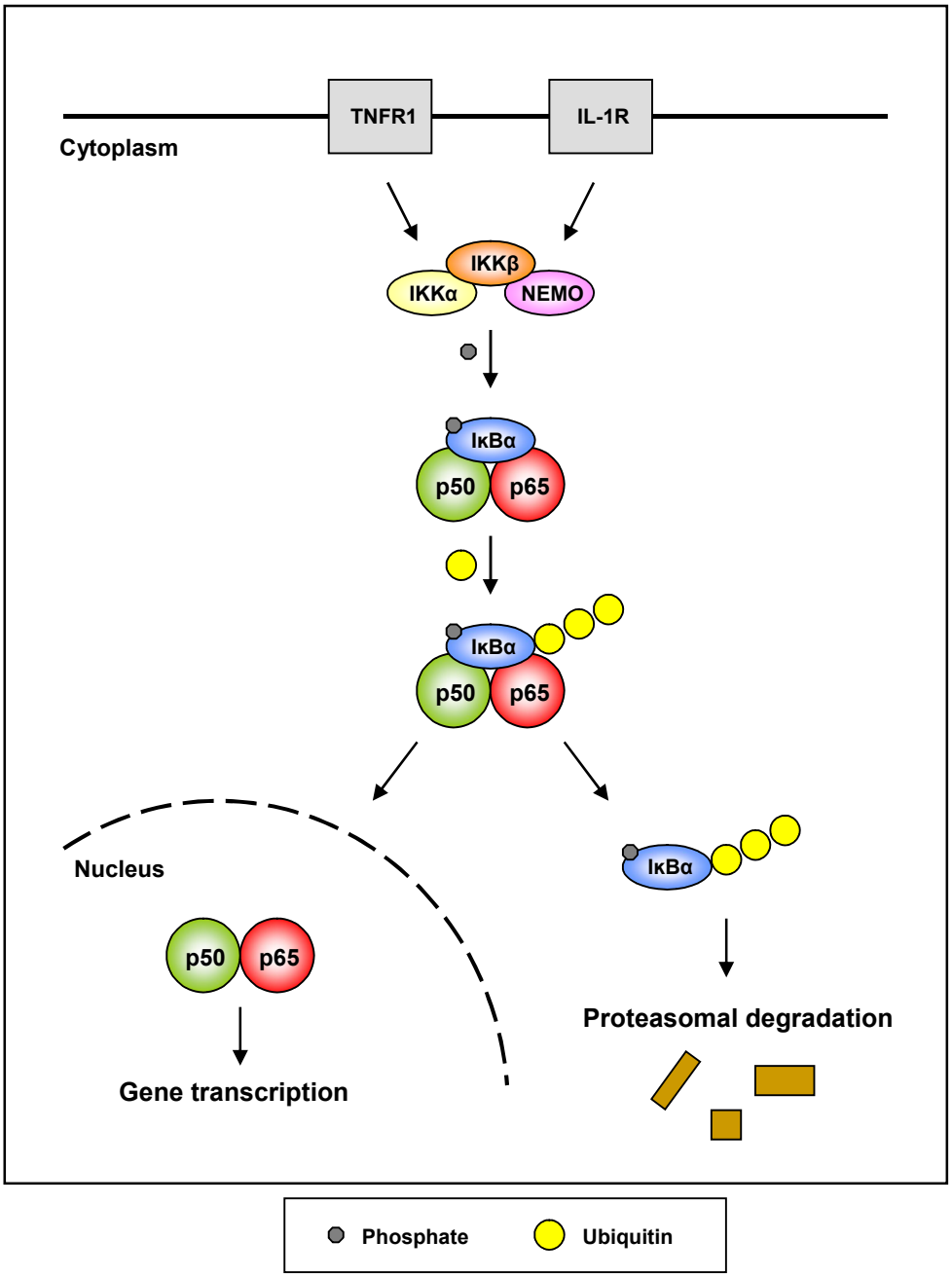

Figure 1.10 The canonical NF-κB pathway

Activation of TNFRs and IL-1Rs induce the IKK complex to phosphorylate IκBα. Consequently, IκBα is ubiquitinated and rapidly degraded through the 26S proteasome. Now free of their IκB binding partners, NF-κB p50-p65 dimers translocate to the nucleus and mediate gene transcription.

Figure adapted from Chen ZJ. Ubiquitin signalling in the NF-κB pathway. *Nat Cell Biol* 2005; **7**: 758-765.

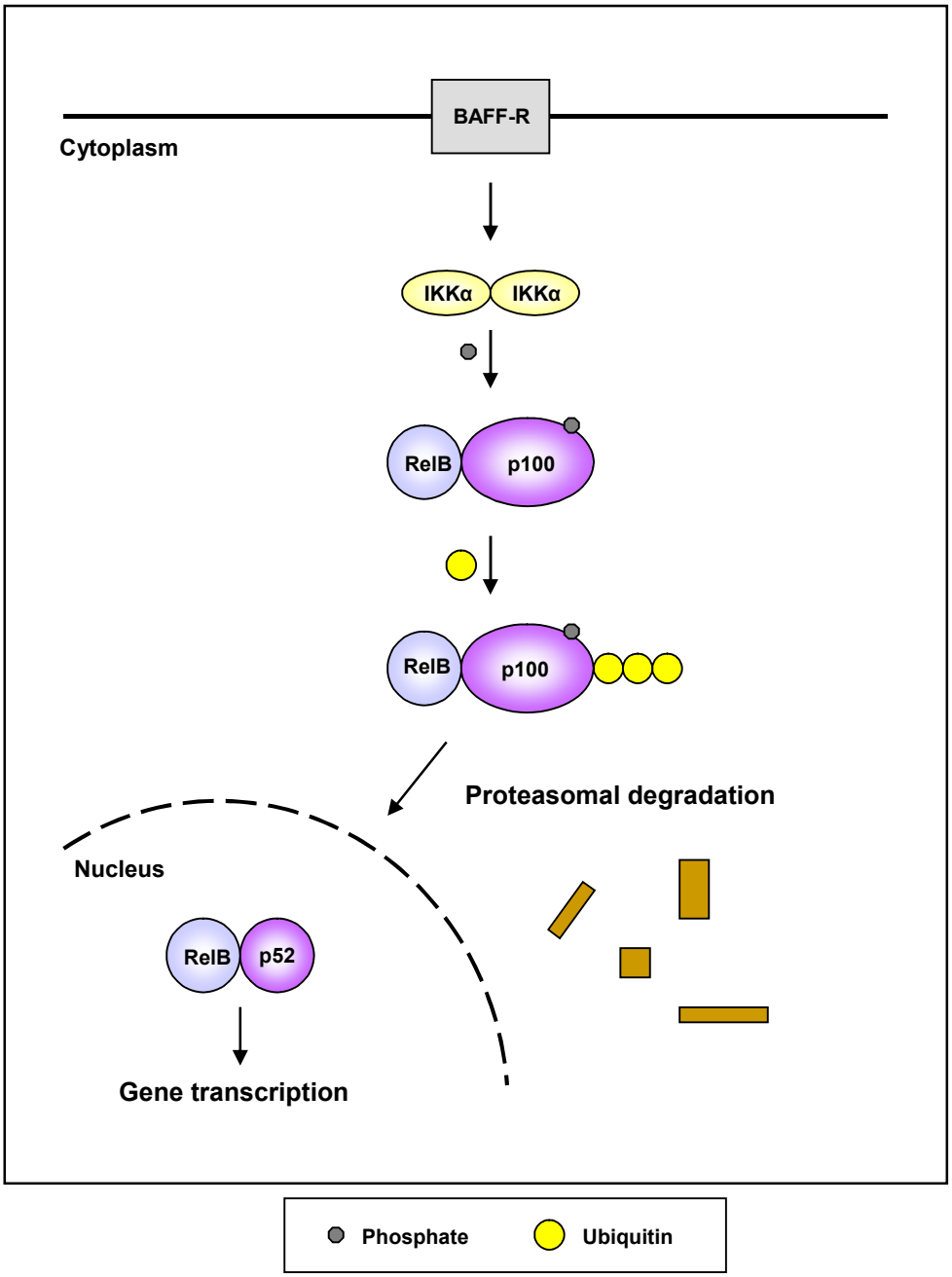

Figure 1.11 The non-canonical NF-κB pathway

The non-canonical NF-κB pathway predominates in B lymphocytes and does not require IKKβ or NEMO. Following cell stimulation, activated NIK leads to IKKα dependent processing of RelB-p100 to RelB-p52. Nuclear accumulation of RelB-p52 promotes the expression of several genes important in adaptive B-cell mediated immunity.

Figure adapted from Chen ZJ. Ubiquitin signalling in the NF-κB pathway. *Nat Cell Biol* 2005; **7**: 758-765.

Genetic mouse models have allowed scientists to investigate the physiological and pathological roles of NF-κB signalling *in vivo* [178]. Increased NF-κB activity, for example, can be achieved by either removing IκB proteins or by overexpressing constitutively active IKKβ. Similarly, NF-κB signalling can be inhibited by either depleting NF-κB family proteins or expressing degradation-resistant IκB (IκB-DR) proteins which are unresponsive to the IKK complex [179]. Ubiquitous inhibition or removal of NF-κB results in embryonic or early postnatal death [180, 181]. Consequently, cell-specific manipulation is required to study the function of NF-κB in tissues [169].

Several *in vivo* mouse studies have demonstrated that NF-κB signalling correlates positively with tissue inflammation [182, 183, 184]. Recently, evidence has emerged in which NF-κB inhibition in non-immune, epithelial or parenchymal cells also triggers a pronounced inflammatory response [185, 186]. This observation has led to the hypothesis that NF-κB activity may contribute to physiological tissue homeostasis via its action on tissue-specific immune cells [187]. In this setting, normal tissue integrity is maintained by balanced NF-κB signalling which ensures a measured innate immune response. Conversely, an imbalance in epithelial or parenchymal NF-κB activation, whether it be positive or negative in nature, triggers and sustains a potentially damaging immune-mediated inflammatory reaction [169].

1.5.5 NF-κB signalling: a link between inflammation and carcinogenesis

Epidemiological studies support the observation that chronic inflammation frequently precedes the onset of cancer in adults. This is particularly evident for oesophageal, gastric, pancreatic and colorectal cancers [188, 189, 190]. Inflammation associated with wound healing is self-limiting where as in chronic inflammation the response is sustained. Cytokines, principally TNFα and IL-1, which initiate and potentiate the inflammatory process also have cardinal effects within the tumour micro-environment. The 'net cytokine effect' fluctuates throughout the various phases of tumour development and is a major determinant of a cancer's growth and behavioural characteristics [191, 192]. NF-κB signalling is the predominant downstream effector of these cytokines and provides a common link between chronic inflammatory disease and malignancy. Its deregulation therefore appears to be at the heart of the transition from normal to neoplastic tissue.

1.5.5.1 Incontinentia pigmenti (IP)

Incontinentia pigmenti (IP) is a rare inherited inflammatory disorder of skin pigmentation that is associated with ocular, dental and neurological abnormalities [193]. Its name is derived from the observation that melanin 'drops out' of the epidermis and forms aggregates within the underlying dermis. IP is now known to be caused by mutations in the gene encoding for NEMO on the X chromososome [194]. NEMO consists of 10 exons and the majority of mutations are deletions which result in a truncated protein. Activation of the IKK complex is therefore impaired leading to a reduction in NF-κB signalling [194]. NEMO-deficient mice exhibit an IP phenotype, male embryonic lethality and heterozygous females develop inflammatory skin disease [195, 196]. Collectively, these observations indicate that NF-κB regulates epithelial maturation and supports the above mentioned hypothesis that a background level of NF-κB activity contributes to skin homeostasis [169].

1.5.5.2 NF-κB deficient epidermal mouse models

Mice with epidermis-specific ablation of transforming growth factor-β-activated kinase ($TAK1^{EKO}$ mice) and IKKβ ($IKK\beta^{EKO}$ mice) develop TNFα-dependent inflammatory dermatoses [197, 198]. Both TAK1 and IKKβ are required for canonical NF-κB signalling. In addition, mice expressing a keratinocyte-specific degradation-resistant form of IκBα (k5-IκBα-DR mice) exhibit inflammatory epidermal hyperplasia shortly after birth and subsequently develop CSCC [199]. When these mice were crossed with TNFR1-deficient mice no cutaneous pathology was observed [200]. In these studies, the source of TNFα was attributed to myeloid-derived cells in the dermis suggesting that keratinocyte and stromal 'communication' is integral to skin homeostasis and inflammatory responses.

1.5.5.3 Psoriasis

Psoriasis is a chronic inflammatory disorder with characteristic cutaneous features (Figure 1.12) and destructive seronegative joint disease [201]. It affects 2-3% of people worldwide and extensive genome-wide linkage studies have identified 9 psoriasis susceptibility loci designated PSORS1-9 [202]. The histopathological features of psoriatic

a

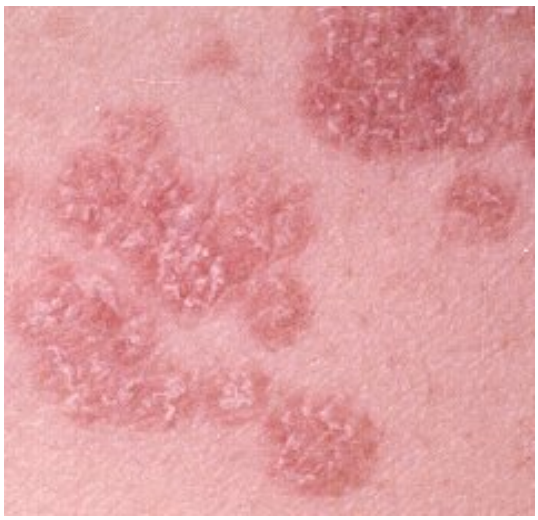

b

Figure 1.12 Psoriasis vulgaris

Photographs of psoriatic plaques. Lesions are typically (**a**) red or (**b**) salmon pink in colour and covered by white or silvery scales. Plaques are classically distributed symmetrically and involve the extensor aspects of the elbows and knees. Images courtesy of Dr Fiona Lewis, Consultant Dermatologist, St John's Institute of Dermatology, St Thomas' Hospital, London.

skin include: hyperkeratosis, epidermal acanthosis, angiogenesis and a leucocyte-rich dermal inflammatory infiltrate. The hyperplastic epidermal changes are associated with parakeratosis, underexpression of keratinocyte differentiation markers, loss of the granular layer, elongation of rete ridges and the presence of Munro microabscesses [203].

The pathogenesis of psoriasis involves epidermal-dermal cytokine interactions which induce the expression of surface adhesion molecules, such as inter-cellular adhesion molecule 1 (ICAM-1), on keratinocytes. This is a significant factor in the regulation of lymphocyte trafficking into psoriatic lesions [204]. In addition, this cytokine network co-ordinates the abnormal dermal vascular proliferation observed in psoriatic plaques and sustains the inflammatory reaction [205]. TNFα induced pro-inflammatory pathways dominate these processes; hence the efficacy of anti-TNFα biological therapies in psoriasis [206].

The risk of developing non-melanoma skin cancer is increased in psoriatic patients. Whether this is related directly to the underlying chronic inflammatory nature of psoriasis or is a consequence of excessive use of phototherapy and systemic immunosuppressant drugs remains unclear [207]. This scenario is further complicated by recent evidence that UV-irradiation induces TNFα mRNA and protein expression in both keratinocytes and dermal fibroblasts [208]. The nature of the mechanism that senses UV light in the TNFα gene promoter is not known [209]. Furthermore, IL-1α is also up-regulated in irradiated skin and has been shown to increase TNFα gene transcription [208]. It acts synergistically with TNFα in a pro-inflammatory manner through NF-κB signalling.

1.5.5.4 Inflammatory bowel disease (IBD)

Inflammatory bowel disease (IBD) is a collective term which encompasses the spectrum of disease seen in Crohn's disease and ulcerative colitis (UC). The aetiology of both conditions is unknown. Crohn's disease occurs mainly in Caucasians and may affect any part of the gastrointestinal tract, including the mouth. Microscopically, there is submucosal chronic non-caseating granulomatous inflammation characterised by multi-nucleate giant cells. UC, in contrast to Crohn's disease, most frequently affects the lower colon and rectum in people aged 15-40 years. Inflammation and ulceration of the superficial layers of the mucosa are followed by pseudopolyp formation. Individuals

with poorly controlled UC for longer than 10 years' duration have a significantly increased risk of colorectal carcinoma. Patients with Crohn's disease are also at an increased risk but less so than those with UC [210].

Complications of IBD include weight loss, a normocytic normochromic anaemia, gastrointestinal obstruction, perianal fissures, fistulae and abscess formation. Non-gastrointestinal features include: conjunctivitis, uveitis, iritis, finger clubbing, sacroileitis, skin disease (erythema nodosum and pyoderma gangrenosum), liver disease (primary sclerosing cholangitis), gallstones and renal calculi [210]. All of the above manifestations reflect the magnitude and chronicity of unchecked inflammation that underlies IBD.

TNFα is a strong stimulus for inflammation in IBD in both mouse models and patients, in whom TNFα-targeted treatment is highly effective [211]. Furthermore, NF-κB activation has been shown to be increased in the mucosa of patients with IBD there by implicating NF-κB pro-inflammatory pathways in the pathogenesis of the disorder [212]. Supportive of this hypothesis are studies involving mouse models of colitis in which the degree of inflammation was reduced by pharmacological inhibition of NF-κB signalling [213, 214]. More significant perhaps is the conclusion, from experiments using mice with NF-κB deficient intestinal epithelium, that NF-κB activation is required for the maintenance of normal mucosal integrity and immune surveillance [215]. This situation mirrors that observed in the skin as discussed previously.

Recent experimental evidence suggests that anti-TNFα therapy in mice reduces the development of colorectal carcinoma associated with chronic colitis; supporting the relationship between TNFα, chronic inflammation and carcinogenesis [216]. In this mouse model of UC, the administration of azaxymethane (AOM) followed by dextran sodium sulphate (DSS) induced severe colitis and multiple colonic cancers [217]. Disease progression in wild-type (WT) mice was associated with increased TNFα expression and a leucocyte-rich inflammatory infiltrate throughout the colonic mucosa and submucosa [218]. When WT mice were treated with etanercept (a human recombinant TNFR-Fc fusion protein) after prior administration of AOM and DSS there was a reduction in the number and size of the tumours. The degree of background colitis was also lessened [218]. The authors concluded that blocking TNFα reversed carcinoma progression, even when well established [218]. Moreover, they suggested that targeting

TNFα may be a useful therapeutic approach for colonic cancers, particularly those arising from chronic inflammation in the setting of IBD [218].

1.5.6 NF-κB and SCCHN

Molecular profiling studies, using a 15,000 element cDNA microarray, of normal, transformed and metastatic keratinocytes from the murine SCC Pam 212 model demonstrated that 308 genes were differentially expressed [219]. Of those identified, NF-κB regulated greater than 60%. The genes were functionally related to cellular processes vital to tumourigenesis such as cell proliferation, cell survival, cell migration, angiogenesis and inflammation [219]. Furthermore, blocking NF-κB signalling by a dominant negative IκBα phosphorylation mutant (IκBαM) inhibited malignant phenotypic features in UM-SCC-9 cells [220]. This data indicates that NF-κB is an important molecular switch for the genotypic and phenotypic changes that are observed during the malignant transformation of normal or dysplastic epithelium to SCC.

NF-κB is constitutively active in both SCCHN cell lines and tumour samples [221, 222]. Its dominant form is the p50-p65 dimer [170, 223]. This modulates several genes involved in the control of cell cycle progression and apoptosis. One such gene, cyclin D1, is overexpressed in 80% of cases and correlates with a poor clinical outcome [224]. NF-κB also inhibits the tumour suppressor p53 by acting upon Mdm2 [225]. Besides regulating anti-apoptotic genes, NF-κB signalling confers chemotherapeutic resistance in SCCHN by inducing γ-glutamylcysteine synthetase; the rate limiting enzyme for glutathione-S-transferase (GST) synthesis [226]. GST overexpression confers resistance to cisplatin therapy in patients with SCCHN [227, 228].

A prominent feature of SCCHN is its propensity for local invasion and metastasis. NF-κB regulates many of the proteins involved in the cellular mechanisms that facilitate these processes [229, 230, 231]. Interleukin-6 (IL-6), interleukin-8 (IL-8), growth-related oncogene 1 (GRO-1) and VEGF promote angiogenesis, cell motility and leucocyte chemotaxis; all are elevated in SCCHN and all have NF-κB DNA binding motifs in their promoters. MMP9 is dependent upon NF-κB for expression and, as previously mentioned in Section 1.3.5, is frequently up-regulated in SCCHN. It correlates positively with nodal metastasis and negatively with patient outcome [120]. Furthermore, NF-κB influences the expression of the MMP activator uPA (urokinase plasminogen

activator) and reciprocally decreases synthesis of TIMP 1 and 2 (tissue inhibitor of MMP) in SCC cells [232].

Although the constitutive activation of NF-κB in SCCHN is well established, the mechanisms which drive it are not fully understood [170]. IL-1α is constitutively expressed in SCCHN and serves as an autocrine stimulus for NF-κB activation [233]. It promotes local and systemic inflammatory responses and potentiates the action of TNFα [192]. The two receptors for TNFα (TNFR1 and TNFR2) are themselves up-regulated in SCCHN, compared to normal epithelium and this creates a positive feedback loop which helps to sustain NF-κB signalling [234]. Epidermal growth factor receptor (EGFR) and its high affinity ligand tumour growth factor alpha (TGFα) are also overexpressed in 90% of cases of SCCHN [235]. EGFR stimulation leads to NF-κB activation by initiating the phosphatidylinositol 3-kinase (PI3K) / Akt protein kinase (Akt) pathway [170]. Mechanistically, PI3K, Akt and 3-phosphoinositide dependent protein kinase-1 (PDK1) collectively activate the IKK complex. Mutations in protein phosphatase and tensin homologue (PTEN) are also found in SCCHN [236]. Consequently, PTEN suppression of Akt activation is impaired which in turn favours NF-κB signalling. Other factors which activate NF-κB in SCC are less well defined. These include infectious agents such as Epstein Barr virus (EBV) and environmental cues such as hypoxia [237, 238].

Besides SCCHN, there is cumulative evidence that NF-κB is also constitutively active in breast, gastric, prostate and colorectal cancers as well as melanoma and lymphoma. It therefore seems likely that NF-κB pathways are of broad importance to cancer in general [239, 240].

1.6 Tumour necrosis factor alpha (TNFα)

1.6.1 TNFα and related proteins

TNFα is a member of the TNF-TNFR cytokine superfamily. Its gene, TNFA, was first cloned in 1985 and maps to chromosome 6 (6p21.3) where it spans approximately 3kb. TNFα is a 185 amino acid (17kDa) polypeptide chain composed of two anti-parallel β-pleated sheets [241]. It is initially expressed as a 212 amino acid (26kDa) transmembrane precursor, pro-TNFα, which is subsequently cleaved at the cell surface by the metalloprotease TNFα converting enzyme (TACE) [242, 243, 244]. The soluble form of

TNFα (sTNFα) is a non-covalently bound trimer of the 17kDa protomer and dissociates at concentrations below the nanomolar range, there by losing its bioactivity. TNFα is synthesised by a variety of cells including T-lymphocytes, macrophages, dendritic cells, endothelial cells, keratinocytes, and fibroblasts [188, 191, 245].

Two TNF receptors (TNFRs) have been identified. TNFR1 (also known as p55/60 or CD120a) is ubiquitously expressed and can be activated by both the membrane-bound and soluble forms of TNFα [246]. TNFR2 (also known as p75/80 or CD120b) is restricted to immune and endothelial cells, and responds to the membrane-bound form of sTNFα. Both receptors have the same extra-cellular domains but differ in that TNFR1 possesses the cytoplasmic death domain (DD) [247, 248].

Ligand binding to TNFR1 initiates signalling through the association of the receptor's DD to TNFR-associated death domain (TRADD) [245]. This serves as a platform for further binding by three adaptor proteins: TNFR-associated factor 2 (TRAF2); receptor interacting protein 1 (RIP1) and Fas-associated-DD (FADD) [249]. Recruitment of TRAF2 and RIP1 triggers NF-κB and activator protein 1 (AP1) signalling [249]. Binding of FADD results in the formation of a cytosolic pro-apoptotic complex containing caspase 8 [250]. Apoptosis mediated through this pathway is reliant on inadequate activation of NF-κB and is therefore a late response to TNFα. Its significance is relatively minor when compared to apoptotic signalling induced by other members of the TNF superfamily such as TRAIL (TNF-related apoptosis-inducing ligand) [251]. Ligand binding to TNFR2 leads to activation of several pathways: NF-κB, MAPK (mitogen activated protein kinase), JNK (c-Jun N-terminal kinase), ERK (extra-cellular signal-regulated kinase) and PI3K [252]. However, the biological significance of this receptor is not well understood.

1.6.2 The biological activities of TNFα

TNFα has a diverse range of biological activities which are central to both innate and adaptive immunity [191]. In both situations, TNFα orchestrates a complex biological cascade involving the production of chemokines, cytokines and the differential expression of adhesion molecules across several cell types [253]. Release of pre-formed TNFα is rapid and occurs early on in the acute phase response [253]. In this setting, it acts

in an autocrine manner, activating NF-κB and inducing further TNFα production along with other cytokines such as IL-1, IL-6, IL-8 and interferon gamma (IFNγ) [245].

Investigations using several animal models, in which local and systemic levels of TNFα have been manipulated, indicate that it is critical to experimental inflammatory and autoimmune diseases [252]. For example, mice in which TNFα mRNA stability has been increased develop arthritis, IBD, anti-double stranded DNA antibodies and cachexia [254]. More importantly perhaps, is the finding that these animal observations are mirrored in human disease. The role of TNFα in the pathogenesis of inflammatory dermatoses and IBD has already been discussed. Other examples of TNFα driven inflammatory disorders include: rheumatoid arthritis, graft versus host disease (GVHD) and TNF receptor-associated periodic syndrome (TRAPS) [255]. The latter condition is caused by mutations in the tumour necrosis factor receptor superfamily member 1A (TNFRSF1A) gene and is characterised by altered cell membrane shedding of the TNFR1 complex. Consequently, the pro-inflammatory effects of TNFα are enhanced and patients present with periodic fevers associated with peritonitis, fasciitis and arthritis [256].

As highlighted in preceding sections, there are several associations between chronic inflammatory disease and cancer. Firstly, cancers arise at sites of chronic inflammation and the incidence of cancer is increased in chronic inflammatory disease [188, 189, 190]. Secondly, both the cellular and cytokine components of the inflammatory and tumour micro-environments are remarkably similar [188, 191]. Finally, interference with or inhibition of the cellular and chemical mediators of inflammation have been shown to influence cancer progression and spread [245, 257]. In view of the above, TNFα has become increasingly recognised as being a pivotal chemical mediator within the tumour micro-environment.

1.6.3 TNFα and cancer

TNFα is not present in plasma or serum of healthy individuals but may be detected in cancer patients with advanced disease [252]. In prostate cancer, for instance, serum TNFα levels correlate with the extent of disease and are elevated in cachectic patients [258]. These findings have also been noted in patients with metastatic breast, pancreatic and renal cancer as well as those with chronic lymphocytic leukaemia (CLL) [259, 260, 261, 262].

Furthermore, TNFα is regularly detected in the epithelial and stromal compartments of human tumour samples [263].

Cancer cell and stromal cell production of TNFα is observed in the development of a variety of experimental tumours [191]. It is also secreted by both cancer and stromal cell lines *in vitro* along with other cytokines such as IL-1, IL-6 and IL-8. Collectively, this phenomenon is responsible for the constitutive activation of NF-κB within these cell cultures [264]. The stimulus for TNFα production *in vitro* and *in vivo*, in the absence of inflammation, is not entirely clear but may be linked to the expression of endogenous molecules such as heat shock proteins [252].

High doses of TNFα are anti-angiogenic and cause haemorrhagic necrosis of tumour blood vessels [265]. This property of TNFα accurately reflects its name and highlights the paradoxical behaviour of TNFα within the tumour micro-environment [257]. Diverse strategies of TNFα use in cancer therapy have been proposed and, when administered locally using an isolated limb perfusion (ILP) circuit, TNFα has proven to be successful in the management of advanced extremity soft tissue sarcoma (STS) [266]. Furthermore, the efficacy of TNFα antagonists in the management of several chronic inflammatory disorders has led to interest in the use of biological agents in cancer chemotherapeutics.

1.7 Interleukin 1 (IL-1)

1.7.1 IL-1 and related proteins

The original members of the interleukin-1 (IL-1) superfamily include IL-1α, IL-1β and the IL-1 antagonist, IL-1RA. The genes encoding for these three proteins cluster together on the long arm of chromosome 2 and span approximately 400kb [192]. Six other members, (IL-1F5 to IL-1F10), have been added to the IL-1 superfamily in recent years. To correspond with this, IL-1α, IL-1β and IL-1RA were reclassified as IL-1F1, IL-1F2 and IL-1F3 respectively [267].

IL-1α is a 155 amino acid (17kDa) polypeptide chain which is cleaved from its precursor molecule, proIL-1α, by a calcium-dependent protease, calpain. An N-terminal cleavage product IL-1NTP, the propiece of IL-1α, is created during this process. The active membrane form of IL-1α is derived from myristoylation of proIL-1α and is

anchored via a mannose-like receptor [268]. IL-1β, like IL-1α, is also synthesised as a precursor peptide and processed to its mature 153 amino acid (17kDa) form by a cysteine protease, IL-1β converting enzyme (ICE). IL-1RA is the physiological inhibitor of IL-1, has a signal recognition peptide and is secreted by the endoplasmic reticulum and Golgi apparatus [269]. With regards to the structural homology of the three proteins, IL-1β is more closely related to IL-1RA than to IL-1α. All members of the IL-1 superfamily have a barrel shaped conformation being composed of 12-14 β-strands. IL-1α, IL-1β and IL-1RA are produced by a variety of cells including macrophages, monocytes and dendritic cells [188, 190].

IL-1 receptors (IL-1Rs) are ubiquitously expressed and belong to the immunoglobulin (Ig) supergene family. IL-1R1 (80kDa) is a signalling receptor where as IL-1R2 (68kDa) serves as a decoy target [192]. Ligand binding to IL-1R1 results in the formation of a complex with IL-1R acceptor protein (IL-1RAcP) and the recruitment of IL-1 receptor-associated kinase (IRAK). Further signal transduction ultimately leads to NF-κB activation. By contrast, the binding of IL-1RA to IL-1R1 or of IL-1 to IL-1R2 does not result in a receptor complex with IL-1RAcP. Consequently, IRAK is not recruited and further downstream events are inhibited [192]. Under physiological conditions, membrane bound IL-1R2, soluble IL-1Rs and IL-1RA limit cell responsiveness to IL-1. Signalling through IL-1R1 is analogous to the *Drosophila* Toll pathway [270]. IL-1R1 has a TIR (Toll-IL-1 receptor) domain in common with other Toll-like receptors (TLRs) expressed on immune cells. TLRs recognise pathogen-associated molecular patterns (PAMPs) and are integral to the innate immune response [271].

1.7.2 The biological activities of IL-1

Currently, the majority of information regarding the biological activities of IL-1 originates from studies involving the use of recombinant IL-1α and IL-1β. Extensive investigations using *in vitro* and *in vivo* experimental systems have demonstrated that in their recombinant form, both IL-1α and IL-1β exert the same spectrum of biological effects [192]. However, the sub-cellular compartments in which IL-1α and IL-1β operate differ dramatically. IL-1α is predominantly active intracellularly or in its membrane bound form and is only marginally active when secreted. IL-1β, on the other hand, is solely active as a secreted product. Its precursor peptide is inactive and IL-1β does not exist in a membrane associated state. With these findings in mind, it has been suggested

that the localisation of IL-1 molecules, in the context of the cell of origin and its surrounding environment, determines the biological function [272].

IL-1α and IL-1β, like TNFα, co-ordinate innate and adaptive immunity [273]. Both induce the expression of pro-inflammatory genes within immune and stromal cells, leading to the cellular and tissue events which typify the inflammatory response. Of particular importance to this process, is the ability of IL-1 and TNFα to stimulate their own and each other's production, thus creating an amplification loop. IL-1 has widespread effects on the proliferation, differentiation, and behaviour of neutrophils, macrophages and natural killer (NK) cells. Many of these actions have been shown to occur indirectly and are dependent upon paracrine signalling from neighbouring stromal cells [192]. IL-1 is also fundamental to the generation of T-cell mediated immune responses and may act as an endogenous adjuvant to self-antigens in the pathogenesis of autoimmune disease [274]. Individuals with mutations in the IL1RN gene do not produce adequate levels of IL-1RA. Since IL-1 activity is unopposed patients develop pustulosis, periostitis and sterile multifocal osteomyelitis. Collectively, this autoimmune inflammatory syndrome is termed DIRA (deficiency of the IL-1 receptor antagonist) [275, 276].

1.7.3 IL-1 and cancer

The intra-cellular forms of IL-1α, (proIL-1α and the IL-1NTP) possess a nuclear localisation sequence (NLS) [277]. They therefore translocate to the nucleus and regulate several cellular functions including gene transcription, protein expression and cell differentiation [278]. In fibroblasts and endothelial cells the accumulation of intracellular IL-1α (icIL-1α) correlates with growth arrest and senescence [279, 280]. The pathways involved in IL-1α intracrine signalling are not well understood but are thought to be active in healthy cells. In malignancy, IL-1α is frequently overexpressed and has been shown to act in an autocrine manner in several types of cancer [281, 282]. What remains unanswered, however, is the functional significance of icIL-1α to cancer cell behaviour.

In an experimental mouse model of skin carcinogenesis, tumour formation was induced by the application of 12-*O*-tetradecanoylphorbol-13-acetate (TPA) as a tumour promoter, after prior treatment with the initiator, 7,12-dimethylbenzanthracene (DMBA). IL-1α expression in the suprabasal keratinocytes was noted and persisted throughout tumour development [283]. An increase in the concentration of intracellular IL-

1RA (icIL-1RA) was also detected [284]. The relationship between IL-1α and IL-1RA expression and its influence in carcinogenesis and tumour progression requires further evaluation.

The importance of TNFα in the tumour micro-environment has been discussed in preceding sections. In the model of skin carcinogenesis described above, TPA was shown to induce TNFα expression at the site of skin application [285]. When TNFα KO mice were used residual tumours developed and this was attributed to the actions of IL-1 [286]. Furthermore, IL-1α was up-regulated in the skin of mice treated with DMBA alone suggesting its involvement in both tumour initiation and promotion [287].

Co-operation between several oncogenes and membrane bound IL-1 has been described in experimental systems of *in vitro* cell transformation [192]. In fibroblasts overexpressing v-JUN, IL-1α and TNFα promote anchorage independent growth [288]. An IL-1 autocrine loop is also involved in Raf-induced transformation of NIH 3T3 cells [289]. IL-1β expression correlates with mutations of Ras in acute myeloid leukaemia (AML) and chronic myeloid leukaemia (CML) [290]. In addition, mutant Ras and constitutive IL-1β activation has been identified in breast, colon, lung, pancreatic, skin and renal cancers. The nature of the relationship between the expression of oncogenes and IL-1 in cancer remains undetermined.

Current literature suggests that the *in vitro* production of IL-1α and IL-1β correlates with cancer cell invasiveness. Only rarely have anti-invasive effects been observed [192]. A diverse group of human cancer cell lines express IL-1 either constitutively or upon appropriate stimulation [291]. What is less clear, however, is whether IL-1 is integral to cell transformation or merely a by-product of the process. Given that normal cells rarely secrete IL-1α, it seems likely that IL-1α production by malignant cells is functionally significant to tumour progression [233]. This statement is supported by the observation that in malignant melanoma, IL-1α secreted by melanoma cells correlates with metastasis. In this setting, IL-1 was shown to act in an autocrine manner on the tumour cells and to have a paracrine influence on neighbouring stromal fibroblasts [292, 293]. Moreover, in a study of patients with gastric carcinoma, IL-1α positive tumours were associated with an increased incidence of liver metastasis and a worse prognosis following resection [294].

In summary, comparative studies which assess the roles of IL-1α, IL-1β, IL-1RA and the IL-1Rs in parallel within the tumour micro-environment are needed. Understanding and characterising the intracrine, autocrine and paracrine activities of IL-1 in the context of tumour development and progression may lead to the development of novel therapeutic strategies.

1.8 Establishing a human tissue bank

1.8.1 The Human Tissue Authority (HTA)

The Human Tissue Authority (HTA) was established on 1st April 2005 under the Human Tissue Act (HT Act) 2004 which extends to England, Wales and Northern Ireland. It is an Executive Non-Department Public Body (ENDPB) appointed by the Secretary of State for Health and consists of a Chair and fourteen members [295]. The HTA Chair and eight members are lay individuals with a wide range of business, commercial and public-sector experience. The remaining six members are medical and scientific professionals selected from some of the groups most directly affected by the HT Act [296].

The HTA protects the public by licensing and inspecting organisations that store and use tissue for research, human application, post-mortem examination, teaching and public exhibitions. It also authorises organ and bone marrow donations for the purpose of transplantation. The HTA acts under two laws: the HT Act 2004 and the Human Tissue (Quality and Safety for Human Application) Regulations 2007.

1.8.2 The Human Tissue Act (HT Act) 2004

The HT Act 2004 replaced previous legislation (the HT Act 1961, the Anatomy Act 1984 and the Human Organ Transplants Act 1989) pertaining to England, Wales and Northern Ireland. Scotland has its own law, the HT (Scotland) Act 2006 [296].

The fundamental principle of the HT Act relates to the issue of patient consent. This must be obtained for the lawful storage and use of bodies, body parts, organs, and tissues from the living or the deceased. The HT Act uses the term ‘appropriate consent’

to refer to the person who can give consent which, in most instances, is the individual concerned. For the deceased, consent may be sought from the next of kin. The Act further stipulates that consent should be given voluntarily by an individual with the capacity to make an informed decision. It is regarded as a positive action and may be implied, verbal or written depending on the circumstances. A person also retains the right to withdraw his or her consent at any time.

The HT Act prohibits the covert collection of biological samples for genetic analysis, but exempts forensic scientific investigations from this offence.

1.8.3 The Human Tissue (Quality and Safety for Human Application) Regulations 2007

This latter piece of legislation provides the framework within which the HTA regulates the removal, storage and use of human tissue. It stems from a European law, the European Union Tissue and Cells Directive (EUTCD) and its remit is the whole of the UK, including Scotland. The EUTCD delineates standards for the handling of human tissue and cells throughout Europe and enables accurate tracing of samples between donors and recipients [295].

1.8.4 The National Research Ethics Service (NRES)

The National Research Ethics Service (NRES) was created in 2006 and is a division of the National Patient Safety Agency (NPSA) [297]. It consists of the former Central Office for Research Ethics Committees (COREC) and the National Health Service Research Ethics Committees (NHS RECs) in England [297]. NRES aims to deliver a system of review that protects the dignity and safety of research participants, whilst promoting ethical research. It is responsible for administering training, accreditation and overseeing quality assurance for the Research Ethics Service [297].

RECs review research projects which involve the collection, storage and use of human tissue. All are recognised as research ethics authorities for the purpose of the HT Act and therefore tissue stored for an ongoing REC approved project does not require an HTA licence. When the research project is completed further storage of any residual

tissue must be covered by the HTA or the samples destroyed. However, the unnecessary destruction of samples donated by patients for research is deemed to be immoral.

1.8.5 The Integrated Research Application System (IRAS)

The Integrated Research Application System (IRAS) was launched in 2008 and was developed to streamline the application process required for approval to perform health care research within the UK. It significantly reduces the volume of paperwork that was previously required by avoiding the duplication of material needed for Site Specific Assessment (SSA). Filters are built into IRAS to ensure that the data collected and collated is appropriate to the type of study and research approvals required.

1.8.6 The National Institute for Health Research Co-ordinated System for gaining NHS Permissions (NIHR CSP)

Any research performed in the NHS requires approval from all the NHS organisations involved. The National Institute for Health Research Co-ordinated System for gaining NHS Permissions (NIHR CSP) was set up in November 2008 [298]. It was developed to standardise the process of gaining Research and Development (R&D) approval in NHS trusts throughout the UK for research studies adopted to the NIHR Clinical Research Network Portfolio. An application to the NIHR CSP is made through IRAS.

For non-NIHR Portfolio research, the new IRAS Site Specific Information Form (SSIF) is used for R&D management approval. Final R&D authorisation is not normally granted until a favourable ethical opinion has been received, funding is in place and a 'research sponsor' has been identified. The sponsor accepts overall responsibility for ensuring that the research meets appropriate standards and that arrangements have been made to monitor the conduct of the individuals involved. Moreover, a system should be in place for the reporting and management of any patient adverse events that arise during the course of the study.

1.8.7 Generic criteria for a human tissue bank

The HTA and the NRES provide guidance for the establishment of human tissue banks for the sole purpose of scientific research [295, 297]. A summary of these guidelines is shown below:

- Prior ethical and R&D approval for the establishment of the Bank should have been obtained from the NRES and the NHS trusts involved as outlined above.

- Chief and Principal Investigators must be appointed for the duration of the study. The Chief or Principal Investigator at each site of tissue collection should assume overall responsibility for data collection, data storage and data analysis relevant to participants recruited to the study. All database systems should be password protected and subject to audit trail in line with current NHS Trust policy.

- The Bank must be stored in a secure facility and its routine handling overseen by a single designated Bank Manager.

- Strict criteria for tissue inclusion, exclusion and withdrawal should be defined prior to recruiting subjects for donation.

- Informed consent, (ideally written), must be obtained from the individual prior to harvesting tissue. Donors should be fully informed of the intended use of their tissue for scientific research, the nature of the investigations to be undertaken and the length of duration their tissue will be stored for. The donor retains the right to withdraw his or her tissue from the bank at anytime without explanation.

- All tissue samples and any associated clinical information pertaining to the donor must be anonymous to the researcher at the point of release. Each sample should be identified by a unique research number.

- The use of tissue samples must comply with the terms of the donor consent. Any contact with donors should be confined to ethically approved arrangements for the feedback of clinically significant information.

- Any serious adverse event, breach of security or confidentiality relating to the Bank which could undermine public confidence in the ethical management of the tissue should be reported to the NRES in accordance with the HT Act 2004.

- A Material Transfer Agreement (MTA) which covers the transfer of tissue from its source (the NHS Trust) to the site of storage and usage (the Research Institute) may be necessary.

- Any substantial amendment to the management of the Bank requires further NRES approval prior to its implementation.

Human tissue banks are a valuable asset to cancer research [299]. The analysis of tumour samples has provided new insights into cancer development and progression. This has subsequently led to improved diagnostic techniques and the development of effective cancer chemotherapeutic agents.

1.9 Aims of this work

A defining feature of cancer is its propensity for invasion. Cell motility is central to this process and is accompanied by dramatic changes of cell phenotype. This requires remodelling of a cell's actin cytoskeleton as well as dynamic interactions with the surrounding ECM.

1.9.1 Hypotheses

- Ubiquitin-linked pathways are key regulators of the actin cytoskeleton.

- Ubiquitin-linked pathways are fundamental to the process of cancer cell invasion.

1.9.2 Objectives

- To identify genes regulating ubiquitin and ubiquitin-like proteins which influence SCC invasion.

- To improve our understanding of the process of SCC invasion by investigating the nature of cellular interactions and signalling pathways at the invasive front.

- To establish a tissue bank of SCCHN tumour specimens, with patient matched control tissue samples.

- Having identified ubiquitin-linked regulators of SCC invasion, to examine their degree of expression in human tumour samples and assess their potential as diagnostic tumour markers.

Chapter 2

Materials and Methods

2.1 Reagents

2.1.1 Buffers and solutions

Buffers and solutions used regularly throughout these experiments are shown below.

Phosphate buffered saline (PBS):

1.5mM KH_2PO_4, 8mM Na_2HPO_4, 2.7mM KCl, 137mM NaCl, pH 7.4

10X Protein buffer

1.92M glycine, 0.25M Trizma® base

1X SDS gel loading buffer

50mM Trizma® HCl pH 6.8, 2% SDS, 10% glycerol, 100mM β-mercaptoethanol, 0.2% bromophenol blue

SDS running buffer

100ml 10X protein buffer, 10ml 10% SDS, 890ml dH_2O

'Stripping' buffer

5.5g glycine, 20g SDS, dH_2O to 500ml, pH 2.7

10X TBE buffer

108g Trizma® base, 55g Boric acid, 9.3g Na_4EDTA, dH_2O to 1 litre, pH 8.3

TE buffer

10mM Trizma® HCl pH 7.5, 1mM EDTA

Transfer buffer

100ml 10X protein buffer, 1ml 10% SDS, 699ml dH_2O, 200ml Methanol

Trizma® buffered saline (TBS)

137mM NaCl, 2.7mM KCl, 20mM Trizma® HCl, pH 7.4

TBS-Tween20 solution

10ml 20% Tween20 and 990ml 1X TBS

2.1.2 Chemicals

Commonly used reagents are shown below. Assay specific reagents are listed in their respective sections.

Adenosine triphosphate (ATP), ammonium persulphate ($(NH_4)_2S_2O_8$), bromophenol blue, bovine serum albumin (BSA), dimethylsulphoxide (DMSO), dithiothreitol (DTT), ethanol (EtOH), ethylene diamine tetra-acetic acid (EDTA), foetal calf serum (FCS), glycine ($C_2H_5NO_2$), hydrochloric acid (HCl), β-mercaptoethanol (C_2H_6OS), Ponceau S, potassium chloride (KCl), potassium phosphate (KH_2PO_4), sodium chloride (NaCl) sodium deoxycholate, sodium orthovanadate ($NaVO_4$), sodium phosphate (Na_2HPO_4), sodium pyrophosphate ($Na_4P_2O_7$), tetramethylethylenediamine (TEMED), Triton® X-100, Trizma® base, Trizma® HCl, Tween20, nonyl phenoxylpolyethoxylethanol (NP-40), were all purchased from Sigma-Aldrich®, UK.

Acetic acid (CH_3COOH), acrylamide solution, boric acid (H_3BO_3), glycerol ($C_3H_5(OH)_3$), magnesium chloride ($MgCl_2$), methanol (MeOH) and sodium dodecyl sulphate (SDS) were purchased from Thermo Fisher Scientific Inc., UK.

BD Matrigel^{TM} basement membrane matrix and rat-tail collagen type I was purchased from BD Biosciences, Europe.

2.2 Mammalian cell culture techniques

2.2.1 Cell lines

A431 cells are human vulval SCC cells and were grown in DMEM with 10% FCS in 10% CO_2 at 37ºC [300]. SCC12 cells (a human CSSC cell line) were cultured in FAD

medium supplemented with 10% FCS, 5µg/ml insulin (Invitrogen, UK), 0.5µg/ml hydrocortisone (Sigma-Aldrich®, UK) and 10ng/ml EGF (Sigma-Aldrich®, UK) hereafter referred to as complete media, in 5% CO_2 at 37ºC [301]. Human HNCAF (head and neck carcinoma-associated fibroblasts) were cultured in DMEM with 10% FCS and insulin-transferrin-selenium (Invitrogen, UK) in 10% CO_2 at 37ºC.

2.2.2 Cell culture

DMEM was made to the following protocol in house by media production services.

E4 - Dulbecco's Modification of Eagles Medium (DMEM)	mg/litre
Inorganic Salts	
$CaCl_2.2H_2O$	265.00
$Fe(NO_3)_3$	0.10
KCl	400.00
$MgSO_4.\ 7H_2O$	200.00
NaCl	6400.00
$NaH_2PO_4.2H_2O$	140.00
Amino Acids	
L- Arginine mono.HCl	84.00
L-Cystine	48.00
L-Histidine mono.HCl	42.00
L-Glutamine	584.00
Glycine	30.00
L-Isoleucine	104.80
L-Leucine	104.80
L-Lysine mono.HCl	146.20
L-Methionine	30.00
L-Phenylalanine	66.00
L-Serine	42.00
L-Threonine	95.20
L-Tryptophan	16.00
L-Tyrosine	72.40
L-Valine	93.60
Inositol	7.00
Vitamins	
Choline Chloride	4.00
Folic acid	4.00
Nicotinamide	4.00
DL-pantothenic acid, Ca salt	4.00
Pyridoxal HCl	4.00
Riboflavin	0.40
Thiamine HCl (aneurine)	4.00
Other Compounds	
D-Glucose	4500.00
Phenol red	15.00

$NaHCO_3$	3700.00
Penicillin	100,000 units
Streptomycin Sulphate	100.00
Sodium pyruvate	110.00
Antimycotic (Butyl-p-hydroxybenzoate)	0.20

FAD medium was also made in house, being a 3:1 formulation of DMEM and Ham's F12.

Cells were sub-cultured every 5-7 days when approximately 90% confluent. After decanting the culture medium, cultures were washed with PBS. The cells were then enzymatically detached by incubating with 0.1% trypsin and 0.02% versene for 5 minutes at 37ºC. The trypsin was subsequently neutralised by adding 10ml of the appropriate culture medium containing 10% FCS.

2.2.3 Storage and retrieval of cells

Stocks of cells were maintained in liquid nitrogen. Cells were frozen in 1.5ml of DMEM with 20% FCS and 10% DMSO in cryotubes containing no more than 10^7 cells. At the time of freezing, cells were typically split 1:10 and cooled in a -80ºC freezer for 12-24 hours before being transferred to liquid nitrogen for long-term storage at -196ºC.

Cells were retrieved from the liquid nitrogen storage facility by rapid thawing of the cryotubes in a 37ºC water bath; the cells were then transferred to 10ml of culture medium. After centrifuging at 12,000rpm for 5 minutes at room temperature, the supernatant was discarded and the cell pellet re-suspended in culture medium before being transferred to the appropriate sized tissue culture flask. Cells were maintained in culture as described previously (Section 2.2.2).

2.2.4 Transient DNA transfections

2 x 10^5 A431 cells were seeded per well in 6 well plates the day before transfection in DMEM with 10% FCS. 100µl of Opti-MEM® (Invitrogen, UK) was mixed with 6µl of FuGENE® 6 transfection reagent (Roche, UK). The contents were left for 15 minutes before adding 1µg of DNA and leaving for a further 15 minutes. Cells were washed once with PBS before being covered with 800µl of Opti-MEM®. The DNA-liposome

mix was then pipetted onto the cells and swirled briefly. After 5 hours of incubation in 10% CO_2 at 37ºC the transfection mix was removed, the cells washed with PBS and fresh DMEM with 10% FCS added. Cells were subsequently recovered for analysis by immunofluorescence (IMF) or immunohistochemistry (IHC).

2.2.5 siRNA transfections

siRNA duplexes were purchased from Dharmacon® or Qiagen® and stock solutions of 20µM made. For the initial A431 screen, Dharmacon® provided SMARTpool siRNA libraries in a 96 well format with each SMARTpool consisting of 4 individual siRNA duplexes per gene. The concentration of oligonucleotides in the libraries was 2.5µM (0.625µM of each duplex).

Cells were cultured in standard conditions. A431 and SCC12 cells were transfected using DharmaFECT™ 2 (Dharmacon®, UK). HNCAF were transfected using DharmaFECT™ 1 (Dharmacon®, UK). The final concentration of siRNA in all transfections was 100nM.

2.2.5.1 siRNA transfections per well (48 well plate)

1 x 10^4 A431 cells or 8 x 10^3 HNCAF cells were plated per well 12-24 hours prior to transfection.

Depending on the stock concentration of the siRNA solution, either transfection mixture A or transfection mixture B was used.

Transfection Mixture A (siRNA stock concentration 2.5µM)

1. 10µl of 2.5µM siRNA solution was mixed with 15µl of Opti-MEM®.
2. 0.5µl of DharmaFECT™ transfection reagent with 24.5µl of Opti-MEM®.

Transfection Mixture B (siRNA stock concentration 20µM)

1. 12.5µl of 2µM siRNA solution was mixed with 12.5µl of Opti-MEM®.
2. 0.5µl of DharmaFECT™ transfection reagent with 24.5µl of Opti-MEM®.

After 5 minutes 1 and 2 were mixed together and left for a further 20 minutes at room temperature to allow siRNA-liposomal complexes to form. During this time cells were washed with PBS and covered with 200µl of Opti-MEM® with 5% FCS. Subsequently, the 50µl siRNA-DharmaFECT™ transfection reagent mix was added. A further 250µl of Opti-MEM® with 5% FCS was then added following 24 hours of standard incubation. Depending on the nature of the experiment, transfections were stopped at 48, 72 or 96 hours.

2.2.5.2 siRNA transfections per well (24 well plate)

1 x 10^4 A431 cells were plated per well 12-24 hours prior to transfection.

Transfection Mixture (siRNA stock concentration 20µM)

1. 25µl of 2µM siRNA solution was mixed with 25µl of Opti-MEM®.
2. 1µl of DharmaFECT™ transfection reagent with 49µl of Opti-MEM®.

After 5 minutes 1 and 2 were mixed together and left for a further 20 minutes at room temperature to allow siRNA-liposomal complexes to form. During this time cells were washed with PBS and covered with 400µl of Opti-MEM® with 5% FCS. The 100µl siRNA-DharmaFECT™ transfection reagent mix was then added to constitute a final transfection volume of 500µl. A further 500µl of Opti-MEM® with 5% FCS was then added following 24 hours of standard incubation.

2.2.5.3 siRNA transfections per well (6 well plate)

2 x 10^5 A431 cells, 3 x 10^5 SCC12 cells or 2 x 10^5 HNCAF were plated per well 12-24 hours prior to transfection.

Transfection Mixture (siRNA stock concentration 20µM)

1. 50µl of 2µM siRNA solution was mixed with 50µl of Opti-MEM®.
2. 2µl of DharmaFECT™ transfection reagent with 98µl of Opti-MEM®.

After 5 minutes 1 and 2 were mixed together and left for a further 20 minutes at room temperature to allow siRNA-liposomal complexes to form. During this time cells were

washed with PBS and covered with 800µl of Opti-MEM® with 5% FCS. The 200µl siRNA-DharmaFECT™ transfection reagent mix was then added to constitute a final transfection volume of 1ml.

2.2.6 siRNA screening

Dharmacon® SMARTpool siRNA libraries targeting 289 E3 ubiquitin ligases and 137 de-ubiquitinating enzymes (DUBs) were used to screen for their potential role in SCC invasion by initially assessing their ability to regulate the actin cytoskeleton of A431 cells.

2.2.6.1 siRNA screening in A431 cells

As detailed in Section 2.2.5, siRNA libraries were presented in a 96 well plate format with each SMARTpool consisting of 4 individual siRNA duplexes per gene. Each plate also contained empty wells and non-targeting siRNA controls. In addition, siRNA duplexes targeting Integrin β1 and Rho A were included. These acted as positive transfection controls since both generate reproducible and characteristic changes in the cytoskeleton of A431 cells. The gene symbols and Dharmacon® catalogue numbers follow.

E3 Ubiquitin Ligase Library

Plate 1

ANKIB1	M-028950-01	ANKRD11	M-027299-01
ARIH2	M-020104-01	MARCH7	M-007055-01
BAZ1A	M-006941-00	BBAP	M-007143-01
BIRC2	M-004390-02	BIRC3	M-004099-02
BIRC4	M-004098-01	C17ORF27	M-023324-02
CBL	M-003003-02	CBLB	M-003004-02
CBLC	M-006962-00	CBLL1	M-007069-00
CCNB1IP1	M-019251-01	CDC26	M-017290-00
CHD5	M-009878-00	RFWD2	M-007049-01
CUL7	M-017673-00	DCST1	M-016740-01
DET1	M-019393-00	DKFZP547C195	M-026520-01
DKFZP564A022	M-007078-01	DKFZP761H1710	M-007082-00
DPF1	M-031779-01	DTX3	M-007156-01
DTX4	M-026663-01	DZIP3	M-006910-00
EGFL9	M-014254-00	FANCL	M-021486-00
FBXL14	M-015718-00	FBXL17	M-024385-00
FBXO17	M-013128-00	FBX018	M-017404-00
FBXO27	M-018558-00	C1ORF164	M-021044-01
FLJ12875	M-007062-02	FLJ20186	M-020685-01
FLJ20315	M-007004-02	FLJ23749	M-007108-01

FLJ30092	M-027115-00	FLJ31951	M-007146-01
FLJ35757	M-007150-02	FLJ36180	M-007174-01
FLJ45273	M-027218-02	FLJ46380	M-032070-01
HACE1	M-007193-01	HECTD2	M-007198-00
FLJ21156	M-027468-03	NEDL1	M-007186-01
HECW2	M-007192-00	HERC2	M-007180-02
HOZFP	M-021465-00	HRD1	M-007090-00
HUWE1	M-007185-01	IBRDC2	M-025119-00
ITCH	M-007196-01	KIAA0317	M-007184-02
KIAA0804	M-023668-00	KIAA1333	M-007014-00
KIAA1542	M-026727-00	KIAA1991	M-032290-00
KIAA2025	M-021878-00	LNX2	M-007164-01
LOC285498	M-008019-00	LOC389822	M-029504-00
LOC442247	M-032292-01	LOC493829	M-032293-00
LOC51136	M-010205-01	LOC51255	M-006985-00
LRSAM1	M-007103-01	MAPKBP1	M-022225-00
FLJ20668	M-007006-02	LOC51257	M-006986-00
MARCH3	M-007116-02	MARCH9	M-015561-01
MDM2	M-003279-04	MGRN1	M-022620-00
LOC142678	M-015287-00	MID2	M-006938-00

Plate 2

MKRN1	M-006959-00	MKRN2	M-006960-01
MKRN3	M-006581-01	MNAB	M-020453-02
MYCBP2	M-006951-01	MYLIP	M-006976-00
MYST3	M-019849-01	NEDD4	M-007178-02
NHLRC1	M-027323-00	NSMCE1	M-007157-01
PDZRN3	M-023265-01	PHF7	M-019179-00
PJA1	M-007045-01	PJA2	M-006916-00
PRP19	M-004668-02	RCHY1	M-006966-01
RFPL1	M-006553-01	RFPL2	M-006935-01
RFPL3	M-006934-00	RFWD3	M-017095-01
RKHD1	M-031965-00	RKHD2	M-006989-00
RKHD3	M-022292-00	RNF10	M-006918-01
RNF103	M-006594-00	RNF11	M-006971-01
RNF111	M-007002-01	RNF12	M-006982-01
RNF121	M-007011-02	RNF122	M-007068-00
RNF123	M-007041-00	RNF125	M-007005-01
RNF126	M-007015-01	RNF127	M-007067-01
RNF128	M-007061-01	TRIM60	M-007153-00
RNF13	M-006944-01	RNF130	M-007021-00
RNF133	M-007155-00	PCGF6	M-007084-01
RNF135	M-007087-01	RNF137	M-007007-01
RNF138	M-006991-01	RNF141	M-006980-00
RNF146	M-007080-00	RNF148	M-010758-00
RNF149	M-007169-00	RNF150	M-010713-01
RNF151	M-030777-00	RNF152	M-007160-00
MARCH5	M-007001-00	RNF157	M-022965-01
RNF159	M-007089-00	RNF166	M-007119-00
RNF167	M-006967-00	FLJ35794	M-007152-00
RNF17	M-007026-00	LOC285533	M-007170-00
RNF18	M-007030-00	LOC285671	M-017714-00
MGC33993	M-007162-00	MGC4734	M-007134-00
FLJ10546	M-020828-00	FLJ38628	M-007107-00
FLJ20225	M-006999-00	RNF187	M-021939-00
RNF19	M-006965-00	RNF2	M-006556-00
RNF20	M-007027-00	RNF24	M-006943-00
RNF25	M-007047-00	RNF26	M-007060-00
RNF28	M-007093-00	TRIM55	M-007092-00
RNF3	M-006926-00	TRIM54	M-007032-00
RNF34	M-007072-00	RNF36	M-007137-00
RNF39	M-007074-00	RNF40	M-006913-00

Plate 3

RNF41	M-006922-00	RNF44	M-006947-00
RNF5	M-006558-00	RUFY1	M-016355-00
SH3MD2	M-007037-00	SH3RF2	M-007145-00
SHPRH	M-007167-00	SIAH1	M-012598-01
SIAH2	M-006561-01	SMC4L1	M-006837-00
SMURF1	M-007191-00	SMURF2	M-007194-00
STUB1	M-007201-01	SUGT1	M-012877-00
MARCH6	M-006925-00	TMEPAI	M-010501-00
TRAF7	M-007086-00	TRIM10	M-006920-00
TRIM11	M-007075-00	TRIM15	M-007102-00
TRIM17	M-006981-00	TRIM2	M-006955-00
TRIM25	M-006585-00	TRIM3	M-006931-00
TRIM31	M-006939-00	TRIM34	M-006997-00
TRIM35	M-006952-01	TRIM36	M-007012-00
TRIM38	M-006929-00	TRIM39	M-007028-00
TRIM4	M-007101-00	TRIM40	M-007129-00
TRIM41	M-007105-00	TRIM42	M-007173-00
TRIM43	M-007127-00	TRIM45	M-007073-00
TRIM46	M-007071-00	TRIM47	M-007106-00
TRIM48	M-007059-00	TRIM5	M-007100-00
TRIM50A	M-007130-00	TRIM50C	M-031736-00
TRIM52	M-007095-00	TRIM56	M-007079-00
TRIM6	M-007121-00	FLJ10759	M-007010-00
LOC201292	M-018490-00	TRIM67	M-032288-00
TRIM7	M-007077-00	TRIM9	M-012974-00
TTC3	M-006570-00	UBE2L6	M-008569-00
UBE2N	M-003920-01	UBQLN2	M-013566-00
VPS11	M-007022-00	VPS41	M-006972-00
KIAA1374	M-023638-00	FLJ36175	M-007203-00
WSB1	M-013015-00	WSB2	M-017223-00
WWP1	M-004251-00	WWP2	M-004252-01
ZC3HDC5	M-022950-00	ZFPL1	M-019375-00
ZFYVE19	M-017961-00	ZNF179	M-006588-00
ZNF183	M-006590-00	ZNF183L1	M-007135-00
ZNF294	M-006968-00	ZNF313	M-007024-00
ZNF364	M-006974-00	ZNF598	M-007104-00
FLJ25735	M-007148-00	ZNF650	M-016653-00
ZNRF1	M-007098-00	ZNRF2	M-007165-00
FLJ12747	M-010747-00	ZNRF4	M-007141-00
ZSWIM2	M-007142-00		

Plate 4

ARIH1	M-019984-00	HERC4	M-021426-00
HERC5	M-005174-01	HERC6	M-005175-02
UBE3C	M-007183-00	UBE3B	M-007197-01
UBE3A	M-005137-00	MID1	M-006537-00
SSA1	M-006563-02	TRIM28	M-005046-01
TRIM32	M-006950-00	TRIM37	M-006538-01
TRIM23	M-006523-00	TRIM33	M-005392-02
TRAF6	M-004712-00	UHRF1	M-006977-00
UHRF2	M-007117-00	UBCE7IP5	M-006949-00
AMFR	M-006522-00	DTX2	M-007114-01
MID1	M-006537-00	PJA2	M-006916-00
RNF139	M-006942-00	RNF144	M-006912-00
RNF14	M-006906-01	RNF7	M-006907-01
RNF8	M-006900-00	RNF6	M-006559-00
RBX1	M-004087-01	LRSAM1	M-007103-00
UBAP1	M-017474-00	UBAP2	M-013168-00
ANUBL1	M-017760-00	UBL3	M-012786-00

UBL4	M-020658-00	UBL5	M-014320-00
BARD1	M-003873-00	MDM4	M-006536-01
UBR1	M-010691-01	UBR2	M-006954-00
EDD1	M-007189-01	CHFR	M-007018-01
TRIAD3	M-017305-00	PARK2	M-003603-00
NEDD4L	M-007187-01	NEDD8	M-020081-00
SAE1	M-006402-00	UBA2	M-005248-00
PML	M-006547-00	RFP	M-006552-00

De-ubiquitinating Enzyme Library

Plate 1

ATXN3L	M-024927-00	BAP1	M-005791-00
COPS5	M-005814-01	CXORF53	M-005798-02
CYLD	M-004609-00	DUB1A	M-028352-00
DUB3	M-027332-00	LOC391622	M-028355-00
FBX07	M-013606-00	FBX08	M-012435-00
FLJ14981	M-018630-00	JOSD1	M-017674-00
MJD	M-012013-00	MYSM1	M-005905-01
OTUB1	M-021061-00	OTUB2	M-010983-00
OTUD1	M-026487-00	OTUD4	M-009927-00
OTUD5	M-013823-00	OTUD6B	M-008553-00
OTUD7A	M-008841-00	PARP11	M-016115-00
PRPF8	M-012252-01	PSMD14	M-006024-00
SBBI54	M-015500-00	SENP2	M-006033-00
SHFM3P1	M-009706-01	STAMBP	M-012202-00
STAMBPL1	M-005783-01	TNFAIP3	M-009919-00
UBE1	M-004509-00	UBE1C	M-005249-00
UBE1DC1	M-006405-00	UBE1L	M-019759-00
UBE2A	M-009424-00	UBE2B	M-009930-00
UBE2C	M-004693-01	UBE2D1	M-009387-01
UBE2D2	M-010383-01	UBE2D3	M-008478-00
UBE2E1	M-008850-01	UBE2E2	M-031782-00
UBE2E3	M-008845-00	UBE2G1	M-010154-01
UBE2G2	M-009095-01	UBE2H	M-009134-00
UBE2I	M-004910-00	UBE2J1	M-007266-00
UBE2J2	M-008614-00	UBE2L3	M-010384-01
UBE2L6	M-008569-00	UBE2M	M-004348-00
UBE2N	M-003920-01	UBE2NL	M-031625-00
UBE2Q	M-008631-01	UBE2R2	M-009700-01
UBE2S	M-009707-00	UBE2V2	M-008823-00
UBE3A	M-005137-00	UBE3B	M-007197-01
UBE4A	M-007200-00	UBE4B	M-007202-01
UBL3	M-012786-00	UBL4	M-020658-00
UBL5	M-014320-00	UBR1	M-010691-01
UBTD1	M-018385-00	UCHL1	M-004309-00
UCHL3	M-006059-00	UCHL5	M-006060-01
UEV3	M-008494-00	UFD1L	M-017918-00
USP1	M-006061-01	USP10	M-006062-01
USP11	M-006063-00	USP12	M-027148-00
USP13	M-006064-00	USP14	M-006065-01
USP15	M-006066-00	USP16	M-006067-00

Plate 2

USP18	M-004236-02	USP19	M-006068-01
USP2	M-006069-00	USP20	M-006070-01
USP21	M-006071-00	USP22	M-006072-00
USP24	M-006073-01	USP25	M-006074-01
USP26	M-006075-01	USP28	M-006076-01

USP29	M-006077-00	USP3	M-006078-01
USP30	M-021294-02	USP31	M-022513-00
USP32	M-006080-01	USP33	M-006081-00
USP34	M-006082-00	USP35	M-006083-01
USP36	M-006084-01	USP37	M-006086-01
USP38	M-006086-01	USP39	M-006087-00
USP4	M-004974-01	USP40	M-006088-00
USP41	M-031434-00	USP42	M-006089-00
USP43	M-023019-00	USP44	M-006091-00
USP45	M-010054-00	USP46	M-006092-02
USP47	M-006093-00	USP48	M-006079-01
TRFP	M-006094-00	USP5	M-006095-00
USP50	M-031837-00	USP51	M-032247-00
USP52	M-021192-00	USP53	M-027186-00
USP54	M-016853-00	USP6	M-006096-02
USP7	M-006097-00	USP8	M-005203-01
USP9X	M-006099-01	USP9Y	M-006100-01
VCPIP1	M-019137-00	YOD1	M-027369-00
ZA20D1	M-008670-00	ZRANB1	M-009270-00
SENP8	M-004071-00	SENP5	M-005946-01
SENP3	M-006034-00	SENP1	M-006357-00
PSMD7	M-009621-01	LOC220594	M-016888-01
MGC5306	M-014314-01	EIF3S3	M-003883-00
COPS8	M-015831-01		

Controls

CTRL #1	D-001210-01	CTRL #2	D-001210-02
ITGB1 #1	D-004506-01	RHOA #1	D-003860-04

For each 96 well plate, 1 x 10^4 A431 cells were seeded per well in two 48 well plates and transfected as previously described (Section 2.2.5.1). Forty-eight hours after transfection, the cells were trypsinised and plated in 250µl of standard media on deformable collagen-Matrigel® gels (Section 2.2.7) in 8 well Lab-Tek™ II chambered coverglasses (NUNC™, UK). Cells were allowed to adhere for a further 24 hours before fixing with 4% paraformaldehyde (PFA) for 10 minutes.

For visualisation, cells were permeabilised with 0.25% Triton® X-100 for 10 minutes, blocked in 3% BSA in PBS for 1 hour and then stained with TRITC phalloidin (Sigma-Aldrich®, UK) and DAPI (Sigma-Aldrich®, UK).

Screening of cell phenotypes was done blindly, in duplicate and scored independently by three individuals.

2.2.6.2 De-convolution of siRNA SMARTpools

SMARTpool upgrade kits were purchased from Dharmacon® and individual siRNA duplexes reconstituted to stock solutions of 20μM. The oligonucleotides were then arranged in a 96 well plate format at a concentration of 2μM to facilitate screening as outlined above.

The gene symbols, gene descriptions and Dharmacon® catalogue numbers of the SMARTpool upgrade kits are shown below.

E3 Ubiquitin Ligases

CDC26	Cell division cycle 26	MU-017290-00
DKFZp761H1710	Hypothetical protein DKFZp761H1710	MU-007082-00
FLJ20315	Hypothetical protein FLJ20315	MU-007004-00
LOC389822	Hypothetical protein LOC389822	MU-029504-00
MARCH3	Membrane-associated ring finger 3	MU-007116-00
MKRN2	Makorin, ring finger protein 2	MU-006960-00
PJA1	Praja 1	MU-007045-00
RFWD3	Ring finger and WD repeat domain 3	MU-017095-00
RKHD2	Ring finger and KH domain containing 2	MU-006989-00
RNF11	Ring finger protein 11	MU-006971-00
RNF12	Ring finger protein 12	MU-006982-00
RNF123	Ring finger protein 123	MU-007041-00
RNF126	Ring finger protein 126	MU-007015-00
FLJ10546	Hypothetical protein FLJ10546	MU-020828-00
RNF2	Ring finger protein 2	MU-006556-00
RNF41	Ring finger protein 41	MU-006922-00
RNF44	Ring finger protein 44	MU-006947-00
RNF5	Ring finger protein 5	MU-006558-00
SUGT1	SGT1, suppressor of G2 allele of SKP1	MU-012877-00
TRIM11	Tripartite motif-containing 11	MU-007075-00
TRIM3	Tripartite motif-containing 3	MU-006931-00
TRIM4	Tripartite motif-containing 4	MU-007101-00
VPS11	Vacuolar protein sorting 11	MU-007022-00
ZNF364	Zinc finger protein 364	MU-006974-00
ZNF598	Zinc finger protein 598	MU-007104-00
FLJ12747	Novel C3HC4 type zinc finger	MU-010747-00
HERC4	Hect domain and RLD 4	MU-021426-00
HERC6	Hect domain and RLD 6	MU-005175-02
UBE3A	Ubiquitin protein ligase E3A	MU-005137-00
TRIM33	Tripartite motif-containing 33	MU-005392-02
TRAF6	TNF receptor-associated factor 6	MU-004712-00
RNF14	Ring finger protein 14	MU-006906-01
Mdm4	Mdm4	MU-006536-01
SAE1	SUMO-1 activating enzyme subunit 1	MU-006402-00

De-ubiquitinating Enzymes

BAP1	BRCA1 associated protein-1	MU-005791-00
DUB1A	De-ubiquitinating enzyme 1A	MU-028352-00
DUB3	De-ubiquitinating enzyme 3	MU-027332-00

OTUD7A	OTU domain containing 7A	MU-008841-00
FLJ14981	Hypothetical protein FLJ14981	MU-018630-00
USP12	Ubiquitin specific protease 12	MU-027148-00
USP2	Ubiquitin specific protease 2	MU-006069-00
TRFP	Trf-proximal homolog	MU-006094-00
ZA20d1	Zinc finger, A20 domain containing 1	MU-008670-00
USP6	Ubiquitin specific protease 6	MU-006096-02
PSMD7	Proteasome 26S subunit, non-ATPase 7	MU-009621-01

2.2.6.3 siRNA screening in HNCAF

Two individual siRNA duplexes were selected for each '2nd Round' gene hit and arranged in a 96 well plate at a concentration of 2μM. 8 x 10^3 HNCAF were plated per well in two 48 well plates and screening carried out as previously described (Sections 2.2.5.1 and 2.2.6.1). If both duplexes produced a consistent phenotype the gene was retained for further study and was designated a 'CAF' hit.

The target gene, oligonucleotide name and Dharmacon® catalogue number for each siRNA duplex included in this screen is listed below.

E3 Ubiquitin Ligases

CDC26	CDC26 #2	D-017290-02
	CDC26 #4	D-017290-04
MARCH3	MARCH3 #1	D-007116-01
	MARCH3 #3	D-007116-03
MKRN2	MKRN2 #1	D-006960-01
	MKRN2 #4	D-006960-04
PJA1	PJA1 #2	D-007045-02
	PJA1 #4	D-007045-04
RFWD3	RFWD3 #2	D-017095-02
	RFWD3 #4	D-017095-04
RKHD2	RKHD2 #1	D-006989-01
	RKHD2 #4	D-006989-04
RNF12	RNF12 #3	D-006982-03
	RNF12 #4	D-006982-04
RNF126	RNF126 #1	D-007015-01
	RNF126 #3	D-007015-03
FLJ10546	FLJ10546 #3	D-020828-03
	FLJ10546 #4	D-020828-04
RNF2	RNF2 #1	D-006556-01
	RNF2 #3	D-006556-03
RNF41	RNF41 #3	D-006922-03
	RNF41 #4	D-006922-04
SUGT1	SUGT1 #3	D-012877-03
	SUGT1 #4	D-012877-04
TRIM11	TRIM11 #2	D-007075-02
	TRIM11 #3	D-007075-03
ZNF598	ZNF598 #2	D-007104-02
	ZNF598 #3	D-007104-03

HERC4	HERC4 #3	D-021426-03
	HERC4 #4	D-021426-04
HERC6	HERC6 #3	D-005175-04
	HERC6 #4	D-005175-06
TRAF6	TRAF6 #2	D-004712-02
	TRAF6 #3	D-004712-03
RNF14	RNF14 #3	D-006906-03
	RNF14 #4	D-006906-04
Mdm4	Mdm4 #2	D-006536-03
	Mdm4 #3	D-006536-04
SAE1	SAE1 #1	D-006402-01
	SAE1 #4	D-006402-04

De-ubiquitinating Enzymes

BAP1	BAP1 #2	D-005791-02
	BAP1 #4	D-005791-04
DUB1A	DUB1A #2	D-028352-02
	DUB1A #3	D-028352-03
FLJ14981	FLJ14981 #2	D-018630-02
	FLJ14981 #3	D-018630-03
USP12	USP12 #3	D-027148-03
	USP12 #4	D-027148-04
USP2	USP2 #1	D-006069-01
	USP2 #4	D-006069-04
TRFP	TRFP #2	D-006094-02
	TRFP #4	D-006094-04
ZA20d1	ZA20d1 #1	D-008670-01
	ZA20d1 #3	D-008670-03
USP6	USP6 #2	D-006096-07
	USP6 #3	D-006096-08
PSMD7	PSMD7 #3	D-009621-03
	PSMD7 #4	D-009621-05

Controls

-	CTRL #1	D-001210-01
-	CTRL #2	D-001210-02
ITGB1	ITGB1 #1	D-004506-01
RHOA	RHOA #1	D-003860-04

2.2.6.4 Qiagen® siRNA screen

For the genes identified as potential candidates for detailed study four further siRNA duplexes were obtained. These were used initially to assess the validity of the cell phenotypes already observed in the A431 cells following gene silencing.

Individual siRNA duplexes were purchased from Qiagen® and reconstituted to stock solutions of either 10μM or 20μM dependent upon their formulation. The

oligonucleotides were then arranged in a 48 well plate format at a concentration of 2μM and screened in A431 cells as previously discussed (Section 2.2.6.1).

The target gene, oligonucleotide name and Qiagen® catalogue number for each siRNA duplex included in this screen is listed below.

E3 Ubiquitin Ligases

RKHD2	RKHD2 #A	S100703696
	RKHD2 #B	S103028487
	RKHD2 #C	S100703675
	RKHD2 #D	S100764862
TRAF6	TRAF6 #A	S103046043
	TRAF6 #B	S103050145
	TRAF6 #C	S100066101
	TRAF6 #D	S100066122

De-ubiquitinating Enzymes

ZA20d1	ZA20d1 #A	S100764869
	ZA20d1 #B	S100764876
	ZA20d1 #C	S100764855
	ZA20d1 #D	S100764862
USP6	USP6 #A	S102633442
	USP6 #B	S103032715
	USP6 #C	S100064512
	USP6 #D	S100064519

2.2.7 Collagen-Matrigel® matrix

The collagen-Matrigel® gel mix which formed the three-dimensional extra-cellular matrix used throughout the stages of siRNA screening consisted of rat tail collagen type 1 (typically 9.03mg/ml) mixed with 5X αMEM containing sodium bicarbonate, 20% Matrigel® (typically 11.2mg/ml) and 10% FCS. The volume was made up with standard media depending on the cell line being used in the assay (Section 2.2.1). The gel mix was then applied to 8 well Lab-Tek™ II chambered coverglasses using a sealed glass pipette; 45μl of gel being sufficient to cover a surface area of 0.7cm^2 per well. Finally, each gel was left to polymerise for 20 minutes at 37ºC to allow the collagen-Matrigel® matrix to be fully formed prior to seeding cells onto its surface.

2.2.8 Organotypic invasion assays

2.2.8.1 The organotypic culture system

The organotypic culture system was set up as previously described [77]. The constituents of a single organotypic collagen gel are listed below:

Organotypic collagen gel mix	µl
Matrigel® (11.2mg/ml)	200
Rat tail collagen type I (9.03mg/ml)	400
5X αMEM with sodium bicarbonate	80
FCS	100
FAD medium with 10% FCS	120
5 x 10^5 HNCAF suspended in FAD medium with 10% FCS	100
Total Volume	1000

The collagen gel mix was prepared on ice and 900µl of this solution aliquoted into wells of a 24 well plate and allowed to polymerise for 30 minutes at 37ºC. The final collagen concentration and Matrigel® concentration per gel was 3.612mg/ml and 2.24mg/ml respectively. Once the gels were set, 1ml of complete media was added per well and the gels left to equilibrate at 37ºC for 24 hours before changing the media daily thereafter.

A fibroblast-free collagen gel mix was also used to coat sterile nylon discs (Millipore™, UK). After incubating at 37ºC for 20 minutes, the gel coated discs were fixed in 1% glutaraldehyde for 1 hour, washed four times in PBS, twice in complete media and then stored at 4ºC.

At 72 hours, 5 x 10^5 SCC12 cells were seeded on to each gel in complete media. The next day, the gels were lifted on to individual collagen coated nylon discs resting on stainless steel bridges placed in 6 well plates. Sufficient complete media was then added to feed each organotypic culture from beneath the bridge thus allowing the epithelial layer to grow at an air-liquid interface. Media was changed daily throughout the duration of the assay.

One week following gel preparation, the cultures were fixed in either 4% paraformaldehyde (PFA) with 0.25% gluteraldehyde in PBS or 10% normal buffered formalin (NBF). After 4 hours, specimens were bisected, transferred to 70% EtOH and embedded in paraffin wax on their cut edge. 4µm sections taken at 50µm intervals were stained with haematoxylin and eosin (H&E) for quantitative analysis (Section 2.10.2). The processing, embedding and staining of samples was performed by the Cancer Research UK Experimental Histopathology Laboratory.

2.2.8.2 SCC invasion screen

SCC12 cells were transfected as outlined in Section 2.2.5.3 and after 24 hours plated on to organotypic collagen gels as above. Two individual siRNA duplexes were selected for each gene hit. The siRNA oligonucleotides included in this screen were those listed in Section 2.2.6.3.

Previous work from our group has established Cdc42 to be a key regulator of SCC12 carcinoma invasion in this system [77]. siRNA targeting Cdc42 was therefore used to assess the effect of gene knockdowns on invasion and acted as a positive control for transfection efficiency. Organotypic cultures in which SCC12 cells had either been transfected with a non-targeting siRNA duplex or were not transfected were also included. A collagen gel without fibroblasts was set up routinely in each assay.

Controls

-	CTRL #1	D-001210-01
CDC42	Cdc42 #2	HOOSA-000009

This screen was carried out over several months and assays which identified genes as being possible regulators of carcinoma invasion were repeated.

2.2.8.3 Inhibition of SCC invasion by HNCAF interference

To assess the influence of the 'CAF' gene hits on the ability of stromal fibroblasts to promote SCC invasion, a modified two-stage organotypic invasion assay was used.

This assay was performed twice and involved knocking down the genes of interest in HNCAF as described in Section 2.2.5.3. The next day, organotypic collagen gels were constructed as outlined in Section 2.2.8. After a further 5 days, the gels were photographed to document the degree of matrix contraction (Section 2.10.3) before being incubated in complete media with puromycin (5µg/ml) for 48 hours at 37ºC to kill the fibroblasts. Complete media was used to wash the gels four times; each wash being greater than 1 hour. 5 x 10^5 SCC12 cells were then plated on top of each gel and the organotypic cultures proceeded as usual.

Inhibition of ROCK in fibroblast-SCC co-cultures is known to reduce carcinoma invasion due to insufficient fibroblast-mediated matrix remodelling [77]. Hence, siRNA targeting ROCK1 and ROCK2 was selected as the positive transfection control. The target gene, oligonucleotide name and Dharmacon® or Qiagen® catalogue number for each siRNA duplex used in this assay is listed below.

<u>E3 Ubiquitin Ligases</u>

MKRN2	MKRN2 #1	D-006960-01
	MKRN2 #4	D-006960-04
RKHD2	RKHD2 #1	D-006989-01
	RKHD2 #4	D-006989-04
HERC4	HERC4 #3	D-021426-03
	HERC4 #4	D-021426-04
TRAF6	TRAF6 #2	D-004712-02
	TRAF6 #3	D-004712-03
Mdm4	Mdm4 #2	D-006536-03
	Mdm4 #3	D-006536-04
SAE1	SAE1 #1	D-006402-01
	SAE1 #4	D-006402-04

<u>De-ubiquitinating Enzymes</u>

ZA20d1	ZA20d1 #1	D-008670-01
	ZA20d1 #3	D-008670-03
USP6	USP6 #2	D-006096-07
	USP6 #3	D-006096-08

<u>Controls</u>

-	CTRL #4	D-001210-04
-	CTRL #Q	1027280
ROCK1	ROCK #1	D-003536-05
ROCK2	ROCK #2	D-004610-05

2.2.8.4 Validation of candidate genes as regulators of SCC invasion

Serial organotypic cultures as described in Section 2.2.8.1 were carried out using the siRNA oligonucleotides shown below:

TRAF6

TRAF6 #1	GGAGAAACCUGUUGUGAUUUU	D-004712-01
TRAF6 #2	GGACAAAGUUGCUGAAAUCUU	D-004712-02
TRAF6 #3	GUUCAUAGUUUGAGCGUUAUU	D-004712-03
TRAF6 #B	UACGCGAACGUGGAAGUCAAU	S103050145
TRAF6 #C	GUCCCUACUCAAAUUUGGGAU	S100066101
TRAF6 #D	GUCGCGACACGUUUGAUAUAU	S100066122

ZA20d1

ZA20d1 #1	GGACAUGGAUGCUGUUCUGUU	D-008670-01
ZA20d1 #2	GAAUCUAUCUGCCUUUGGAUU	D-008670-02
ZA20d1 #3	GAAGGAGAAUACCAAGGAAUU	D-008670-03
ZA20d1 #A	UUCCUCCGAUUUGUUUCAAUU	S100764869
ZA20d1 #B	GGCCGCCUUCCUCUUCAGUUU	S100764876
ZA20d1 #C	UUCCUCCAAGAGUCAGUUAUU	S100764855

Controls

CTRL #1	UAGCGACUAAACACAUCAA	D-001210-01
CTRL #Q	Sequence not specified	1027280
Cdc42 #2	AGACUCCUUUCUUGCUUGUUU	HOOSA-000009

In experiments where cells were depleted of both TRAF6 and ZA20d1, siRNA duplexes were added in equal concentration in the transfection mix. The final concentration of siRNA was 100nM.

2.2.8.5 A431 organotypic cultures

Organotypic assays were performed with A431 cells. Compared to SCC12 cells, A431 cells were intrinsically less invasive in this system and therefore the duration of the assays were lengthened to 2 weeks. Organotypic collagen gels were set up as described in Section 2.2.8 and allowed to remodel for 7 days before adding 5 x 10^5 A431 cells. The cultures then proceeded as normal until fixation on Day 14.

2.2.8.6 Investigating NF-κB signalling in SCC invasion

NF-κB signalling in our organotypic system was investigated using several cytokines and small molecule inhibitors. These were added to the medium which was changed daily throughout the duration of the assay. Doses varied according to the assay performed and are specified in the relevant section. The cytokines, inhibitors and their targets are listed below:

Cytokine / Inhibitor		Target	Source
Tumour Necrosis Factor alpha	TNFα	TNFRs	First Link UK Ltd.
Interleukin 1 alpha	IL-1α	IL-1Rs / TLRs	Calbiochem®, UK
IKK Inhibitor II	IKKI-II	IKKα / IKKβ	Calbiochem®, UK
IKK-2 Inhibitor	IKKI-2	IKKβ	Calbiochem®, UK
IKK Inhibitor III	IKKI-III	IKKβ	Calbiochem®, UK
IKK Inhibitor X	IKKI-X	IKK complex	Calbiochem®, UK

* Vehicles: IL-1α ~ BSA (0.1%) and IKK Inhibitors ~ DMSO (>99%)

Organotypic cultures were also performed with the daily addition of infliximab (Centocor BV, The Netherlands), a monoclonal antibody to TNFα in clinical use. This was a gift from Professor Martin Gore (The Royal Marsden Hospital, London).

2.3 Bacterial techniques

2.3.1 Bacterial media and plates

Escherichia coli (*E.coli*) bacteria were grown in suspension in either Luria-Bertani medium (LB) or Terrific Broth (TB) containing the appropriate antibiotic to select for the DNA construct of interest. Similarly, transformations were plated on to 10cm dishes with agar containing either ampicillin (50μg/ml), blasticidin (50μg/ml) or kanamycin (50μg/ml).

2.3.2 Bacterial strains

Novablue Competent Cells™ (Novagen®, UK) were used for transformations of all plasmids. Competent *E.coli* bacteria were generated as follows.

E.coli were grown overnight in 20ml LB medium at 37 °C. The next day 5ml of the 20ml culture was added to 500ml of fresh LB medium and the culture re-incubated at 37°C on a rotary shaker. When the optical density of the culture (measured at a wavelength of 600nm) reached 0.6, the flask was chilled on ice and centrifuged at 4,000rpm for 20 minutes at 4ºC. The supernatant was discarded and the pelleted bacteria re-suspended in 100ml of sterile Transformation Buffer 1 (TFB1).

The bacteria were again centrifuged at 4,000rpm at 4°C for 20 minutes, the supernatant removed and the pellet re-suspended in 20ml of chilled sterile Transformation Buffer 2 (TFB2). The bacterial suspension was kept on ice for 15 minutes before being aliquoted into 1.5ml Eppendorf tubes. The samples were then snap frozen in dry ice and placed in a -80ºC freezer for long-term storage.

Transformation Buffer 1 (TFB1)

Potassium acetate (CH_3COOK)	30mM
Manganese chloride ($MnCl_2$)	50mM
Potassium chloride (KCl)	100mM
Calcium chloride, ($CaCl_2$)	10mM
Glycerol	15 %

Transformation Buffer 2 (TFB2)

4-morpholinepropanesulfonic acid (MOPS)	10mM
Calcium chloride ($CaCl_2$)	76mM
Potassium chloride (KCl)	10mM
Glycerol	15 %
pH	7.0

2.3.3 Bacterial transformation

Competent *E.coli* bacteria were thawed on ice for 15 minutes. 130µl of bacterial suspension was mixed with 1µg of plasmid DNA and incubated on ice for a further 15 minutes. The competent cell-DNA mix was then heated in a water bath at 42ºC for exactly 90 seconds and returned to ice for 2 minutes. 800µl of LB was added to the bacteria before incubating them again for another 45 minutes at 37ºC. After centrifuging

at 4,000rpm for 5 minutes, the bacterial pellet was re-suspended in 200µl of LB. This bacterial suspension was spread over an agar plate containing the appropriate antibiotic and incubated overnight at 37ºC. The next day the plate was inspected for colony formation.

2.4 Plasmids

2.4.1 pUNO-hTRAF6-HA

The plasmid pUNO-hTRAF6-HA was purchased from InvivoGen™, (Autogen Bioclear UK Ltd.) and contained the hTRAF6 gene fused to the influenza haemagglutinin epitope tag (YPYDVPDYA x 3) at the 3' end. Features of the pUNO expression vector included: the human EF-1α / HTLV hybrid promoter, a multiple cloning region with convenient restriction enzyme sites, a polyadenylation signal, and the blasticidin resistance gene (*bsr*) driven by the SV40 promoter in tandem with the bacterial EM7 promoter.

2.5 Nucleic acid methods

2.5.1 Preparation of plasmid DNA

The preparation and purification of plasmid DNA from small volume overnight bacterial cultures was performed using the QIAfilter Plasmid Midi Kit (Qiagen®, UK). All buffers were supplied with the kit and all the steps were carried out at room temperature unless otherwise indicated.

Single colonies of *E.coli* bacteria transformed with the pUNO-hTRAF6-HA construct were inoculated into 50ml of InvivoGen™ BLAS TB medium (Autogen Bioclear UK Ltd.) and left to incubate overnight in 5% CO_2 at 37ºC. The next day pelleted bacteria were re-suspended in 4ml of Buffer P1, mixed with 4ml of Buffer P2 and left to stand for 5 minutes. After adding 4ml of chilled Buffer P3 the mixture was inverted gently

and left on ice for 20 minutes. The sample was then centrifuged at full speed at 4ºC for 30 and 15 minutes respectively.

After each centrifugation the DNA containing supernatant was removed and placed into a QIAGEN-tip which had previously been equilibrated with Buffer QBT. The tip was then washed twice with two 10ml aliquots of Buffer QC following which the DNA was eluted with 5ml of Buffer QF. DNA, precipitated by the subsequent addition of 3.5ml of isopropanol, was pelleted by centrifuging at 10,000rpm at 4ºC for 30 minutes. After washing with 2ml of 70% EtOH and a final centrifugation at 10,000rpm at 4ºC for 10 minutes, the DNA was air dried for 10 minutes and then dissolved in 500µl distilled water.

Buffer P1

Trizma® HCl	50mM
EDTA	10mM
RNase A	100µg/ml
pH	8.0

Buffer P2

Sodium hydroxide (NaOH)	200mM
SDS	1%

Buffer P3

Potassium acetate (CH_3COOK)	3M
pH	5.5

Buffer QBT

Sodium chloride (NaCl)	750mM
4-morpholinepropanesulfonic acid (MOPS)	50mM
Isopropanol (C_3H_7OH)	15%
Triton® X-100	15%
pH	5.5

Buffer QC

Sodium chloride (NaCl)	1M
4-morpholinepropanesulfonic acid (MOPS)	50mM
Isopropanol (C_3H_7OH)	15%
pH	7.0

Buffer QF

Sodium chloride (NaCl)	1.25M
Trizma® HCl	50mM
Isopropanol (C_3H_7OH)	15%
pH	8.5

2.5.2 Nucleic acid quantification

The concentration of nucleic acid from Midipreps was determined using a NanoDrop™ spectrophotometer (Thermo Fisher Scientific Inc., UK) which measures the absorbance of a 1µl sample at a wavelength of 260nm.

2.5.3 Preparation of RNA

The preparation and purification of RNA from cells grown in culture was performed using the RNeasy Mini Kit (Qiagen®, UK). All buffers were supplied with the kit and all the steps were carried out at room temperature unless otherwise stated. RNase-free tubes and pipette tips were used.

Typically 3 x 10^5 cells in a single well of a 6 well plate were lysed directly by the addition of 600µl of Buffer RLT containing 6µl of β-mercaptoethanol (β-ME). The lysate was homogenised in an RNase-free tube by passing it through a 20-gauge needle (0.9mm diameter) 15 times and 600µl of 70% EtOH was added. Up to 700µl of the sample was loaded into an RNeasy spin column and centrifuged at 10,000rpm for 15 seconds. The flow through was discarded and this step repeated until the whole sample had been transferred to the spin column. The column membrane was now washed by centrifuging with 350µl of Buffer RW1 at 10,000rpm for 15 seconds.

To reduce the risk of genomic DNA contamination, DNase digestion was carried out for 15 minutes on the column according to the manufacturer's instructions using the RNase-Free DNase Set (Qiagen®, UK). Following this, the membrane was washed again with Buffer RW1 as described above.

Finally, 500µl of Buffer RPE was spun through the column at 10,000rpm for 15 seconds twice. Once dry, the RNA was eluted in 50µl of RNase-free water and quantified using a NanoDrop™ spectrophotometer (Section 2.5.2).

Buffer RLT

Proprietary buffer containing guanindine thiocyanate ($C_2H_6N_4S$).

Buffer RW1

Proprietary buffer containing EtOH and guanindine thiocyanate ($C_2H_6N_4S$).

Buffer RPE

Proprietary buffer of unspecified composition.

2.5.4 Preparation of cDNA

Complementary DNA (cDNA) was prepared by reverse transcription as follows:

	µg
RNA template	2.0
Random Primer Mix (500µg/ml) *	1.0

The RNA-random primer mix was made up to a total volume of 14µl using nuclease-free water before heating to 75ºC for 5 minutes. After cooling on ice for a further 5 minutes, the following were added.

	µl
5X M-MLV Reverse Transcriptase Buffer *	5.0
dNTPs (10µM) *	5.0
M-MLV Reverse Transcriptase *	1.0
Reaction Volume	25.0

* Purchased from Promega, UK

The reaction mixture was allowed to equilibrate at room temperature for 10 minutes, before being heated to 40ºC for 50 minutes. 75µl of nuclease-free water was then added

to the resultant cDNA solution to a total volume of 100µl. cDNA samples were stored at -20ºC.

2.5.4.1 Generating a cDNA library

cDNA was generated from A431 gene depleted cells as described in Sections 2.2.5.2, 2.5.3 and 2.5.4. The siRNA oligonucleotides used for gene depletion are listed below:

E3 Ubiquitin Ligases	
RKHD2	RKHD2 #1, #2, #3, #4, #A, #B, #C and #D
TRAF6	TRAF6 #1, #2, #3, #4, #A, #B, #C and #D
De-ubiquitinating Enzymes	
ZA20d1	ZA20d1 #1, #2, #3, #4, #A, #B, #C and D
Controls	
MOCK	-
-	CTRL #1
RHOA	RHOA #1

2.5.5 Polymerase chain reaction (PCR)

Polymerase chain reactions (PCRs) were carried out using a GeneAmp® PCR System 2700 thermal cycler (Applied Biosystems™, UK) with the protocol detailed below.

PCR mix	µl
5X Phusion™ GC Buffer containing 7.7mM $MgCl_2$ **	5.0
dNTPs (10µM) *	2.0
DNA template (10ng)	0.5
Phusion™ DNA Polymerase **	0.5
Forward primer (10µM)	5.0
Reverse primer (10µM)	5.0
dH_2O	7.0
Reaction Volume	25.0

* Purchased from Promega, UK. ** Purchased from Finnzymes Inc., USA.

PCR temperature cycles

95ºC	5 minutes	

25-28 cycles of:

95ºC	1 minute	Denaturing
54ºC	1 minute	Annealing
72ºC	1 minute	Extension
72ºC	10 minutes	
4ºC	Hold	

2.5.5.1 Primer design

Primer 3 software (Whitehead Institute for Biomedical Research, USA) was used to design forward and reverse DNA primers which would generate gene products of 150-250 base pairs. A BLAST search for each oligonucleotide sequence was conducted against the human genome to assess gene specificity prior to ordering it from Sigma-Aldrich®, UK. At least 2 pairs of primers were constructed for each gene of interest and their respective PCR products verified by agarose gel electrophoresis (Section 2.5.7). The details of regularly used primers are shown below.

E3 Ubiquitin Ligases

Gene	Primer	Sequence	TmºC	Product Size (bp)
RKHD2	1F	GGAGAAAGAGCGTCAACACC	59.85	190
	1R	GCCATGGCAACATCTTCTTT	60.08	
	2F	GGAGAAAGAGCGTCAACACC	59.85	248
	2R	GTTTCGAGATGCACGAATCA	59.81	
TRAF6	1F	CTGCAAAGCCTGCATCATAA	59.98	224
	1R	GGGGACAATCCATAAGAGCA	59.89	
	2F	TGCCATGAAAAGATGCAGAG	59.95	174
	2R	AAGGCGACCCTCTAACTGGT	60.13	

De-ubiquitinating Enzymes

Gene	Primer	Sequence	TmºC	Product Size (bp)
ZA20d1	1F	CACGTCTTTGTCCTTGCTCA	60.02	202
	1R	TGGACACGAGTGCAGAAAAG	60.02	
	2F	CATTTGCCCCTATTCCCTTT	60.14	195
	2R	GCAAGGGCAGCAGCTTATAC	60.01	

Control Genes	Primer	Sequence	TmºC	Product Size (bp)
GAPDH	1F	CGACCACTTTGTCAAGCTCA	60.02	203
	1R	AGGGGAGATTCAGTGTGGTG	59.96	
	2F	ACGGATTTGGTCGTATTGGGC	65.17	157
	2R	TTGACGGTGCCATGGAATTTG	66.10	
RHOA	1F	AAGGACCAGTTCCCAGAGGT	59.97	228
	1R	TTCTGGGGTCCACTTTTCTG	60.08	
	2F	GTGCCCACAGTGTTTGAGAA	59.73	171
	2R	ACTATCAGGGCTGTCGATGG	60.10	

DNA oligonucleotides were reconstituted to stock solutions of 100µM using Milli-Q™ water according to the manufacturer's instruction. For PCR, 10µM secondary stock solutions were used.

2.5.6 Quantitative PCR (qPCR)

Platinum® SYBR® Green qPCR SuperMix-UDG with ROX (Invitrogen, UK) was used for the amplification and detection of DNA in real-time quantitative PCR (qPCR) in conjunction with the 7900HT Fast Real-Time PCR System (Applied Biosystems™, UK).

Platinum® SYBR® Green qPCR SuperMix-UDG with ROX

Platinum® *Taq* DNA polymerase	
SYBR® Green I dye	
Trizma® HCl	
Potassium chloride (KCl)	
Magnesium chloride ($MgCl_2$)	6mM
dGTP	400µM
dATP	400µM
dCTP	400µM
dUTP	800µM
Uracil DNA glycosylase (UDG)	
ROX Reference Dye	1µM
Stabilizers	

All real-time polymerase chain reactions (qPCRs) were carried out in an ABI Prism™ 96 well optical reaction plate (Applied Biosystems™, UK) and were set up on ice. The protocol for a single reaction is detailed below.

qPCR mix	µl
DNA template (10ng)	0.5
Platinum® SYBR® Green qPCR SuperMix-UDG with ROX	12.5
Forward primer (10µM)	0.5
Reverse primer (10µM)	0.5
Milli-Q™ H_2O	11.0
Reaction Volume	25.0

PCR temperature cycles

50ºC	2 minutes	UDG incubation
95ºC	2 minutes	

40 cycles of:

95ºC	15 seconds	Denaturing
60ºC	30 seconds	Annealing / Extension
4ºC	Hold	

2.5.7 Agarose gel electrophoresis

DNA samples (10µl) were mixed with 5µl of 6X gel loading buffer (0.25% bromophenol blue and 0.25% xylene cyanol in 30% glycerol) and loaded into the lanes of an agarose gel. 0.8% to 2% agarose gels were selected according to the size of the DNA fragments being separated. Ethidium bromide (Sigma-Aldrich®, UK), at a final concentration of 5µg/ml, was added to the agarose during the gel casting process and gel electrophoresis was performed in 0.5X TBE buffer at 70 volts for 1-2 hours. The DNA was visualised using a UV transilluminator with a wavelength of 254nm.

2.5.8 Purification of DNA from agarose gels

DNA bands cut from agarose gels were purified using an illustra™ GFX™ PCR DNA and Gel Band Purification Kit (GE Healthcare UK Ltd.) according to the manufacturer's instructions.

In summary, the agarose band containing DNA was dissolved in 300µl of Capture Buffer Type 3 by heating to 60ºC for 15 minutes before being transferred to an assembled GFX MicroSpin™ column and collection tube. After centrifugation at 13,000rpm for 30 seconds, the column was washed with 500µl of Wash Buffer Type 1. Once dry, the DNA was eluted in 20-50µl of distilled water and quantified using a NanoDrop™ spectrophotometer (Section 2.5.2).

Capture Buffer Type 3

Proprietary buffer of unspecified composition containing a pH indicator to visually identify the optimal time for DNA binding to the silica membrane of the column.

Wash Buffer Type 1

Proprietary buffer of unspecified composition containing EtOH.

2.5.9 DNA sequencing

DNA constructs were sequenced using the Big Dye® Terminator (BDT) Kit (Applied Biosystems™, UK) in accordance with the manufacturer's instructions. Each sequencing reaction consisted of:

Sequencing mix	µl
DNA template (100ng)	1.0
BDT reaction mix	8.0
Primer (3.2pmol)	1.0
dH_2O	10.0
Reaction Volume	20.0

Sequence temperature cycles

95ºC	1 minute	

25 cycles of:

96ºC	10 seconds	Denaturing
61ºC	5 seconds	Annealing
60ºC	4 minutes	Extension
4ºC	Hold	

Sequencing reactions were purified using PERFORMA® DTR Gel Filtration Cartridges (EdgeBio,USA). After air drying at room temperature, the DNA was analysed by an in house research services laboratory (Cancer Research UK Equipment Park).

2.6 Protein methods

2.6.1 Preparation of cell lysates for Western blotting

Cells were cultured in 6 well plates. After washing once with PBS on ice, cells were lysed directly by the addition of 150-250µl of 1X SDS gel loading buffer per well. Lysates were sonicated three times for 5 seconds each and heated to 95ºC for 5 minutes prior to being stored at -80ºC.

2.6.2 SDS-PAGE gel electrophoresis

Samples were separated by electrophoresis under reducing conditions using 1.5mm 10% SDS-polyacrylamide mini-gels constructed as follows:

Running Gel Layer		µl
SDS	10%	100
Trizma® HCl at pH 8.8	1M	3,750
Acrylamide	40%	2,500
Ammonium persulphate	20%	50
TEMED		10
dH_2O		3,590
Total Volume		10,000

Once poured, the running gel was overlaid with water and allowed to polymerise for 20 minutes. When set, a 5% stacking gel was prepared as shown below:

Stacking Gel Layer		µl
SDS	10%	50
Trizma® HCl at pH 6.8	1M	625
Acrylamide	40%	625
Ammonium persulphate	20%	25
TEMED		5
dH_2O		3,670
Total Volume		5,000

The overlay water was decanted and the stacking gel poured. A 10 or 15 well comb was then inserted into the stacking gel mix, being careful not to introduce any air bubbles. The stacking gel layer was allowed to set over 45 minutes.

The comb was removed and the wells rinsed with distilled water. The SDS-PAGE mini-gel was now transferred to a running tank (Bio-Rad Laboratories Ltd., UK) which was in turn filled with SDS running buffer (Section 2.1.1). Each well was loaded with up to 25µl of sample and one lane was used to run a pre-stained protein ladder with the range of 10-200kDa (Benchmark™, Invitrogen, UK). Gels were run at 25mA for 2 hours.

2.6.3 Western blotting

After protein separation was complete and having removed the stacking gel layer, the SDS-PAGE mini-gel was allowed to equilibrate in transfer buffer (Section 2.1.1) for 15 minutes. The Protran™ nitrocellulose membrane (Whatman™, UK) on to which the proteins were to be blotted was also equilibrated for a similar period.

The membrane, closely apposed to the gel, was placed between two sheets of 3MM chromatography paper (Whatman™, UK) and two fibre pads. This ‘gel sandwich’ was positioned in a transfer cassette and loaded into a Mini Trans-Blot® electrophoretic transfer cell (Bio-Rad Laboratories Ltd., UK). A frozen Bio-Ice cooling unit was put in the transfer tank which was then filled with chilled transfer buffer. Electrophorectic transfer was performed at 100volts over 90 minutes on ice.

The uniformity and overall effectiveness of the transfer of protein from the gel to the membrane was assessed by staining the membrane with Ponceau S solution (0.1% Ponceau S and 5% acetic acid). This was then removed by washing with distilled water before blocking the membrane for 1 hour in 5% milk (Marvel™, Cadbury, UK) + TBS-Tween20 solution (Section 2.1.1) at room temperature. Primary antibodies, generally used at a dilution of 1:1000 in 5% BSA + TBS-Tween20 solution, were applied to the membrane by incubating overnight at 4ºC.

The next day, the membrane was washed three times in TBS-Tween20 solution (5 minutes per wash) and incubated for a further hour at room temperature with an HRP-conjugated secondary antibody (Thermo Fisher Scientific Inc., UK). Secondary antibodies were diluted 1:50,000 in 5% milk + TBS-Tween20 solution. After three further washes as above, the membrane was rinsed for 5 minutes in 2ml of either 'West Dura' or 'West Pico' SuperSignal® Chemiluminescent Substrate (Thermo Fisher Scientific Inc., UK). Finally, the blot was developed by exposing the membrane to chemiluminescent film (GE Healthcare UK Ltd.).

2.6.4 Primary antibodies used for Western blotting

Antibody / Target	Mol Wt*	Dilution	Species	Source
TRAF6	64	1:2000	Rabbit	Abcam®
Phospho-NF-κB p65 (Ser536)	65	1:1000	Rabbit	Cell Signaling Technology®
Phospho-IκBα (Ser32)	41	1:1000	Rabbit	Cell Signaling Technology®
Phospho-IKKα/β	85 / 87	1:1000	Rabbit	Cell Signaling Technology®
NF-κB p65	65	1:1000	Rabbit	Cell Signaling Technology®
IκBα	39	1:1000	Mouse	Cell Signaling Technology®
IKKα	85	1:1000	Rabbit	Cell Signaling Technology®
β-Tubulin 1	55	1:200000	Mouse	Sigma-Aldrich®

* Molecular Weight in kilodaltons (kDa)

2.6.5 Secondary probing of Western blots

Nitrocellulose membranes were "stripped" of antibodies by washing for 10 minutes twice with stripping buffer (Section 2.1.1). After washing two times in TBS-Tween20 solution (5 minutes per wash), the 'stripped' membrane was blocked for 1 hour in 5% milk + TBS-Tween20 solution at room temperature and then re-probed with primary antibody as outlined above.

2.7 Immunohistochemistry (IHC)

The following techniques were performed in conjunction with Emma Nye (Operational Head of the Cancer Research UK Experimental Histopathology Laboratory).

2.7.1 Optimisation of antibodies

A431 cell pellets were used to optimise antibodies for immunohistochemistry (IHC). Dependent upon the antibody, cells were gene depleted / DNA transfected or cytokine stimulated / inhibited prior to pelleting.

For a single cell pellet approximately 1 x 10^6 A431 cells were washed with PBS before being gently lifted and pipetted into an Eppendorf tube. After centrifugation at 10,000rpm for 1 minute, the cells were fixed in 500µl of 10% NBF for 30 minutes. The NBF was then replaced by 70% EtOH and the pellet embedded in paraffin wax for processing by standard methods thereafter.

2.7.2 Paraffin sections

Paraffin embedded specimens (4µm thick) were mounted on poly-L-lysine coated slides before being de-waxed in xylene and dehydrated by passage through graded alcohols to water. Endogenous peroxidase activity was blocked using 1.6% hydrogen peroxide (H_2O_2) in PBS for 10 minutes followed by washing in distilled water. Antigen retrieval was performed by immersing samples in sodium citrate buffer and microwaving three times for 5 minutes at full power. Sections were then cooled to room temperature in running water and washed in PBS prior to blocking in goat serum diluted to 10% in 1% BSA for 30 minutes. This step was included to reduce non-specific staining.

Slides were incubated with primary antibody (Section 2.7.3) in 1% BSA for 1 hour at room temperature. After washing in PBS-Tween20 solution for 1 minute, biotinylated goat anti-rabbit secondary antibody (1:250 in 1% BSA) was then applied to the sections for 45 minutes, also at room temperature. Samples were washed as above and developed microscopically with VECTASTAIN® Elite ABC Reagent and Vector DAB substrate (Vector Laboratories Ltd., UK). A final wash in water was performed before the sections were counterstained lightly with haematoxylin, dehydrated, cleared and mounted.

Omission of the primary antibody acted as a negative control. Positive controls varied according to the nature of the assay and are specified in the relevant sections. A single section of all samples was routinely stained with H&E.

Sodium Citrate Buffer

Sodium Citrate	10mM
Tween20	0.05%
pH	6.0

PBS-Tween20 solution

10ml 20% Tween20 and 990ml 1X PBS

2.7.3 Primary antibodies used for IHC (paraffin sections)

Antibody / Target	Dilution	Species	Source
TRAF6	1:20	Rabbit	Abcam®
NF-κB p65	1:50	Rabbit	Cell Signaling Technology®
IκBα	1:20	Mouse	Cell Signaling Technology®
Vimentin	1:200	Rabbit	Abcam®
Pan-cytokeratin AE1 / AE3	1:100	Mouse	Dako

2.7.4 Frozen sections

Frozen sections (5µm thick) were cut on to poly-L-lysine coated glass slides and stored at -80ºC. Staining was performed at room temperature unless otherwise indicated and all steps were separated by three 5 minute washes with PBS.

Once thawed, sections were fixed in 4% PFA for 10 minutes and permeabilised with 0.2% Triton® X-100 for a further 10 minutes. Samples were then treated with sodium borohydride 2mg/ml (Sigma-Aldrich®, UK) for 5 minutes and blocked for 1 hour with 3% BSA.

Following blocking, slides were incubated with primary antibody (Section 2.7.5) in 3% BSA overnight at 4ºC. For visualisation, Alexa Fluor® secondary antibodies (Invitrogen, UK), TRITC phalloidin and DAPI each diluted to a concentration of 1:500 in 3% BSA were applied to the sections over 2 hours in darkness. After three final washes, the tissue samples were mounted and imaged by confocal microscopy.

Omission of the primary antibody acted as a negative control. As with paraffin embedded specimens, a single section of all frozen tissue samples was routinely stained with H&E.

2.7.5 Primary antibodies used for IHC (frozen sections)

Antibody / Target	Dilution	Species	Source
TRAF6	1:100	Rabbit	Abcam®
Collagen IV	1:100	Mouse	Abcam®

2.7.6 Commercial tissue microarrays

To investigate the clinical relevance of TRAF6 as a potential biological marker and therapeutic target, paraffin embedded tissue microarrays were purchased from US Biomax Inc. for immunohistochemical analysis. These are listed below.

Tissue Microarray	Cores	Cases		Catalogue No.
		Tumour	Normal	
SCCHN	63	20	3	BC34011
OSCC	60	50	10	OR601
Vulval SCC	24	10	2	UV241
CSCC	48	40	8	SK483

Microarrays were bought in triplicate and processed as outlined in Section 2.7.2. Paraffin embedded A431 cell pellets with and without TRAF6-HA expressing cells (Section 2.7.1) acted as positive controls and were stained alongside the tissue arrays. The analysis of and quantification of TRAF6 expression in these samples is described in Section 2.10.5. Several cores were missing from the supplied arrays and therefore the number of samples included in the final analysis of each array differed from that listed above.

2.8 Human tissue banking

Ethical and R&D approval was obtained for the establishment of a human tissue bank of SCCHN specimens with patient matched control tissue samples. The process of setting up the tissue bank and its management are described in detail in Chapter 8, Section 8.2.

2.9 Microscopy techniques

2.9.1 Immunofluorescence (IMF)

Approximately 1 x 10^4 A431 cells were seeded on to glass coverslips in 24 well plates. Twenty-four hours later the cells were washed once with PBS and fixed in 4% PFA for 20 minutes on ice. After being permeabilised with 0.2% Triton® X-100 for 10 minutes, the cells were washed three times with PBS and blocked for 1 hour with 2% BSA.

Following blocking, the cells were incubated with primary antibody (Section 2.9.2) in 2% BSA for 2 hours at room temperature. For visualisation, Alexa Fluor® secondary antibodies (1:300), TRITC phalloidin (1:500) and DAPI (1:500) in 2% BSA were applied over 2 hours in darkness. After three further washes, the coverslips were mounted using Mowiol® medium (Sigma-Aldrich®, UK) and imaged by confocal microscopy. Omission of the primary antibody acted as a negative control.

2.9.2 Primary antibodies used for IMF

Antibody / Target	Dilution	Species	Source
TRAF6	1:50	Rabbit	Abcam®
TRAF6	1:50	Rabbit	Santa Cruz Biotechnology, Inc
NF-κB p65	1:50	Rabbit	Cell Signaling Technology®
Integrin β1	1:250	Mouse	Santa Cruz Biotechnology, Inc

2.9.3 Imaging

A Nikon TE2000-S equipped with a Nikon DS-5M camera was used for routine viewing of cell cultures and to capture images of H&E and immunostained sections. All other imaging was performed using a Zeiss LSM 510 inverted confocal microscope.

2.9.4 Confocal imaging of human tissue samples

Frozen sections of SCCHN and matched normal tissue samples were prepared for confocal microscopy as described in Section 2.7.4. GFP, TRITC and Cy5 fluorophores were imaged using standard lasers and filter sets. DAPI was imaged using two-photon excitation in response to an 840nm pulsed titanium sapphire laser.

2.10 Data analysis

2.10.1 Assessment of cell morphology

Gene silencing in A431 cells and HNCAF was accompanied by a variety of cell phenotypes compared to control cells. These included cell rounding, cell elongation, actin-rich micro-spikes, lamellipodial extensions and membrane blebbing. For the siRNA screens previously described, cell morphology was assessed qualitatively and scored descriptively by at least two independent observers. Each screen was blind and performed twice. Genes were retained for further study if there was a high degree of concordance with respect to the cytoskeletal changes recorded amongst observers.

Representative confocal images were taken of the cell phenotypes induced by gene silencing at successive rounds of screening. Zeiss LSM Image Browser was used to examine the F-actin cytoskeleton and cell morphology of gene knockdowns more closely but a detailed quantitative morphometric analysis was not undertaken.

2.10.2 The Invasion Index

Carcinoma cell invasion in the organotypic gel culture system was assessed using an Invasion Index as previously described [77, 302].

H&E stained sections of organotypic cultures were viewed at 20x magnification and 5 areas of each gel captured. The digital images were loaded into Image J software (NIMH, USA) and for each image the 'invading' and non-invading areas measured. The 'invading' area included both the region of SCC dispersion within the gel and the surface or 'epithelial' layer of non-invading cells.

The Invasion Index was defined as 1 - (Non-invading Area / Invading Area) where a value of 0 represented no invasion. For each organotypic culture, the Invasion Index was an average of 5 measurements.

2.10.3 The Contraction Index

For two-stage organotypic assays (Section 2.2.8.3) gels were photographed after 5 days of matrix remodelling just prior to the removal of HNCAF with puromycin. The degree of gel contraction was then assessed by using Image J software to measure the surface area of the gel relative to its well. The Contraction Index was subsequently calculated by using the formula 1 - (Gel Area / Well Area) where a value of 0 represented no contraction [303].

2.10.4 Apoptotic counts in gene depleted cells

DAPI stained siRNA gene depleted A431 cells on collagen-Matrigel® gels were imaged at 20x magnification 72 hours following transfection. Five images per sample were captured and the percentage of apoptotic cells per visual field calculated.

2.10.5 Quantitative analysis of TRAF6 IHC

TRAF6 immunostained sections were viewed at 20x magnification and 3 images per sample captured. Digital images were loaded into NIS Elements software (Nikon UK Ltd) and 10 representative immunostained areas were selected for analysis per sample. TRAF6 immunostaining was cytosolic in nature and therefore cell nuclei were not included in the regions analysed to avoid positively skewing the data. The mean absolute pixel intensity within each region of interest was measured and normalised to a 'white balanced' area of the image by subtracting the background pixel intensity. This normalised value was then expressed on a scale of 0 to 1, with 0 representing absolute whiteness and 1 absolute blackness. The mean and standard error of the 10 measurements was calculated to give an overall measure of mean pixel intensity for TRAF6 immunostained regions per sample. Neither the relative proportion of TRAF6 positive cells nor their distribution within each sample was recorded.

2.10.6 Statistical analysis

NCSS Statistical Power & Analysis software was used to perform:

(a) ANOVA for randomized block design tests to assess statistical significance of differences in carcinoma cell invasion within single and between duplicate organotypic assays. p values were Bonferroni corrected depending on the nature of the assay and ranged from $p < 0.007$ to $p < 0.05$.

(b) Kruskal-Wallis non-parametric ANOVA to assess statistical significance of the percentage of apoptotic cells following siRNA gene depletion compared to mock transfected samples; p value < 0.05 (Chapter 5, Section 5.4.5).

Chapter 3

Morphological siRNA screening

3.1 Introduction

Cancer cell invasion and cell motility are accompanied by dramatic changes of cell phenotype as well as dynamic interactions with the surrounding ECM. To test the hypothesis that ubiquitin-linked pathways are key regulators of the actin cytoskeleton a series of morphological screens using siRNA targeting 289 E3 ubiquitin ligases and 137 DUBs were performed. This chapter details the results of this screening process.

3.2 Morphological siRNA screening

3.2.1 Screening for regulators of cortical actin organization in SCC cells

Dharmacon® SMARTpool siRNA libraries targeting 289 E3 ubiquitin ligases and 137 DUBs were used to screen for their potential role in SCC invasion by initially assessing their ability to regulate the actin cytoskeleton. Transfected A431 cells were plated on deformable collagen-Matrigel® gels and after 24 hours stained with DAPI and TRITC phalloidin to visualise the F-actin cytoskeleton. Gene silencing was accompanied by a variety of cell phenotypes compared to control cells. These included cell rounding, cell elongation, actin-rich spikes, membrane blebs, and a disrupted actin cell cortex. Cell morphology was assessed qualitatively and scored descriptively by three independent observers. A SMARTpool was retained for further investigation if it achieved a score of at least 5 out of 6 for altered cell morphology compared to the control. Each screen was blind and performed twice. Descriptions of the cell phenotypes observed for the highest scoring gene knockdowns are shown in Tables 3.1-3.6.

Control, non-targeting siRNA transfected cells (Figure 3.1b) were phenotypically indistinguishable from non-transfected cells (Figure 3.1a). siRNA duplexes targeting Integrin β1 and Rho A were included as positive controls since both generated reproducible and characteristic changes in the cytoskeleton of A431 cells. Integrin β1

gene depletion produced rounded cells (Figure 3.1c) where as Rho A knockdown resulted in elongated cells with a thickened actin cortex (Figure 3.1d).

Figures 3.2-3.4 show representative images of the various cell phenotypes observed. Knocking down RKHD2, for example, resulted in elongated cells with prominent cortical actin (Figure 3.2c). In contrast to this, silencing SUGT1 caused the cells to cluster with a rounded morphology (Figure 3.2f). Several gene knockdowns led to the formation of actin-rich spikes (Figures 3.3c, 3.3d and 3.3e) where as membrane blebs were less frequently seen (Figure 3.3f). Interference with a number of other genes, such as TRIM11 and MARCH3, produced a flattened cell phenotype (Figures 3.4c and 3.4d). Occasionally, the actin cytoskeleton appeared to be disrupted (Figures 3.4e and 3.4f).

Tables 3.7 and 3.8 list the symbol, description and accession number of each of the 45 genes identified. These '1st Round' hits were subsequently de-convoluted.

3.2.2 De-convolution of siRNA SMARTpools

To confirm that the cell phenotypes observed in my initial round of screening were not 'off-target' phenomena; the respective 45 SMARTpools were de-convoluted in A431 cells using individual siRNA duplexes. If at least two of the four duplexes comprising the SMARTpool produced the same phenotype, the gene was retained for further study. This screen was blind, performed twice and scored by two independent observers.

Figures 3.5, 3.6 and 3.7 illustrate the de-convolution of siRNA SMARTpools targeting SAE1, USP12 and Mdm4 respectively. In these examples, gene silencing with at least three of the four siRNA duplexes of each SMARTpool produced the phenotype originally observed in the '1st Round'. Knocking down SAE1 resulted in rounded cells. USP12 gene depletion was characterised by flat, elongated cells and interference with Mdm4 led to cells with pronounced actin-rich spikes.

Following SMARTpool de-convolution, 29 genes emerged as '2nd Round' hits. These are listed in Table 3.9.

GENE	Screen 1			Screen 2			SCORE
	Scorer 1	Scorer 2	Scorer 3	Scorer 1	Scorer 2	Scorer 3	
DKFZ-p761H1710	single rounded	clusters rounded	rounded	single rounded	control	single rounded	**5**
MARCH3	elongated spikes	elongated	control	elongated flat	elongated	elongated	**5**
CDC26	elongated spikes	control	elongated	elongated flat	disrupted	disrupted flat	**5**
LOC-389822	elongated spikes	control	elongated	spikes	spikes	spikes	**5**
FLJ20315	elongated	elongated	elongated	elongated	collapsed	elongated	**6**

Table 3.1 Screening for regulators of cortical actin organization in A431 cells with Dharmacon® SMARTpool siRNA: E3 ubiquitin ligases Plate 1

Cells were plated on deformable collagen-Matrigel® gels, fixed at 72 hours following transfection and stained with TRITC phalloidin. Each screen was blind and performed twice. Cell phenotype was assessed qualitatively and scored descriptively by three independent observers. A SMARTpool was retained for de-convolution if it achieved a score of at least 5 out of 6 for altered cell morphology compared to the control.

GENE	Screen 1			Screen 2			SCORE
	Scorer 1	Scorer 2	Scorer 3	Scorer 1	Scorer 2	Scorer 3	
RNF123	single rounded	spikes	spikes rounded	single rounded	control	rounded	**5**
MKRN2	elongated spikes	elongated spikes	bipolar	spikes	spikes	elongated spikes	**6**
RKHD2	elongated	bipolar	bipolar	bipolar	bipolar	spikes flat	**6**
PJA1	spikes	spikes	spikes	spikes	spikes	spikes	**6**
RNF126	spikes	control	spikes	spikes	spikes	spikes	**5**
FLJ10546	elongated spikes	flat	elongated	flat	control	elongated flat	**5**
RNF11	spikes rounded	spikes	single spikes	spikes rounded	spikes	spikes	**6**
RNF12	elongated	elongated	elongated	elongated	elongated	elongated	**6**
RNF2	spikes	spikes	spikes	spikes	control	spikes	**5**
RFWD3	spikes rounded	single spikes	spikes	spikes	spikes	spikes	**6**

Table 3.2 Screening for regulators of cortical actin organization in A431 cells with Dharmacon® SMARTpool siRNA: E3 ubiquitin ligases Plate 2

Cells were plated on deformable collagen-Matrigel® gels, fixed at 72 hours following transfection and stained with TRITC phalloidin. Each screen was blind and performed twice. Cell phenotype was assessed qualitatively and scored descriptively by three independent observers. A SMARTpool was retained for de-convolution if it achieved a score of at least 5 out of 6 for altered cell morphology compared to the control.

GENE	Screen 1			Screen 2			SCORE
	Scorer 1	Scorer 2	Scorer 3	Scorer 1	Scorer 2	Scorer 3	
RNF41	elongated spikes	spikes	elongated	elongated spikes	control	flat	**5**
TRIM4	elongated blebs	control	spikes	spikes	spikes	spikes	**5**
ZNF364	elongated spikes	control	spikes	spikes	spikes	bipolar spikes	**5**
RNF44	spikes	clusters	spikes	clusters spikes	control	spikes	**5**
ZNF598	bipolar	bipolar	elongated	elongated	control	elongated flat	**5**
RNF5	clusters rounded	rounded	single	clusters rounded	control	mixed	**5**
SUGT1	single rounded	rounded	single rounded	single rounded	single rounded	rounded	**6**
TRIM3	control	spikes	spikes	spikes	spikes	spikes	**5**
VPS11	spikes	spikes	spikes	spikes	spikes	spikes	**6**
FLJ12747	spikes	spikes	spikes	spikes	spikes	spikes	**6**
TRIM11	elongated spikes	elongated spikes	bipolar	spikes	control	flat	**5**

Table 3.3 Screening for regulators of cortical actin organization in A431 cells with Dharmacon® SMARTpool siRNA: E3 ubiquitin ligases Plate 3

Cells were plated on deformable collagen-Matrigel® gels, fixed at 72 hours following transfection and stained with TRITC phalloidin. Each screen was blind and performed twice. Cell phenotype was assessed qualitatively and scored descriptively by three independent observers. A SMARTpool was retained for de-convolution if it achieved a score of at least 5 out of 6 for altered cell morphology compared to the control.

GENE	Screen 1			Screen 2			SCORE
	Scorer 1	Scorer 2	Scorer 3	Scorer 1	Scorer 2	Scorer 3	
HERC4	single rounded	control	single rounded	single rounded	spikes	rounded	**5**
HERC6	elongated flat	control	blebs	elongated flat	bipolar	bipolar	**5**
TRIM33	elongated spikes	spikes	elongated spikes	spikes	control	disrupted	**5**
TRAF6	elongated flat	control	elongated flat	elongated	flat	elongated	**5**
RNF14	elongated spikes	spikes	bipolar	flat	elongated	control	**5**
UBE3A	single rounded	single	single rounded	single rounded	rounded	rounded	**6**
SAE1	spikes	disrupted cortex	single rounded	single rounded	clusters	rounded	**6**
Mdm4	spikes	spikes	spikes	spikes	control	spikes	**5**

Table 3.4 Screening for regulators of cortical actin organization in A431 cells with Dharmacon® SMARTpool siRNA: E3 ubiquitin ligases Plate 4

Cells were plated on deformable collagen-Matrigel® gels, fixed at 72 hours following transfection and stained with TRITC phalloidin. Each screen was blind and performed twice. Cell phenotype was assessed qualitatively and scored descriptively by three independent observers. A SMARTpool was retained for de-convolution if it achieved a score of at least 5 out of 6 for altered cell morphology compared to the control.

GENE	Screen 1			Screen 2			SCORE
	Scorer 1	Scorer 2	Scorer 3	Scorer 1	Scorer 2	Scorer 3	
FLJ14981	flat	blebs	disrupted	flat	flat	flat	**6**
OTUD7A	clusters spikes	spikes	spikes	rounded blebs	spikes	spikes	**6**
BAP1	rounded spikes	clusters spikes	spikes	rounded spikes	spikes	spikes	**6**
DUB1A	flat spikes	spikes	spikes	flat spikes	flat	flat	**6**
USP12	elongated	elongated	elongated	elongated	control	elongated	**5**
DUB3	elongated blebs	spikes	spikes	clusters spikes	spikes	spikes	**6**

Table 3.5 Screening for regulators of cortical actin organization in A431 cells with Dharmacon® SMARTpool siRNA: De-ubiquitinating enzymes Plate 1

Cells were plated on deformable collagen-Matrigel® gels, fixed at 72 hours following transfection and stained with TRITC phalloidin. Each screen was blind and performed twice. Cell phenotype was assessed qualitatively and scored descriptively by three independent observers. A SMARTpool was retained for de-convolution if it achieved a score of at least 5 out of 6 for altered cell morphology compared to the control.

GENE	Screen 1			Screen 2			SCORE
	Scorer 1	Scorer 2	Scorer 3	Scorer 1	Scorer 2	Scorer 3	
USP2	elongated spikes	spikes	spikes	elongated spikes	elongated	disrupted	**6**
TRFP	elongated	elongated	elongated	elongated spikes	elongated	elongated	**6**
PSMD7	single rounded	single rounded	rounded	single rounded	few cells	single rounded	**6**
ZA20d1	spikes	spikes	spikes	elongated spikes	spikes	spikes	**6**
USP6	elongated blebs	clusters blebs	control	elongated	elongated	elongated	**5**

Table 3.6 Screening for regulators of cortical actin organization in A431 cells with Dharmacon® SMARTpool siRNA: De-ubiquitinating enzymes Plate 2

Cells were plated on deformable collagen-Matrigel® gels, fixed at 72 hours following transfection and stained with TRITC phalloidin. Each screen was blind and performed twice. Cell phenotype was assessed qualitatively and scored descriptively by three independent observers. A SMARTpool was retained for de-convolution if it achieved a score of at least 5 out of 6 for altered cell morphology compared to the control.

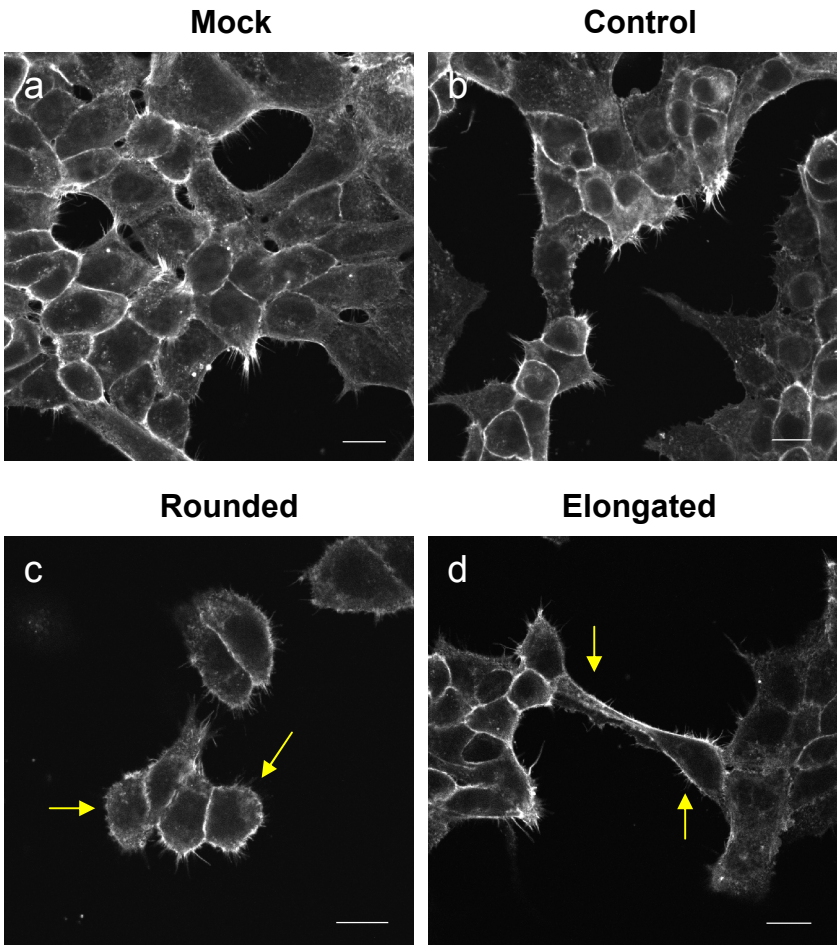

Figure 3.1 'Reference' F-actin phenotype categories in A431 cells: Integrin β1 and Rho A gene depletion

Cells were plated on deformable collagen-Matrigel® gels and fixed 72 hours following transfection. Cells stained with TRITC phalloidin. (**a**) Mock; (**b**) Control siRNA; (**c**) Integrin β1 siRNA and (**d**) Rho A siRNA. Scale bar indicates 20μm.

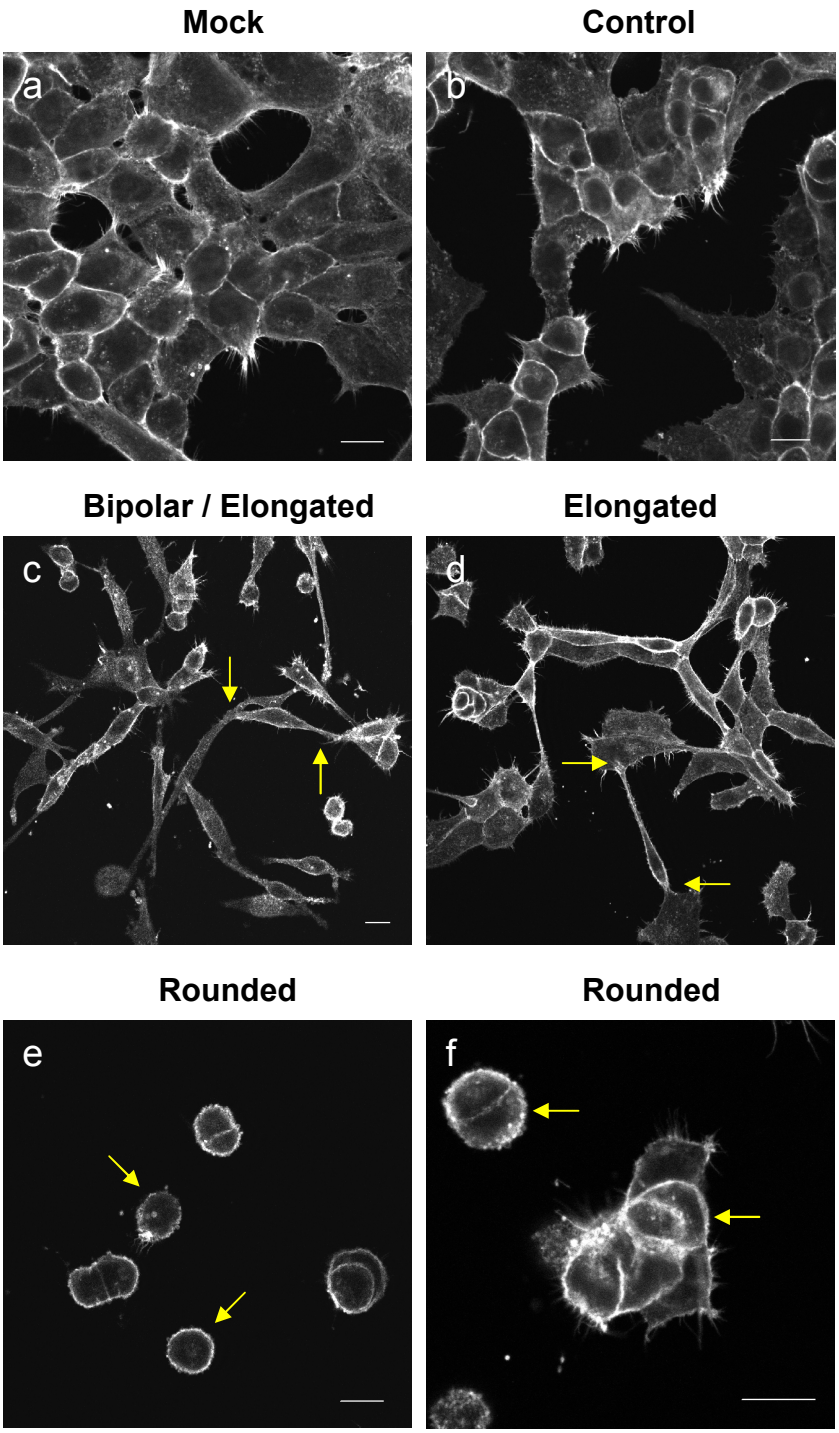

Figure 3.2 Examples of F-actin phenotype categories in A431 cells: bipolar, elongated and rounded

Cells were plated on deformable collagen-Matrigel® gels and fixed 72 hours after transfection with Dharmacon® SMARTpool siRNA libraries. Cells stained with TRITC phalloidin. (**a**) Mock; (**b**) Control siRNA; (**c**) RKHD2 siRNA and (**d**) HERC6 siRNA; (**e**) DKFZp761H1710 siRNA and (**f**) SUGT1 siRNA. Scale bar indicates 20µm.

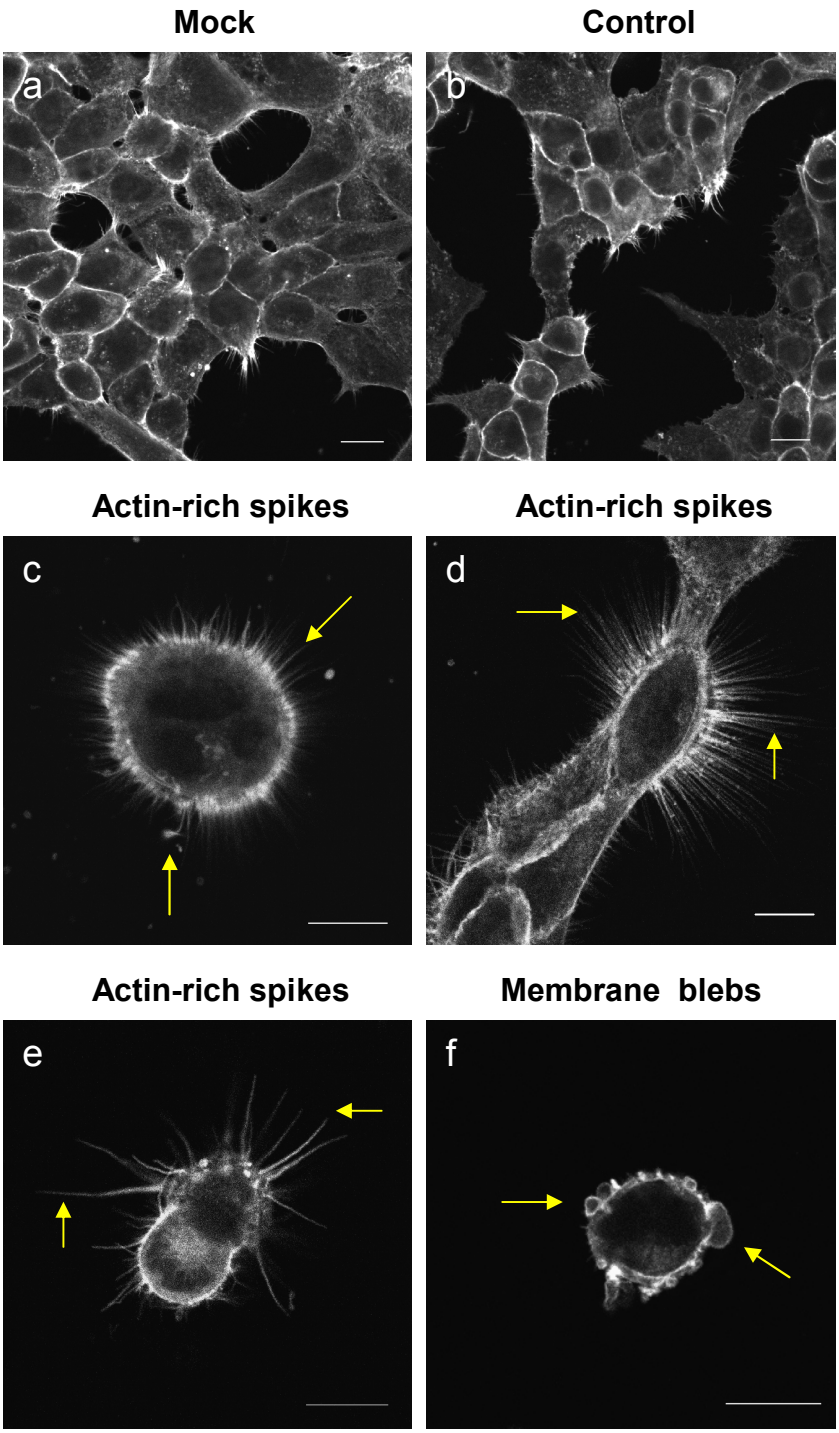

Figure 3.3 Examples of F-actin phenotype categories in A431 cells: actin-rich spikes and membrane blebs

Cells were plated on deformable collagen-Matrigel® gels and fixed 72 hours after transfection with Dharmacon® SMARTpool siRNA libraries. Cells stained with TRITC phalloidin. (**a**) Mock; (**b**) Control siRNA; (**c**) OTUD7A siRNA and (**d**) DUB1A siRNA; (**e**) RNF2 siRNA and (**f**) PSMD7 siRNA. Scale bar indicates 20μm.

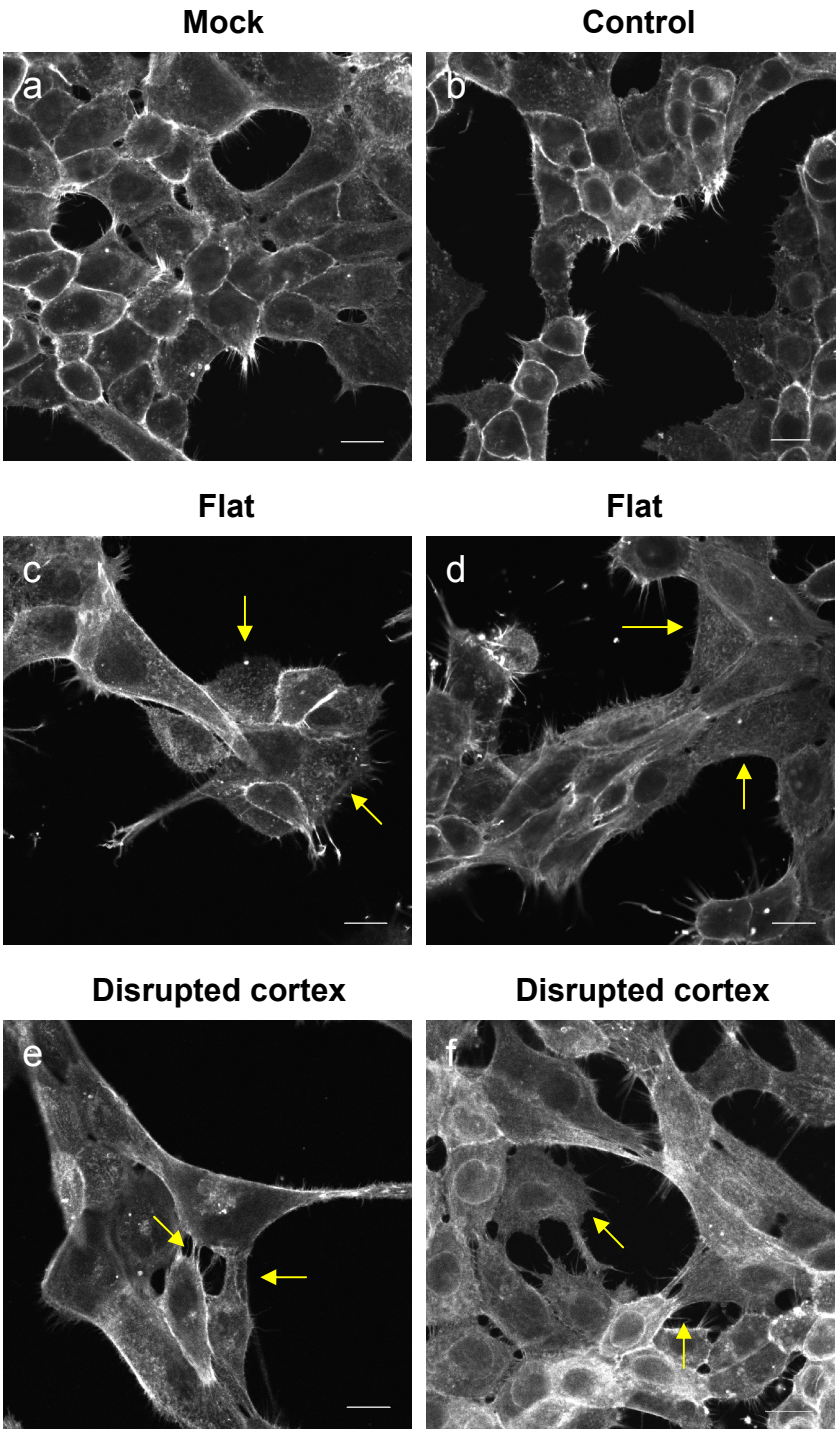

Figure 3.4 Examples of F-actin phenotype categories in A431 cells: flat and disrupted cortex

Cells were plated on deformable collagen-Matrigel® gels and fixed 72 hours after transfection with Dharmacon® SMARTpool siRNA libraries. Cells stained with TRITC phalloidin. (**a**) Mock; (**b**) Control siRNA; (**c**) TRIM11 siRNA and (**d**) MARCH3 siRNA; (**e**) ZNF598 siRNA and (**f**) RNF14 siRNA. Scale bar indicates 20µm.

E3 Ubiquitin Ligases

	Gene Symbol	Gene Description	Accession
Plate 1	CDC26	Cell division cycle 26	NM_139286
	DKFZp761H1710	Hypothetical protein DKFZp761H1710	NM_031297
	FLJ20315	Hypothetical protein FLJ20315	NM_017763
	LOC389822	Hypothetical protein LOC389822	XM_372169
	MARCH3	Membrane-associated ring finger 3	NM_178450
Plate 2	MKRN2	Makorin ring finger protein 2	NM_014160
	PJA1	Praja 1	NM_022368
	RFWD3	Ring finger and WD repeat domain 3	NM_018124
	RKHD2	Ring finger and KH domain containing 2	NM_016626
	RNF11	Ring finger protein 11	NM_014372
	RNF12	Ring finger protein 12	NM_016120
	RNF123	Ring finger protein 123	NM_022064
	RNF126	Ring finger protein 126	NM_017876
	FLJ10546	Hypothetical protein FLJ10546	NM_018133
	RNF2	Ring finger protein 2	NM_007212
Plate 3	RNF41	Ring finger protein 41	NM_005785
	RNF44	Ring finger protein 44	NM_014901
	RNF5	Ring finger protein 5	NM_006913
	SUGT1	SGT1, suppressor of G2 allele of SKP1	NM_006704
	TRIM11	Tripartite motif-containing 11	NM_145214
	TRIM3	Tripartite motif-containing 3	NM_006458
	TRIM4	Tripartite motif-containing 4	NM_033017
	VPS11	Vacuolar protein sorting 11	NM_021729
	ZNF364	Zinc finger protein 364	NM_014455
	ZNF598	Zinc finger protein 598	NM_178167
	FLJ12747	Novel C3HC4 type zinc finger	XM_290972
Plate 4	HERC4	Hect domain and RLD 4	NM_015601
	HERC6	Hect domain and RLD 6	NM_017912
	UBE3A	Ubiquitin protein ligase E3A	NM_000462
	TRIM33	Tripartite motif-containing 33	NM_015906
	TRAF6	TNF receptor-associated factor 6	NM_004620
	RNF14	Ring finger protein 14	NM_004290
	Mdm4	Mdm4	NM_002393
	SAE1	SUMO-1 activating enzyme subunit 1	NM_005500

Table 3.7 Regulators of cortical actin organization in A431 cells: '1st Round' Dharmacon® SMARTpool hits

De-ubiquitinating Enzymes

	Gene Symbol	Gene Description	Accession
Plate 1	BAP1	BRCA1 associated protein-1	NM_004656
	DUB1A	De-ubiquitinating enzyme 1A	XM_377830
	DUB3	De-ubiquitinating enzyme 3	NM_201402
	FLJ14981	Hypothetical protein FLJ14981	NM_032868
	OTUD7A	OTU domain containing 7A	NM_130901
	USP12	Ubiquitin specific protease 12	NM_182488
Plate 2	USP2	Ubiquitin specific protease 2	NM_004205
	TRFP	Trf-proximal homolog	NM_004275
	ZA20d1	Zinc finger, A20 domain containing 1	NM_020205
	USP6	Ubiquitin specific protease 6	NM_004505
	PSMD7	Proteasome 26S subunit, non-ATPase 7	NM_02811

Table 3.8 Regulators of cortical actin organization in A431 cells: '1st Round' Dharmacon® SMARTpool hits

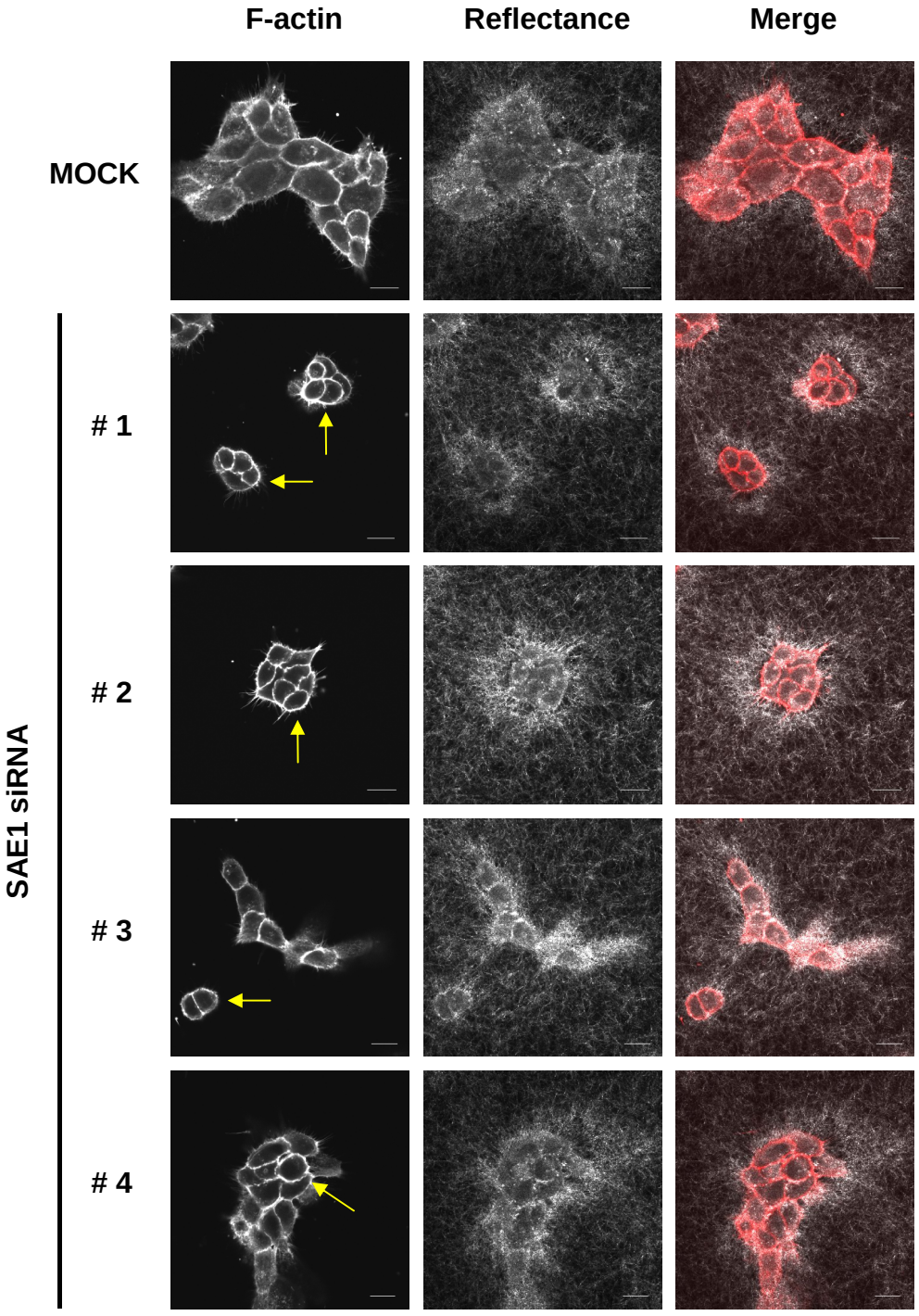

Figure 3.5 Example of de-convolution of Dharmacon® SMARTpool siRNA in A431 cells: 'rounded' cell phenotype

Knockdown of SAE1 with the individual siRNA duplexes comprising the SMARTpool results in a rounded cell phenotype. Cells stained for F-actin with TRITC phalloidin 72 hours after transfection. Collagen-Matrigel® matrix imaged by reflectance. Scale bar indicates 20µm.

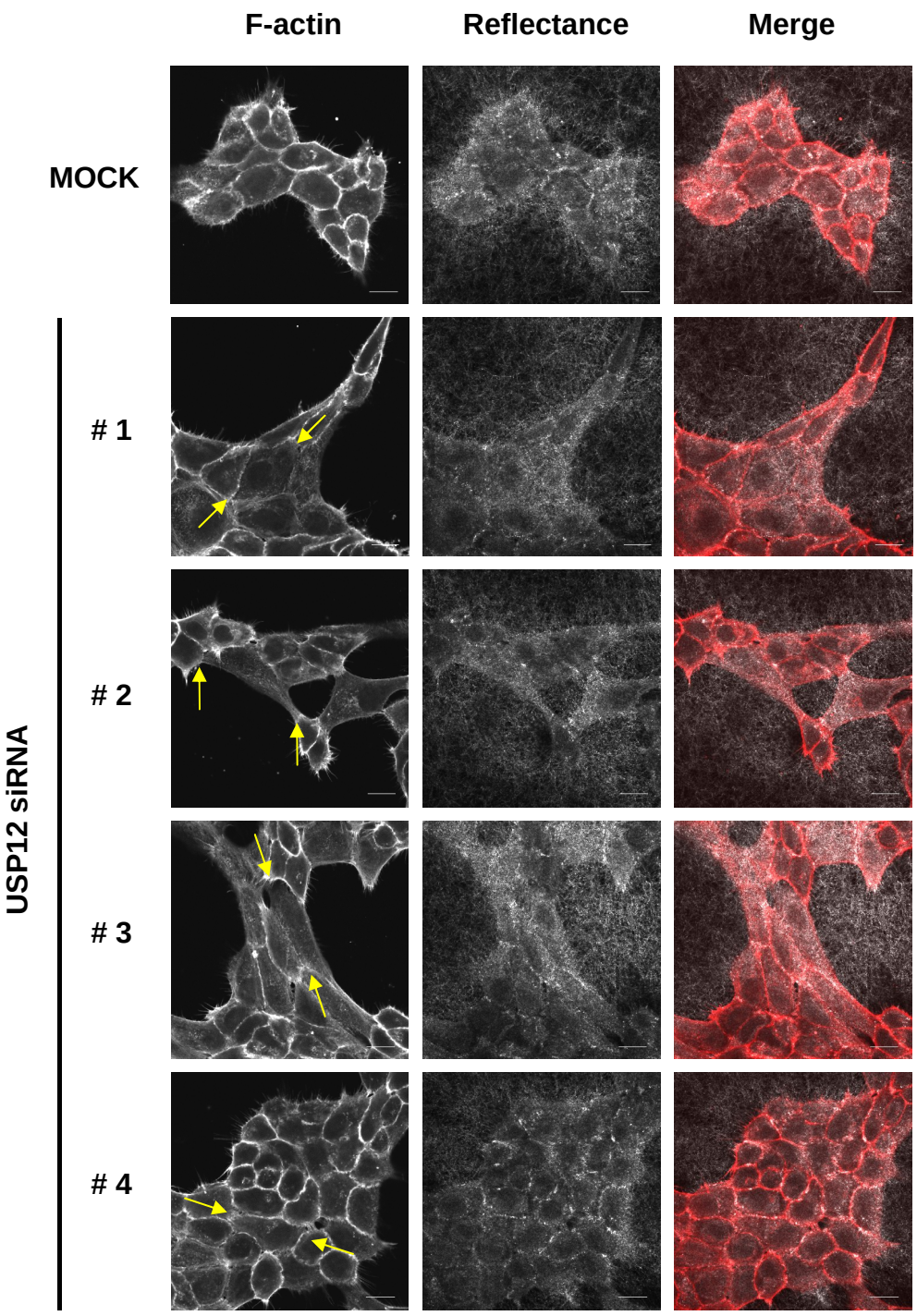

Figure 3.6 Example of de-convolution of Dharmacon® SMARTpool siRNA in A431 cells: 'elongated' cell phenotype

Knockdown of USP12 with the individual siRNA duplexes comprising the SMARTpool results in an elongated cell phenotype. The phenotype induced by duplex 4 is less impressive compared to that observed with the other three oligonucleotides. Cells stained for F-actin with TRITC phalloidin 72 hours after transfection. Collagen-Matrigel® matrix imaged by reflectance. Scale bar indicates 20µm.

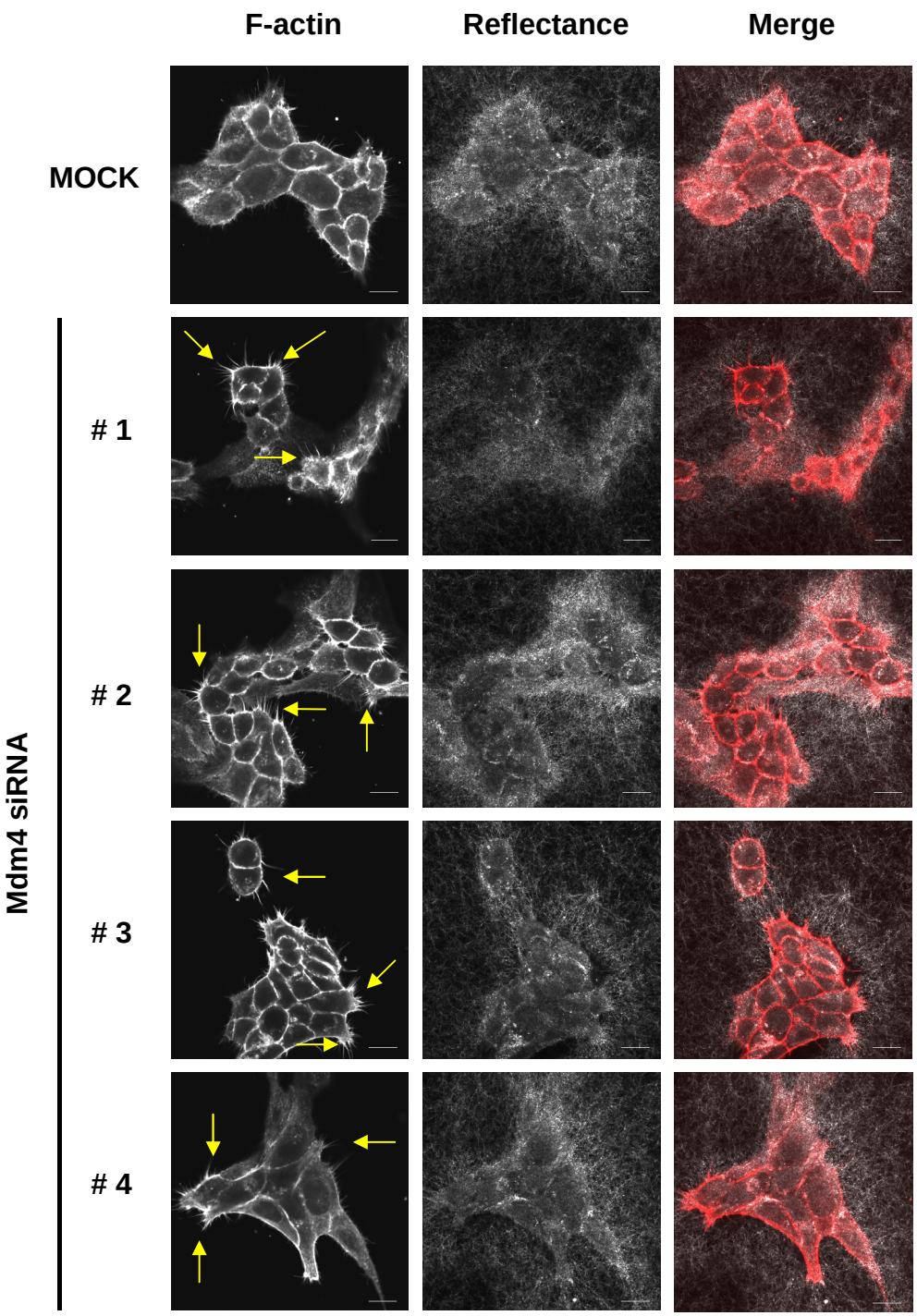

Figure 3.7 Example of de-convolution of Dharmacon® SMARTpool siRNA in A431 cells: 'spiky' cell phenotype

Knockdown of Mdm4 with the individual siRNA duplexes comprising the SMARTpool results in cells with prominent actin-rich spikes. Cells stained for F-actin with TRITC phalloidin 72 hours after transfection. Collagen-Matrigel® matrix imaged by reflectance. Scale bar indicates 20µm.

E3 Ubiquitin Ligases

Gene Symbol	Gene Description	Predominant Phenotype
CDC26	Cell division cycle 26	elongated
MARCH3	Membrane-associated ring finger 3	elongated
MKRN2	Makorin, ring finger protein 2	spiky
PJA1	Praja 1	spiky
RFWD3	Ring finger and WD repeat domain 3	spiky
RKHD2	Ring finger and KH domain containing 2	elongated
RNF12	Ring finger protein 12	elongated
RNF126	Ring finger protein 126	spiky
FLJ10546	Hypothetical protein FLJ10546	elongated
RNF2	Ring finger protein 2	spiky
RNF41	Ring finger protein 41	elongated
SUGT1	SGT1, suppressor of G2 allele of SKP1	rounded
TRIM11	Tripartite motif-containing 11	elongated
ZNF598	Zinc finger protein 598	elongated
HERC4	Hect domain and RLD 4	rounded
HERC6	Hect domain and RLD 6	elongated
TRAF6	TNF receptor-associated factor 6	elongated
RNF14	Ring finger protein 14	elongated
Mdm4	Mdm4	spiky
SAE1	SUMO-1 activating enzyme subunit 1	rounded

De-ubiquitinating Enzymes

BAP1	BRCA1 associated protein-1	spiky
DUB1A	De-ubiquitinating enzyme 1A	spiky
FLJ14981	Hypothetical protein FLJ14981	elongated
USP12	Ubiquitin specific protease 12	elongated
USP2	Ubiquitin specific protease 2	spiky
TRFP	Trf-proximal homolog	elongated
ZA20d1	Zinc finger, A20 domain containing 1	spiky
USP6	Ubiquitin specific protease 6	elongated
PSMD7	Proteasome 26S subunit, non-ATPase 7	rounded

Table 3.9 De-convolution of Dharmacon® SMARTpool siRNA in A431 cells: '2nd Round' gene hits

The 45 '1st Round' SMARTpool hits were de-convoluted. If at least two of the four individual duplexes comprising the SMARTpool produced the same phenotype the gene was retained for further study.

3.2.3 Screening for regulators of cortical actin organization in HNCAF

The importance of stromal interactions with epithelial cells is well established in carcinogenesis and although the characteristics of activated CAF are not completely understood their tumour promoting role is well documented [50, 66.]

To further test my 29 '2nd Round' gene hits as regulators of the actin cytoskeleton and to investigate their potential role in CAF function an additional siRNA screen was undertaken. This screen was blind, performed twice and scored by two independent observers. Eight 'CAF' hits were identified (Table 3.10) and representative images of the cell phenotypes observed are shown in Figures 3.8-3.12.

siRNA duplexes targeting Integrin β1 and Rho A were again included as positive controls (Figure 3.8). Integrin β1 knockdown caused loss of the bipolar appearance typical of CAF, whilst Rho A depletion resulted in the formation of prominent stress fibres (Figure 3.13a). The majority of CAF hits (MKRN2, RKHD2, TRAF6, Mdm4, SAE1, ZA20d1 and USP6) were characterised by abnormal cell bodies which had fewer stress fibres and an increased spread area (Figure 3.13c). In 'normal' CAF, stress fibres were orientated parallel to each other and the long axis of the cell (Figure 3.13b). Knocking down HERC4 led to a dramatic rounding of cells which still retained some capacity to contract their associated ECM (Figure 3.11).

Stromal fibroblasts are able to alter their surrounding ECM via a combination of force-mediated and protease-mediated matrix remodelling [77]. Figure 3.14 shows reflectance imaging of collagen-Matrigel® gels after 24 hours of fibroblast remodelling. Holes in the matrix are clearly visible. Transmission Electron Microscopy (TEM) has demonstrated that these structures represent migration tracks, being devoid of matrix at their centre and composed of thick collagen bundles at their periphery [77]. They are also associated with the deposition of matrix components such as fibronectin and tenascin-C Remodelled ECM facilitates the collective invasion of carcinoma cells, where as naïve unconditioned matrix does not [77].

E3 Ubiquitin Ligases

Gene Symbol	Gene Description	Accession
MKRN2	Makorin, ring finger protein 2	NM_014160
RKHD2	Ring finger and KH domain containing 2	NM_016626
TRAF6	TNF receptor-associated factor 6	NM_004620
Mdm4	Mdm4	NM_002393
HERC4	Hect domain and RLD 4	NM_015601
SAE1	SUMO-1 activating enzyme subunit 1	NM_005500

De-ubiquitinating Enzymes

ZA20d1	Zinc finger, A20 domain containing 1	NM_020205
USP6	Ubiquitin specific protease 6	NM_004505

Table 3.10 Regulators of cortical actin organization in HNCAF: 'CAF' hits

Screening in HNCAF was undertaken with two siRNA duplexes per '2nd Round' gene hit to further investigate their role as regulators of the actin cytoskeleton. The screen was blind, performed twice and scored by two independent observers. Eight 'CAF' hits were identified in which gene depletion by both oligonucleotides resulted in an abnormal cell phenotype.

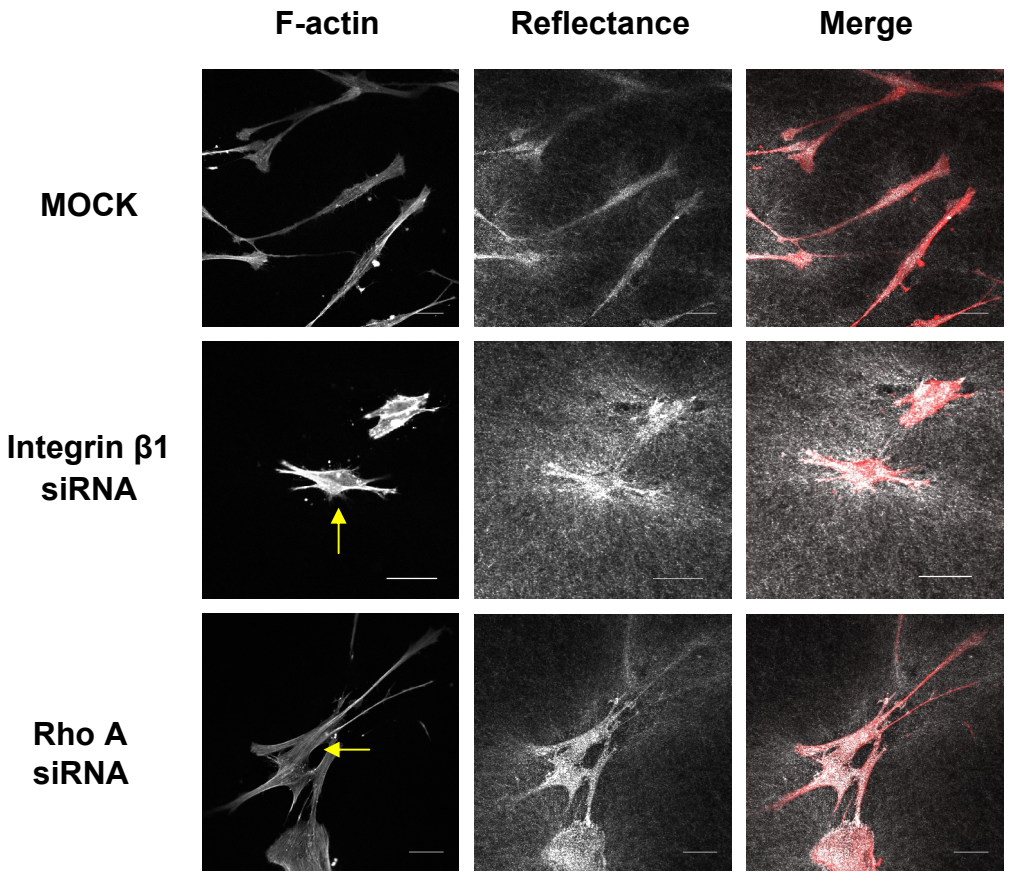

Figure 3.8 'Reference' F-actin phenotypes in HNCAF: Integrin β1 and Rho A gene depletion

Cell phenotypes observed in HNCAF following siRNA gene depletion. Arrows indicate abnormal cell bodies. Cells stained for F-actin with TRITC phalloidin 72 hours after transfection. Collagen-Matrigel® matrix imaged by reflectance. The scale bars represent 50µm.

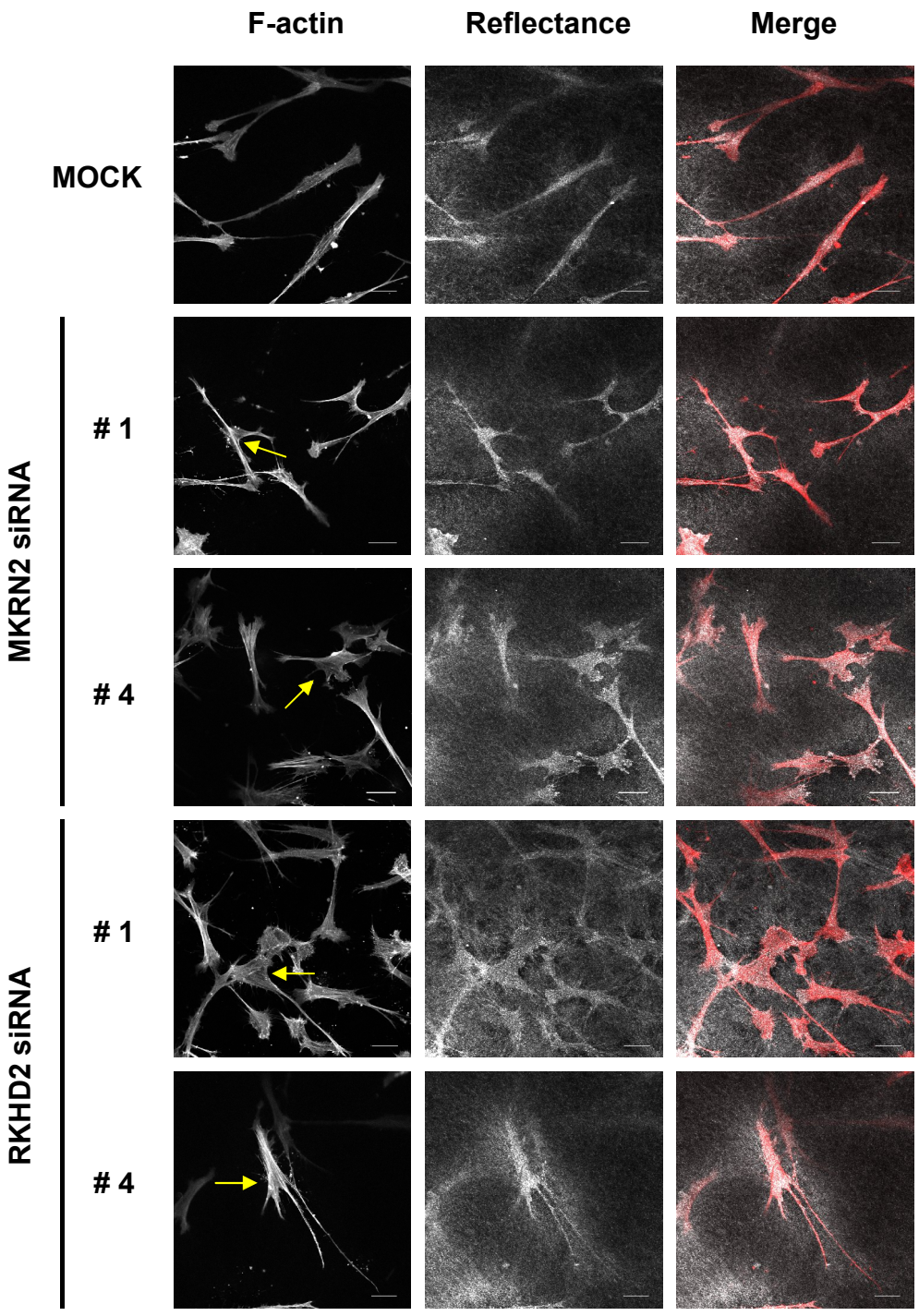

Figure 3.9 F-actin phenotypes in HNCAF: MKRN2 and RKHD2 gene depletion

Cell phenotypes observed in HNCAF following siRNA gene depletion. Arrows indicate abnormal cell bodies. Cells stained for F-actin with TRITC phalloidin 72 hours after transfection. Collagen-Matrigel® matrix imaged by reflectance. The scale bars represent 50µm.

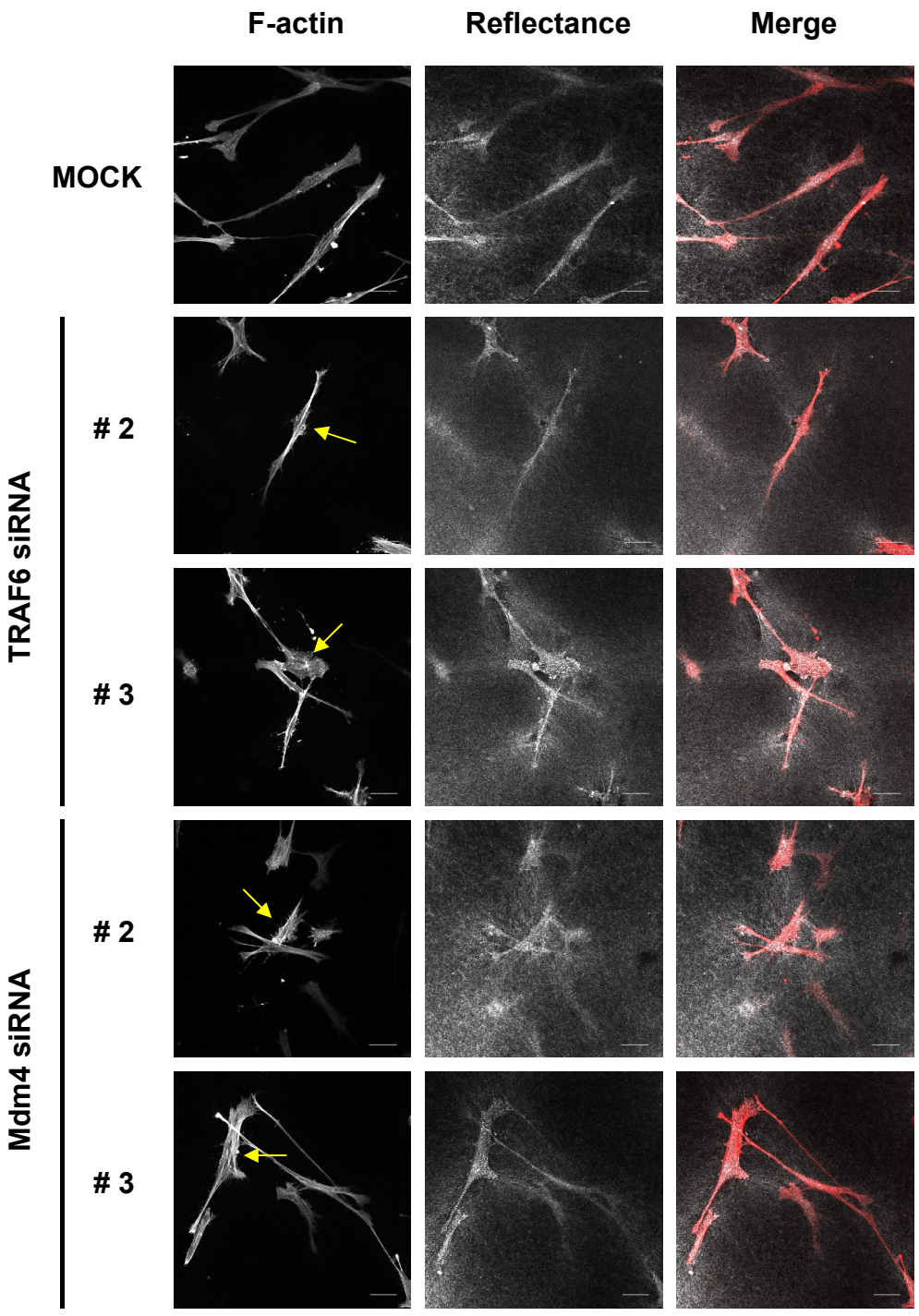

Figure 3.10 F-actin phenotypes in HNCAF: TRAF6 and Mdm4 gene depletion

Cell phenotypes observed in HNCAF following siRNA gene depletion. Arrows indicate abnormal cell bodies. Cells stained for F-actin with TRITC phalloidin 72 hours after transfection. Collagen-Matrigel® matrix imaged by reflectance. The scale bars represent 50µm.

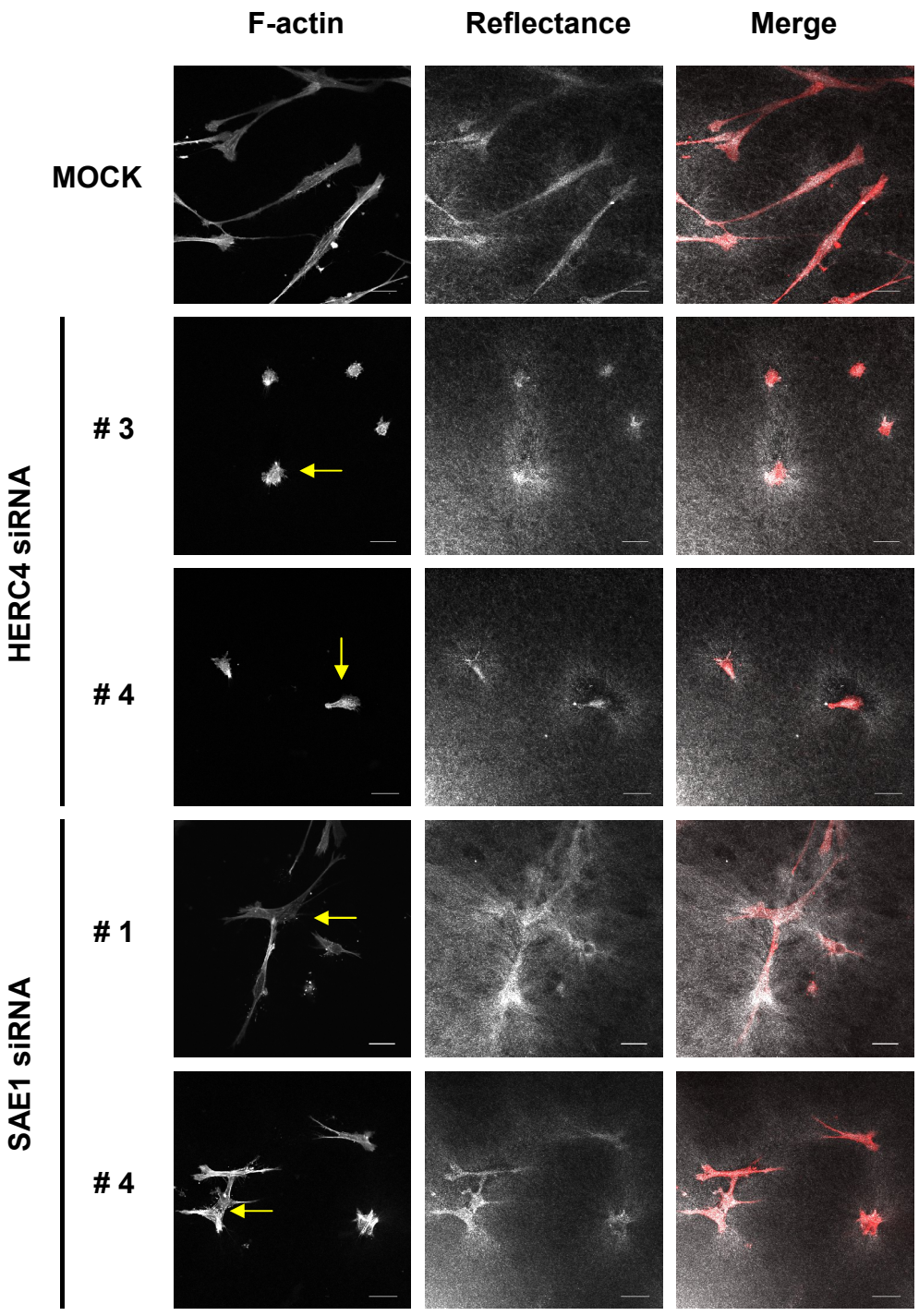

Figure 3.11 F-actin phenotypes in HNCAF: HERC4 and SAE1 gene depletion

Cell phenotypes observed in HNCAF following siRNA gene depletion. Arrows indicate abnormal cell bodies. Cells stained for F-actin with TRITC phalloidin 72 hours after transfection. Collagen-Matrigel® matrix imaged by reflectance. The scale bars represent 50µm.

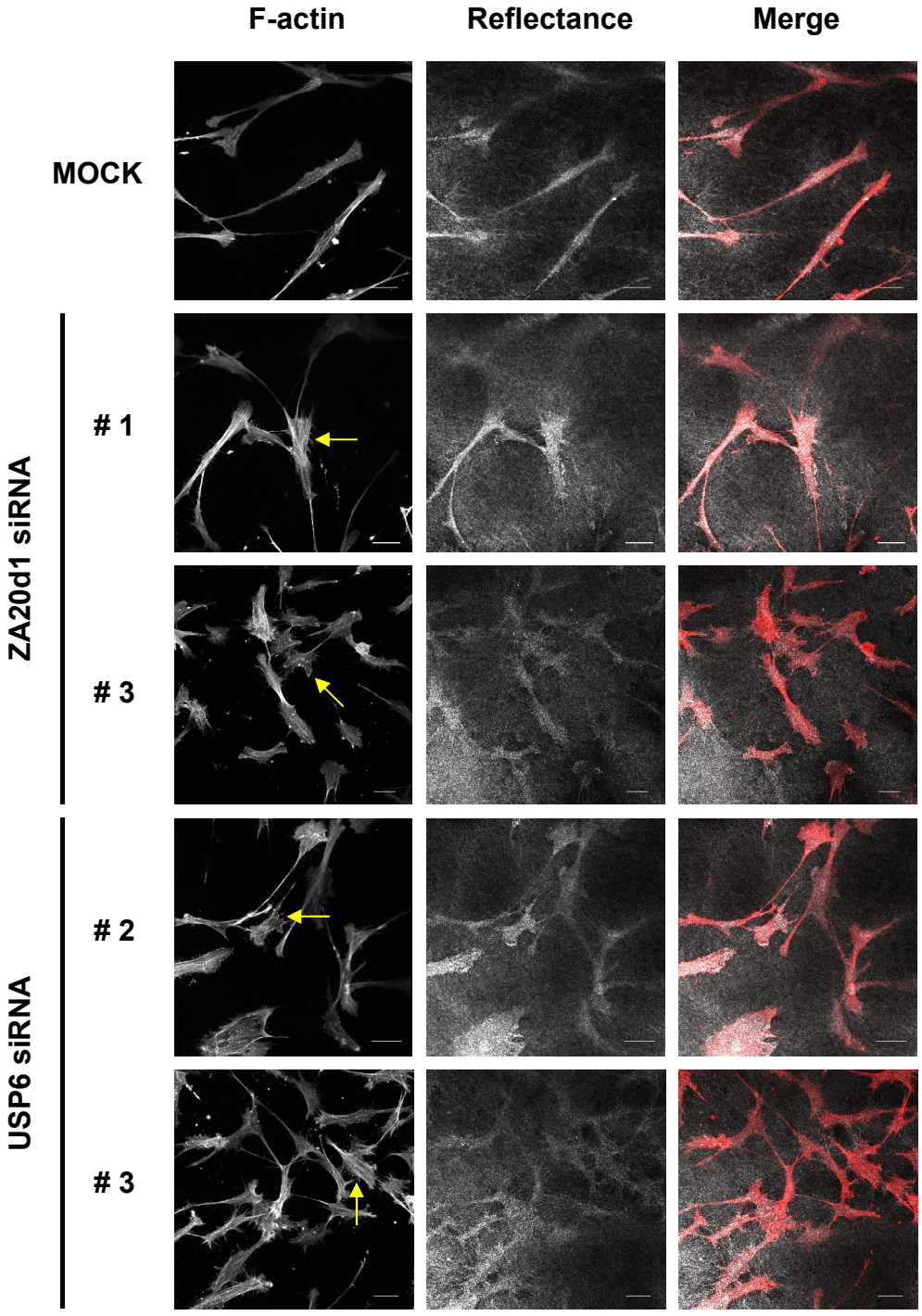

Figure 3.12 F-actin phenotypes in HNCAF: ZA20d1 and USP6 gene depletion

Cell phenotypes observed in HNCAF following siRNA gene depletion. Arrows indicate abnormal cell bodies. Cells stained for F-actin with TRITC phalloidin 72 hours after gene depletion. Collagen-Matrigel® matrix imaged by reflectance. The scale bars represent 50µm.

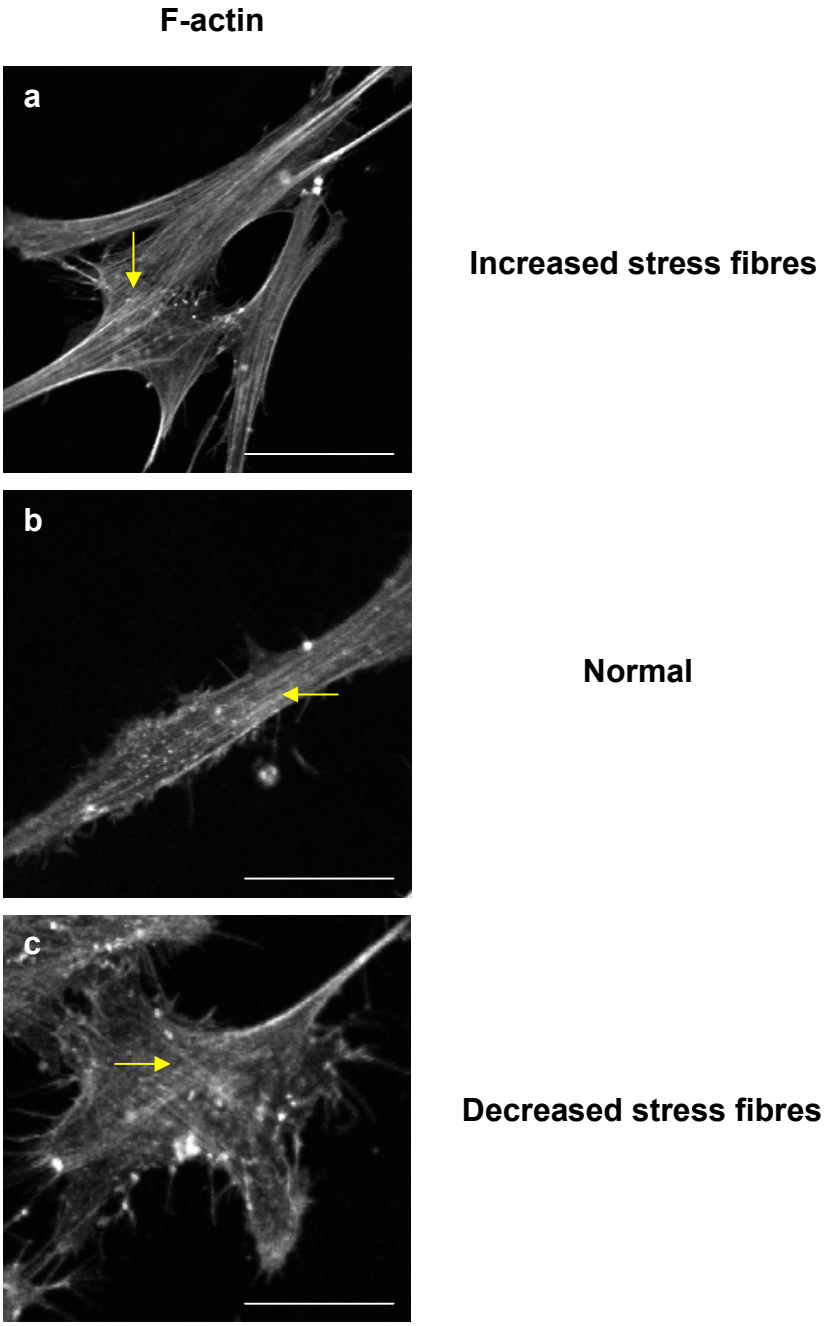

Figure 3.13 F-actin phenotypes in HNCAF: stress fibres.

Cell phenotypes observed in HNCAF based upon the effect on the actin cytoskeleton. Arrows indicate stress fibres. A decrease in stress fibres was associated with an increase in cell spread area. Cells stained for F-actin with TRITC phalloidin 72 hours after transfection. The scale bars represent 50µm.

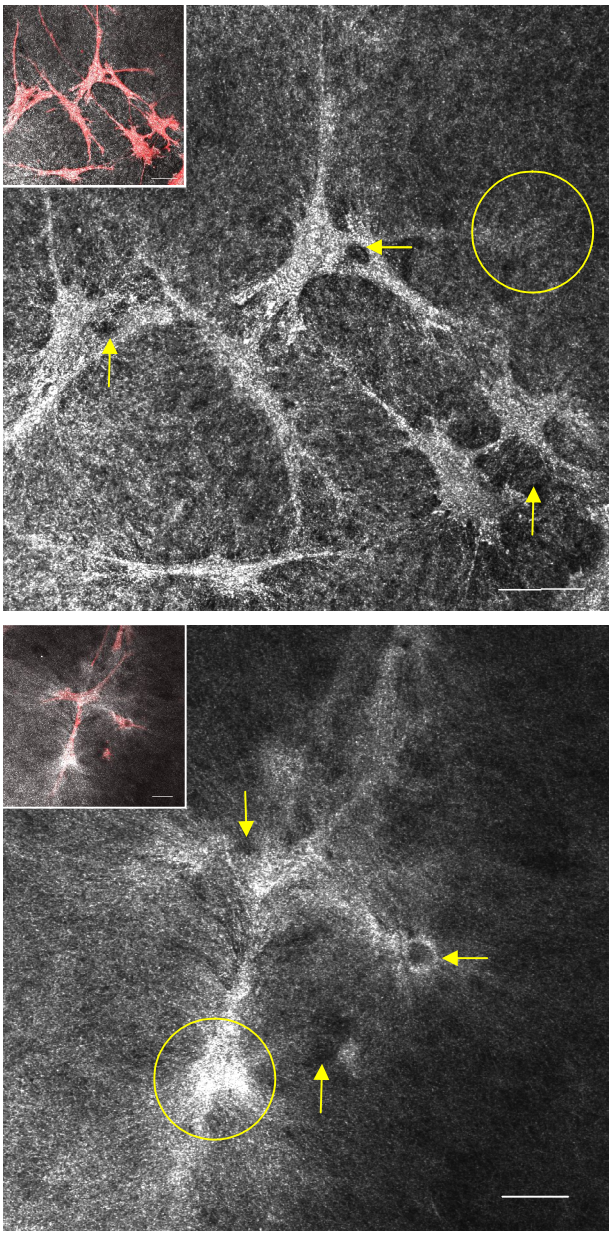

Figure 3.14 Examples of matrix remodelling and track generation by carcinoma-associated fibroblasts

Reflectance images of collagen-Matrigel® extra-cellular matrix (white) after 24 hours of fibroblast remodelling. Fibroblasts stained with TRITC phalloidin (red) shown in insets. Arrows indicate holes generated in the matrix. Circles indicate areas of remodelled matrix. The scale bars represent 50µm.

3.3 Summary

- Dharmacon® SMARTpool siRNA libraries targeting 289 E3 ubiquitin ligases and 137 DUBs were used to screen for their potential role in SCC invasion by assessing their ability to regulate the actin cytoskeleton of A431 cells. Forty-five '1st Round' hits were identified.

- To confirm that the cell phenotypes observed in the initial morphological screen were not 'off-target' phenomena, the SMARTpools of the 45 '1st Round' hits were de-convoluted using individual siRNA duplexes. From this screen in A431 cells, 29 genes emerged as '2nd Round' hits.

- To further test my 29 '2nd Round' gene hits as regulators of the actin cytoskeleton, an additional siRNA screen in stromal fibroblasts was performed. Eight genes (MKRN2, RKHD2, TRAF6, Mdm4, HERC4, SAE1, ZA20d1 and USP6) when individually depleted in fibroblasts resulted in markedly abnormal cell phenotypes. These were designated 'CAF' hits.

Chapter 4

Functional siRNA screening

4.1 Introduction

To investigate the role of my 29 '2nd Round' gene hits (Chapter 3, Table 3.9) on SCC invasion a functional siRNA screen using an organotypic culture system was performed (Figure 4.1). This system involved culturing carcinoma cells (SCC12) over a matrix predominantly composed of Type I collagen. Each culture was supported by a metal bridge which enabled the epithelial layer to develop at an air-liquid interface. Media was changed daily throughout the duration of the assay. When HNCAF were introduced, the collagen-Matrigel® ECM was remodelled and carcinoma cells invaded as collective chains without having undergone an EMT [77]. The extent of SCC invasion was reproducibly assessed by calculating the Invasion Index [302].

Matrix remodelling by fibroblasts is an important aspect of several physiological and pathological processes such as wound healing and tissue fibrosis. It is also critical to carcinoma invasion [304, 305]. Fibroblast-mediated remodelling of the ECM can be visualised microscopically by reflectance imaging and TEM [77]. Fibroblasts also have the ability to contract collagen gels; a phenomenon that can be observed at the macroscopic level [303, 306]. Furthermore, a good correlation between the degree of macroscopic gel contraction and the extent of microscopic matrix remodelling exists [77]. Given that our organotypic system is fibroblast-dependent and that a remodelled conditioned ECM is necessary to support SCC invasion, I also investigated the influence of my 8 'CAF' gene hits (Chapter 3, Table 3.10) on the ability of stromal fibroblasts to promote SCC invasion and gel contraction.

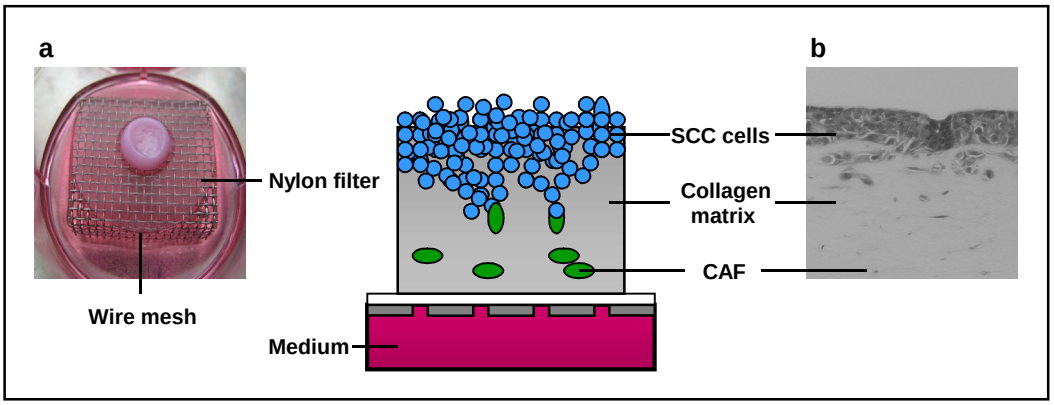

Figure 4.1 Organotypic culture system for studying SCC invasion

(**a**) Photograph and diagram showing experimental set-up. This system involved culturing carcinoma cells over a collagen-Matrigel® matrix supported by a collagen coated nylon filter resting on a stainless steel bridge. Sufficient medium was added to feed the culture from beneath the bridge thus allowing the epithelial layer to develop at an air-liquid interface. (**b**) Photomicrograph of an H&E section showing invasion of carcinoma cells. When carcinoma-associated fibroblasts are introduced into the matrix the SCC cells invade as collective chains and retain the expression of epithelial markers.

4.2 Functional siRNA screening

4.2.1 SCC invasion screen

Cdc42 is a key regulator of SCC12 invasion in our organotypic system [77]. siRNA targeting Cdc42 was therefore used as a positive control for transfection efficiency and to assess the effect of gene depletion on invasion. Organotypic cultures in which SCC12 cells had been transfected with a non-targeting siRNA duplex or were not transfected were also included. In addition, a collagen gel without fibroblasts was set up routinely in each assay to act as a negative control. Two individual siRNA oligonucleotides were selected for each of the 29 '2nd Round' gene hits per assay. Serial assays were performed and the genes assessed with respect to the degree of inhibition of carcinoma invasion observed following their depletion. Silencing 21 of the 29 genes identified as cytoskeletal regulators had no obvious functional effect on SCC invasion (data not shown).

Figures 4.2-4.9 illustrate the results of the organotypic assays of the genes which emerged as potential candidates for further study. Each figure consists of (a) photomicrographs of H&E sections demonstrating the degree of carcinoma infiltration into the underlying matrix, (b) quantification of carcinoma invasion using the Invasion Index and (c) randomized block ANOVA statistical analysis. Depletion of RKHD2 (Figure 4.3), TRAF6 (Figure 4.4), and ZA20d1 (Figure 4.8) achieved statistically significant inhibition of carcinoma invasion with at least one of the two targeting siRNA duplexes chosen.

a

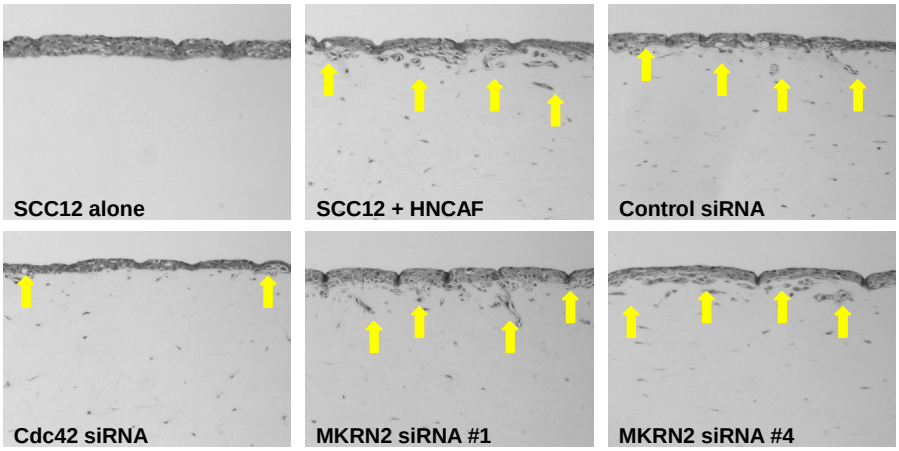

b

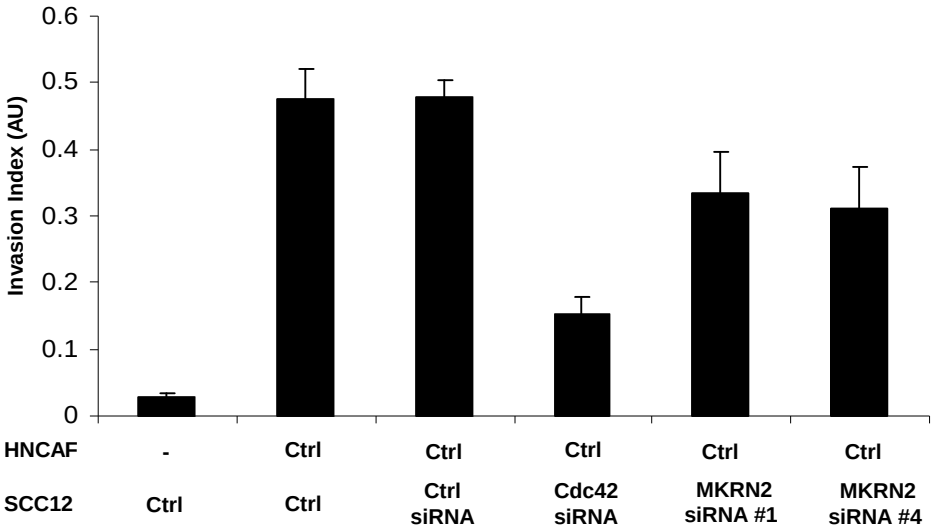

c

Randomized Block ANOVA	p Value	Decision p<0.025
Contol vs Control siRNA	0.972741	Do not reject
Control siRNA vs MKRN2 siRNA #1	0.360851	Do not reject
Control siRNA vs MKRN2 siRNA #4	0.304217	Do not reject

Figure 4.2 SCC organotypic invasion screen: MKRN2 gene depletion

(**a**) H&E stained sections of SCC12 cells cultured in organotypic gels. Arrows point to the invading front of carcinoma cells. (**b**) Quantification of carcinoma invasion in organotypic gels in the absence of stromal fibroblasts, in the presence of stromal fibroblasts and with Cdc42 or MKRN2 inhibited by siRNA in SCC12 cells. The average of 10 visual fields from 2 experiments is shown. The error bars represent the s.e. (**c**) Randomized block ANOVA statistical analysis. Null hypothesis (NØ) rejected if $p < 0.025$.

a

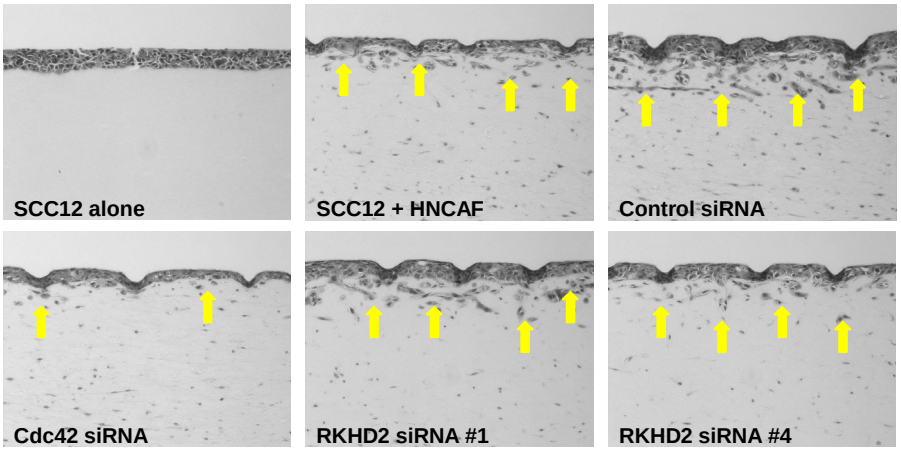

b

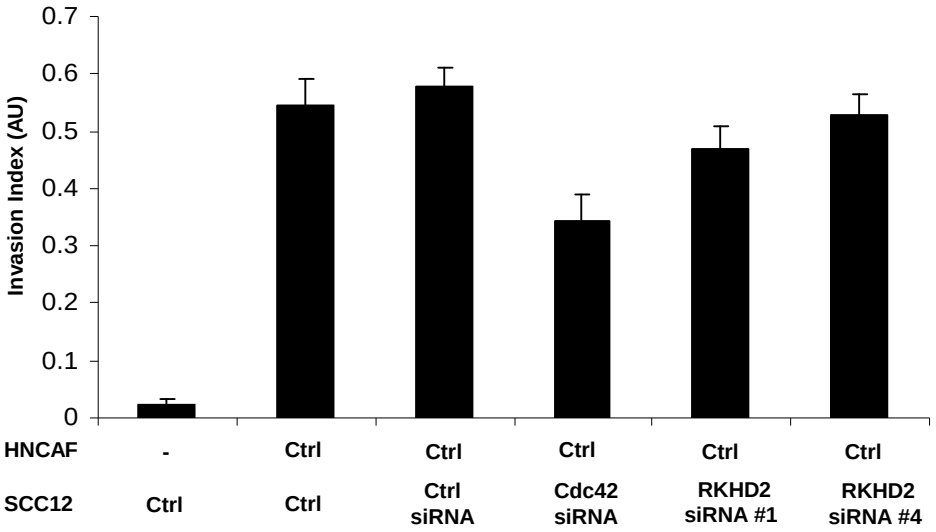

c

Randomized Block ANOVA	p Value	Decision p<0.025
Control vs Control siRNA	0.370949	Do not reject
Control siRNA vs RKHD2 siRNA #1	0.019921	Reject
Control siRNA vs RKHD2 siRNA #4	0.092371	Do not reject

Figure 4.3 SCC organotypic invasion screen: RKHD2 gene depletion

(**a**) H&E stained sections of SCC12 cells cultured in organotypic gels. Arrows point to the invading front of carcinoma cells. (**b**) Quantification of carcinoma invasion in organotypic gels in the absence of stromal fibroblasts, in the presence of stromal fibroblasts and with Cdc42 or RKHD2 inhibited by siRNA in SCC12 cells. The average of 10 visual fields from 2 experiments is shown. The error bars represent the s.e. (**c**) Randomized block ANOVA statistical analysis. Null hypothesis (NØ) rejected if $p < 0.025$.

a

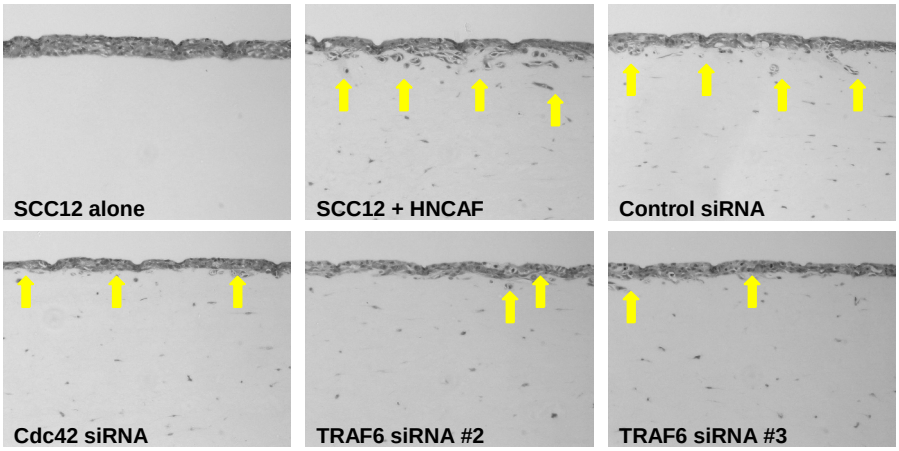

b

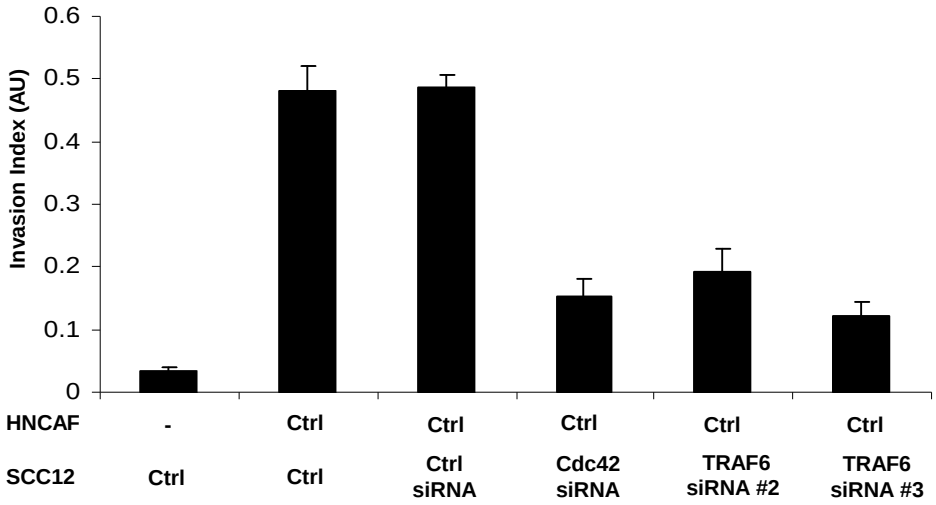

c

Randomized Block ANOVA	p Value	Decision p<0.025
Control vs Control siRNA	0.945694	Do not reject
Control siRNA vs TRAF6 siRNA #2	0.000010	Reject
Control siRNA vs TRAF6 siRNA #3	0.000006	Reject

Figure 4.4 SCC organotypic invasion screen: TRAF6 gene depletion

(**a**) H&E stained sections of SCC12 cells cultured in organotypic gels. Arrows point to the invading front of carcinoma cells. (**b**) Quantification of carcinoma invasion in organotypic gels in the absence of stromal fibroblasts, in the presence of stromal fibroblasts and with Cdc42 or TRAF6 inhibited by siRNA in SCC12 cells. The average of 10 visual fields from 2 experiments is shown. The error bars represent the s.e. (**c**) Randomized block ANOVA statistical analysis. Null hypothesis (NØ) rejected if $p < 0.025$.

a

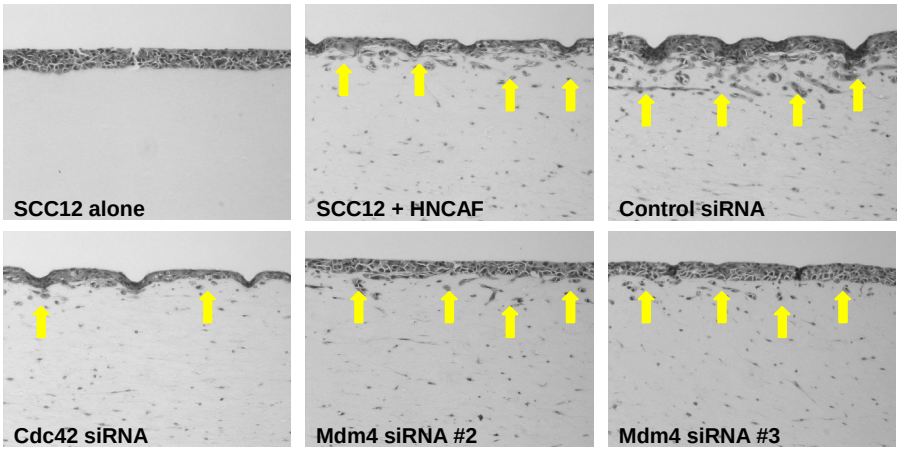

b

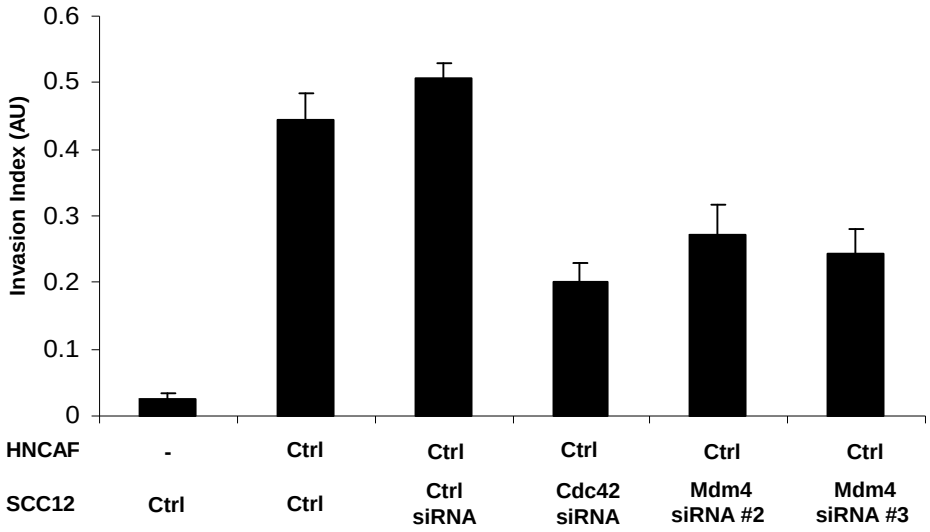

c

Randomized Block ANOVA	p Value	Decision p<0.025
Control vs Control siRNA	0.086477	Do not reject
Control siRNA vs Mdm4 siRNA #2	0.076099	Do not reject
Control siRNA vs Mdm4 siRNA #3	0.061711	Do not reject

Figure 4.5 SCC organotypic invasion screen: Mdm4 gene depletion

(**a**) H&E stained sections of SCC12 cells cultured in organotypic gels. Arrows point to the invading front of carcinoma cells. (**b**) Quantification of carcinoma invasion in organotypic gels in the absence of stromal fibroblasts, in the presence of stromal fibroblasts and with Cdc42 or Mdm4 inhibited by siRNA in SCC12 cells. The average of 10 visual fields from 2 experiments is shown. The error bars represent the s.e. (**c**) Randomized block ANOVA statistical analysis. Null hypothesis (NØ) rejected if $p < 0.025$.

a

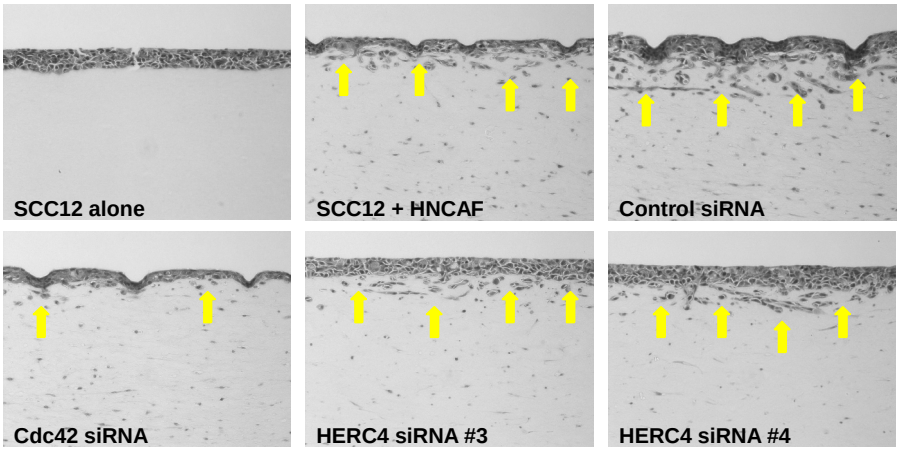

b

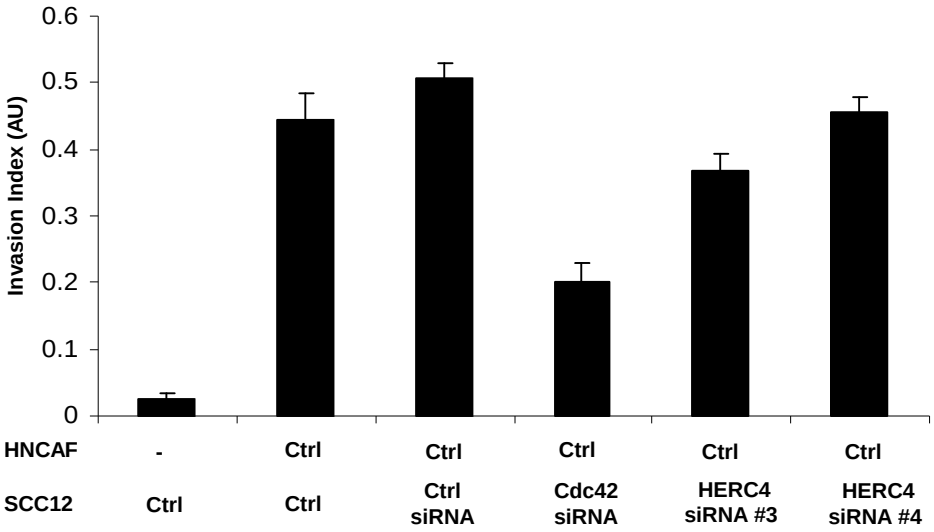

c

Randomized Block ANOVA	p Value	Decision p<0.025
Control vs Control siRNA	0.086477	Do not reject
Control siRNA vs HERC4 siRNA #3	0.029069	Do not reject
Control siRNA vs HERC4 siRNA #4	0.167189	Do not reject

Figure 4.6 SCC organotypic invasion screen: HERC4 gene depletion

(**a**) H&E stained sections of SCC12 cells cultured in organotypic gels. Arrows point to the invading front of carcinoma cells. (**b**) Quantification of carcinoma invasion in organotypic gels in the absence of stromal fibroblasts, in the presence of stromal fibroblasts and with Cdc42 or HERC4 inhibited by siRNA in SCC12 cells. The average of 10 visual fields from 2 experiments is shown. The error bars represent the s.e. (**c**) Randomized block ANOVA statistical analysis. Null hypothesis (NØ) rejected if $p < 0.025$.

a

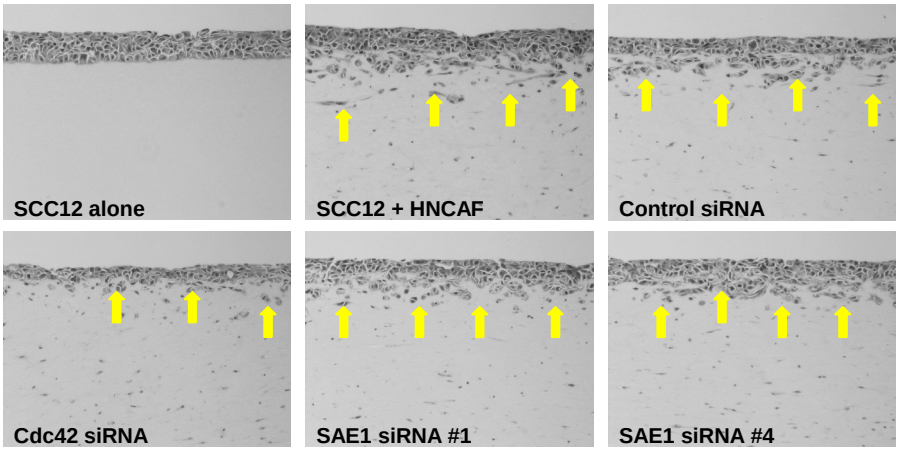

b

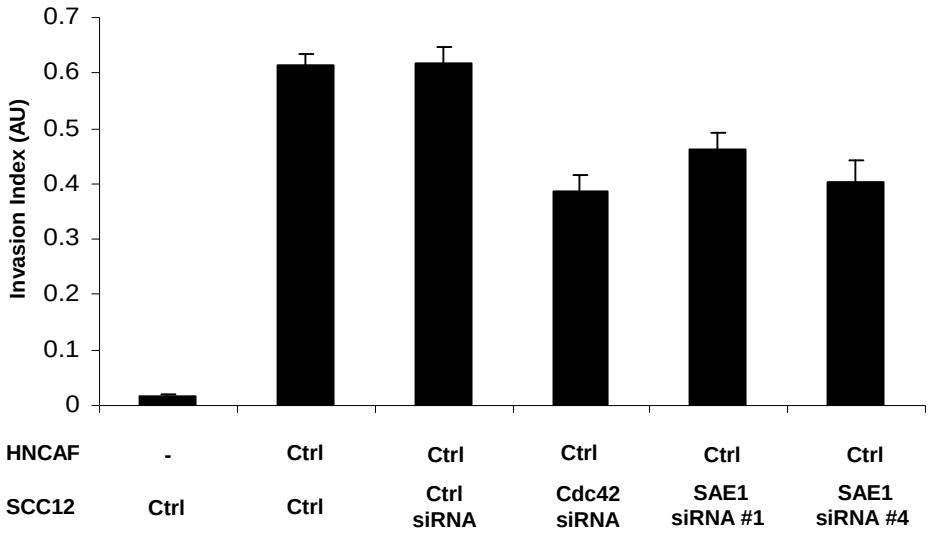

c

Randomized Block ANOVA	p Value	Decision p<0.025
Control vs Control siRNA	0.953404	Do not reject
Control siRNA vs SAE1 siRNA #1	0.069820	Do not reject
Control siRNA vs SAE1 siRNA #4	0.037713	Do not reject

Figure 4.7 SCC organotypic invasion screen: SAE1 gene depletion

(**a**) H&E stained sections of SCC12 cells cultured in organotypic gels. Arrows point to the invading front of carcinoma cells. (**b**) Quantification of carcinoma invasion in organotypic gels in the absence of stromal fibroblasts, in the presence of stromal fibroblasts and with Cdc42 or SAE1 inhibited by siRNA in SCC12 cells. The average of 10 visual fields from 2 experiments is shown. The error bars represent the s.e. (**c**) Randomized block ANOVA statistical analysis. Null hypothesis (NØ) rejected if $p < 0.025$.

a

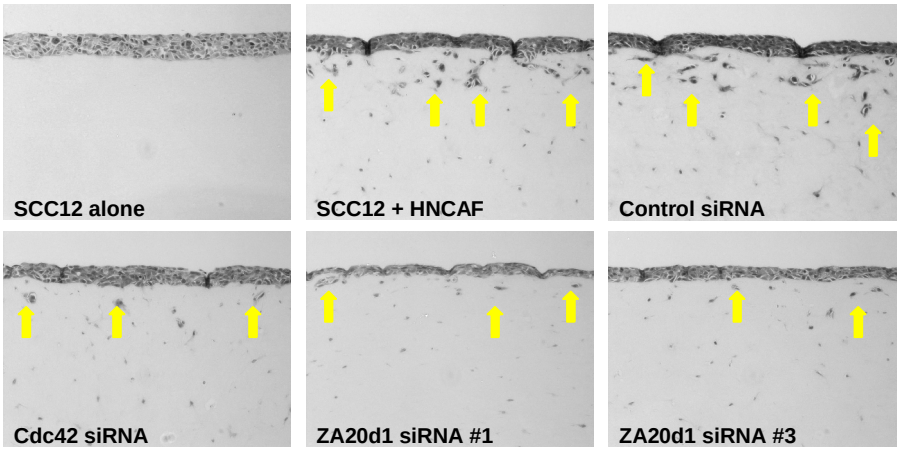

b

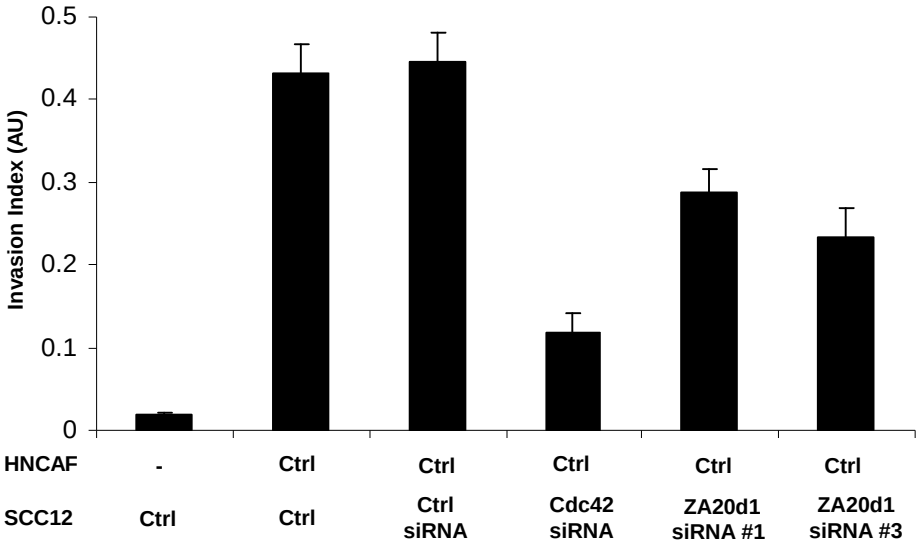

c

Randomized Block ANOVA	p Value	Decision p<0.025
Control vs Control siRNA	0.858188	Do not reject
Control siRNA vs ZA20d1 siRNA #1	0.040391	Do not reject
Control siRNA vs ZA20d1 siRNA #3	0.022693	Reject

Figure 4.8 SCC organotypic invasion screen: ZA20d1 gene depletion

(**a**) H&E stained sections of SCC12 cells cultured in organotypic gels. Arrows point to the invading front of carcinoma cells. (**b**) Quantification of carcinoma invasion in organotypic gels in the absence of stromal fibroblasts, in the presence of stromal fibroblasts and with Cdc42 or ZA20d1 inhibited by siRNA in SCC12 cells. The average of 10 visual fields from 2 experiments is shown. The error bars represent the s.e. (**c**) Randomized block ANOVA statistical analysis. Null hypothesis (NØ) rejected if $p < 0.025$.

a

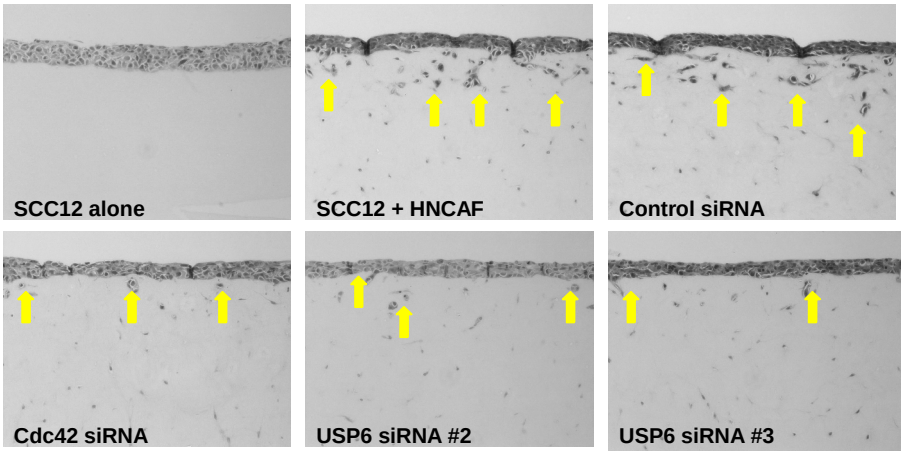

b

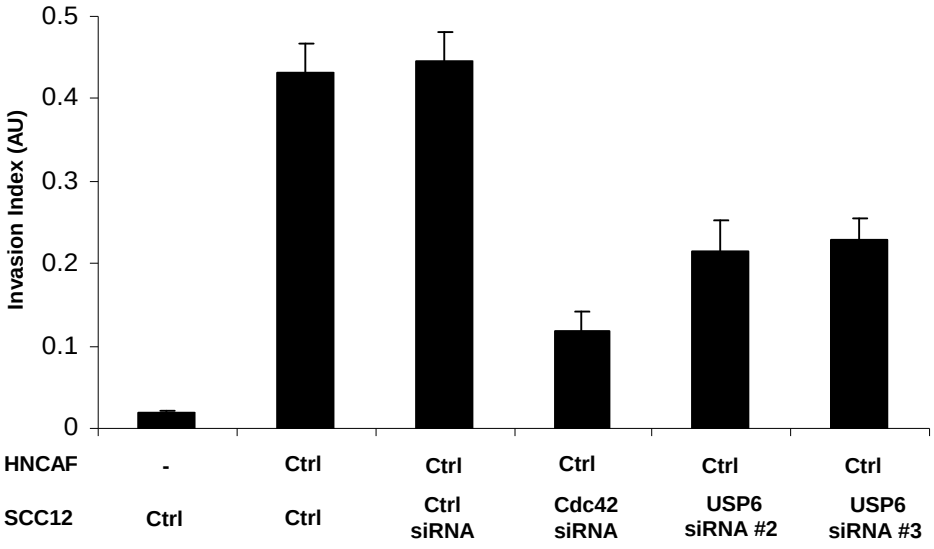

c

Randomized Block ANOVA	p Value	Decision p<0.025
Control vs Control siRNA	0.858188	Do not reject
Control siRNA vs USP6 siRNA #2	0.027850	Do not reject
Control siRNA vs USP6 siRNA #3	0.031790	Do not reject

Figure 4.9 SCC organotypic invasion screen: USP6 gene depletion

(**a**) H&E stained sections of SCC12 cells cultured in organotypic gels. Arrows point to the invading front of carcinoma cells. (**b**) Quantification of carcinoma invasion in organotypic gels in the absence of stromal fibroblasts, in the presence of stromal fibroblasts and with Cdc42 or USP6 inhibited by siRNA in SCC12 cells. The average of 10 visual fields from 2 experiments is shown. The error bars represent the s.e. (**c**) Randomized block ANOVA statistical analysis. Null hypothesis (NØ) rejected if $p < 0.025$.

4.2.2 Inhibition of SCC invasion by HNCAF interference

To assess the influence of the 8 'CAF' cytoskeletal gene hits on the ability of stromal fibroblasts to promote SCC invasion, a modified two-stage organotypic assay was used as described in Chapter 2, Section 2.2.8.3.

This assay was performed twice and involved the construction of collagen-Matrigel® gels containing siRNA gene depleted HNCAF. After 5 days of matrix remodelling, the fibroblasts were extracted and SCC12 seeded on to the conditioned ECM. The organotypic cultures were then allowed to proceed to completion and the extent of carcinoma invasion quantified. Inhibition of ROCK in fibroblast-SCC co-cultures has been shown to reduce carcinoma invasion by impairing fibroblast-dependent force-mediated matrix contraction [77]. siRNA targeting ROCK1 and ROCK2 was therefore chosen as the positive transfection control.

The results of this invasive screen are displayed in Figures 4.10-4.12. Five genes, (MKRN2, RKHD2, TRAF6, ZA20d1 and USP6), when individually depleted in stromal fibroblasts impaired their ability to promote SCC invasion.

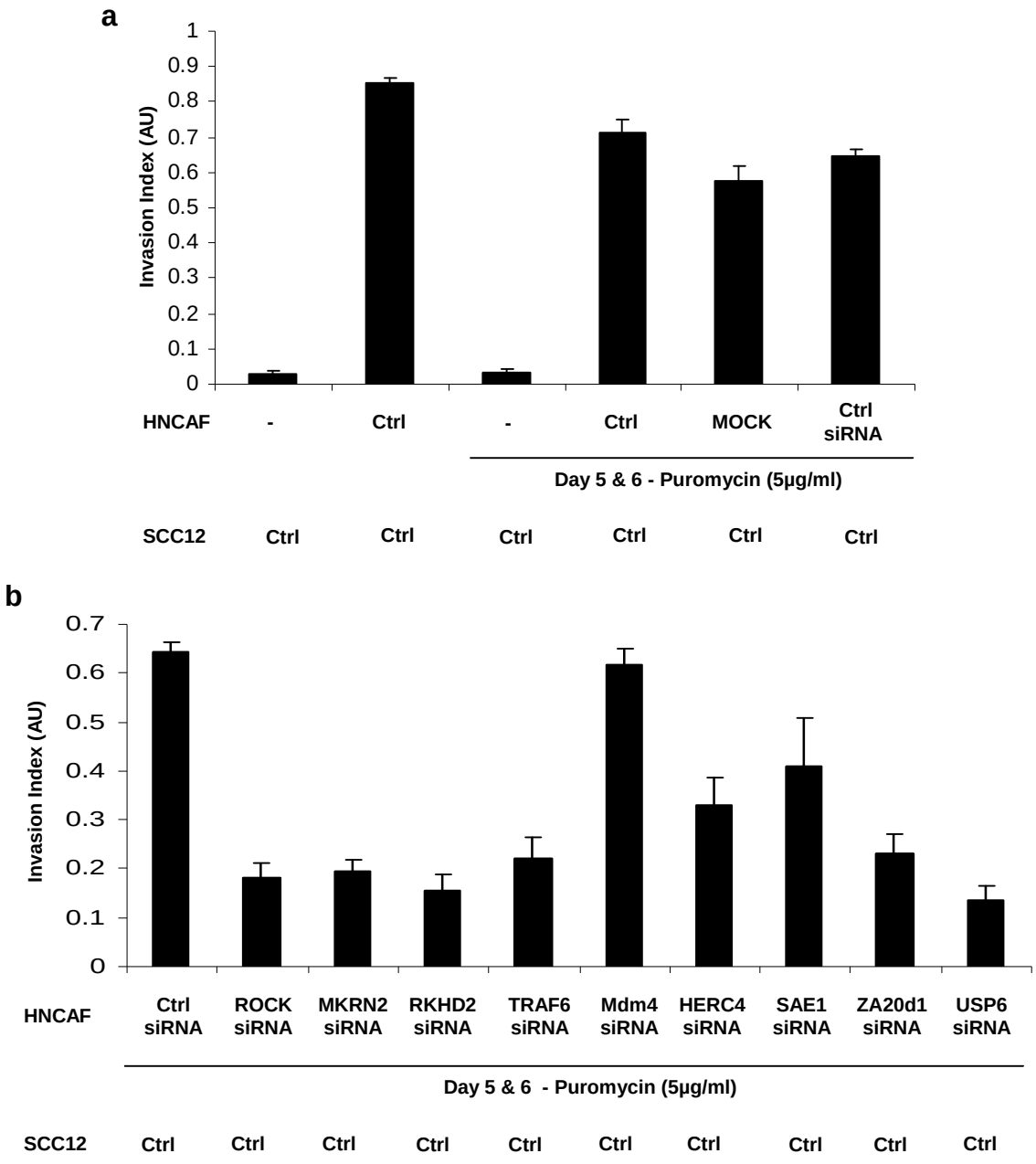

Figure 4.10 Inhibition of SCC invasion by HNCAF interference. (a) 'Control' gels and (b) siRNA gene depleted HNCAF gels

Quantification of carcinoma invasion in organotypic gels that previously contained gene depleted stromal fibroblasts. ROCK, MKRN2, RKHD2, TRAF6, Mdm4, HERC4, SAE1, ZA20d1 and USP6 function inhibited by siRNA in HNCAF. Gels treated with puromycin (5µg/ml) daily for 48 hours after 5 days of matrix remodelling and fibroblasts removed prior to the addition of SCC12 cells. The average of 10 visual fields from 2 experiments is shown. The error bars represent the s.e.

a

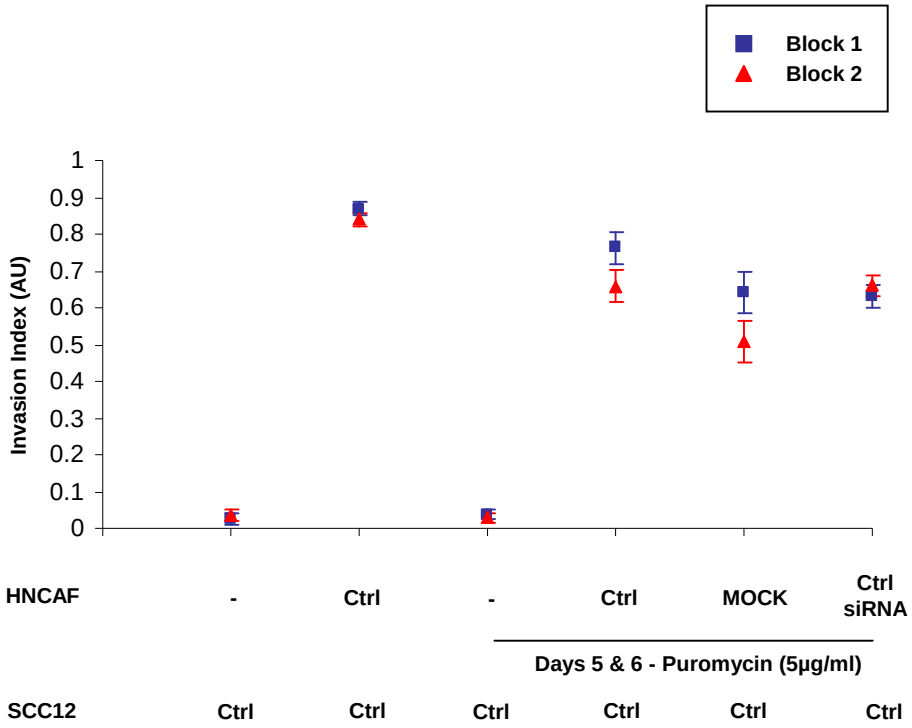

b

Randomized Block ANOVA	p Value	Decision p<0.025
Control vs MOCK	0.155424	Do not reject
MOCK vs Control siRNA	0.367520	Do not reject

Figure 4.11 Inhibition of SCC invasion by HNCAF interference. (a) 'Control' gels and (b) randomized block ANOVA statistical analysis

(**a**) Scatter plot displaying quantification of carcinoma invasion in the 'control' gels of the organotypic assay illustrated in Figure 4.10. Individual experimental blocks are illustrated. The average of 5 visual fields is shown and error bars represent the s.e. (**b**) Randomized block ANOVA statistical analysis. Null hypothesis (NØ) rejected if $p < 0.025$.

a

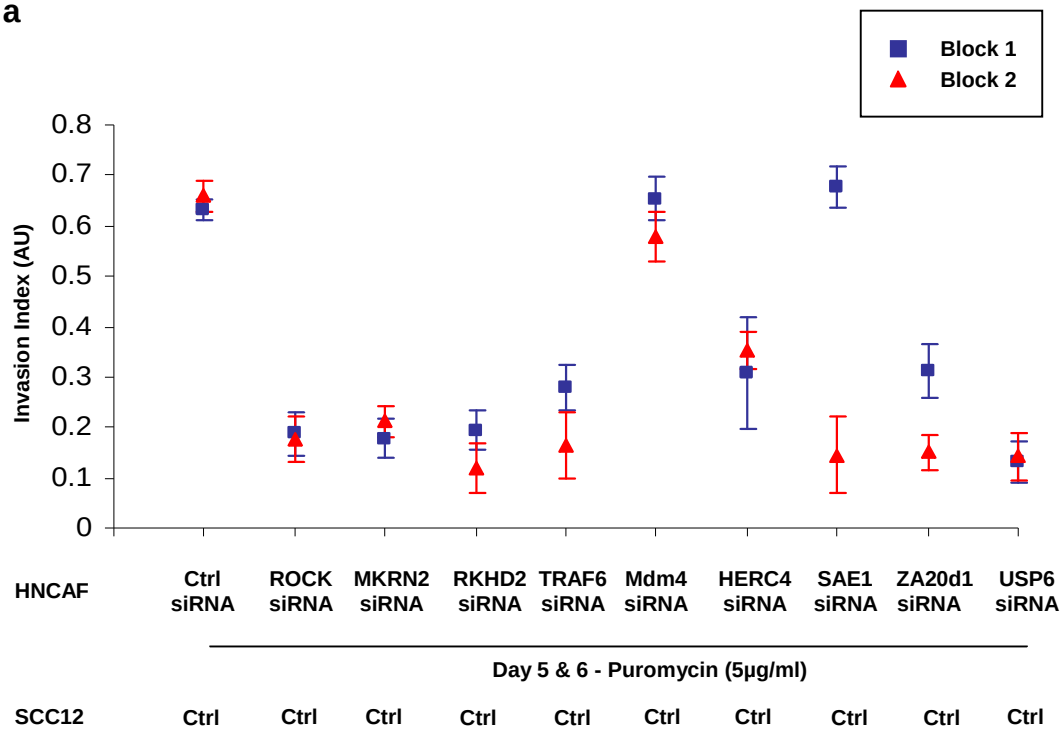

b

Randomized Block ANOVA	p Value	Decision p<0.025
Control siRNA vs MKRN2 siRNA #1+ #4	0.006113	Reject
Control siRNA vs RKHD2 siRNA #1+ #4	0.003809	Reject
Control siRNA vs TRAF6 siRNA #2 + #3	0.008562	Reject
Control siRNA vs Mdm4 siRNA #2 + #3	0.0820224	Do not reject
Control siRNA vs HERC4 siRNA #3 + #4	0.034362	Do not reject
Control siRNA vs SAE1 siRNA #1 + #4	0.096878	Do not reject
Control siRNA vs ZA20d1 siRNA #1 + #3	0.009604	Reject
Control siRNA vs USP6 siRNA #1 + #3	0.003008	Reject

Figure 4.12 Inhibition of SCC invasion by HNCAF interference. (a) siRNA gene depleted HNCAF gels and (b) randomized block ANOVA statistical analysis

(**a**) Scatter plot displaying quantification of carcinoma invasion in the gene depleted HNCAF gels of organotypic assay illustrated in Figure 4.10. Individual experimental blocks are illustrated. The average of 5 visual fields is shown and error bars represent the s.e. (**b**) Randomized block ANOVA statistical analysis. Null hypothesis (NØ) rejected if $p < 0.025$.

4.3 Fibroblast-dependent collagen-Matrigel® matrix remodelling

4.3.1 The Contraction Index

The collagen-Matrigel® gels constructed for the assays detailed in Section 4.2.2 were photographed after 5 days of fibroblast-mediated matrix remodelling (Figures 4.13a and 4.15a) and the Contraction Index for each gel calculated (Figures 4.13b and 4.15b). Figures 4.14a and 4.16a show scatter plots of the individual experimental blocks for the 'Control' gels and the siRNA gene depleted HNCAF gels respectively.

Gels containing HNCAF transfected with non-targeting siRNA contracted to a similar degree to those with mock transfected or non-transfected stromal fibroblasts (Figure 4.14b). As expected, fibroblast-deficient gels did not contract.

Predictably, ROCK depleted HNCAF exhibited a noticeably reduced ability to contract their ECM (Figure 4.15). The contraction indices of the siRNA gene depleted HNCAF gels were not statistically different when compared to the control (Figure 4.16b).

4.3.2 The relationship between SCC invasion and collagen-Matrigel® matrix contraction

Figure 4.17 shows scatterplots of the mean Invasion Index and the mean Contraction Index for the two-stage organotypic assays investigating the functional significance of my 8 'CAF' cytoskeletal gene hits (Section 4.2.2). The relationship between these two parameters for my genes of interest was inconsistent.

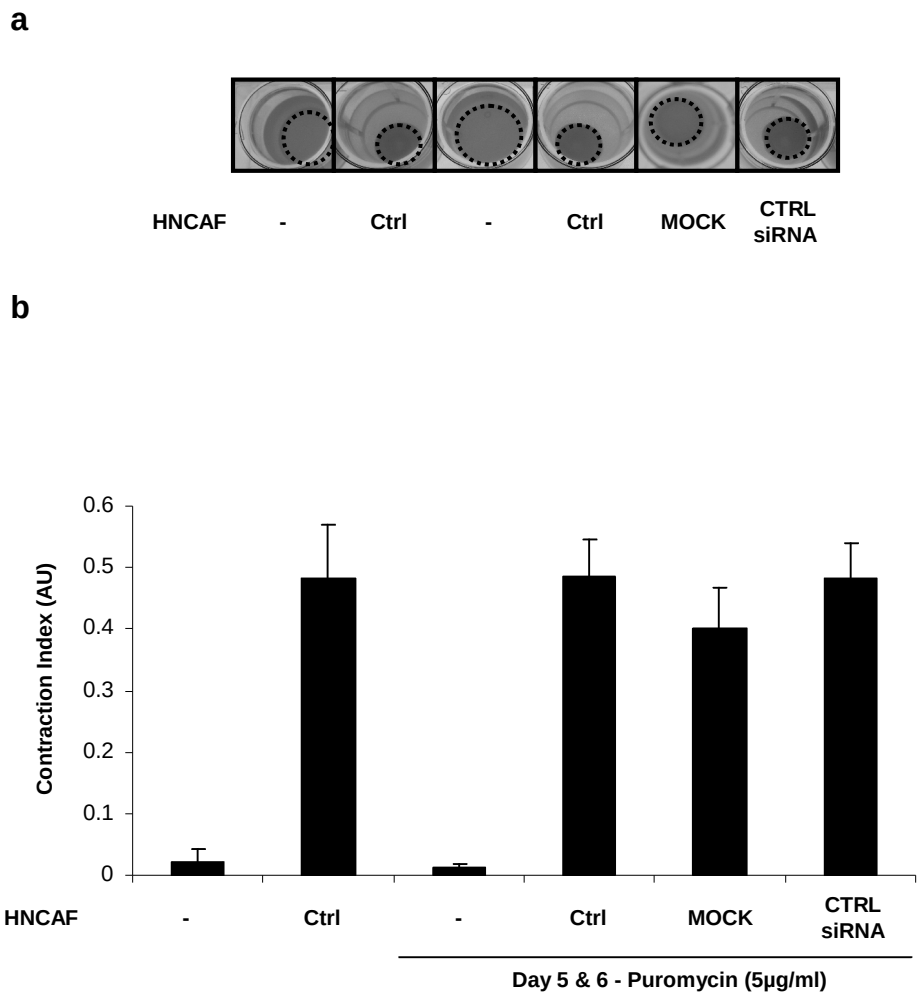

Figure 4.13 Assessment of fibroblast-dependent collagen-Matrigel® matrix contraction: 'Control' gels

(**a**) Images of organotypic gels after 5 days of matrix remodelling prior to the removal of HNCAF from the organotypic assay described in Figure 4.10. The dotted line represents the area of the gel. (**b**) Quantification of the degree of matrix remodelling. The Contraction Index was calculated using the formula 1 - (Gel Area / Well Area). The average of 2 experiments is shown and error bars represent the s.e.

a

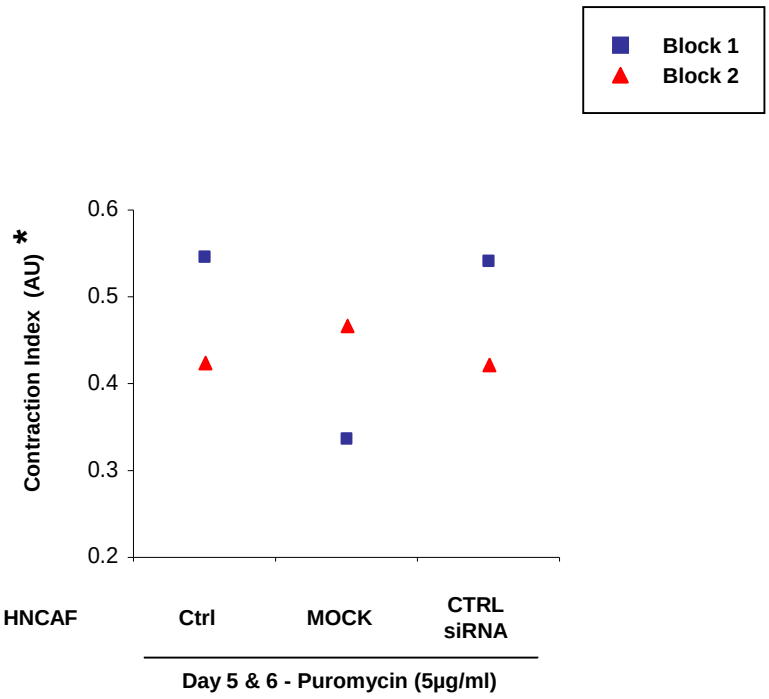

b

Randomized Block ANOVA	p Value	Decision p<0.025
Control vs MOCK	0.501702	Do not reject
MOCK vs Control siRNA	0.516166	Do not reject

Figure 4.14 Assessment of fibroblast-dependent collagen-Matrigel® matrix contraction: 'Control' gels. (a) Scatter plot and (b) randomized block ANOVA statistical analysis

(**a**) Scatter plot displaying the Contraction Index of the 'Control' gels illustrated in Figure 4.13. Individual experimental blocks are shown. *****Denotes an expanded Y-axis. (**b**) Randomized block ANOVA statistical analysis. Null hypothesis (NØ) rejected if $p < 0.025$.

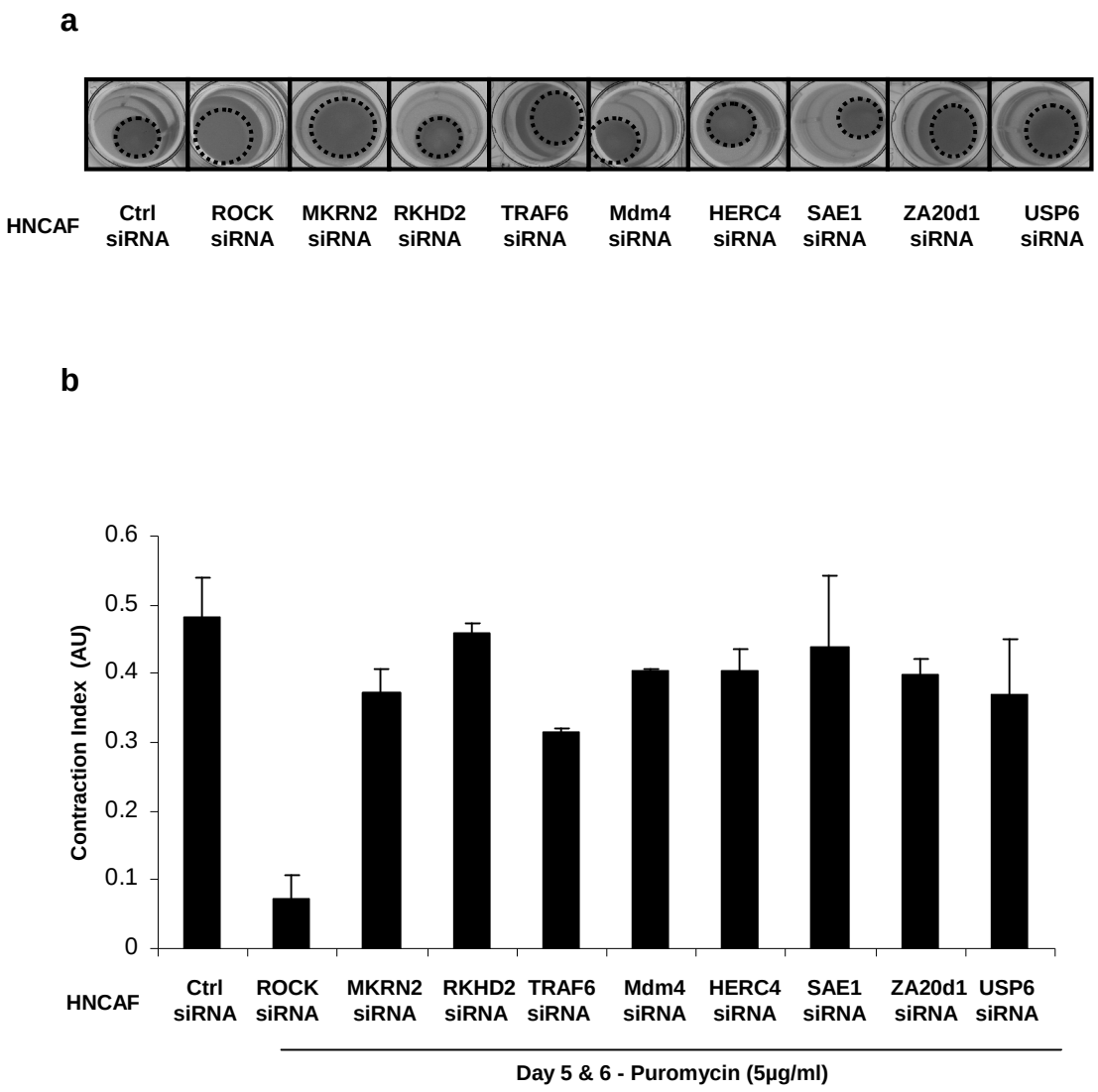

Figure 4.15 Assessment of fibroblast-dependent collagen-Matrigel® matrix contraction: siRNA gene depleted HNCAF gels

(**a**) Images of organotypic gels after 5 days of matrix remodelling prior to the removal of HNCAF from the organotypic assay illustrated in Figure 4.10 The dotted line represents the area of the gel. (**b**) Quantification of the degree of matrix remodelling. The Contraction Index was calculated using the formula 1 - (Gel Area / Well Area). The average of 2 experiments is shown and error bars represent the s.e.

a

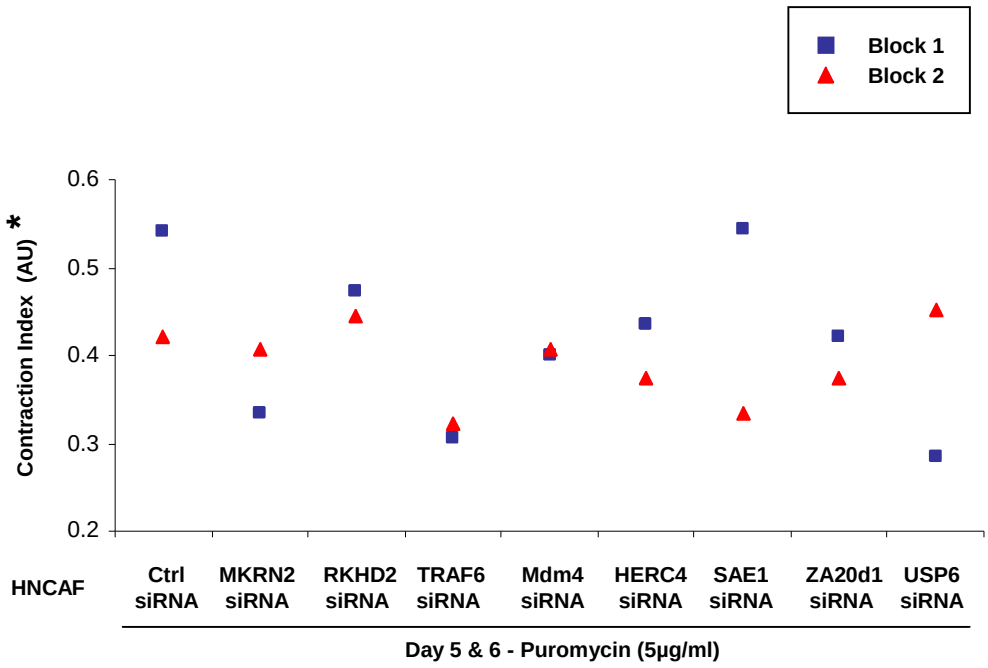

b

Randomized Block ANOVA	p Value	Decision p<0.025
Control siRNA vs MKRN2 siRNA #1+ #4	0.185677	Do not reject
Control siRNA vs RKHD2 siRNA #1+ #4	0.779174	Do not reject
Control siRNA vs TRAF6 siRNA #2 + #3	0.058996	Do not reject
Control siRNA vs Mdm4 siRNA #2 + #3	0.338575	Do not reject
Control siRNA vs HERC4 siRNA #3 + #4	0.344147	Do not reject
Control siRNA vs SAE1 siRNA #1 + #4	0.585704	Do not reject
Control siRNA vs ZA20d1 siRNA #1 + #3	0.310840	Do not reject
Control siRNA vs USP6 siRNA #1 + #3	0.177399	Do not reject

Figure 4.16 Assessment of fibroblast-dependent collagen-Matrigel® matrix contraction: siRNA gene depleted HNCAF gels. (a) Line plot and (b) randomized block ANOVA statistical analysis

(**a**) Scatter plot displaying the Contraction Index of the siRNA gene depleted HNCAF gels illustrated in Figure 4.15. Individual experimental blocks are shown. *Denotes an expanded Y-axis. (**b**) Randomized block ANOVA statistical analysis. Null hypothesis (NØ) rejected if $p < 0.025$.

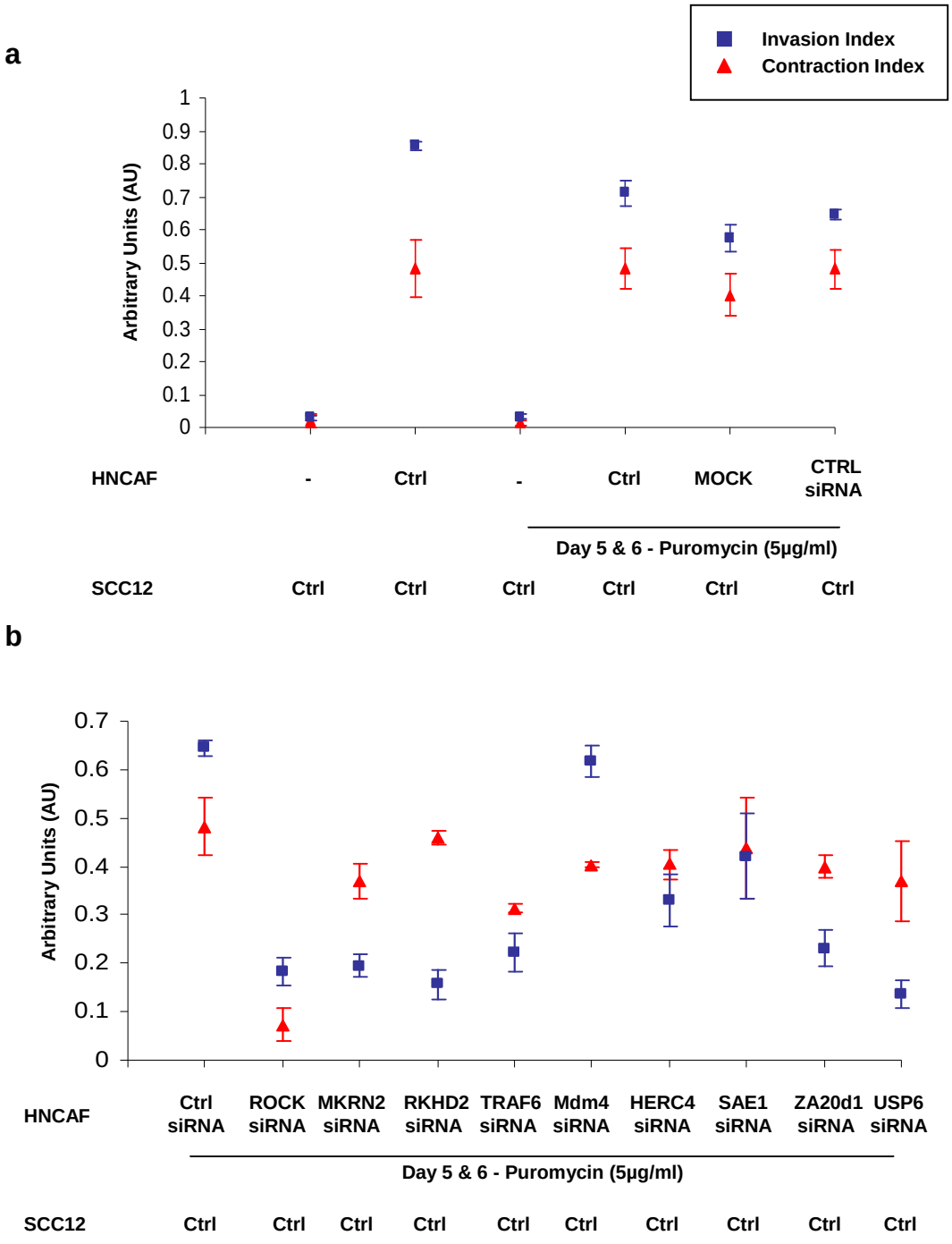

Figure 4.17 Relationship between SCC invasion and collagen-Matrigel® matrix contraction

Scatter plots displaying the relationship between mean carcinoma invasion (blue) and mean gel contraction (red) of the organotypic assay illustrated in Figure 4.10. (**a**) 'Control' gels and (**b**) siRNA gene depleted HNCAF gels. Error bars represent the s.e.

4.4 Summary of siRNA screening

A summary of the results of the various morphological and functional screens described in Chapters 3 and 4 is presented diagrammatically in Figure 4.18.

4.4.1 Gene hits

Five genes: 3 E3 ubiquitin ligases (MKRN2, RKHD2, and TRAF6) and 2 de-ubiquitinating enzymes (ZA20d1 and USP6) were identified as potential candidate genes for detailed study.

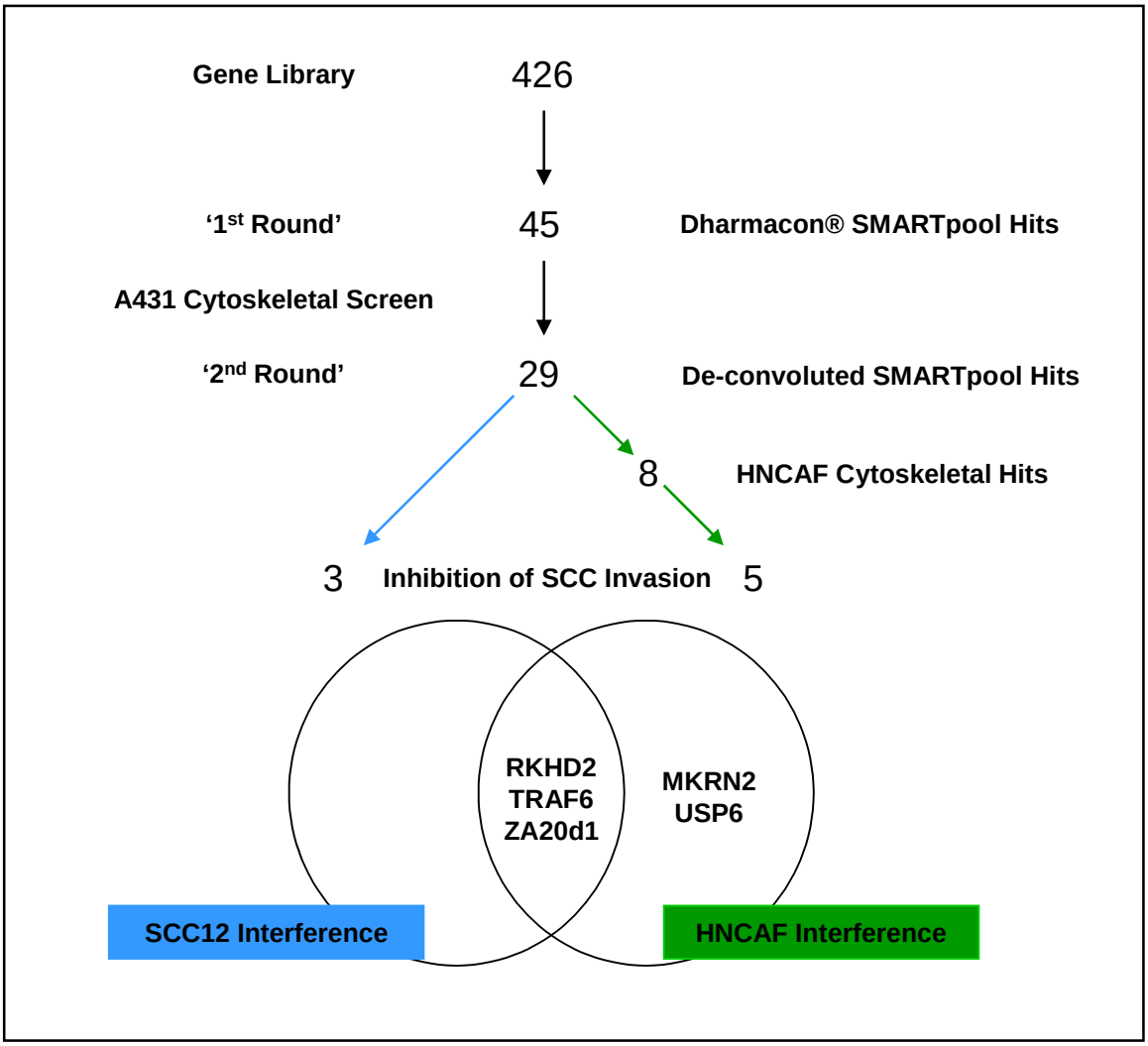

Figure 4.18 Summary of siRNA screening

Diagrammatic representation of the morphological and functional screens undertaken to identify regulators of SCC invasion using Dharmacon® SMARTpool siRNA libraries targeting 289 E3 ubiquitin ligases and 137 de-ubiquitinating enzymes.

4.5 Summary

- To investigate the role of my 29 '2nd Round' gene hits on SCC invasion a functional siRNA screen using an organotypic culture system was performed. Three genes, (RKHD2, TRAF6 and ZA20d1), when individually depleted in SCC12 cells were associated with a statistically significant reduction in carcinoma invasion.

- To assess the influence of my 8 'CAF' gene hits on the ability of stromal fibroblasts to promote carcinoma invasion, a modified two-stage organotypic assay was conducted. Five genes, (MKRN2, RKHD2, TRAF6, ZA20d1 and USP6), when individually depleted in HNCAF impaired their ability to promote SCC invasion.

- Previous work from our group has shown a good correlation between the extent of collagen-Matrigel® matrix contraction and the ability of stromal fibroblasts to promote carcinoma invasion [77]. The relationship between these two parameters for my genes of interest was inconsistent.

- Following morphological and functional screening, 3 E3 ubiquitin ligases (MKRN2, RKHD2 and TRAF6) and 2 de-ubiquitinating enzymes (ZA20d1 and USP6), emerged from the original 426 siRNA gene library as potential candidates for detailed study.

Chapter 5

Validation of gene hits and candidate genes

5.1 Introduction

Of the 5 genes identified from the various cytoskeletal and functional screens outlined in Chapters 3 and 4, RKHD2, TRAF6, ZA20d1 and USP6 were selected for further validation. At this stage, results suggested that RKHD2, TRAF6 and ZA20d1 were functionally important to carcinoma invasion in both SCC12 cells and HNCAF. MKRN2 was 'dropped' at this time on the basis of its poor performance in the SCC organotypic invasion screen compared to that of USP6 (Chapter 4, Figures 4.2 and 4.9).

The results of this validation process, the selection of candidate genes and their subsequent confirmation as regulators of carcinoma invasion are presented here.

5.2 Validation of gene hits

5.2.1 Qiagen® siRNA screen

For each of RKHD2, TRAF6, ZA20d1 and USP6 four additional siRNA duplexes were purchased from Qiagen®. These oligonucleotides were screened in A431 cells (as described in Chapter 3, Section 3.2.1) to assess the legitimacy of the morphological changes previously noted following gene depletion. Figures 5.1 and 5.2 show representative images of the cell phenotypes observed.

The results of this cytoskeletal screen were consistent with those obtained using Dharmacon® siRNA. The predominant cell phenotypes observed following gene depletion in A431 cells were: RKHD2 - elongated, TRAF6 - elongated, ZA20d1 - spiky and USP6 - elongated.

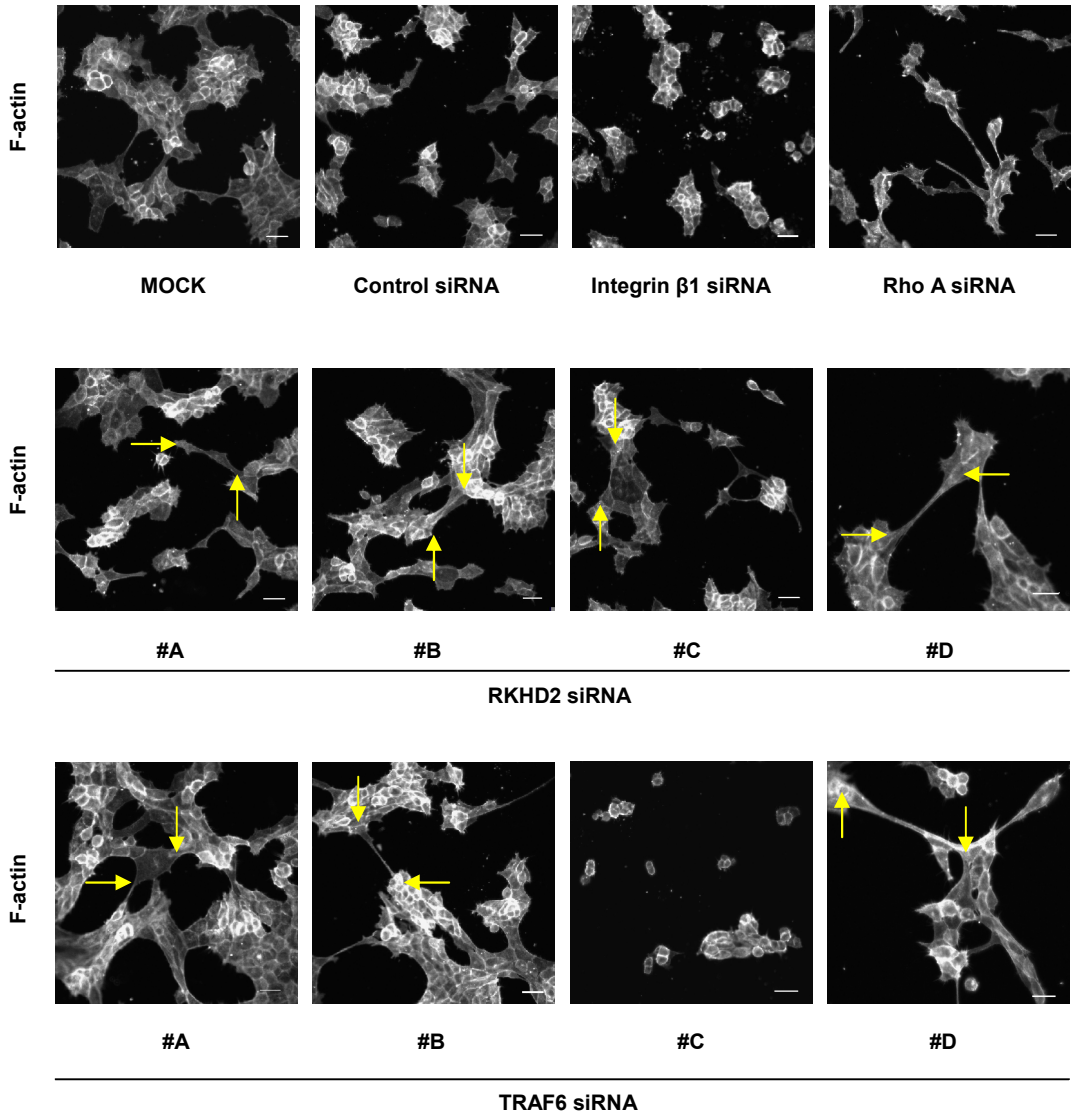

Figure 5.1 Qiagen® siRNA screen in A431 cells: RKHD2 and TRAF6 gene depletion

Phenotypes of A431 cells on deformable collagen-Matrigel® gels 72 hours following transfection with control, Integrin β1, Rho A, RKHD2, and TRAF6 siRNA duplexes. Arrows indicate examples of elongated cells. Cells stained with TRITC phalloidin. Scale bar represents 50μm.

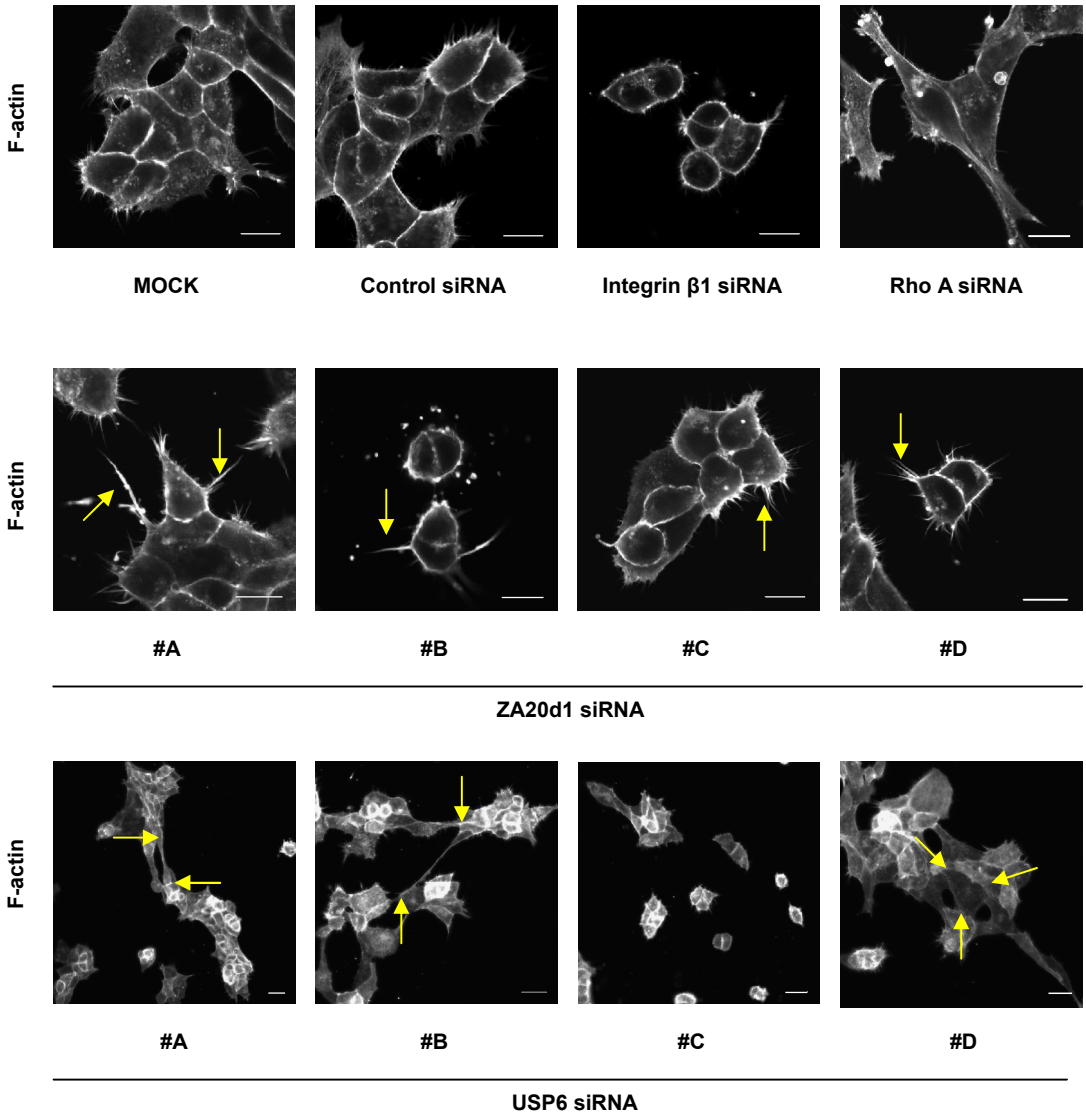

Figure 5.2 Qiagen® siRNA screen in A431 cells: ZA20d1 and USP6 gene depletion

Phenotypes of A431 cells on deformable collagen-Matrigel® gels 72 hours following transfection with control, Integrin β1, Rho A, ZA20d1 and USP6 siRNA duplexes. Arrows indicate examples of actin-rich spikes. Cells stained with TRITC phalloidin. Scale bar represents 20μm.

5.2.2 Quantitative polymerase chain reaction (qPCR)

For RKHD2, TRAF6 and ZA20d1 quantitative polymerase chain reaction (qPCR) assays were performed to assess the knockdown efficiency of each siRNA duplex for its target gene. USP6 was 'dropped' at this stage since I was unable to design a functional set of forward and reverse DNA primers necessary to generate the desired PCR product.

RNA was extracted from A431 cells 72 hours following transfection and mRNA transcriptional output correlated to the cell phenotype observed on a collagen-Matrigel® gel. qPCR assays were performed in triplicate and normalised to GAPDH which was chosen as a house-keeping gene.

Figure 5.3 illustrates the elongated cell phenotypes observed in A431 cells following RKHD2 gene depletion. Figures 5.4a and 5.4b show the relative knockdown efficiencies of the Dharmacon® and Qiagen® siRNA duplexes respectively. All eight oligonucleotides resulted in approximately 60% or greater reduction in mRNA transcriptional output compared to the mock sample. Figures 5.4c and 5.5 confirm transfection efficiency.

Figure 5.6 illustrates the elongated cell phenotypes observed in A431 cells following TRAF6 gene depletion. Figures 5.7a and 5.7b show the relative knockdown efficiencies of the Dharmacon® and Qiagen® siRNA duplexes respectively. Four of the eight oligonucleotides, #1, #2, #3 and #B, resulted in approximately 50% or greater reduction in mRNA transcriptional output compared to the mock sample. Figures 5.7c and 5.8 confirm transfection efficiency.

Figure 5.9 illustrates the actin-rich spikes observed in A431 cells following ZA20d1 gene depletion. Figures 5.10a and 5.10b show the relative knockdown efficiencies of the Dharmacon® and Qiagen® siRNA duplexes respectively. All of the oligonucleotides, other than #4, resulted in approximately 50% or greater reduction in mRNA transcriptional output compared to the mock sample. Figures 5.10c and 5.11 confirm transfection efficiency.

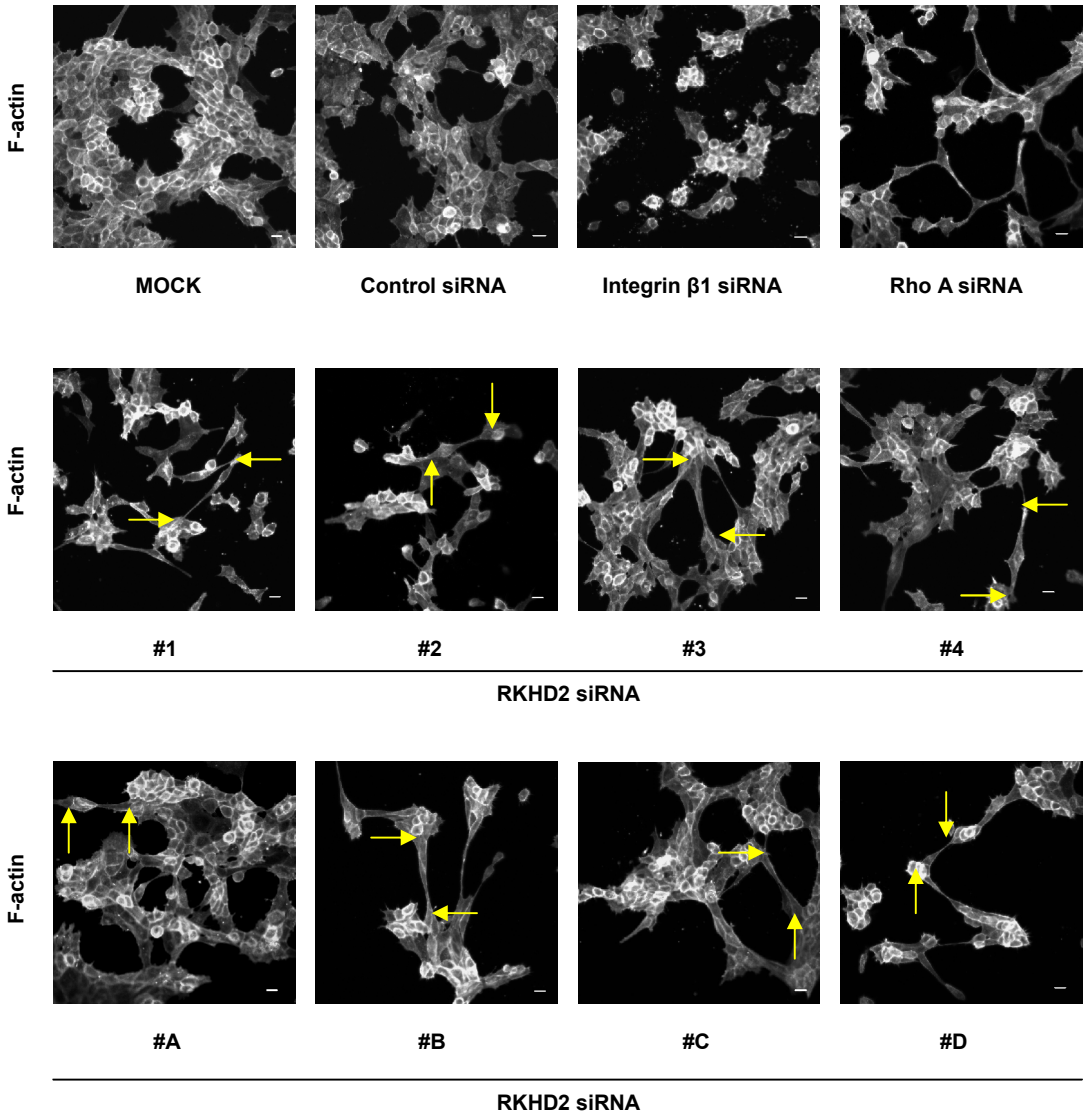

Figure 5.3 Validation of Dharmacon® and Qiagen® RKHD2 siRNA duplexes: A431 cell phenotypes

Phenotypes of A431 cells on deformable collagen-Matrigel® gels 72 hours following transfection with control, Integrin β1, Rho A and RKHD2 siRNA duplexes. Arrows indicate examples of elongated cells. Cells stained with TRITC phalloidin. Scale bar represents 20μm.

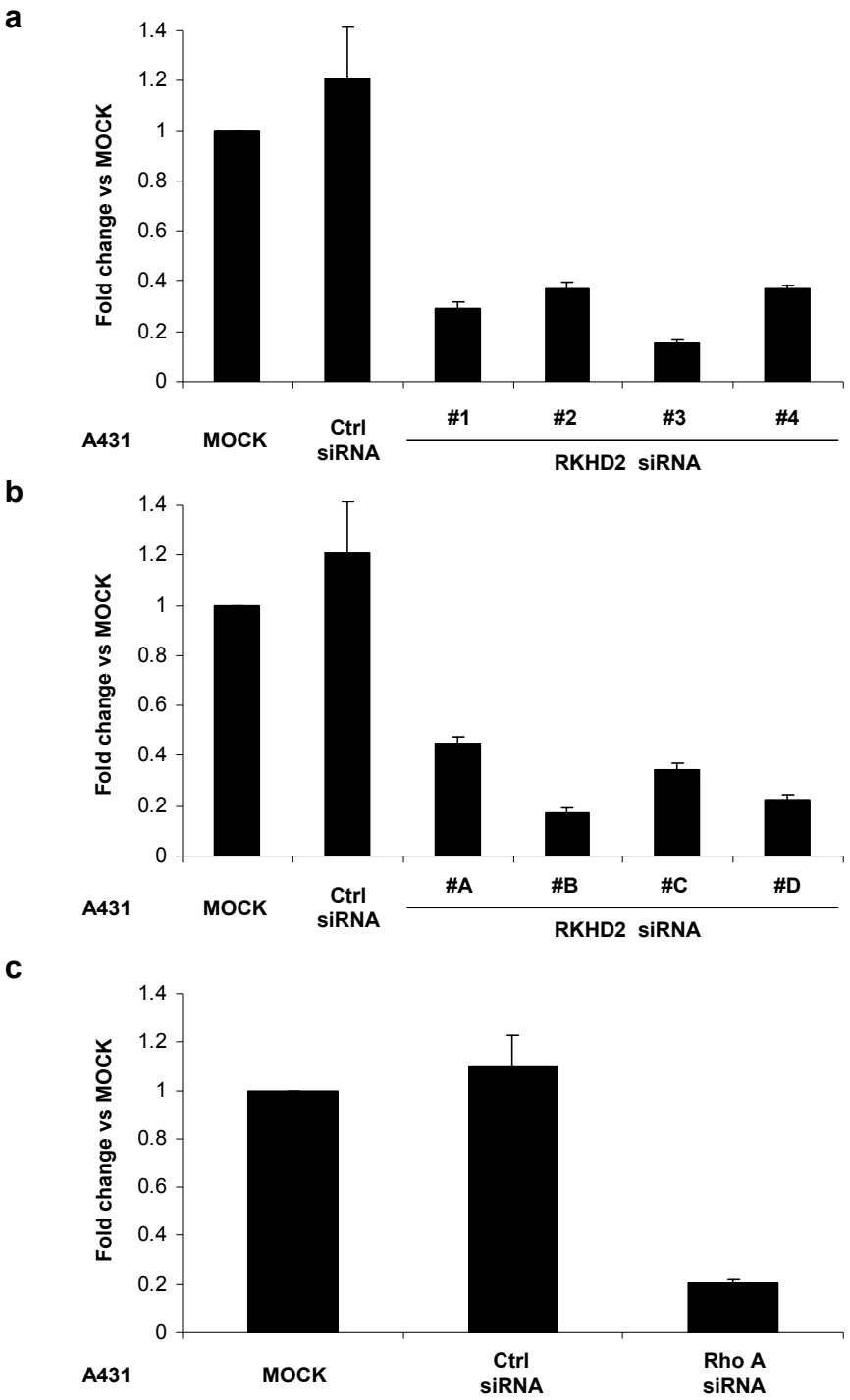

Figure 5.4 Validation of Dharmacon® and Qiagen® RKHD2 siRNA duplexes: quantitative polymerase chain reaction (qPCR)

qPCR assays were performed to assess mRNA transcriptional output in A431 cells 72 hours following siRNA transfection. Values were normalised to GAPDH which was selected as a house-keeping gene. The average value of 3 independent experiments is shown and error bars indicate the s.e. (**a**) Dharmacon® RKHD2 siRNA duplexes. (**b**) Qiagen® RKHD2 siRNA duplexes. (**c**) Rho A siRNA duplex. This was included as a positive transfection control.

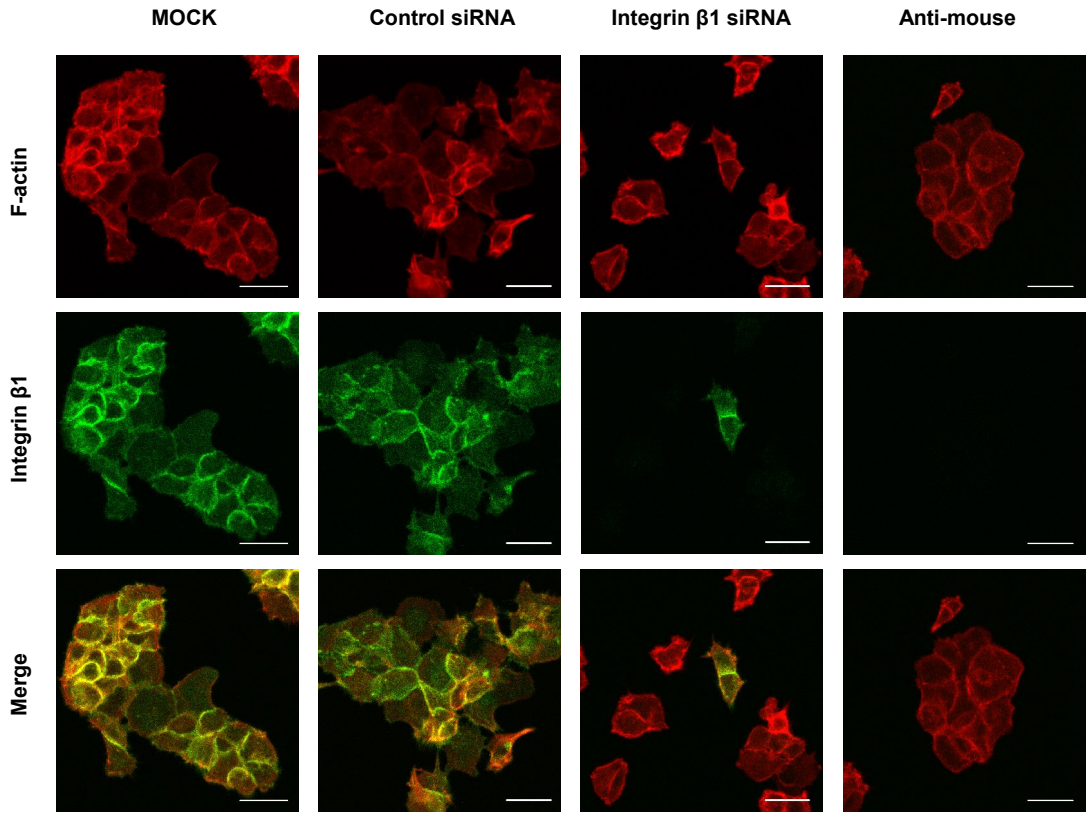

Figure 5.5 Validation of Dharmacon® and Qiagen® RKHD2 siRNA duplexes: Integrin β1 immunofluoresence

Immunofluoresence staining of A431 cells on glass 72 hours following transfection with Integrin β1 siRNA confirming gene knockdown efficiency. This acted as an additional positive transfection control. Cells also stained with TRITC phalloidin. Scale bar represents 50μm.

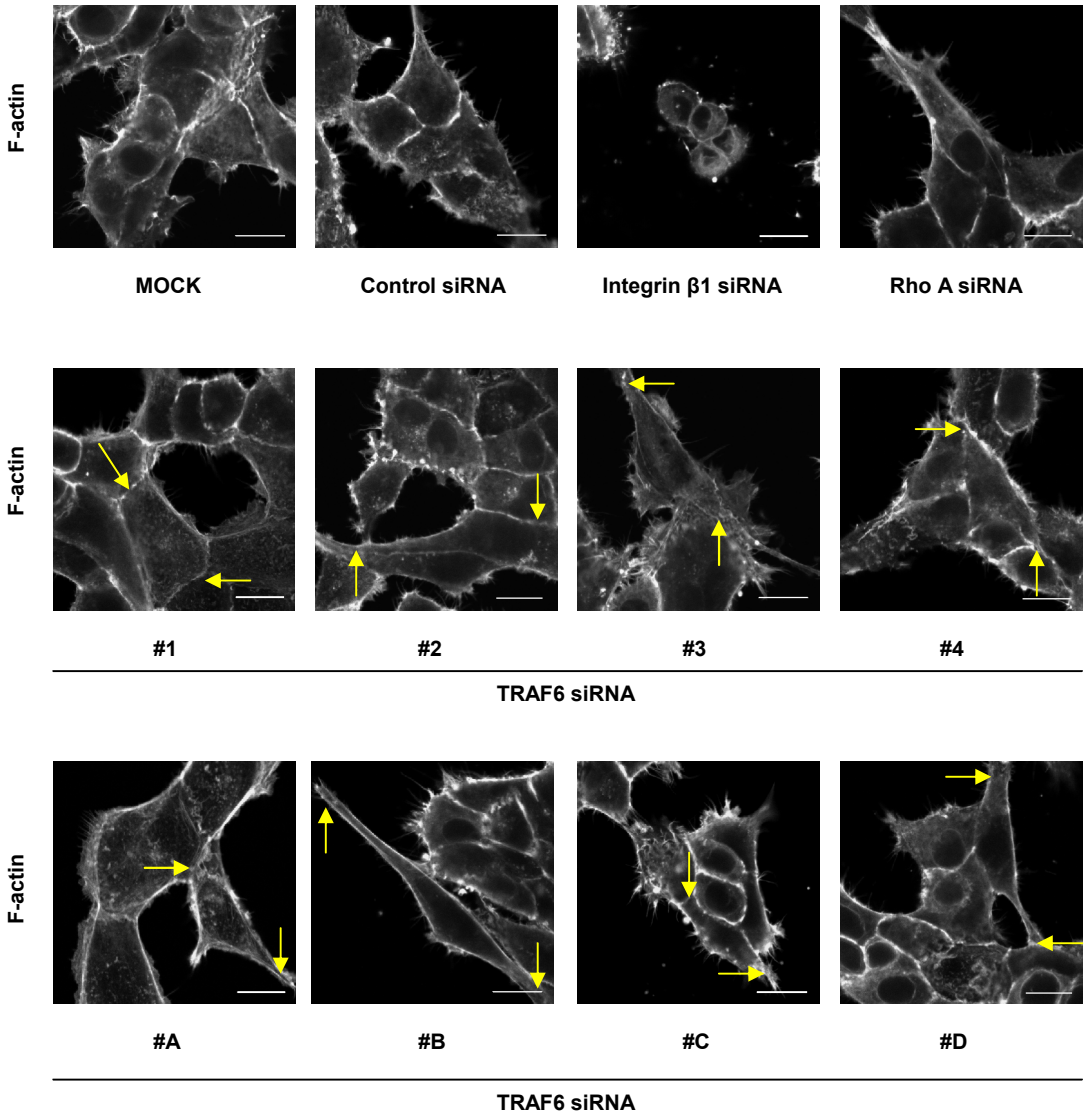

Figure 5.6 Validation of Dharmacon® and Qiagen® TRAF6 siRNA duplexes: A431 cell phenotypes

Phenotypes of A431 cells on deformable collagen-Matrigel® gels 72 hours following transfection with control, Integrin β1, Rho A and TRAF6 siRNA duplexes. Arrows indicate examples of elongated flat cells. Cells stained with TRITC phalloidin. Scale bar represents 20μm.

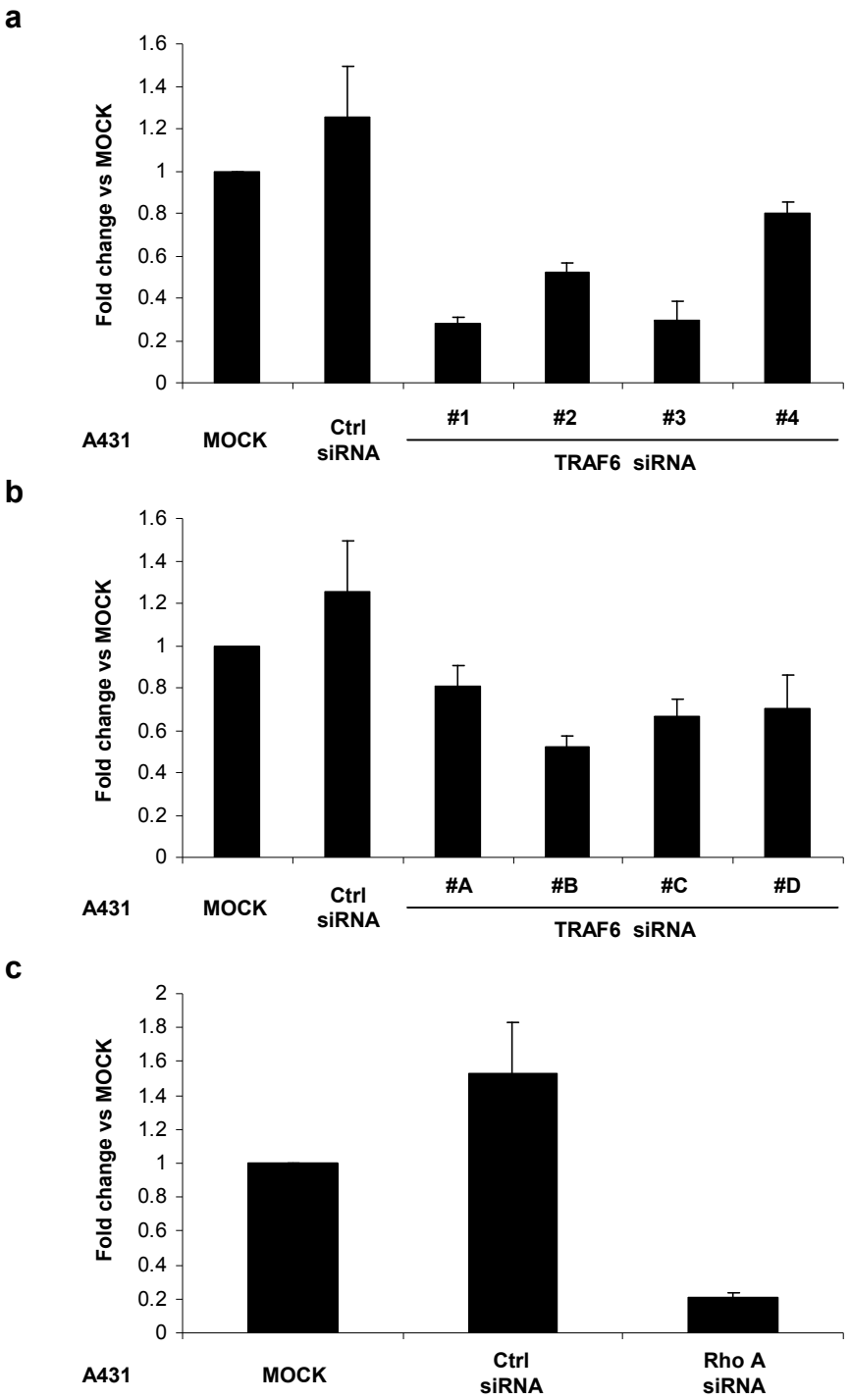

Figure 5.7 Validation of Dharmacon® and Qiagen® TRAF6 siRNA duplexes: quantitative polymerase chain reaction (qPCR)

qPCR assays were performed to assess mRNA transcriptional output in A431 cells 72 hours following siRNA transfection. Values were normalised to GAPDH which was selected as a house-keeping gene. The average value of 3 independent experiments is shown and error bars indicate the s.e. (**a**) Dharmacon® TRAF6 siRNA duplexes. (**b**) Qiagen® TRAF6 siRNA duplexes. (**c**) Rho A siRNA duplex. This was included as a positive transfection control.

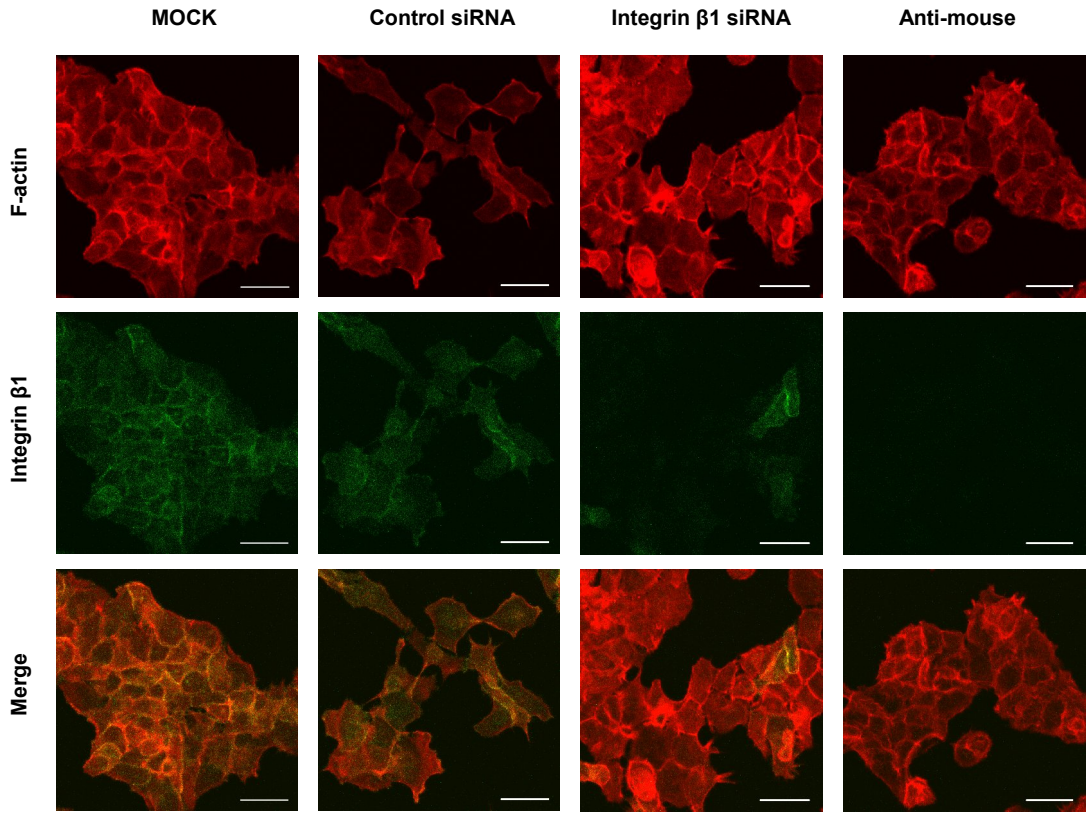

Figure 5.8 Validation of Dharmacon® and Qiagen® TRAF6 siRNA duplexes: Integrin β1 immunofluoresence

Immunofluoresence staining of A431 cells on glass 72 hours following transfection with Integrin β1 siRNA confirming gene knockdown efficiency. This acted as an additional positive transfection control. Cells also stained with TRITC phalloidin. Scale bar represents 50μm.

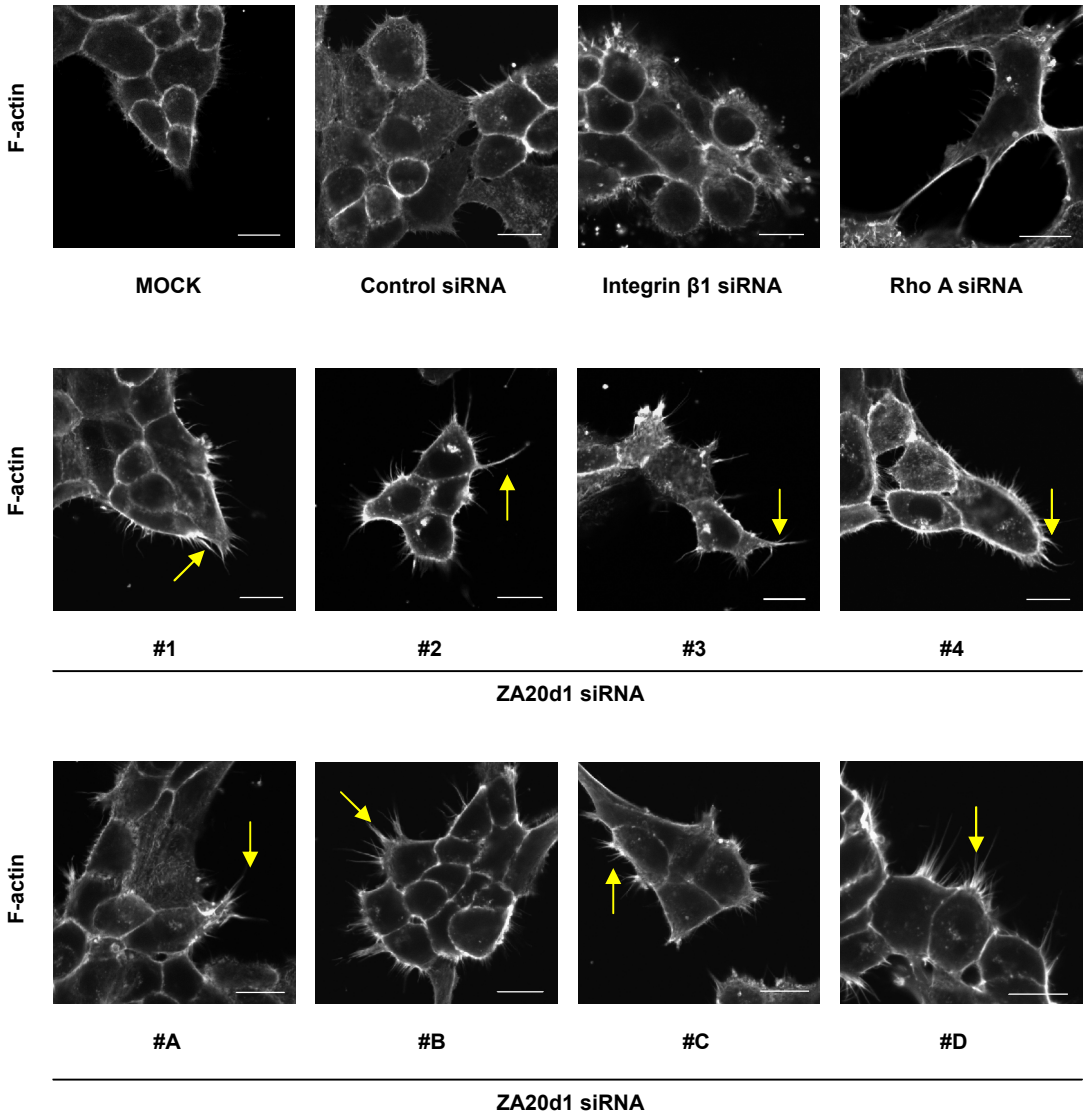

Figure 5.9 Validation of Dharmacon® and Qiagen® ZA20d1 siRNA duplexes: A431 cell phenotypes

Phenotypes of A431 cells on deformable collagen-Matrigel® gels 72 hours following transfection with control, Integrin β1, Rho A and ZA20d1 siRNA duplexes. Arrows indicate examples of actin-rich spikes. Cells stained with TRITC phalloidin. Scale bar represents 20μm.

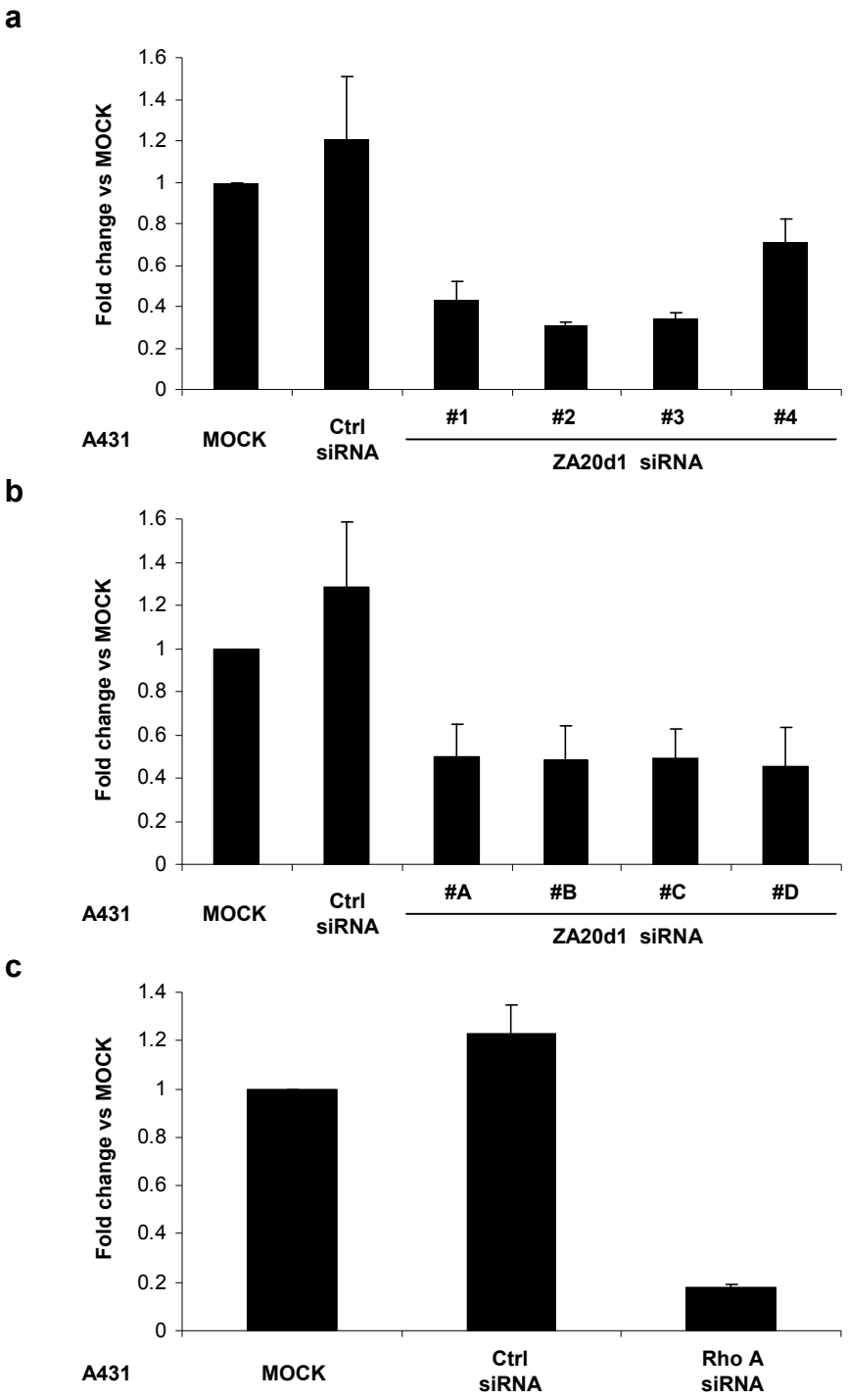

Figure 5.10 Validation of Dharmacon® and Qiagen® ZA20d1 siRNA duplexes: quantitative polymerase chain reaction (qPCR)

qPCR assays were performed to assess mRNA transcriptional output in A431 cells 72 hours following siRNA transfection. Values were normalised to GAPDH which was selected as a house-keeping gene. The average value of 3 independent experiments is shown and error bars indicate the s.e. (**a**) Dharmacon® ZA20d1 siRNA duplexes. (**b**) Qiagen® ZA20d1 siRNA duplexes. (**c**) Rho A siRNA duplex. This was included as a positive transfection control.

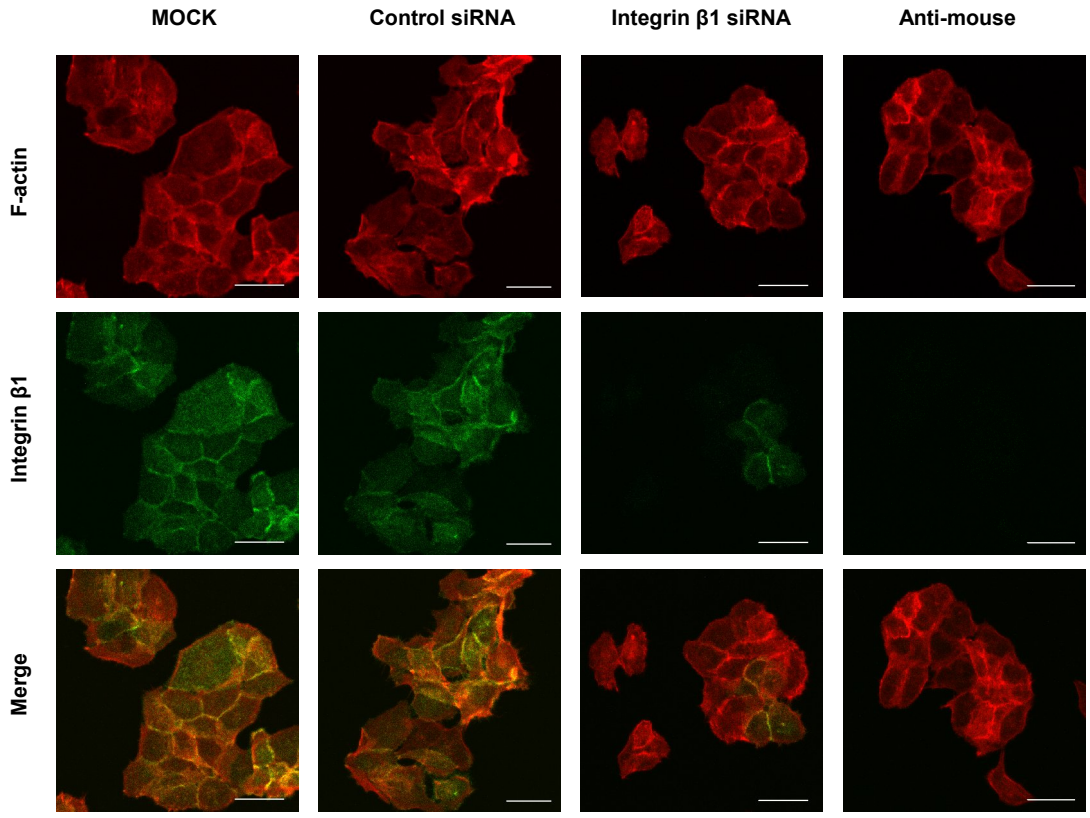

Figure 5.11 Validation of Dharmacon® and Qiagen® ZA20d1 siRNA duplexes: Integrin β1 immunofluoresence

Immunofluoresence staining of A431 cells on glass 72 hours following transfection with Integrin β1 siRNA confirming gene knockdown efficiency. This acted as an additional positive transfection control. Cells also stained with TRITC phalloidin. Scale bar represents 50μm.

5.2.3 TRAF6 immunofluoresence (IMF)

Of my potential candidate genes, RKHD2, TRAF6 and ZA20d1, antibodies were only available commercially for TRAF6. Anti-TRAF6 antibodies were therefore purchased from Abcam® and Santa Cruz Biotechnology Inc.

Figure 5.12 demonstrates IMF staining for TRAF6 in A431 cells on glass 72 hours following transfection with the pUNO-hTRAF6-HA construct. Images were captured to optimally show TRAF6-HA positive cells. TRAF6 expression was cytosolic.

The rabbit monoclonal antibody manufactured by Abcam® was considered to be the better of the two anti-TRAF6 antibodies and was further validated in TRAF6-HA positive cells using 12CA5, a HA-tag antibody (Figure 5.13).

5.3 The selection of candidate genes

5.3.1 TRAF6 and ZA20d1

At this stage of my research, a review of the scientific literature indicated that TRAF6 and ZA20d1 were positive and negative regulators of canonical NF-κB signalling in epithelial cells [163, 307]. Co-immunoprecipitation studies also suggested that ZA20d1 was the complementary DUB to TRAF6 and that its interaction with TRAF6 was critical to downstream signalling events following TNFR and IL-1R activation [308]. In view of this, and given the importance of NF-κB pathways in the pathogenesis of SCC, TRAF6 and ZA20d1 were selected as candidate genes for detailed study.

5.3.2 RKHD2

RKHD2 was not selected as a candidate gene for detailed study. Currently there is no experimental data regarding its function other than a single study which speculatively links its E3 ligase activity to the pathogenesis of essential hypertension [309].

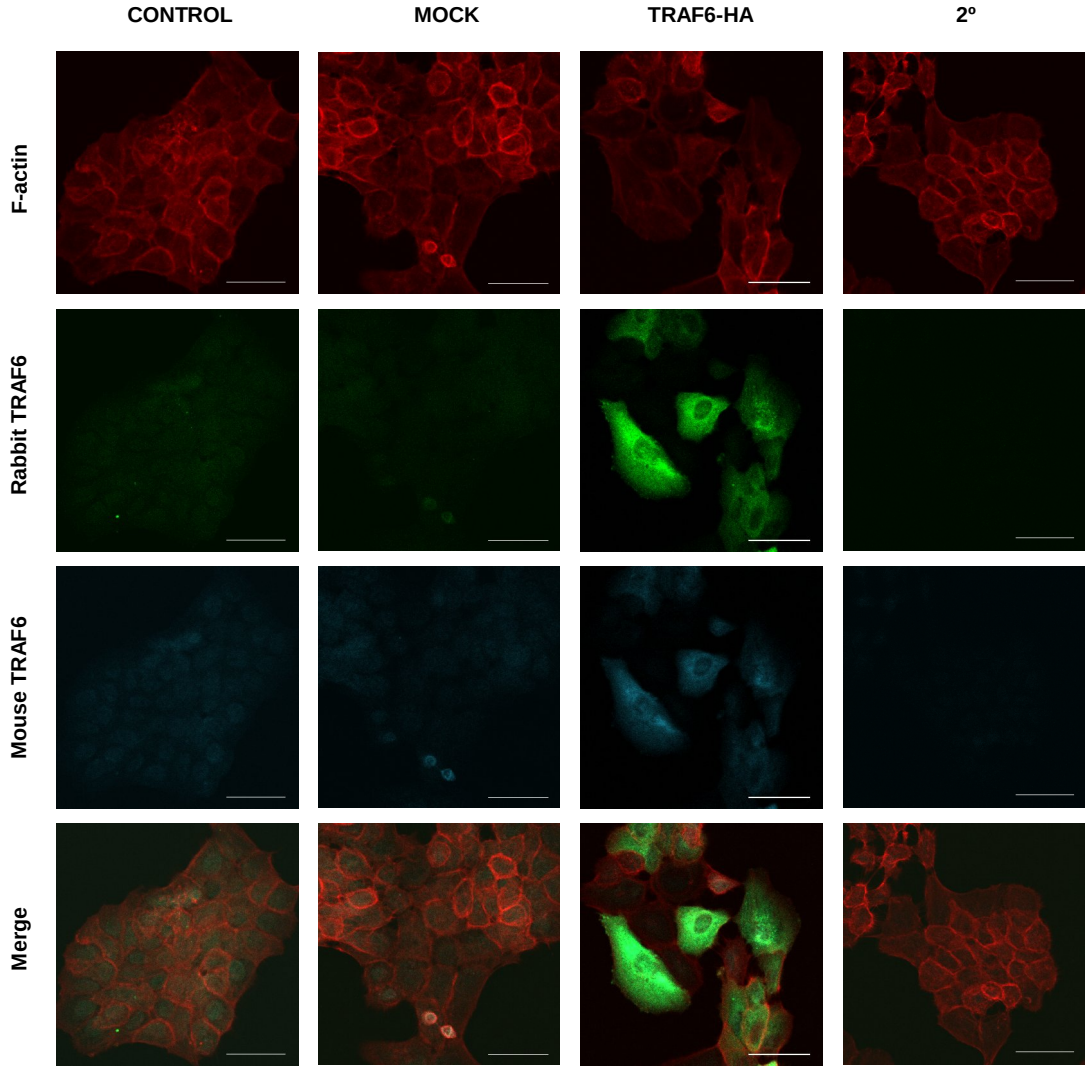

Figure 5.12 TRAF6 immunofluoresence

Immunofluoresence staining of A431 cells on glass 72 hours following transfection with the pUNO-hTRAF6-HA construct. Cells stained with rabbit anti-TRAF6 (1:50) and mouse anti-TRAF6 (1:50) antibodies. Cells also stained with TRITC phalloidin. Scale bar represents 50µm.

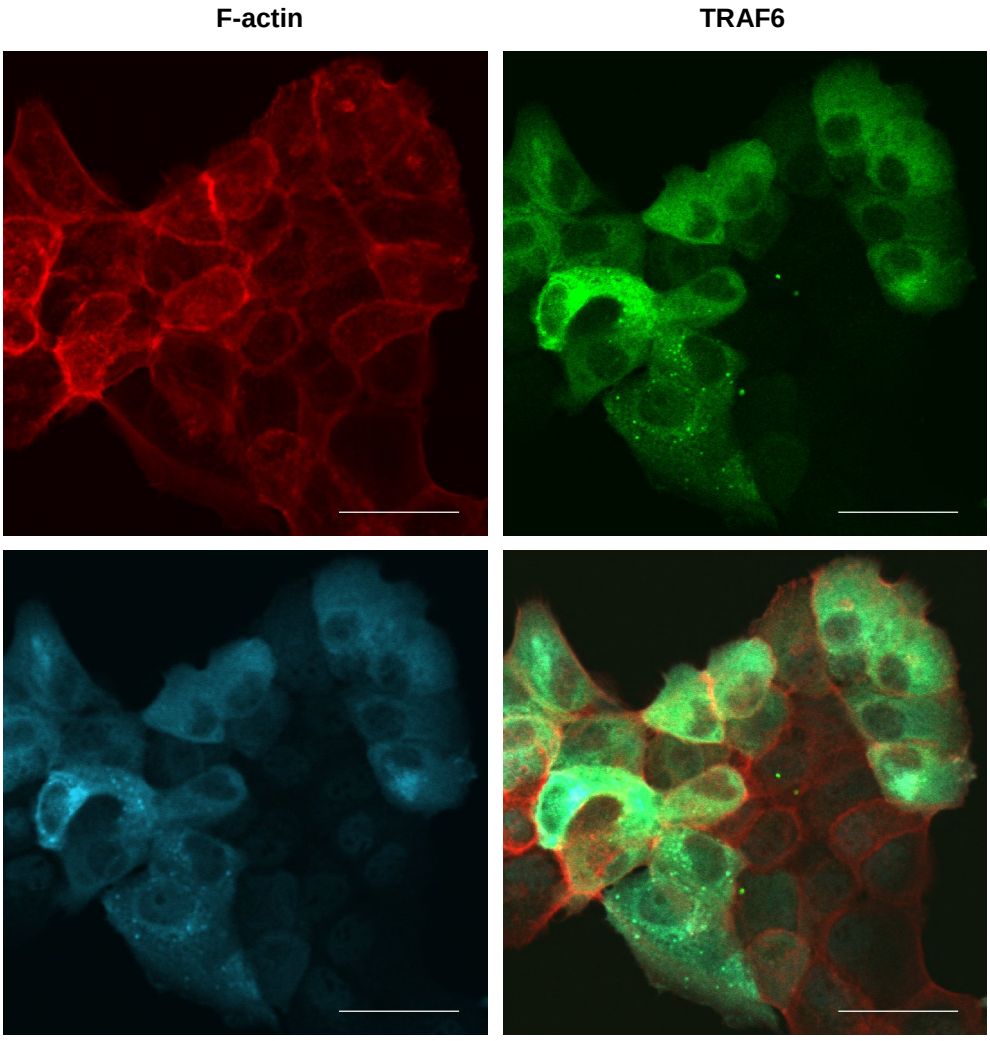

Figure 5.13 TRAF6-HA positive A431 cells

Immunofluoresence staining of A431 cells on glass 72 hours following transfection with the pUNO-hTRAF6-HA construct. Cells stained with rabbit anti-TRAF6 (1:50) and mouse 12CA5 (1:50) antibodies. 12CA5 is a HA-tag antibody. Cells also stained with TRITC phalloidin. Scale bar represents 50µm.

5.4 Functional validation of candidate genes

Having chosen TRAF6 and ZA20d1 as candidate genes, I sought to validate their function as regulators of carcinoma invasion in SCC12 cells by performing organotypic assays using six targeting siRNA duplexes for each gene. These were selected on the basis of their ability to knockdown TRAF6 (Figure 5.7) and ZA20d1 (Figure 5.10) respectively.

5.4.1 TRAF6 is required in SCC12 cells for carcinoma invasion *in vitro*

Figure 5.14a consists of representative photomicrographs of H&E sections from these assays. Silencing of TRAF6 with each of the six siRNA oligonucleotides inhibited carcinoma invasion compared to the control samples, evident by the reduced number of cancer cells infiltrating the ECM. Figure 5.14b shows the quantification of carcinoma invasion. A scatter plot of the individual experimental blocks is presented in Figure 5.15a. The reduction in carcinoma invasion observed following TRAF6 gene depletion was statistically significant for all six duplexes (Figure 5.15b).

Figure 5.16 demonstrates the efficacy of TRAF6 siRNA gene depletion in SCC12 cells 72 hours following transfection. Cell lysates were made in parallel with Block 1 of the organotypic assay illustrated in Figure 5.14.

5.4.2 ZA20d1 is required in SCC12 cells for carcinoma invasion *in vitro*

Figure 5.17a consists of representative photomicrographs of H&E sections from these assays. Silencing of ZA20d1 with each of the six siRNA oligonucleotides inhibited carcinoma invasion compared to the control samples, evident by the reduced number of cancer cells infiltrating the ECM. Figure 5.17b shows the quantification of carcinoma invasion. A scatter plot of the individual experimental blocks is also presented in Figure 5.18a. The reduction in carcinoma invasion observed following ZA20d1 gene depletion was statistically significant for five of the six duplexes (Figure 5.18b).

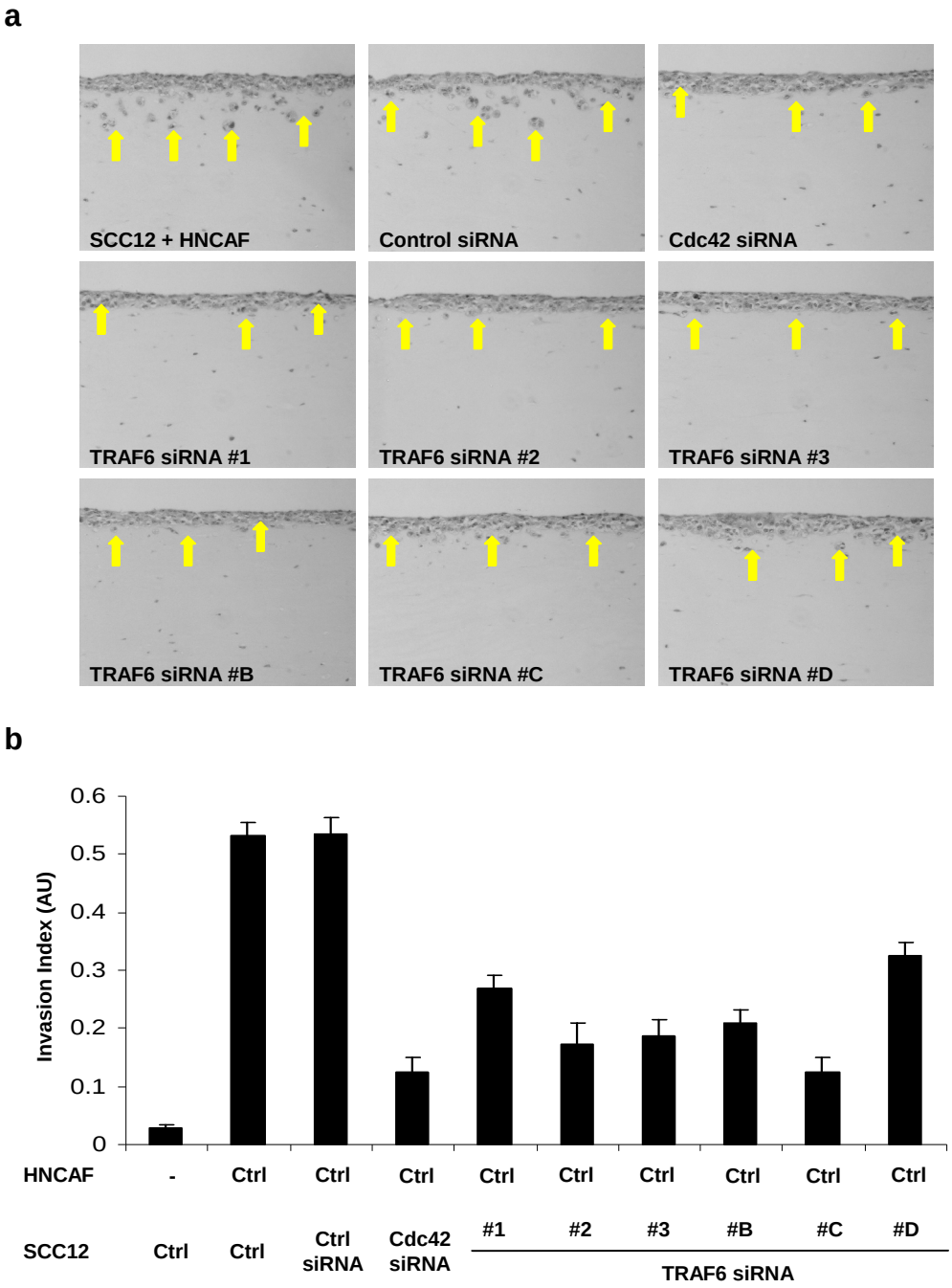

Figure 5.14 SCC12 organotypic invasion assay: TRAF6 gene depletion

(**a**) H&E stained sections of SCC12 cells cultured in organotypic gels. Arrows point to the invading front of carcinoma cells. (**b**) Quantification of carcinoma invasion in organotypic gels in the absence of stromal fibroblasts, in the presence of stromal fibroblasts and with Cdc42 or TRAF6 inhibited by siRNA in SCC12 cells. The average of 15 visual fields from 3 experiments is shown. The error bars represent the s.e.

a

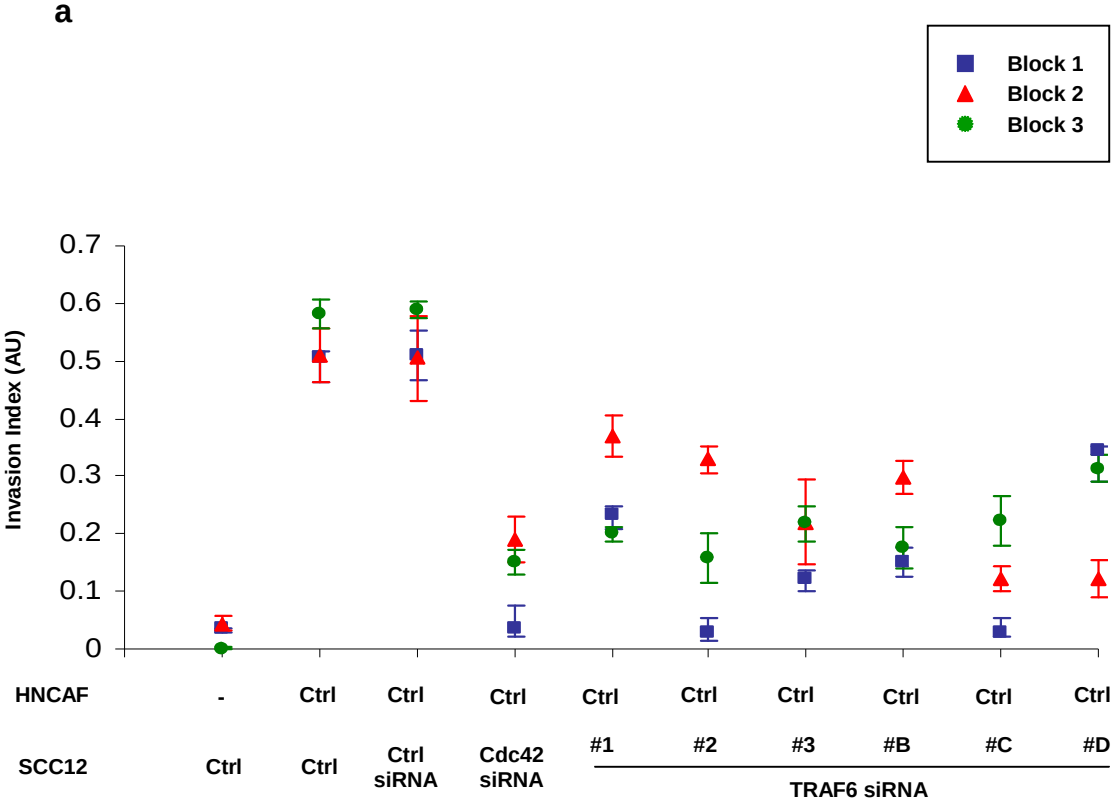

b

Randomized Block ANOVA	p Value	Decision p<0.007
Control vs Control siRNA	0.979053	Do not reject
Control siRNA vs TRAF6 siRNA #1	0.000428	Reject
Control siRNA vs TRAF6 siRNA #2	0.00022	Reject
Control siRNA vs TRAF6 siRNA #3	0.00034	Reject
Control siRNA vs TRAF6 siRNA #B	0.000066	Reject
Control siRNA vs TRAF6 siRNA #C	0.000006	Reject
Control siRNA vs TRAF6 siRNA #D	0.003054	Reject

Figure 5.15 TRAF6 is required in SCC12 cells for carcinoma invasion *in vitro*

(**a**) Scatter plot displaying quantification of carcinoma invasion of the organotypic assay illustrated in Figure 5.14. Individual experimental blocks are illustrated. The average of 5 visual fields is shown and error bars represent the s.e. (**b**) Randomized block ANOVA statistical analysis. Null hypothesis (NØ) rejected if $p < 0.007$.

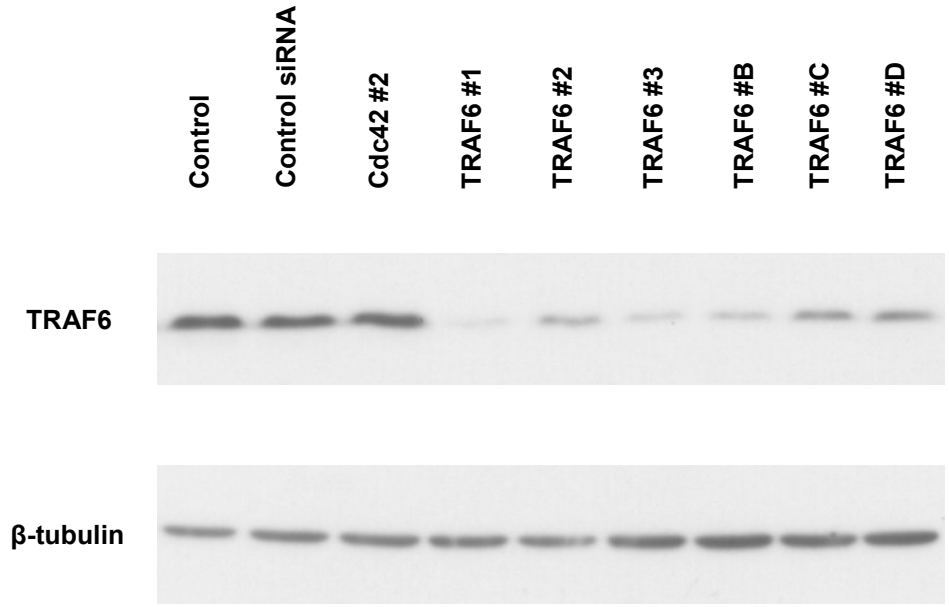

Figure 5.16 Western blot demonstrating the efficacy of TRAF6 siRNA gene depletion in SCC12 cells

Western blot of SCC12 cell lysates 72 hours post-transfection showing the efficient knockdown of TRAF6. These lysates were made in parallel with Block 1 of the organotypic assay illustrated in Figure 5.14.

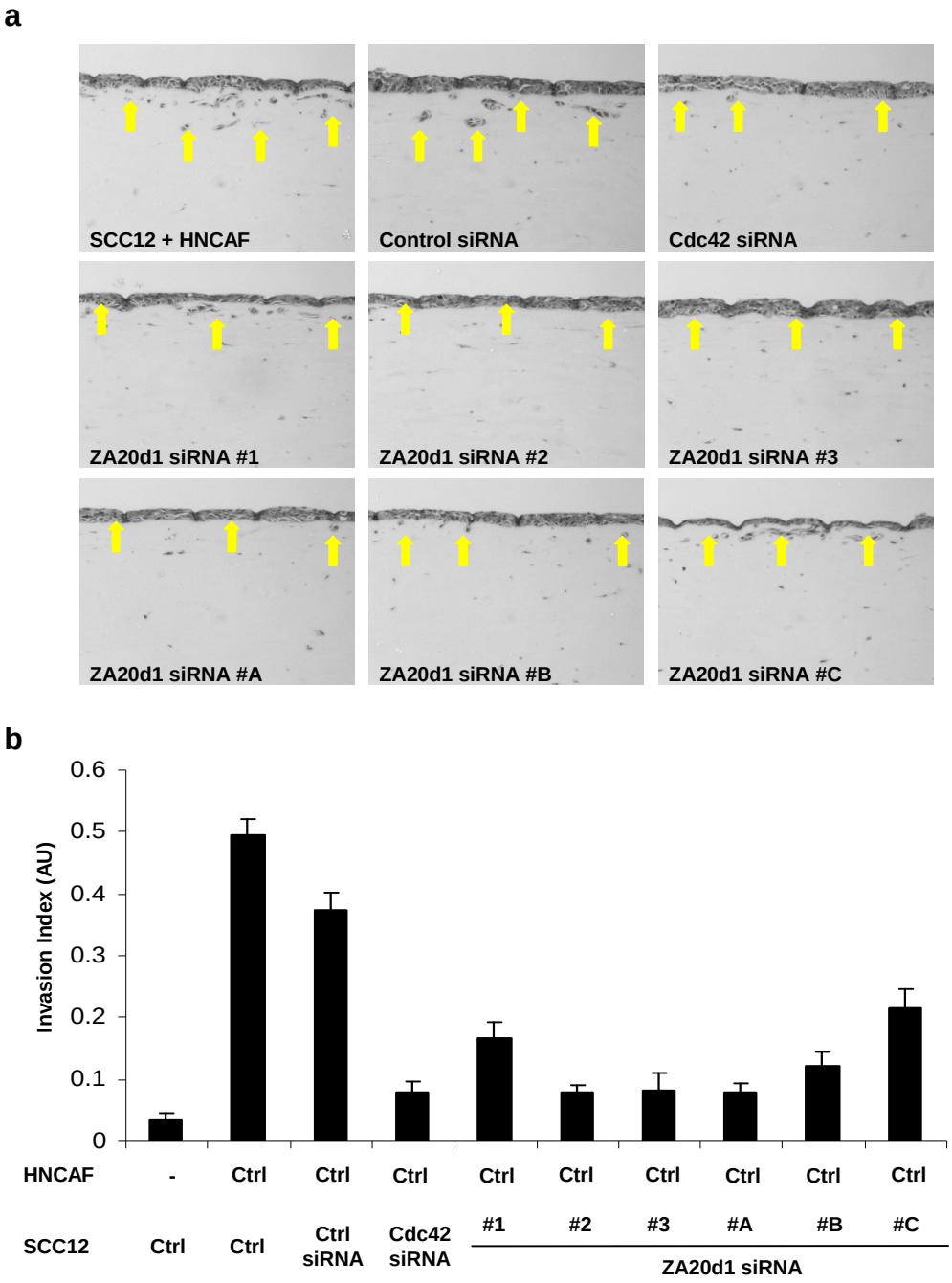

Figure 5.17 SCC12 organotypic invasion assay: ZA20d1 gene depletion

(**a**) H&E stained sections of SCC12 cells cultured in organotypic gels. Arrows point to the invading front of carcinoma cells. (**b**) Quantification of carcinoma invasion in organotypic gels in the absence of stromal fibroblasts, in the presence of stromal fibroblasts and with Cdc42 or ZA20d1 inhibited by siRNA in SCC12 cells. The average of 10 visual fields from 2 experiments is shown. The error bars represent the s.e.

a

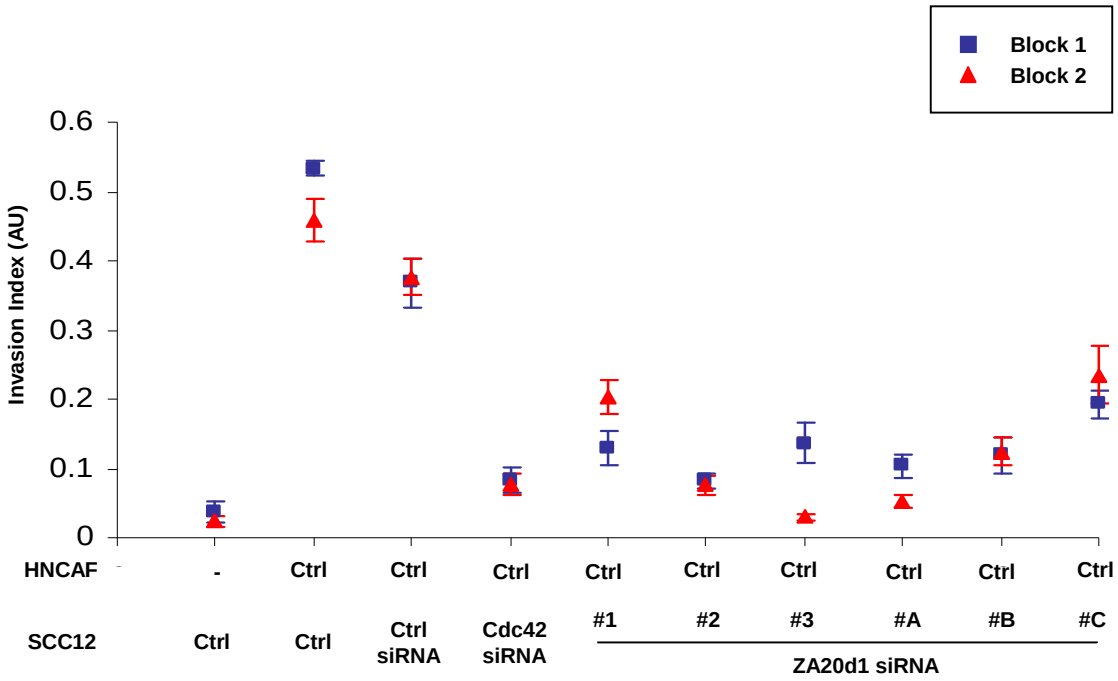

b

Randomized Block ANOVA	p Value	Decision p<0.007
Control vs Control siRNA	0.23079	Do not reject
Control siRNA vs ZA20d1 siRNA #1	0.001917	Reject
Control siRNA vs ZA20d1 siRNA #2	0.000233	Reject
Control siRNA vs ZA20d1 siRNA #3	0.000253	Reject
Control siRNA vs ZA20d1 siRNA #A	0.000230	Reject
Control siRNA vs ZA20d1 siRNA #B	0.000606	Reject
Control siRNA vs ZA20d1 siRNA #C	0.007477	Do not reject

Figure 5.18 ZA20d1 is required in SCC12 cells for carcinoma invasion *in vitro*

(**a**) Scatter plot displaying quantification of carcinoma invasion of the organotypic assay illustrated in Figure 5.17. Individual experimental blocks are illustrated. The average of 5 visual fields is shown and error bars represent the s.e. (**b**) Randomized block ANOVA statistical analysis. Null hypothesis (NØ) rejected if $p < 0.007$.

5.4.3 TRAF6 and ZA20d1 double gene depletion in SCC12 cells

Having validated TRAF6 and ZA20d1 as regulators of carcinoma invasion in SCC12 cells, I performed invasion assays in which carcinoma cells were depleted of both proteins. Double knockdown of TRAF6 and ZA20d1 was achieved by adding equal concentrations of the respective siRNA duplexes to the transfection mix (Chapter 2, Section 2.2.8.4).

Figures 5.19-5.21 illustrate the results of these double knockdown experiments. As expected, double gene depletion of TRAF6 and ZA20d1 in SCC12 cells resulted in statistically significant inhibition of carcinoma invasion (Figure 5.21a).

However, double gene depletion when compared to single gene depletion of either TRAF6 or ZA20d1 did not lead to greater inhibition of SCC12 cell invasion and was not statistically significant (Figure 5.21b).

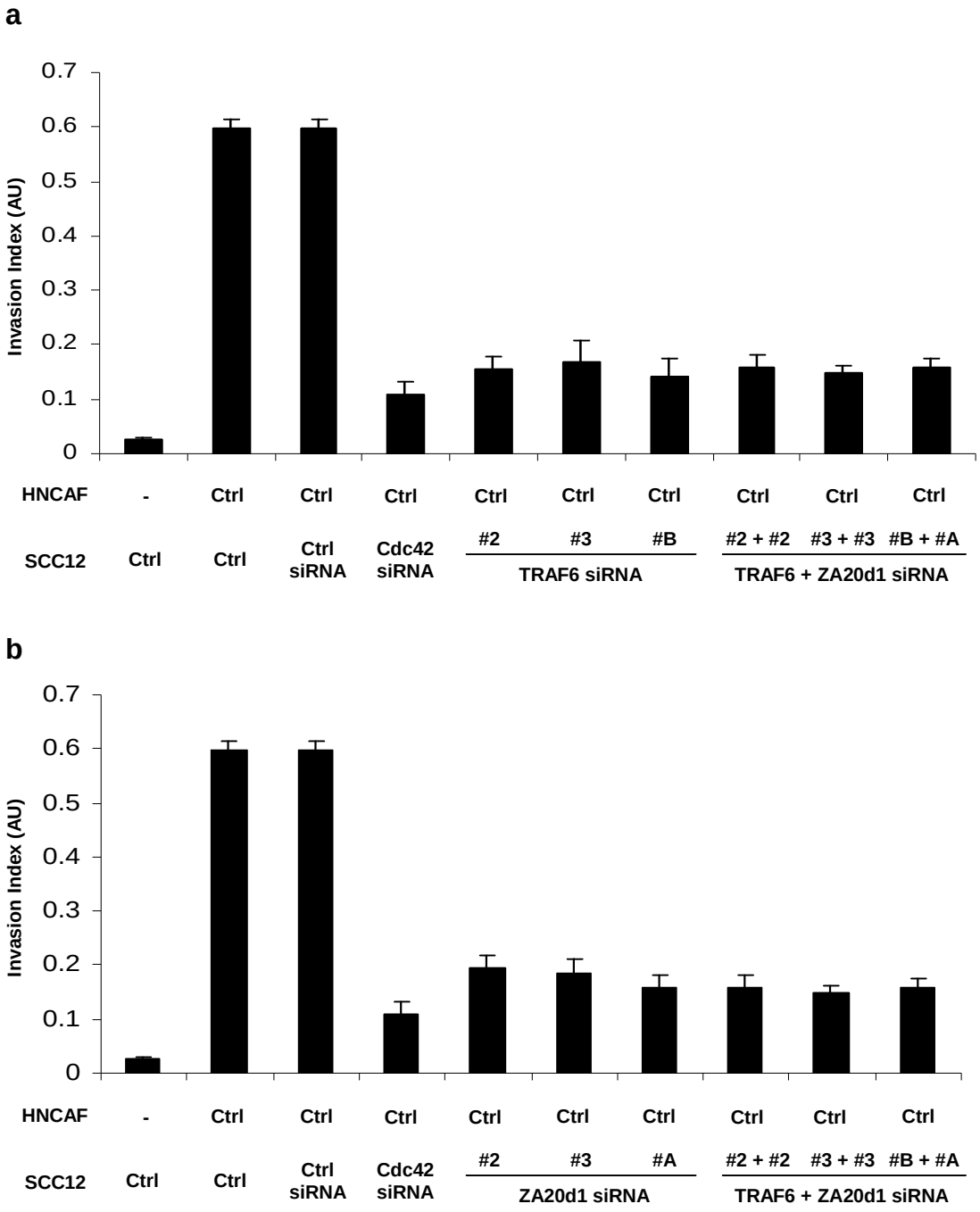

Figure 5.19 SCC12 organotypic invasion assay: TRAF6 and ZA20d1 double gene depletion

Quantification of carcinoma invasion in organotypic gels in the absence of stromal fibroblasts, in the presence of stromal fibroblasts and with Cdc42, TRAF6 and ZA20d1 inhibited by siRNA in SCC12 cells. Double gene depletions were performed by co-transfection of the specified oligonucleotides in equal concentration. The average of 10 visual fields from 2 experiments is shown. The error bars represent the s.e.

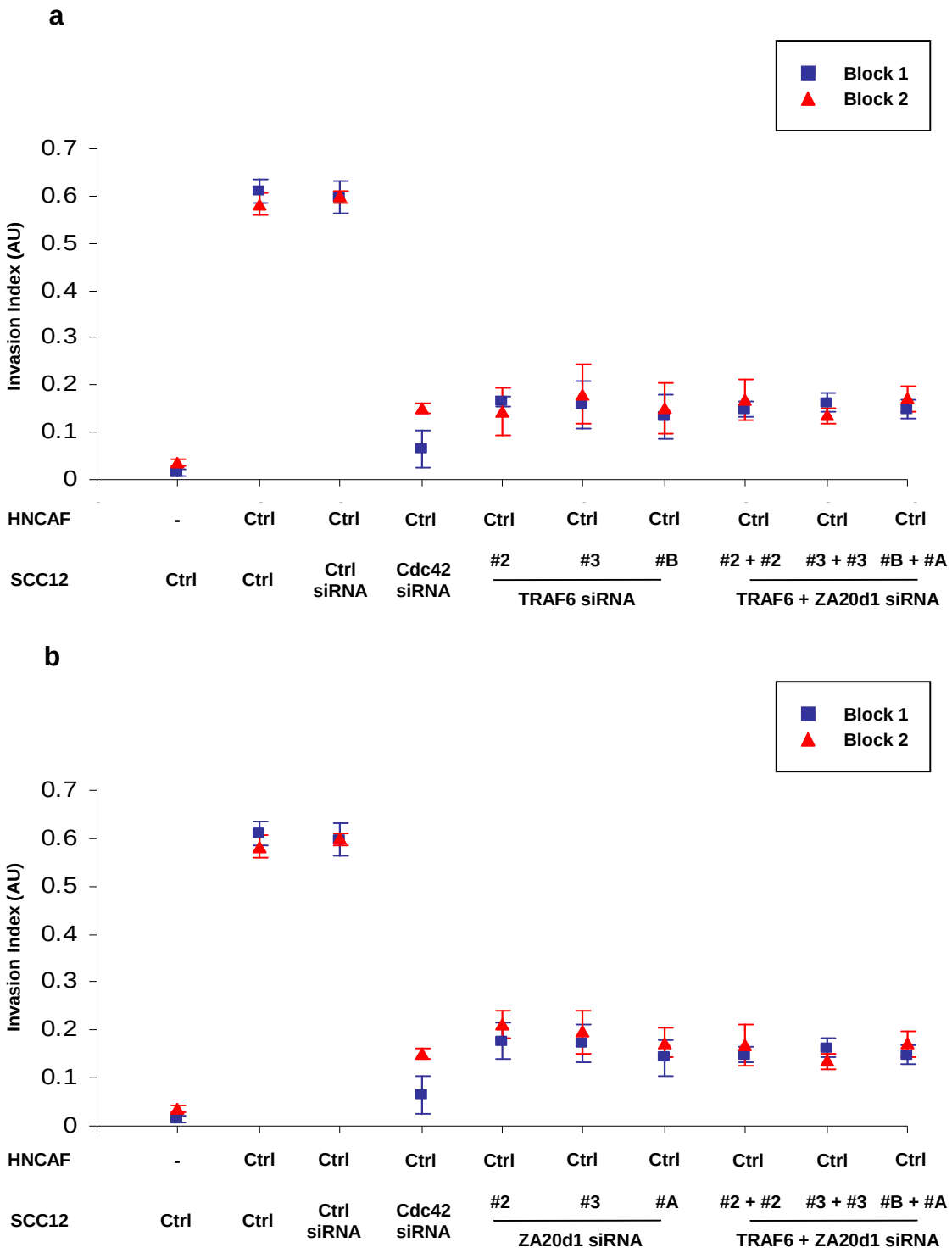

Figure 5.20 SCC12 organotypic invasion assay: TRAF6 and ZA20d1 double gene depletion - scatter plots

Scatter plots displaying quantification of carcinoma invasion of the organotypic assay illustrated in Figure 5.19. Individual experimental blocks are illustrated. The average of 5 visual fields is shown and error bars represent the s.e.

a

Randomized Block ANOVA	p Value	Decision p<0.0166
Control siRNA vs TRAF6 siRNA #2	0.000125	Reject
Control siRNA vs TRAF6 siRNA #3	0.000143	Reject
Control siRNA vs TRAF6 siRNA #B	0.000017	Reject
Control siRNA vs ZA20d1 siRNA #2	0.000167	Reject
Control siRNA vs ZA20d1 siRNA #3	0.000159	Reject
Control siRNA vs ZA20d1 siRNA #A	0.000019	Reject
Control siRNA vs TRAF6 + ZA20d1 siRNA #2 + #2	0.000130	Reject
Control siRNA vs TRAF6 + ZA20d1 siRNA #3 + #3	0.000125	Reject
Control siRNA vs TRAF6 + ZA20d1 siRNA #B + #A	0.000019	Reject

b

Randomized Block ANOVA	p Value	Decision p<0.025
TRAF6 siRNA #2 vs TRAF6 + ZA20d1 siRNA #2 + #2	0.816283	Do not reject
TRAF6 siRNA #3 vs TRAF6 + ZA20d1 siRNA #3 + #3	0.438116	Do not reject
TRAF6 siRNA #B vs TRAF6 + ZA20d1 siRNA #B + #A	0.076399	Do not reject
ZA20d1 siRNA #2 vs TRAF6 + ZA20d1 siRNA #2 + #2	0.224467	Do not reject
ZA20d1 siRNA #3 vs TRAF6 + ZA20d1 siRNA #3 + #3	0.239008	Do not reject
ZA20d1 siRNA #A vs TRAF6 + ZA20d1 siRNA #B + #A	0.784810	Do not reject

Figure 5.21 SCC12 organotypic invasion assay: TRAF6 and ZA20d1 double gene depletion - randomized block ANOVA statistical analysis

Randomized block ANOVA statistical analysis of organotypic assay illustrated in Figures 5.19. Null hypothesis (NØ) rejected if (**a**) $p < 0.0166$ and (**b**) $p < 0.025$.

5.4.4 TRAF6 and ZA20d1 are required in A431 cells for carcinoma invasion *in vitro*

Having shown TRAF6 and ZA20d1 to be regulators of carcinoma invasion in SCC12 cells, I wanted to see if they also exerted a similar functional influence in A431 cells. Since A431 cells were intrinsically less invasive in our organotypic system, the standard assay was modified to optimise carcinoma invasion (Chapter 2, Section 2.2.8.5).

Figure 5.22a consists of representative photomicrographs of H&E sections from these assays. Gene depletion of either TRAF6 or ZA20d1 inhibited carcinoma invasion compared to the control samples, evident by the reduced number of cancer cells infiltrating the ECM. Figure 5.22b shows the quantification of carcinoma invasion. A scatter plot of the individual experimental blocks is presented in Figure 5.23a. The reduction in carcinoma invasion observed following either TRAF6 or ZA20d1 gene depletion was statistically significant for each of the siRNA duplexes (Figure 5.23b).

Figure 5.24 demonstrates the efficacy of TRAF6 siRNA gene depletion in A431 cells 96 hours following transfection. Cell lysates were made in parallel with Block 1 of the organotypic assay illustrated in Figure 5.22.

5.4.5 Apoptotic counts in gene depleted A431 cells

Figures 5.25 and 5.26 show the percentage of apoptotic A431 cells per visual field 72 hours following TRAF6 and ZA20d1 gene depletion respectively. Knocking down either TRAF6 or ZA20d1 was not associated with an increase in cell apoptosis compared to the control samples.

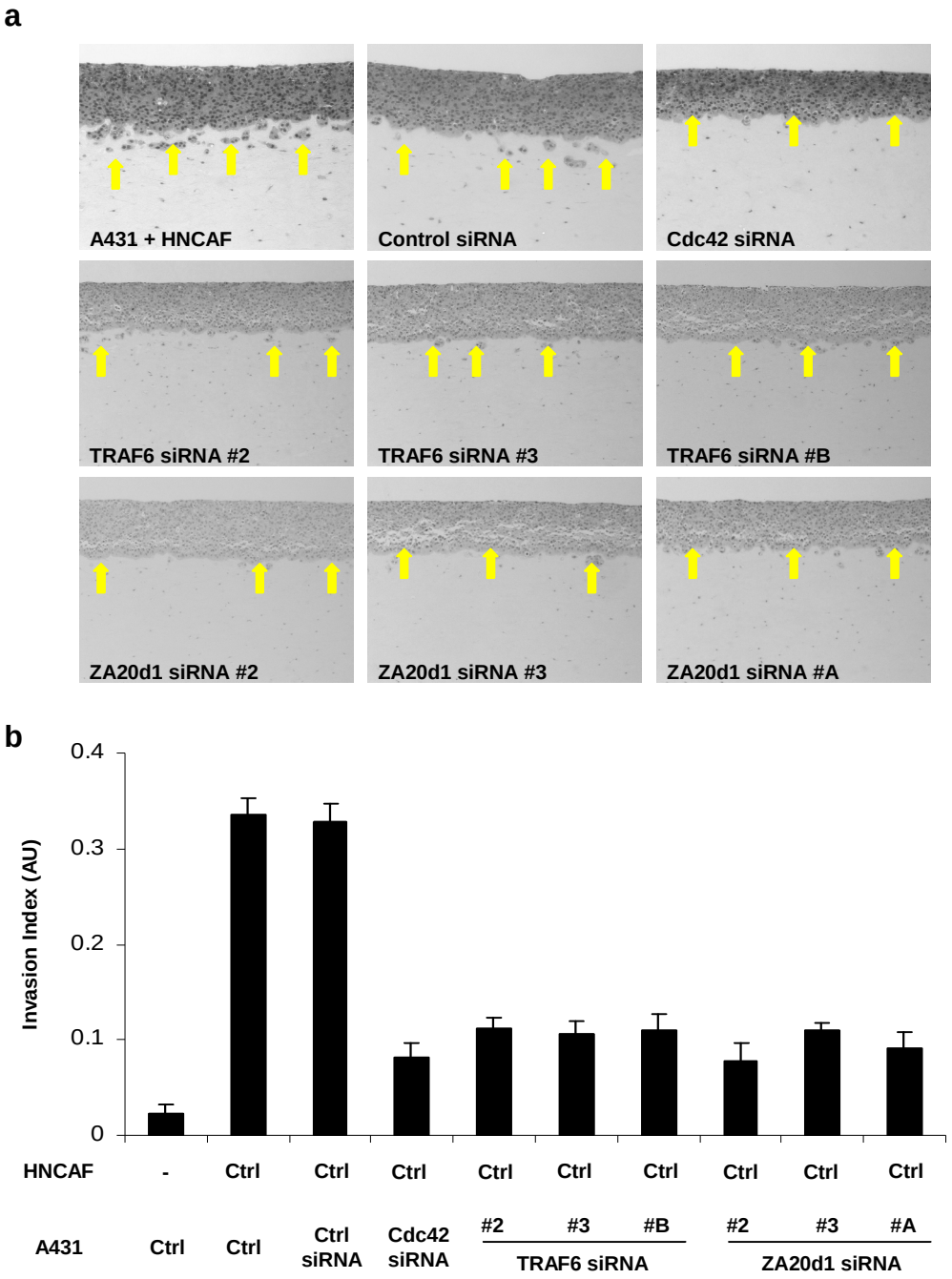

Figure 5.22 A431 organotypic invasion assay: TRAF6 and ZA20d1 gene depletion

(**a**) H&E stained sections of A431 cells cultured in organotypic gels. Arrows point to the invading front of carcinoma cells. (**b**) Quantification of carcinoma invasion in organotypic gels in the absence of stromal fibroblasts, in the presence of stromal fibroblasts and with Cdc42, TRAF6 or ZA20d1 inhibited by siRNA in A431 cells. The average of 10 visual fields from 2 experiments is shown. The error bars represent the s.e.

a

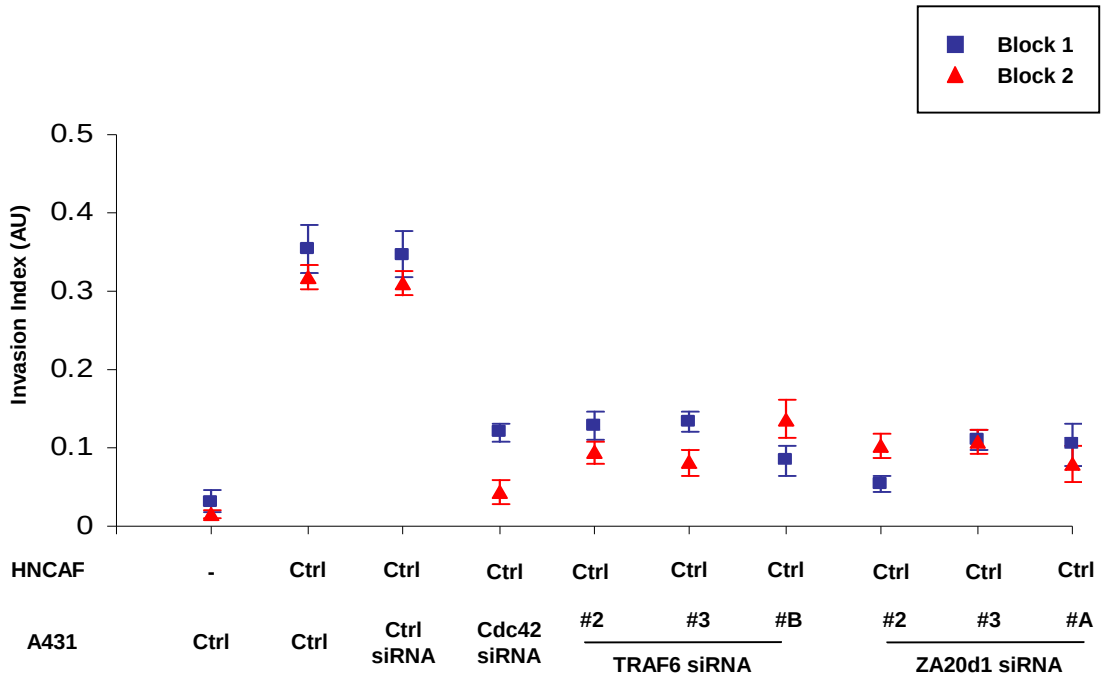

b

Randomized Block ANOVA	p Value	Decision p<0.007
Control vs Control siRNA	0.806627	Do not reject
Control siRNA vs TRAF6 siRNA #2	0.000126	Reject
Control siRNA vs TRAF6 siRNA #3	0.000112	Reject
Control siRNA vs TRAF6 siRNA #B	0.000051	Reject
Control siRNA vs ZA20d1 siRNA #2	0.000051	Reject
Control siRNA vs ZA20d1 siRNA #3	0.000119	Reject
Control siRNA vs ZA20d1 siRNA #A	0.000073	Reject

Figure 5.23 TRAF6 and ZA20d1 are required in A431 cells for carcinoma invasion *in vitro*

(**a**) Scatter plot displaying quantification of carcinoma invasion of the organotypic assay illustrated in Figure 5.22. Individual experimental blocks are illustrated. The average of 5 visual fields is shown and error bars represent the s.e. (**b**) Randomized block ANOVA statistical analysis. Null hypothesis (NØ) rejected if $p < 0.007$.

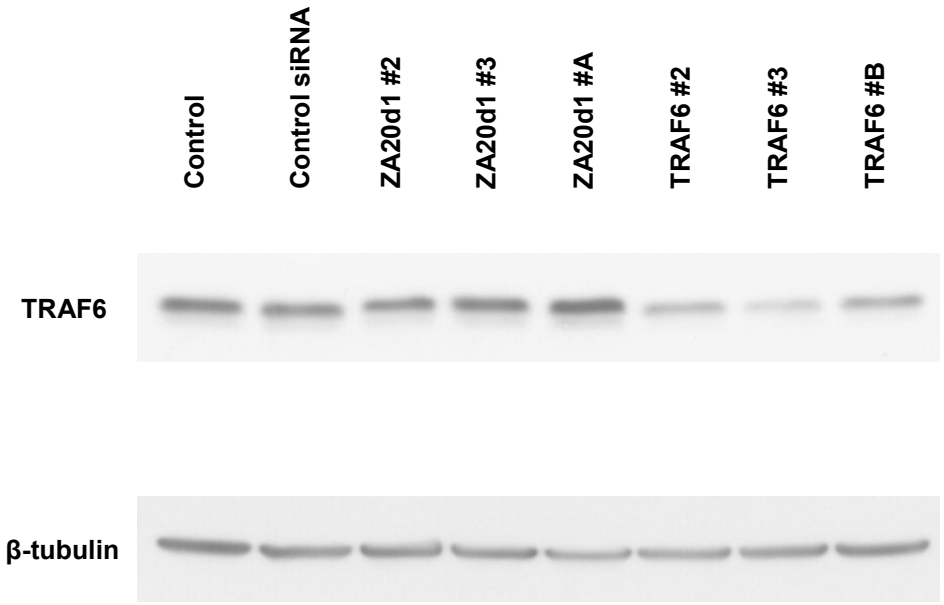

Figure 5.24 Western blot demonstrating the efficacy of TRAF6 siRNA gene depletion in A431 cells

Western blot of A431 cell lysates 96 hours post-transfection showing the efficient knockdown of TRAF6. These lysates were made in parallel with Block 1 of the organotypic assay illustrated in Figure 5.22.

a

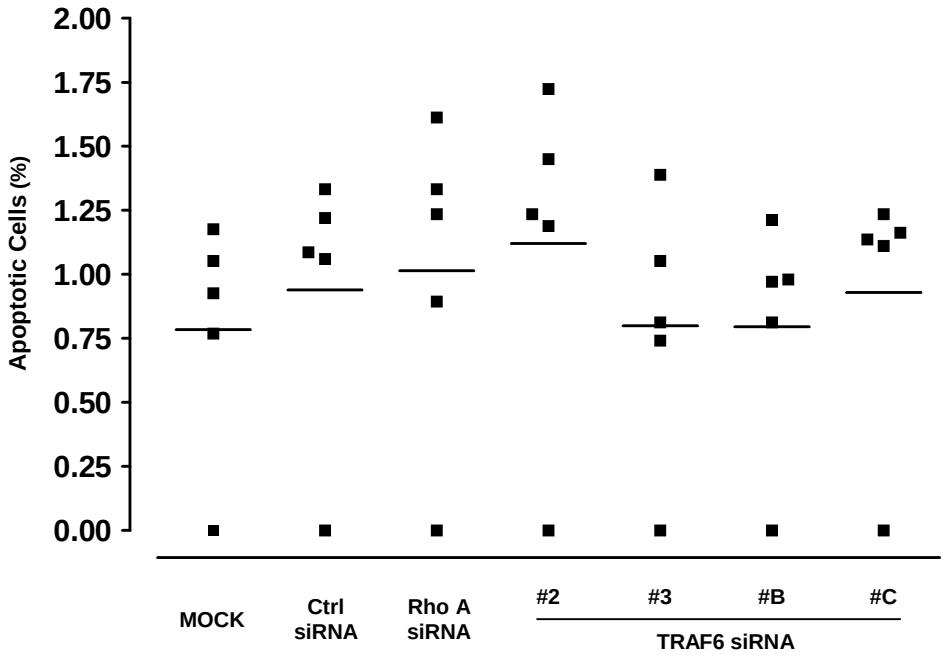

b

Kruskal-Wallis non-parametric ANOVA	p Value	Decision p<0.05
MOCK vs siRNA duplexes	0.491971	Do not reject

NØ - All medians are equal

Figure 5.25 Apoptotic counts in TRAF6 gene depleted A431 cells

(**a**) Scatter plot displaying the percentage of apoptotic A431 cells per visual field 72 hours following transfection with control, Rho A and TRAF6 siRNA duplexes. (**b**) Kruskal-Wallis non-parametric ANOVA statistical analysis. Null hypothesis (NØ) rejected if $p < 0.05$.

a

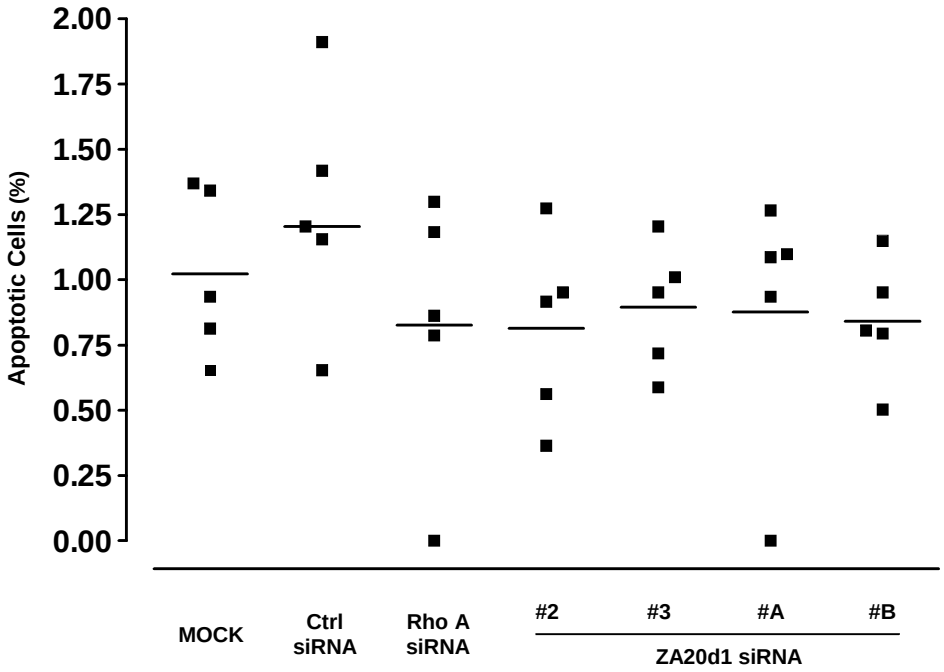

b

Kruskal-Wallis non-parametric ANOVA	p Value	Decision p<0.05
MOCK vs siRNA duplexes	0.914924	Do not reject

NØ - All medians are equal

Figure 5.26 Apoptotic counts in ZA20d1 gene depleted A431 cells

(**a**) Scatter plot displaying the percentage of apoptotic A431 cells per visual field 72 hours following transfection with control, Rho A and ZA20d1 siRNA duplexes. (**b**) Kruskal-Wallis non-parametric ANOVA statistical analysis. Null hypothesis (NØ) rejected if $p < 0.05$.

5.5 Summary

- Following further validation of my 5 gene hits using Qiagen® siRNA, qPCR and IMF, 3 genes (RKHD2, TRAF6 and ZA20d1) remained as potential candidates for detailed study.

- A review of the scientific literature indicated that ZA20d1 was the complementary DUB to TRAF6 and that both were key regulators of canonical NF-κB signalling in epithelial cells [163, 307]. Given the importance of NF-κB pathways in the pathogenesis of SCC, TRAF6 and ZA20d1 were selected as candidate genes for further study.

- Currently there is no experimental data regarding the function of RKHD2 other than a single study which speculatively links its E3 ligase activity to the pathogenesis of essential hypertension [309]. The role RKHD2 in carcinoma invasion was not studied beyond the point of validation.

- Having selected TRAF6 and ZA20d1 as candidate genes, both were functionally validated as regulators of carcinoma invasion *in vitro* in SCC12 and A431 cells.

Chapter 6

NF-κB signalling in SCC invasion

6.1 Introduction

Having selected TRAF6 and ZA20d1 as my candidate genes for detailed study and validated them as regulators of carcinoma invasion in our organotypic system (Chapter 5), the next phase of my research was focused on elucidating the signalling mechanisms underlying their pro-invasive effects.

Literature suggested that TRAF6 and ZA20d1 were positive and negative regulators of canonical NF-κB signalling in epithelial cells [163, 307]. Co-immunoprecipitation studies also indicated that ZA20d1 was the complementary DUB to TRAF6 and that both proteins were critical to downstream events following TNFR and IL-1R activation [308]. Given the importance of NF-κB signalling in the pathogenesis of SCC, I wondered whether TRAF6 and ZA20d1 were influencing cancer cell invasion in an NF-κB dependent manner.

To address the above hypothesis I initially examined the significance of NF-κB pathways in carcinoma invasion in our organotypic system using TNFα, IL-1α, several IKK inhibitors and infliximab (a monoclonal antibody to TNFα in clinical use). The results of these investigations are presented in this chapter.

6.2 Tumour necrosis factor alpha (TNFα)

The importance of TNFα in the development and progression of a number of cancers is well established [191, 310]. I therefore investigated its influence on carcinoma invasion in our organotypic system.

6.2.1 TNFα promotes A431 carcinoma invasion *in vitro* in a dose responsive manner

Figure 6.1a consists of representative photomicrographs of H&E sections from A431 invasion assays in which both the stromal and epithelial components of the organotypic cultures were stimulated daily with TNFα at concentrations of 1, 3.1, 10 and 31ng/ml. Figure 6.1b shows the quantification of carcinoma invasion. A scatter plot of the individual experimental blocks is presented in Figure 6.2a. The Invasion Index increased with escalating concentrations of TNFα and was statistically significant at a dose of 31ng/ml (Figure 6.2b).

Figure 6.3 illustrates the log linear relationship of mean carcinoma invasion in response to TNFα stimulation.

6.2.2 TNFα activates NF-κB signalling in A431 cells and HNCAF

Cancer cell and stromal cell production of TNFα has been observed in a variety of experimental tumours [191]. Collectively, this phenomenon is responsible for the constitutive activation of NF-κB [264].

Figure 6.4 demonstrates the activation of IKK in A431 cells following stimulation with TNFα (31ng/ml). This results in the phosphorylation and reciprocal degradation of IκBα (Figure 6.5). Consequently, NF-κB p65 is activated (Figure 6.6).

Figure 6.7 demonstrates the activation of IKK in HNCAF following stimulation with TNFα (31ng/ml). This results in the phosphorylation and reciprocal degradation of IκBα (Figure 6.8). Consequently, NF-κB p65 is activated (Figure 6.9).

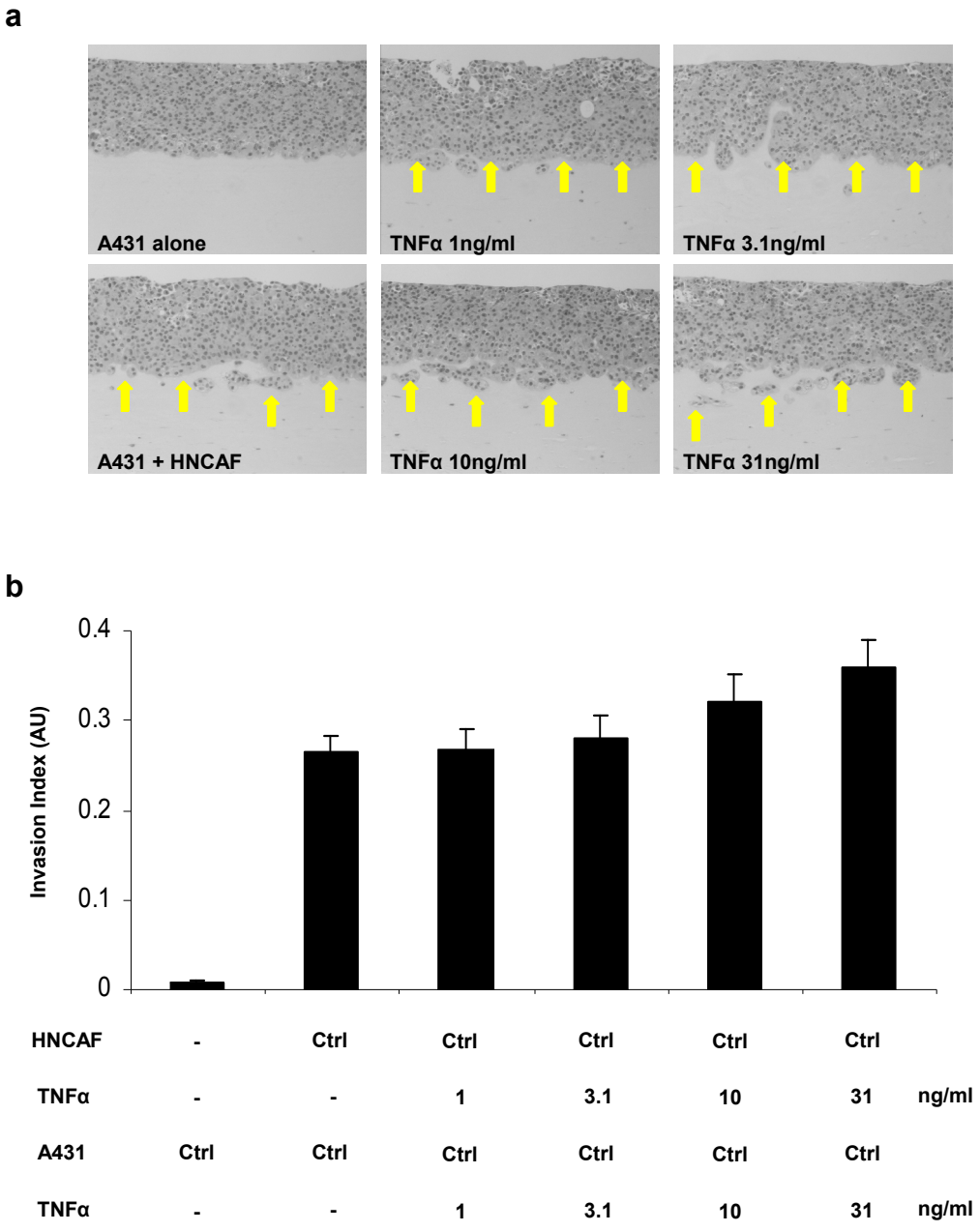

Figure 6.1 Organotypic invasion assay: HNCAF and A431 TNFα stimulation

(**a**) H&E stained sections of A431 cells cultured in organotypic gels. Arrows point to the invading front of carcinoma cells. (**b**) Quantification of carcinoma invasion. Both the stromal and epithelial components of the organotypic cultures were stimulated daily with TNFα at the specified concentrations. The average of 10 visual fields from 2 experiments is shown. The error bars represent the s.e.

a

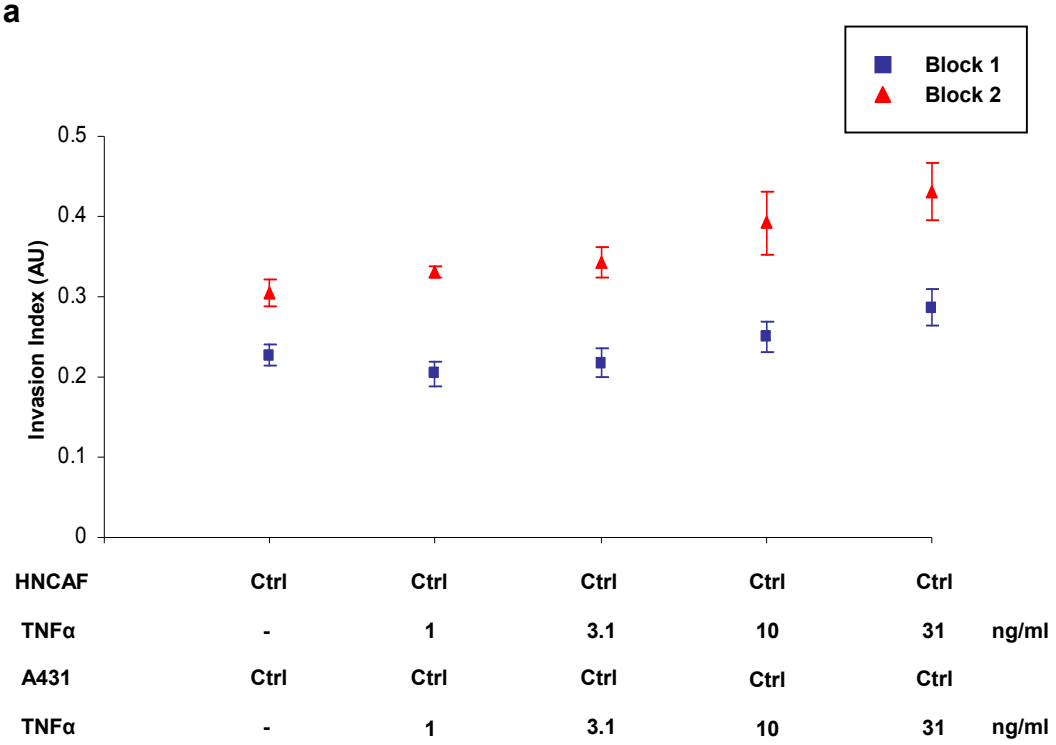

b

Randomized Block ANOVA	p Value	Decision p<0.0125
Control vs TNFα 1	0.926714	Do not reject
Control vs TNFα 3.1	0.483890	Do not reject
Control vs TNFα 10	0.042689	Do not reject
Control vs TNFα 31	0.007867	Reject

Figure 6.2 Organotypic invasion assay: HNCAF and A431 TNFα stimulation. (a) Scatter plot and (b) randomized block ANOVA statistical analysis

(**a**) Scatter plot displaying quantification of carcinoma invasion in cultures from the organotypic assay illustrated in Figure 6.1. Individual experimental blocks are illustrated. The average of 5 visual fields is shown and error bars represent the s.e. (**b**) Randomized block ANOVA statistical analysis. Null hypothesis (NØ) rejected if $p < 0.0125$.

a

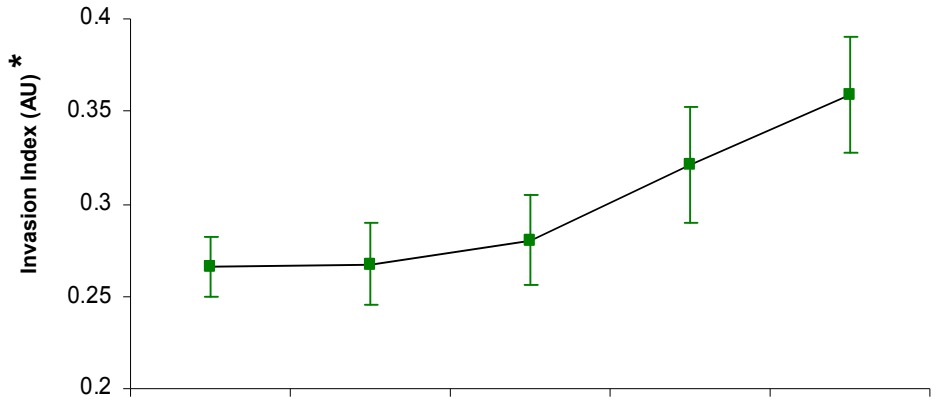

HNCAF	**Ctrl**	**Ctrl**	**Ctrl**	**Ctrl**	**Ctrl**	
TNFα	**-**	**1**	**3.1**	**10**	**31**	**ng/ml**
A431	**Ctrl**	**Ctrl**	**Ctrl**	**Ctrl**	**Ctrl**	
TNFα	**-**	**1**	**3.1**	**10**	**31**	**ng/ml**

b

ANOVA test for linear trend

Group	Count	Mean Invasion Index	Comparison Coefficient
Control	10	0.2656842	-0.6324555
TNFα 1	10	0.2675425	-0.3162278
TNFα 3.1	10	0.2803116	0
TNFα 10	10	0.3213504	0.3162278
TNFα 31	10	0.3592749	0.6324555

p = 0.006782

Figure 6.3 TNFα promotes A431 cell invasion *in vitro* in a dose responsive manner

(**a**) Line plot displaying the log linear relationship of mean carcinoma invasion in response to TNFα stimulation. The average of 10 fields is shown and error bars represent the s.e. *Denotes an expanded Y-axis. (**b**) ANOVA test for linear trend. Null hypothesis (NØ) rejected if $p < 0.05$.

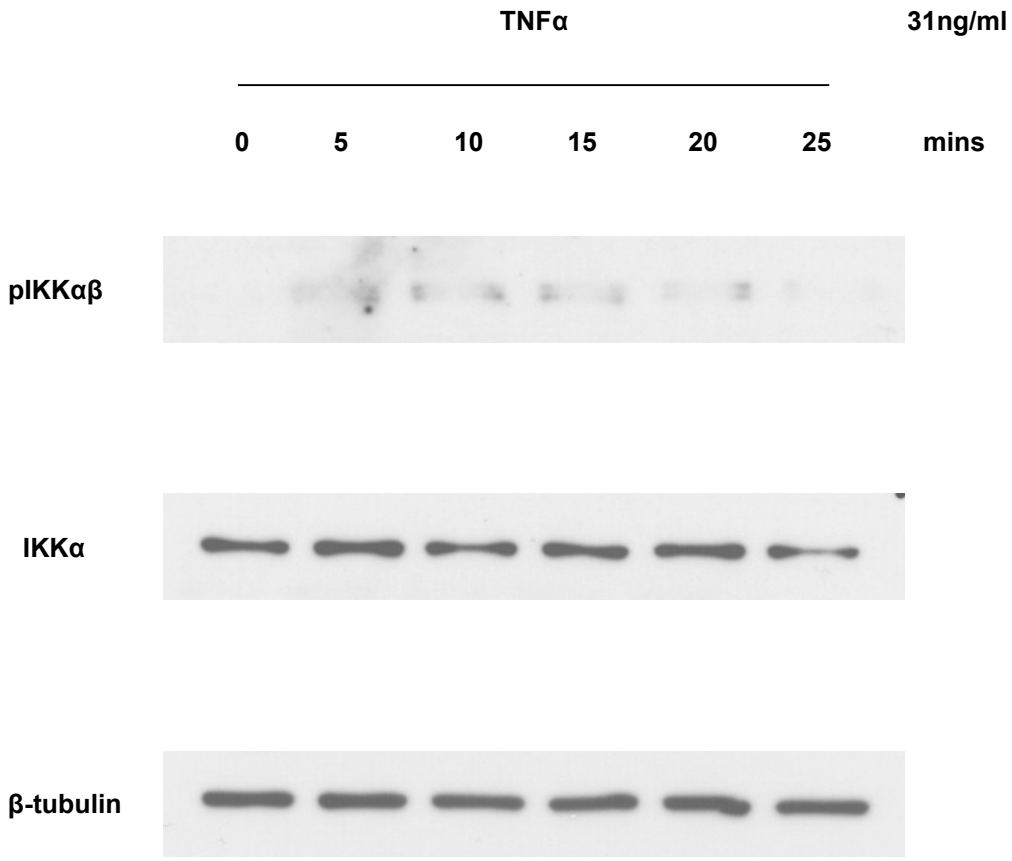

Figure 6.4 TNFα activates IKK in A431 cells

Western blots of A431 cell lysates showing the activation of IKK in response to stimulation with TNFα (31ng/ml). This leads to the degradation of IκBα (Figure 6.5) with the subsequent activation of NF-κB (Figure 6.6).

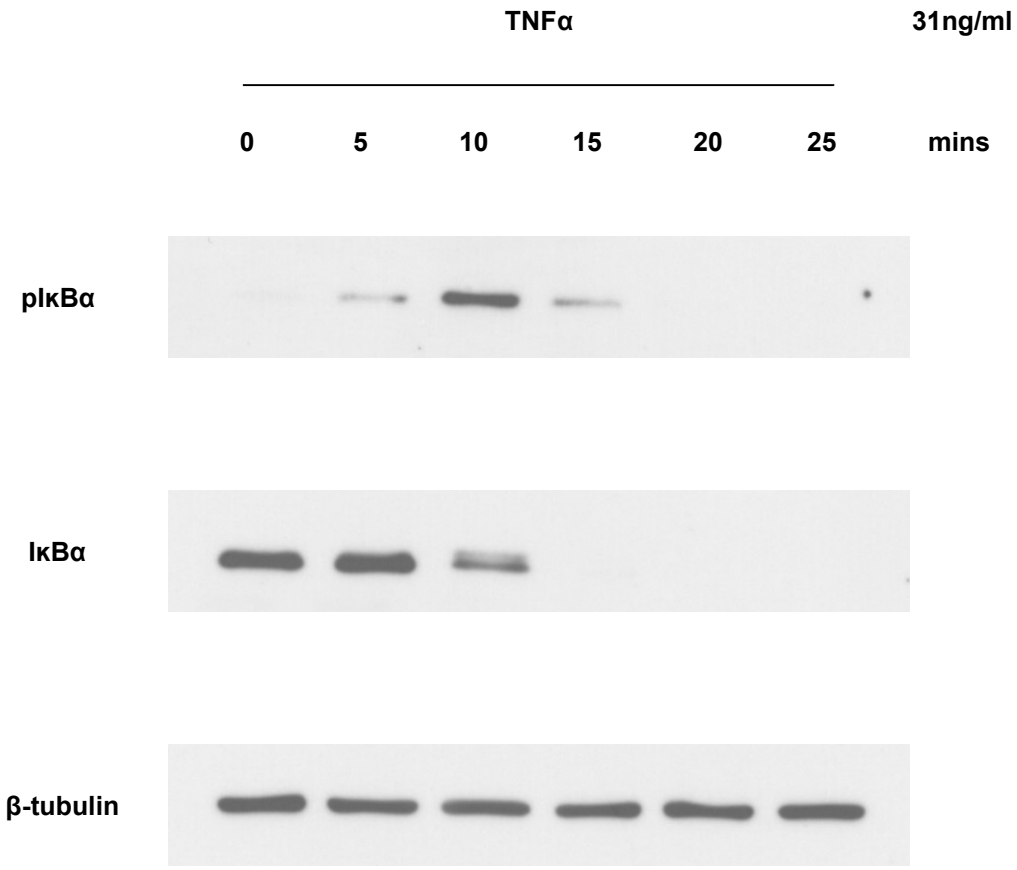

Figure 6.5 TNFα induced NF-κB activation is associated with the phosphorylation and reciprocal degradation of IκBα in A431 cells

Western blots of A431 cell lysates showing the phosphorylation and reciprocal degradation of IκBα in response to stimulation with TNFα (31ng/ml).

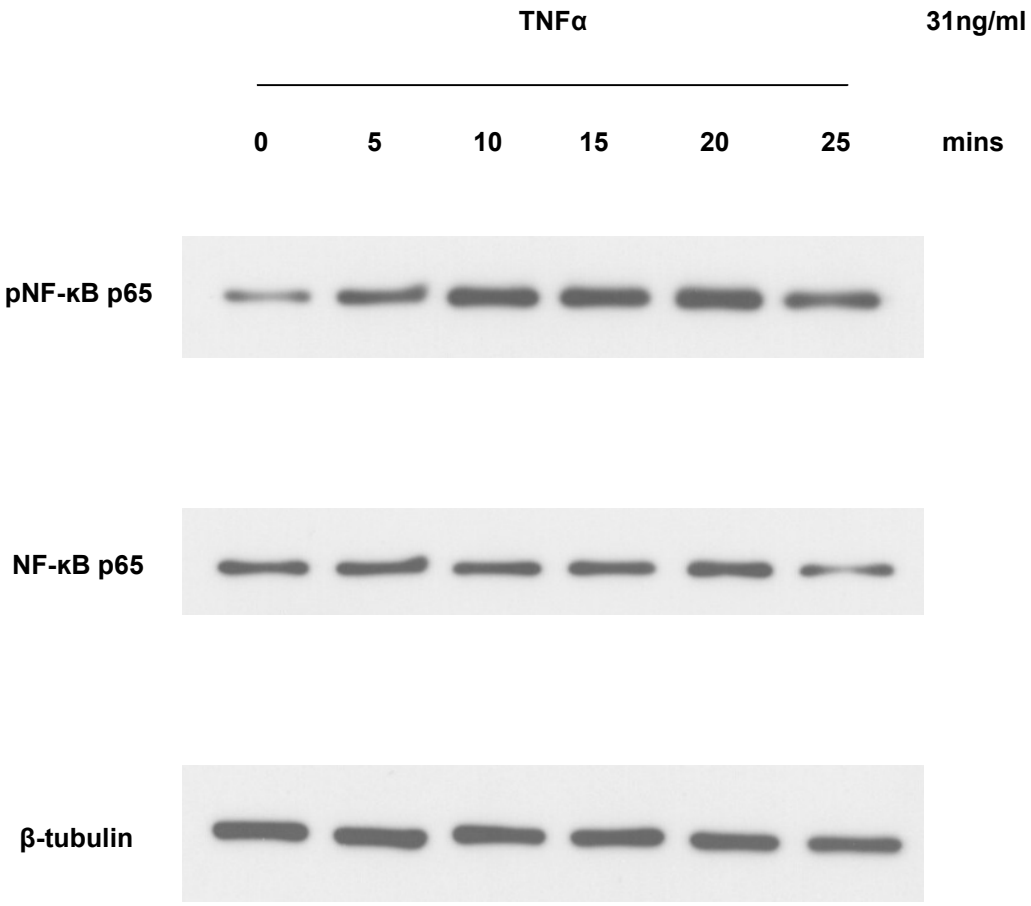

Figure 6.6 TNFα activates NF-κB in A431 cells

Western blots of A431 cell lysates showing the phosphorylation of NF-κB p65 in response to stimulation with TNFα (31ng/ml).

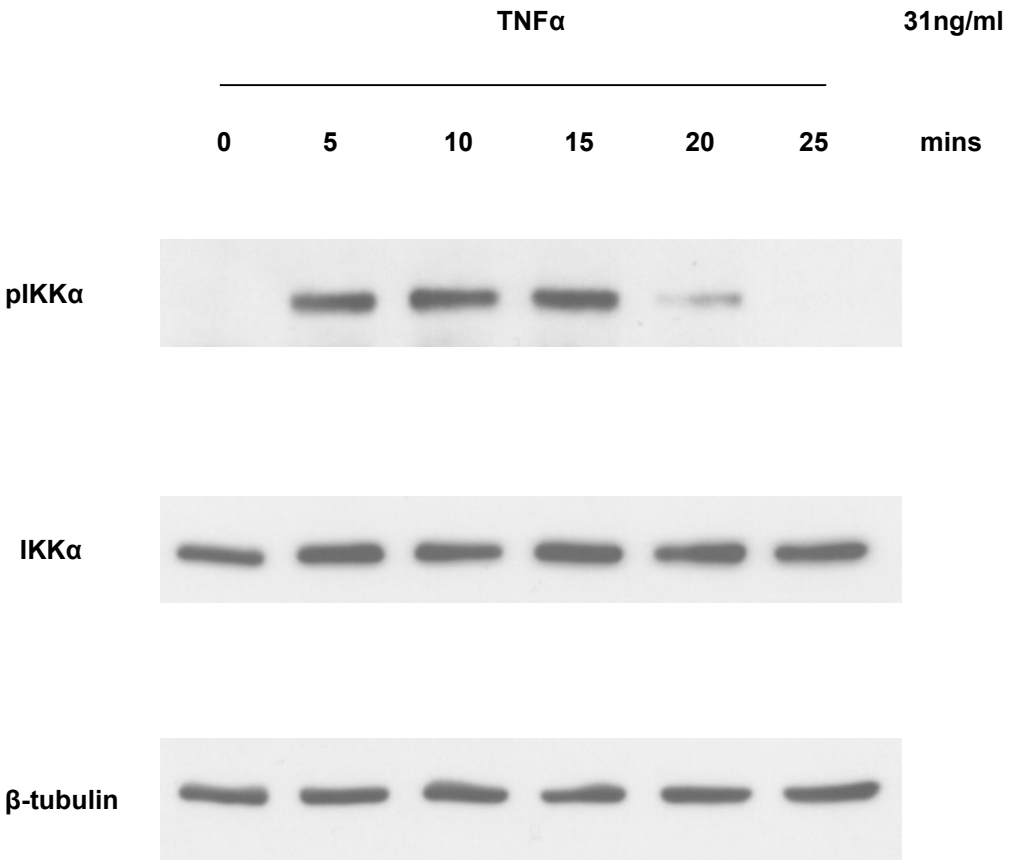

Figure 6.7 TNFα activates IKK in HNCAF

Western blots of HNCAF cell lysates showing the activation of IKK in response to stimulation with TNFα (31ng/ml). This leads to the degradation of IκBα (Figure 6.8) with the subsequent activation of NF-κB (Figure 6.9).

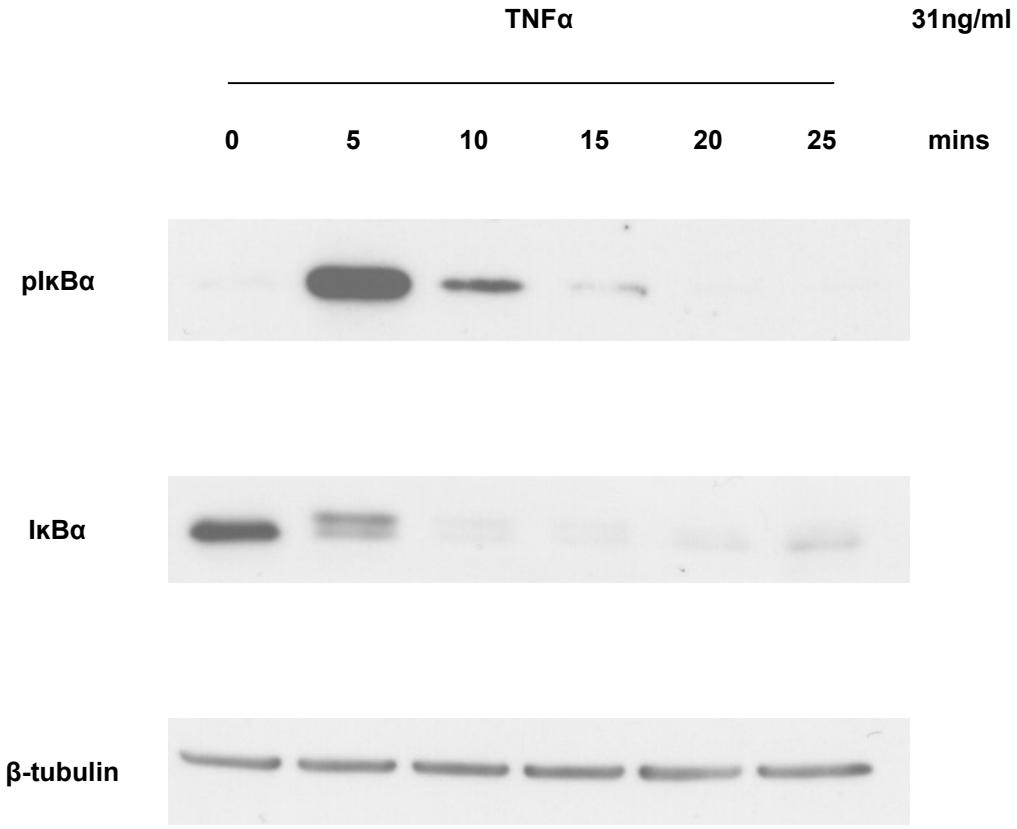

Figure 6.8 TNFα induced NF-κB activation is associated with the phosphorylation and reciprocal degradation of IκBα in HNCAF

Western blots of HNCAF cell lysates showing the phosphorylation and reciprocal degradation of IκBα in response to stimulation with TNFα (31ng/ml).

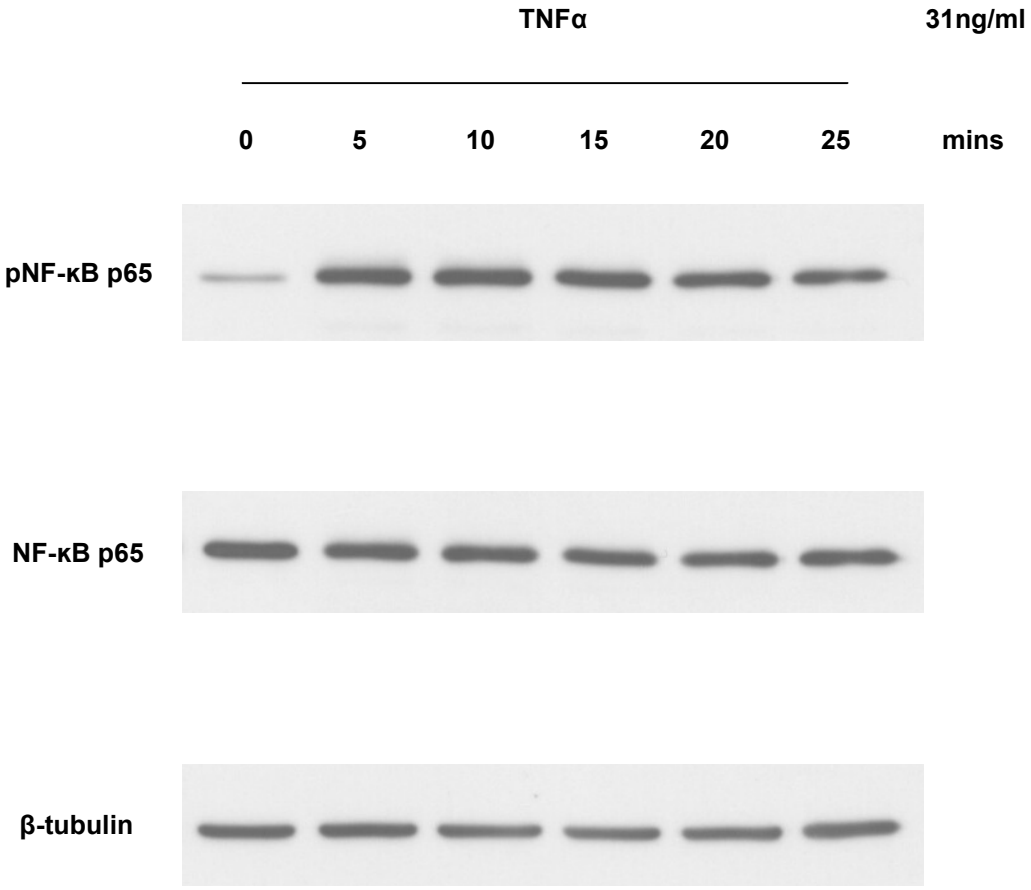

Figure 6.9 TNFα activates NF-κB in HNCAF

Western blots of HNCAF cell lysates showing the phosphorylation of NF-κB p65 in response to stimulation with TNFα (31ng/ml).

6.2.3 TNFα promotes SCC12 carcinoma invasion *in vitro* in a dose responsive manner

Figure 6.10a consists of representative photomicrographs of H&E sections from SCC12 invasion assays in which both the stromal and epithelial components of the organotypic cultures were stimulated daily with TNFα at concentrations of 1, 3.1, 10 and 31ng/ml. Figure 6.10b shows the quantification of carcinoma invasion. A scatter plot of the individual experimental blocks is presented in Figure 6.11a. The Invasion Index increased with escalating concentrations of TNFα and was statistically significant at doses of 10 and 31ng/ml (Figure 6.11b).

Figure 6.12 illustrates the log linear relationship of mean carcinoma invasion in response to TNFα stimulation.

6.2.4 TNFα stimulation of SCC12 cells promotes carcinoma invasion in remodelled collagen-Matrigel® matrix in a dose responsive manner in the absence of stromal fibroblasts

TNFα, through its ability to activate several signalling pathways in a variety of cells, has been shown to be integral to the cytokine network that exists within the tumour micro-environment [257]. Having established A431 and SCC12 carcinoma invasion to be TNFα driven, I investigated the influence of TNFα on the epithelial and stromal components of our organotypic system independently of each other.

Figure 6.13 shows the quantification of SCC12 invasion in organotypic cultures in which only the epithelial component was stimulated daily with TNFα at concentrations of 1, 3.1, 10 and 31ng/ml. Fibroblasts were removed from the collagen-Matrigel® gels after five days of matrix remodelling by treating with puromycin (5µg/ml) daily for 48 hours prior to the addition of SCC12 cells. A scatter plot of the individual experimental blocks is presented in Figure 6.14a. The Invasion Index increased with escalating concentrations of TNFα but did not achieve statistical significance (Figure 6.14b).

Figure 6.15 illustrates the log linear relationship of mean carcinoma invasion in response to SCC12 TNFα stimulation.

Figure 6.16 confirms that TNFα stimulated SCC12 cells do not invade 'naïve' collagen-Matrigel® matrix in fibroblast-deficient organotypic cultures.

6.2.5 TNFα stimulation of HNCAF promotes carcinoma invasion in a dose responsive manner in the absence of direct stimulation of SCC12 cells

Figure 6.17 shows the quantification of SCC12 invasion in organotypic cultures in which only the stromal component was stimulated daily with TNFα at concentrations of 1, 3.1, 10 and 31ng/ml. Fibroblasts were removed from the collagen-Matrigel® gels after five days of matrix remodelling by treating with puromycin (5μg/ml) daily for 48 hours prior to the addition of SCC12 cells. A scatter plot of the individual experimental blocks is presented in Figure 6.18a. The Invasion Index increased with escalating concentrations of TNFα but did not achieve statistical significance (Figure 6.18b).

Figure 6.19 illustrates the log linear relationship of mean carcinoma invasion in response to HNCAF TNFα stimulation.

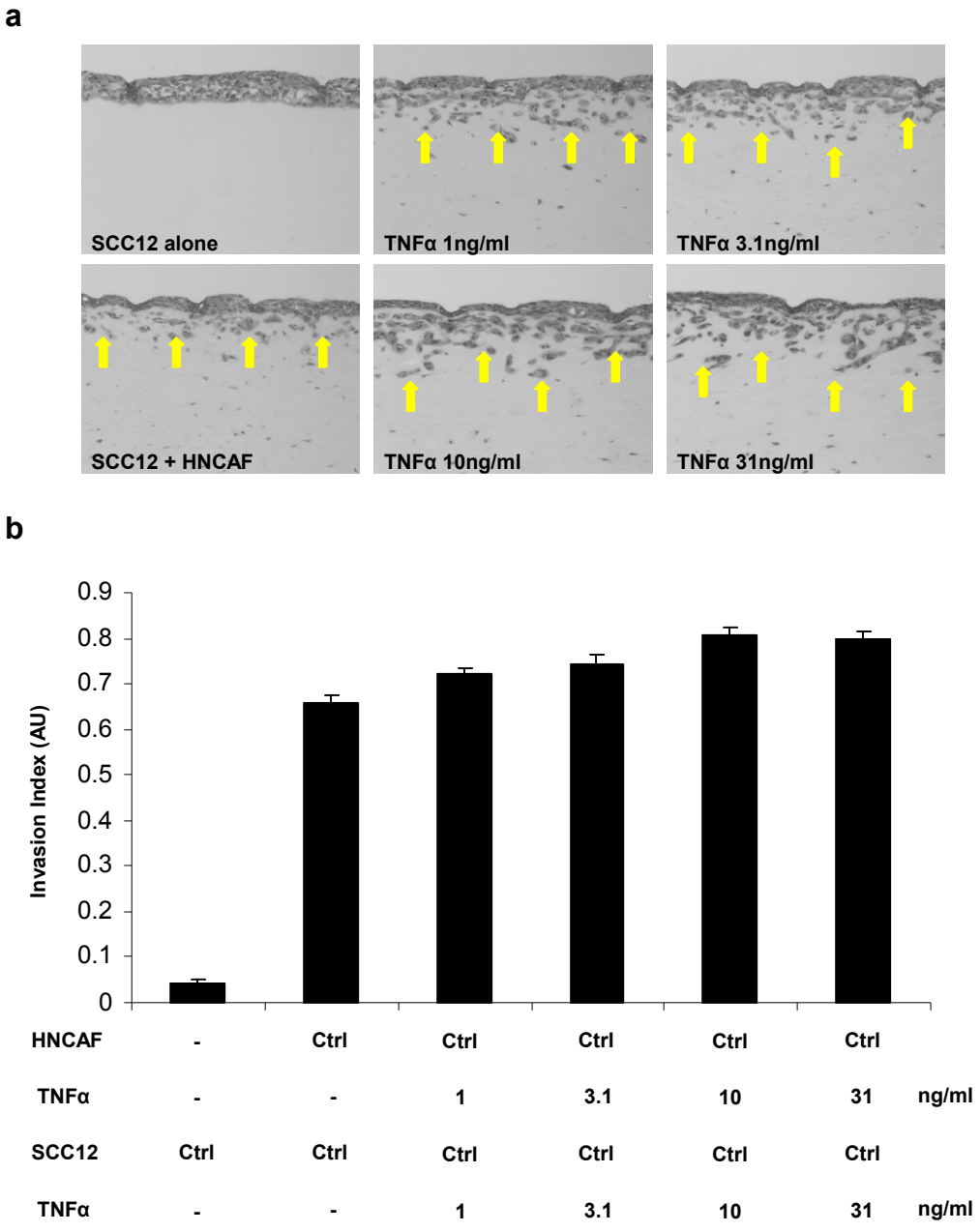

Figure 6.10 Organotypic invasion assay: HNCAF and SCC12 TNFα stimulation

(**a**) H&E stained sections of SCC12 cells cultured in organotypic gels. Arrows point to the invading front of carcinoma cells. (**b**) Quantification of carcinoma invasion. Both the stromal and epithelial components of the organotypic cultures were stimulated daily with TNFα at the specified concentrations. The average of 10 visual fields from 2 experiments is shown. The error bars represent the s.e.

a

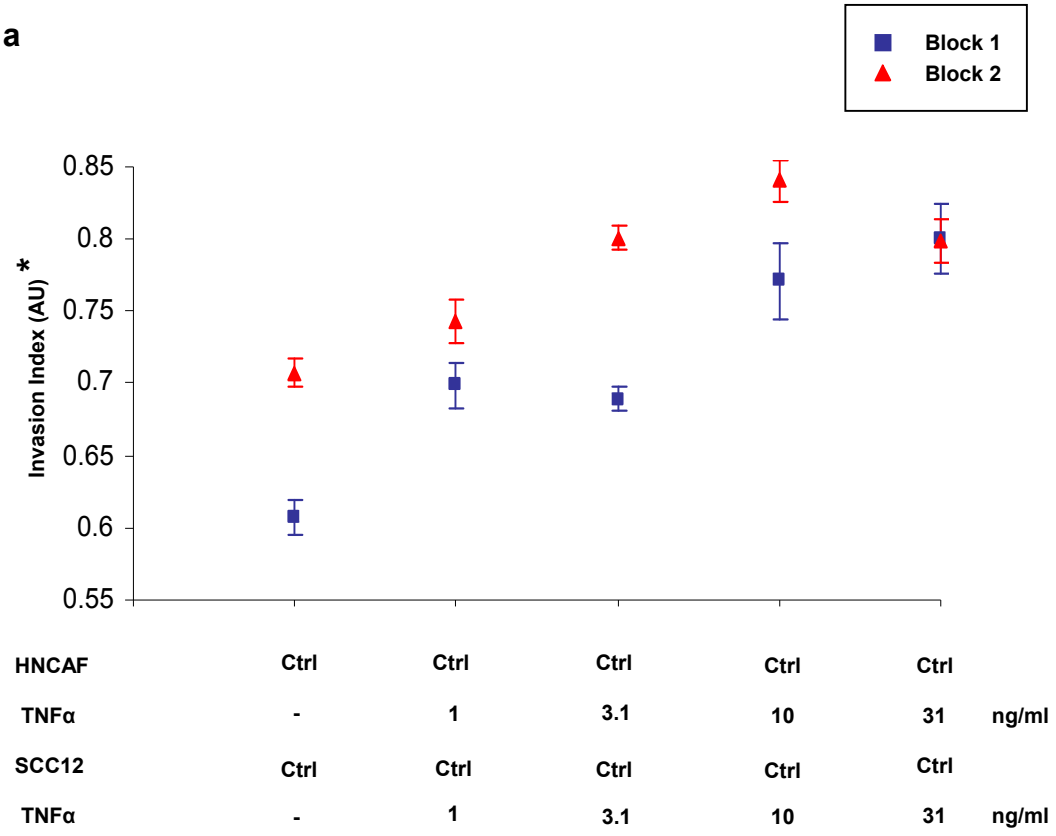

b

Randomized Block ANOVA	p Value	Decision p<0.0125
Control vs TNFα 1	0.120165	Do not reject
Control vs TNFα 3.1	0.052562	Do not reject
Control vs TNFα 10	0.009951	Reject
Control vs TNFα 31	0.011434	Reject

Figure 6.11 Organotypic invasion assay: HNCAF and SCC12 TNFα stimulation. (a) Scatter plot and (b) randomized block ANOVA statistical analysis

(**a**) Scatter plot displaying quantification of carcinoma invasion in cultures from the organotypic assay illustrated in Figure 6.10. Individual experimental blocks are illustrated. The average of 5 visual fields is shown and error bars represent the s.e. *Denotes an expanded Y-axis. (**b**) Randomized block ANOVA statistical analysis. Null hypothesis (NØ) rejected if $p < 0.0125$.

a

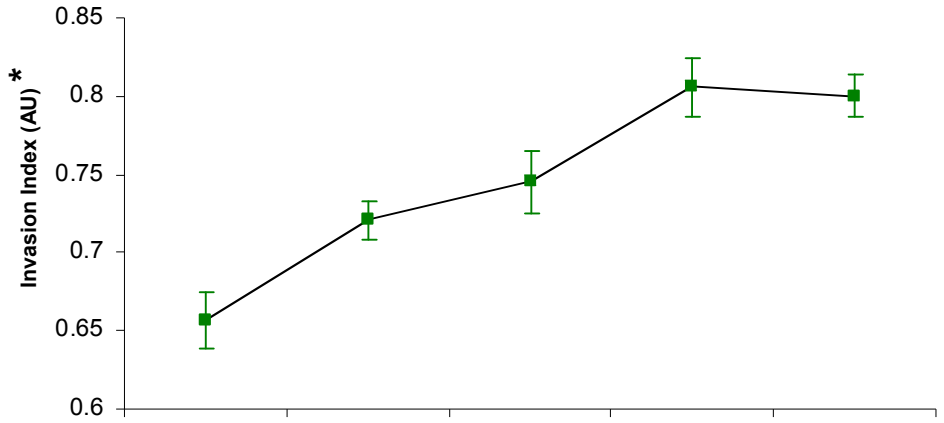

b

ANOVA test for linear trend

Group	Count	Mean Invasion Index	Comparison Coefficient
Control	10	0.6571336	-0.6324555
TNFα 1	10	0.7205902	-0.3162278
TNFα 3.1	10	0.7449988	0
TNFα 10	10	0.8056464	0.3162278
TNFα 31	10	0.7997851	0.6324555

p = 0.006782

Figure 6.12 TNFα promotes SCC12 cell invasion *in vitro* in a dose responsive manner

(**a**) Line plot displaying the log linear relationship of mean carcinoma invasion in response to TNFα stimulation. The average of 10 visual fields is shown and error bars represent the s.e. *Denotes an expanded Y-axis. (**b**) ANOVA test for linear trend. Null hypothesis (NØ) rejected if $p < 0.05$.

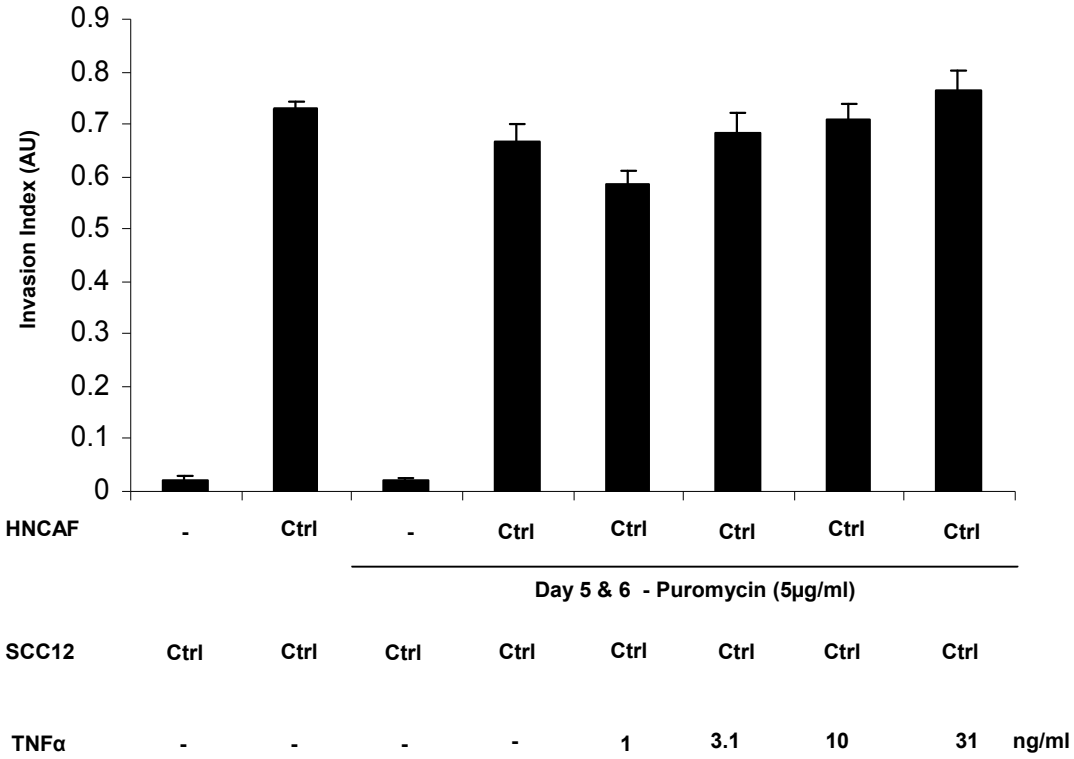

Figure 6.13 Organotypic invasion assay: SCC12 TNFα stimulation

Quantification of carcinoma invasion in organotypic cultures in which gels were treated with puromycin (5µg/ml) daily for 48 hours after 5 days of matrix remodelling. Fibroblasts were removed prior to the addition of SCC12 cells which were then stimulated daily with TNFα at the specified concentrations. The average of 10 visual fields from 2 experiments is shown. The error bars represent the s.e.

a

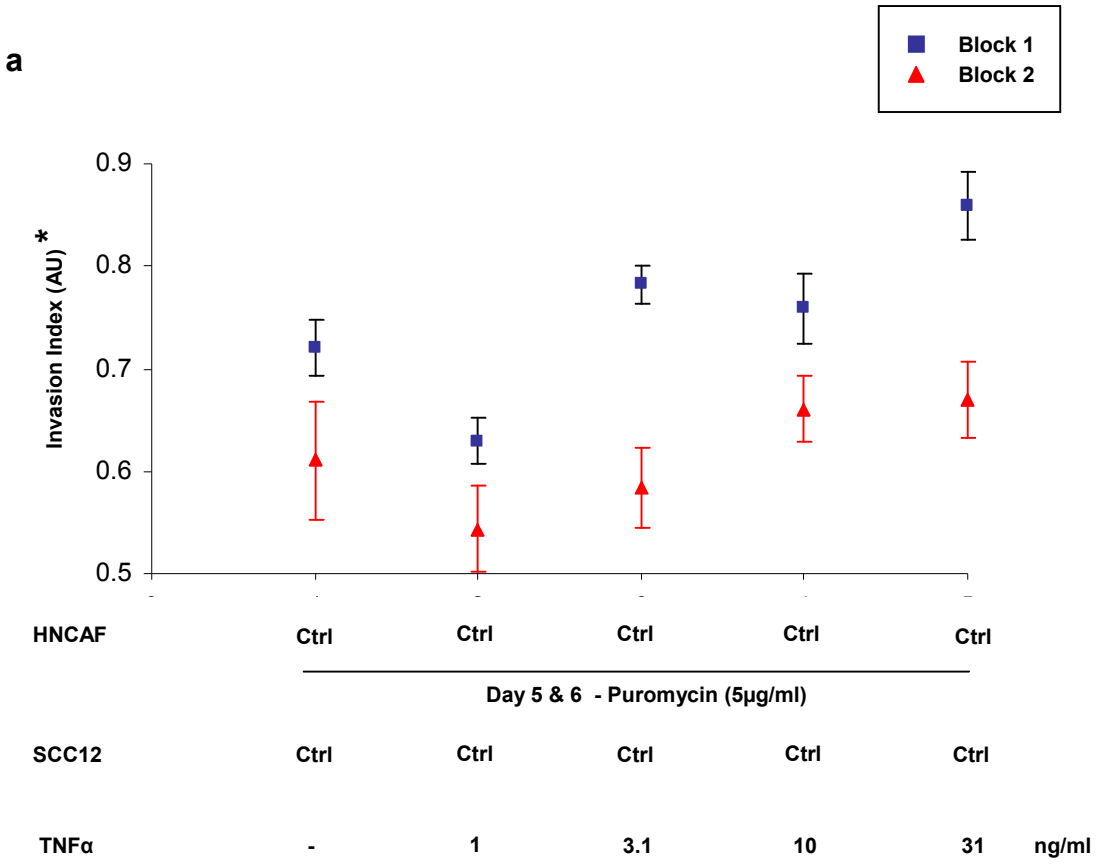

b

Randomized Block ANOVA	p Value	Decision p<0.0125
Control vs TNFα 1	0.102226	Do not reject
Control vs TNFα 3.1	0.667032	Do not reject
Control vs TNFα 10	0.305689	Do not reject
Control vs TNFα 31	0.058552	Do not reject

Figure 6.14 Organotypic invasion assay: SCC12 TNFα stimulation. (a) Scatter plot and (b) randomized block ANOVA statistical analysis

(**a**) Scatter plot displaying quantification of carcinoma invasion in cultures from the organotypic assay illustrated in Figure 6.13. Individual experimental blocks are illustrated. The average of 5 visual fields is shown and error bars represent the s.e. *Denotes an expanded Y-axis. (**b**) Randomized block ANOVA statistical analysis. Null hypothesis (NØ) rejected if $p < 0.0125$.

a

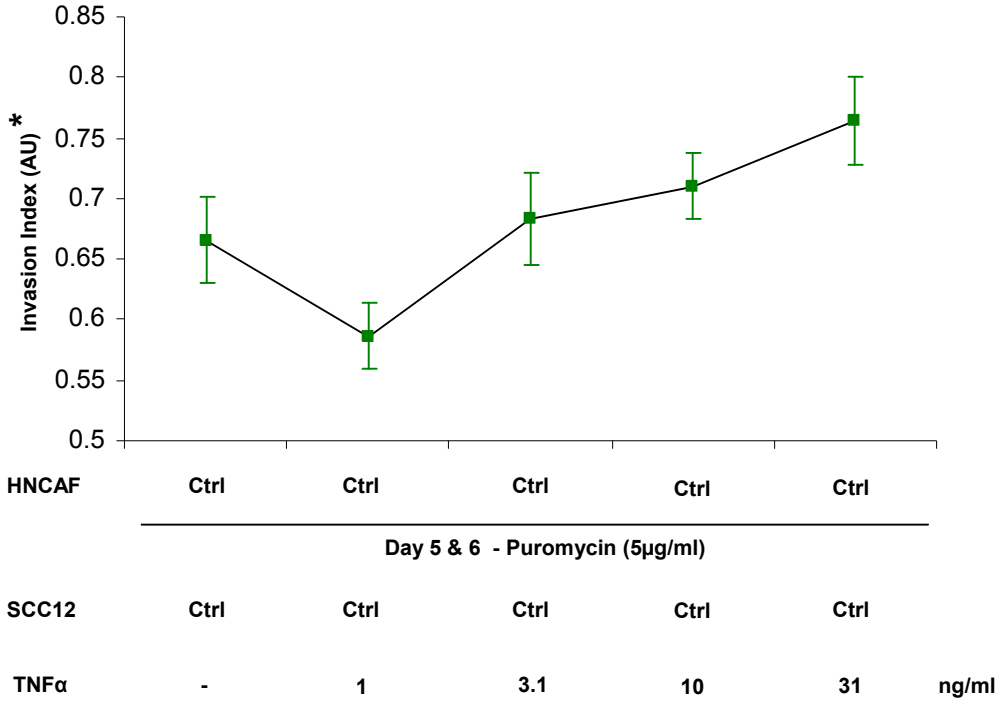

b

ANOVA test for linear trend

Group	Count	Mean Invasion Index	Comparison Coefficient
Control	10	0.6658506	-0.6324555
TNFα 1	10	0.5866195	-0.3162278
TNFα 3.1	10	0.6832404	0
TNFα 10	10	0.7098694	0.3162278
TNFα 31	10	0.7642763	0.6324555

p = 0.018836

Figure 6.15 TNFα stimulation of SCC12 cells promotes carcinoma invasion in remodelled collagen-Matrigel® matrix in a dose responsive manner in the absence of stromal fibroblasts

(**a**) Line plot displaying the log linear relationship of mean carcinoma invasion in response to TNFα stimulation. The average of 10 fields is shown and error bars represent the s.e. *Denotes an expanded Y-axis. (**b**) Linear trend ANOVA analysis. Null hypothesis (NØ) rejected if $p < 0.05$.

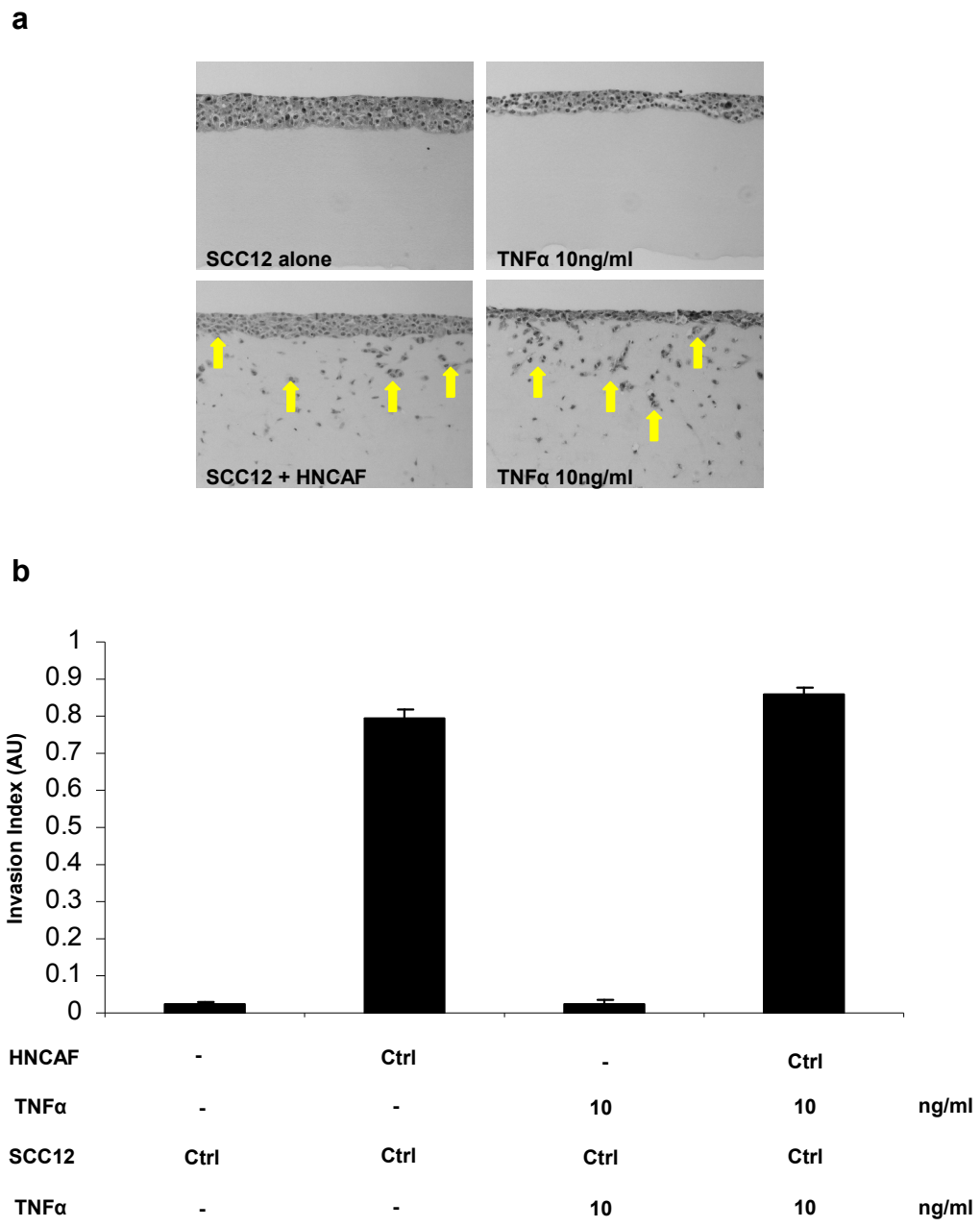

Figure 6.16 TNFα stimulated SCC12 cells do not invade 'naïve' collagen-Matrigel® matrix

(**a**) H&E stained sections of SCC12 cells cultured in organotypic gels. Arrows point to the invading front of carcinoma cells. (**b**) Quantification of carcinoma invasion. SCC12 cells were stimulated daily with TNFα (10ng/ml) on gels with and with out stromal fibroblasts. The average of 10 visual fields from 2 experiments is shown. The error bars represent the s.e.

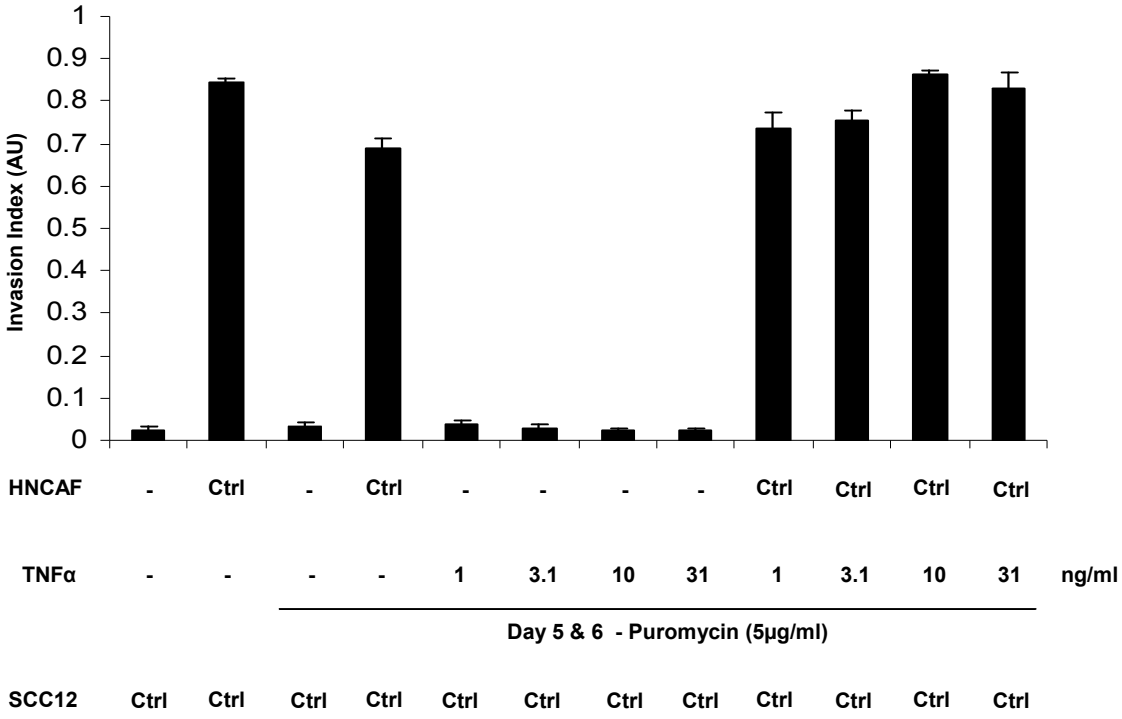

Figure 6.17 Organotypic invasion assay: HNCAF TNFα stimulation

Quantification of carcinoma invasion in organotypic cultures in which gels were stimulated daily with TNFα at the specified concentrations and then treated with puromycin (5µg/ml) daily for 48 hours after 5 days of matrix remodelling. Fibroblasts were removed prior to the addition of SCC12 cells and the cultures allowed to proceed to completion. The average of 10 visual fields from 2 experiments is shown. The error bars represent the s.e.

a

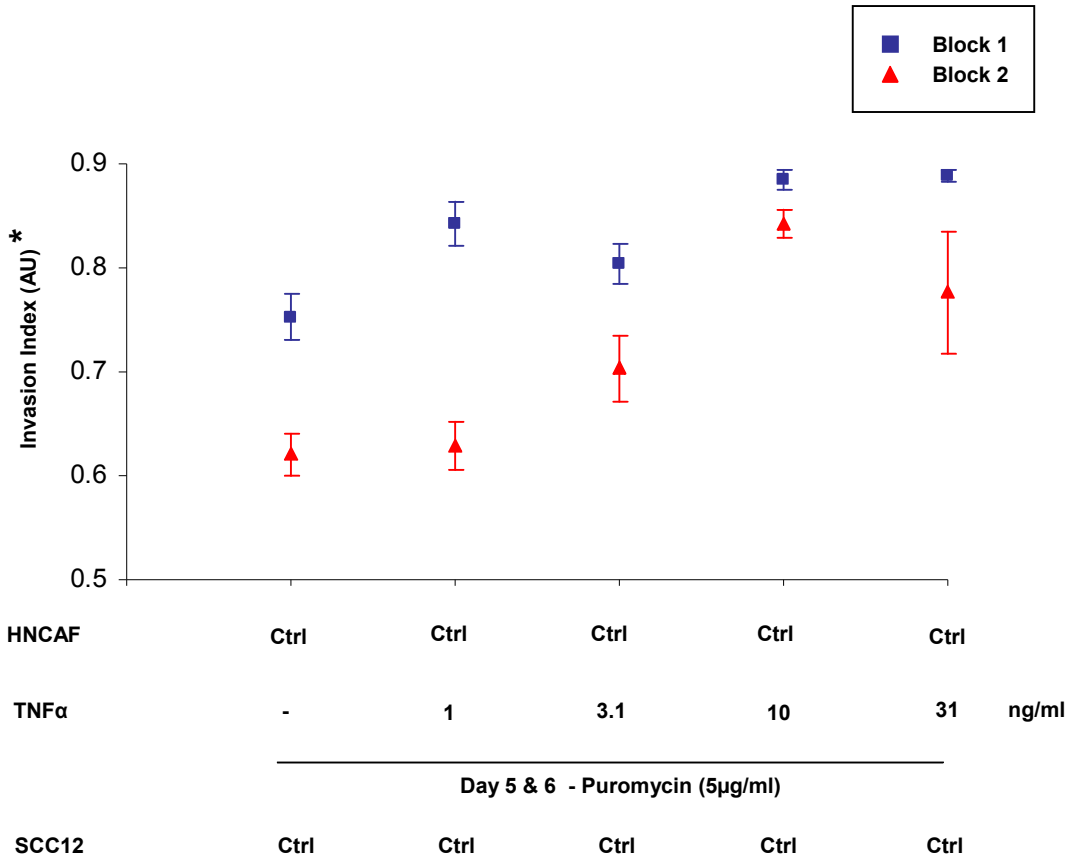

b

Randomized Block ANOVA	p Value	Decision p<0.0125
Control vs TNFα 1	0.324620	Do not reject
Control vs TNFα 3.1	0.798249	Do not reject
Control vs TNFα 10	0.015440	Do not reject
Control vs TNFα 31	0.028632	Do not reject

Figure 6.18 Organotypic invasion assay: HNCAF TNFα stimulation. (a) Scatter plot and (b) randomized block ANOVA statistical analysis

(**a**) Scatter plot displaying quantification of carcinoma invasion in cultures from the organotypic assay illustrated in Figure 6.17. Individual experimental blocks are illustrated. The average of 5 visual fields is shown and error bars represent the s.e. *Denotes an expanded Y-axis. (**b**) Randomized block ANOVA statistical analysis. Null hypothesis (NØ) rejected if $p < 0.0125$.

a

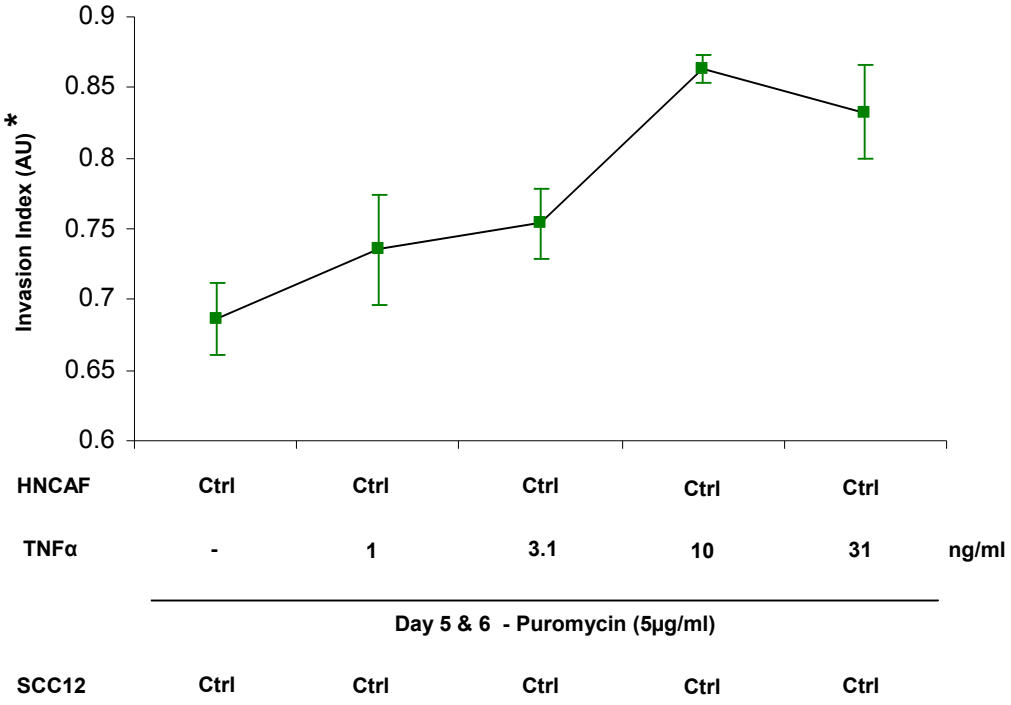

b

ANOVA test for linear trend

Group	Count	Mean Invasion Index	Comparison Coefficient
Control	10	0.6864706	-0.6324555
TNFα 1	10	0.7353746	-0.3162278
TNFα 3.1	10	0.7536159	0
TNFα 10	10	0.8631001	0.3162278
TNFα 31	10	0.8328683	0.6324555

p = 0.012597

Figure 6.19 TNFα stimulation of HNCAF promotes carcinoma invasion in a dose responsive manner in the absence of direct stimulation of SCC12 cells

(**a**) Line plot displaying the log linear relationship of mean carcinoma invasion in response to TNFα stimulation. The average of 10 visual fields is shown and error bars represent the s.e. *Denotes an expanded Y-axis. (**b**) ANOVA test for linear trend. Null hypothesis (NØ) rejected if $p < 0.05$.

6.2.6 TNFα promotes fibroblast-dependent collagen-Matrigel® matrix contraction in a dose responsive manner which correlates positively with carcinoma invasion

As highlighted in Chapter 4, a good correlation between the degree of macroscopic gel contraction and the extent of microscopic matrix remodelling exists [77, 303]. The latter is in turn intimately associated with the ability of stromal fibroblasts to promote SCC invasion [77, 303]. Therefore, I also assessed the effect of TNFα stimulation on fibroblast-dependent collagen-Matrigel® matrix contraction.

The collagen-Matrigel® gels constructed for the assays detailed in Section 6.2.5 were photographed after 5 days of fibroblast-mediated matrix remodelling (Figure 6.20a) and the Contraction Index for each gel calculated (Figure 6.20b). As expected, TNFα stimulated fibroblast-deficient gels did not contract. A line plot of the individual experimental blocks is presented in Figure 6.21a. Gel contraction was statistically significant at all concentrations of TNFα (Figure 6.21b).

Figure 6.22 illustrates the log linear relationship of mean collagen-Matrigel® matrix contraction in response to HNCAF TNFα stimulation.

To exclude the possibility that the TNFα-induced HNCAF effects on carcinoma invasion and matrix contraction were secondary to an enhanced proliferative response, fibroblast number per unit area was assessed on Day 1 and Day 5 of the assays in gels with and without daily TNFα stimulation (Figure 6.23). TNFα at concentrations of 1-31ng/ml did not affect HNCAF proliferation (Figure 6.24).

Figure 6.25 is a scatter plot displaying the relationship between the mean Invasion Index and the mean Contraction Index for the TNFα stimulated HNCAF-containing organotypic cultures presented in Section 6.2.5. TNFα stimulation of HNCAF at concentrations of 1-31ng/ml resulted in an increase in both collagen-Matrigel® matrix contraction and carcinoma invasion.

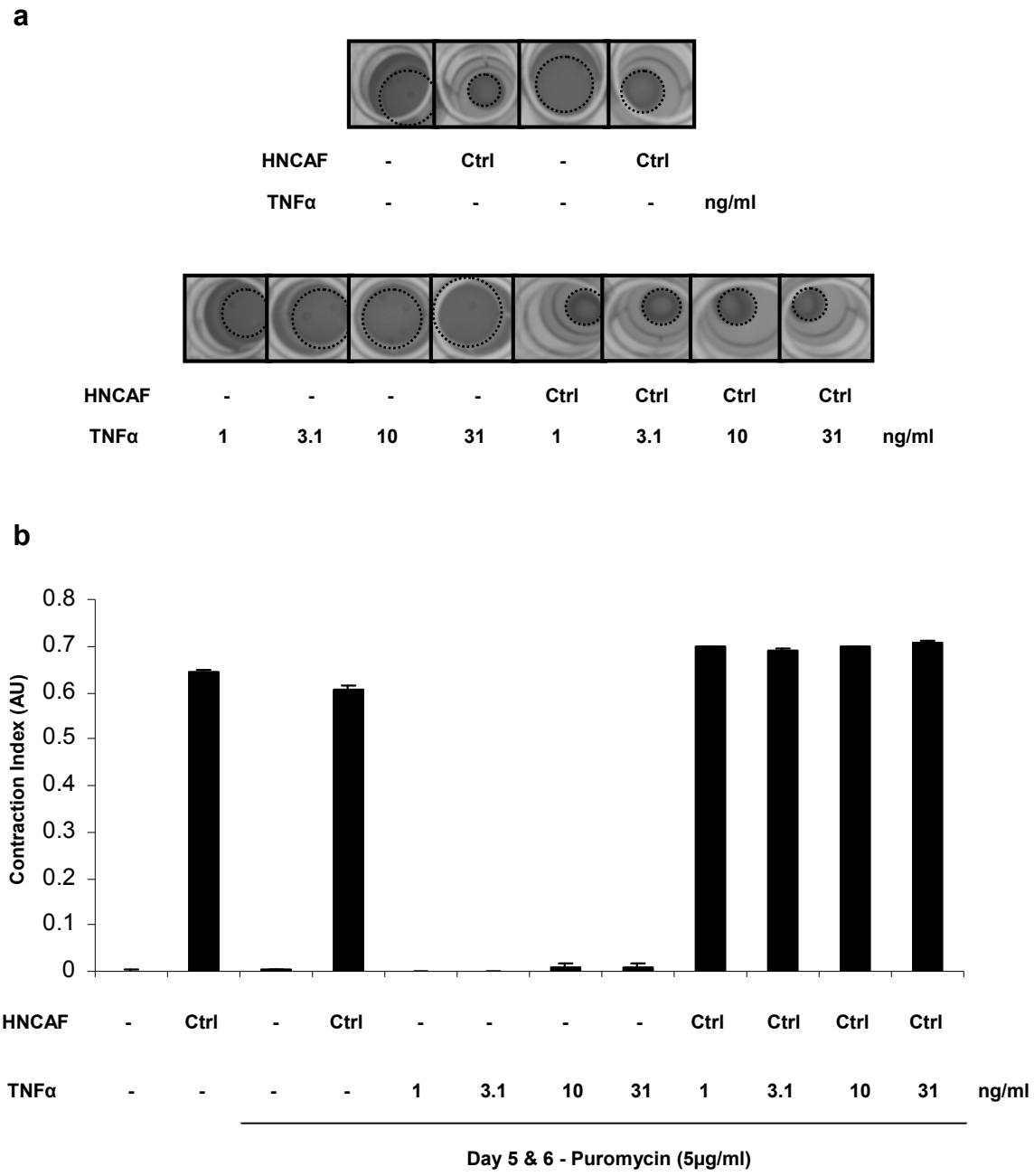

Figure 6.20 Assessment of TNFα stimulated fibroblast-dependent collagen-Matrigel® matrix contraction

(**a**) Images of organotypic gels after 5 days of matrix remodelling and daily TNFα stimulation at the specified concentrations prior to the removal of HNCAF. The dotted line represents the area of the gel. (**b**) Quantification of the degree of matrix remodelling. The Contraction Index was calculated using the formula 1 - (Gel Area / Well Area). The average of 2 experiments is shown and error bars represent the s.e.

a

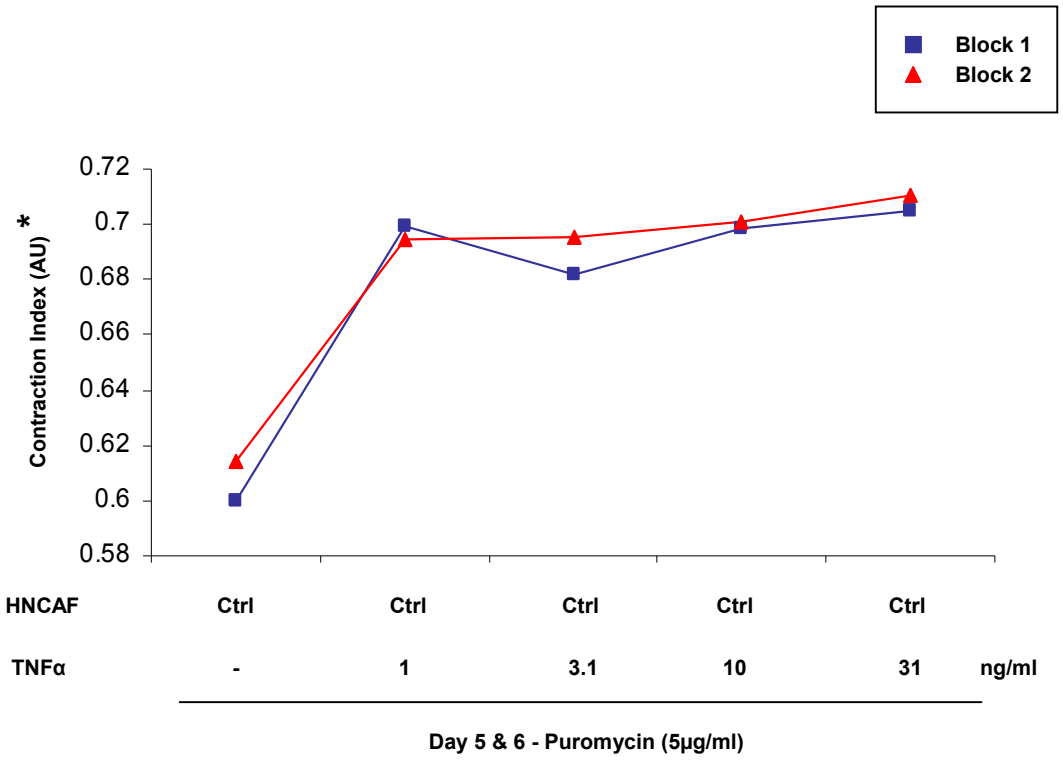

b

Randomized Block ANOVA	p Value	Decision p<0.0125
Control vs TNFα 1	0.000088	Reject
Control vs TNFα 3.1	0.000129	Reject
Control vs TNFα 10	0.000077	Reject
Control vs TNFα 31	0.000056	Reject

Figure 6.21 TNFα promotes fibroblast-dependent collagen-Matrigel® matrix contraction

(**a**) Line plot displaying the Contraction Index of the TNFα stimulated fibroblast containing gels of the organotypic assay illustrated in Figure 6.20. Individual experimental blocks are shown. *Denotes an expanded Y-axis. (**b**) Randomized block ANOVA statistical analysis. Null hypothesis (NØ) rejected if $p < 0.0125$.

a

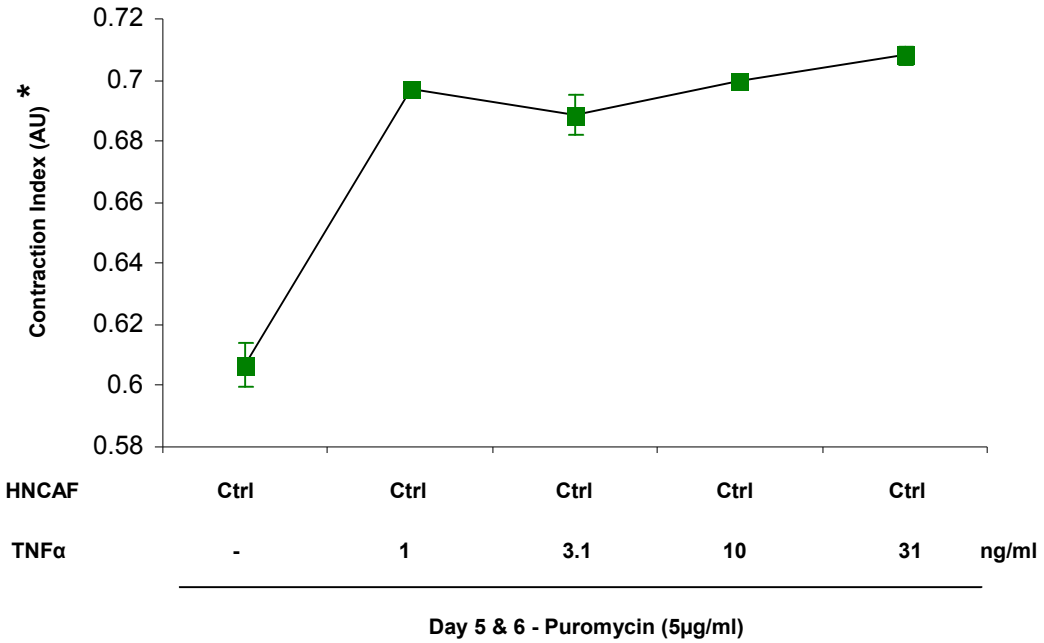

b

ANOVA test for linear trend

Group	Count	Mean Contraction Index	Comparison Coefficient
Control	2	0.6069958	-0.6324555
TNFα 1	2	0.6970044	-0.3162278
TNFα 3.1	2	0.6886168	0
TNFα 10	2	0.6998724	0.3162278
TNFα 31	2	0.707998	0.6324555

p = 0.000082

Figure 6.22 TNFα stimulation of HNCAF promotes collagen-Matrigel® matrix contraction in a dose responsive manner

(**a**) Line plot displaying the log linear relationship of the Contraction Index in response to TNFα stimulation of the fibroblast containing gels of the organotypic assay illustrated in Figure 6.20. *Denotes an expanded Y-axis. (**b**) ANOVA test for linear trend. Null hypothesis (NØ) rejected if $p < 0.05$.

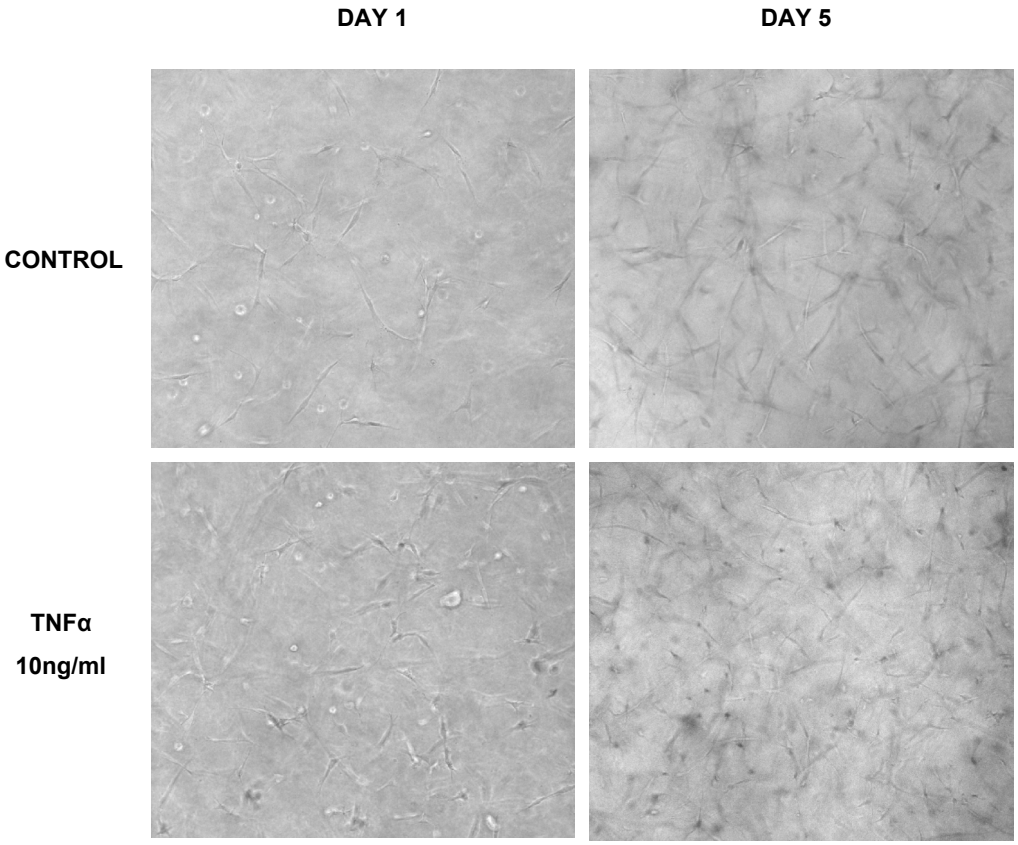

Figure 6.23 Assessment of fibroblast number in organotypic cultures after 5 days of collagen-Matrigel® matrix remodelling with and without daily TNFα stimulation

Examples of low power phase images of HNCAF in collagen-Matrigel® matrix taken on Day 1 and Day 5 of the organotypic gels illustrated in Figure 6.20. The number of fibroblasts per unit area was quantified from 6 representative regions of each culture and corrected for the degree of gel contraction. (n=2)

a

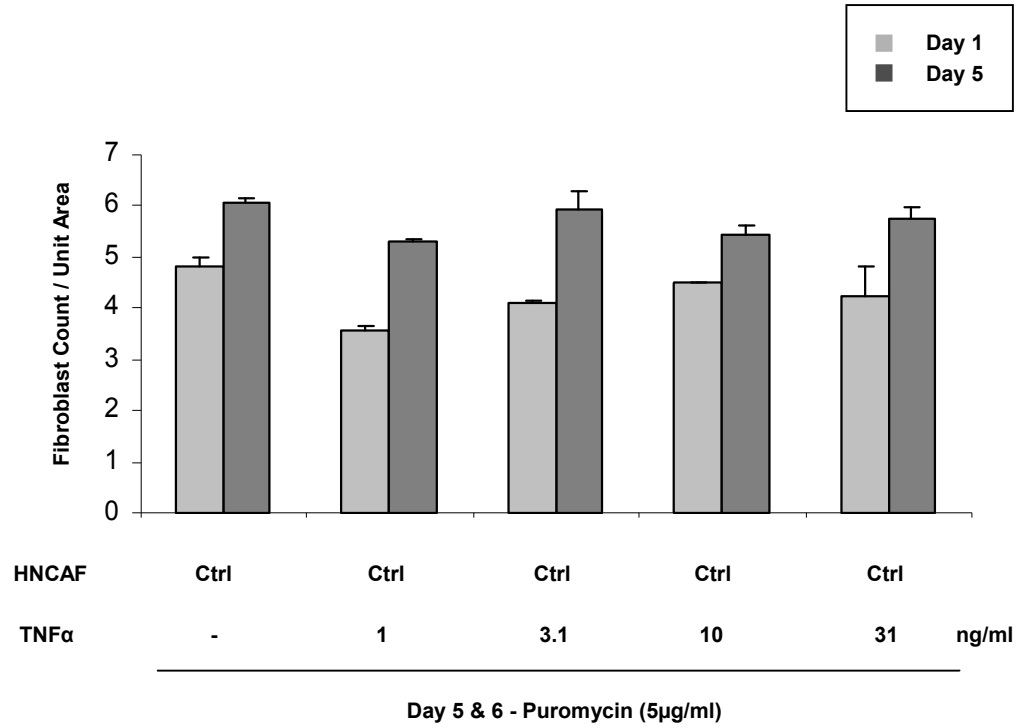

b

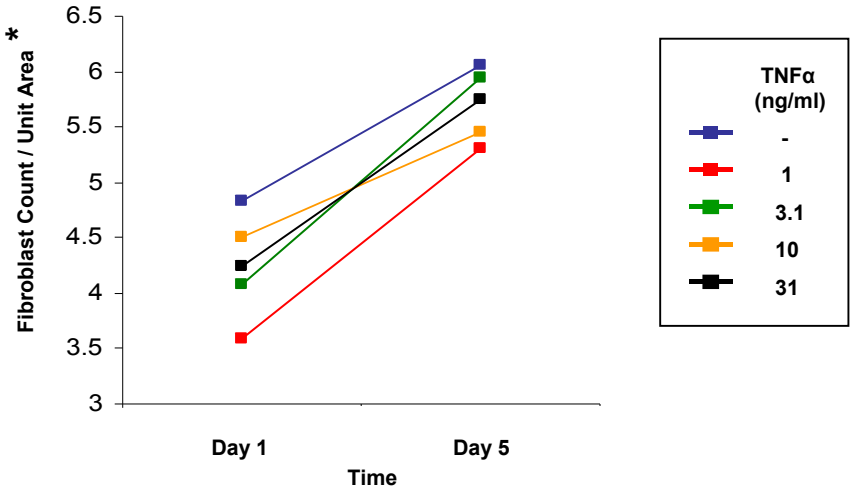

c

Randomized Block ANOVA	p Value	Decision p<0.05
Control vs TNFα (1, 3.1, 10, 31)	0.220800	Do not reject

Figure 6.24 TNFα at concentrations of 1-31ng/ml does not affect HNCAF proliferation

Fibroblast count per unit area (corrected for degree of gel contraction) after 5 days of matrix remodelling and daily TNFα stimulation at the specified concentrations (**a**) bar chart and (**b**) line plot. The average of 12 fields from 2 experiments is shown. The error bars represent the s.e. *Denotes an expanded Y-axis. (**c**) Randomized block ANOVA statistical analysis. Null hypothesis (NØ) rejected if $p < 0.05$.

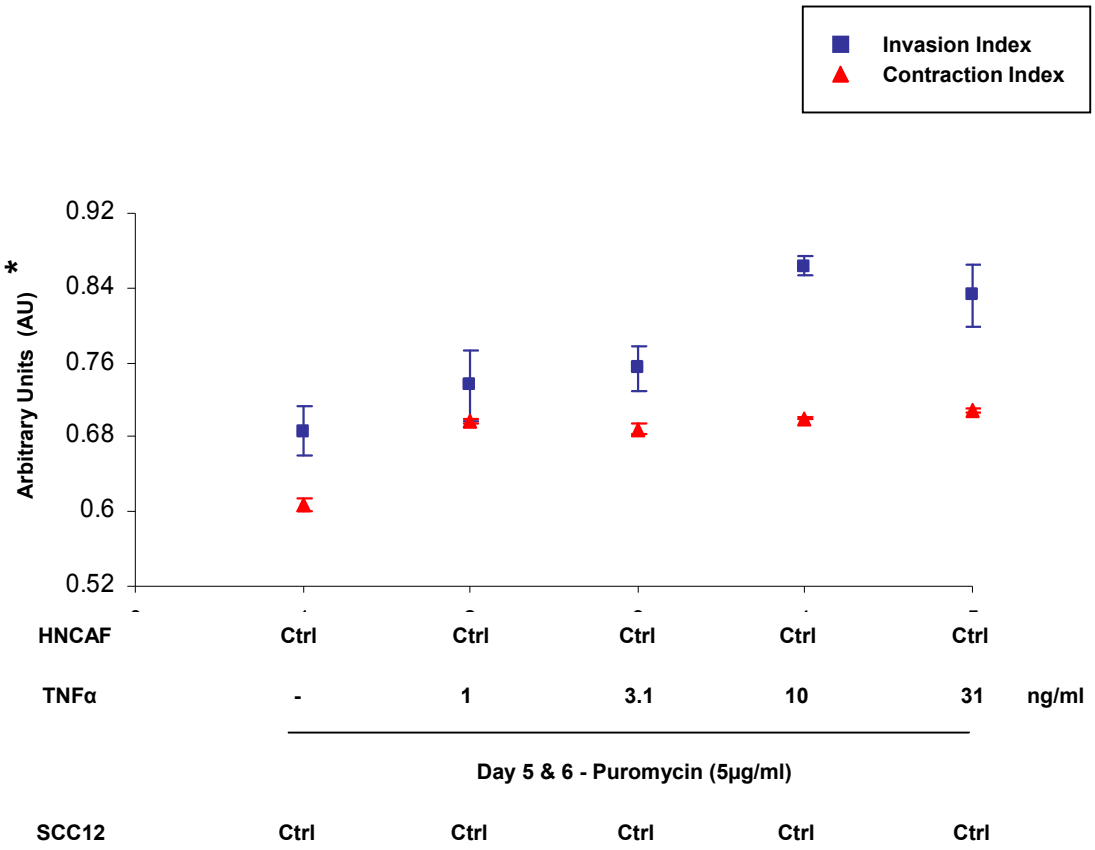

Figure 6.25 TNFα stimulation of HNCAF promotes collagen-Matrigel® matrix contraction in a dose responsive manner which correlates positively with carcinoma invasion

Scatter plot displaying the relationship between mean carcinoma invasion and mean gel contraction in response to TNFα stimulation. Error bars represent the s.e. *Denotes an expanded Y-axis.

6.3 Interleukin-1α (IL-1α)

Like TNFα, current literature suggests that IL-1α production by malignant cells regulates tumour progression and correlates with cancer cell invasiveness [281]. As well as acting in an autocrine manner, IL-1α has also been shown to have a paracrine influence on neighbouring stromal fibroblasts [192]. Given the responsiveness of our organotypic system to TNFα stimulation, I investigated whether IL-1α exerted a similar influence on carcinoma invasion.

6.3.1 IL-1α promotes SCC12 carcinoma invasion *in vitro* in a dose responsive manner

Figure 6.26 shows the quantification of SCC12 invasion assays in which both the stromal and epithelial components of the organotypic cultures were stimulated daily with IL-1α at concentrations of 100, 213, 467 and 1000pg/ml. Vehicle controls (0.1% BSA at concentrations comparable to those of IL-1α) were also included. The Invasion Index increased with escalating concentrations of IL-1α and was statistically significant at doses of 467 and 1000pg/ml (Figures 6.27-6.30).

Figure 6.31 illustrates the log linear relationship of mean carcinoma invasion in response to IL-1α stimulation.

6.3.2 IL-1α stimulation of SCC12 cells promotes carcinoma invasion in remodelled collagen-Matrigel® matrix in a dose responsive manner in the absence of stromal fibroblasts

Having determined SCC12 carcinoma invasion to be IL-1α driven, as for TNFα, I examined the effect of IL-1α stimulation on the epithelial and stromal components of our organotypic system independently of each other.

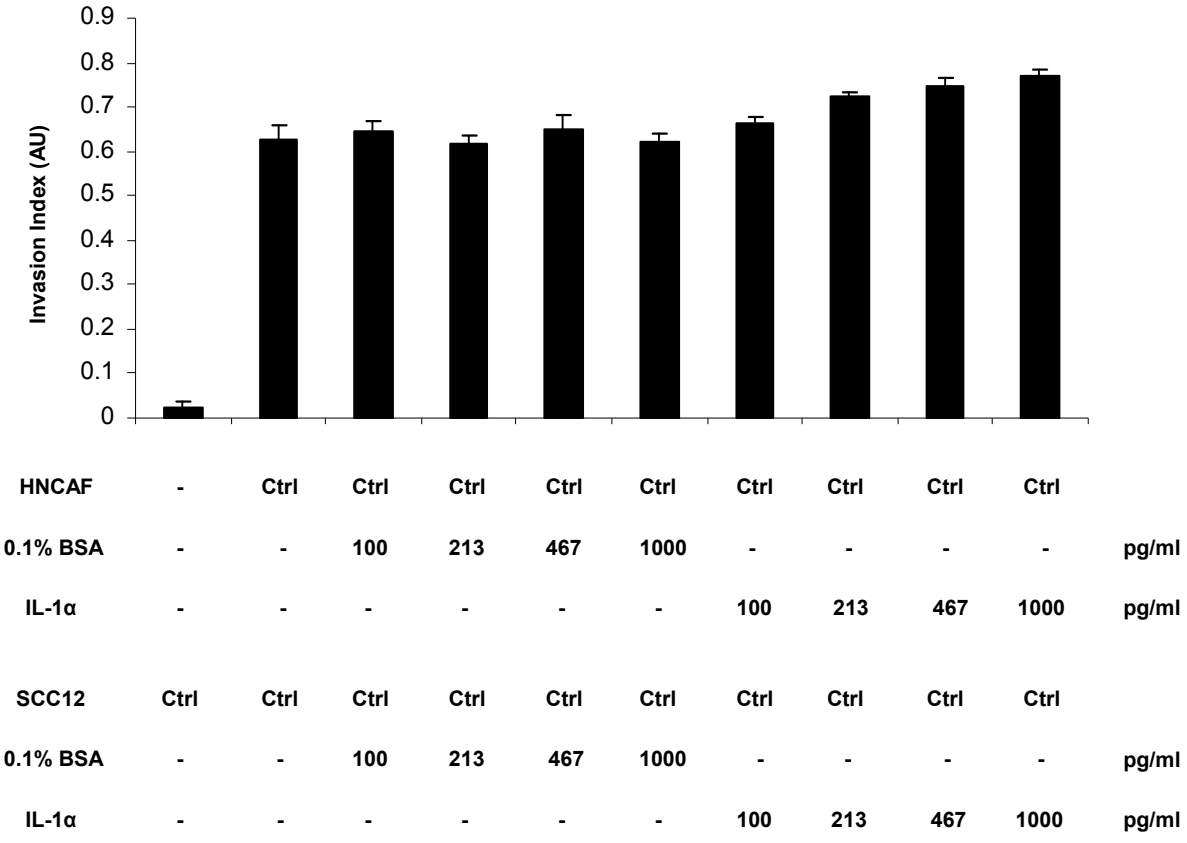

Figure 6.26 Organotypic invasion assay: HNCAF and SCC12 IL-1α stimulation

Quantification of carcinoma invasion. Both the stromal and epithelial components of the organotypic cultures were stimulated daily with IL-1α at the specified concentrations. Vehicle controls (0.1% BSA at concentrations comparable to those of IL-1α) were also included in the assay. The average of 10 visual fields from 2 experiments is shown. The error bars represent the s.e.

a

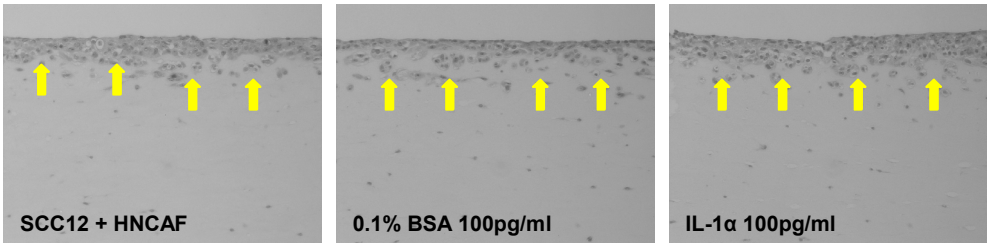

b

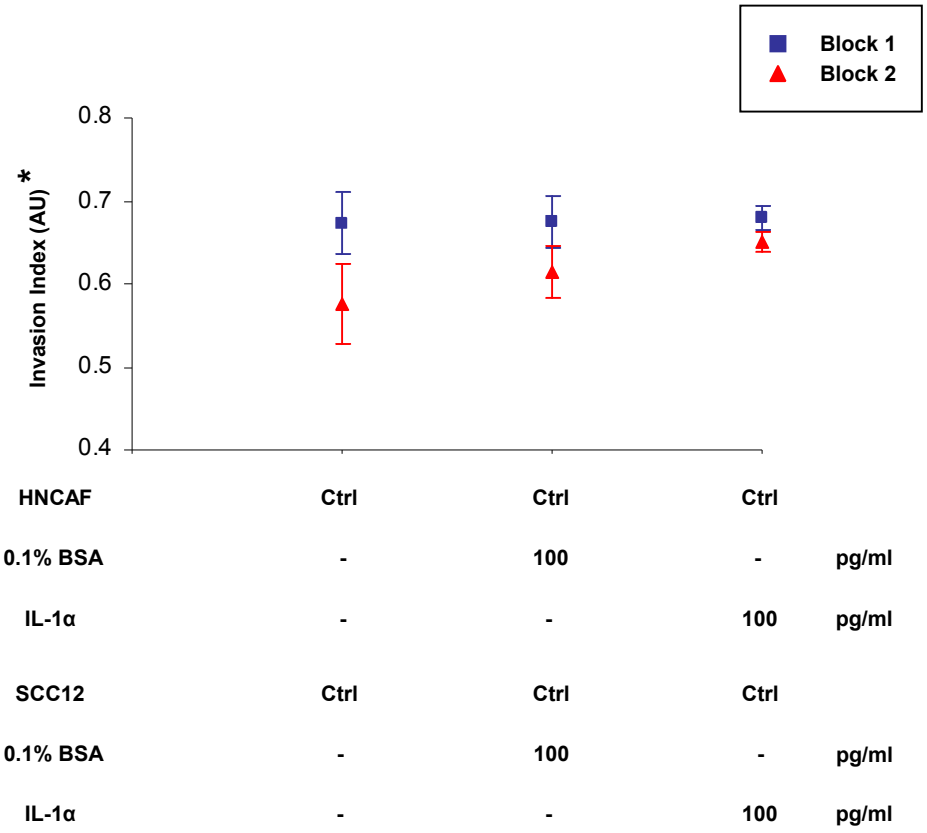

c

Randomized Block ANOVA	p Value	Decision p<0.025
Control vs 0.1% BSA 100	0.502987	Do not reject
0.1% BSA 100 vs IL-1α 100	0.482476	Do not reject

Figure 6.27 Organotypic invasion assay: HNCAF and SCC12 IL-1α stimulation (100pg/ml)

(**a**) H&E stained sections of SCC12 cells cultured in organotypic gels. Arrows point to the invading front of carcinoma cells. (**b**) Scatter plot displaying quantification of carcinoma invasion. Individual experimental blocks are illustrated. The average of 5 visual fields is shown and error bars represent the s.e. *Denotes an expanded Y-axis. (**c**) Randomized block ANOVA statistical analysis. Null hypothesis (NØ) rejected if $p < 0.025$.

a

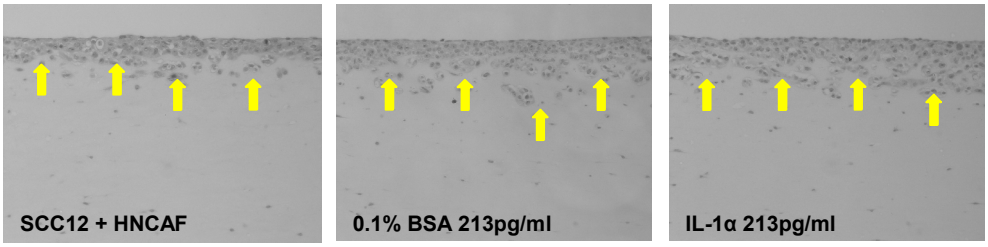

b

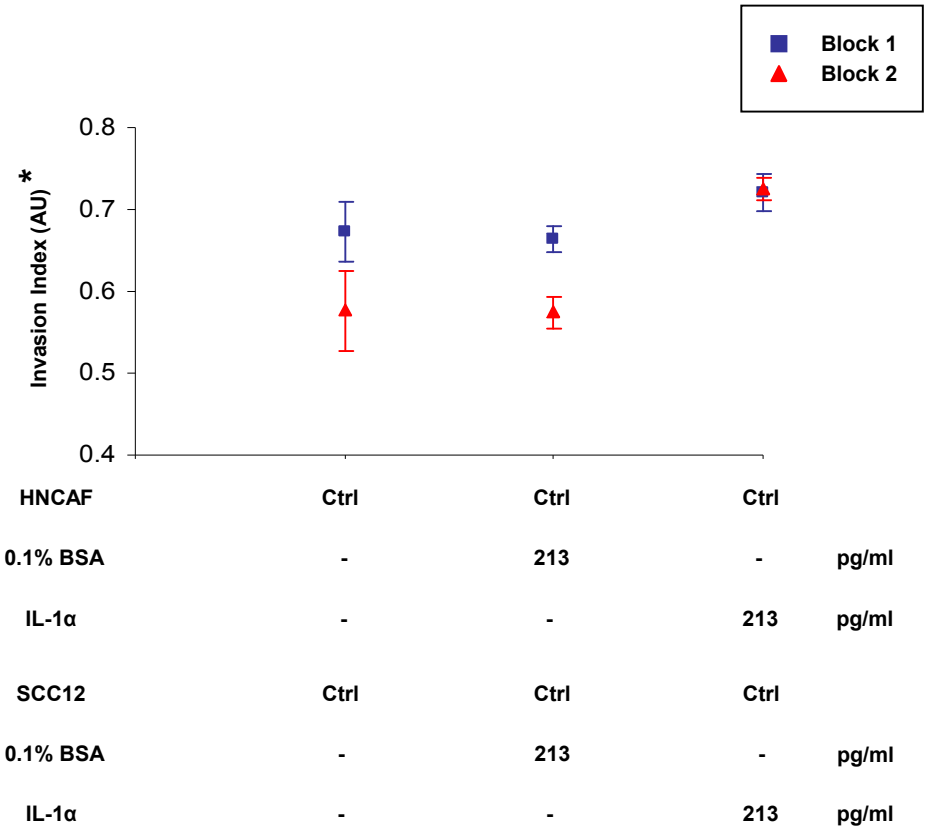

c

Randomized Block ANOVA	p Value	Decision p<0.025
Control vs 0.1% BSA 213	0.900636	Do not reject
0.1% BSA 213 vs IL-1α 213	0.122179	Do not reject

Figure 6.28 Organotypic invasion assay: HNCAF and SCC12 IL-1α stimulation (213pg/ml)

(**a**) H&E stained sections of SCC12 cells cultured in organotypic gels. Arrows point to the invading front of carcinoma cells. (**b**) Scatter plot displaying quantification of carcinoma invasion. Individual experimental blocks are illustrated. The average of 5 visual fields is shown and error bars represent the s.e. *Denotes an expanded Y-axis. (**c**) Randomized block ANOVA statistical analysis. Null hypothesis (NØ) rejected if $p < 0.025$.

a

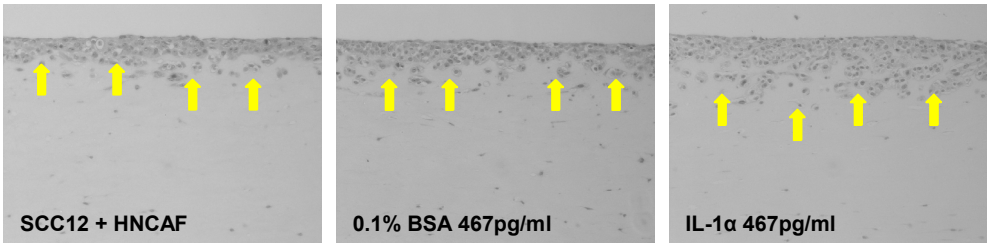

b

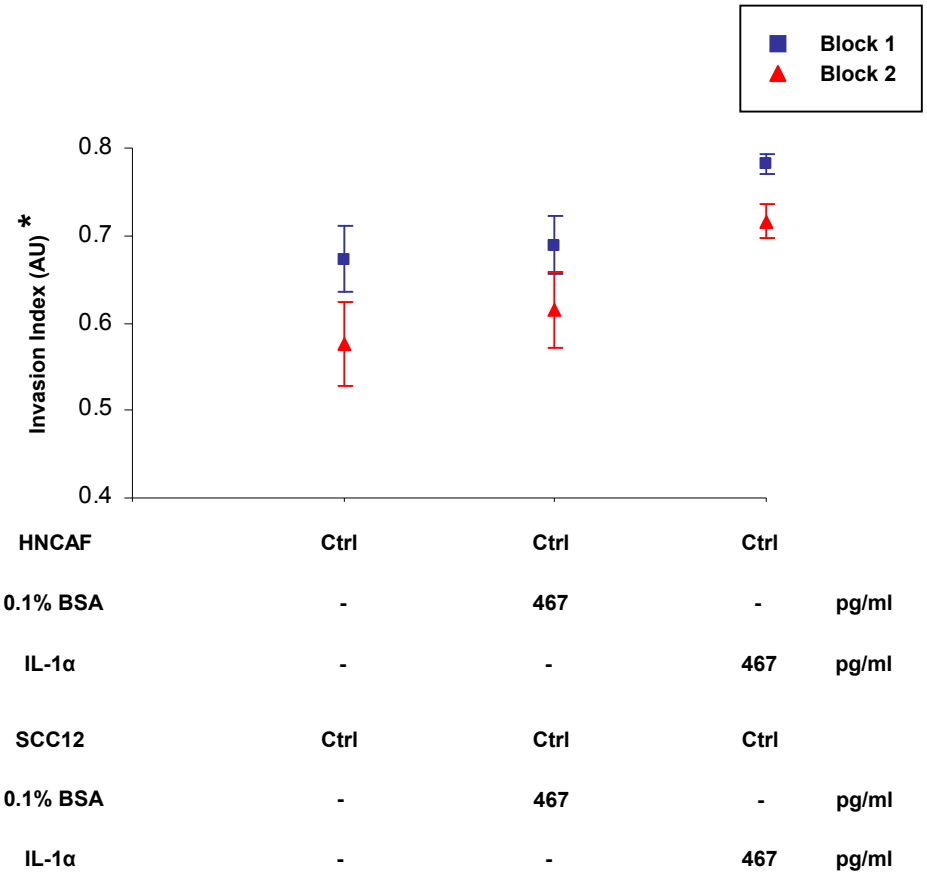

c

Randomized Block ANOVA	p Value	Decision p<0.025
Control vs 0.1% BSA 467	0.142616	Do not reject
0.1% BSA 467 vs IL-1α 467	0.013920	Reject

Figure 6.29 Organotypic invasion assay: HNCAF and SCC12 IL-1α stimulation (467pg/ml)

(**a**) H&E stained sections of SCC12 cells cultured in organotypic gels. Arrows point to the invading front of carcinoma cells. (**b**) Scatter plot displaying quantification of carcinoma invasion. Individual experimental blocks are illustrated. The average of 5 visual fields is shown and error bars represent the s.e. *Denotes an expanded Y-axis. (**c**) Randomized block ANOVA statistical analysis. Null hypothesis (NØ) rejected if $p < 0.025$.

a

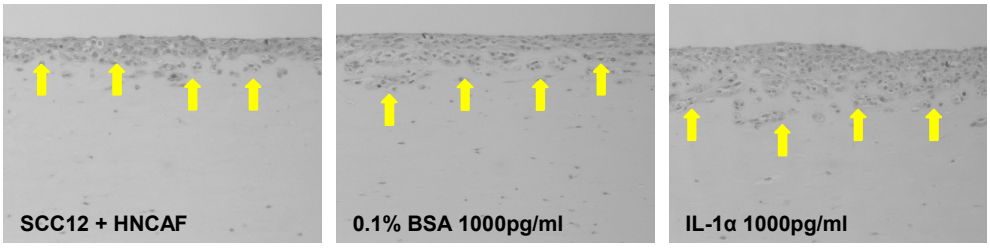

b

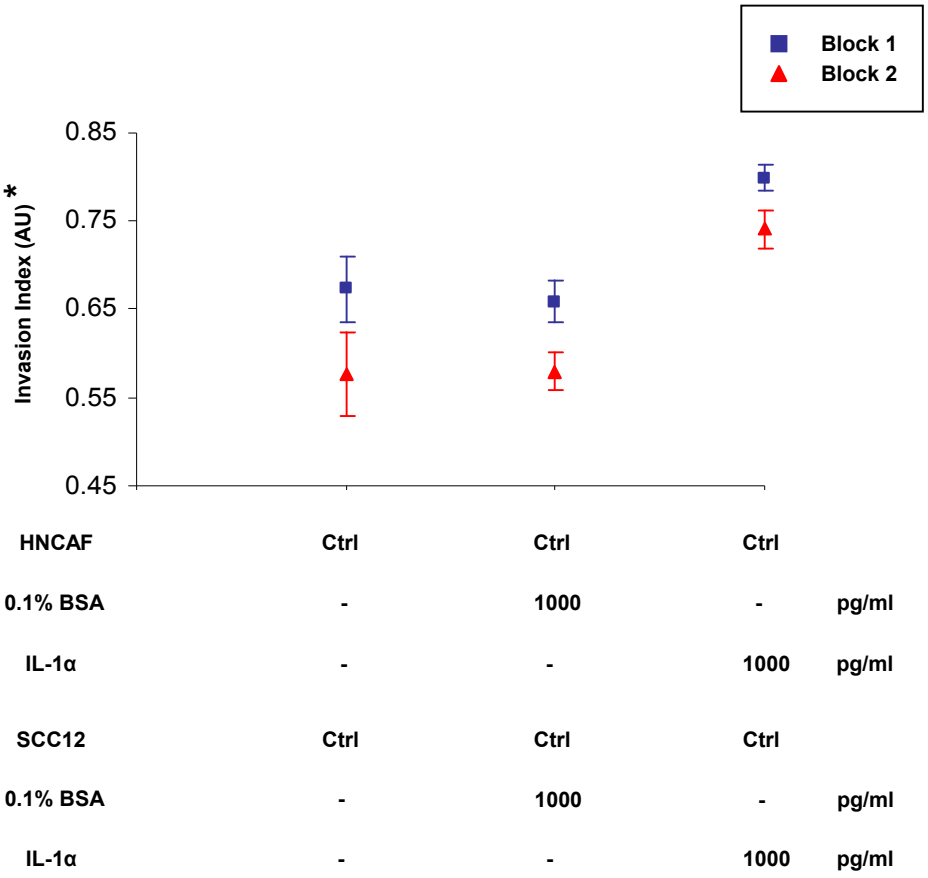

c

Randomized Block ANOVA	p Value	Decision p<0.025
Control vs 0.1% BSA 1000	0.735387	Do not reject
0.1% BSA 1000 vs IL-1α 1000	0.008129	Reject

Figure 6.30 Organotypic invasion assay: HNCAF and SCC12 IL-1α stimulation (1000pg/ml)

(**a**) H&E stained sections of SCC12 cells cultured in organotypic gels. Arrows point to the invading front of carcinoma cells. (**b**) Scatter plot displaying quantification of carcinoma invasion. Individual experimental blocks are illustrated. The average of 5 visual fields is shown and error bars represent the s.e. *Denotes an expanded Y-axis. (**c**) Randomized block ANOVA statistical analysis. Null hypothesis (NØ) rejected if $p < 0.025$.

a

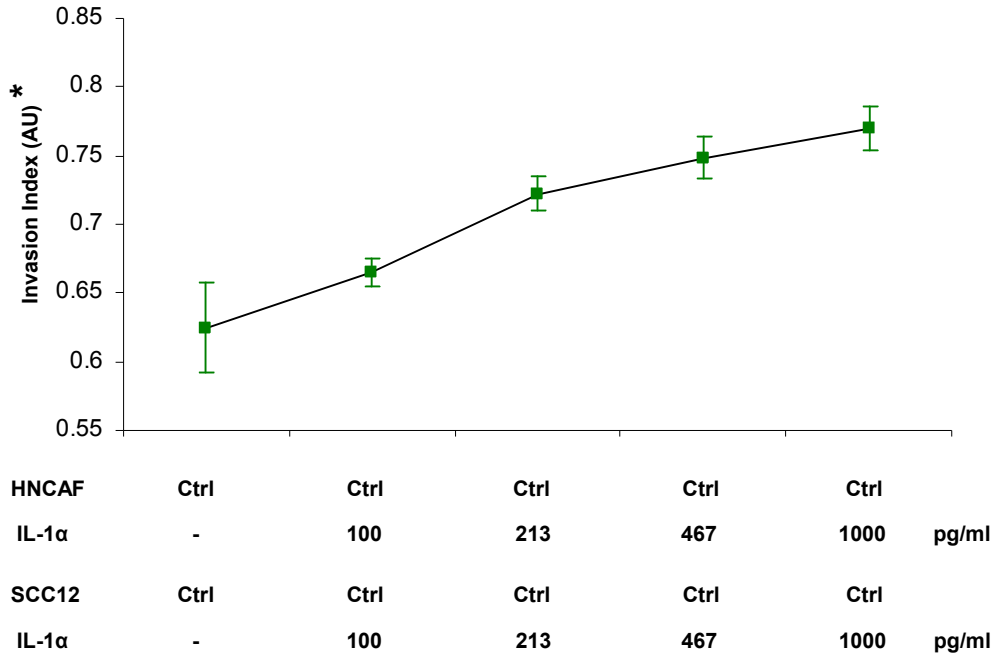

b

ANOVA test for linear trend

Group	Count	Mean Invasion Index	Comparison Coefficient
Control	10	0.6246637	-0.6324555
IL-1α 100	10	0.6650797	-0.3162278
IL-1α 213	10	0.7223568	0
IL-1α 467	10	0.7483929	0.3162278
IL-1α 1000	10	0.7698712	0.6324555

p = 0.003543

Figure 6.31 IL-1α promotes SCC12 carcinoma invasion *in vitro* in a dose responsive manner

(**a**) Line plot displaying the log linear relationship of mean carcinoma invasion in response to IL-1α. The average of 10 visual fields is shown and error bars represent the s.e. *Denotes an expanded Y-axis. (**b**) ANOVA test for linear trend. Null hypothesis (NØ) rejected if $p < 0.05$.

Figure 6.32 shows the quantification of SCC12 invasion in organotypic cultures in which only the epithelial component was stimulated daily with IL-1α at concentrations of 100, 213, 467 and 1000pg/ml. Vehicle controls (0.1% BSA at concentrations comparable to those of IL-1α) were also included. Fibroblasts were removed from the collagen-Matrigel® gels after five days of matrix remodelling by treating with puromycin (5μg/ml) daily for 48 hours prior to the addition of SCC12 cells. A scatter plot of the individual experimental blocks is presented in Figure 6.33. The Invasion Index increased with escalating concentrations of IL-1α (Figure 6.34a) and was statistically significant at doses of 100, 467 and 1000pg/ml (Figure 6.34b).

Figure 6.35 illustrates the log linear relationship of mean carcinoma invasion in response to SCC12 IL-1α stimulation.

6.3.3 IL-1α stimulation of HNCAF does not promote carcinoma invasion in a dose responsive manner in the absence of direct stimulation of SCC12 cells

Figure 6.36 shows the quantification of SCC12 invasion in organotypic cultures in which only the stromal component was stimulated daily with IL-1α at concentrations of 100, 213, 467 and 1000pg/ml. Vehicle controls (0.1% BSA at concentrations comparable to those of IL-1α) were also included. Fibroblasts were removed from the collagen-Matrigel® gels after five days of matrix remodelling by treating with puromycin (5μg/ml) daily for 48 hours prior to the addition of SCC12 cells. A scatter plot of the individual experimental blocks is presented in Figure 6.37. The Invasion Index remained relatively constant with escalating concentrations of IL-1α (Figure 6.38).

In contrast to TNFα, IL-1α did not potentiate the ability of HNCAF to promote SCC12 carcinoma invasion. A log linear relationship of mean Invasion Index in response to IL-1α stimulation was not observed (Figure 6.39).

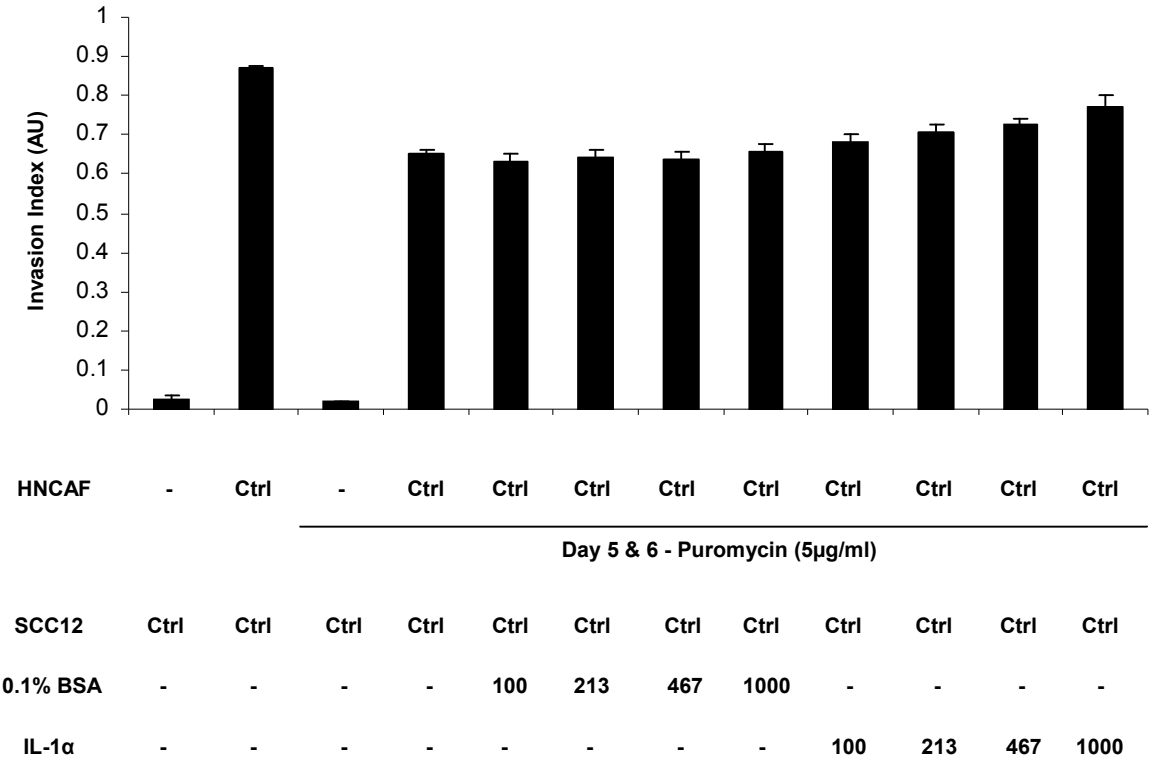

Figure 6.32 Organotypic invasion assay: SCC12 IL-1α stimulation

Quantification of carcinoma invasion in organotypic cultures in which gels were treated with puromycin (5µg/ml) daily for 48 hours after 5 days of matrix remodelling. Fibroblasts were removed prior to the addition of SCC12 cells which were then stimulated daily with IL-1α at the specified concentrations. Vehicle controls (0.1% BSA at concentrations comparable to those of IL-1α) were also included in the assay. The average of 10 visual fields from 2 experiments is shown. The error bars represent the s.e.

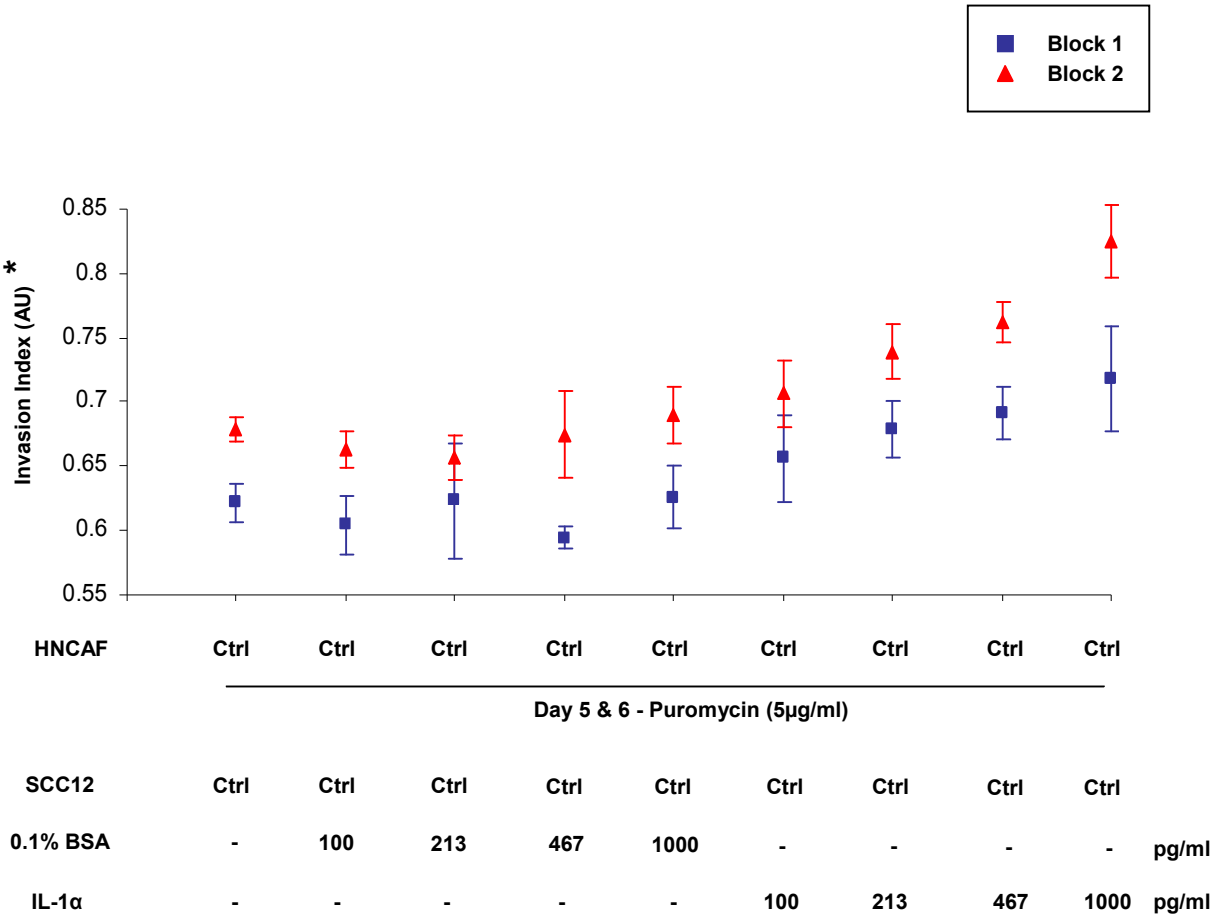

Figure 6.33 Organotypic invasion assay: SCC12 IL-1α stimulation - scatter plot

Scatter plot displaying quantification of carcinoma invasion in cultures from the organotypic assay illustrated in Figure 6.32. Individual experimental blocks are illustrated. The average of 5 visual fields is shown and error bars represent the s.e. *Denotes an expanded Y-axis.

a

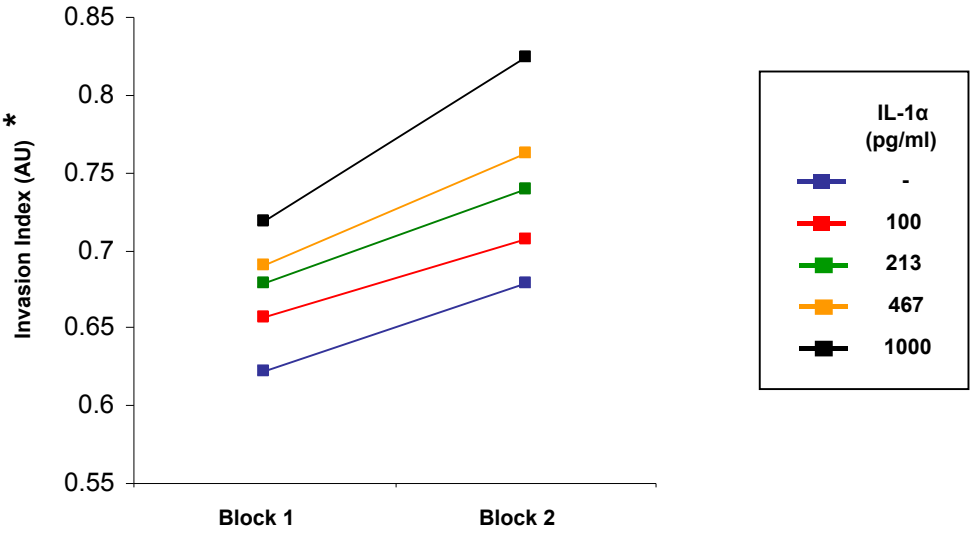

b

Randomized Block ANOVA	p Value	Decision p<0.025
Control vs 0.1% BSA 100	0.036905	Do not reject
0.1% BSA 100 vs IL-1α 100	0.010736	Reject
Control vs 0.1% BSA 213	0.426776	Do not reject
0.1% BSA 213 vs IL-1α 213	0.028848	Do not reject
Control vs 0.1% BSA 467	0.188575	Do not reject
0.1% BSA 467 vs IL-1α 467	0.010983	Reject
Control vs 0.1% BSA 1000	0.723961	Do not reject
0.1% BSA 1000 vs IL-1α 1000	0.023132	Reject

Figure 6.34 IL-1α stimulation of SCC12 cells results in statistically significant carcinoma invasion which is independent of its potential effect on carcinoma associated fibroblasts

(a) Line plot of quantification of carcinoma invasion of the IL-1α stimulated cultures from the organotypic assay illustrated in Figure 6.32 Individual experimental blocks are illustrated. The average of 5 visual fields is shown. *Denotes an expanded Y-axis. (b) Randomized block ANOVA statistical analysis. Null hypothesis (NØ) rejected if $p < 0.025$.

a

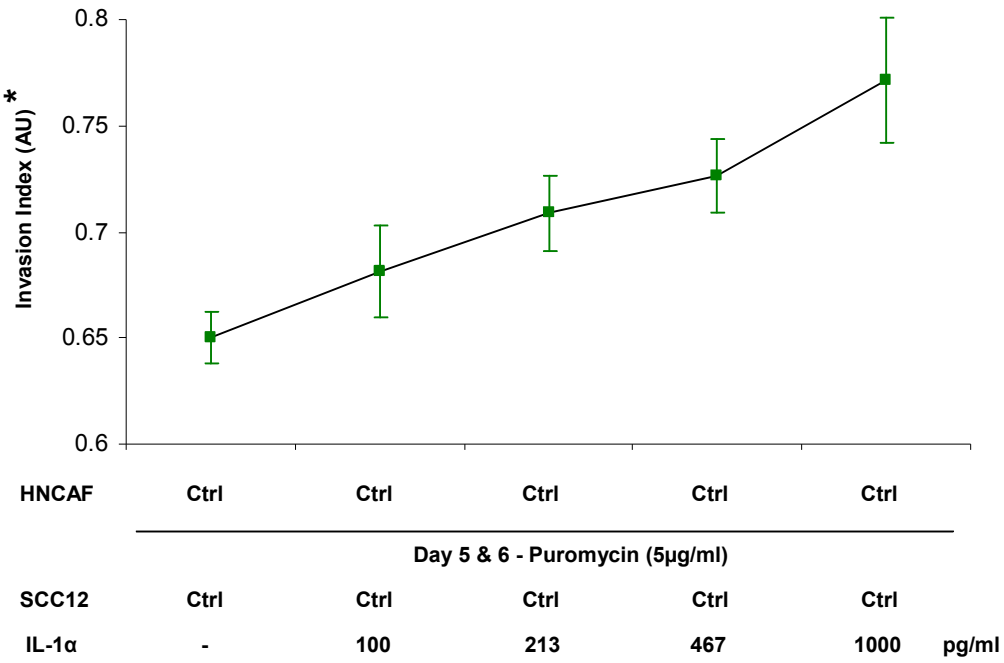

b

ANOVA test for linear trend

Group	Count	Mean Invasion Index	Comparison Coefficient
Control	10	0.6502563	-0.6324555
IL-1α 100	10	0.6814149	-0.3162278
IL-1α 213	10	0.7087712	0
IL-1α 467	10	0.7263905	0.3162278
IL-1α 1000	10	0.7713237	0.6324555

p = 0.001202

Figure 6.35 IL-1α stimulation of SCC12 cells promotes carcinoma invasion in remodelled collagen-Matrigel® matrix in a dose responsive manner in the absence of stromal fibroblasts

(**a**) Line plot displaying the log linear relationship of mean carcinoma invasion in response to IL-1α. The average of 10 visual fields is shown and error bars represent the s.e. *Denotes an expanded Y-axis. (**b**) ANOVA test for linear trend. Null hypothesis (NØ) rejected if $p < 0.05$.

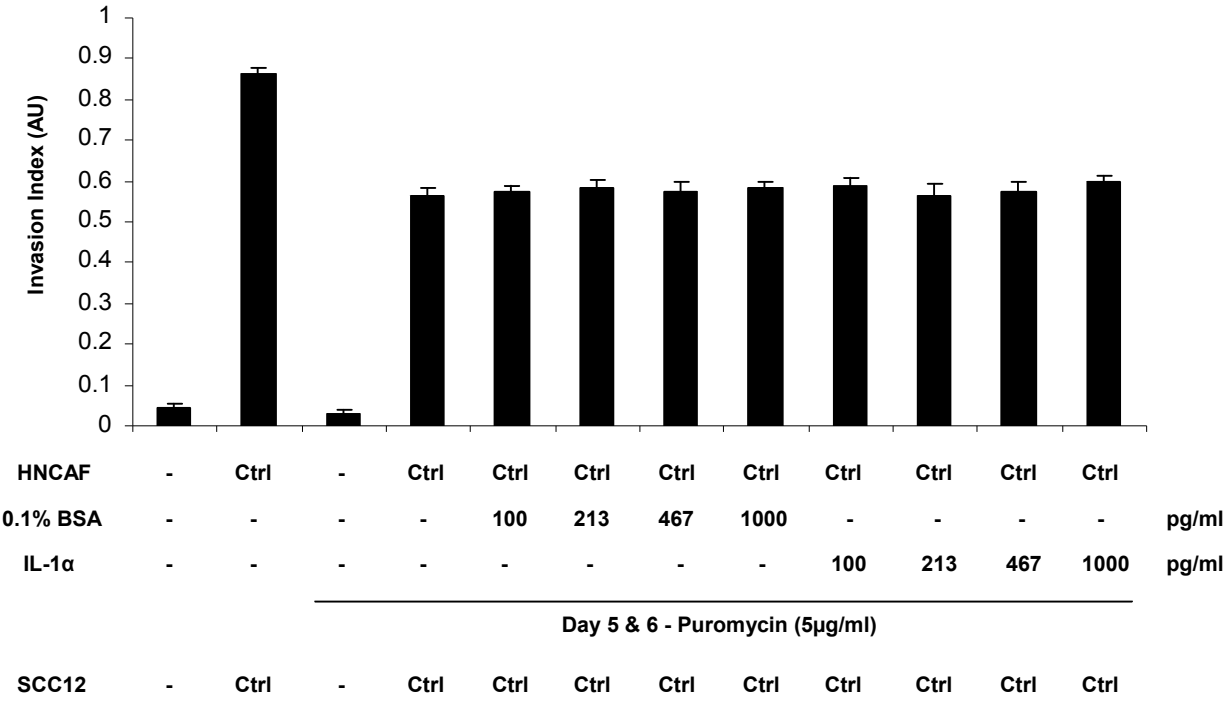

Figure 6.36 Organotypic invasion assay: HNCAF IL-1α stimulation

Quantification of carcinoma invasion in organotypic cultures in which gels were stimulated daily with IL-1α at the specified concentrations and then treated with puromycin (5µg/ml) daily for 48 hours after 5 days of matrix remodelling. Fibroblasts were removed prior to the addition of SCC12 cells and the cultures allowed to proceed to completion. Vehicle controls (0.1% BSA at concentrations comparable to those of IL-1α) were also included in the assay. The average of 10 visual fields from 2 experiments is shown. The error bars represent the s.e.

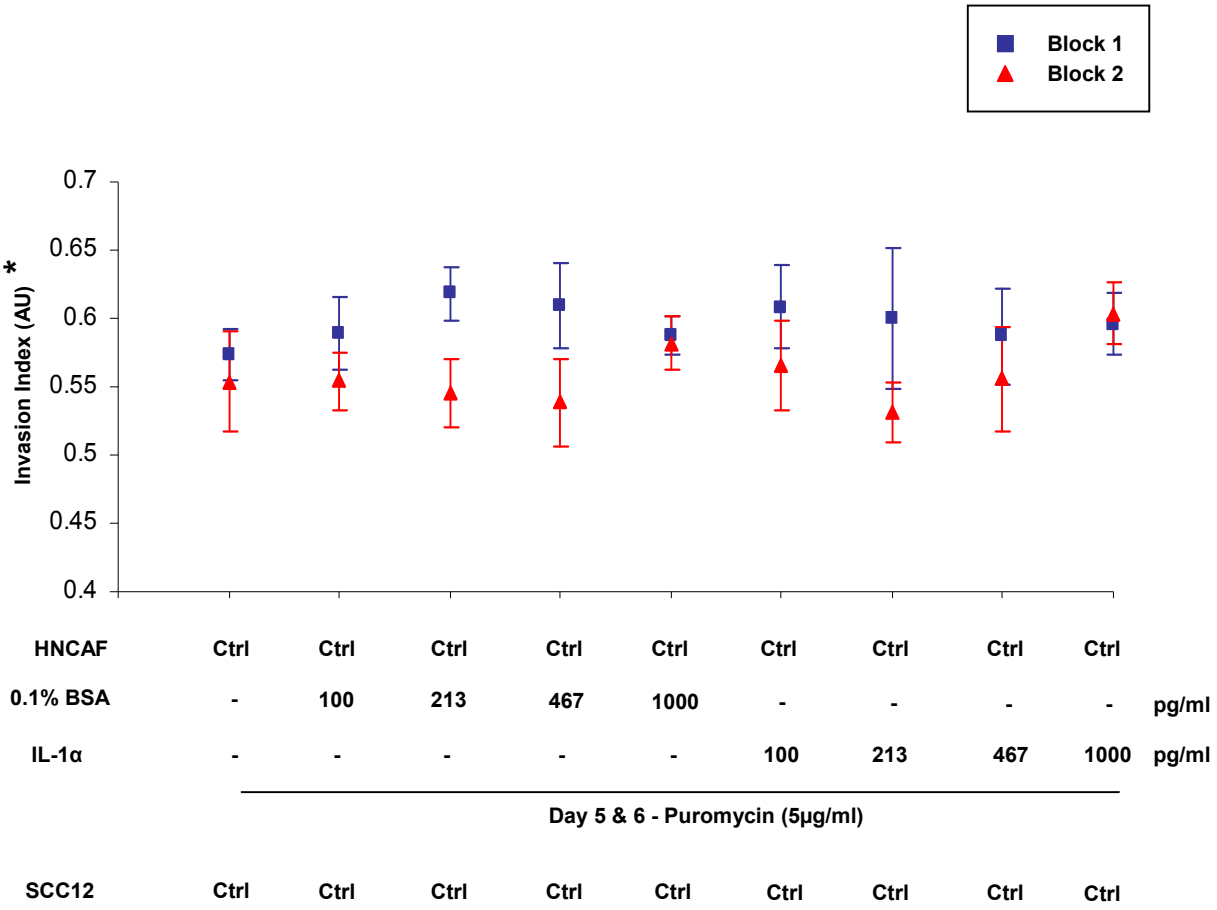

Figure 6.37 Organotypic invasion assay: HNCAF IL-1α stimulation - scatter plot

Scatter plot displaying quantification of carcinoma invasion in cultures from the organotypic assay illustrated in Figure 6.36. Individual experimental blocks are illustrated. The average of 5 visual fields is shown and error bars represent the s.e. *Denotes an expanded Y-axis.

a

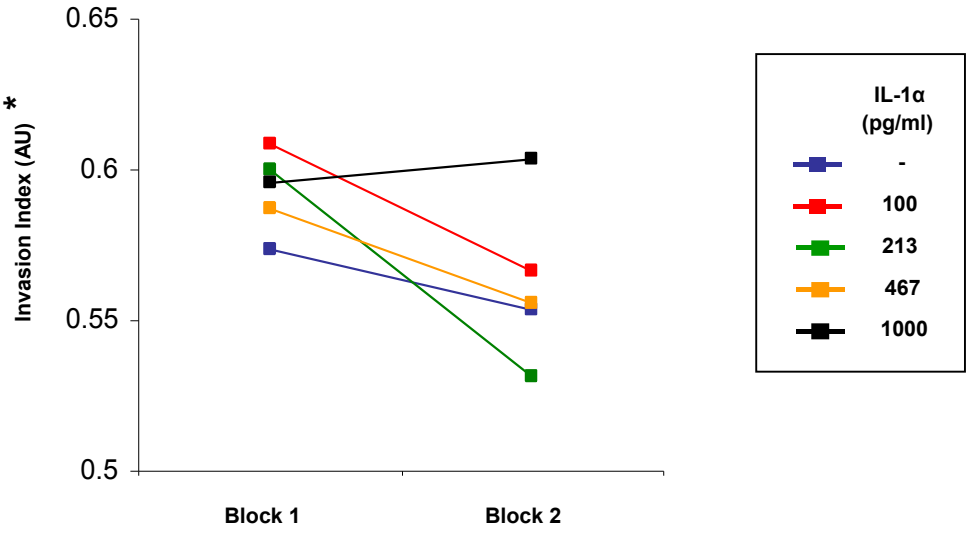

b

Randomized Block ANOVA	p Value	Decision p<0.025
Control vs 0.1% BSA 100	0.407704	Do not reject
0.1% BSA 100 vs IL-1α 100	0.096919	Do not reject
Control vs 0.1% BSA 213	0.912660	Do not reject
0.1% BSA 213 vs IL-1α 213	0.463720	Do not reject
Control vs 0.1% BSA 467	0.627861	Do not reject
0.1% BSA 467 vs IL-1α 467	0.714702	Do not reject
Control vs 0.1% BSA 1000	0.160454	Do not reject
0.1% BSA 1000 vs IL-1α 1000	0.066092	Do not reject

Figure 6.38 Organotypic invasion assay: HNCAF IL-1α stimulation. (a) Line plot and (b) randomized block ANOVA statistical analysis

(**a**) Line plot of quantification of carcinoma invasion of the IL-1α stimulated cultures from the organotypic assay illustrated in Figure 6.36 Individual experimental blocks are illustrated. The average of 5 visual fields is shown. *Denotes an expanded Y-axis. (**b**) Randomized block ANOVA statistical analysis. Null hypothesis (NØ) rejected if $p < 0.025$

a

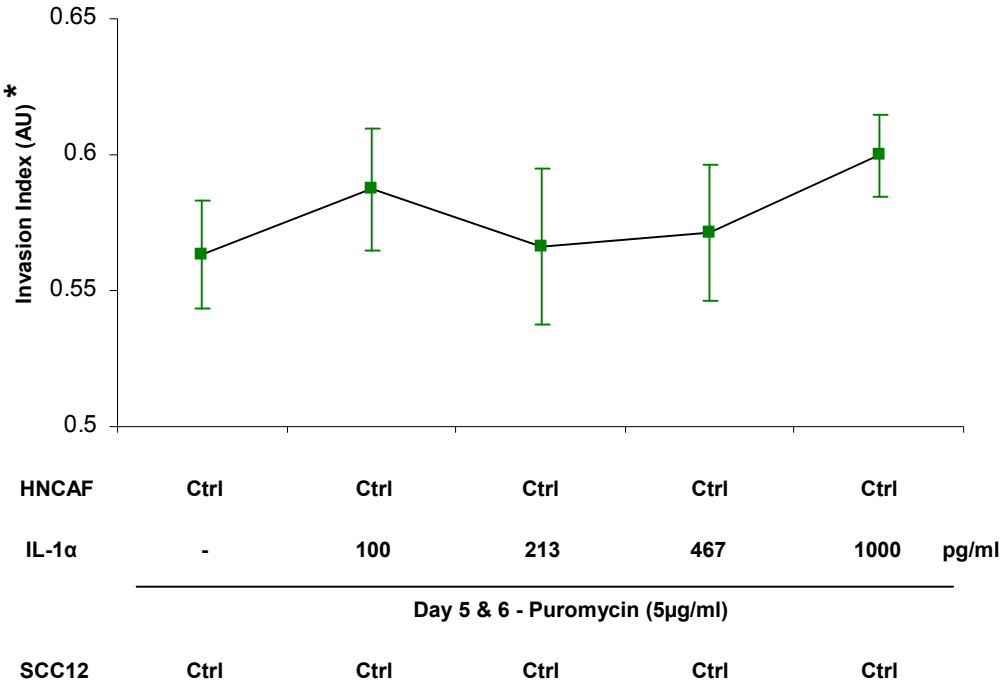

b

ANOVA test for linear trend

Group	Count	Mean Invasion Index	Comparison Coefficient
Control	10	0.563355	-0.6324555
IL-1α 100	10	0.5872568	-0.3162278
IL-1α 213	10	0.565947	0
IL-1α 467	10	0.5713912	0.3162278
IL-1α 1000	10	0.5997415	0.6324555

p = 0.271633

Figure 6.39 IL-1α stimulation of HNCAF does not promote carcinoma invasion in a dose responsive manner in the absence of direct stimulation of SCC12 cells

(**a**) Line plot displaying the log linear relationship of mean carcinoma invasion in response to IL-1α. The average of 10 visual fields is shown and error bars represent the s.e. *Denotes an expanded Y-axis. (**b**) ANOVA test for linear trend. Null hypothesis (NØ) rejected if $p < 0.05$.

6.3.4 IL-1α does not potentiate fibroblast-dependent collagen-Matrigel® matrix contraction

As for TNFα, I also assessed the effect of IL-1α stimulation on fibroblast-dependent collagen-Matrigel® matrix contraction.

The collagen-Matrigel® gels constructed for the assays detailed in Section 6.3.3 were photographed after 5 days of fibroblast-mediated matrix remodelling (Figure 6.40a) and the Contraction Index for each gel calculated (Figure 6.40b). Scatter plots of the individual experimental blocks for each concentration of IL-1α are presented in Figure 6.41. IL-1α stimulation of HNCAF did not potentiate fibroblast-dependent collagen-Matrigel® matrix contraction at any of the tested concentrations (Figure 6.42).

To exclude the possibility that IL-1α was inhibiting HNCAF proliferation, fibroblast number per unit area was assessed on Day 1 and Day 5 of the assays in gels with and without daily IL-1α stimulation (Figure 6.43). IL-1α at concentrations of 100-1000pg/ml did not affect HNCAF proliferation (Figures 6.44-6.47).

6.3.5 IL-1α activates NF-κB signalling in A431 cells but not in HNCAF

IL1-α and TNFα are potent activators of canonical NF-κB signalling. Given the disparity between the effects of TNFα and IL-1α stimulation on the ability of HNCAF to promote carcinoma invasion, I wondered whether this was a reflection of the underlying NF-κB response.

Figure 6.48 demonstrates the activation of IKK in A431 cells following stimulation with IL-1α (1000pg/ml). This results in the phosphorylation and reciprocal degradation of IκBα (Figure 6.49). Consequently, NF-κB p65 is activated (Figure 6.50).

Figure 6.51 demonstrates that IKK is not activated in HNCAF following stimulation with IL-1α (1000pg/ml). Consequently, IκBα is not degraded (Figure 6.52) and NF-κB p65 is not phosphorylated (Figure 6.53).

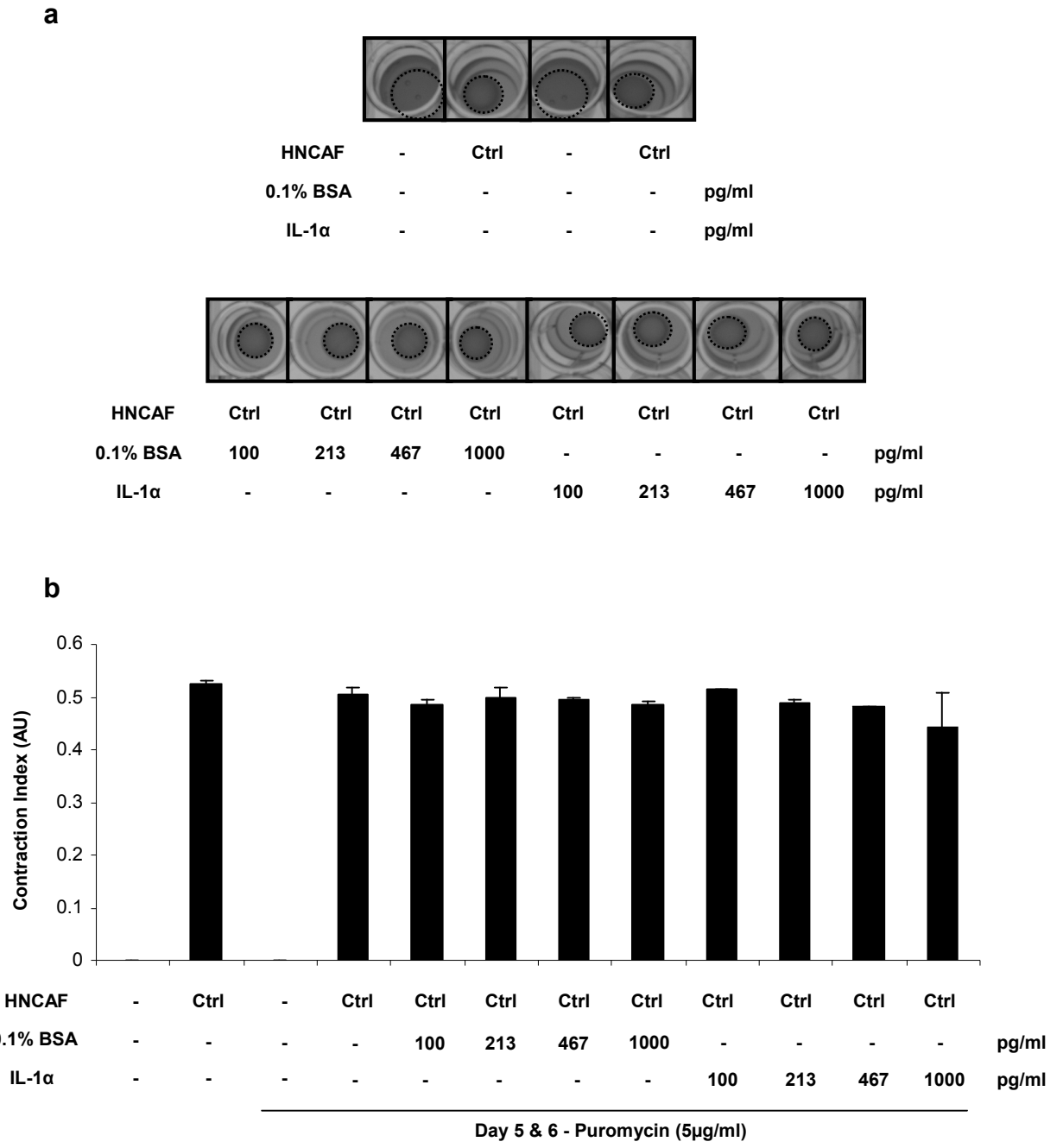

Figure 6.40 Assessment of the influence of IL-1α on fibroblast-dependent collagen-Matrigel® matrix contraction

(**a**) Images of organotypic gels after 5 days of matrix remodelling and daily treatment with either IL-1α or vehicle (0.1% BSA) at the specified concentrations prior to the removal of HNCAF. The dotted line represents the area of the gel. (**b**) Quantification of the degree of matrix remodelling. The Contraction Index was calculated using the formula 1 - (Gel Area / Well Area). The average of 2 experiments is shown and error bars represent the s.e.

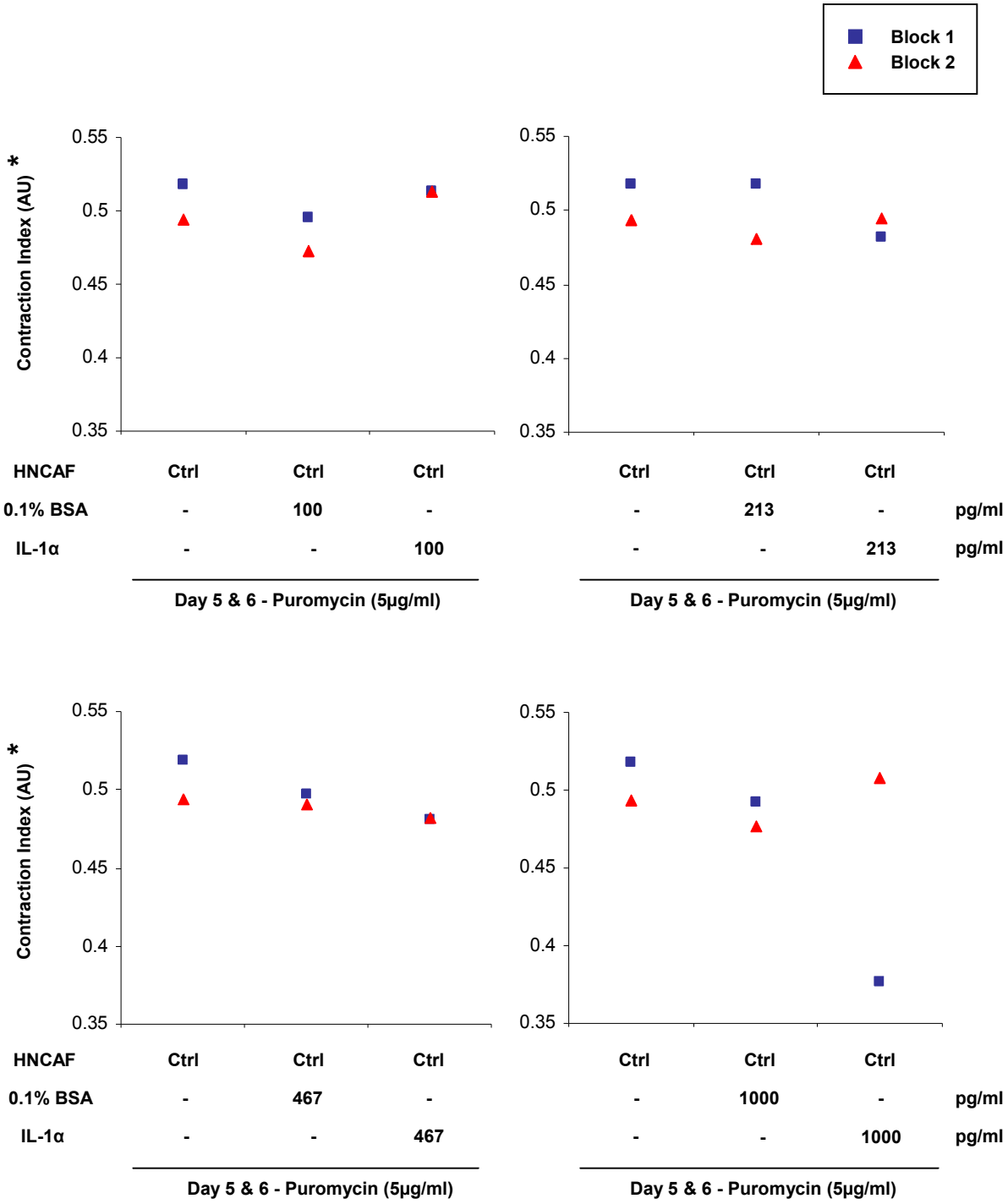

Figure 6.41 Assessment of the influence of IL-1α on fibroblast-dependent collagen-Matrigel® matrix contraction - scatter plots

Scatter plots displaying the Contraction Index of the fibroblast containing gels treated with either IL-1α or vehicle (0.1% BSA) of the organotypic assay illustrated in Figure 6.40. Individual experimental blocks are shown. *Denotes an expanded Y-axis.

Randomized Block ANOVA	p Value	Decision p<0.025
Control vs 0.1% BSA 100	0.160396	Do not reject
0.1% BSA 100 vs IL-1α 100	0.100300	Do not reject
Control vs 0.1% BSA 213	0.743311	Do not reject
0.1% BSA 213 vs IL-1α 213	0.609959	Do not reject
Control vs 0.1% BSA 467	0.337494	Do not reject
0.1% BSA 467 vs IL-1α 467	0.302743	Do not reject
Control vs 0.1% BSA 1000	0.759417	Do not reject
0.1% BSA 1000 vs IL-1α 1000	0.561672	Do not reject

Figure 6.42 IL-1α does not potentiate fibroblast-dependent collagen-Matrigel® matrix contraction

Randomized block ANOVA statistical analysis of the Contraction Indices of the fibroblast containing gels treated with either IL-1α or vehicle (0.1% BSA) from the organotypic assay illustrated in Figure 6.40. Null hypothesis (NØ) rejected if $p < 0.025$.

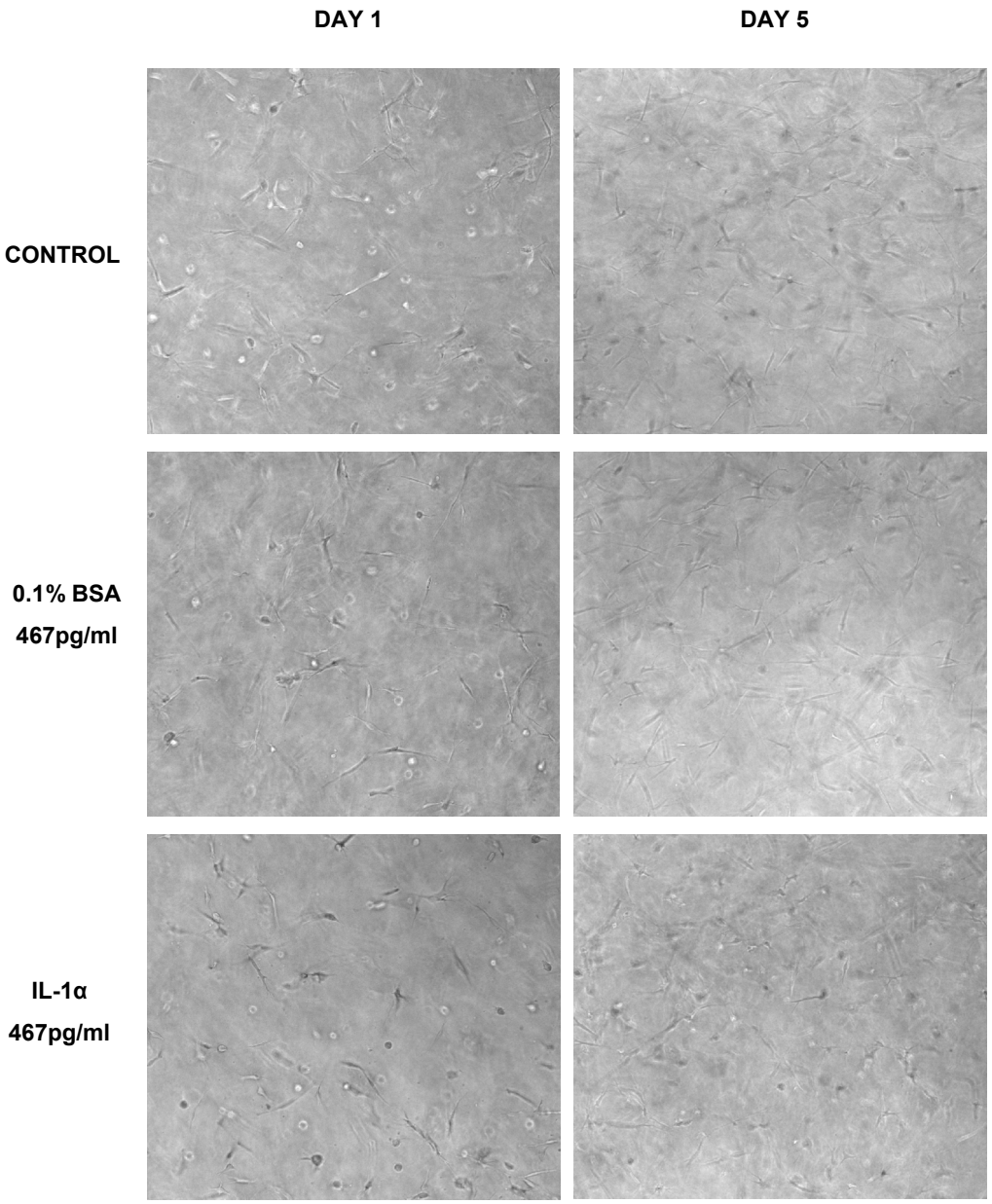

Figure 6.43 Assessment of fibroblast number in organotypic cultures after 5 days of collagen-Matrigel® matrix remodelling with and without daily treatment with IL-1α

Examples of low power phase images of HNCAF in collagen-Matrigel® matrix taken on Day 1 and Day 5 of the organotypic gels illustrated in Figure 6.40. The number of fibroblasts per unit area was quantified from 6 representative regions of each culture and corrected for the degree of gel contraction. (n=2)

a

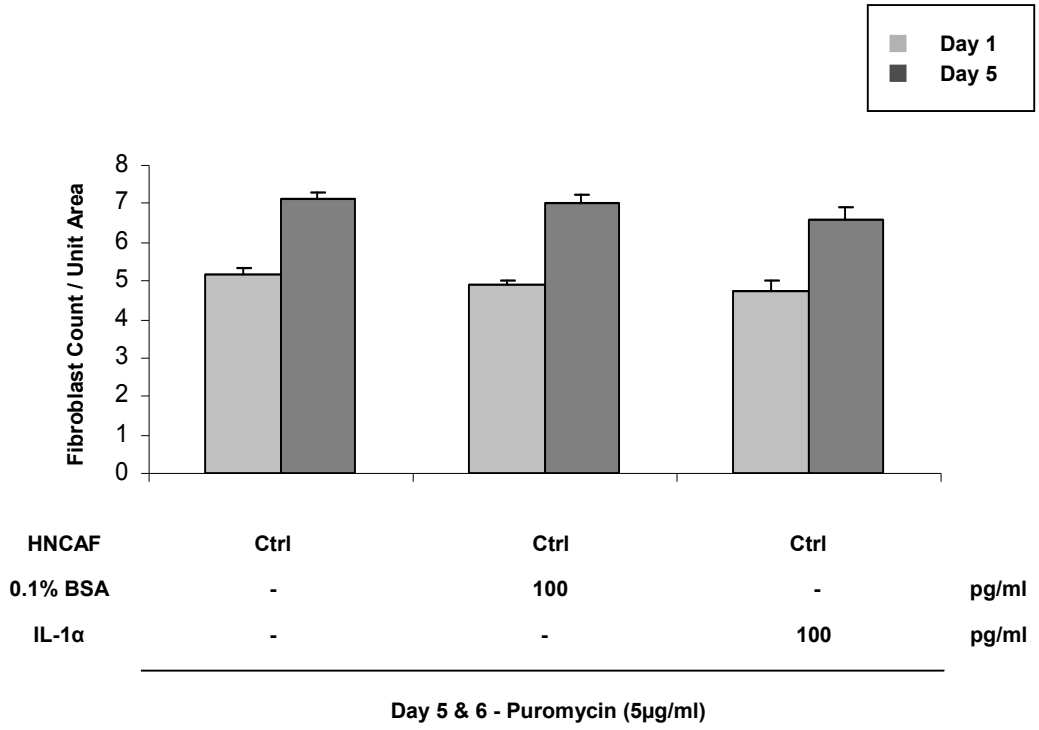

b

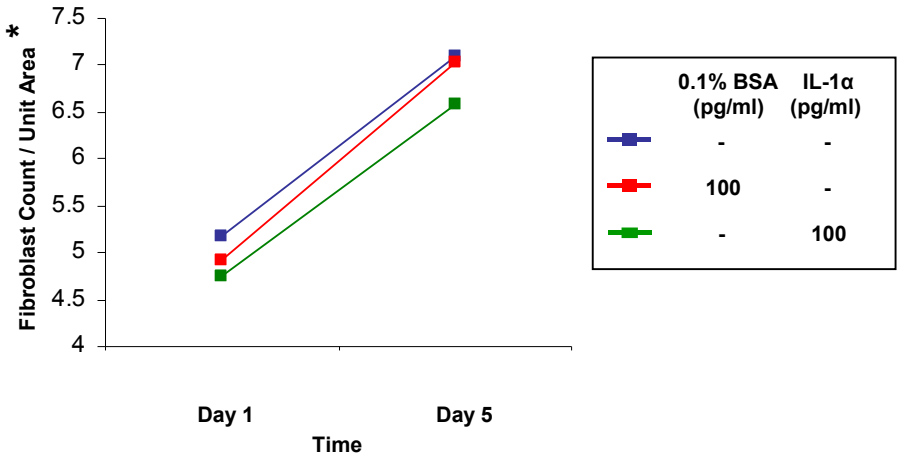

c

Randomized Block ANOVA	p Value	Decision p<0.05
Control vs 0.1% BSA 100 vs IL-1α 100	1.000000	Do not reject

Figure 6.44 IL-1α at a concentration of 100pg/ml does not affect HNCAF proliferation

Fibroblast count per unit area (corrected for degree of gel contraction) after 5 days of matrix remodelling and daily treatment with IL-1α at a concentration of 1pg/ml (**a**) bar chart and (**b**) line plot. The average of 12 fields from 2 experiments is shown. The error bars represent the s.e. *Denotes an expanded Y-axis. (**c**) Randomized block ANOVA statistical analysis. Null hypothesis (NØ) rejected if $p < 0.05$.

a

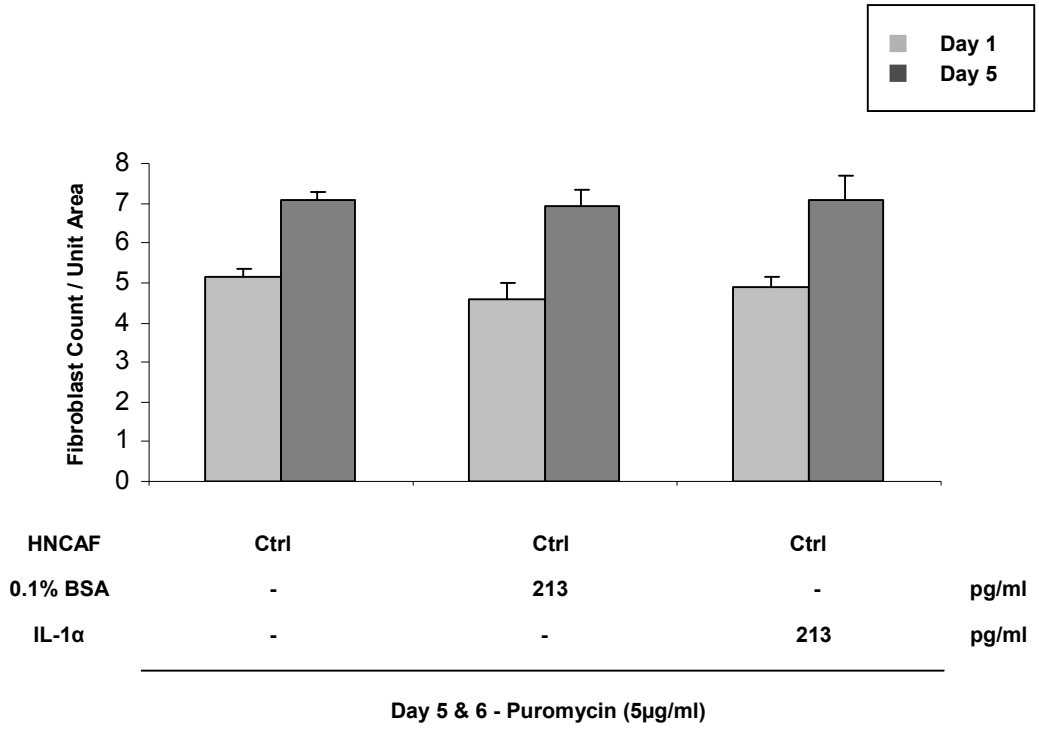

b

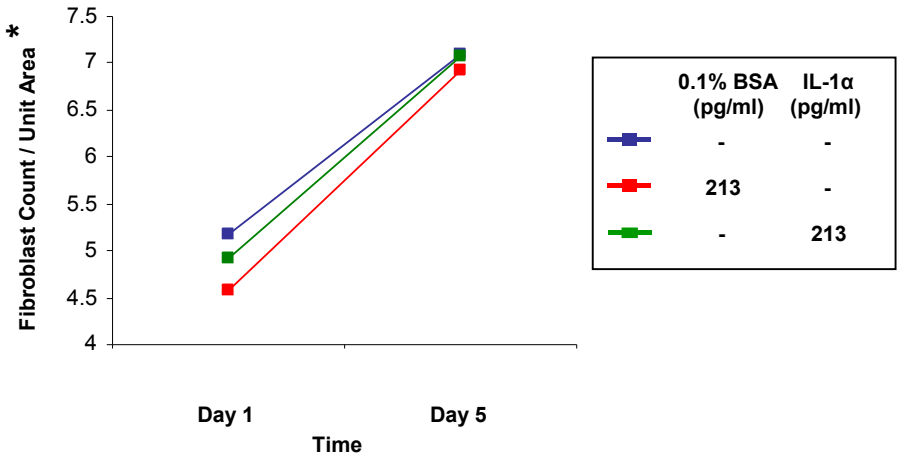

c

Randomized Block ANOVA	p Value	Decision p<0.05
Control vs 0.1% BSA 213 vs IL-1α 213	1.000000	Do not reject

Figure 6.45 IL-1α at a concentration of 213pg/ml does not affect HNCAF proliferation

Fibroblast count per unit area (corrected for degree of gel contraction) after 5 days of matrix remodelling and daily treatment with IL-1α at a concentration of 213pg/ml (**a**) bar chart and (**b**) line plot. The average of 12 fields from 2 experiments is shown. The error bars represent the s.e. *Denotes an expanded Y-axis. (**c**) Randomized block ANOVA statistical analysis. Null hypothesis (NØ) rejected if $p < 0.05$.

a

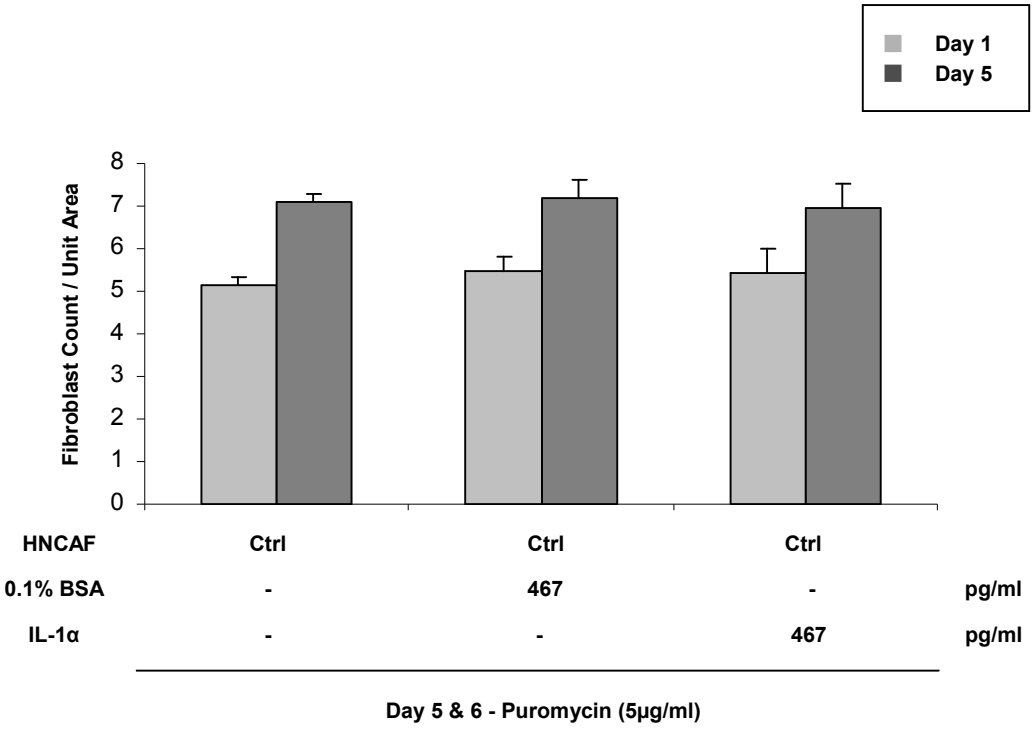

b

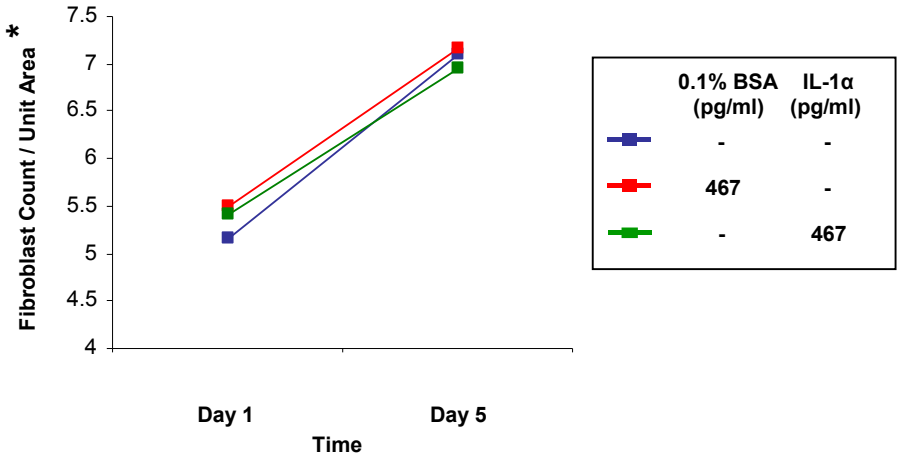

c

Randomized Block ANOVA	p Value	Decision p<0.05
Control vs 0.1% BSA 467 vs IL-1α 467	1.000000	Do not reject

Figure 6.46 IL-1α at a concentration of 467pg/ml does not affect HNCAF proliferation

Fibroblast count per unit area (corrected for degree of gel contraction) after 5 days of matrix remodelling and daily treatment with IL-1α at a concentration of 467pg/ml (**a**) bar chart and (**b**) line plot. The average of 12 fields from 2 experiments is shown. The error bars represent the s.e. *Denotes an expanded Y-axis. (**c**) Randomized block ANOVA statistical analysis. Null hypothesis (NØ) rejected if $p < 0.05$.

a

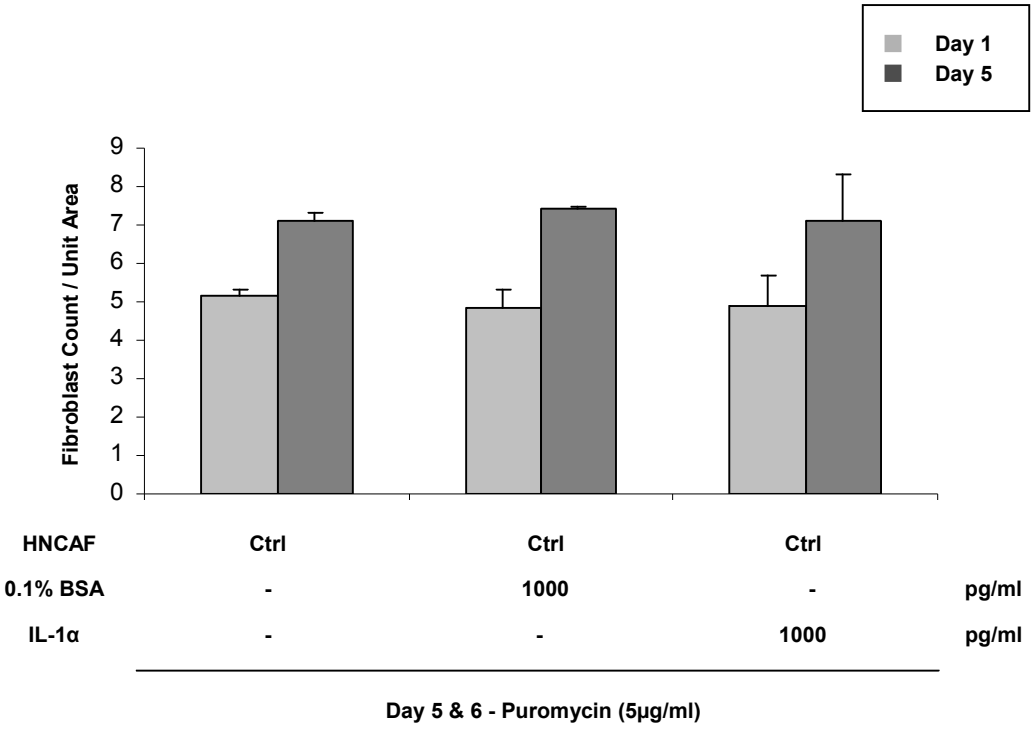

b

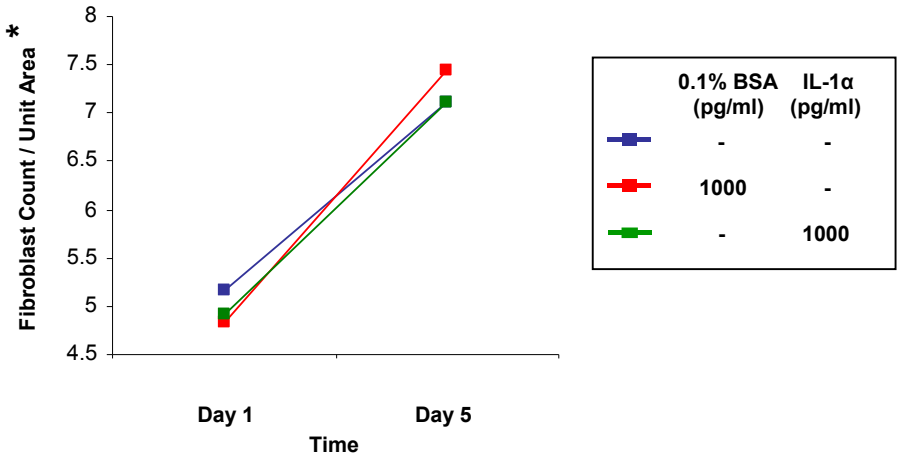

c

Randomized Block ANOVA	p Value	Decision p<0.05
Control vs 0.1% BSA 1000 vs IL-1α 1000	1.000000	Do not reject

Figure 6.47 IL-1α at a concentration of 1000pg/ml does not affect HNCAF proliferation

Fibroblast count per unit area (corrected for degree of gel contraction) after 5 days of matrix remodelling and daily treatment with IL-1α at a concentration of 1000pg/ml (**a**) bar chart and (**b**) line plot. The average of 12 fields from 2 experiments is shown. The error bars represent the s.e. *Denotes an expanded Y-axis. (**c**) Randomized block ANOVA statistical analysis. Null hypothesis (NØ) rejected if $p < 0.05$.

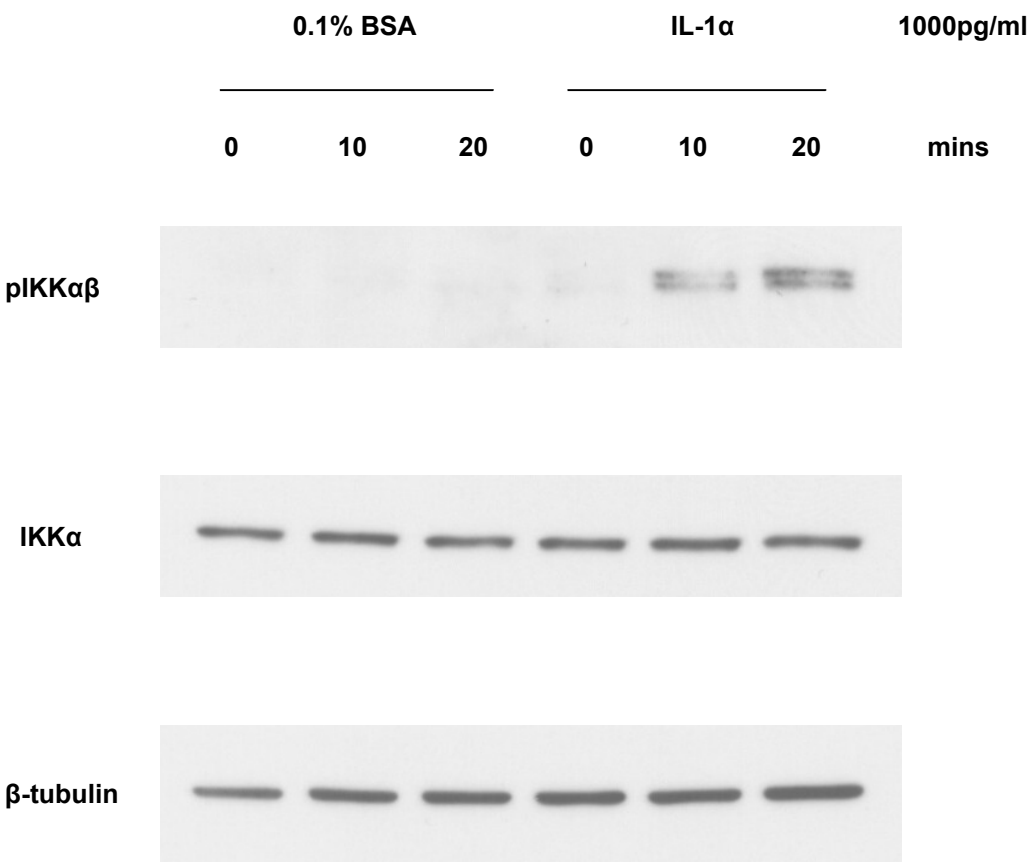

Figure 6.48 IL-1α activates IKK in A431 cells

Western blots of A431 cell lysates showing the activation of IKK in response to stimulation with IL-1α (1000pg/ml). This leads to the degradation of IκBα (Figure 6.49) with the subsequent activation of NF-κB (Figure 6.50). Control samples in which cells were treated with the vehicle (0.1% BSA at a concentration comparable to that of IL-1α) are also included.

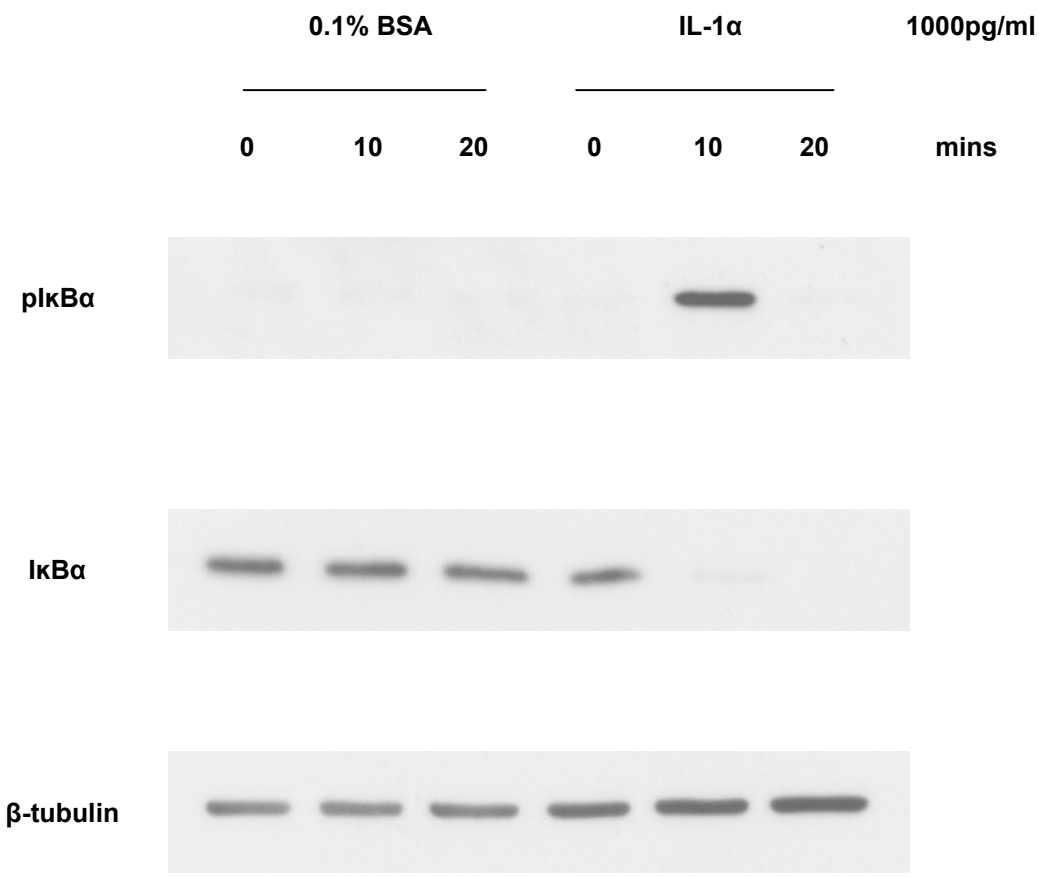

Figure 6.49 IL-1α induced NF-κB activation is associated with the phosphorylation and reciprocal degradation of IκBα in A431 cells

Western blots of A431 cell lysates showing the phosphorylation and reciprocal degradation of IκBα in response to stimulation with IL-1α (1000pg/ml). Control samples in which cells were treated with the vehicle (0.1% BSA at a concentration comparable to that of IL-1α) are also included.

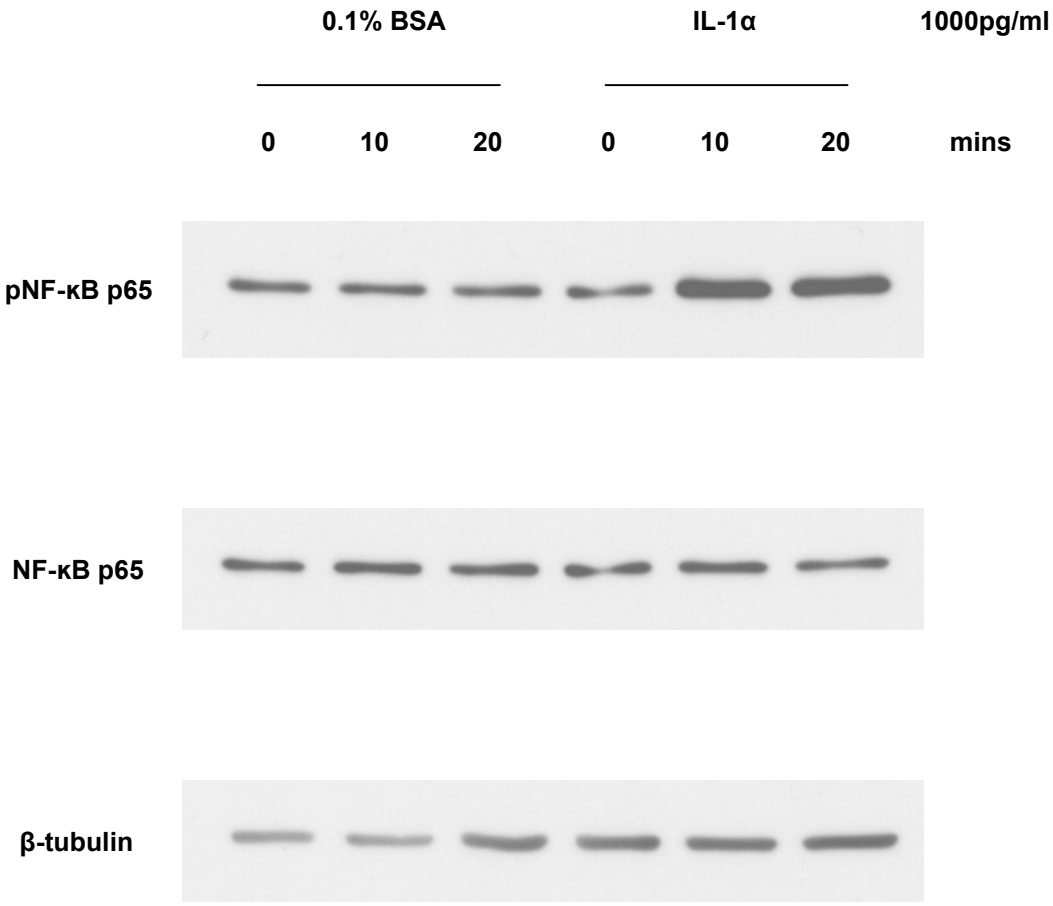

Figure 6.50 IL-1α activates NF-κB in A431 cells

Western blots of A431 cell lysates showing the phosphorylation of NF-κB p65 in response to stimulation with IL-1α (1000pg/ml). Control samples in which cells were treated with the vehicle (0.1% BSA at a concentration comparable to that of IL-1α) are also included.

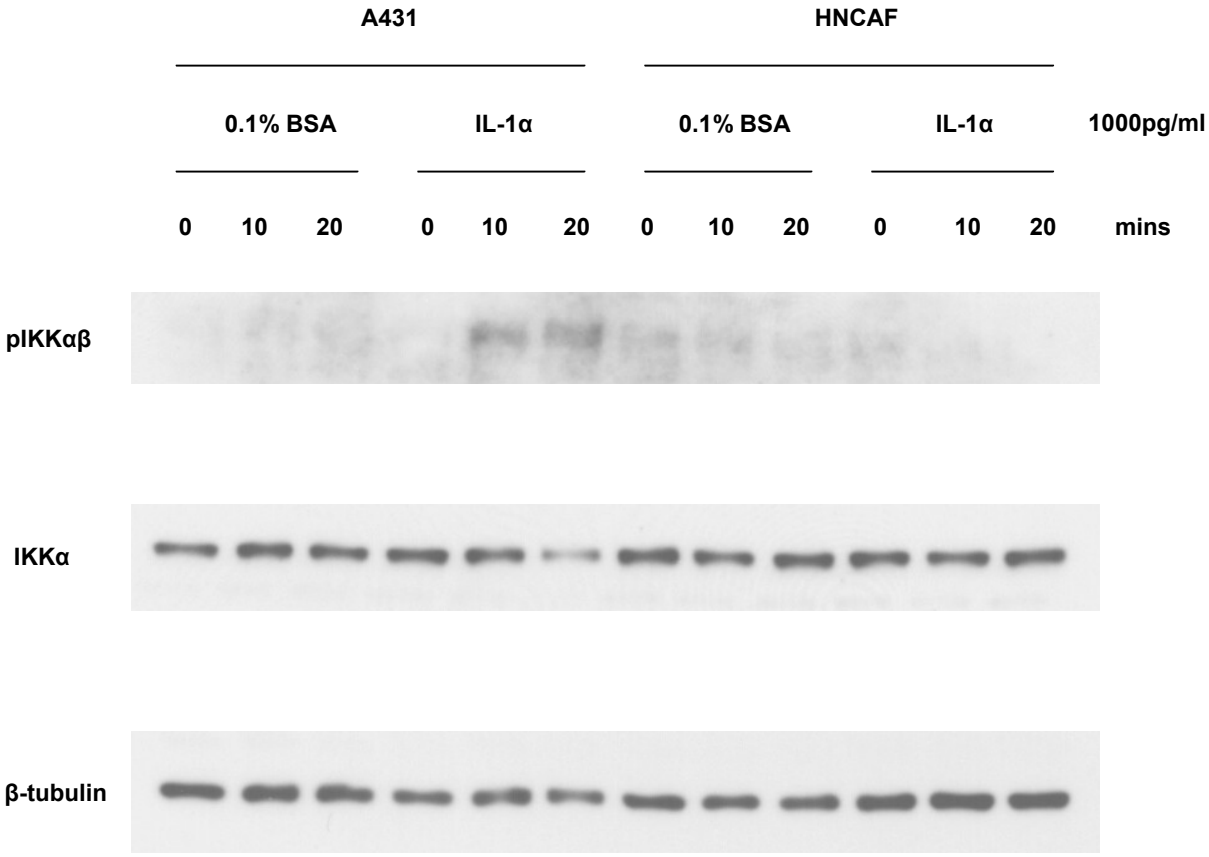

Figure 6.51 IL-1α does not activate IKK in HNCAF

Western blots of A431 and HNCAF cell lysates demonstrating that IL-1α (1000pg/ml) does not activate IKK in HNCAF and consequently does not induce NF-κB signalling (Figures 6.52 and 6.53). This is in contrast to its action on A431 cells. Control samples in which cells were treated with the vehicle (0.1% BSA at a concentration comparable to that of IL-1α) are also included.

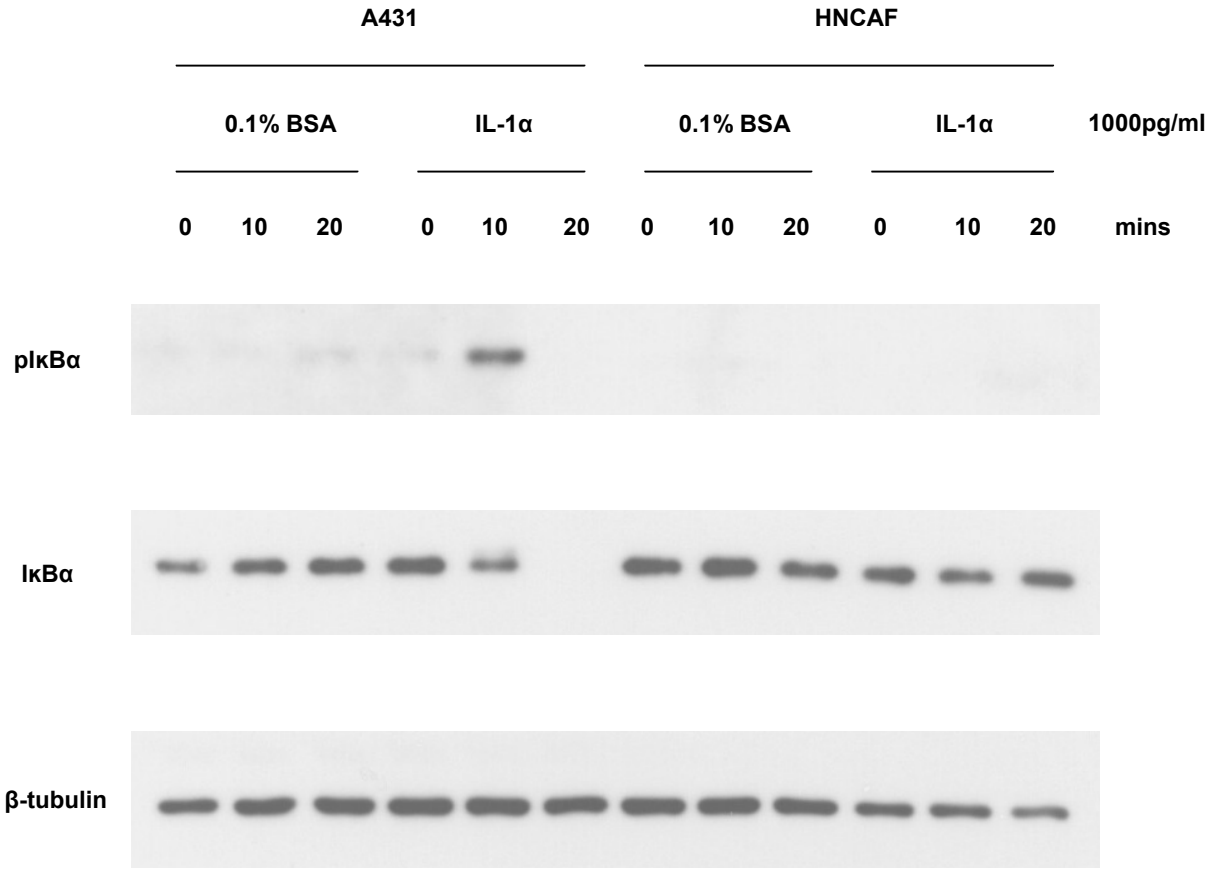

Figure 6.52 IL-1α does not result in the phosphorylation and reciprocal degradation of IκBα in HNCAF

Western blots of A431 and HNCAF cell lysates demonstrating that IL-1α (1000pg/ml) does not induce the phosphorylation and reciprocal degradation of IκBα in HNCAF. This is in contrast to its action on A431 cells. Control samples in which cells were treated with the vehicle (0.1% BSA at a concentration comparable to that of IL-1α) are also included.

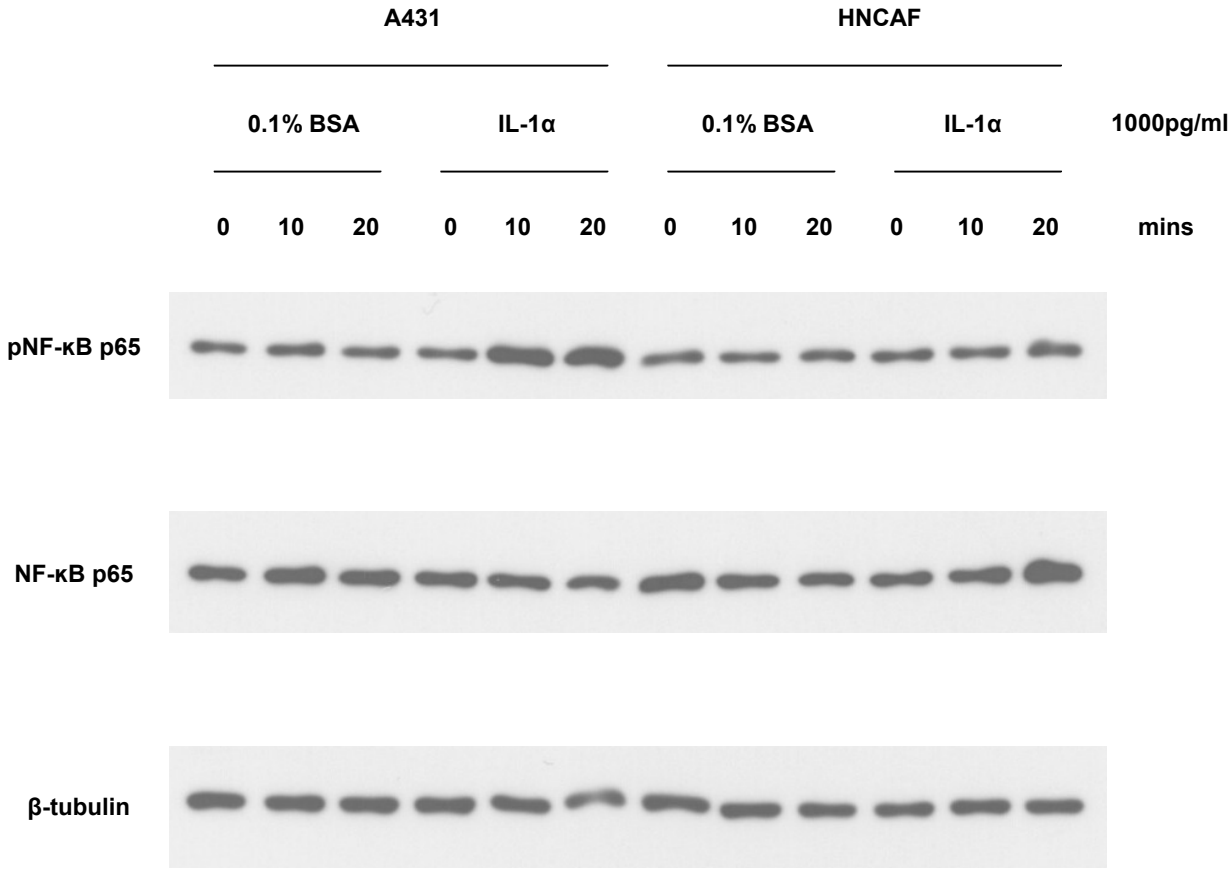

Figure 6.53 IL-1α does not activate NF-κB in HNCAF

Western blots of A431 and HNCAF cell lysates demonstrating that IL-1α (1000pg/ml) does not induce NF-κB p65 phosphorylation in HNCAF. This is in contrast to its action on A431 cells. Control samples in which cells were treated with the vehicle (0.1% BSA at a concentration comparable to that of IL-1α) are also included.

6.4 The IKK complex

Having demonstrated cancer cell invasion within our organotypic system to be TNFα and IL-1α driven, I sought to substantiate or refute the data from my Western blots which suggested that carcinoma progression in this setting was NF-κB dependent. My initial approach involved examining the action of a single IKK inhibitor, IKKI-II, on A431 and SCC12 cell invasion.

6.4.1 IKKI-II reduces A431 carcinoma invasion *in vitro*

Figure 6.54 shows the quantification of A431 invasion assays in which both the stromal and epithelial components of the organotypic cultures were inhibited daily with IKKI-II at concentrations of 1 and 10μM. Vehicle controls (DMSO at concentrations comparable to those of IKKI-II) were also included. Figures 6.55 and 6.56 consist of (a) photomicrographs of H&E sections demonstrating the degree of carcinoma infiltration into the underlying matrix, (b) a scatter plot of the individual experimental blocks and (c) randomized block ANOVA statistical analysis. Statistically significant reductions in the Invasion Index were seen at both concentrations of IKKI-II.

6.4.2 IKKI-II reduces SCC12 carcinoma invasion *in vitro*

Figure 6.57 shows the quantification of SCC12 invasion assays in which both the stromal and epithelial components of the organotypic cultures were inhibited daily with IKKI-II at concentrations of 1 and 10μM. Vehicle controls (DMSO at concentrations comparable to those of IKKI-II) were also included. Figures 6.58 and 6.59 consist of (a) photomicrographs of H&E sections demonstrating the degree of carcinoma infiltration into the underlying matrix, (b) a scatter plot of the individual experimental blocks and (c) randomized block ANOVA statistical analysis. Statistically significant reductions in the Invasion Index were seen at both concentrations of IKKI-II.

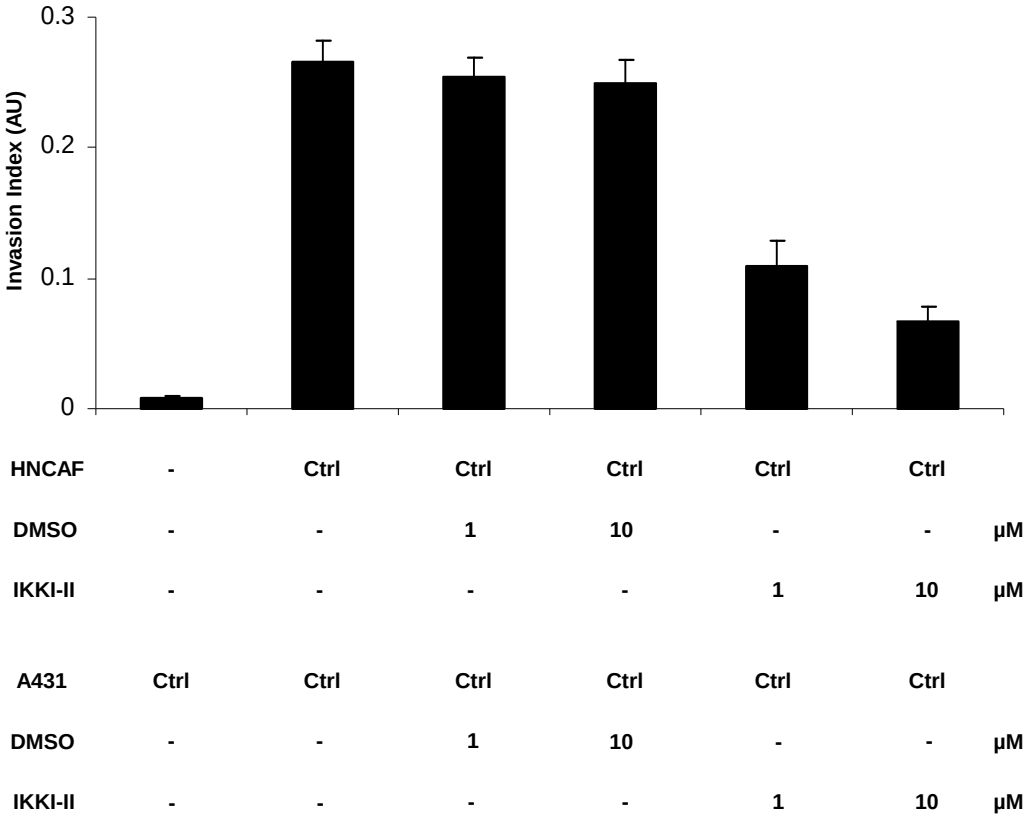

Figure 6.54 Organotypic invasion assay: inhibition of HNCAF and A431 with IKKI-II

Quantification of carcinoma invasion. Both the stromal and epithelial components of the organotypic cultures were treated daily with IKKI-II at the specified concentrations. Vehicle controls (DMSO at concentrations comparable to those of IKKI-II) were also included in the assay. The average of 10 visual fields from 2 experiments is shown. The error bars represent the s.e.

a

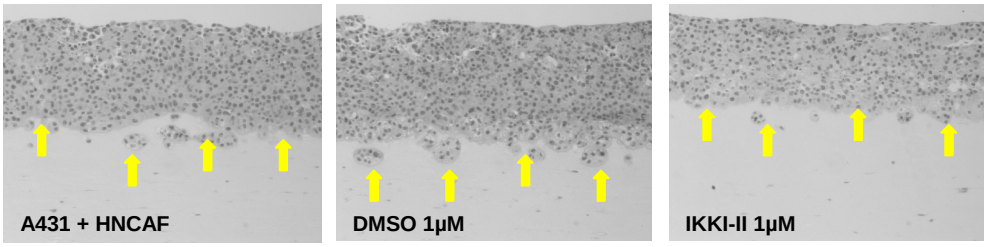

b

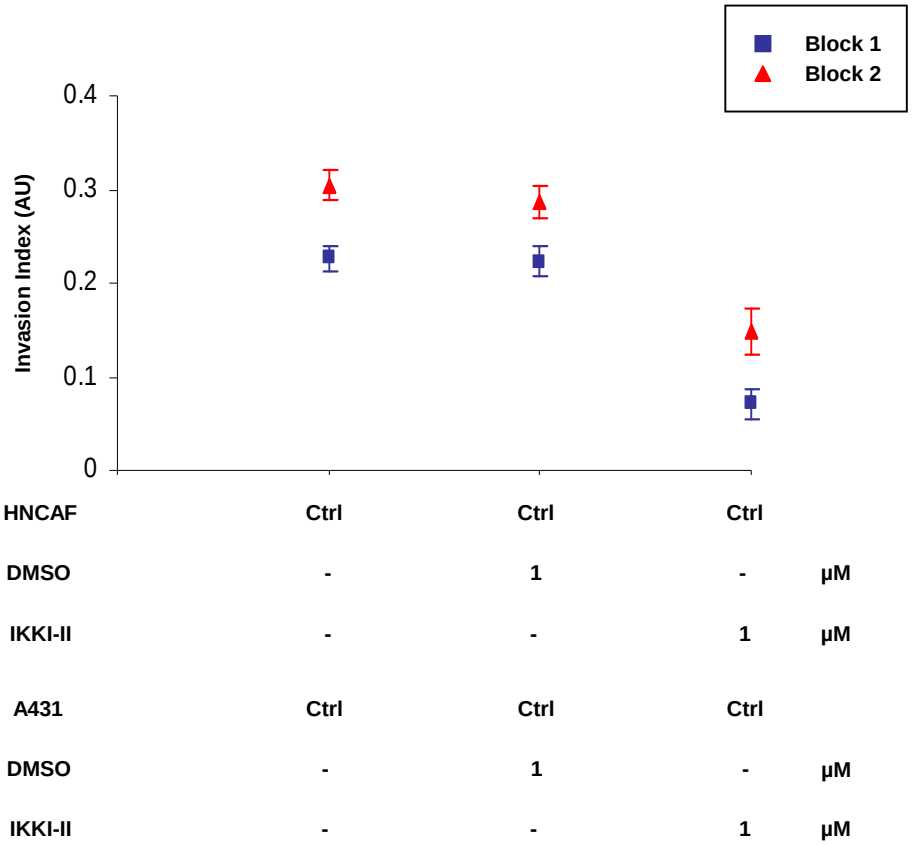

c

Randomized Block ANOVA	p Value	Decision p<0.025
Control vs DMSO 1	0.187832	Do not reject
DMSO 1 vs IKKI-II 1	0.001607	Reject

Figure 6.55 Organotypic invasion assay: inhibition of HNCAF and A431 with IKKI-II (1µM)

(**a**) H&E stained sections of A431 cells cultured in organotypic gels. Arrows point to the invading front of carcinoma cells. (**b**) Scatter plot displaying quantification of carcinoma invasion. Individual experimental blocks are illustrated. The average of 5 visual fields is shown and error bars represent the s.e. (**c**) Randomized block ANOVA statistical analysis. Null hypothesis (NØ) rejected if $p < 0.025$.

a

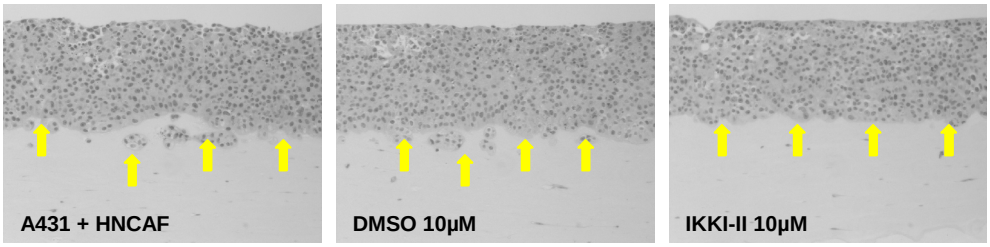

b

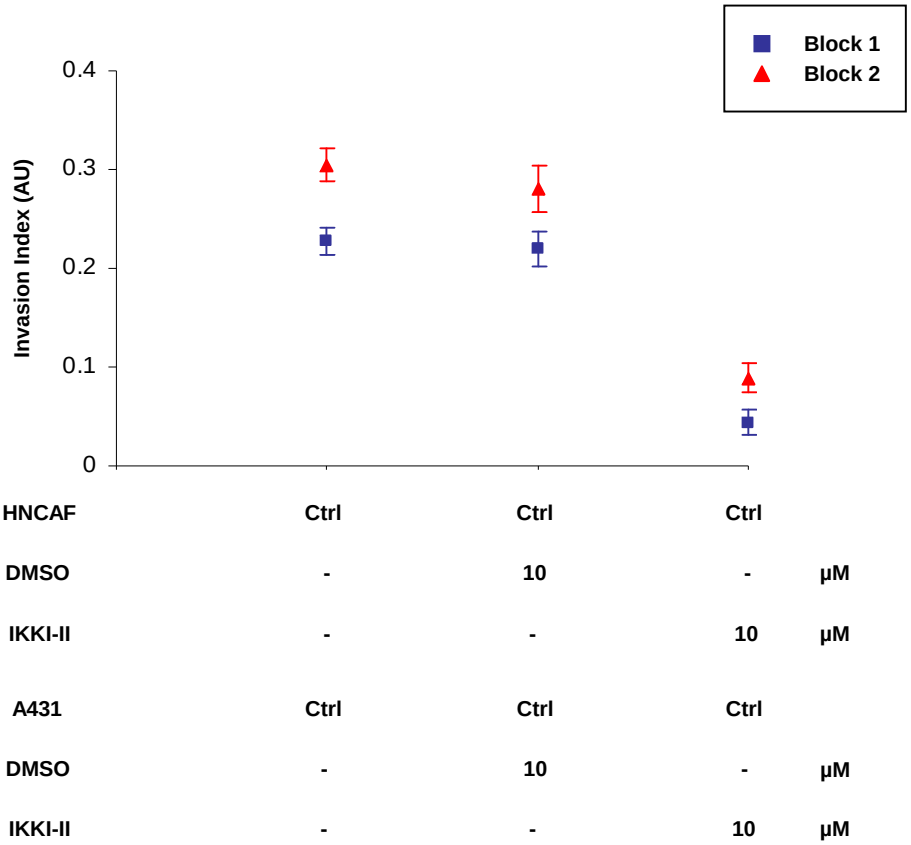

c

Randomized Block ANOVA	p Value	Decision p<0.025
Control vs DMSO 10	0.299627	Do not reject
DMSO 10 vs IKKI-II 10	0.003789	Reject

Figure 6.56 Organotypic invasion assay: inhibition of HNCAF and A431 with IKKI-II (10μM)

(**a**) H&E stained sections of A431 cells cultured in organotypic gels. Arrows point to the invading front of carcinoma cells. (**b**) Scatter plot displaying quantification of carcinoma invasion. Individual experimental blocks are illustrated. The average of 5 visual fields is shown and error bars represent the s.e. (**c**) Randomized block ANOVA statistical analysis. Null hypothesis (NØ) rejected if $p < 0.025$.

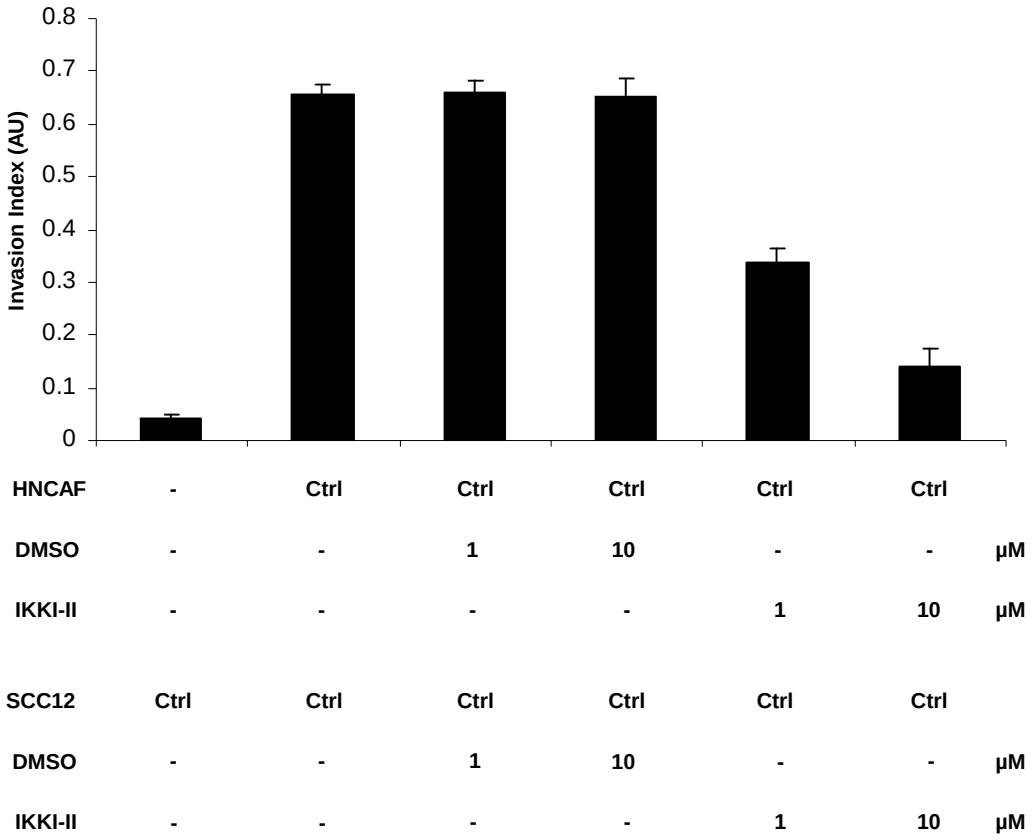

Figure 6.57 Organotypic invasion assay: inhibition of HNCAF and SCC12 with IKKI-II

Quantification of carcinoma invasion. Both the stromal and epithelial components of the organotypic cultures were treated daily with IKKI-II at the specified concentrations. Vehicle controls (DMSO at concentrations comparable to those of IKKI-II) were also included in the assay. The average of 10 visual fields from 2 experiments is shown. The error bars represent the s.e.

a

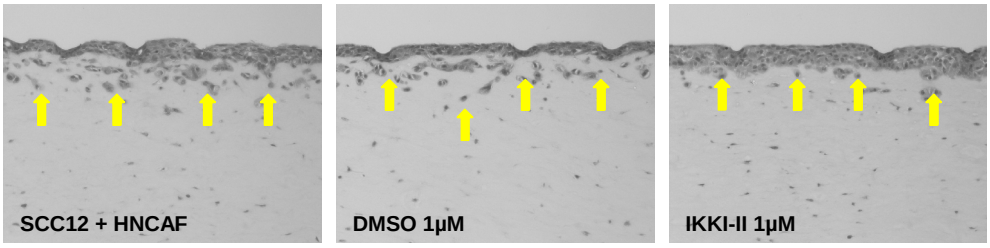

b

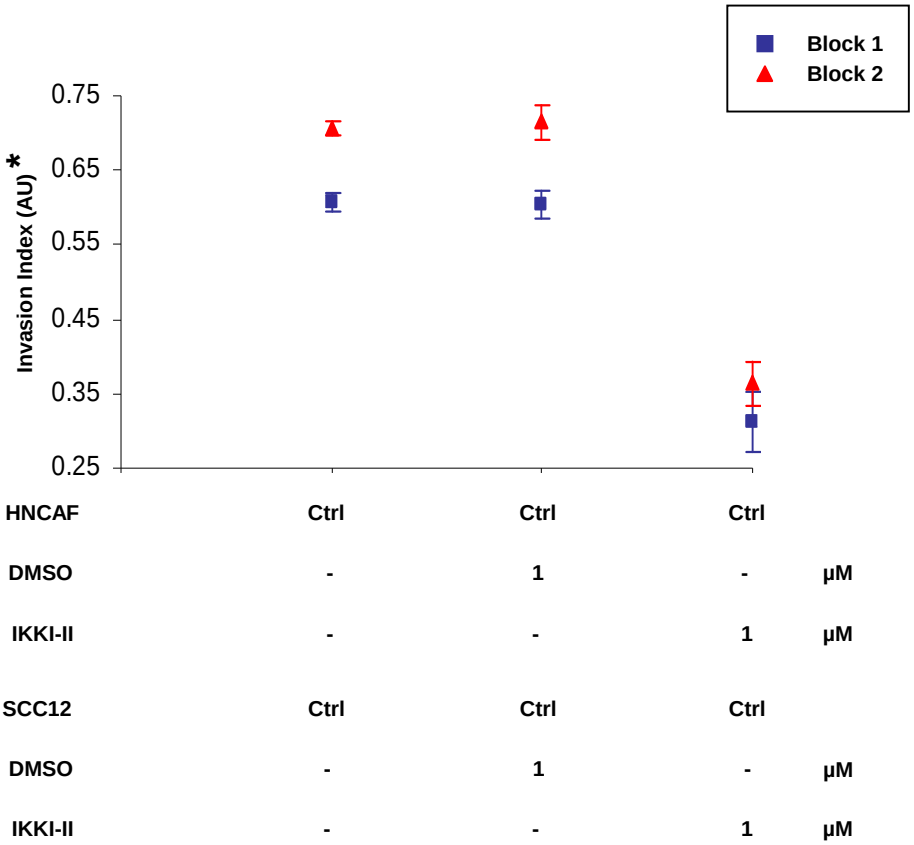

c

Randomized Block ANOVA	p Value	Decision p<0.025
Control vs DMSO 1	0.939281	Do not reject
DMSO 1 vs IKKI-II 1	0.004852	Reject

Figure 6.58 Organotypic invasion assay: inhibition of HNCAF and SCC12 with IKKI-II (1μM)

(**a**) H&E stained sections of SCC12 cells cultured in organotypic gels. Arrows point to the invading front of carcinoma cells. (**b**) Scatter plot displaying quantification of carcinoma invasion. Individual experimental blocks are illustrated. The average of 5 visual fields is shown and error bars represent the s.e. *Denotes an expanded Y-axis. (**c**) Randomized block ANOVA statistical analysis. Null hypothesis (NØ) rejected if $p < 0.025$.

a

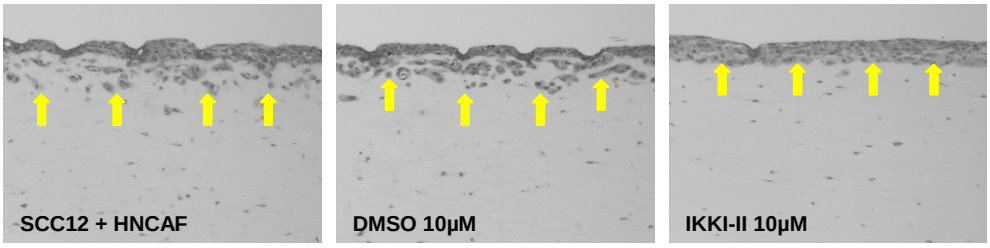

b

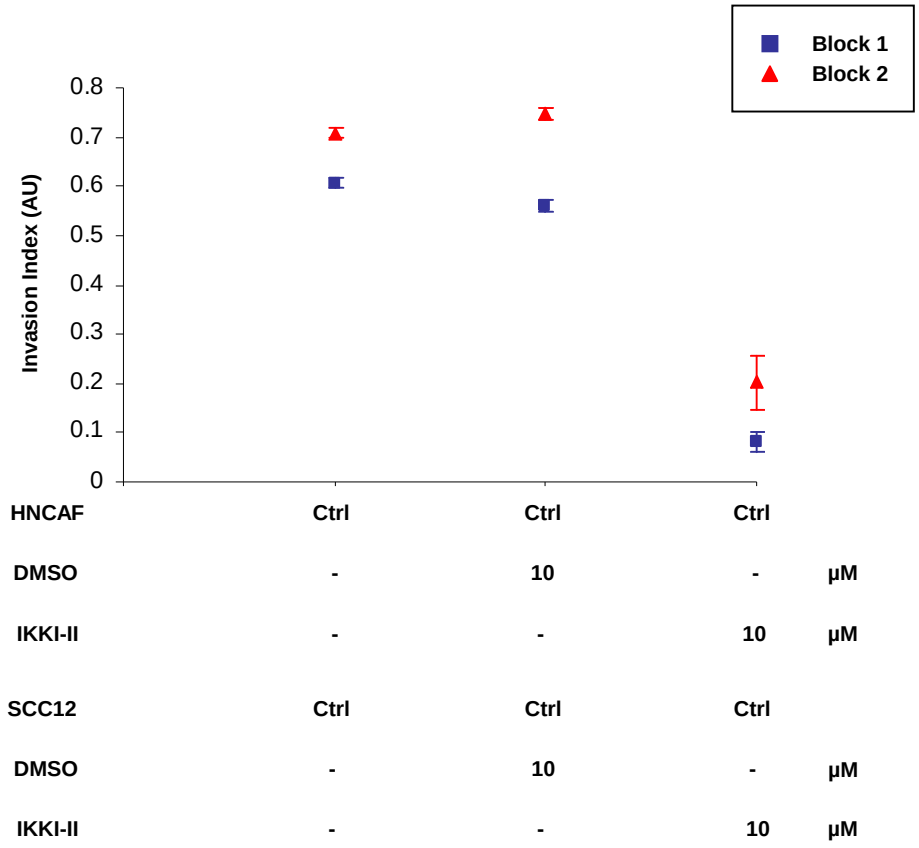

c

Randomized Block ANOVA	p Value	Decision p<0.025
Control vs DMSO 10	0.920340	Do not reject
DMSO 10 vs IKKI-II 10	0.003689	Reject

Figure 6.59 Organotypic invasion assay: inhibition of HNCAF and SCC12 with IKKI-II (10μM)

(**a**) H&E stained sections of SCC12 cells cultured in organotypic gels. Arrows point to the invading front of carcinoma cells. (**b**) Scatter plot displaying quantification of carcinoma invasion. Individual experimental blocks are illustrated. The average of 5 visual fields is shown and error bars represent the s.e. (**c**) Randomized block ANOVA statistical analysis. Null hypothesis (NØ) rejected if $p < 0.025$.

6.4.3 Inhibition of SCC12 cells with IKKI-II reduces carcinoma invasion in remodelled collagen-Matrigel® matrix in the absence of stromal fibroblasts

I next investigated the effect of IKKI-II on the epithelial and stromal components of our organotypic system independently of each other. These experiments mirrored those previously performed using TNFα (Sections 6.2.4-6.2.6) and IL-1α (Sections 6.3.2-6.3.4).

Figure 6.60 shows the quantification of SCC12 invasion in organotypic cultures in which only the epithelial component was inhibited daily with IKKI-II at concentrations of 1 and 10μM. Vehicle controls (DMSO at concentrations comparable to those of IKKI-II) were also included. Fibroblasts were removed from the collagen-Matrigel® gels after five days of matrix remodelling by treating with puromycin (5μg/ml) daily for 48 hours prior to the addition of SCC12 cells. A scatter plot of the individual experimental blocks is presented in Figure 6.61a. A statistically significant reduction in the Invasion Index was seen at a 10μM concentration of IKKI-II (Figure 6.61b).

6.4.4 Inhibition of HNCAF with IKKI-II reduces carcinoma invasion in the absence of direct inhibition of SCC12 cells

Figure 6.62 shows the quantification of SCC12 invasion in organotypic cultures in which only the stromal component was inhibited daily with IKKI-II at concentrations of 1 and 10μM. Vehicle controls (DMSO at concentrations comparable to those of IKKI-II) were also included. Fibroblasts were removed from the collagen-Matrigel® gels after five days of matrix remodelling by treating with puromycin (5μg/ml) daily for 48 hours prior to the addition of SCC12 cells. A scatter plot of the individual experimental blocks is presented in Figure 6.63a. A statistically significant reduction in the Invasion Index was seen at a 10μM concentration of IKKI-II (Figure 6.63b).

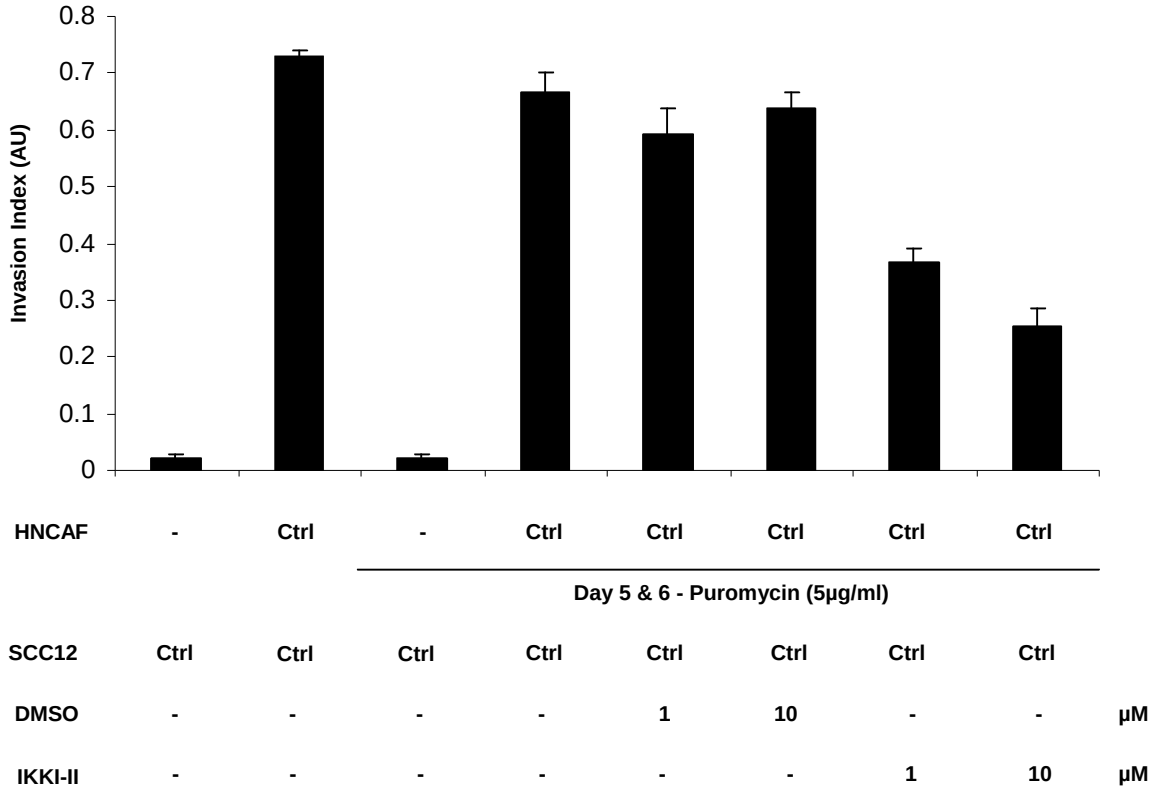

Figure 6.60 Organotypic invasion assay: Inhibition of SCC12 with IKKI-II

Quantification of carcinoma invasion in organotypic cultures in which gels were treated with puromycin (5µg/ml) daily for 48 hours after 5 days of matrix remodelling. Fibroblasts were removed prior to the addition of SCC12 cells which were then treated daily with IKKI-II at the specified concentrations. Vehicle controls (DMSO at concentrations comparable to those of IKKI-II) were also included in the assay. The average of 10 visual fields from 2 experiments is shown. The error bars represent the s.e.

a

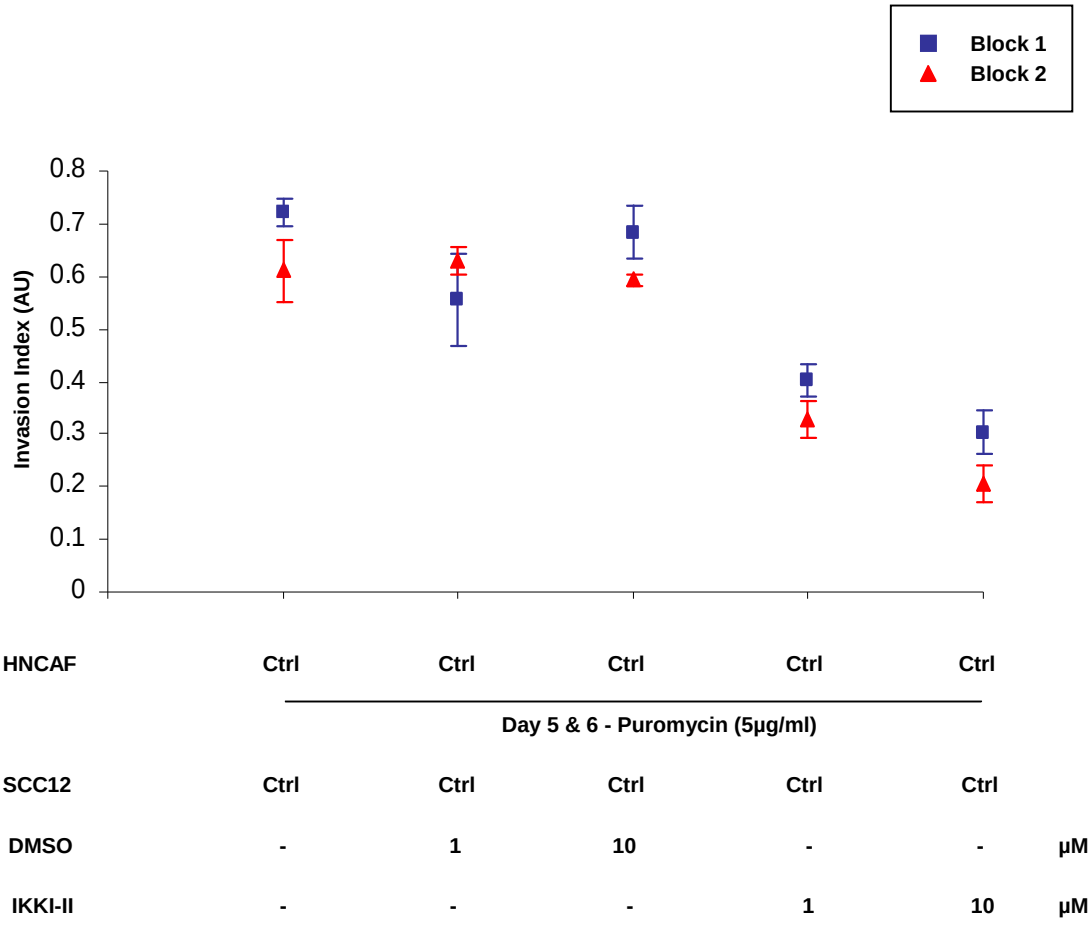

b

Randomized Block ANOVA	p Value	Decision p<0.025
Control vs DMSO 1	0.401784	Do not reject
DMSO 1 vs IKKI-II 1	0.081051	Do not reject
Control vs DMSO 10	0.62134	Do not reject
DMSO 10 vs IKKI-II 10	0.000344	Reject

Figure 6.61 Organotypic invasion assay: inhibition of SCC12 with IKKI-II. (a) Scatter plot and (b) randomized block ANOVA statistical analysis

(**a**) Scatter plot displaying quantification of carcinoma invasion in cultures from the organotypic assay illustrated in Figure 6.60. Individual experimental blocks are illustrated. The average of 5 fields is shown and error bars represent the s.e. (**b**) Randomized block ANOVA statistical analysis. Null hypothesis (NØ) rejected if $p < 0.025$.

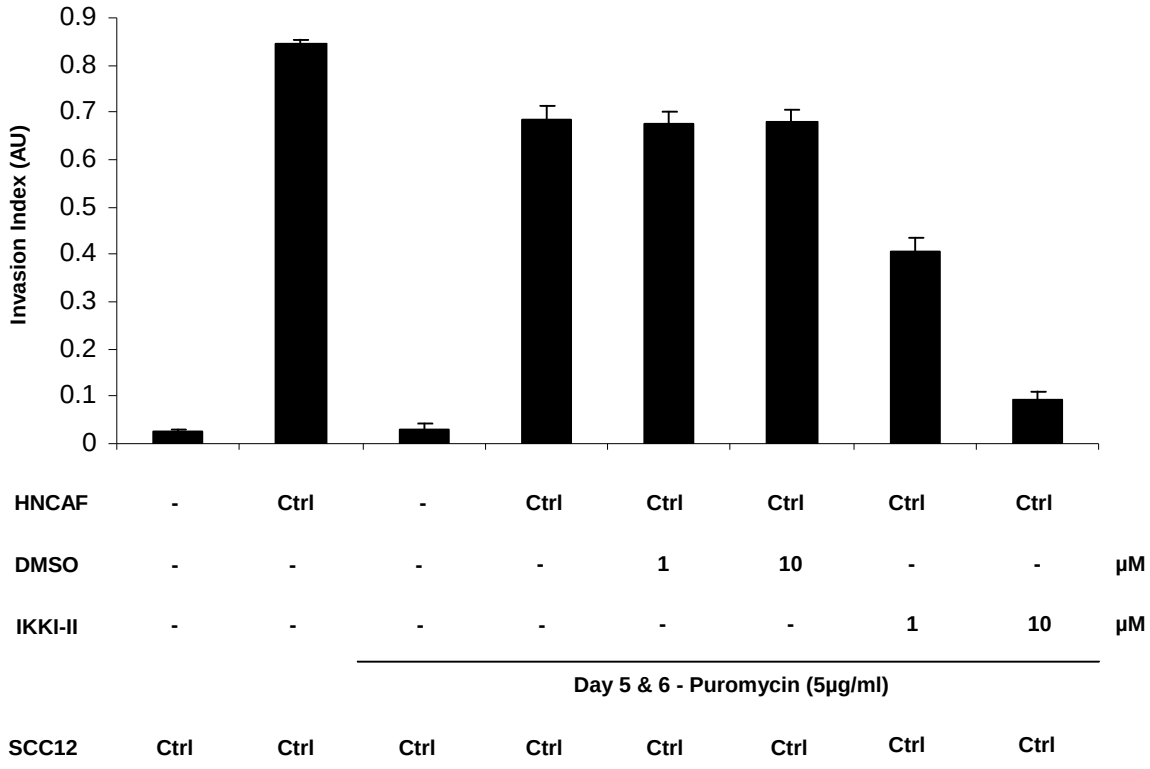

Figure 6.62 Organotypic invasion assay: inhibition of HNCAF with IKKI-II

Quantification of carcinoma invasion in organotypic cultures in which gels were treated daily with IKKI-II at the specified concentrations followed by puromycin (5µg/ml) daily for 48 hours after 5 days of matrix remodelling. Fibroblasts were removed prior to the addition of SCC12 cells and the cultures allowed to proceed to completion. Vehicle controls (DMSO at concentrations comparable to those of IKKI-II) were also included in the assay. The average of 10 visual fields from 2 experiments is shown. The error bars represent the s.e.

a

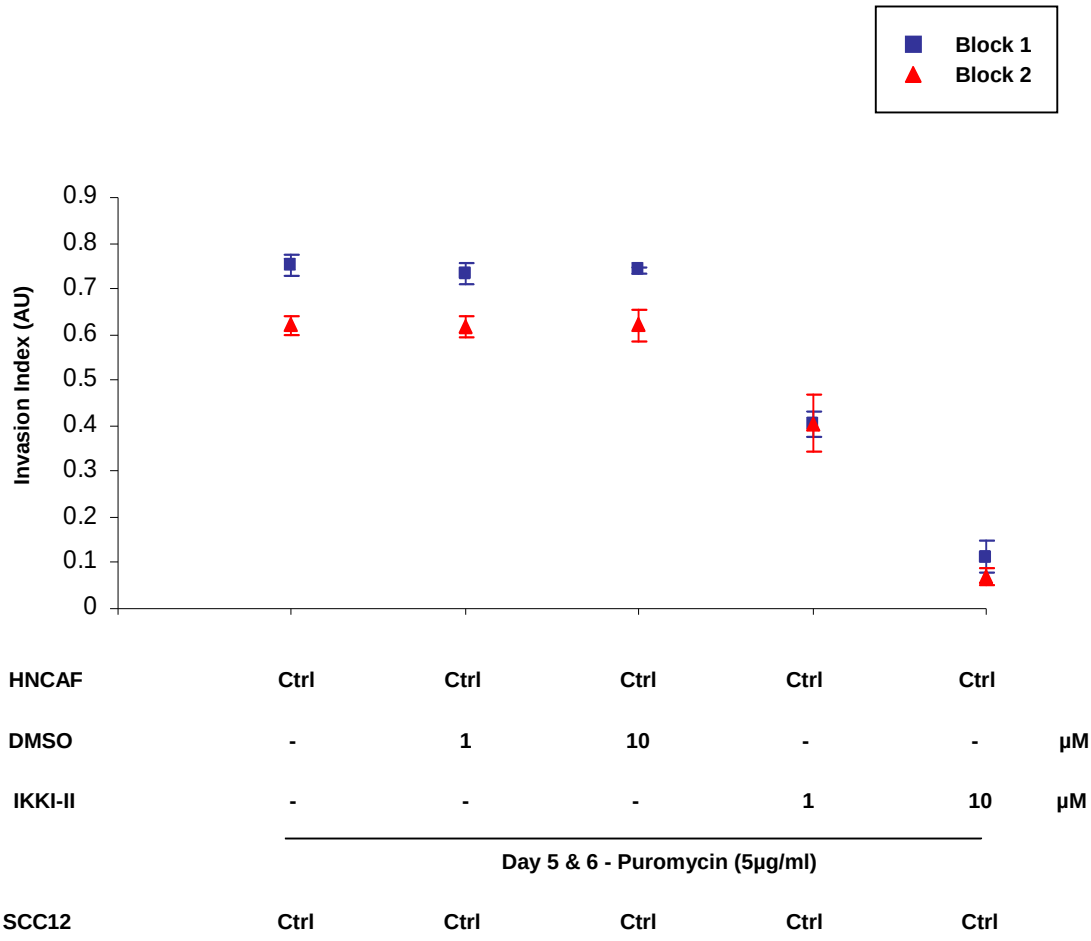

b

Randomized Block ANOVA	p Value	Decision p<0.025
Control vs DMSO 1	0.846297	Do not reject
DMSO 1 vs IKKI-II 1	0.035059	Do not reject

Control vs DMSO 10	0.875228	Do not reject
DMSO 10 vs IKKI-II 10	0.003339	Reject

Figure 6.63 Organotypic invasion assay: inhibition of HNCAF with IKKI-II. (a) Scatter plot and (b) randomized block ANOVA statistical analysis

(**a**) Scatter plot displaying quantification of carcinoma invasion in cultures from the organotypic assay illustrated in Figure 6.62. Individual experimental blocks are illustrated. The average of 5 fields is shown and error bars represent the s.e. (**b**) Randomized block ANOVA statistical analysis. Null hypothesis (NØ) rejected if $p < 0.025$.

6.4.5 IKKI-II reduces fibroblast-dependent collagen-Matrigel® matrix contraction

As for TNFα and IL-1α, I also recorded the effect of IKKI-II inhibition on fibroblast-dependent collagen-Matrigel® matrix contraction.

The collagen-Matrigel® gels constructed for the assays detailed in Section 6.4.4 were photographed after 5 days of fibroblast-mediated matrix remodelling (Figure 6.64a) and the Contraction Index for each gel calculated (Figure 6.64b). Scatter plots of the individual experimental blocks for each concentration of IKKI-II are presented in Figure 6.65a. Statistically significant reductions in the Contraction Index were seen at both concentrations of IKKI-II (Figure 6.65b).

To exclude the possibility that IKKI-II was inhibiting HNCAF proliferation, fibroblast number per unit area was assessed on Day 1 and Day 5 of the assays in gels with and without daily IKKI-II inhibition (Figure 6.66). IKKI-II at concentrations of 1 and10μM did not affect HNCAF proliferation (Figures 6.67 and 6.68).

Figure 6.69 consists of scatter plots displaying the relationship between the mean Invasion Index and the mean Contraction Index for the organotypic cultures presented in Section 6.4.4. IKKI-II at concentrations of 1 and 10μM resulted in a reduction in both collagen-Matrigel® matrix contraction and carcinoma invasion.

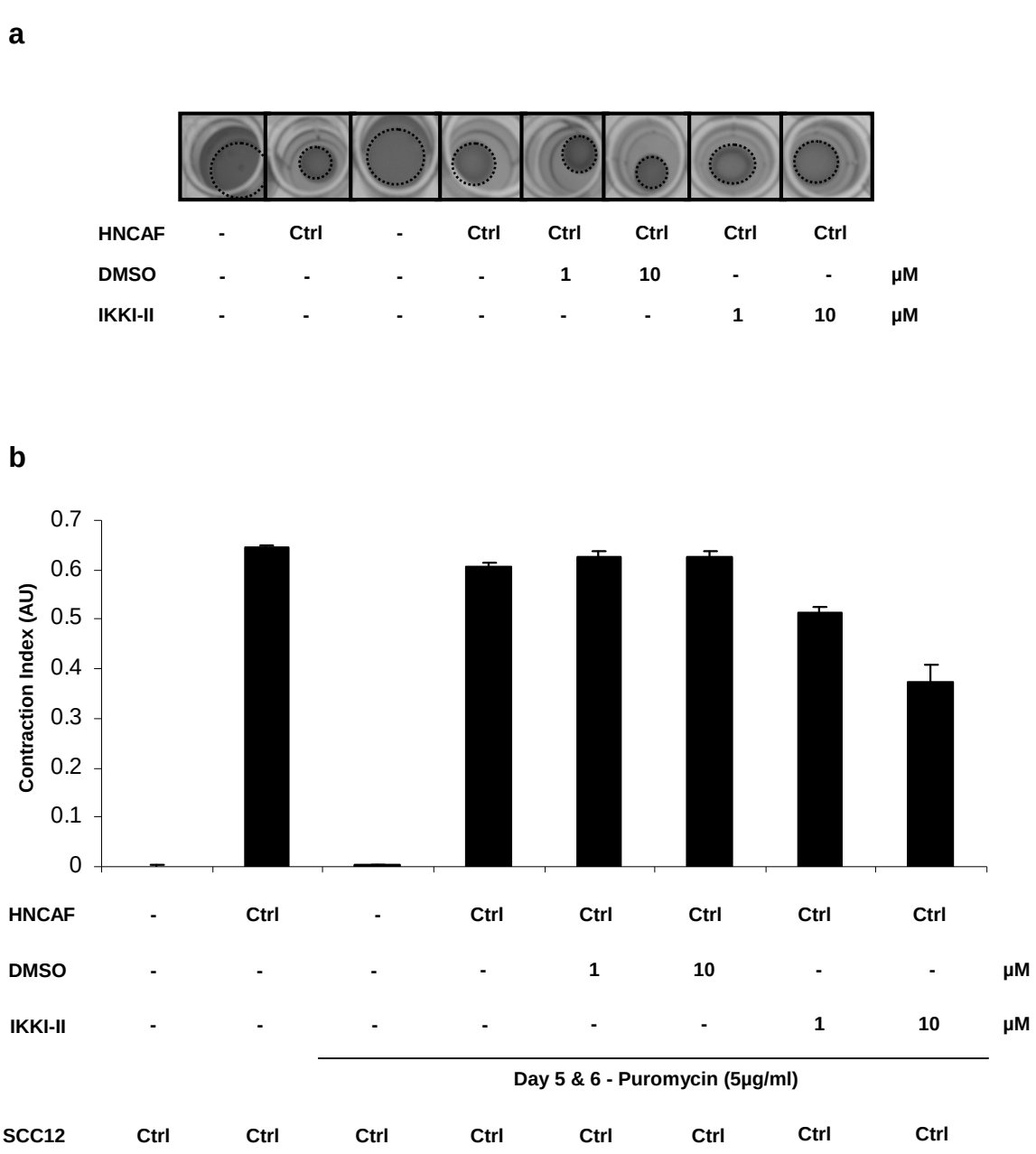

Figure 6.64 Assessment of the influence of IKKI-II on fibroblast-dependent collagen-Matrigel® matrix contraction

(**a**) Images of organotypic gels after 5 days of matrix remodelling and daily treatment with IKKI-II at the specified concentrations prior to the removal of HNCAF. The dotted line represents the area of the gel. (**b**) Quantification of the degree of matrix remodelling. The Contraction Index was calculated using the formula 1 - (Gel Area / Well Area). The average of 2 experiments is shown and error bars represent the s.e.

a

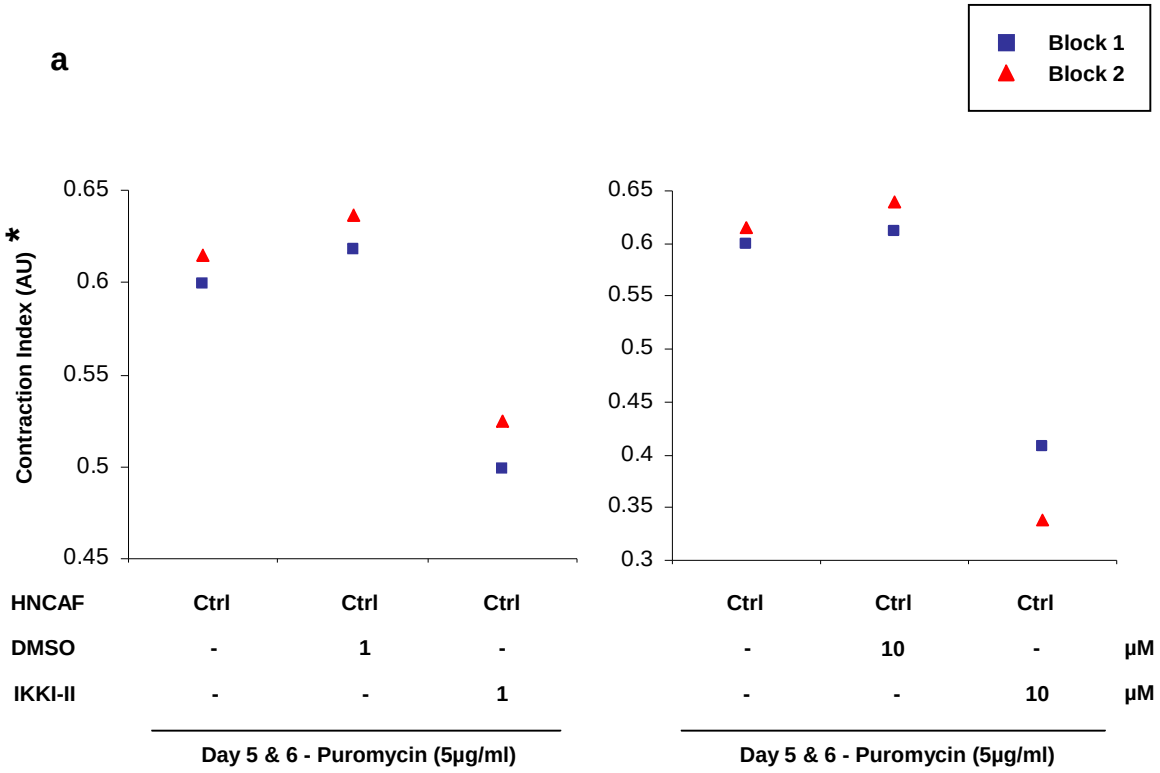

b

Randomized Block ANOVA	p Value	Decision p<0.025
Control vs DMSO 1	0.039070	Do not reject
DMSO 1 vs IKKI-II 1	0.001267	Reject

Control vs DMSO 10	0.672463	Do not reject
DMSO 10 vs IKKI-II 10	0.020889	Reject

Figure 6.65 IKKI-II reduces fibroblast-dependent collagen-Matrigel® matrix contraction

(**a**) Scatter plots displaying the Contraction Index of the fibroblast containing gels treated with IKKI-II illustrated in Figure 6.64. Individual experimental blocks are shown. *Denotes an expanded Y-axis. (**b**) Randomized block ANOVA statistical analysis. Null hypothesis (NØ) rejected if $p < 0.025$.

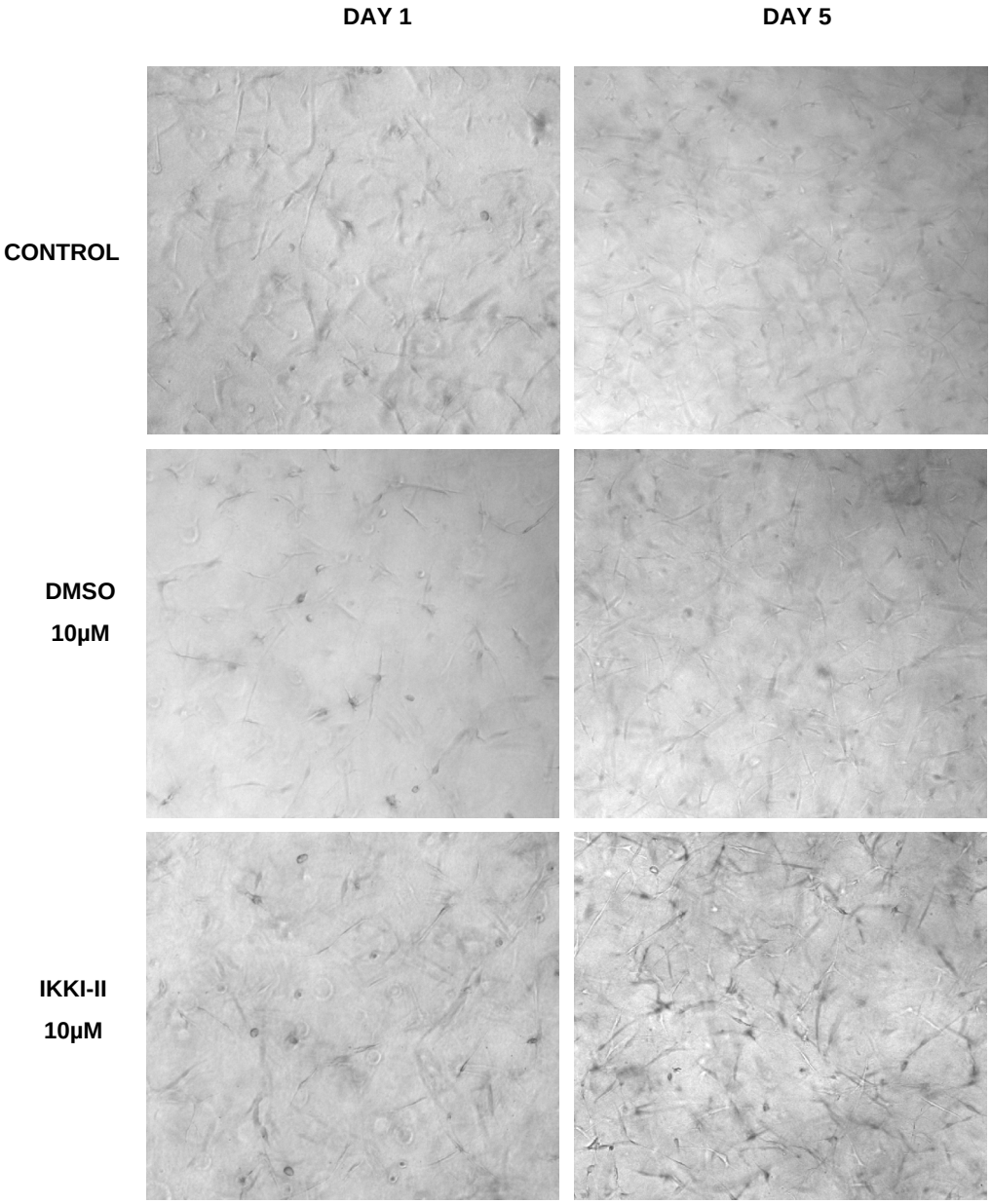

Figure 6.66 Assessment of fibroblast number in organotypic cultures after 5 days of collagen-Matrigel® matrix remodelling with and without daily treatment with IKKI-II

Examples of low power phase images of HNCAF in collagen-Matrigel® matrix taken on Day 1 and Day 5 of the organotypic gels illustrated in Figure 6.64. The number of fibroblasts per unit area was quantified from 6 representative regions of each culture and corrected for the degree of gel contraction. (n=2)

a

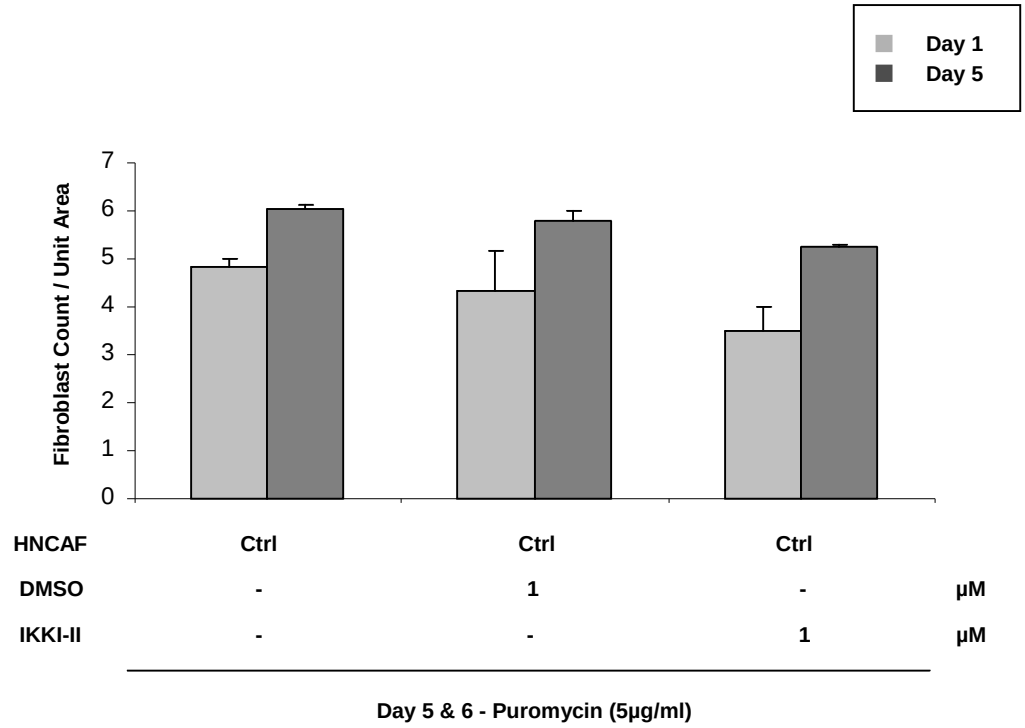

b

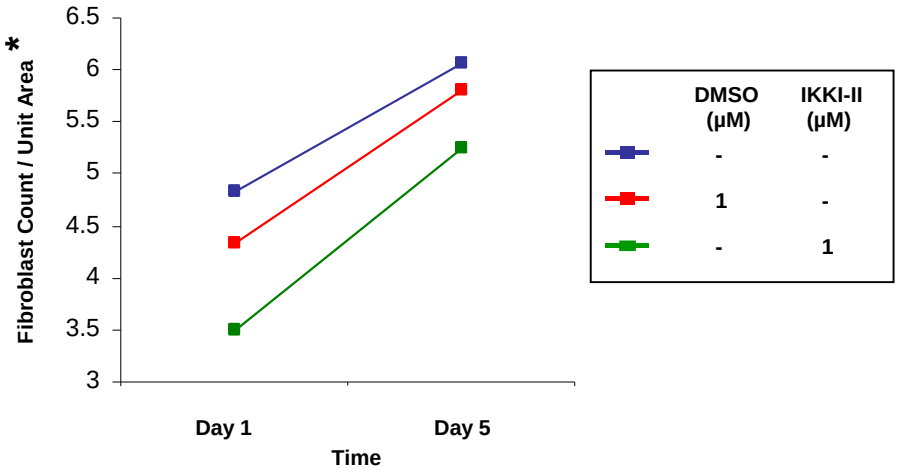

c

Randomized Block ANOVA	p Value	Decision p<0.05
Control vs DMSO 1 vs IKKI-II 1	1.000000	Do not reject

Figure 6.67 IKKI-II at a concentration of 1µM does not affect HNCAF proliferation

Fibroblast count per unit area (corrected for degree of gel contraction) after 5 days of matrix remodelling and daily treatment with IKKI-II at a concentration of 1µM (**a**) bar chart and (**b**) line plot. The average of 12 fields is shown from 2 experiments. The error bars represent the s.e. *Denotes an expanded Y-axis. (**c**) Randomized block ANOVA statistical analysis. Null hypothesis (NØ) rejected if $p < 0.05$.

a

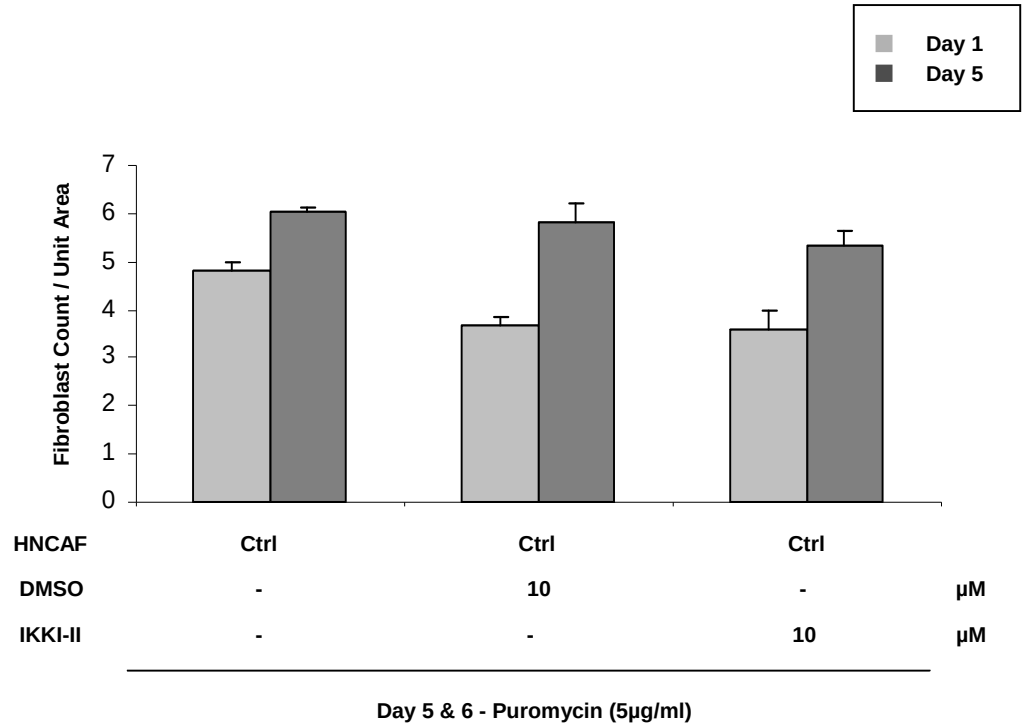

b

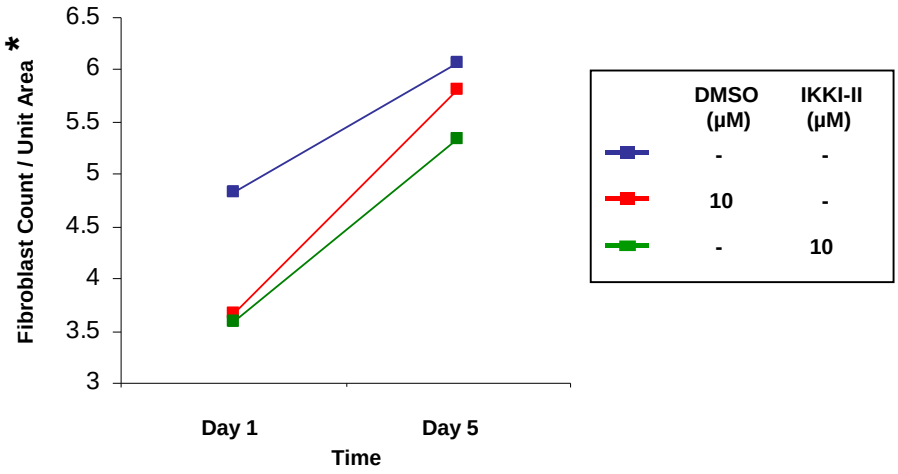

c

Randomized Block ANOVA	p Value	Decision p<0.05
Control vs DMSO 10 vs IKKI-II 10	0.312518	Do not reject

Figure 6.68 IKKI-II at a concentration of 10µM does not affect HNCAF proliferation

Fibroblast count per unit area (corrected for degree of gel contraction) after 5 days of matrix remodelling and daily treatment with IKKI-II at a concentration of 10µM (**a**) bar chart and (**b**) line plots. The average of 12 fields from 2 experiments is shown. The error bars represent the s.e. *Denotes an expanded Y-axis. (**c**) Randomized block ANOVA statistical analysis. Null hypothesis (NØ) rejected if $p < 0.05$.

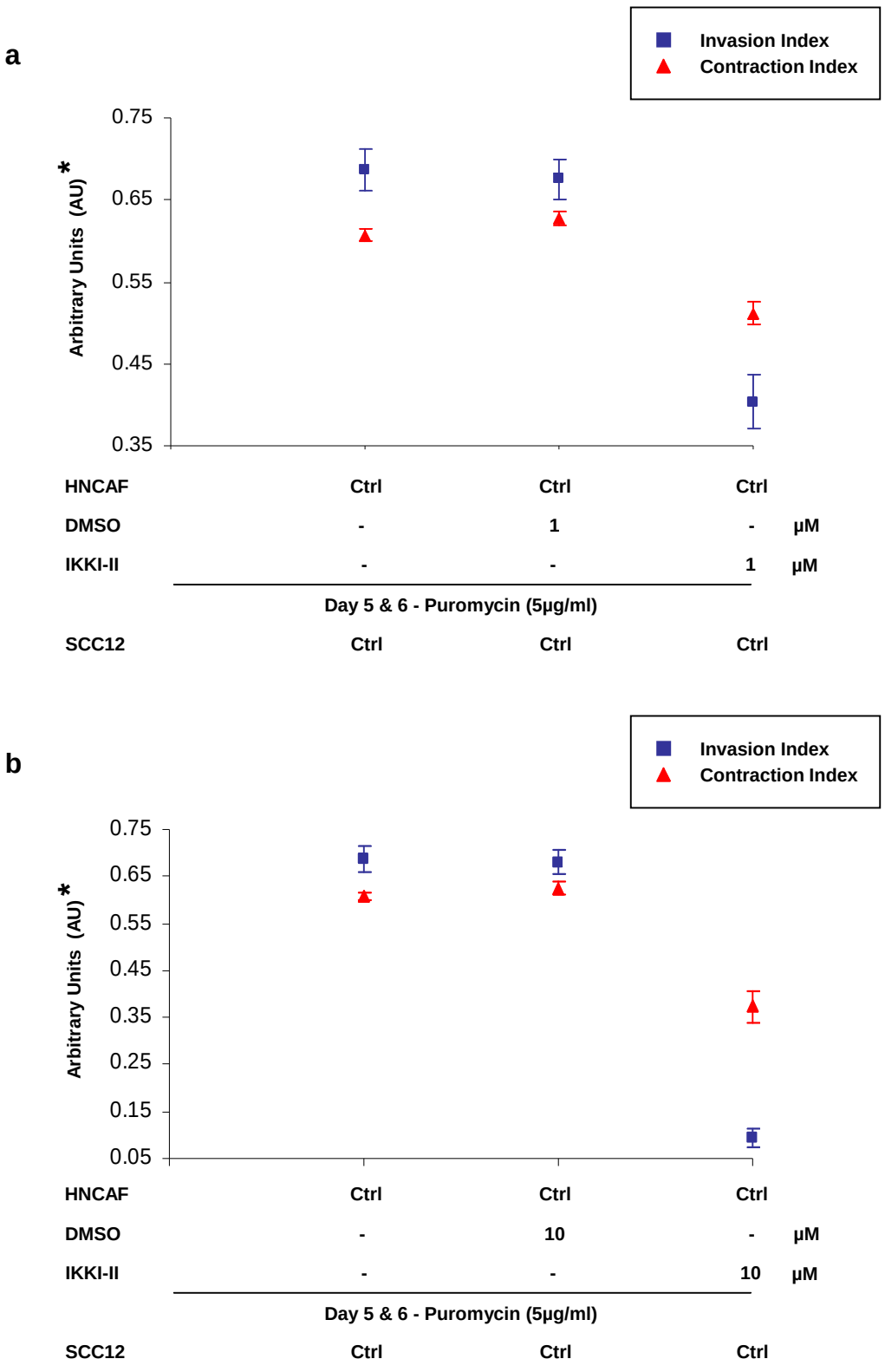

Figure 6.69 Inhibition of HNCAF with IKKI-II reduces collagen-Matrigel® matrix remodelling and is associated with a reduction in carcinoma invasion

Scatter plots displaying the relationship between mean carcinoma invasion and mean gel contraction in response to treatment with IKKI-II at (**a**) 1µM and (**b**) 10µM. Error bars represent the s.e. *Denotes an expanded Y-axis.

6.4.6 Validation of IKK inhibitor influence

The results of my IKKI-II experiments indicated that carcinoma invasion in our organotypic system could be blocked by inhibiting NF-κB signalling at the level of the IKK complex. To validate these findings, I tested three other IKK inhibitors.

Figure 6.70 shows the quantification of SCC12 invasion assays in which both the stromal and epithelial components of the organotypic cultures were inhibited daily with either IKKI-II, IKKI-2, IKKI-III or IKKI-X at concentrations of 1 and 10μM. Vehicle controls (DMSO at concentrations comparable to those of the IKK inhibitors) were also included. Figures 6.71-6.74 illustrate the results with respect to each inhibitor and consist of (a) scatter plots of the individual experimental blocks and (b) randomized block ANOVA statistical analyses. Daily treatment with IKKI-II, IKKI-2 and IKKI-III at a concentration of 10μM resulted in statistically significant reductions in carcinoma invasion.

6.4.7 IKKI-II and IKKI-III inhibit TNFα induced activation of NF-κB signalling in A431 cells and HNCAF

Figure 6.75 demonstrates that pre-treating A431 cells with either IKKI-II (10μM) or IKKI-III (10μM) inhibits TNFα (10ng/ml) induced IKK activation. Consequently, IκBα is not degraded (Figure 6.76) and NF-κB p65 is not phosphorylated (Figure 6.77).

Figure 6.78 demonstrates that pre-treating HNCAF with either IKKI-II (10μM) or IKKI-III (10μM) inhibits TNFα (10ng/ml) induced IKK activation. Consequently, IκBα is not degraded (Figure 6.79) and NF-κB p65 is not phosphorylated (Figure 6.80).

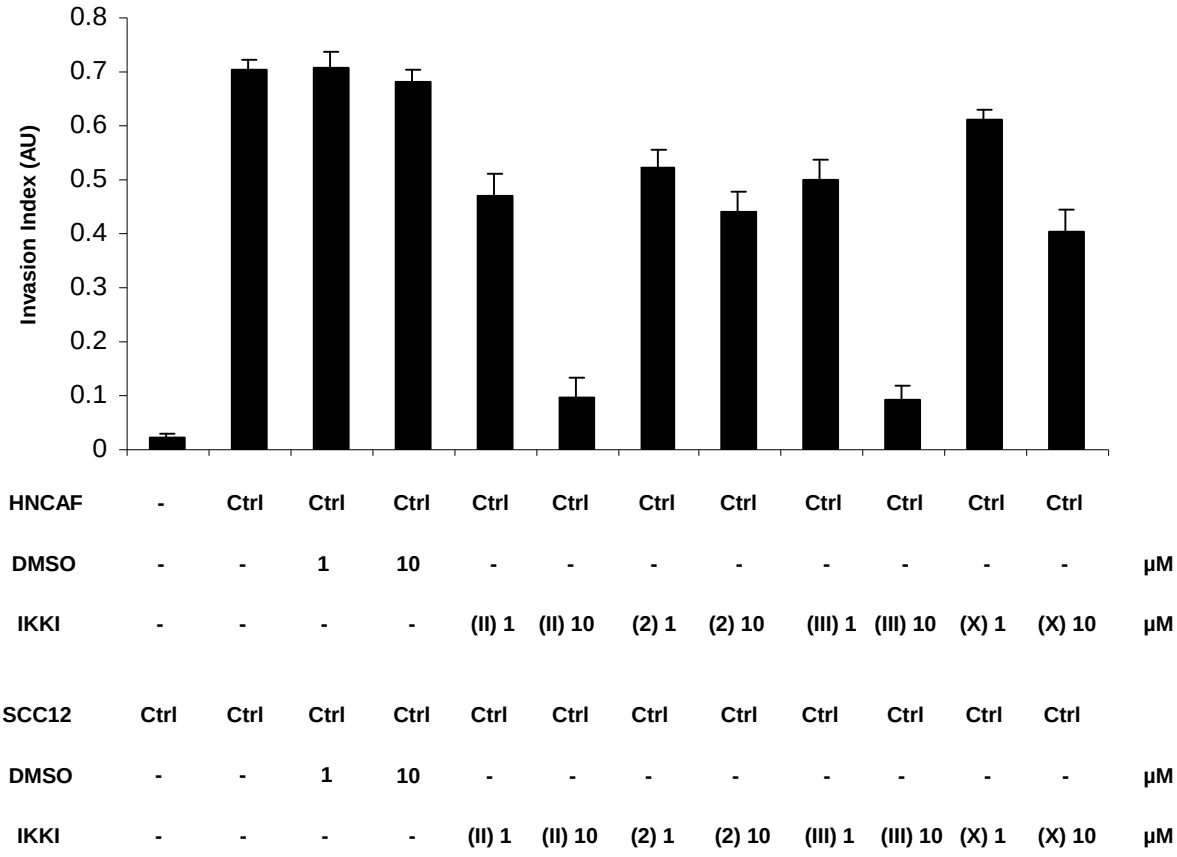

Figure 6.70 Organotypic invasion assay: validation of IKK inhibitor influence

Quantification of carcinoma invasion. Both the stromal and epithelial components of the organotypic cultures were treated daily with IKKI-II, IKKI-2, IKKI-III and IKKI-X at the specified concentrations. Vehicle controls (DMSO at concentrations comparable to those of the IKK inhibitors) were also included in the assay. The average of 10 visual fields from 2 experiments is shown. The error bars represent the s.e.

a

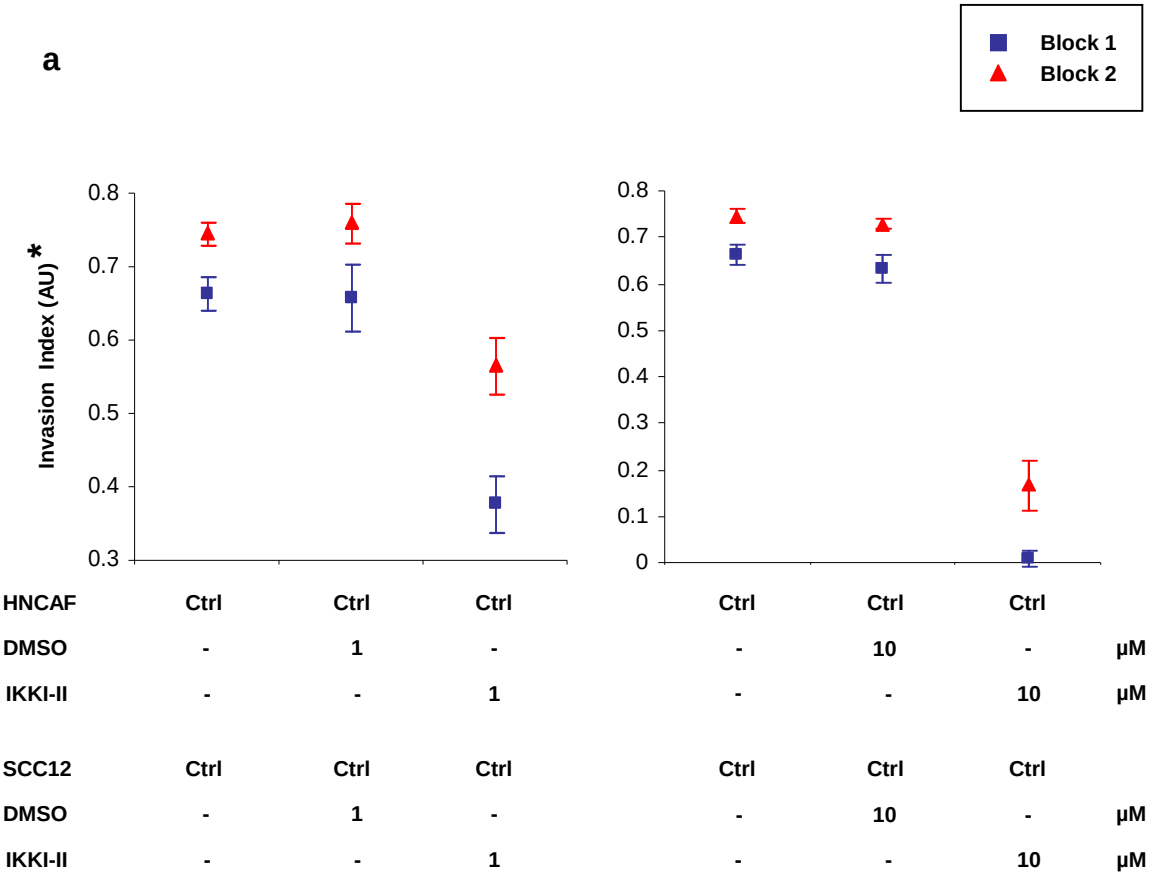

b

Randomized Block ANOVA	p Value	Decision p<0.025
Control vs DMSO 1	0.921791	Do not reject
DMSO 1 vs IKKI-II 1	0.026771	Do not reject

Control vs DMSO 10	0.514963	Do not reject
DMSO 10 vs IKKI-II 10	0.002318	Reject

Figure 6.71 Validation of IKK inhibitor influence: IKKI-II

(**a**) Scatter plots displaying the quantification of carcinoma invasion of IKKI-II treated cultures from the organotypic assay illustrated in Figure 6.70. Individual experimental blocks are illustrated. The average of 5 visual fields is shown and error bars represent the s.e. *Denotes an expanded Y-axis. (**b**) Randomized block ANOVA statistical analysis. Null hypothesis (NØ) rejected if $p < 0.025$.

a

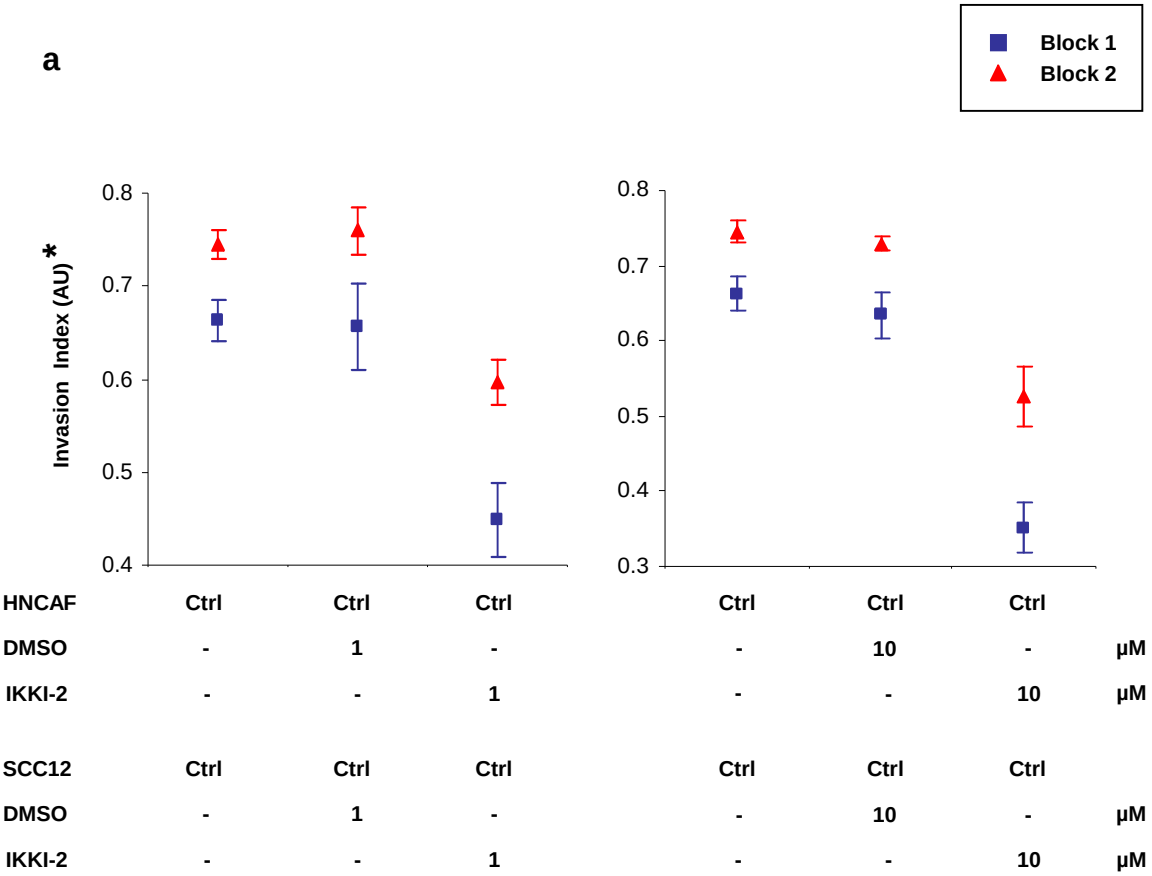

b

Randomized Block ANOVA	p Value	Decision p<0.025
Control vs DMSO 1	0.871061	Do not reject
DMSO 1 vs IKKI-2 1	0.016358	Reject

Control vs DMSO 10	0.591249	Do not reject
DMSO 10 vs IKKI-2 10	0.020757	Reject

Figure 6.72 Validation of IKK inhibitor influence: IKKI-2

(**a**) Scatter plots displaying the quantification of carcinoma invasion of IKKI-2 treated cultures from the organotypic assay illustrated in Figure 6.70. Individual experimental blocks are illustrated. The average of 5 visual fields is shown and error bars represent the s.e. *Denotes an expanded Y-axis. (**b**) Randomized block ANOVA statistical analysis. Null hypothesis (NØ) rejected if $p < 0.025$.

a

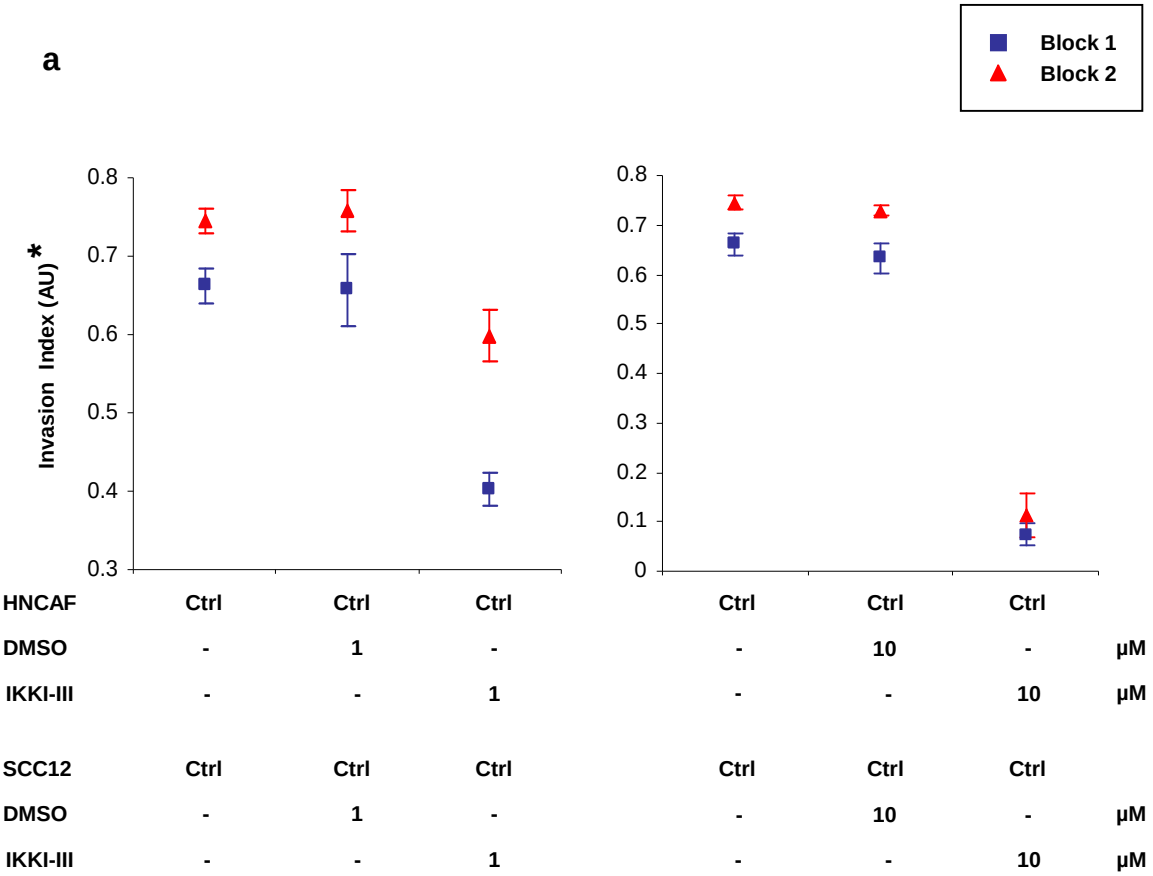

b

Randomized Block ANOVA	p Value	Decision p<0.025
Control vs DMSO 1	0.927591	Do not reject
DMSO 1 vs IKKI-III 1	0.026771	Do not reject

Control vs DMSO 10	0.040051	Do not reject
DMSO 10 vs IKKI-III 10	0.001266	Reject

Figure 6.73 Validation of IKK inhibitor influence: IKKI-III

(**a**) Scatter plots displaying the quantification of carcinoma invasion of IKKI-III treated cultures from the organotypic assay illustrated in Figure 6.70. Individual experimental blocks are illustrated. The average of 5 visual fields is shown and error bars represent the s.e. *Denotes an expanded Y-axis. (**b**) Randomized block ANOVA statistical analysis. Null hypothesis (NØ) rejected if $p < 0.025$.

a

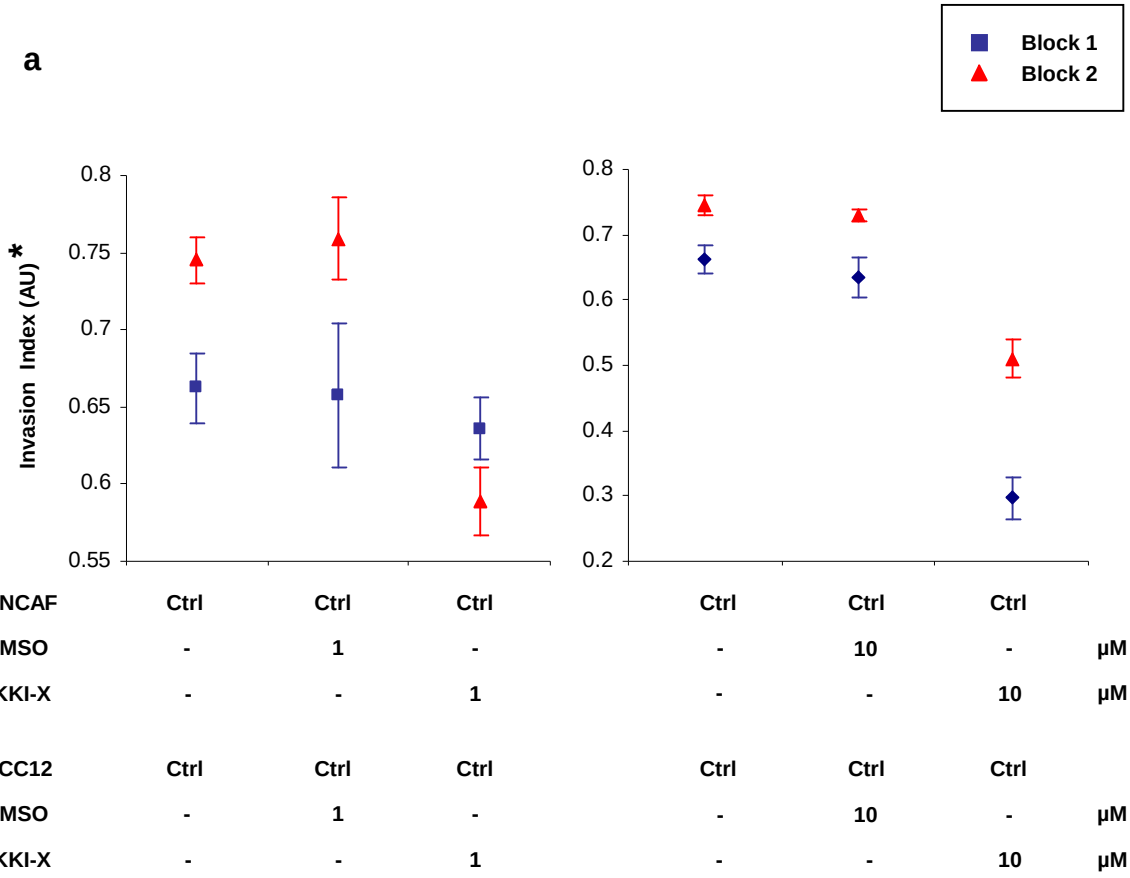

b

Randomized Block ANOVA	p Value	Decision p<0.025
Control vs DMSO 1	0.945833	Do not reject
DMSO 1 vs IKKI-X 1	0.237537	Do not reject

Control vs DMSO 10	0.704095	Do not reject
DMSO 10 vs IKKI-X10	0.032340	Do not reject

Figure 6.74 Validation of IKK inhibitor influence: IKKI-X

(**a**) Scatter plots displaying the quantification of carcinoma invasion of IKKI-X treated cultures from the organotypic assay illustrated in Figure 6.70. Individual experimental blocks are illustrated. The average of 5 visual fields is shown and error bars represent the s.e. *Denotes an expanded Y-axis. (**b**) Randomized block ANOVA statistical analysis. Null hypothesis (NØ) rejected if $p < 0.025$.

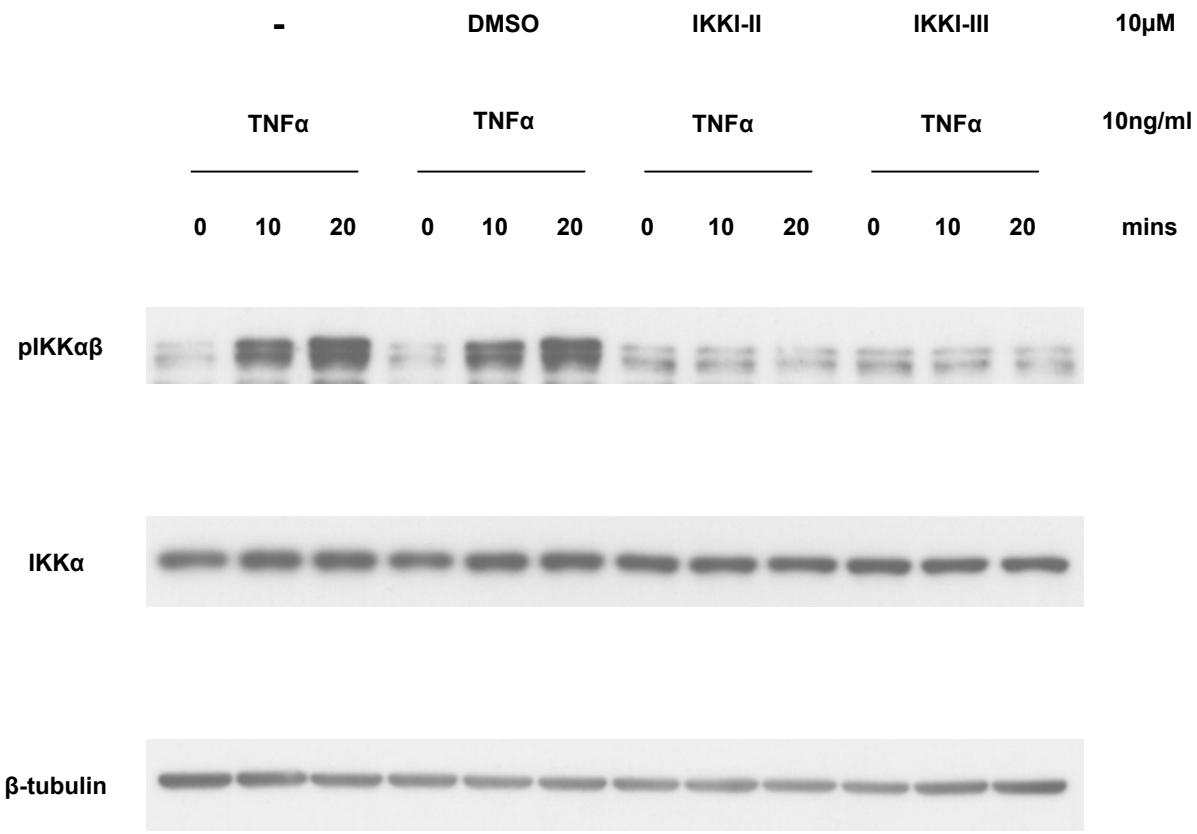

Figure 6.75 IKKI-II and IKKI-III inhibit TNFα induced activation of IKK in A431 cells

Western blots of lysates of A431 cells which had been treated with either IKKI-II or IKKI-III at a concentration of 10μM for 2 hours prior to stimulation with TNFα (10ng/ml). Both IKK inhibitors prevented TNFα induced activation of IKK and consequently inhibited NF-κB signalling. Control samples in which cells had either not been treated or were treated with the vehicle (DMSO at a concentration comparable to that of the IKK inhibitors) are also included.

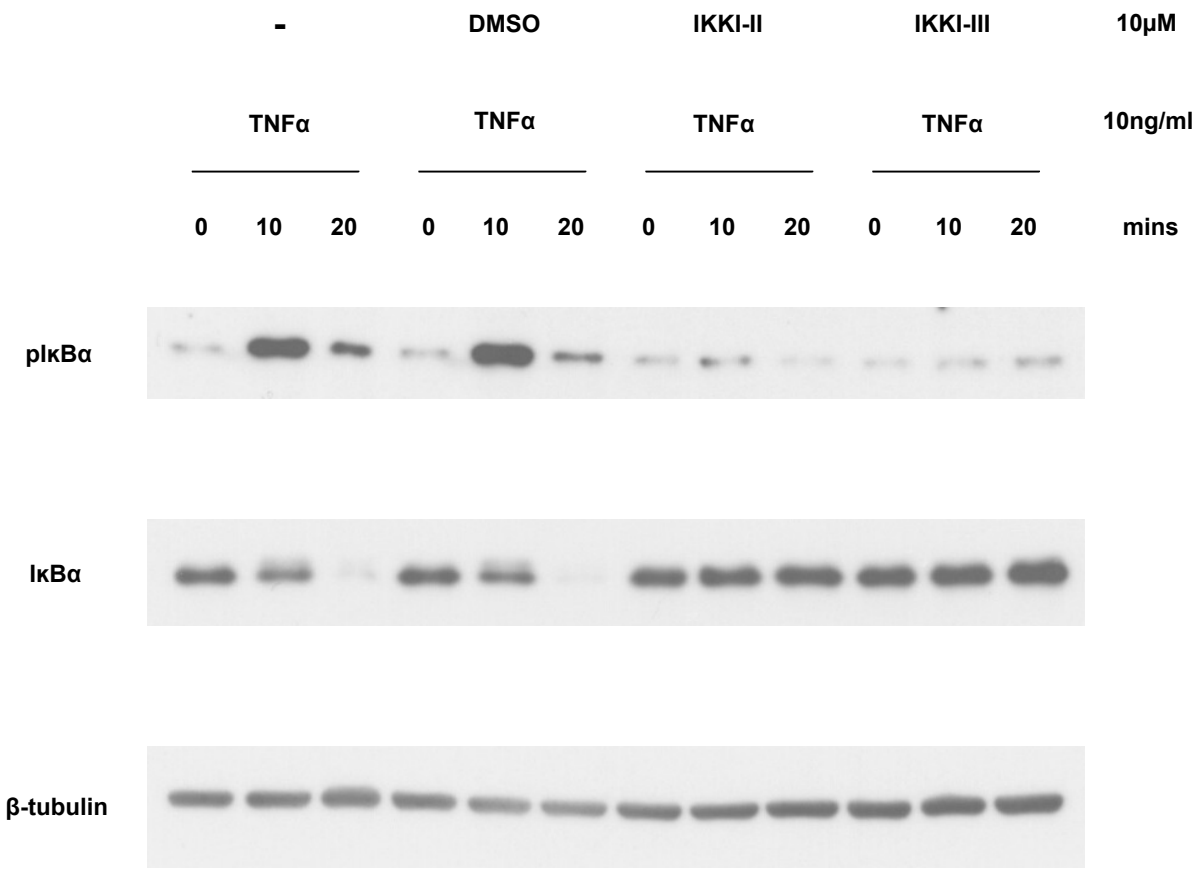

Figure 6.76 IKKI-II and IKKI-III inhibit TNFα induced phosphorylation and reciprocal degradation of IκBα in A431 cells

Western blots of lysates of A431 cells which had been treated with either IKKI-II or IKKI-III at a concentration of 10μM for 2 hours prior to stimulation with TNFα (10ng/ml). Both IKK inhibitors prevented TNFα induced phosphorylation and reciprocal degradation of IκBα. Control samples in which cells had either not been treated or were treated with the vehicle (DMSO at a concentration comparable to that of the IKK inhibitors) are also included.

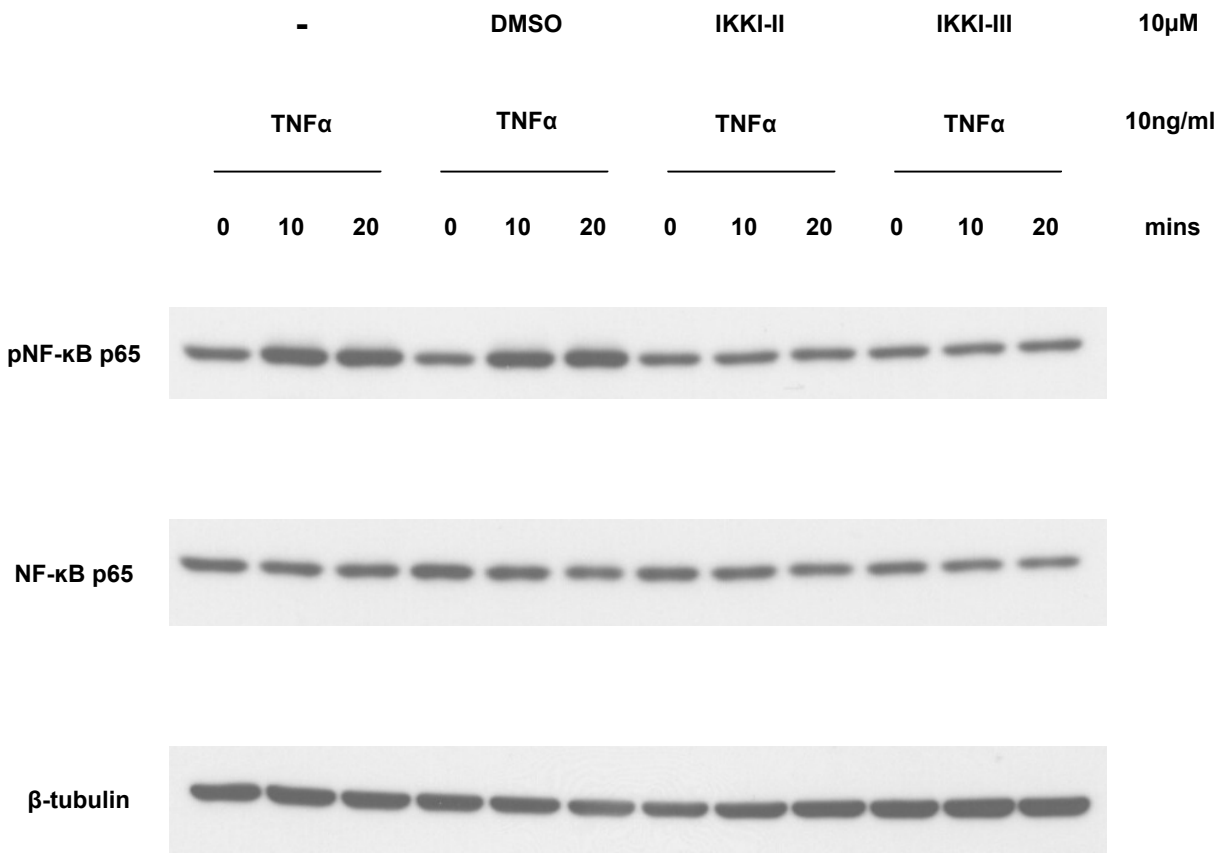

Figure 6.77 IKKI-II and IKKI-III inhibit TNFα induced activation of NF-κB in A431 cells

Western blots of lysates of A431 cells which had been treated with either IKKI-II or IKKI-III at a concentration of 10μM for 2 hours prior to stimulation with TNFα (10ng/ml). Both IKK inhibitors prevented TNFα induced activation of NF-κB p65. Control samples in which cells had either not been treated or were treated with the vehicle (DMSO at a concentration comparable to that of the IKK inhibitors) are also included.

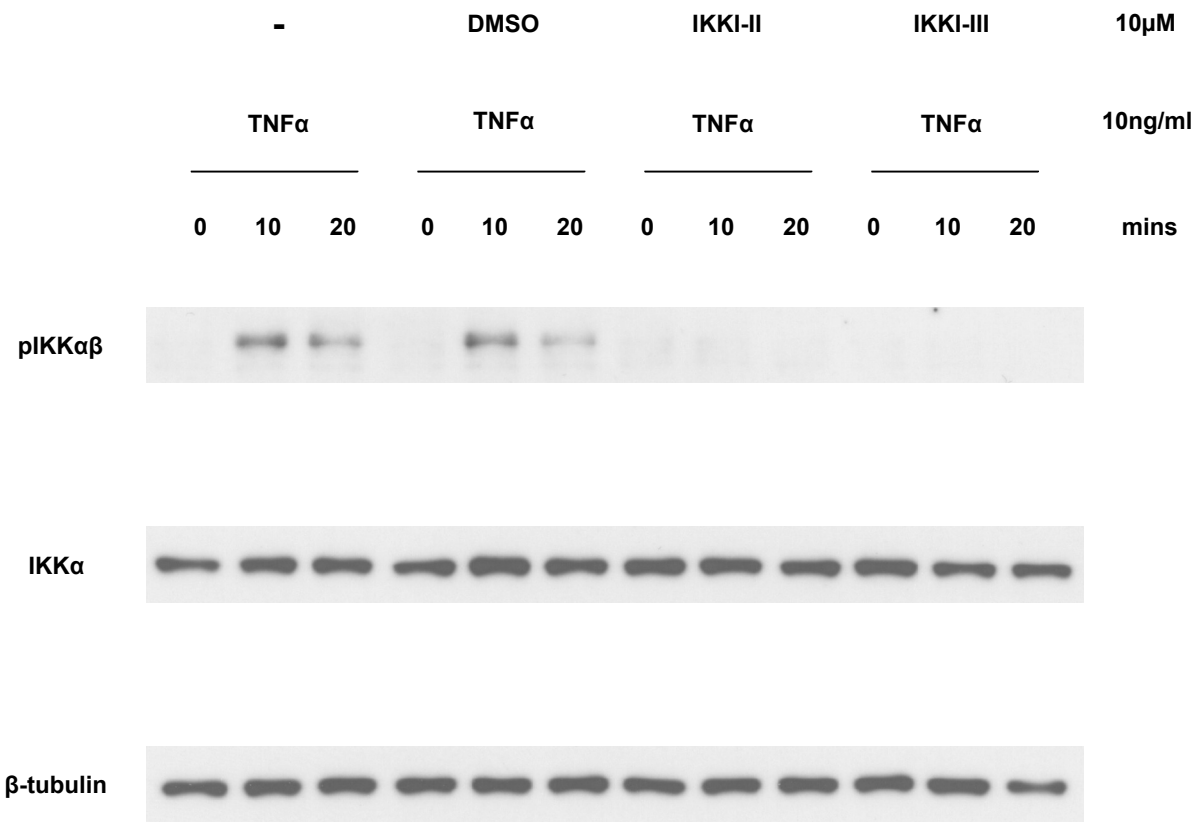

Figure 6.78 IKKI-II and IKKI-III inhibit TNFα induced activation of IKK in HNCAF

Western blots of lysates of HNCAF which had been treated with either IKKI-II or IKKI-III at a concentration of 10μM for 2 hours prior to stimulation with TNFα (10ng/ml). Both IKK inhibitors prevented TNFα induced activation of IKK and consequently inhibited NF-κB signalling. Control samples in which cells had either not been treated or were treated with the vehicle (DMSO at a concentration comparable to that of the IKK inhibitors) are also included.

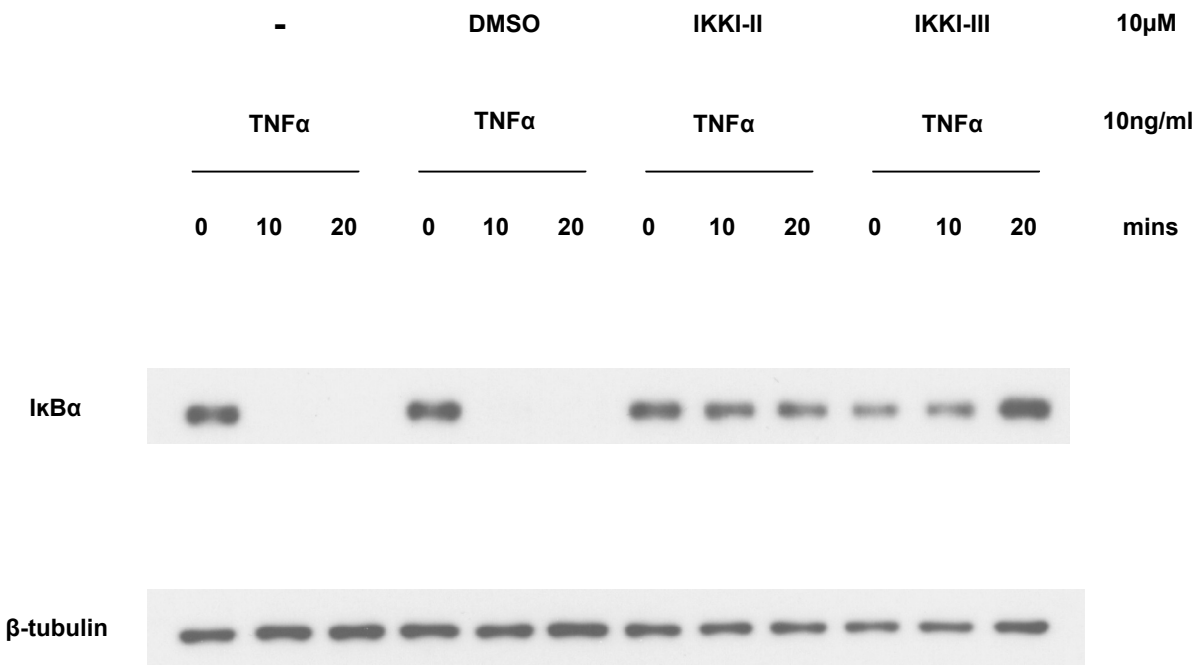

Figure 6.79 IKKI-II and IKKI-III inhibit TNFα induced degradation of IκBα in HNCAF

Western blots of lysates of HNCAF which had been treated with either IKKI-II or IKKI-III at a concentration of 10μM for 2 hours prior to stimulation with TNFα (10ng/ml). Both IKK inhibitors prevented TNFα induced degradation of IκBα. Control samples in which cells had either not been treated or were treated with the vehicle (DMSO at a concentration comparable to that of the IKK inhibitors) are also included.

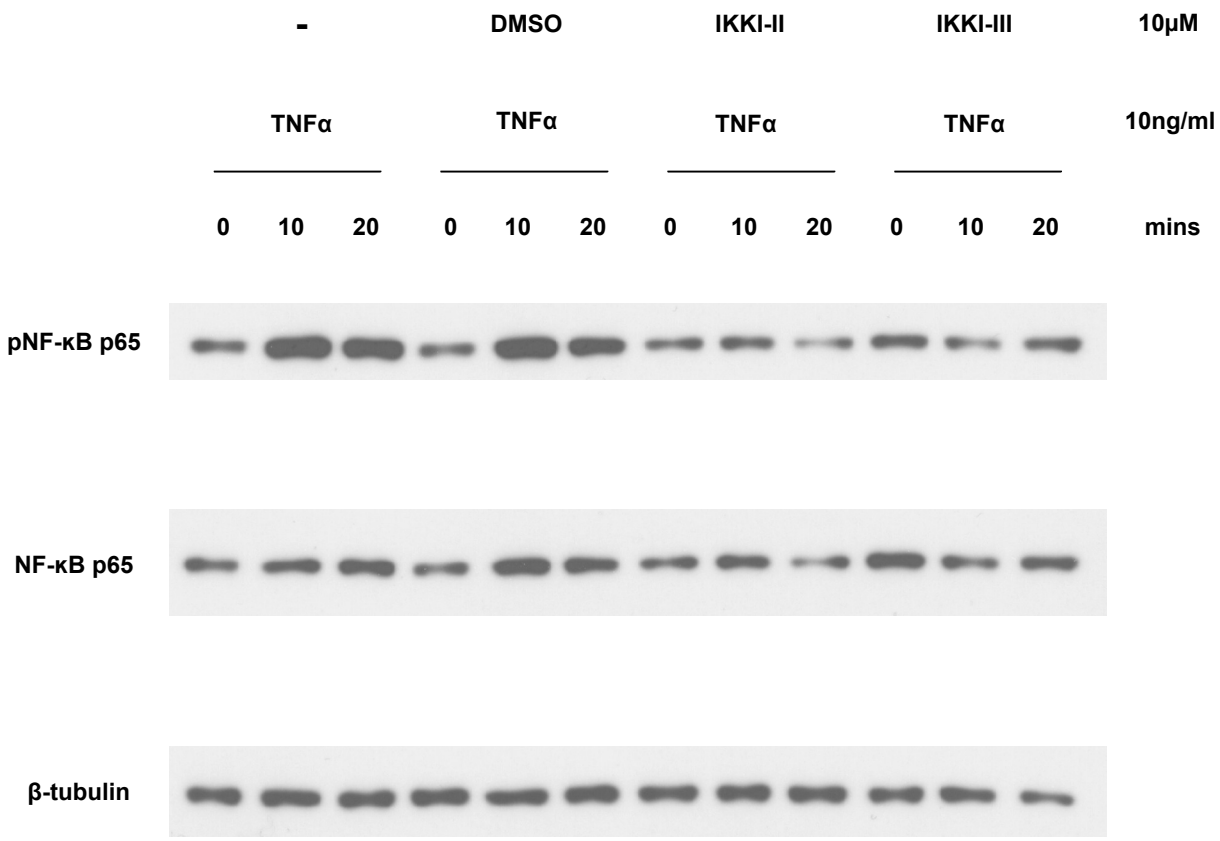

Figure 6.80 IKKI-II and IKKI-III inhibit TNFα induced activation of NF-κB in HNCAF

Western blots of lysates of HNCAF which had been treated with either IKKI-II or IKKI-III at a concentration of 10μM for 2 hours prior to stimulation with TNFα (10ng/ml). Both IKK inhibitors prevented TNFα induced activation of NF-κB p65. Control samples in which cells had either not been treated or were treated with the vehicle (DMSO at a concentration comparable to that of the IKK inhibitors) are also included.

6.5 Anti-TNFα therapy

Collectively, my experimental data strongly supported the notion that carcinoma invasion in our organotypic model was both TNFα driven and NF-κB dependent. To further corroborate these findings I investigated whether infliximab (a monoclonal anti-TNFα antibody in clinical use) could block cancer cell invasion in this setting.

6.5.1 Infliximab reduces SCC12 carcinoma invasion *in vitro*

Figure 6.81 shows the quantification of SCC12 invasion assays in which both the stromal and epithelial components of the organotypic cultures were treated daily with infliximab at concentrations of 10 and 31μg/ml. Controls treated with TNFα (31ng/ml) and TNFα (31ng/ml) + infliximab (31μg/ml) were also included. Figures 6.82 and 6.83 consist of (a) photomicrographs of H&E sections demonstrating the degree of carcinoma infiltration into the underlying matrix, (b) a line plot of the individual experimental blocks and (c) randomized block ANOVA statistical analysis. Statistically significant reductions in the Invasion Index were seen at both concentrations of infliximab.

6.5.2 Infliximab reduces fibroblast-dependent collagen-Matrigel® matrix contraction

The collagen-Matrigel® gels constructed for the assays detailed in Section 6.5.1 were photographed after 3 days of fibroblast-mediated matrix remodelling (Figure 6.84a) and the Contraction Index for each gel calculated. A line plot of the individual experimental blocks for each concentration of infliximab is presented in Figure 6.84b. A statistically significant reduction in the Contraction Index was seen at a 31μg/ml concentration of infliximab (Figure 6.84c).

To exclude the possibility that infliximab was inhibiting HNCAF proliferation, fibroblast number per unit area was assessed on Day 1 and Day 3 of the assays in gels with and without daily infliximab (Figure 6.85). Infliximab at concentrations of 10 and 31μg/ml did not affect HNCAF proliferation (Figures 6.86).

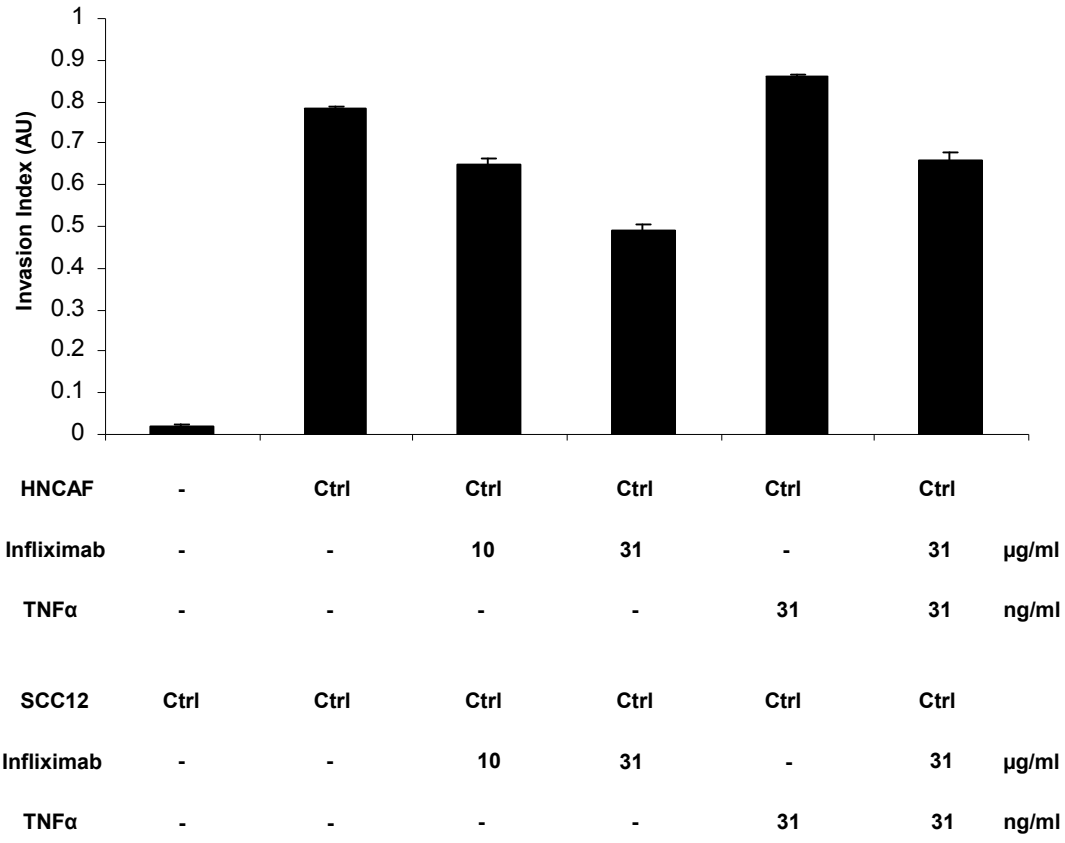

Figure 6.81 Organotypic invasion assay: treatment of HNCAF and SCC12 with infliximab

Quantification of carcinoma invasion. Both the stromal and epithelial components of the organotypic cultures were treated daily with infliximab at the specified concentrations. TNFα and TNFα with infliximab controls were also included in the assay. The average of 10 visual fields from 2 experiments is shown. The error bars represent the s.e.

a

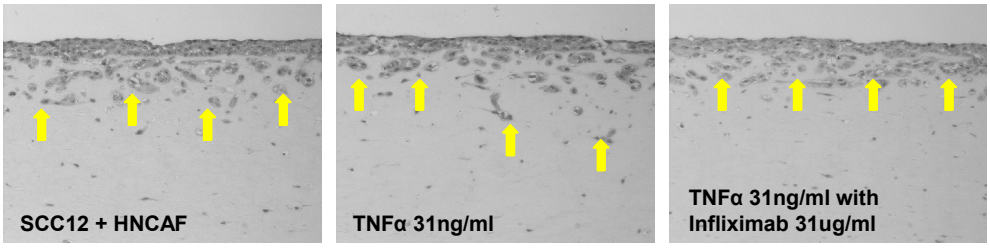

b

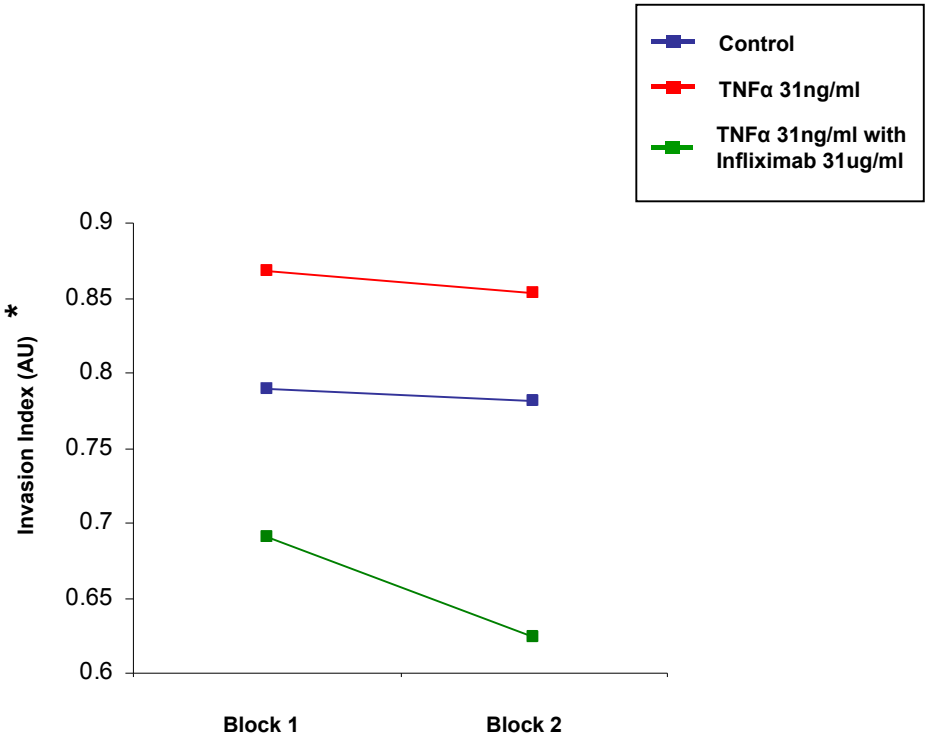

c

Randomized Block ANOVA	p Value	Decision p<0.025
TNFα 31 vs TNFα 31 with Infliximab 31	0.012269	Reject

Figure 6.82 Treatment of HNCAF and SCC12 with infliximab: TNFα and TNFα with infliximab controls

(**a**) H&E stained sections of SCC12 cells cultured in organotypic gels. Arrows point to the invading front of carcinoma cells. (**b**) Line plot displaying quantification of carcinoma invasion. Individual experimental blocks are illustrated. The average of 5 visual fields is shown. *Denotes an expanded Y-axis. (**c**) Randomized block ANOVA statistical analysis. Null hypothesis (NØ) rejected if $p < 0.025$.

a

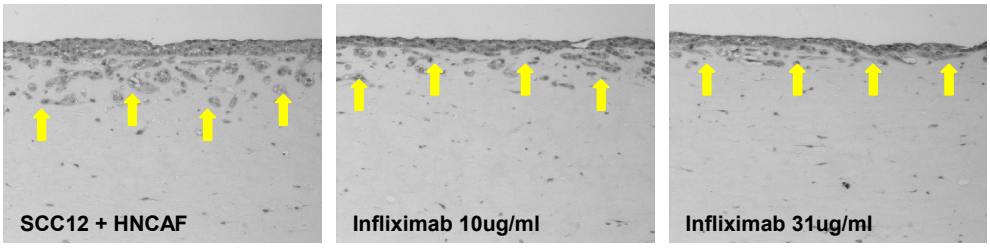

b

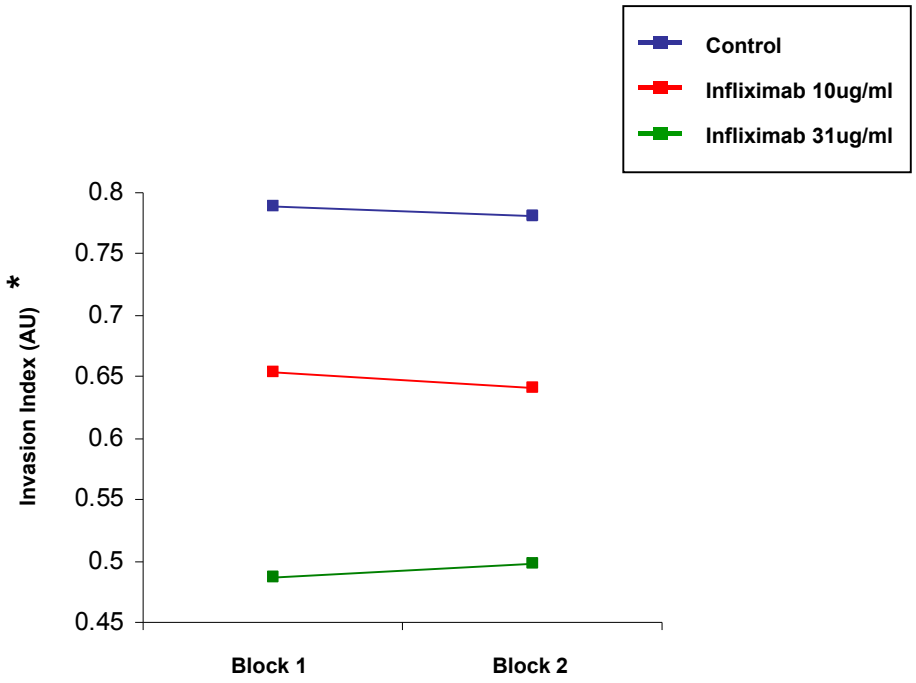

c

Randomized Block ANOVA	p Value	Decision p<0.025
Control vs Infliximab 10	0.003809	Reject
Control vs Infliximab 31	0.008490	Reject

Figure 6.83 Treatment of HNCAF and SCC12 with infliximab at 10µg/ml and 31µg/ml reduces carcinoma invasion *in vitro*

(**a**) H&E stained sections of SCC12 cells cultured in organotypic gels. Arrows point to the invading front of carcinoma cells. (**b**) Line plot displaying quantification of carcinoma invasion. Individual experimental blocks are illustrated. The average of 5 visual fields is shown. *Denotes an expanded Y-axis. (**c**) Randomized block ANOVA statistical analysis. Null hypothesis (NØ) rejected if $p < 0.025$.

a

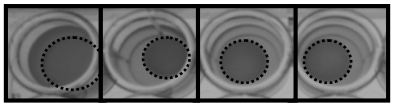

HNCAF	-	Ctrl	Ctrl	Ctrl	
Infliximab	-	-	10	31	µg/ml

b

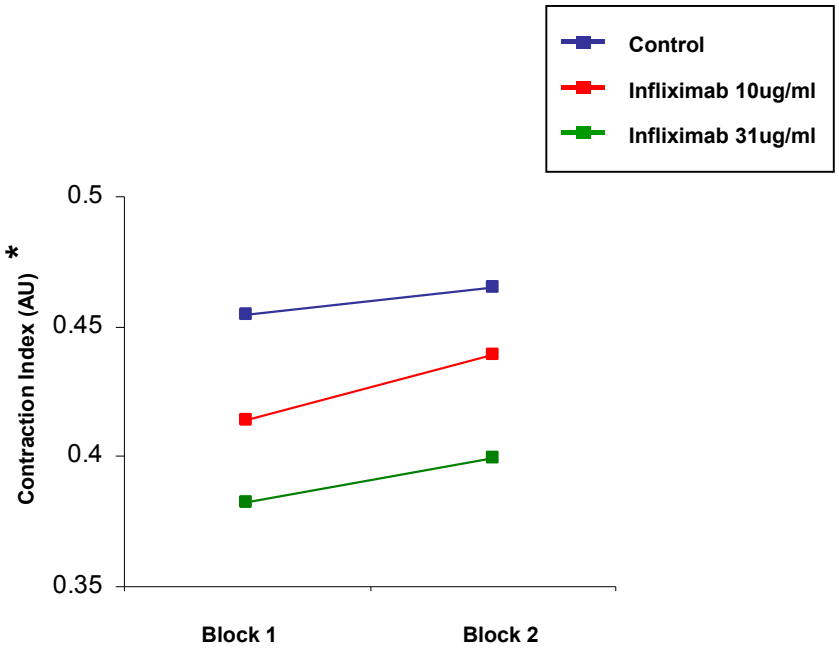

c

Randomized Block ANOVA	p Value	Decision p<0.025
Control vs Infliximab 10	0.027299	Do not reject
Control vs Infliximab 31	0.006499	Reject
Infliximab 10 vs Infliximab 31	0.023437	Reject

Figure 6.84 Assessment of the influence of infliximab on fibroblast-dependent collagen-Matrigel® matrix remodelling

(**a**) Images of organotypic gels after 3 days of matrix remodelling and daily treatment with infliximab at the specified concentrations. The dotted line represents the area of the gel. (**b**) Line plot displaying quantification of the degree of matrix remodelling. The Contraction Index was calculated using the formula 1 - (Gel Area / Well Area). Individual experimental blocks are illustrated. *Denotes an expanded Y-axis. (**c**) Randomized block ANOVA statistical analysis. Null hypothesis (NØ) rejected if $p < 0.025$.

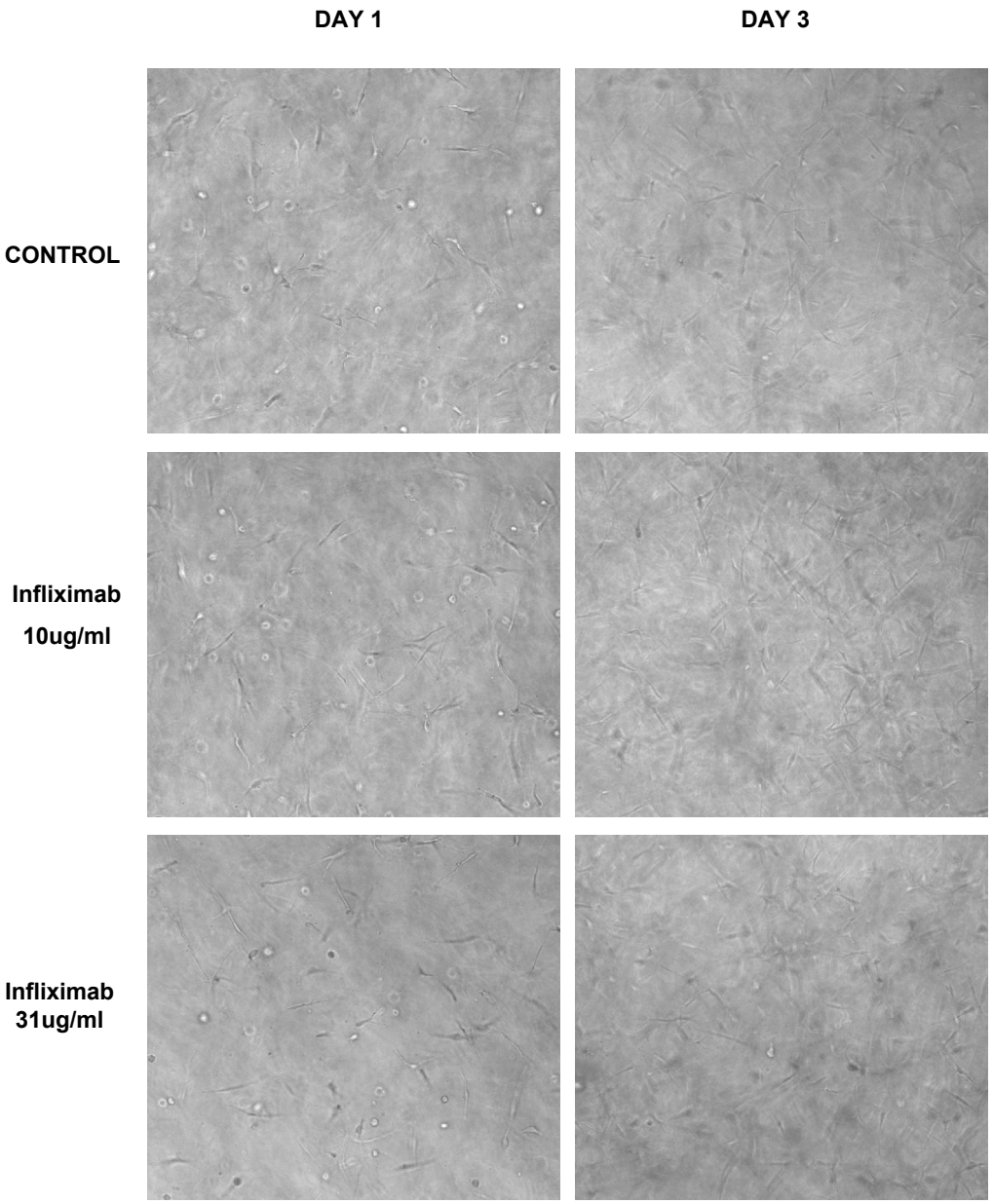

Figure 6.85 Assessment of fibroblast number in organotypic cultures after 3 days of collagen-Matrigel® matrix remodelling with and without daily treatment with infliximab

Examples of low power phase images of HNCAF in collagen-Matrigel® matrix taken on Day 1 and Day 3 of the organotypic gels illustrated in Figure 6.84. The number of fibroblasts per unit area was quantified from 6 representative regions of each culture and corrected for the degree of gel contraction. (n=2)

a

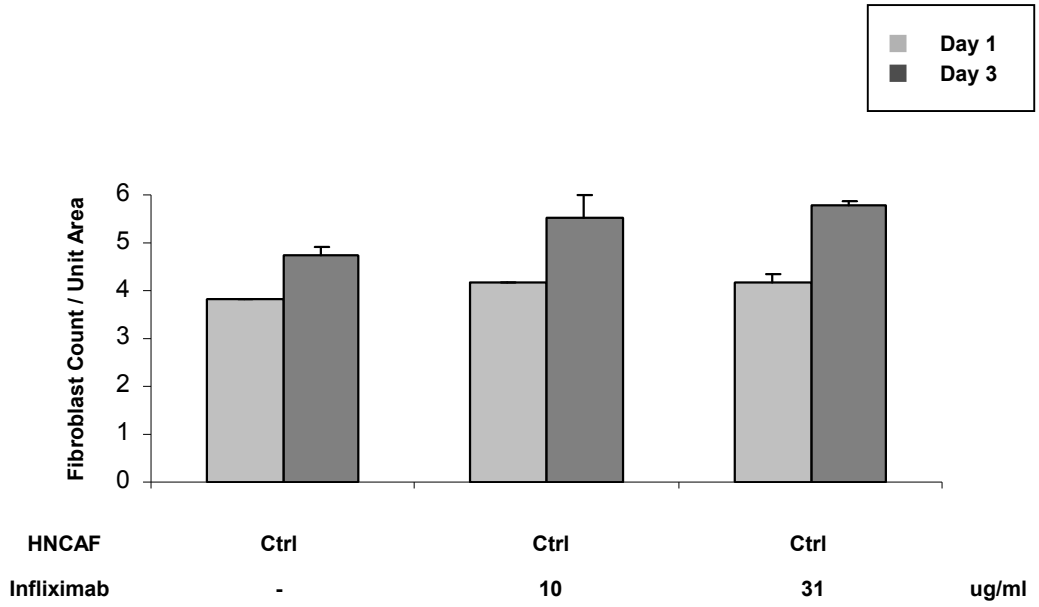

b

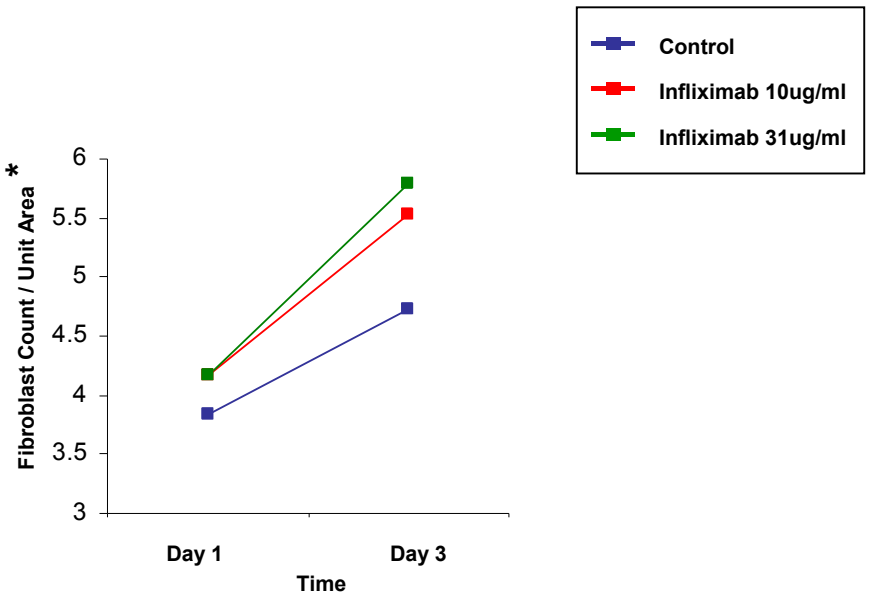

c

Randomized Block ANOVA	p Value	Decision p<0.05
Control vs Infliximab 10 vs Infliximab 31	0.134615	Do not reject

Figure 6.86 Infliximab at concentrations of 10µg/ml and 31µg/ml does not affect HNCAF proliferation

Fibroblast count per unit area (corrected for degree of gel contraction) after 3 days of matrix remodelling and daily treatment with infliximab at the specified concentrations (**a**) bar chart and (**b**) line plot. The average of 12 fields from 2 experiments is shown. The error bars represent the s.e. *Denotes an expanded Y-axis. (**c**) Randomized block ANOVA statistical analysis. Null hypothesis (NØ) rejected if $p < 0.05$.

6.5.3 Infliximab inhibits TNFα induced activation of NF-κB signalling in A431 cells and HNCAF

Figure 6.87 demonstrates that pre-treating A431 cells with infliximab (10μg/ml) inhibits TNFα (31ng/ml) induced IKK activation. Consequently, IκBα is not degraded (Figure 6.88) and NF-κB p65 is not phosphorylated (Figure 6.89).

Figure 6.90 demonstrates that pre-treating HNCAF with infliximab (10μg/ml) inhibits TNFα (31ng/ml) induced IKK activation. Consequently, IκBα is not degraded (Figure 6.91) and NF-κB p65 is not phosphorylated (Figure 6.92).

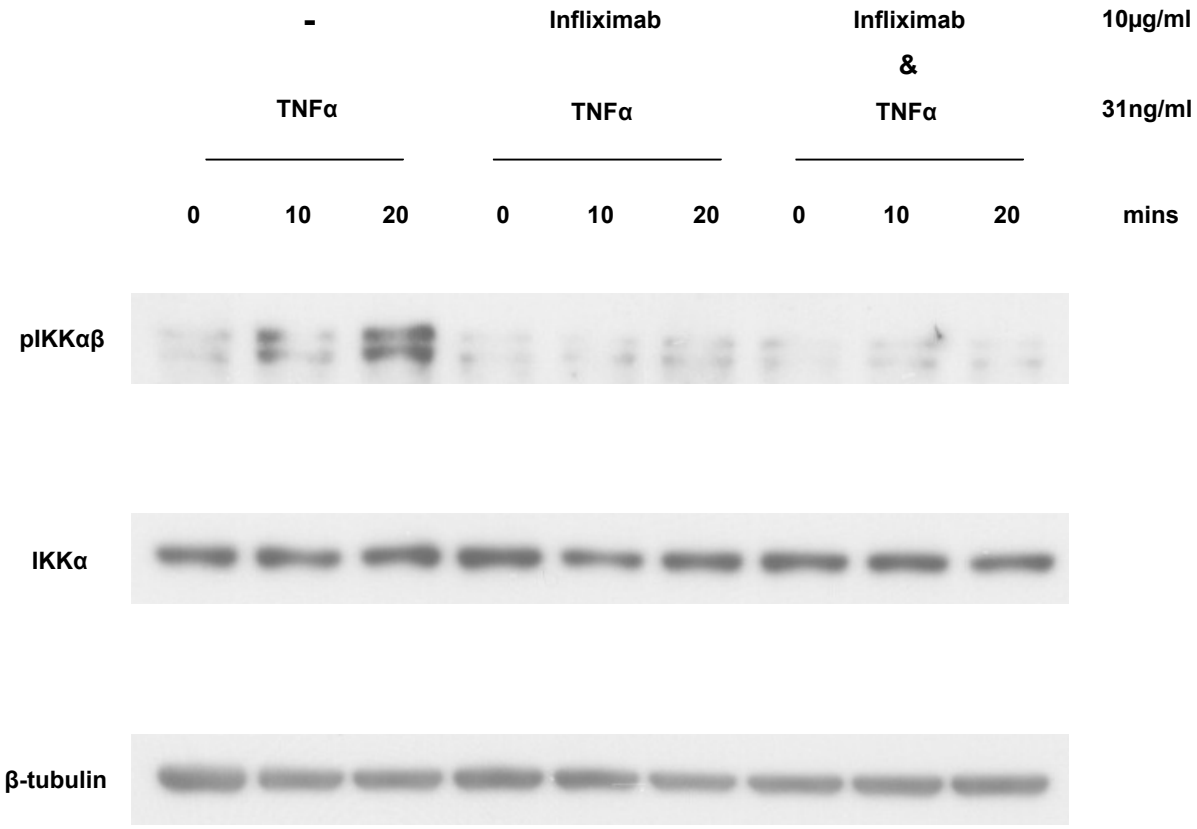

Figure 6.87 Infliximab inhibits TNFα induced activation of IKK in A431 cells

Western blots of lysates of A431 cells which had been treated with infliximab at a concentration of 10µg/ml for 1 hour prior to stimulation with TNFα (31ng/ml). Infliximab prevented TNFα induced activation of IKK and consequently inhibited NF-κB signalling. Control samples in which cells had not been treated with infliximab or were treated with both infliximab and TNFα simultaneously are also included.

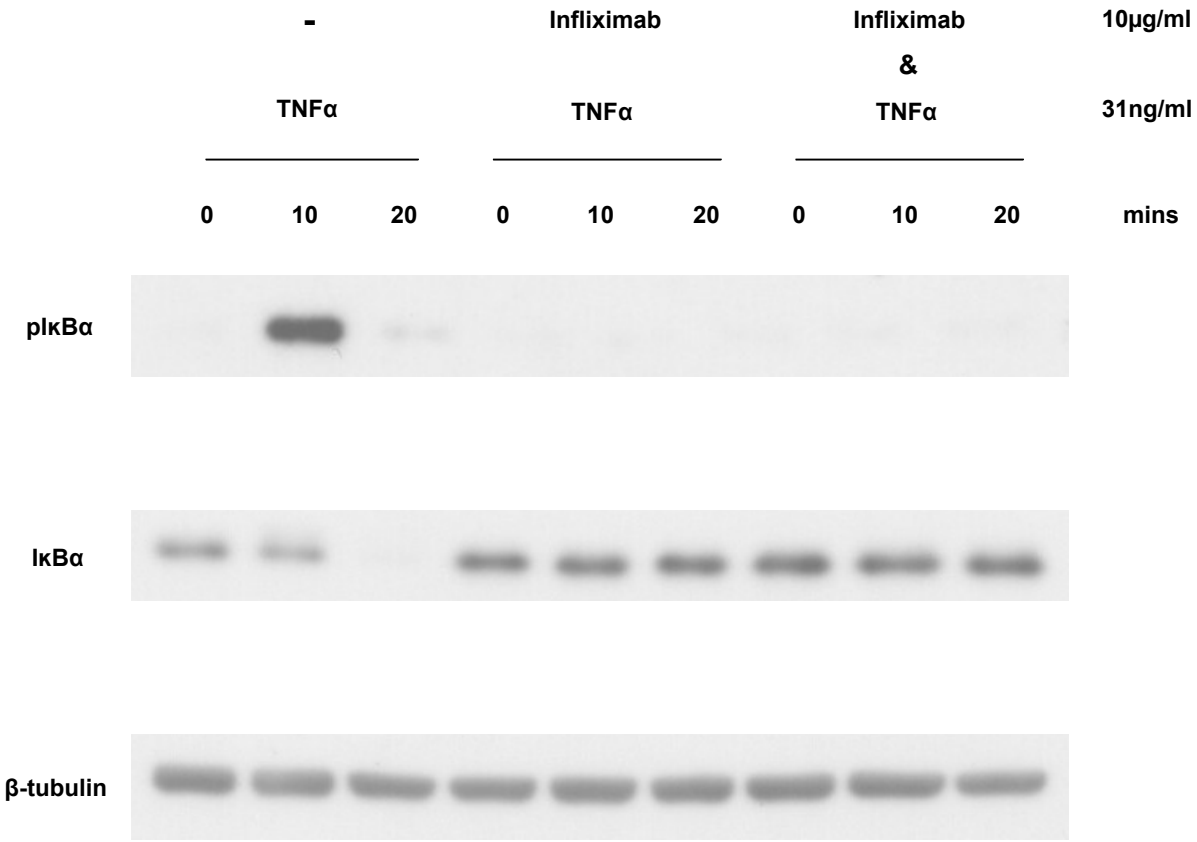

Figure 6.88 Infliximab inhibits TNFα induced phosphorylation and reciprocal degradation of IκBα in A431 cells

Western blots of lysates of A431 cells which had been treated with infliximab at a concentration of 10µg/ml for 1 hour prior to stimulation with TNFα (31ng/ml). Infliximab prevented TNFα induced phosphorylation and reciprocal degradation of IκBα. Control samples in which cells had not been treated with infliximab or were treated with both infliximab and TNFα simultaneously are also included.

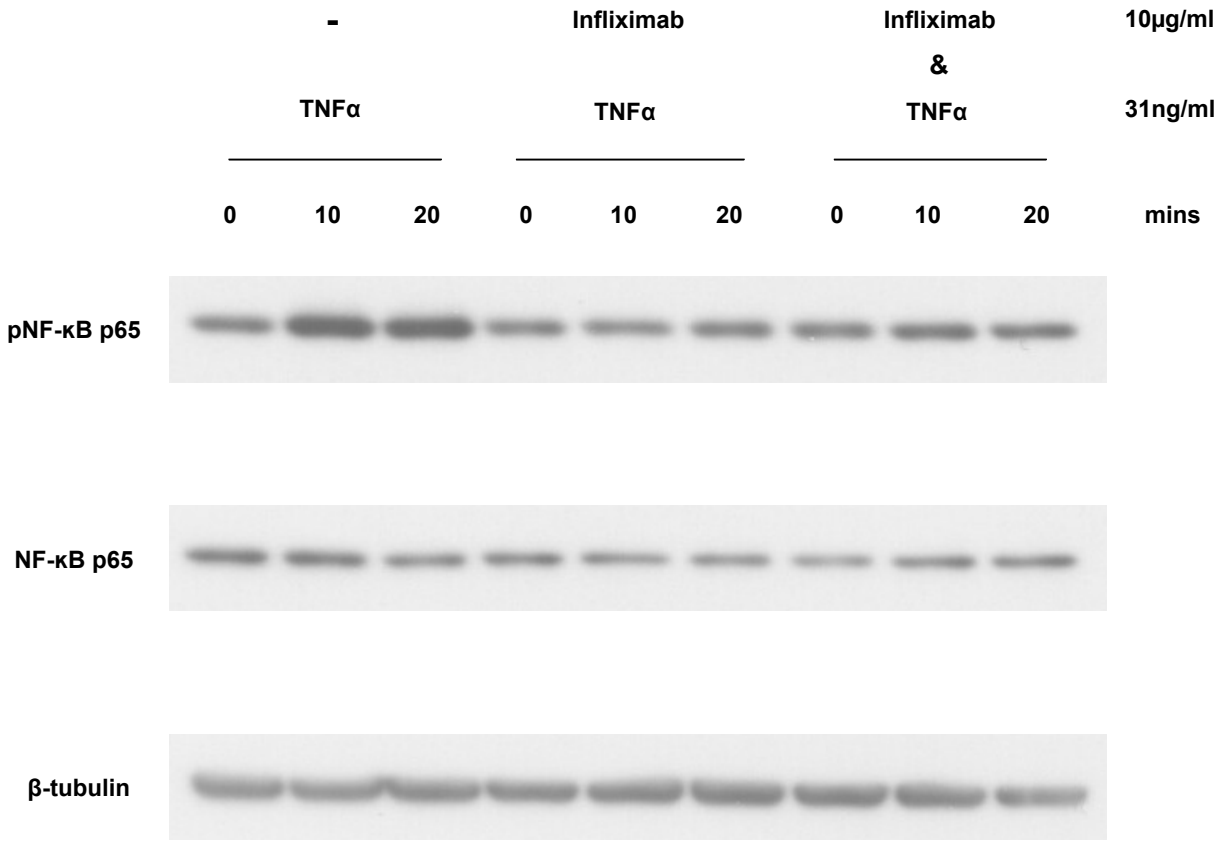

Figure 6.89 Infliximab inhibits TNFα induced activation of NF-κB in A431 cells

Western blots of lysates of A431 cells which had been treated with infliximab at a concentration of 10µg/ml for 1 hour prior to stimulation with TNFα (31ng/ml). Control samples in which cells had not been treated with infliximab or were treated with both infliximab and TNFα simultaneously are also included.

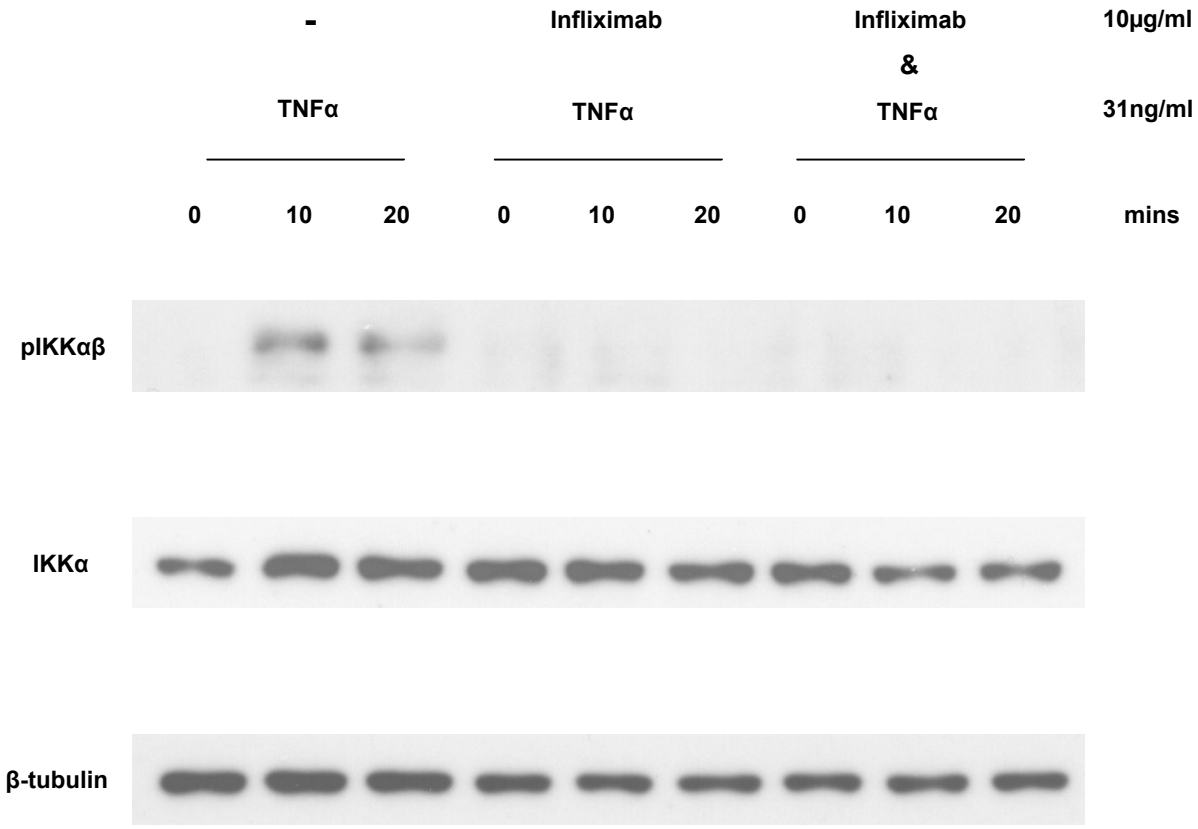

Figure 6.90 Infliximab inhibits TNFα induced activation of IKK in HNCAF

Western blots of lysates of HNCAF which had been treated with infliximab at a concentration of 10µg/ml for 1 hour prior to stimulation with TNFα (31ng/ml). Infliximab prevented TNFα induced activation of IKK and consequently inhibited NF-κB signalling. Control samples in which cells had not been treated with infliximab or were treated with both infliximab and TNFα simultaneously are also included.

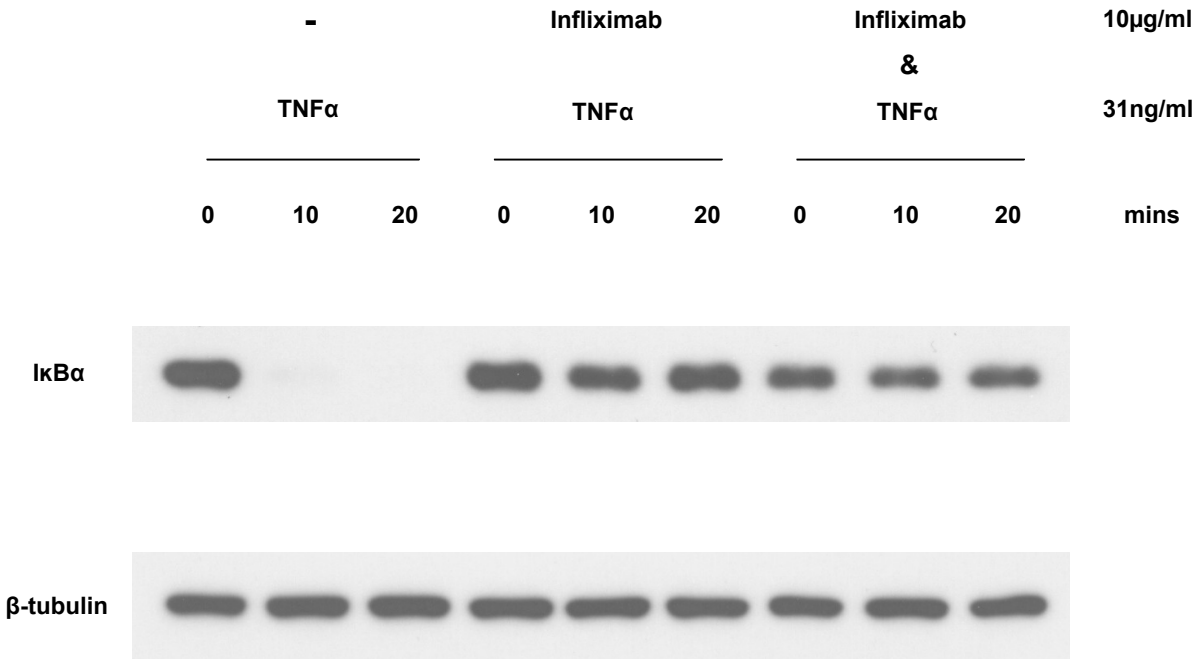

Figure 6.91 Infliximab inhibits TNFα induced degradation of IκBα in HNCAF

Western blots of lysates of HNCAF which had been treated with infliximab at a concentration of 10µg/ml for 1 hour prior to stimulation with TNFα (31ng/ml). Infliximab prevented TNFα induced degradation of IκBα. Control samples in which cells had not been treated with infliximab or were treated with both infliximab and TNFα simultaneously are also included.

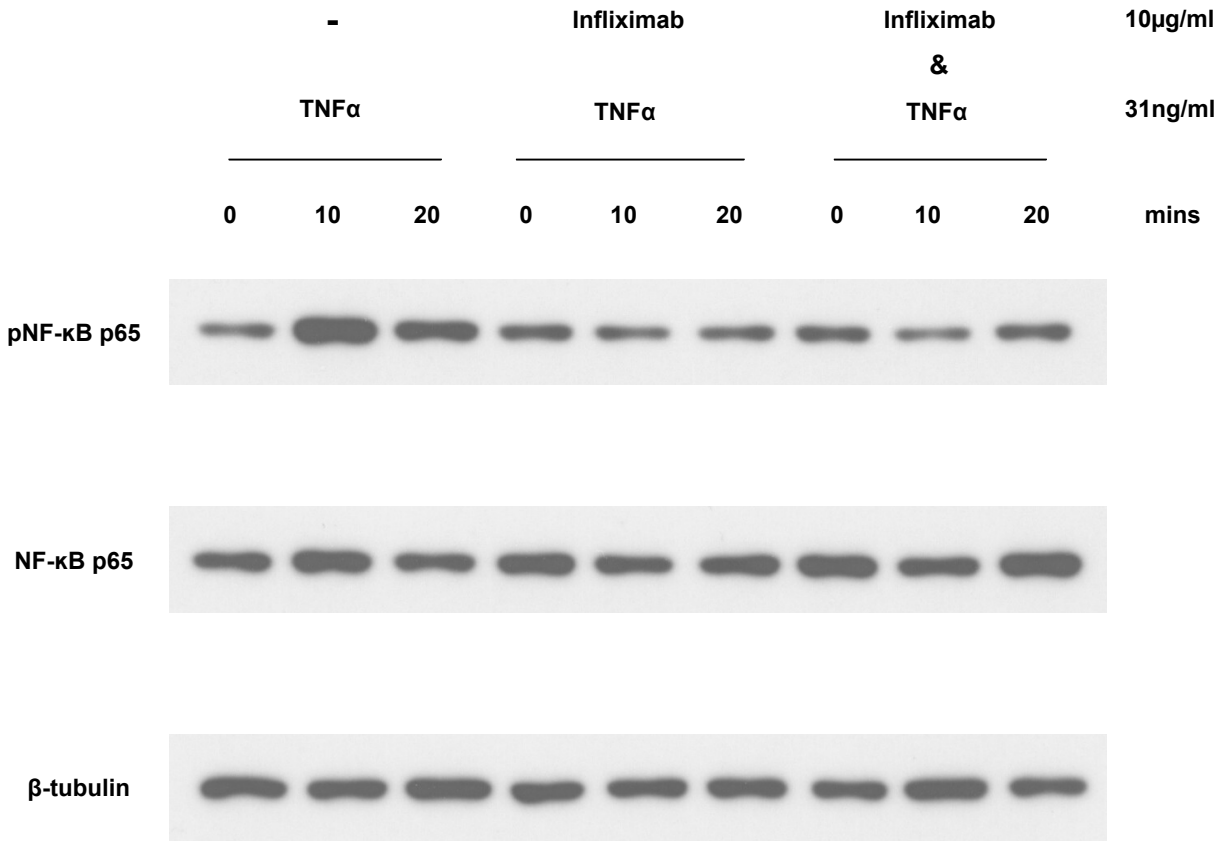

Figure 6.92 Infliximab inhibits TNFα induced activation of NF-κB in HNCAF

Western blots of lysates of HNCAF which had been treated with infliximab at a concentration of 10µg/ml for 1 hour prior to stimulation with TNFα (31ng/ml). Control samples in which cells had not been treated with infliximab or were treated with both infliximab and TNFα simultaneously are also included.

6.6 Summary

- TNFα promotes A431 carcinoma invasion *in vitro* in a dose responsive manner.

- TNFα promotes SCC12 carcinoma invasion *in vitro* in a dose responsive manner via a combined effect on both the epithelial and stromal components of the organotypic culture.

- TNFα promotes fibroblast-dependent collagen-Matrigel® matrix contraction in a dose responsive manner which correlates positively with carcinoma invasion.

- IL-1α promotes SCC12 carcinoma invasion *in vitro* in a dose responsive manner but, in contrast to TNFα, does not potentiate the invasive promoting and ECM remodelling functions of HNCAF.

- SCC invasion in our organotypic sytem is NF-κB dependent. Inhibition of NF-κB signalling at the level of the IKK complex reduces A431 and SCC12 carcinoma invasion *in vitro* in a dose responsive manner.

- The disparity between the effects of TNFα and IL-1α stimulation on the ability of HNCAF to promote carcinoma invasion was a reflection of the underlying NF-κB response.

- Infliximab, (a monoclonal anti-TNFα antibody in clinical use), blocks NF-κB signalling in both A431 cells and HNCAF, inhibits fibroblast-dependent collagen-Matrigel® matrix contraction and reduces SCC12 carcinoma invasion *in vitro* in a dose responsive manner.

Chapter 7

TRAF6, ZA20d1 and NF-κB signalling in SCC invasion

7.1 Introduction

The results in Chapter 5 confirmed that both TRAF6 and ZA20d1 were functionally important for SCC12 and A431 cell invasion in our organotypic carcinoma model. Moreover, the investigations undertaken in Chapter 6 demonstrated that the extent of carcinoma infiltration into the collagen-Matrigel® ECM was NF-κB dependent and could be driven by stimulation with both TNFα and IL-1α. The data also suggested that TNFα promoted SCC12 carcinoma invasion by exerting a duel influence on both the stromal and epithelial compartments of the system. This was not the case with respect to IL-1α, to which the stromal fibroblasts were essentially unresponsive. Furthermore, gel contraction data indicated that TNFα stimulation potentiated fibroblast-dependent force-mediated matrix remodelling of the ECM.

In view of the above and given current literature concerning the regulatory functions of my candidate genes in NF-κB signalling, I investigated the influence of TNFα stimulation on carcinoma invasion using SCC12 cells depleted of either TRAF6 or ZA20d1.

7.2 The influence of TNFα on carcinoma invasion of siRNA gene depleted SCC12 cells

Two-stage organotypic assays were performed in which collagen-Matrigel® gels were stimulated daily with TNFα (31ng/ml) to promote fibroblast-dependent matrix remodelling. After five days, the HNCAF were removed by treating with puromycin (5μg/ml) for 48 hours prior to the addition of siRNA gene depleted SCC12 cells. Cultures were set up in duplicate with one half being stimulated daily with TNFα (31ng/ml) thereafter.

Figures 7.1-7.3 show the quantification and statistical analysis of SCC12 invasion in the 'Control' gels of these assays. Interestingly, prolonged daily TNFα stimulation of HNCAF and SCC12 did not result in statistically significant carcinoma invasion when compared to an unstimulated control (Figure 7.2).

7.2.1 TNFα rescues carcinoma invasion in TRAF6 gene depleted SCC12 cells

Figure 7.4 shows the quantification of TRAF6 gene depleted SCC12 cell invasion in organotypic cultures with and without daily stimulation with TNFα (31ng/ml). Figure 7.5 consists of (a) scatter plots of the individual experimental blocks and (b) randomized block ANOVA statistical analyses. As expected, TRAF6 gene depletion resulted in a statistically significant reduction in carcinoma invasion compared to the control under basal conditions. In contrast, the invasion of TNFα stimulated TRAF6 gene depleted SCC12 cells was not impaired.

Figure 7.6 illustrates the magnitude of the carcinoma invasion response of SCC12 cells following stimulation with TNFα (31ng/ml) normalised to each individual TRAF6 siRNA duplex.

7.2.2 TNFα rescues carcinoma invasion in ZA20d1 gene depleted SCC12 cells

Figure 7.7 shows the quantification of ZA20d1 gene depleted SCC12 cell invasion in organotypic cultures with and without daily stimulation with TNFα (31ng/ml). Figure 7.8 consists of (a) scatter plots of the individual experimental blocks and (b) randomized block ANOVA statistical analyses. As expected, ZA20d1 gene depletion resulted in a statistically significant reduction in carcinoma invasion compared to the control under basal conditions. In contrast, the invasion of TNFα stimulated ZA20d1 gene depleted SCC12 cells was not impaired.

Figure 7.9 illustrates the magnitude of the carcinoma invasion response of SCC12 cells following stimulation with TNFα (31ng/ml) normalised to each individual ZA20d1 siRNA duplex.

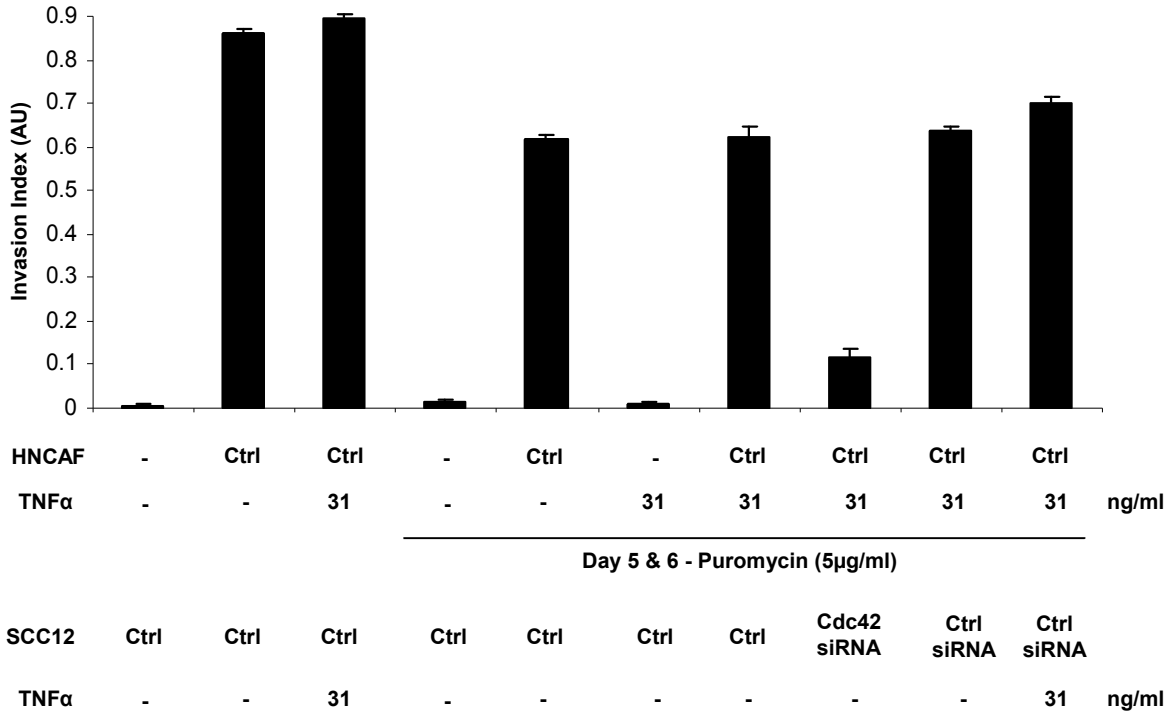

Figure 7.1 Organotypic invasion assay: TNFα stimulation of siRNA gene depleted SCC12 cells - 'Control' gels

Quantification of carcinoma invasion in organotypic cultures which acted as the controls for the assessment of the influence of TNFα stimulation on siRNA gene depleted SCC12 cells as illustrated in Figures 7.4 and 7.7. The average of 10 visual fields from 2 experiments is shown. The error bars represent the s.e.

a

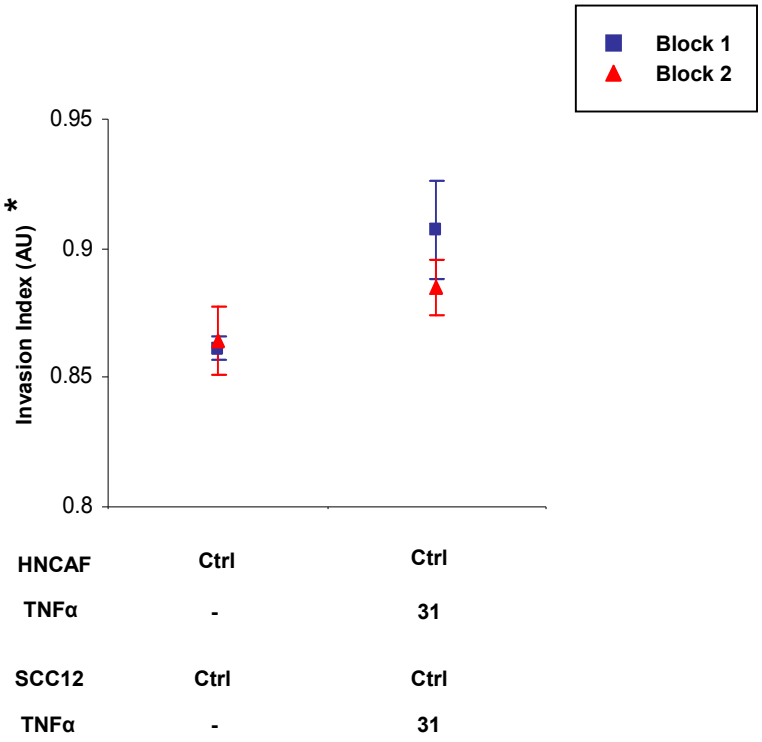

b

Randomized Block ANOVA	p Value	Decision p<0.05
Control vs TNFα 31	0.233892	Do not reject

Figure 7.2 Prolonged daily TNFα stimulation of HNCAF and SCC12 does not result in statistically significant carcinoma invasion when compared to an unstimulated control

(**a**) Scatter plots displaying quantification of carcinoma invasion in cultures from the organotypic assay illustrated in Figure 7.1. Both the stromal and epithelial components of the TNFα-stimulated culture were treated daily for 11 days. Individual experimental blocks are illustrated. The average of 5 visual fields is shown and error bars represent the s.e. *Denotes an expanded Y-axis. (**b**) Randomized block ANOVA statistical analysis. Null hypothesis (NØ) rejected if $p < 0.05$.

a

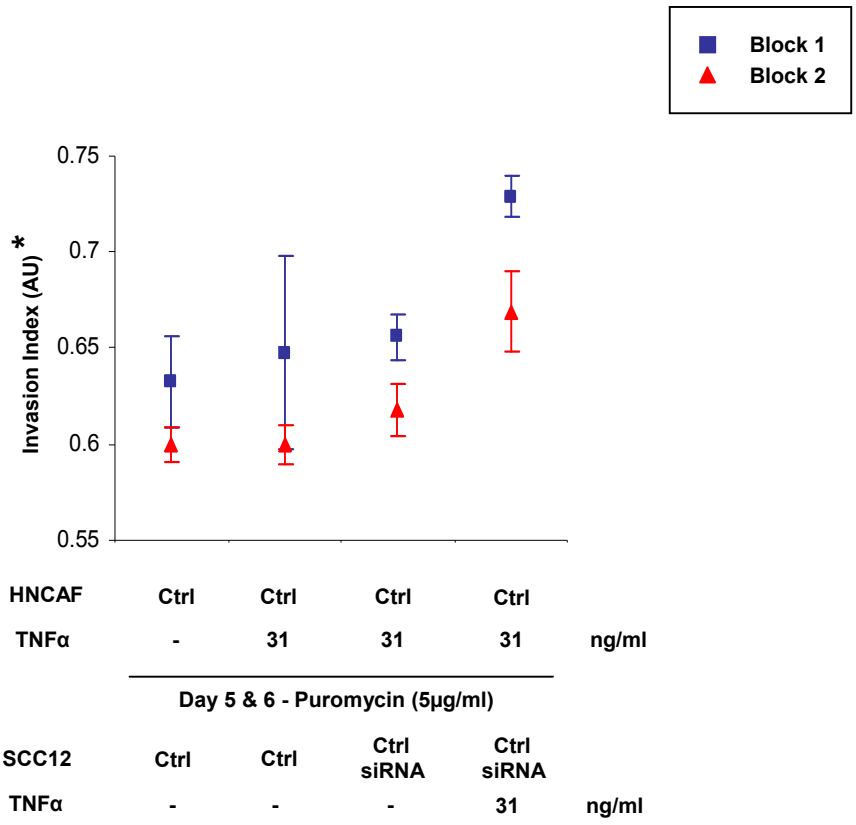

b

Randomized Block ANOVA	p Value	Decision p<0.05
Control vs HNCAF (T) Control	0.493025	Do not reject
HNCAF (T) Control vs HNCAF (T) Control siRNA	0.236554	Do not reject
HNCAF (T) Control siRNA vs HNCAF (T) Control siRNA (T)	0.113050	Do not reject

(T) - Daily stimulation with TNFα (31ng/ml)

Figure 7.3 Organotypic invasion assay: TNFα stimulation of siRNA gene depleted SCC12 cells - 'Control' gels. (a) Scatter plot and (b) randomized block ANOVA statistical analysis

(**a**) Scatter plot displaying quantification of carcinoma invasion in cultures from the organotypic assay illustrated in Figure 7.1. Individual experimental blocks are illustrated. The average of 5 visual fields is shown and error bars represent the s.e. *Denotes an expanded Y-axis. (**b**) Randomized block ANOVA statistical analysis. Null hypothesis (NØ) rejected if $p < 0.05$.

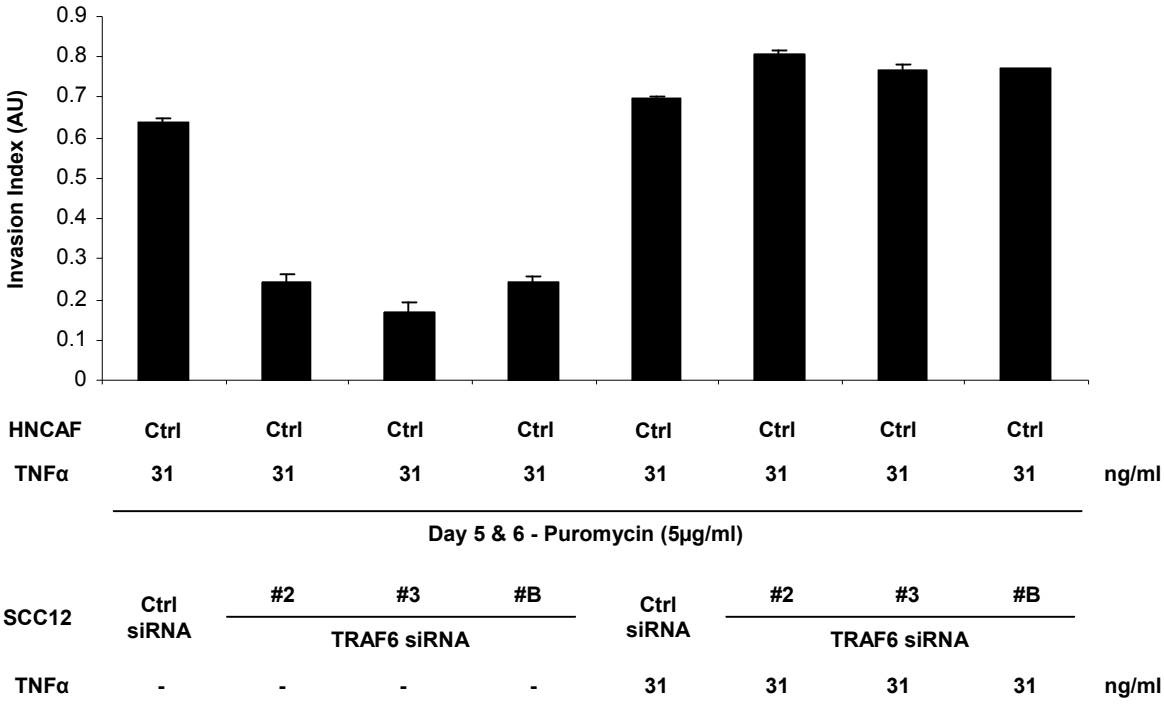

Figure 7.4 Organotypic invasion assay: TNFα stimulation of TRAF6 gene depleted SCC12 cells

Quantification of carcinoma invasion in organotypic gels in which stromal fibroblasts were stimulated daily with TNFα (31ng/ml) and then treated with puromycin (5µg/ml) daily for 48 hours after 5 days of matrix remodelling. Fibroblasts were removed prior to the addition of TRAF6 siRNA gene depleted SCC12 cells. Cultures were performed in duplicate with one half being stimulated daily by TNFα (31ng/ml) thereafter. The average of 10 visual fields from 2 experiments is shown. The error bars represent the s.e.

a

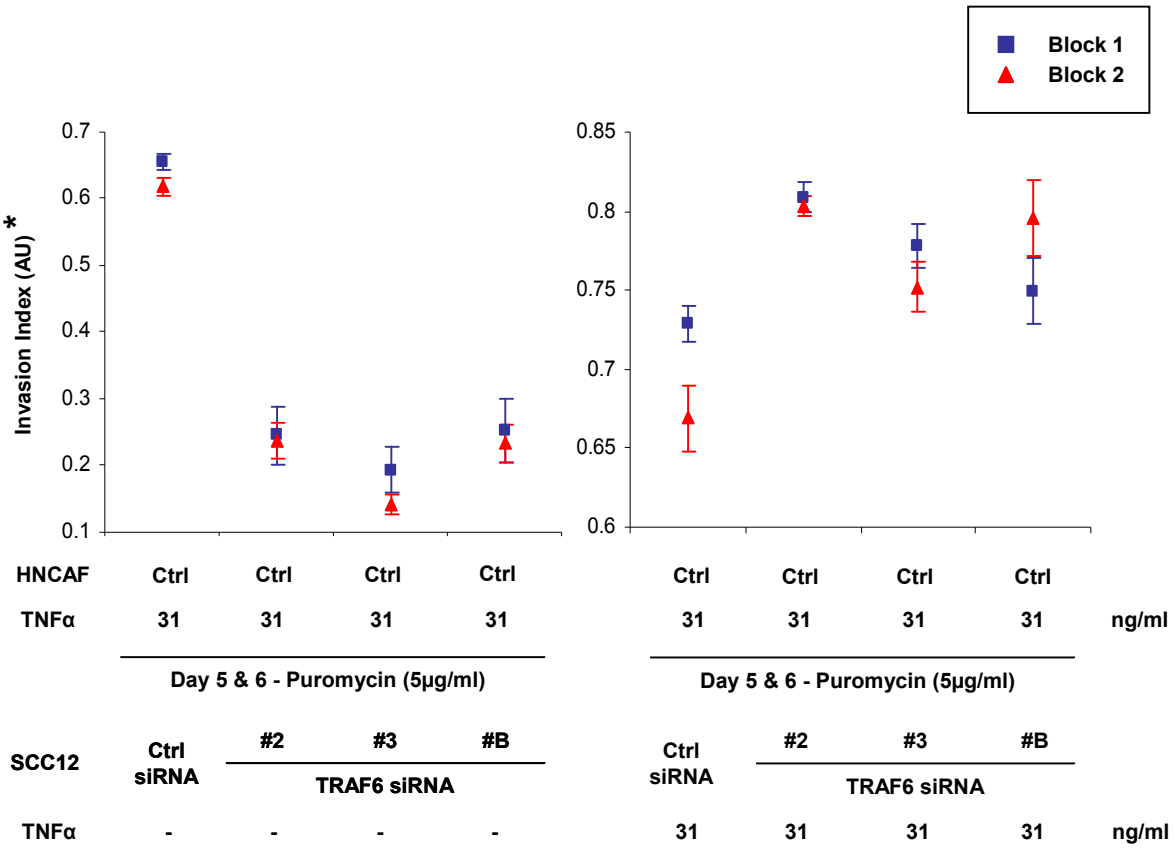

b

Unstimulated SCC12

Randomized Block ANOVA	p Value	Decision p<0.0083
Control siRNA vs TRAF6 siRNA #2	0.000073	Reject
Control siRNA vs TRAF6 siRNA #3	0.000027	Reject
Control siRNA vs TRAF6 siRNA #B	0.000075	Reject

TNFα stimulated SCC12

Control siRNA vs TRAF6 siRNA #2	0.010654	Do not reject
Control siRNA vs TRAF6 siRNA #3	0.064481	Do not reject
Control siRNA vs TRAF6 siRNA #B	0.045352	Do not reject

Figure 7.5 Organotypic invasion assay: TNFα stimulation of TRAF6 gene depleted SCC12 cells. (a) Scatter plot and (b) randomized block ANOVA statistical analysis

(**a**) Scatter plots displaying quantification of carcinoma invasion in cultures from the organotypic assay illustrated in Figure 7.4. Individual experimental blocks are illustrated. The average of 5 visual fields is shown and error bars represent the s.e. *Denotes an expanded Y-axis. (**b**) Randomized block ANOVA statistical analysis. Null hypothesis (NØ) rejected if $p < 0.05$.

a

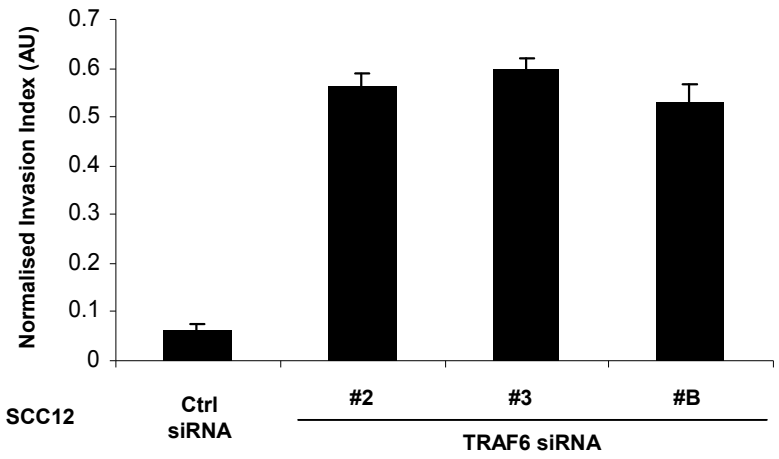

b

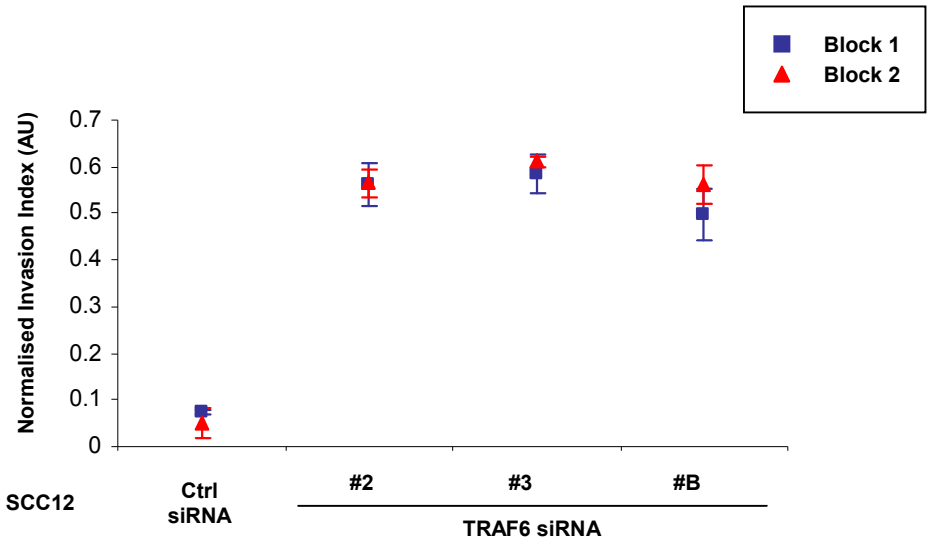

c

Randomized Block ANOVA	p Value	Decision p<0.0083
Control siRNA vs TRAF6 siRNA #2	0.000004	Reject
Control siRNA vs TRAF6 siRNA #3	0.000003	Reject
Control siRNA vs TRAF6 siRNA #B	0.000007	Reject

Figure 7.6 TNFα stimulation at a concentration of 31ng/ml rescues carcinoma invasion in TRAF6 gene depleted SCC12 cells

(**a**) Bar chart depicting the magnitude of the carcinoma invasion response of SCC12 cells following stimulation with TNFα (31ng/ml) normalised to the siRNA duplex for cultures from the organotypic assay illustrated in Figure 7.4. The average of 10 visual fields is shown. The error bars represent the s.e. (**b**) Scatter plot. Individual experimental blocks are illustrated. The average of 5 visual fields is shown and error bars represent the s.e. (**c**) Randomized block ANOVA statistical analysis. Null hypothesis (NØ) rejected if $p < 0.05$.

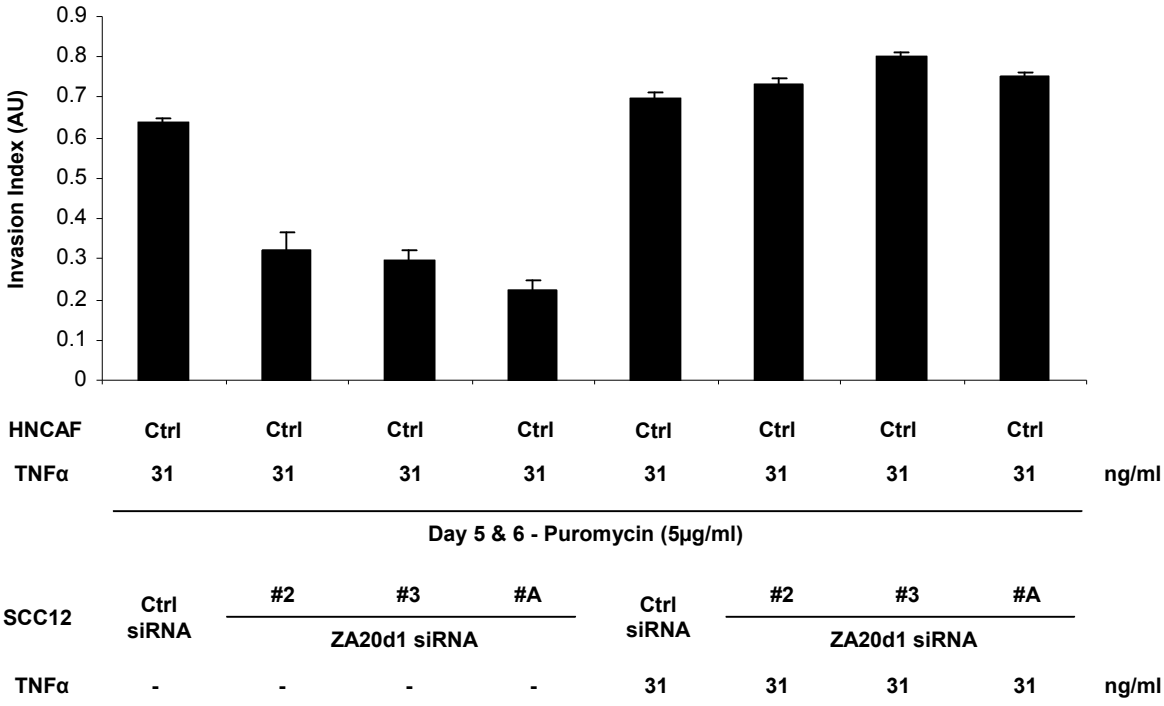

Figure 7.7 Organotypic invasion assay: TNFα stimulation of ZA20d1 gene depleted SCC12 cells

Quantification of carcinoma invasion in organotypic gels in which stromal fibroblasts were stimulated daily with TNFα (31ng/ml) and then treated with puromycin (5µg/ml) daily for 48 hours after 5 days of matrix remodelling. Fibroblasts were removed prior to the addition of ZA20d1 siRNA gene depleted SCC12 cells. Cultures were performed in duplicate with one half being stimulated daily by TNFα (31ng/ml) thereafter. The average of 10 visual fields from 2 experiments is shown. The error bars represent the s.e.

a

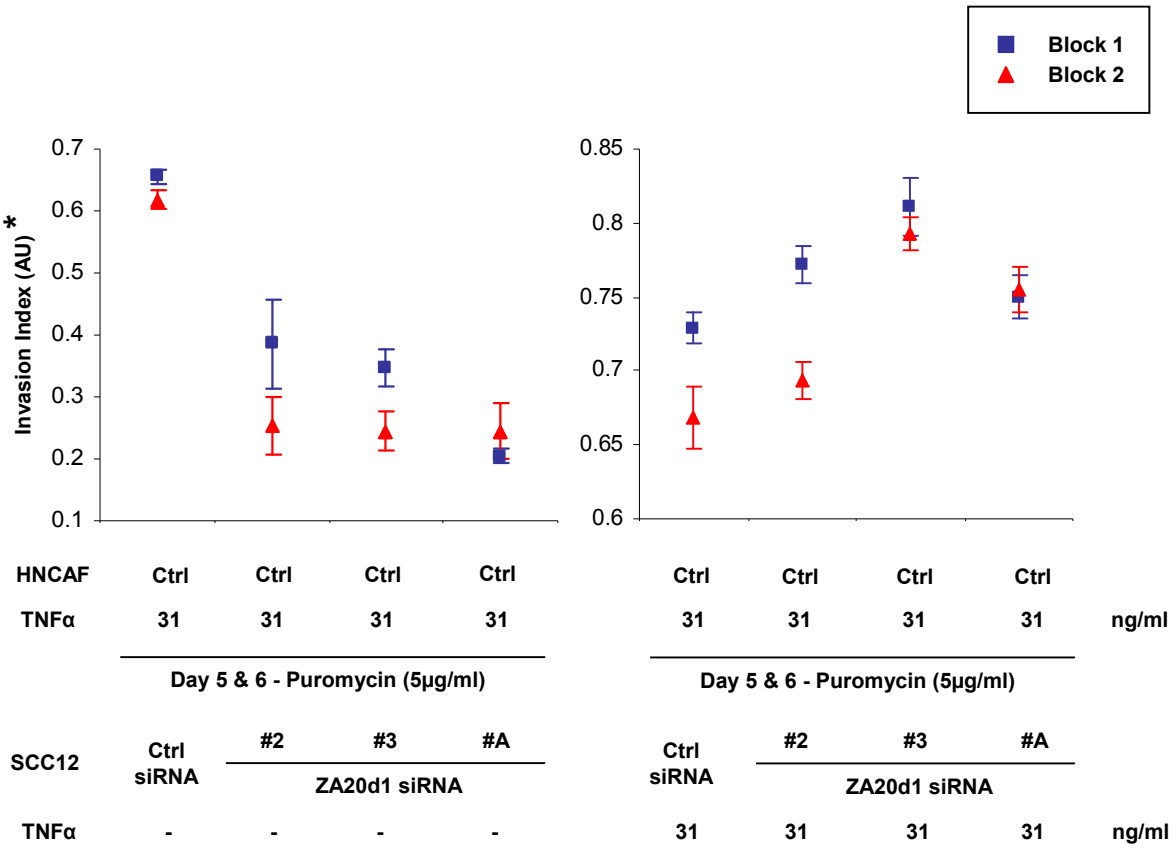

b

Unstimulated SCC12

Randomized Block ANOVA	p Value	Decision p<0.0083
Control siRNA vs ZA20d1 siRNA #2	0.000249	Reject
Control siRNA vs ZA20d1 siRNA #3	0.000169	Reject
Control siRNA vs ZA20d1 siRNA #A	0.000057	Reject

TNFα stimulated SCC12

Control siRNA vs ZA20d1 siRNA #2	0.292387	Do not reject
Control siRNA vs ZA20d1 siRNA #3	0.012711	Do not reject
Control siRNA vs ZA20d1 siRNA #A	0.011727	Do not reject

Figure 7.8 Organotypic invasion assay: TNFα stimulation of ZA20d1 gene depleted SCC12 cells. (a) Scatter plot and (b) randomized block ANOVA statistical analysis

(**a**) Scatter plots displaying quantification of carcinoma invasion in cultures from the organotypic assay illustrated in Figure 7.7. Individual experimental blocks are illustrated. The average of 5 visual fields is shown and error bars represent the s.e. *Denotes an expanded Y-axis. (**b**) Randomized block ANOVA statistical analysis. Null hypothesis (NØ) rejected if $p < 0.0083$.

a

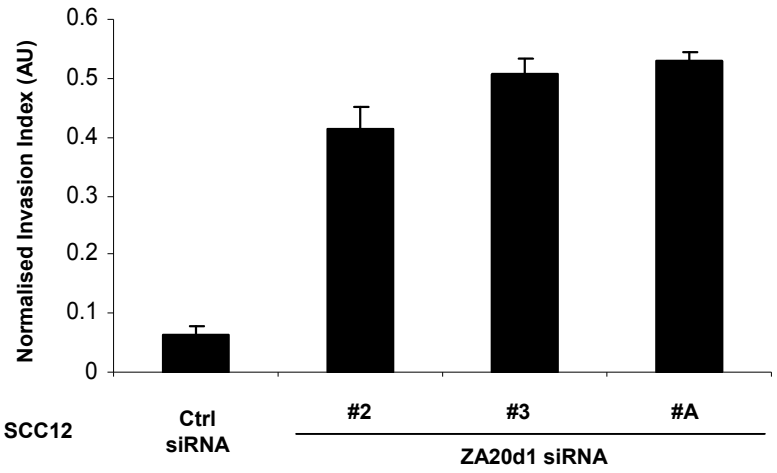

b

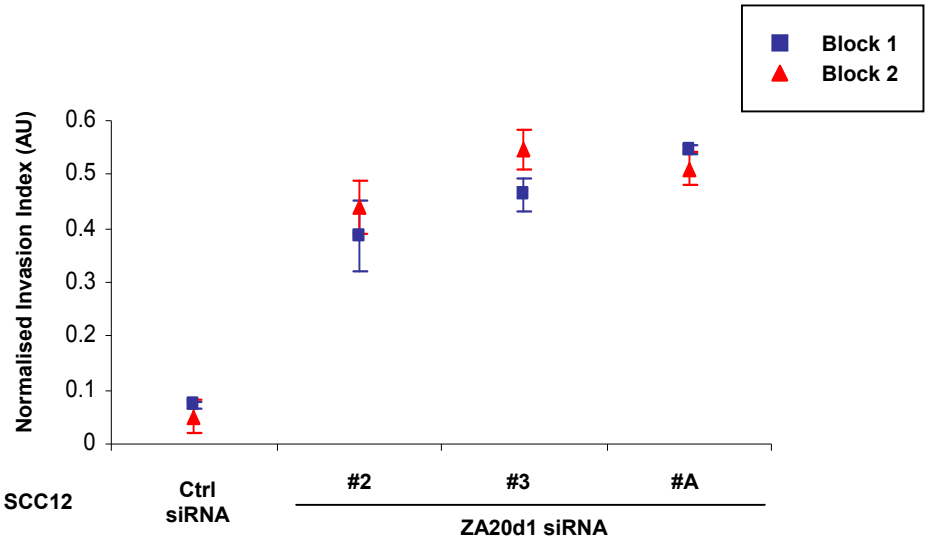

c

Randomized Block ANOVA	p Value	Decision p<0.0083
Control siRNA vs ZA20d1 siRNA #2	0.000035	Reject
Control siRNA vs ZA20d1 siRNA #3	0.000009	Reject
Control siRNA vs ZA20d1 siRNA #B	0.000007	Reject

Figure 7.9 TNFα stimulation at a concentration of 31ng/ml rescues carcinoma invasion in ZA20d1 gene depleted SCC12 cells

(**a**) Bar chart depicting the magnitude of the carcinoma invasion response of SCC12 cells following stimulation with TNFα (31ng/ml) normalised to the siRNA duplex for cultures from the organotypic assay illustrated in Figure 7.7. The average of 10 visual fields is shown. The error bars represent the s.e. (**b**) Scatter plot. Individual experimental blocks are illustrated. The average of 5 visual fields is shown and error bars represent the s.e. (**c**) Randomized block ANOVA statistical analysis. Null hypothesis (NØ) rejected if $p < 0.0083$.

7.3 The influence of TRAF6 and ZA20d1 gene depletion on NF-κB signalling

7.3.1 TRAF6 gene depletion in SCC12 cells influences the degradation of IκBα

Figure 7.10 demonstrates a reduction in the phosphorylation and reciprocal degradation of IκBα in TRAF6 gene depleted SCC12 cells compared to the control 96 hours following transfection. Figure 7.11 confirms the efficacy of TRAF6 gene depletion in these samples. Cell lysates were made in parallel with Block 2 of the organotypic assay illustrated in Figure 7.4.

7.3.2 ZA20d1 gene depletion in SCC12 cells does not influence the degradation of IκBα

Figure 7.12 shows the phosphorylation and reciprocal degradation of IκBα in ZA20d1 gene depleted SCC12 cells 96 hours following transfection. In contrast to TRAF6 gene depletion, silencing of ZA20d1 did not affect IκBα degradation. Cell lysates were made in parallel with Block 2 of the organotypic assay illustrated in Figure 7.7.

7.3.3 TRAF6 gene depletion in A431 cells influences the degradation of IκBα

Figure 7.13 shows the phosphorylation and reciprocal degradation of IκBα in TRAF6 and ZA20d1 gene depleted A431 cells 96 hours following transfection. Unlike ZA20d1, silencing of TRAF6 was associated with a reduction in the degradation of IκBα compared to the control. Figure 7.14 confirms the efficacy of TRAF6 gene depletion in these samples. Cell lysates were made in parallel with Block 2 of the organotypic assay illustrated in Figure 5.22.

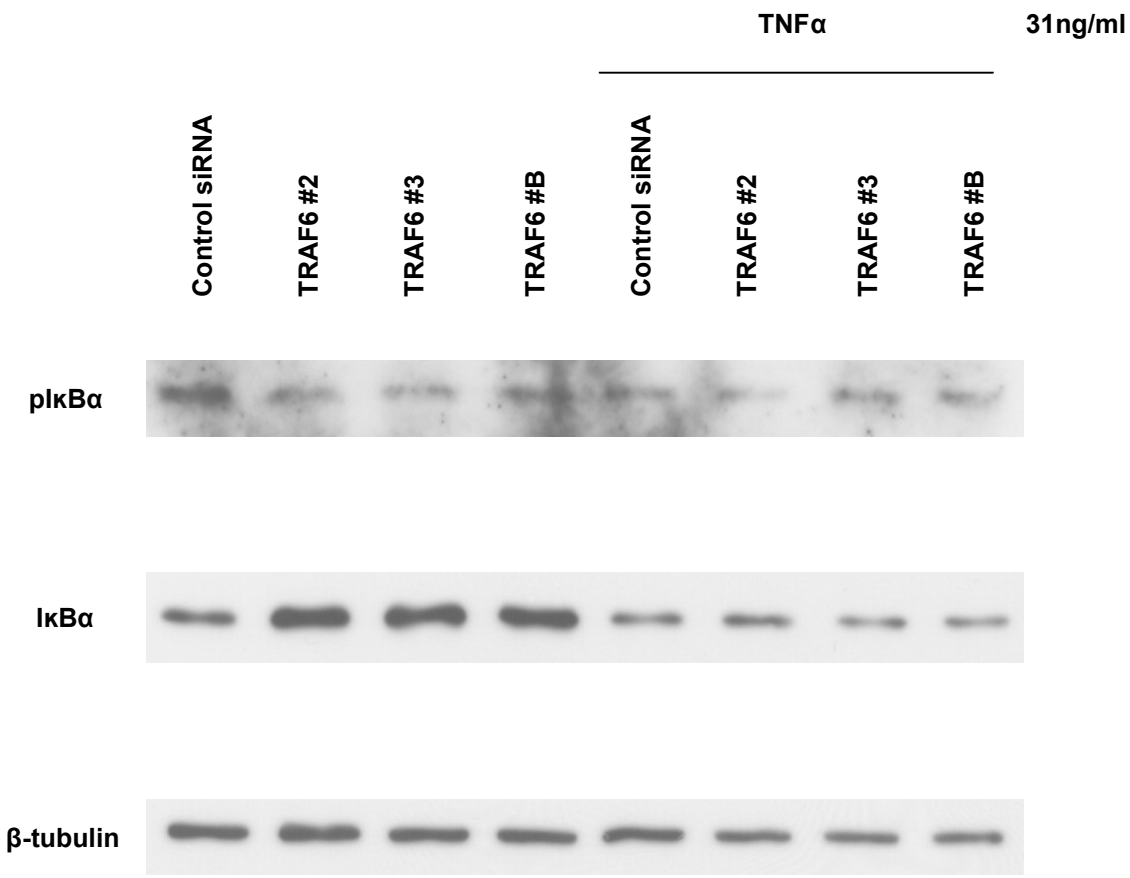

Figure 7.10 TRAF6 siRNA gene depletion in SCC12 cells is associated with a reduction in the phosphorylation and reciprocal degradation of IκBα

Western blots of SCC12 cell lysates 96 hours post-transfection showing a reduction in the phosphorylation and reciprocal degradation of IκBα in TRAF6 gene depleted cells. Lanes 6-8 contain lysates in which TRAF6 gene depleted SCC12 cells had been stimulated daily with TNFα at a concentration of 31ng/ml. In this TNFα enriched environment, IκBα phosphorylation and degradation was restored to a similar magnitude to that observed in the control siRNA samples. These lysates were made in parallel with Block 2 of the organotypic assay illustrated in Figure 7.4.

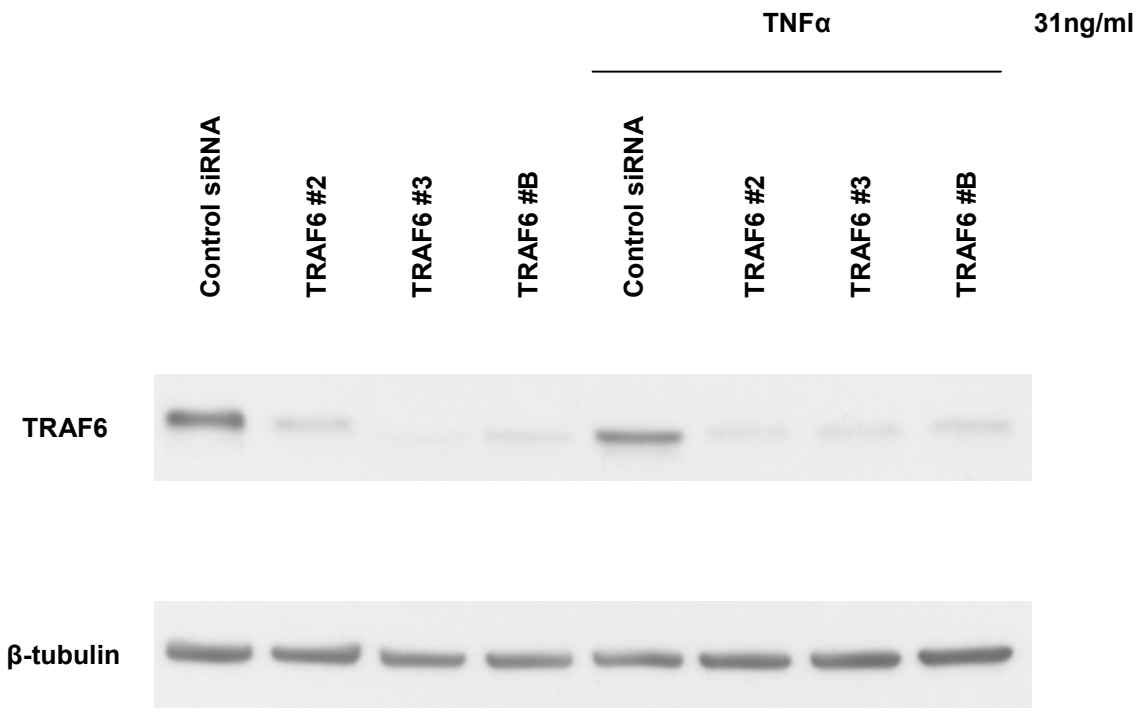

Figure 7.11 Western blot demonstrating the efficacy of TRAF6 siRNA gene depletion in SCC12 cells

Western blot of SCC12 cell lysates 96 hours post-transfection showing the efficient knockdown of TRAF6. These lysates were made in parallel with Block 2 of the organotypic assay illustrated in Figure 7.4.

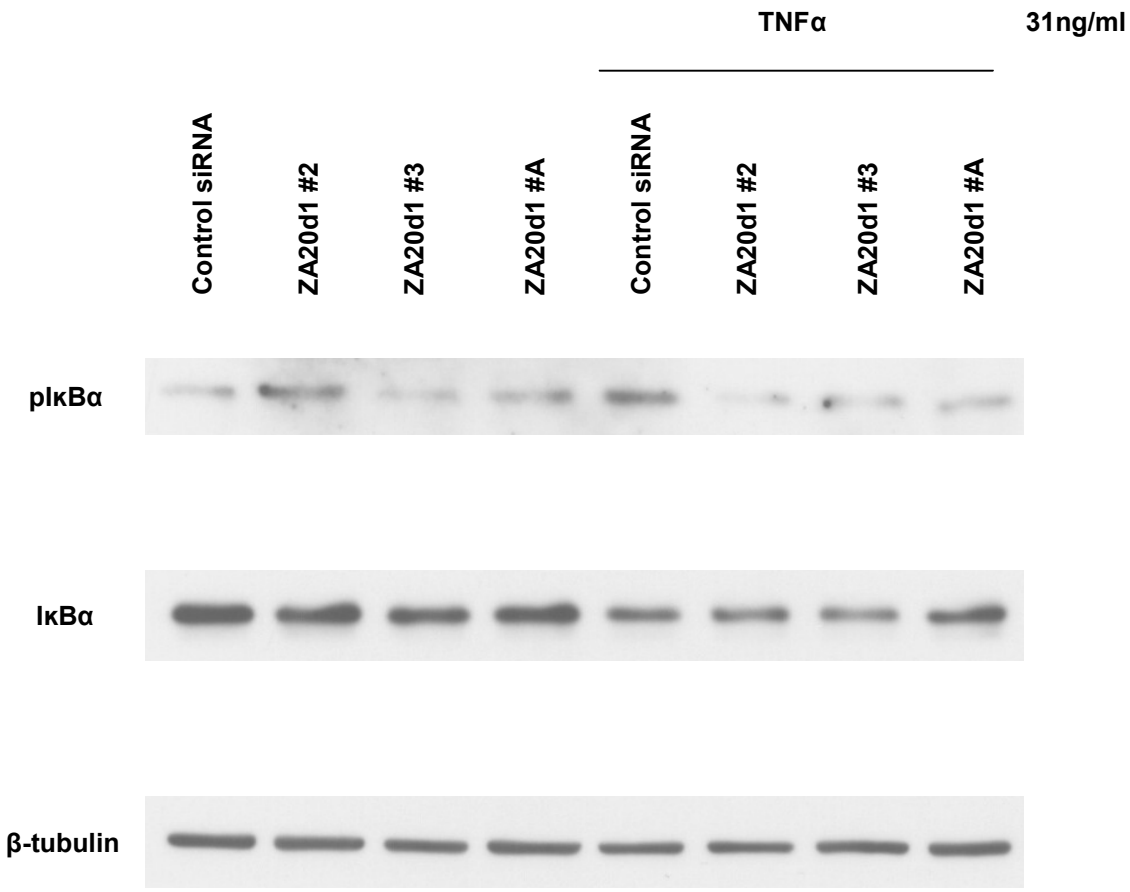

Figure 7.12 ZA20d1 siRNA gene depletion in SCC12 cells is not associated with a reduction in the phosphorylation and reciprocal degradation of IκBα

Western blots of SCC12 cell lysates 96 hours post-transfection showing that the phosphorylation and reciprocal degradation of IκBα was unaffected by ZA20d1 gene depletion. Lanes 6-8 contain lysates in which ZA20d1 gene depleted SCC12 cells had been stimulated daily with TNFα at a concentration of 31ng/ml. These lysates were made in parallel with Block 2 of the organotypic assay illustrated in Figure 7.7.

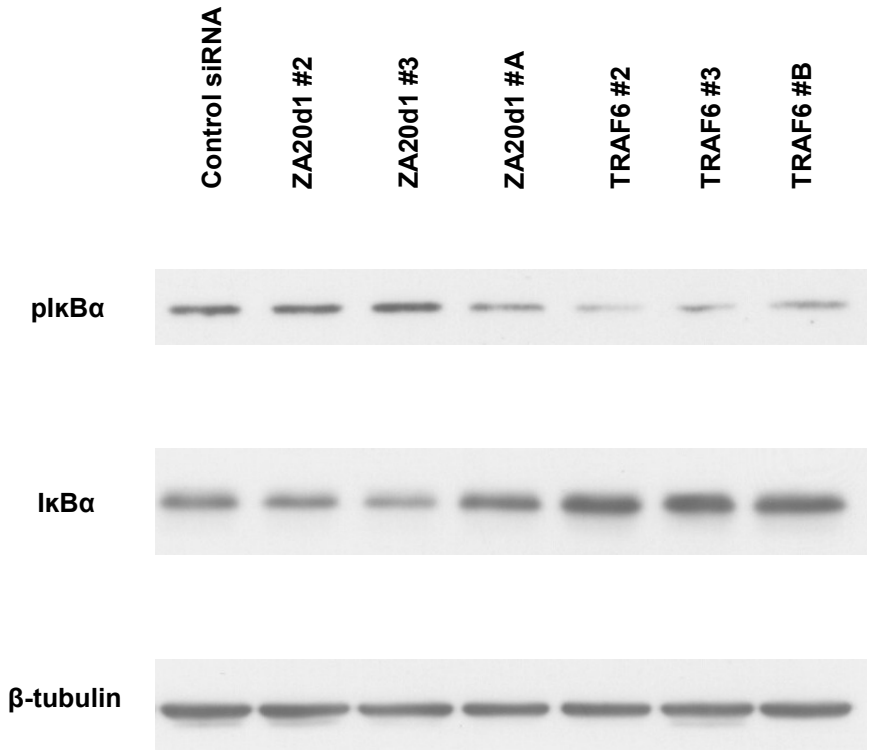

Figure 7.13 TRAF6 siRNA gene depletion in A431 cells is associated with a reduction in the phosphorylation and reciprocal degradation of IκBα

Western blots of A431 cell lysates 96 hours post-transfection showing a reduction in the phosphorylation and reciprocal degradation of IκBα in TRAF6 gene depleted cells. This observation was inconclusive with respect to the lysates of the ZA20d1 gene depleted cells. These lysates were made in parallel with Block 2 of the organotypic assay illustrated in Figure 5.22.

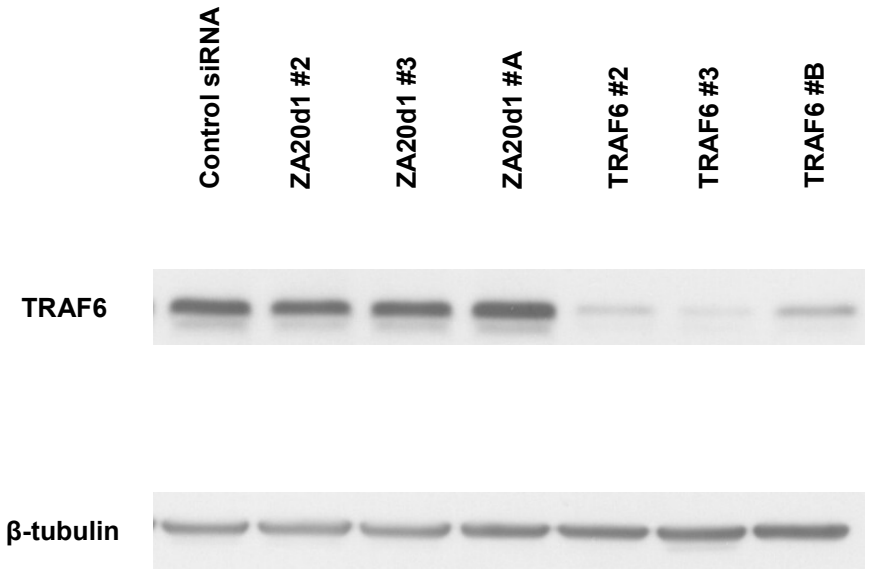

Figure 7.14 Western blot demonstrating the efficacy of TRAF6 siRNA gene depletion in A431 cells

Western blot of A431 cell lysates 96 hours post-transfection showing the efficient knockdown of TRAF6. These lysates were made in parallel with Block 2 of the organotypic assay illustrated in Figure 5.22.

7.4 Summary

- TNFα (31ng/ml) stimulation of either TRAF6 or ZA20d1 gene depleted SCC12 cells rescued carcinoma invasion *in vitro*.

- TRAF6 gene depletion in SCC12 and A431 cells was associated with a reduction in the phosphorylation and reciprocal degradation of IκBα.

- In contrast to TRAF6 gene depletion, silencing of ZA20d1 in SCC12 and A431 cells did not influence IκBα degradation.

Chapter 8

Tissue banking and analysis of tumour samples

8.1 Introduction

Human tissue banks are integral to cancer research [299]. The analysis of tumour samples has led to new insights into cancer development and progression, as well as improved diagnostic techniques and more effective chemotherapeutic agents.

This chapter details the establishment and management of a human tissue bank of SCCHN tumour specimens with patient matched control tissue. These samples and commercial tissue microarrays were analysed to investigate the expression of TRAF6 in several types of SCC as well as its potential as a diagnostic tumour marker.

8.2 Establishing a SCCHN tissue bank

8.2.1 Ethical and R&D approval

NHS Research Ethics Committee (NREC) approval was obtained following Site Specific Assessment (SSA) for the recruitment of patients and the collection of tissue samples at three Acute Teaching NHS Trusts in London (REC reference: 06/Q0403/125).

The Chief or Principal Investigators at each site were as follows: Dr Kevin Harrington (Senior Lecturer and Honorary Consultant in Clinical Oncology) - The Royal Marsden NHS Foundation Trust, Mr Peter Clarke (Consultant ENT / Head & Neck Surgeon) - The Hammersmith Hospitals NHS Trust and Mr Peter Williamson (Consultant ENT / Head & Neck Surgeon) - St George's Healthcare NHS Trust.

NHS R&D approval was authorised by the Committee for Clinical Research (CCR) at the Royal Marsden NHS Trust (CCR reference: 2924) and the Research Office (RO) at St George's Healthcare NHS Trust (RO reference: 07.0003).

The Royal Marsden NHS Foundation Trust granted sponsorship across all sites for the establishment of the tissue bank. A Material Transfer Agreement (MTA) was also set up to cover the transfer of samples from their source to the Cancer Research UK London Research Institute for storage and subsequent analysis. Dr Erik Sahai (Tumour Cell Biology Laboratory) is the Principal Investigator at this site.

8.2.2 Tissue freezing

In preparation for the collection of human tissue samples, I assessed the quality of tissue preservation upon freezing using various fixation reagents. These experiments were performed in conjunction with Dr Erik Sahai.

Figure 8.1 shows photomicrographs of H&E sections of mouse skin fixed in (a) dry ice, (b) isopentane and (c) liquid nitrogen. Snap freezing of samples in liquid nitrogen was most effective at preserving epidermal and dermal tissue architecture.

8.2.3 Banking and storage of tissue

Individuals with histopathologically confirmed SCCHN considered to be medically fit for surgery under general anaesthesia were identified by the Head & Neck Surgeon responsible for their care during regular hospital attendance. Patients under the age of 18 years and those who had received either local radiotherapy or systemic chemotherapy within four weeks prior to their scheduled surgery were excluded from the study.

Posters advertising the need for tissue donation were placed in clinic and ward patient waiting areas (Appendix I). An information sheet detailing the purpose of the tumour bank was provided to patients (Appendix II) and written consent for tissue donation obtained by their Head & Neck Surgeon prior to surgery (Appendix III). A letter confirming the patients' participation in the study was also sent to their general medical practitioner (Appendix IV).

Samples were collected under general anaesthesia whilst the patient underwent head and neck surgery for excision of their primary tumour. Tissue was harvested from: (a) the

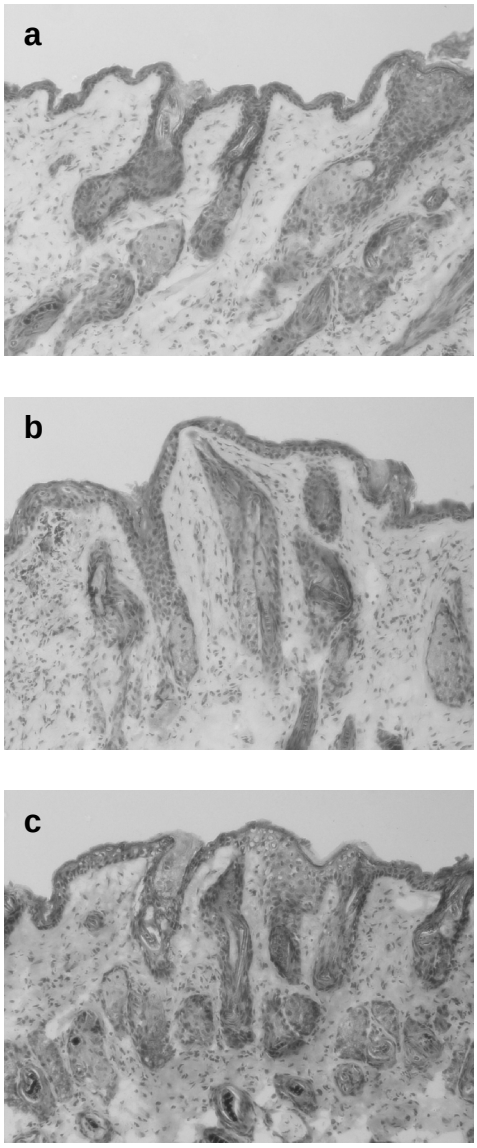

Figure 8.1 Tissue freezing

H&E stained sections of mouse skin comparing tissue fixation reagents (**a**) dry ice, (**b**) isopentane and (**c**) liquid nitrogen. Image magnification 20x.

resected SCC specimen and (b) clinically healthy mucosa adjacent to the surgical margin. Samples were fixed by snap freezing in liquid nitrogen at -80ºC and transferred to the Cancer Research UK London Research Institute for long-term storage in a secure facility. Each specimen has been given a unique research number, the key to which is known only to the Principal Investigator at each NHS Trust site. To date, 40 pairs of matched samples have been accrued. All database systems are password protected and subject to audit trail in line with current NHS Trust policy.

Patients were followed up post-operatively by their Head & Neck Surgeon as dictated by their routine clinical care with no further participation beyond the point of tissue donation. Individuals retain the right to withdraw consent to the use of their tissues at any time.

8.3 TRAF6 immunohistochemistry (IHC)

8.3.1 Optimisation of TRAF6 IHC

Figure 8.2a consists of representative photomicrographs of immunostained sections of A431 cells showing endogenous TRAF6 at primary antibody concentrations of 1:60 and 1:20 72 hours following transfection.

TRAF6 immunostaining was cytosolic in nature and was assessed as detailed in Chapter 2, Section 2.10.5. Figure 8.2b illustrates the quantification of TRAF6 positive regions. TRAF6 expression was best demonstrated with a primary antibody concentration of 1:20.

To validate the above finding, endogenous and exogenous TRAF6 expression in A431 cells 72 hours following transfection with the pUNO-hTRAF6-HA construct was examined (Figure 8.3a). The TRAF6 level in TRAF6-HA positive cells was approximately twice that of untransfected cells (Figure 8.3b).

Finally, I assessed TRAF6 expression in A431 cells 72 hours following siRNA gene depletion (Figure 8.4a). A 60% or greater reduction in normalised mean intensity of immunostaining was noted compared to the mock sample (Figure 8.4b).

a

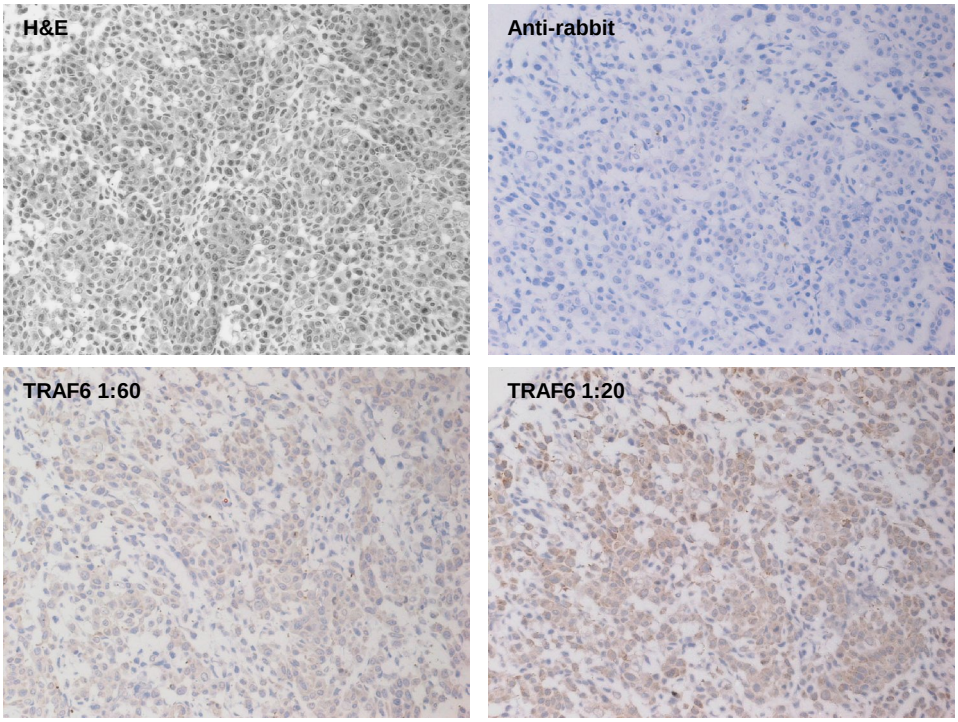

b

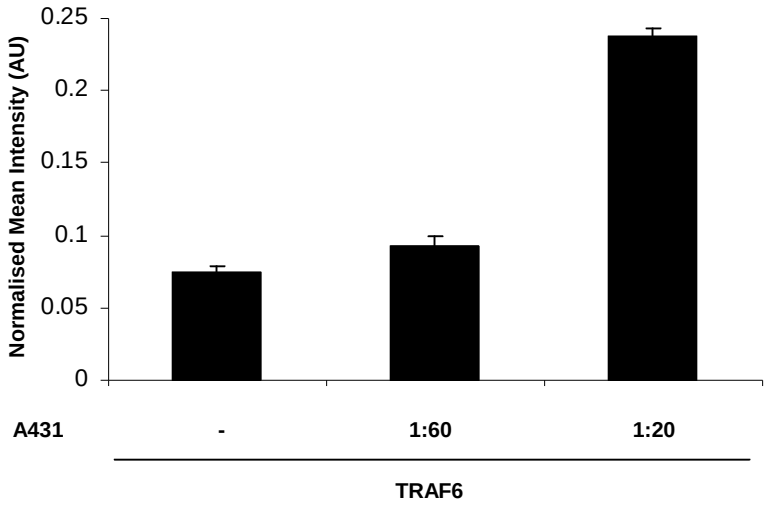

Figure 8.2 Optimisation of TRAF6 IHC in A431 cells

(**a**) Immunostained sections of A431 cells showing the expression of endogenous TRAF6 at primary antibody concentrations of 1:60 and 1:20 72 hours following transfection. Sections stained with H&E and the anti-rabbit secondary antibody are also shown. Image magnification 20x. (**b**) Quantitative analysis of TRAF6 immunostaining. The average of 10 representative immunostained areas is shown and error bars represent the s.e.

a

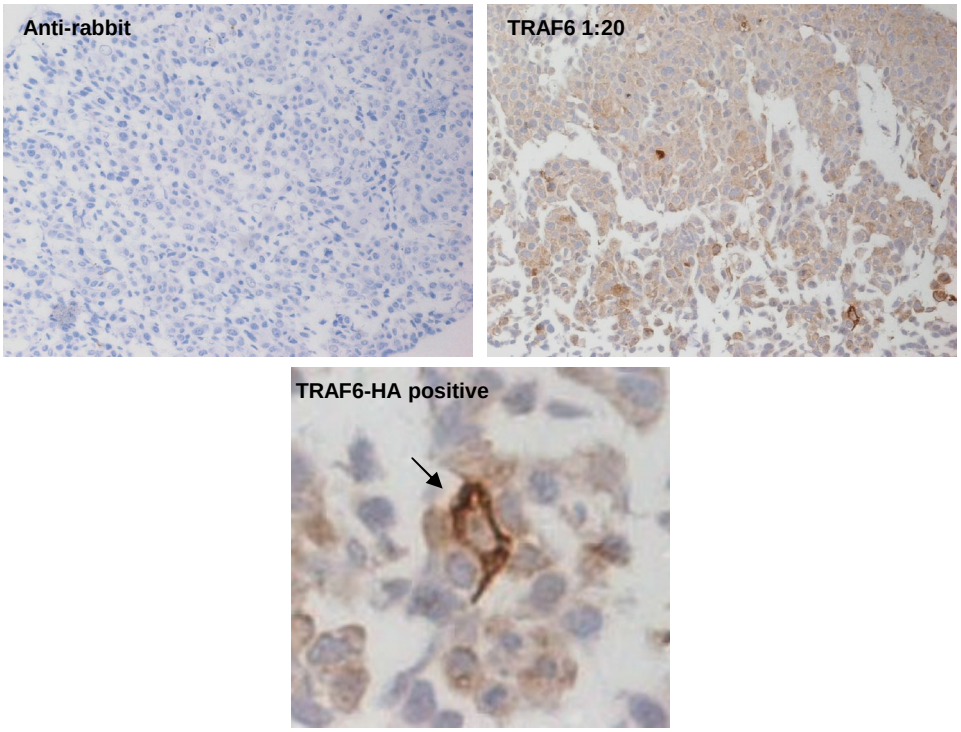

b

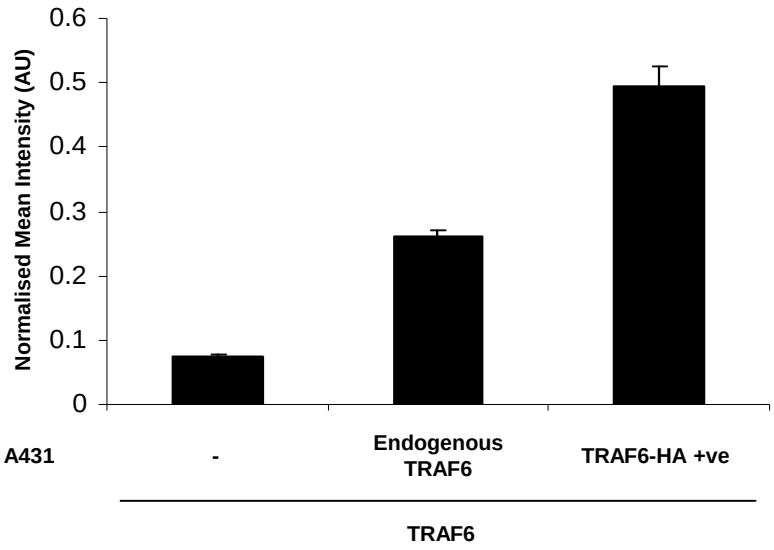

Figure 8.3 Optimisation of TRAF6 IHC: TRAF6-HA positive A431 cells

(**a**) Immunostained sections of A431 cells showing the expression of endogenous and exogenous TRAF6 72 hours following transfection with the pUNO-hTRAF6-HA construct. Cells stained with rabbit anti-TRAF6 (1:20). Image magnification 20x. (**b**) Quantitative analysis of TRAF6 immunostaining. The average of 10 representative immunostained areas is shown and error bars represent the s.e.

a

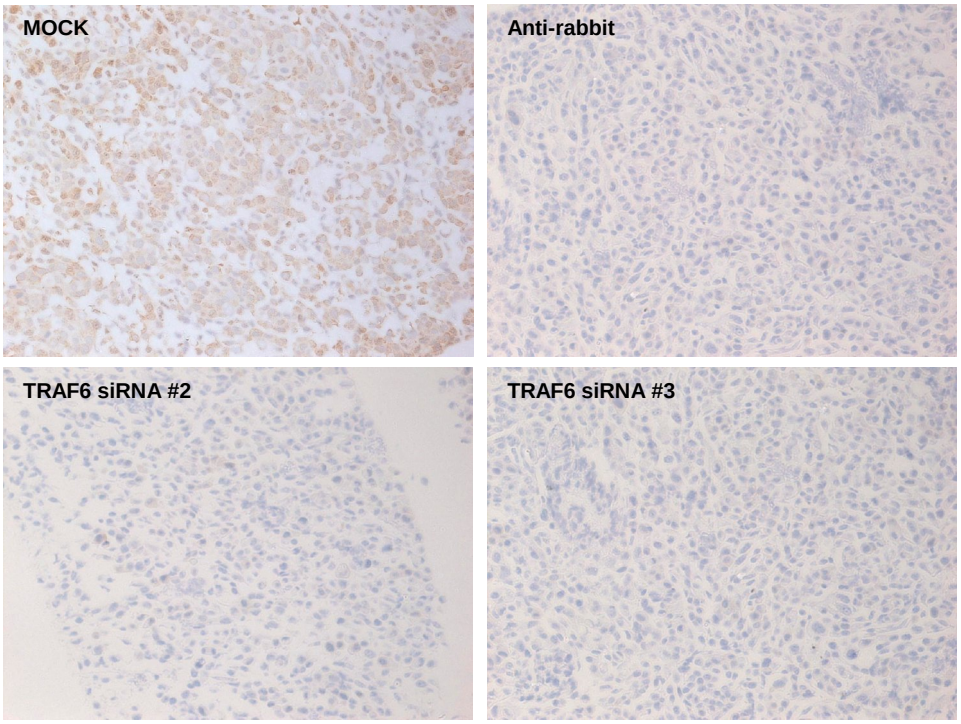

b

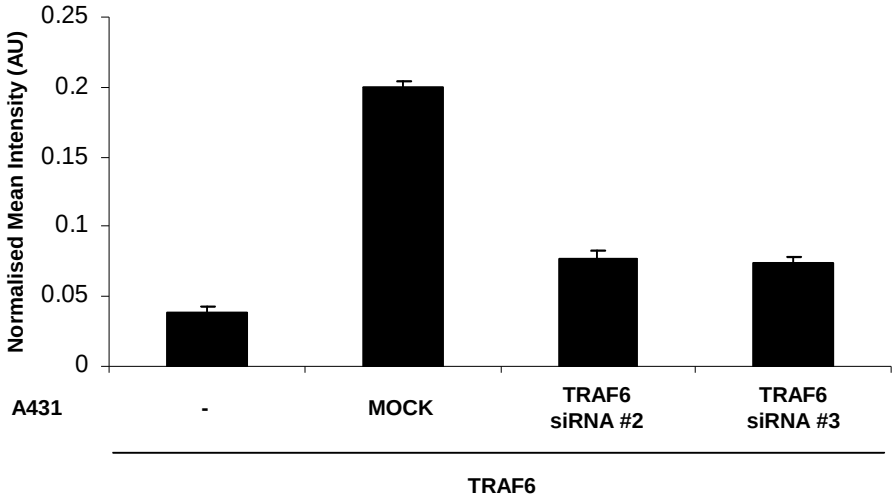

Figure 8.4 Optimisation of TRAF6 IHC: TRAF6 siRNA gene depleted A431 cells

(**a**) Immunostained sections of A431 cells showing TRAF6 expression 72 hours following transfection with TRAF6 siRNA duplexes. Cells stained with rabbit anti-TRAF6 (1:20). (**b**) Quantitative analysis of TRAF6 immunostaining. The average of 10 representative immunostained areas is shown and error bars represent the s.e.

8.4 Analysis of commercial tissue microarrays

To investigate the relevance of TRAF6 as a potential tumour marker, a variety of paraffin embedded tissue microarrays were purchased for analysis. For each tumour, TRAF6 expression was assessed by measuring the normalised mean pixel intensity of 10 representative immunostained areas as described in Chapter 2, Section 2.10.5. Neither the relative proportion of TRAF6 positive cells nor their distribution within each sample was recorded. Consequently, the data that follows does not signify the absolute or total TRAF6 expression level.

8.4.1 TRAF6 expression in SCCHN

Table 8.1 summarises the clinical cases included in the SCCHN tissue microarray purchased from US Biomax Inc. (BC34011). The patient's age, gender, tumour site and histological grade are listed. Cases 21 and 22 were unmatched samples of normal tissue.

Representative photomicrographs of H&E and TRAF6 immunostained sections of tumour tissue and normal tissue included in this array are shown in Figure 8.5. The normalised mean intensity of TRAF6 positive regions for each case is presented in Figure 8.6a. Paraffin embedded A431 cell pellets with and without TRAF6-HA expressing cells were also stained alongside the tissue array (Figure 8.6b).

Five of the 15 tumours (33%) had TRAF6 positive regions with a normalised mean intensity equal to or greater than that expressed in A431 cells.

Case	Age	Gender	Site	Grade
1	51	F	Buccal mucosa	I
2	53	M	Tongue	II
3	65	M	Larynx	II
4	52	M	Buccal mucosa	II
5	60	M	Tongue	III
6	52	M	Larynx	III
7	49	M	Buccal mucoas	I
8	57	M	Tongue	II
9	56	M	Larynx	I
10	52	F	Buccal mucosa	III
11	48	F	Tongue	I
12	46	M	Larynx	III
13	54	M	Maxilla	II
14	50	M	Tongue	II
15	69	F	Larynx	II
16	51	M	Larynx	II
17	50	M	Nasopharynx	III
18	62	M	Nasopharynx	III
19	50	M	Nasopharynx	III
20	56	F	Nasopharynx	III
21	33	M	Gingiva	Normal
22	41	M	Gingiva	Normal

Histological Grade			
I	Well differentiated	II	Moderately differentiated
III	Poorly differentiated	IV	Undifferentiated

Table 8.1 SCCHN tissue microarray: summary of cases

Cases included in the SCCHN tissue microarray purchased from US Biomax Inc. (BC34011). The patient's age, gender, tumour site and histological grade are shown. Cases 21 and 22 were unmatched samples of normal tissue.

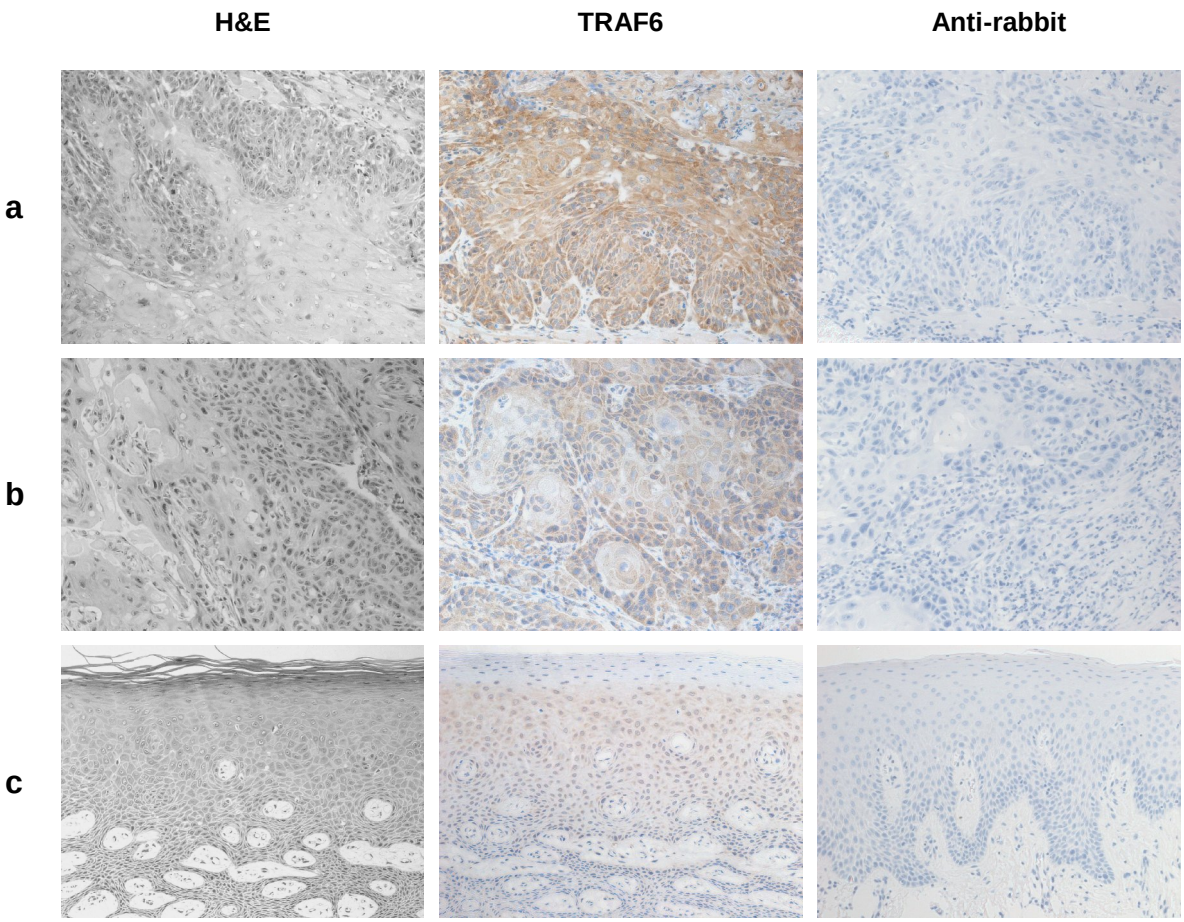

Figure 8.5 SCCHN tissue microarray: TRAF6 IHC

Examples of cases included in the SCCHN tissue microarray purchased from US Biomax Inc. (BC34011). (**a**) Case 2. 53 year old male with Grade II SCC of the tongue. (**b**) Case 16. 51 year old male with Grade II SCC of the larynx. (**c**) Case 22. 41 year old male. Normal mucosa from the gingiva. Sections stained with H&E, rabbit anti-TRAF6 (1:20), and anti-rabbit secondary antibody. Image magnification 20x.

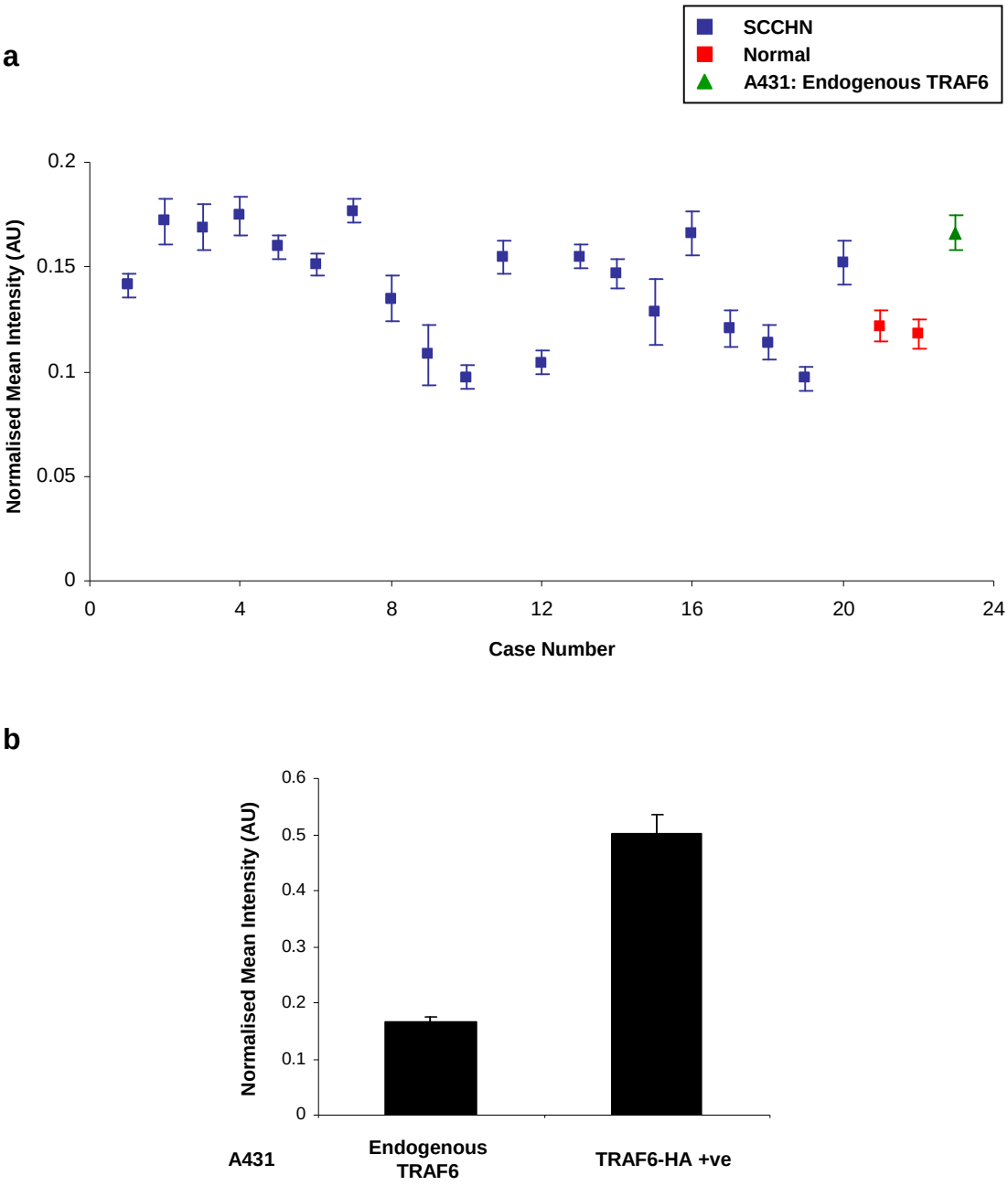

Figure 8.6 SCCHN tissue microarray: analysis of TRAF6 positive regions

Quantitative analysis of TRAF6 immunostaining. (**a**) SCCHN tissue microarray and A431 cells (endogenous TRAF6 expression). (**b**) A431 cells 72 hours following transfection with the pUNO-hTRAF6-HA construct. This sample was stained alongside the tissue microarray and acted as a positive control. The average of 10 representative immunostained areas is shown and error bars represent the s.e.

8.4.2 TRAF6 expression in OSCC

Tables 8.2 and 8.3 summarise the clinical cases included in the OSCC tissue microarray purchased from US Biomax Inc. (OR601). The patient's age, gender, tumour site and histological grade are listed. Cases 51-59 were unmatched samples of normal tissue.

Representative photomicrographs of H&E and TRAF6 immunostained sections of tumour tissue and normal tissue included in this array are shown in Figure 8.7. The normalised mean intensity of TRAF6 positive regions for each case is presented in Figure 8.8a. Paraffin embedded A431 cell pellets with and without TRAF6-HA expressing cells were also stained alongside the tissue array (Figure 8.8b).

40 of the 50 tumours (80%) had TRAF6 positive regions with a normalised mean intensity equal to or greater than that expressed in A431 cells.

Case	Age	Gender	Site	Grade
1	57	M	Tongue	I-II
2	51	F	Buccal mucosa	I-II
3	65	F	Buccal mucosa	I-II
4	66	M	Gingiva	I-II
5	56	F	Buccal mucosa	I-II
6	35	F	Tongue	II
7	78	M	Tongue	I
8	60	M	Gingiva	I-II
9	39	F	Tongue	I-II
10	46	F	Tongue	I-II
11	64	M	Lip	I-II
12	53	M	Buccal mucosa	Not graded
13	57	F	Tongue	I-II
14	36	F	Tongue	Not graded
15	58	M	Not specified	I
16	52	M	Buccal mucosa	I
17	63	M	Not specified	I-II
18	47	F	Tongue	I-II
19	63	F	Tongue	I
20	56	M	Tongue	I-II
21	49	M	Buccal mucosa	I-II
22	55	F	Tongue	Not graded
23	76	M	Tongue	I-II
24	50	F	Tongue	I-II
25	61	M	Lip	I-II
26	55	M	Tongue	I
27	55	M	Buccal mucosa	I
28	60	M	Gingiva	I
29	60	M	Tongue	I
30	49	M	Buccal mucosa	II

Histological Grade			
I	Well differentiated	II	Moderately differentiated
III	Poorly differentiated	IV	Undifferentiated

Table 8.2 OSCC tissue microarray: summary of cases 1-30

Cases included in the OSCC tissue microarray purchased from US Biomax Inc. (OR601). The patient's age, gender, tumour site and histological grade are shown.

Case	Age	Gender	Site	Grade
31	64	M	Tongue	I
32	52	F	Tongue	II
33	50	F	Tongue	II
34	46	F	Tongue	II
35	45	F	Tongue	II
36	35	M	Tongue	I-II
37	46	F	Tongue	II
38	48	F	Tongue	II
39	80	M	Lip	II
40	45	M	Buccal mucosa	I-II
41	55	M	Gingiva	II-III
42	48	F	Tongue	II
43	60	M	Tongue	II
44	37	M	Tongue	II
45	40	F	Not specified	Not graded
46	60	M	Tongue	II-III
47	56	F	Not specified	II
48	60	M	Tongue	II-III
49	77	M	Not specified	II
50	73	M	Tongue	III
51	48	M	Tongue	Normal
52	38	M	Tongue	Normal
53	66	M	Tongue	Normal
54	45	F	Tongue	Normal
55	49	F	Tongue	Normal
56	42	F	Tongue	Normal
57	49	M	Tongue	Normal
58	40	M	Gingiva	Normal
59	62	M	Palate	Normal

Histological Grade			
I	Well differentiated	II	Moderately differentiated
III	Poorly differentiated	IV	Undifferentiated

Table 8.3 OSCC tissue microarray: summary of cases 31-59

Cases included in the OSCC tissue microarray purchased from US Biomax Inc. (OR601). The patient's age, gender, tumour site and histological grade are shown. Cases 51-59 were unmatched samples of normal tissue.

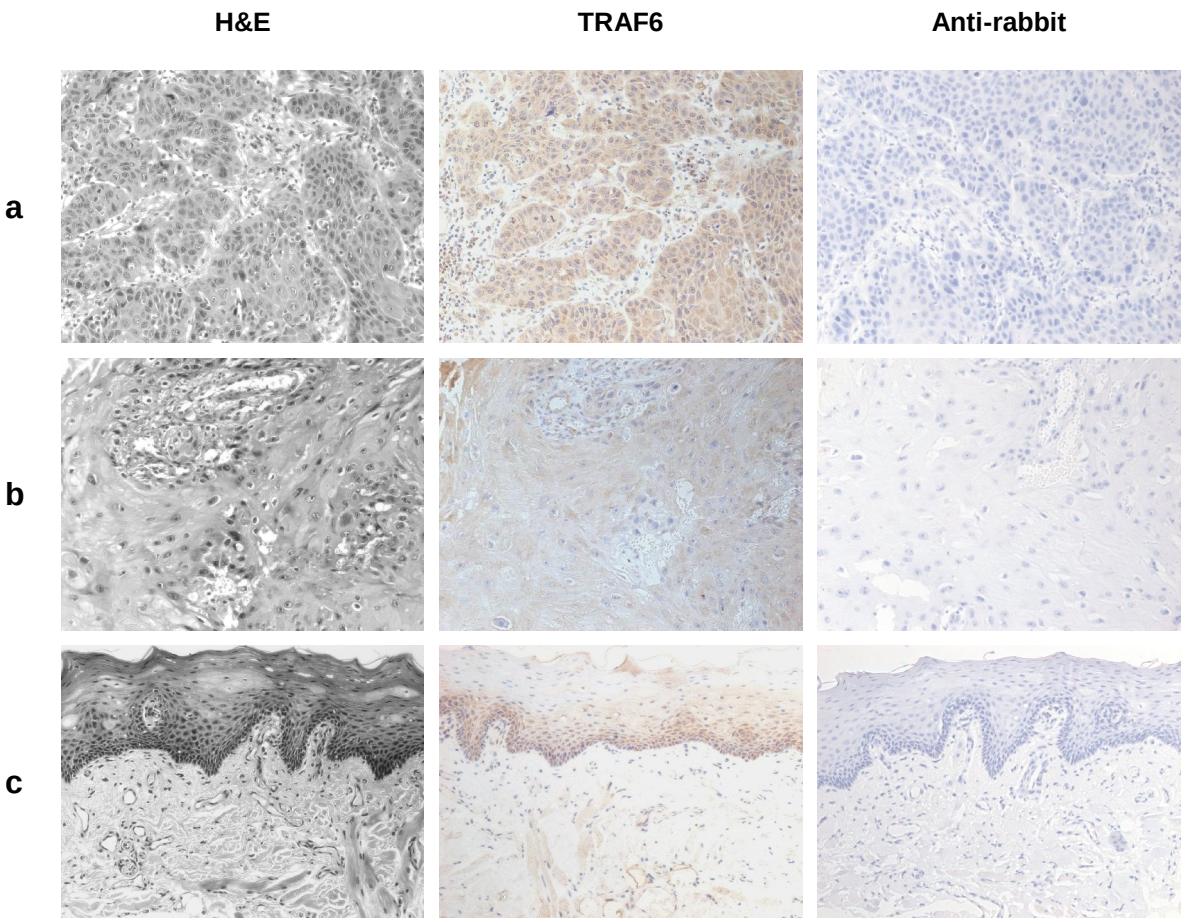

Figure 8.7 OSCC tissue microarray: TRAF6 IHC

Examples of cases included in the OSCC tissue microarray purchased from US Biomax Inc. (OR601). (**a**) Case 6. 35 year old female with Grade II SCC of the tongue. (**b**) Case 40. 45 year old male with Grade I-II SCC of the buccal mucosa. (**c**) Case 54. 45 year old female. Normal mucosa from the tongue. Sections stained with H&E, rabbit anti-TRAF6 (1:20), and anti-rabbit secondary antibody. Image magnification 20x.

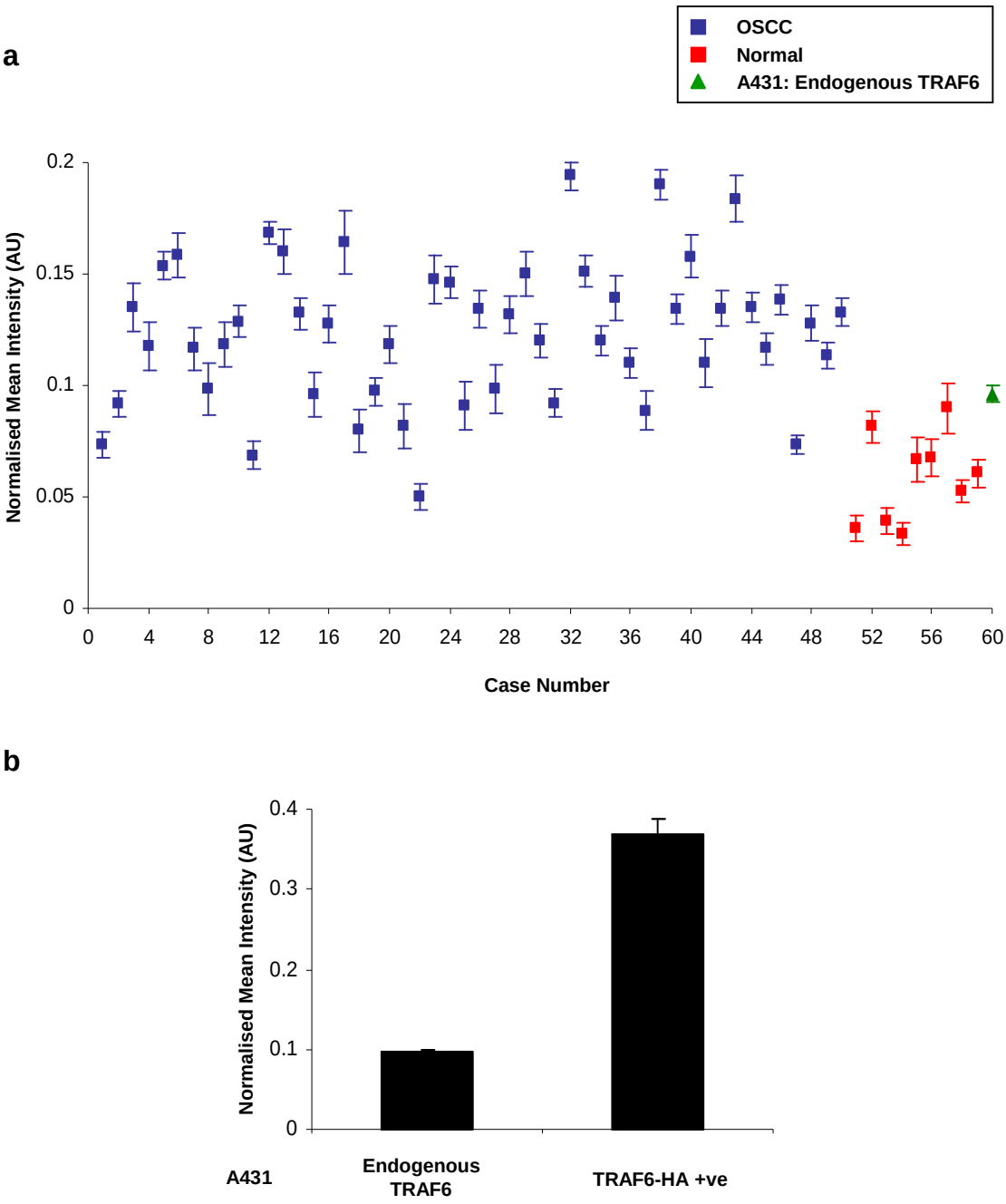

Figure 8.8 OSCC tissue microarray: analysis of TRAF6 positive regions

Quantitative analysis of TRAF6 immunostaining. (**a**) OSCC tissue microarray and A431 cells (endogenous TRAF6 expression). (**b**) A431 cells 72 hours following transfection with the pUNO-hTRAF6-HA construct. This sample was stained alongside the tissue microarray and acted as a positive control. The average of 10 representative immunostained areas is shown and error bars represent the s.e.

8.4.3 TRAF6 expression in CSCC

Tables 8.4 and 8.5 summarise the clinical cases included in the CSCC tissue microarray purchased from US Biomax Inc. (SK483). The patient's age, gender, tumour site and histological grade are listed. Cases 40-46 were unmatched samples of normal tissue.

Representative photomicrographs of H&E and TRAF6 immunostained sections of tumour tissue and normal tissue included in this array are shown in Figure 8.9. The normalised mean intensity of TRAF6 positive regions for each case is presented in Figure 8.10a. Paraffin embedded A431 cell pellets with and without TRAF6-HA expressing cells were also stained alongside the tissue array (Figure 8.10b).

22 of the 39 tumours (56%) had TRAF6 positive regions with a normalised mean intensity equal to or greater than that expressed in A431 cells.

Case	Age	Gender	Site	Grade
1	68	M	Right temple	I
2	78	M	Left temple	I
3	64	M	Right thigh	I
4	63	M	Scalp	I
5	51	F	Right leg	I
6	62	F	Right leg	I
7	63	M	Occiput	I
8	37	M	Left upper arm	I
9	77	F	Sacrum	I
10	79	F	Left orbit	I
11	53	F	Tongue	I
12	62	F	Not specified	I
13	52	M	Head	I
14	52	F	Right upper arm	I
15	53	F	Not specified	I
16	48	F	Right groin	I
17	69	M	Vertex	I
18	64	F	Vulva	I
19	70	F	Vulva	I
20	42	F	Right heel	I
21	70	M	Not specified	I
22	64	F	Left leg	I
23	76	F	Sacrum	I

Histological Grade			
I	Well differentiated	II	Moderately differentiated
III	Poorly differentiated	IV	Undifferentiated

Table 8.4 CSCC tissue microarray: summary of cases 1-23

Cases included in the CSCC tissue microarray purchased from US Biomax Inc. (SK483). The patient's age, gender, tumour site and histological grade are shown.

Case	Age	Gender	Site	Grade
24	82	F	Left face	I-II
25	67	M	Occiput	I
26	60	M	Not specified	I
27	74	F	Left cheek	I
28	50	F	Right thigh	I-II
29	48	F	Scalp	I-II
30	87	F	Right cheek	II
31	51	M	Back	I
32	65	M	Abdomen	II
33	83	F	Head	II
34	25	M	Scalp	II
35	35	F	Not specified	I
36	56	M	Back	II
37	82	F	Not specified	II
38	32	M	Right buttock	II
39	65	F	Face	II
40	22	M	Not specified	Normal
41	35	M	Neck	Normal
42	40	M	Not specified	Normal
43	40	M	Not specified	Normal
44	21	F	Not specified	Normal
45	21	F	Not specified	Normal
46	47	M	Wrist	Normal

Histological Grade			
I	Well differentiated	II	Moderately differentiated
III	Poorly differentiated	IV	Undifferentiated

Table 8.5 CSCC tissue microarray: summary of cases 24-46

Cases included in the CSCC tissue microarray purchased from US Biomax Inc. (SK483). The patient's age, gender, tumour site and histological grade are shown. Cases 40-46 were unmatched samples of normal tissue.

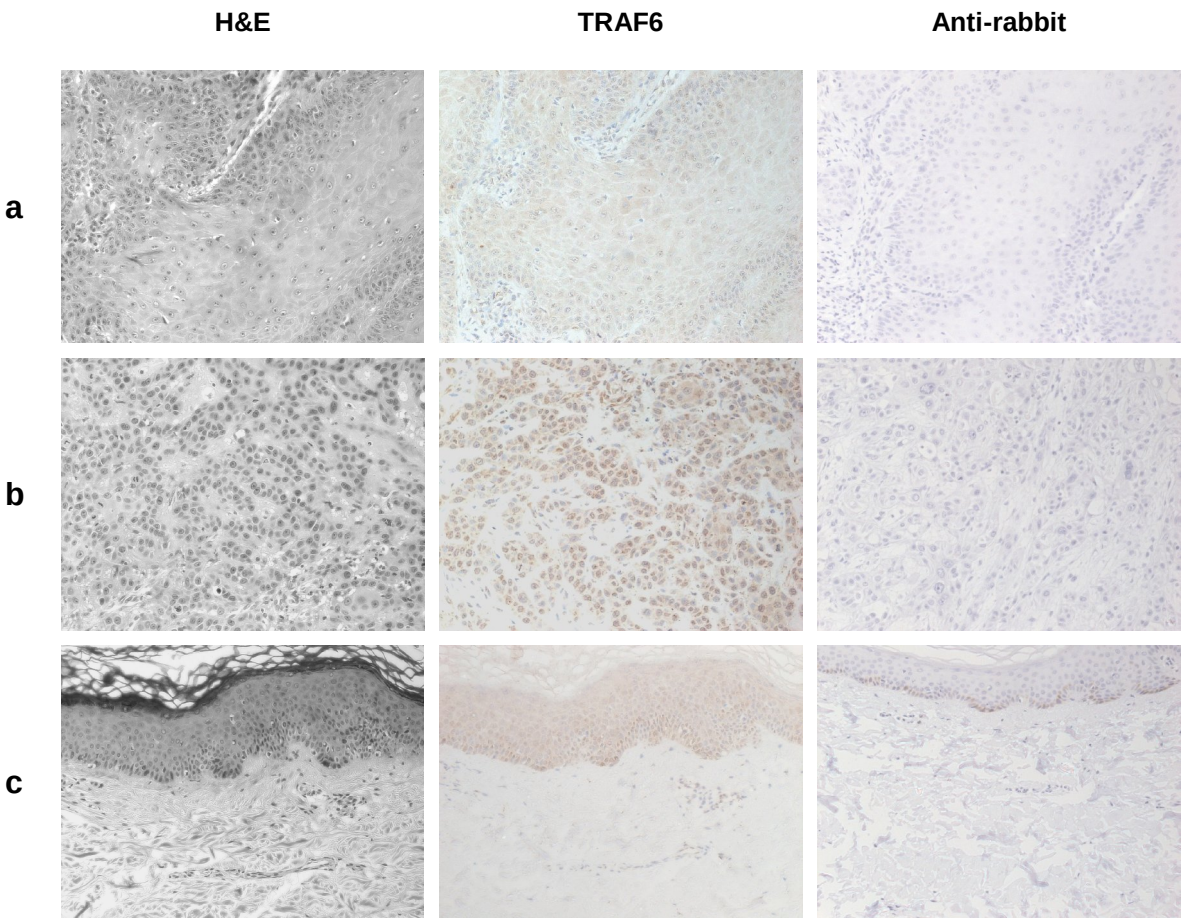

Figure 8.9 CSCC tissue microarray: TRAF6 IHC

Examples of cases included in the CSCC tissue microarray purchased from US Biomax Inc. (SK483). (**a**) Case 20. 42 year old female with Grade I SCC of the right heel. (**b**) Case 30. 87 year old female with Grade II SCC of the right cheek. (**c**) Case 41. 35 year old female. Normal skin from the neck. Sections stained with H&E, rabbit anti-TRAF6 (1:20), and anti-rabbit secondary antibody. Image magnification 20x.

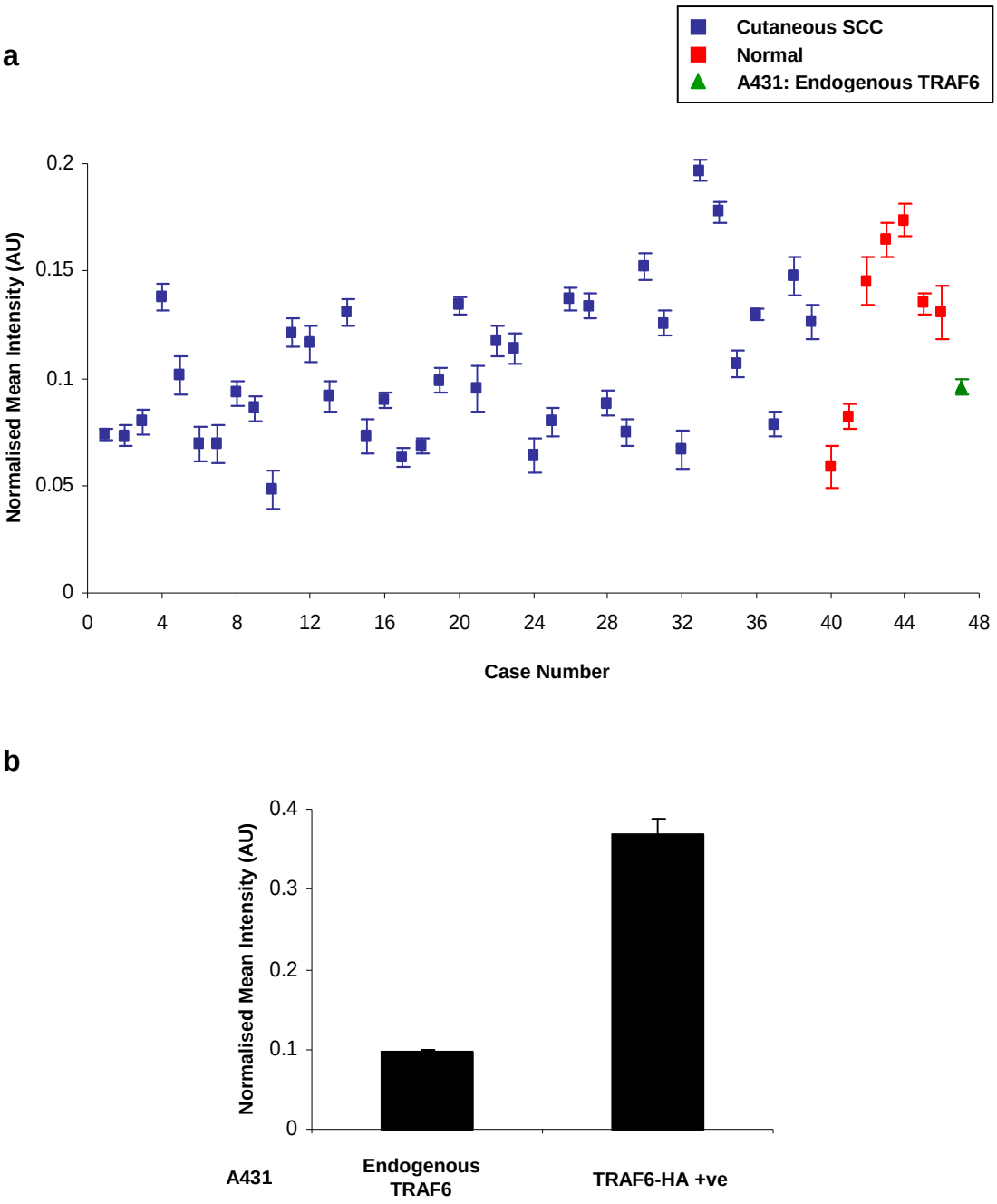

Figure 8.10 CSCC tissue microarray: analysis of TRAF6 positive regions

Quantitative analysis of TRAF6 immunostaining. (**a**) CSCC tissue microarray and A431 cells (endogenous TRAF6 expression). (**b**) A431 cells 72 hours following transfection with the pUNO-hTRAF6-HA construct. This sample was stained alongside the tissue microarray and acted as a positive control. The average of 10 representative immunostained areas is shown and error bars represent the s.e.

8.4.4 TRAF6 expression in vulval SCC

Table 8.6 summarises the clinical cases included in the vulval SCC tissue microarray purchased from US Biomax Inc. (UV241). The patient's age, gender, tumour site and histological grade are listed. Cases 11 and 12 were unmatched samples of normal tissue.

Representative photomicrographs of H&E and TRAF6 immunostained sections of tumour tissue and normal tissue included in this array are shown in Figure 8.11. The normalised mean intensity of TRAF6 positive regions for each case is presented in Figure 8.12a. Paraffin embedded A431 cell pellets with and without TRAF6-HA expressing cells were also stained alongside the tissue array (Figure 8.12b).

7 of the 10 tumours (70%) had TRAF6 positive regions with a normalised mean intensity equal to or greater than that expressed in A431 cells.

Case	Age	Gender	Site	Grade
1	29	F	Vulva	I
2	59	F	Vulva	II
3	85	F	Vulva	I
4	42	F	Vulva	II
5	56	F	Vulva	I
6	51	F	Vulva	I
7	46	F	Vulva	II
8	58	F	Vulva	I
9	50	F	Vulva	I
10	48	F	Vulva	I
11	42	F	Vulva-adjacent skin	Normal
12	48	F	Vulva-adjacent skin	Normal

Histological Grade			
I	Well differentiated	II	Moderately differentiated
III	Poorly differentiated	IV	Undifferentiated

Table 8.6 Vulval SCC tissue microarray: summary of cases

Cases included in the vulval SCC tissue microarray purchased from US Biomax Inc. (UV241). The patient's age, gender, tumour site and histological grade are shown. Cases 11 and 12 were unmatched samples of normal tissue.

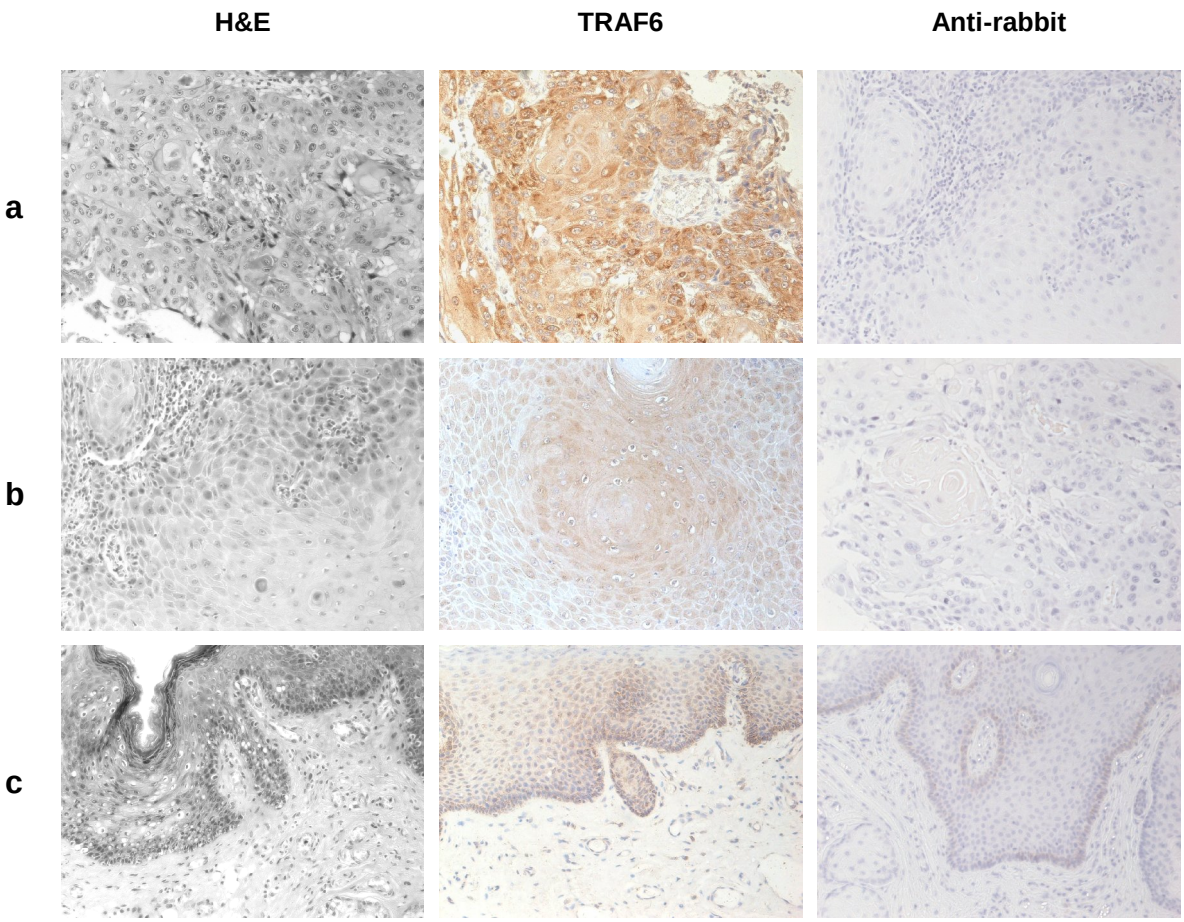

Figure 8.11 Vulval SCC tissue microarray: TRAF6 IHC

Examples of cases included in the vulval SCC tissue microarray purchased from US Biomax Inc. (UV241). (**a**) Case 1. 29 year old female with Grade I SCC of the vulva. (**b**) Case 10. 48 year old female with Grade I SCC of the vulva. (**c**) Case 11. 42 year old female. Normal vulva-adjacent skin. Sections stained with H&E, rabbit anti-TRAF6 (1:20), and anti-rabbit secondary antibody. Image magnification 20x.

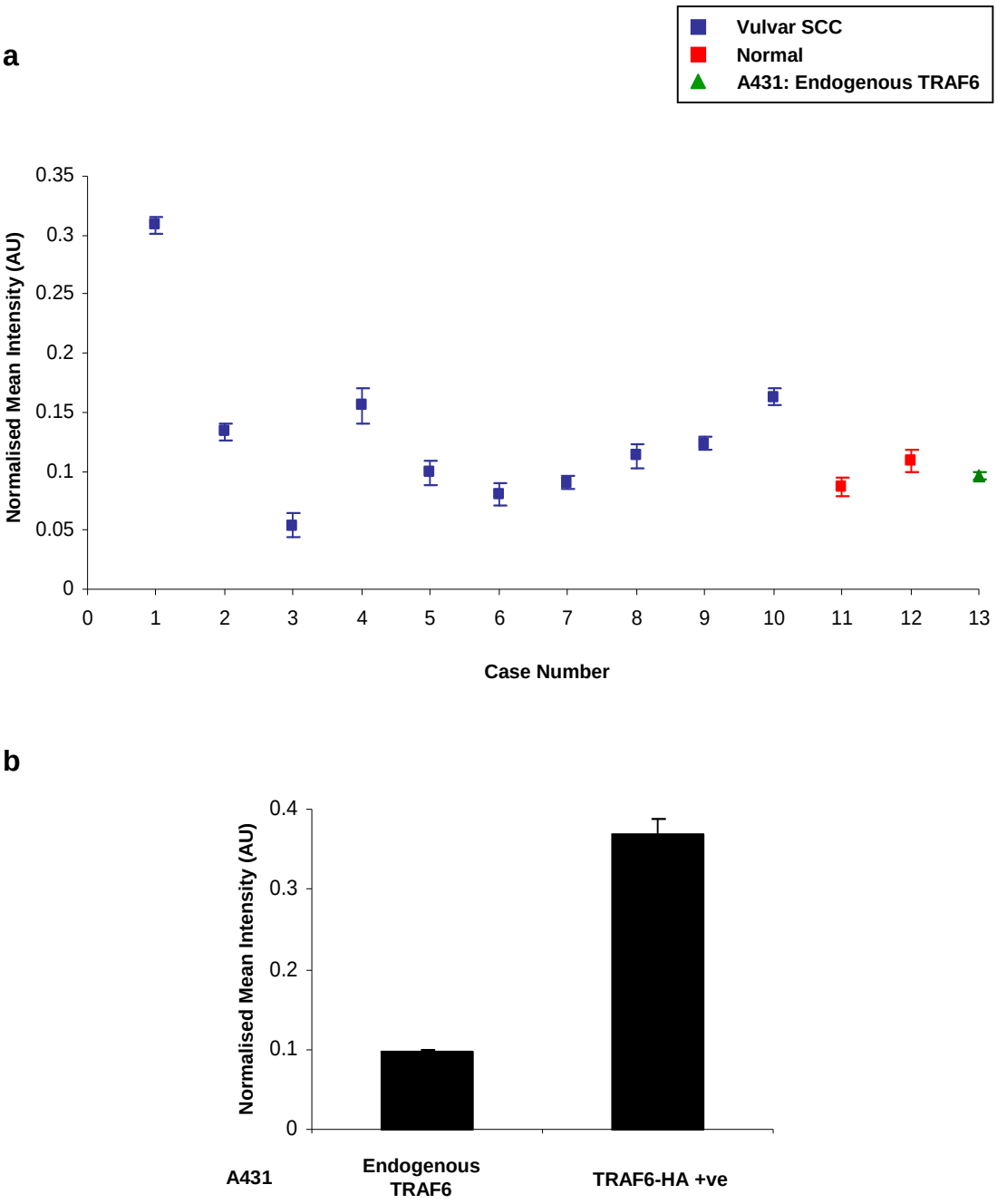

Figure 8.12 Vulval SCC tissue microarray: analysis of TRAF6 positive regions

Quantitative analysis of TRAF6 immunostaining. (**a**) Vulval SCC tissue microarray and A431 cells (endogenous TRAF6 expression). (**b**) A431 cells 72 hours following transfection with the pUNO-hTRAF6-HA construct. This sample was stained alongside the tissue microarray and acted as a positive control. The average of 10 representative immunostained areas is shown and error bars represent the s.e.

8.5 Analysis of SCCHN tissue bank samples

8.5.1 Immunohistochemistry (IHC)

TRAF6 expression in these samples was assessed as previously detailed in Sections 8.3 and 8.4.

Representative photomicrographs of H&E and TRAF6 immunostained sections of tumour tissue from three SCCHN tissue bank cases are shown in Figure 8.13. The normalised mean intensity of TRAF6 positive regions is presented in Figure 8.14. Paraffin embedded A431 cell pellets with and without TRAF6-HA expressing cells were also stained alongside the tissue array.

Figures 8.15-8.18 demonstrate NF-κB p65, IκBα, pan-cytokeratin and vimentin immunostaining of the SCCHN tissue bank samples illustrated in Figure 8.13. The optimisation of these antibodies for IHC was performed by Emma Nye of the Cancer Research UK Experimental Histopathology Laboratory (data not shown).

TRAF6 expression in Case (c) - a 53 year old male with SCC of the right tonsil (T_2N_2) was similar to that of TRAF6-HA positive A431 cells. Furthermore, stromal fibroblasts were also TRAF6 positive. These observations were accompanied by the loss of pan-cytokeratin markers and strong vimentin immunostaining (Figure 8.19).

8.5.2 Confocal imaging

Immunofluoresence staining of matched normal and tumour tissue from the three SCCHN tissue bank cases illustrated in Figures 8.13-8.18 is shown in Figures 8.20-8.22. Tissue architecture was well preserved and detailed imaging of cytoskeletal structures was possible (Figure 8.23).

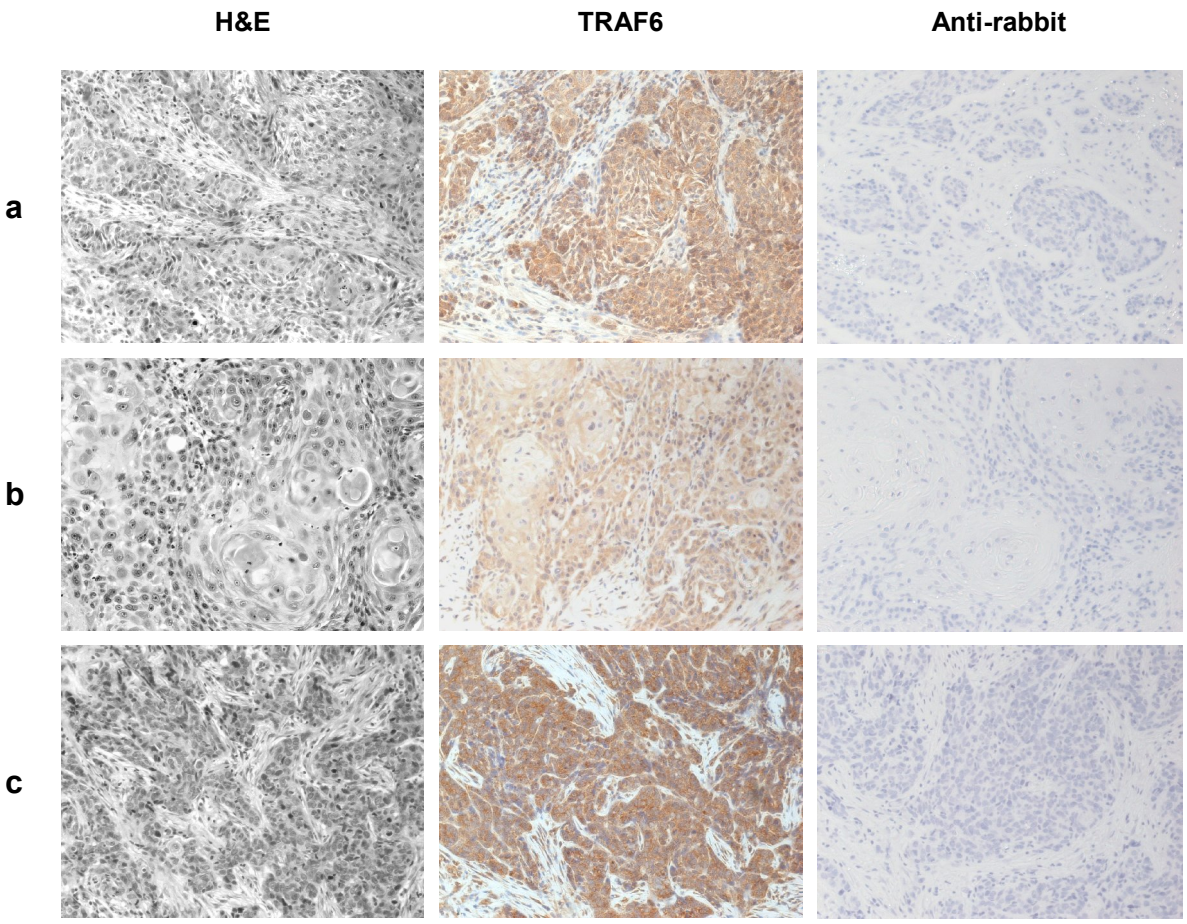

Figure 8.13 SCCHN tissue bank: TRAF6 IHC

Examples of cases from the SCCHN tissue bank. (**a**) 53 year old male with SCC of the left tonsil (T_4N_3). (**b**) 70 year old male with SCC of the right floor of the mouth (T_2N_2). (**c**) 53 year old male with SCC of the right tonsil (T_2N_2). Sections stained with H&E, rabbit anti-TRAF6 (1:20), and anti-rabbit secondary antibodies. Image magnification 20x.

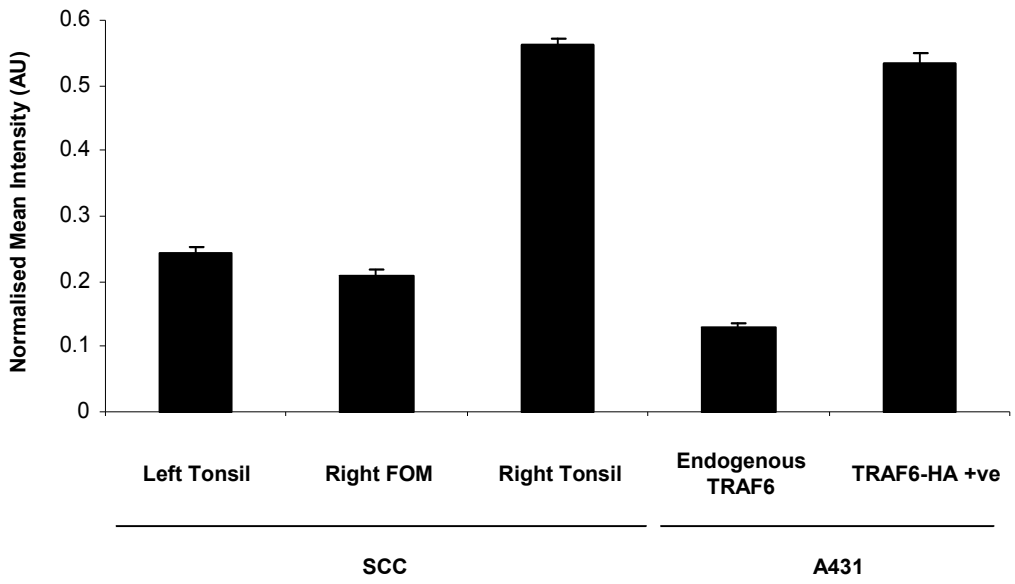

Figure 8.14 SCCHN tissue bank: analysis of TRAF6 positive regions

Quantitative analysis of TRAF6 immunostaining of the SCCHN samples illustrated in Figure 8.13 compared to that of A431 cells 72 hours following transfection with the pUNO-hTRAF6-HA construct. The A431 cell pellet was stained alongside the tissue bank samples and acted as a positive control. The average of 10 representative immunostained areas is shown and error bars represent the s.e.

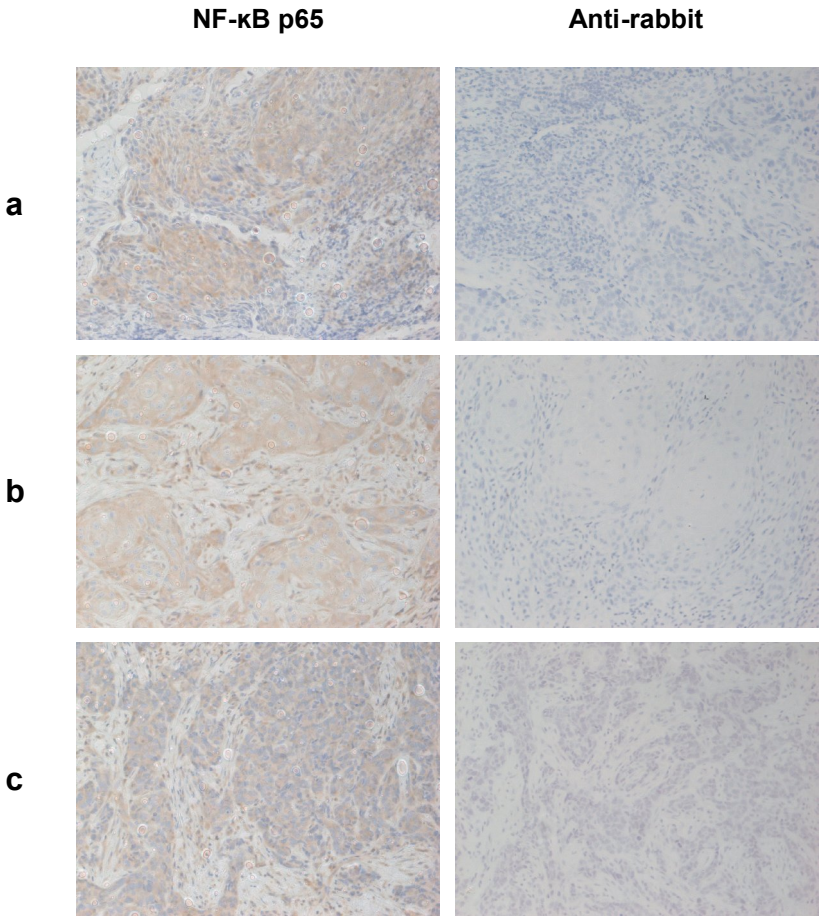

Figure 8.15 SCCHN tissue bank: NF-κB p65 IHC

NF-κB p65 immunostaining of the SCCHN tissue bank samples previously illustrated in Figure 8.13. (**a**) 53 year old male with SCC of the left tonsil (T_4N_3). (**b**) 70 year old male with SCC of the right floor of the mouth (T_2N_2). (**c**) 53 year old male with SCC of the right tonsil (T_2N_2). Sections stained with rabbit anti-NF-κB (1:20) and anti-rabbit secondary antibodies. Image magnification 20x.

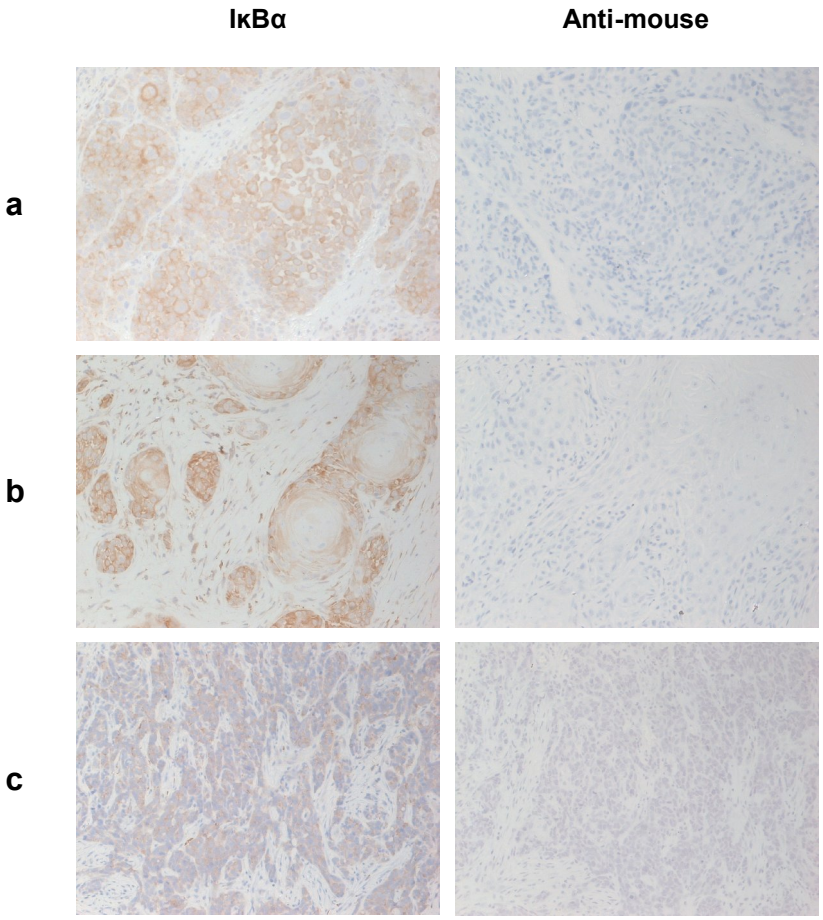

Figure 8.16 SCCHN tissue bank: IκBα IHC

IκBα immunostaining of the SCCHN tissue bank samples previously illustrated in Figure 8.13. (**a**) 53 year old male with SCC of the left tonsil (T_4N_3). (**b**) 70 year old male with SCC of the right floor of the mouth (T_2N_2). (**c**) 53 year old male with SCC of the right tonsil (T_2N_2). Sections stained with mouse anti-IκBα (1:20) and anti-mouse secondary antibodies. Image magnification 20x.

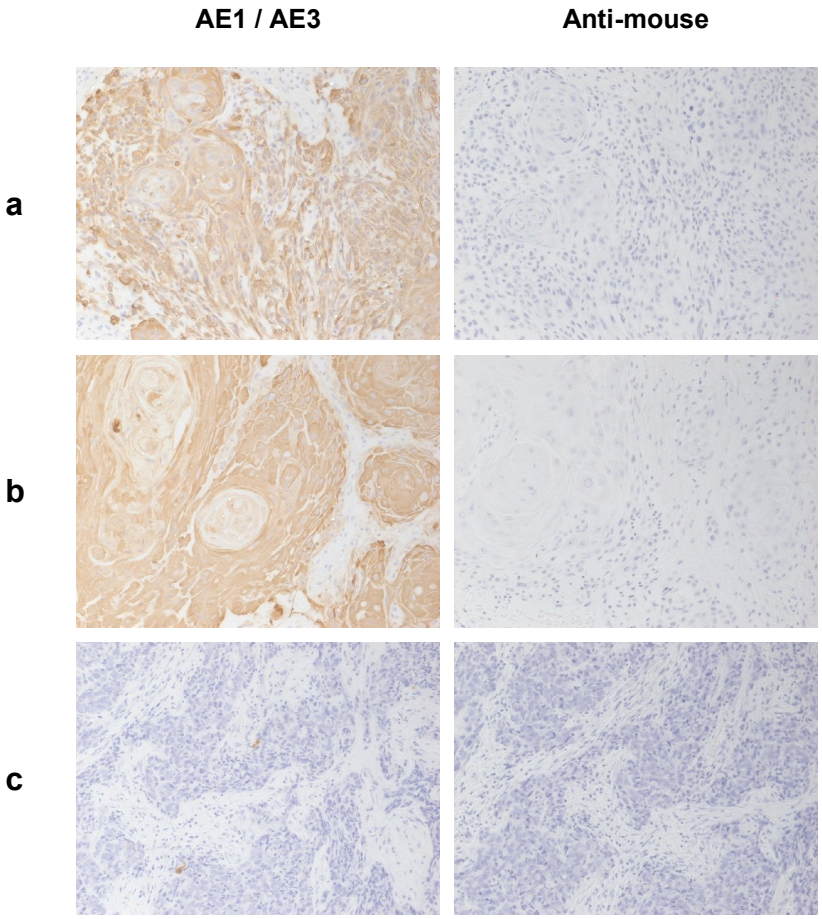

Figure 8.17 SCCHN tissue bank: pan-cytokeratin IHC

Pan-cytokeratin immunostaining of the SCCHN tissue bank samples previously illustrated in Figure 8.13. (**a**) 53 year old male with SCC of the left tonsil (T_4N_3). (**b**) 70 year old male with SCC of the right floor of the mouth (T_2N_2). (**c**) 53 year old male with SCC of the right tonsil (T_2N_2). Sections stained with mouse AE1 / AE3 (1:100) and anti-mouse secondary antibodies. Image magnification 20x.

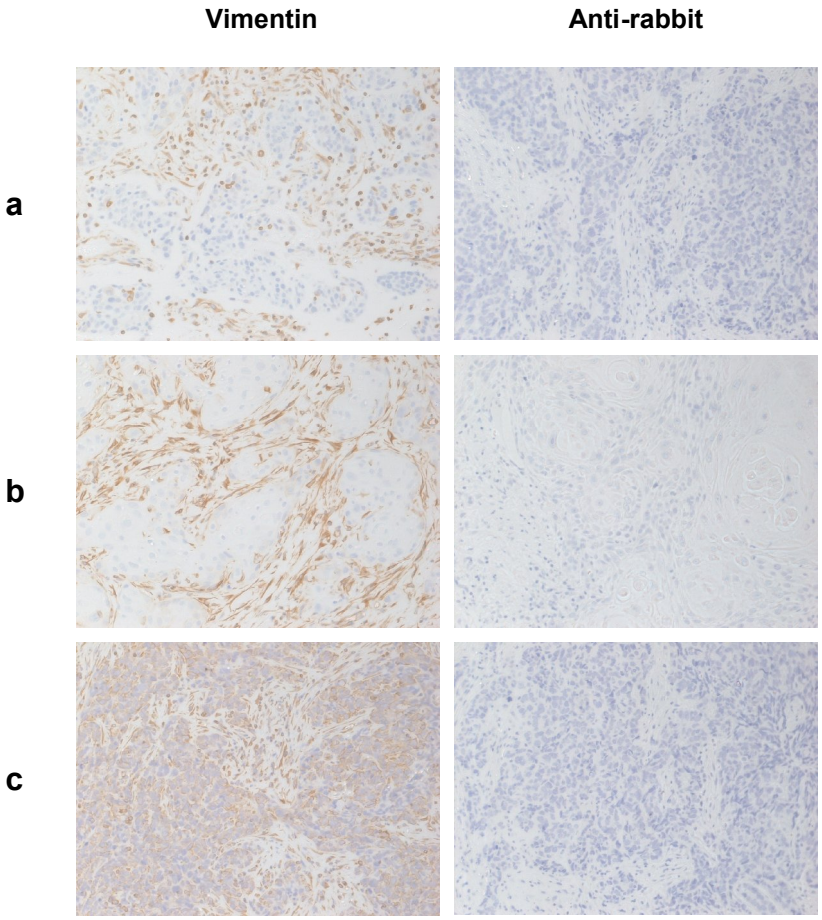

Figure 8.18 SCCHN tissue bank: vimentin IHC

Vimentin immunostaining of the SCCHN tissue bank samples previously illustrated in Figure 8.13. (**a**) 53 year old male with SCC of the left tonsil (T_4N_3). (**b**) 70 year old male with SCC of the right floor of the mouth (T_2N_2). (**c**) 53 year old male with SCC of the right tonsil (T_2N_2). Sections stained with rabbit anti-vimentin (1:50) and anti-rabbit secondary antibodies. Image magnification 20x.

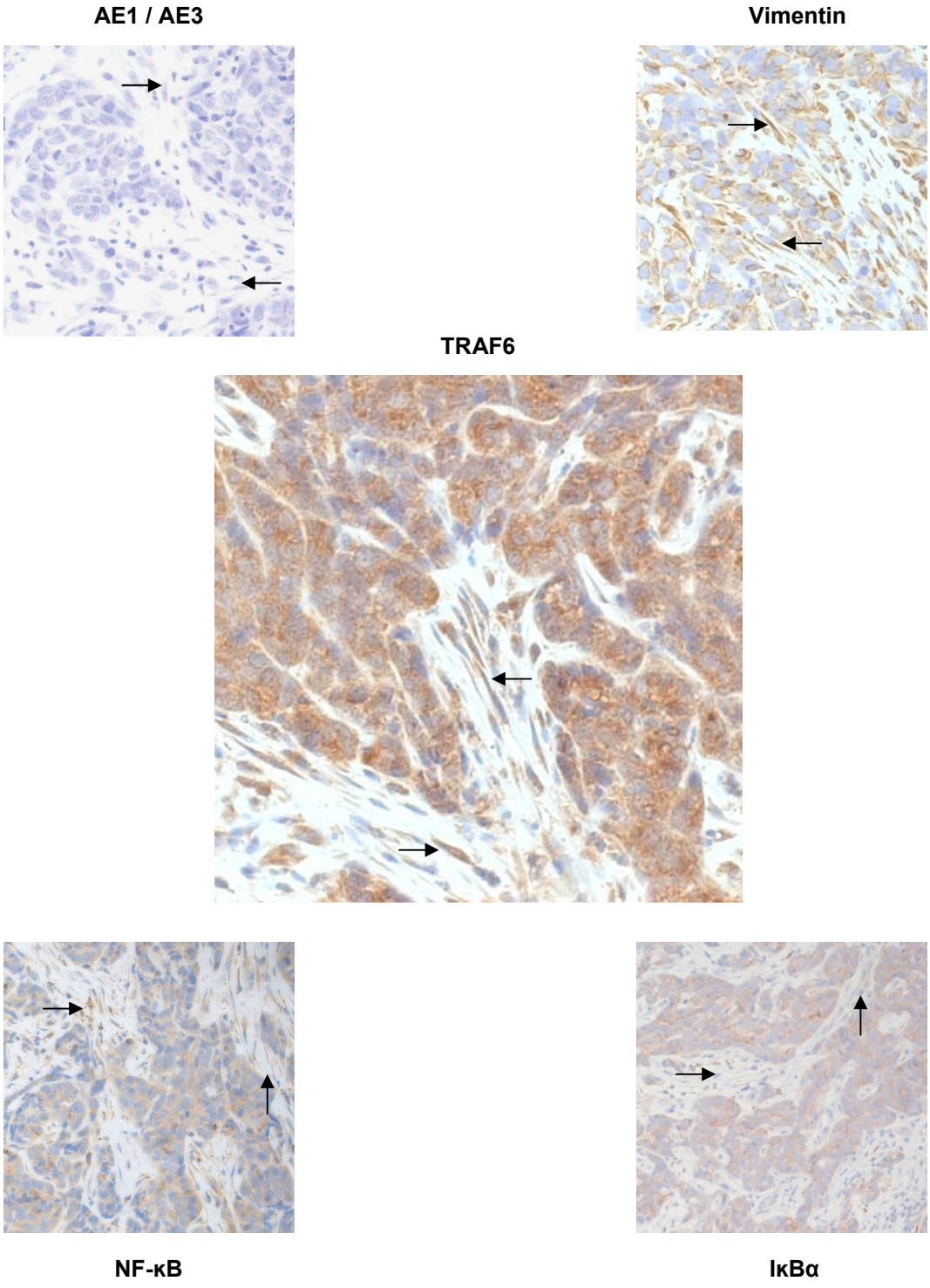

Figure 8.19 IHC of SCC of the right tonsil

SCC of the right tonsil (T_2N_2) from a 53 year old male: Case (**c**) of the SCCHN tissue bank samples previously illustrated in Figure 8.13. Arrows indicate carcinoma-associated fibroblasts. Sections stained with rabbit anti-TRAF6 (1:20), mouse AE1 / AE3 (1:100), rabbit anti-vimentin (1:50), rabbit anti-NF-κB p65 (1:20), and mouse anti-IκBα (1:50) antibodies.

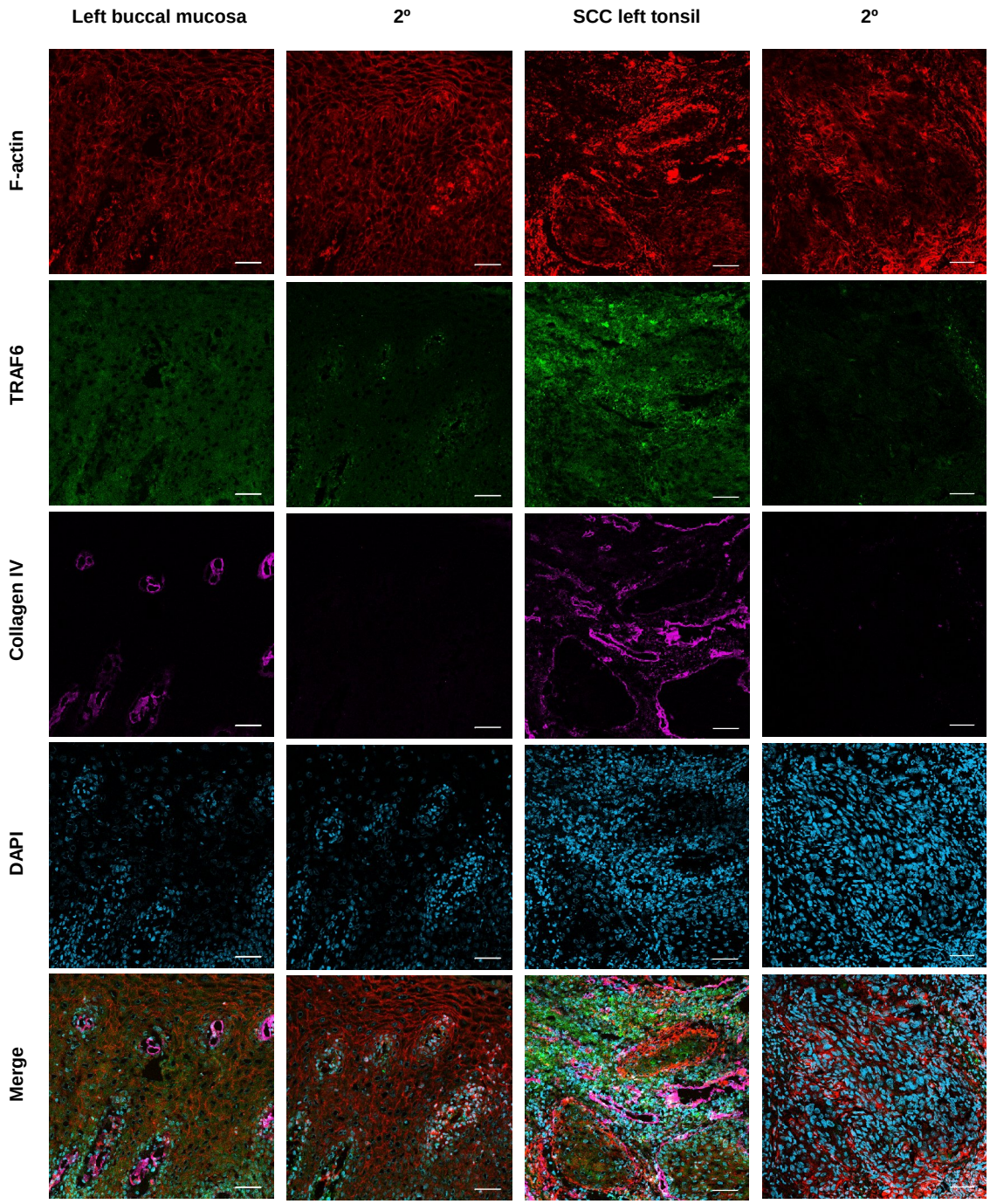

Figure 8.20 Confocal imaging: SCC of the left tonsil

Immunofluoresence staining of matched normal and tumour tissue from a 53 year old male with SCC of the left tonsil (T_4N_3): Case (**a**) of the SCCHN tissue bank samples illustrated in Figures 8.13-8.18. Sections stained with TRITC phalloidin (1:500), rabbit anti-TRAF6 (1:100), mouse anti-collagen IV (1:100) and DAPI (1:500). Scale bars represent 50µm.

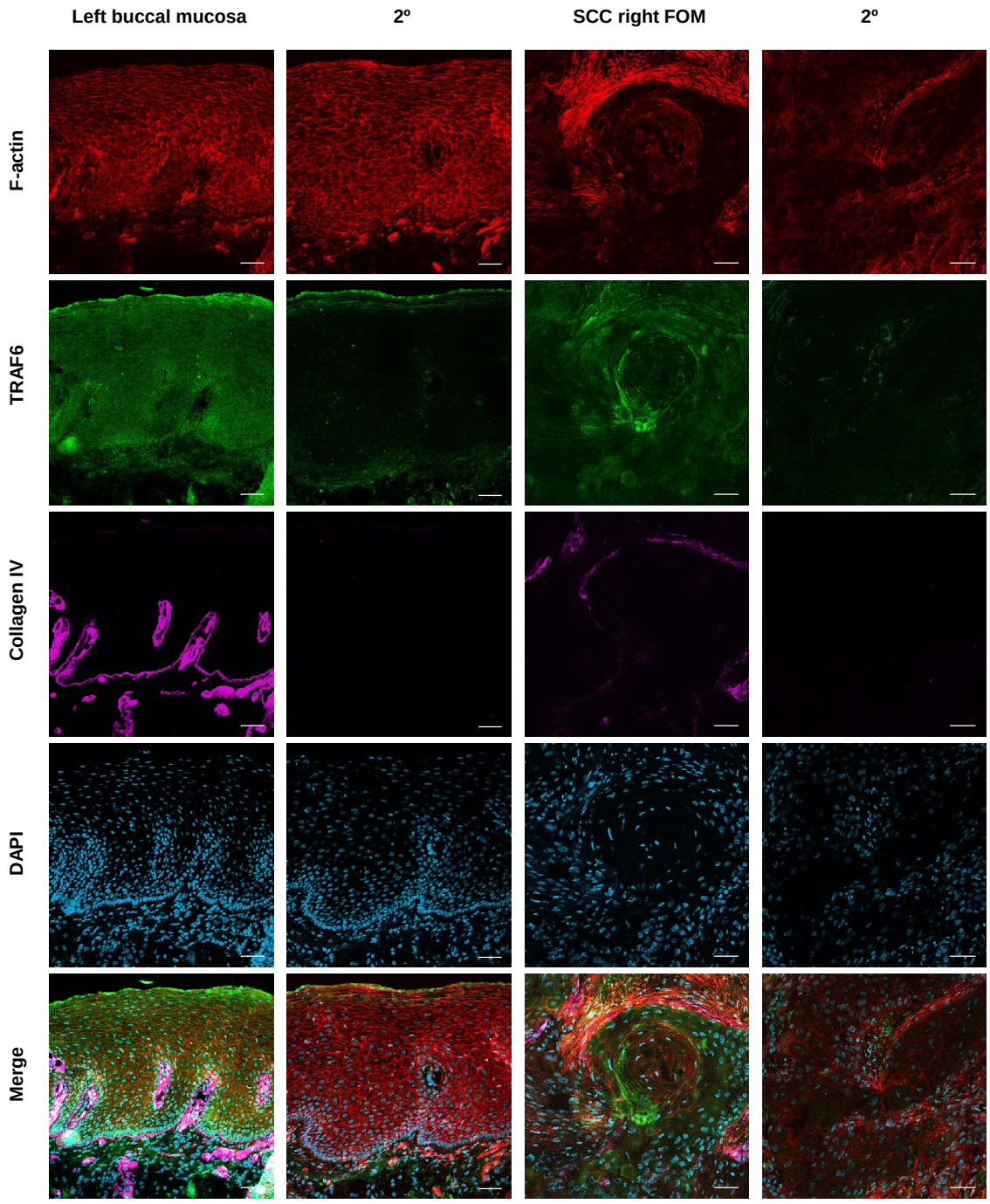

Figure 8.21 Confocal imaging: SCC of the right FOM

Immunofluoresence staining of matched normal and tumour tissue from a 70 year old male with SCC of the right floor of the mouth (T_2N_2): Case (**b**) of the SCCHN tissue bank samples illustrated in Figures 8.13-8.18. Sections stained with TRITC phalloidin (1:500), rabbit anti-TRAF6 (1:100), mouse anti-collagen IV (1:100) and DAPI (1:500). Scale bars represent 50µm.

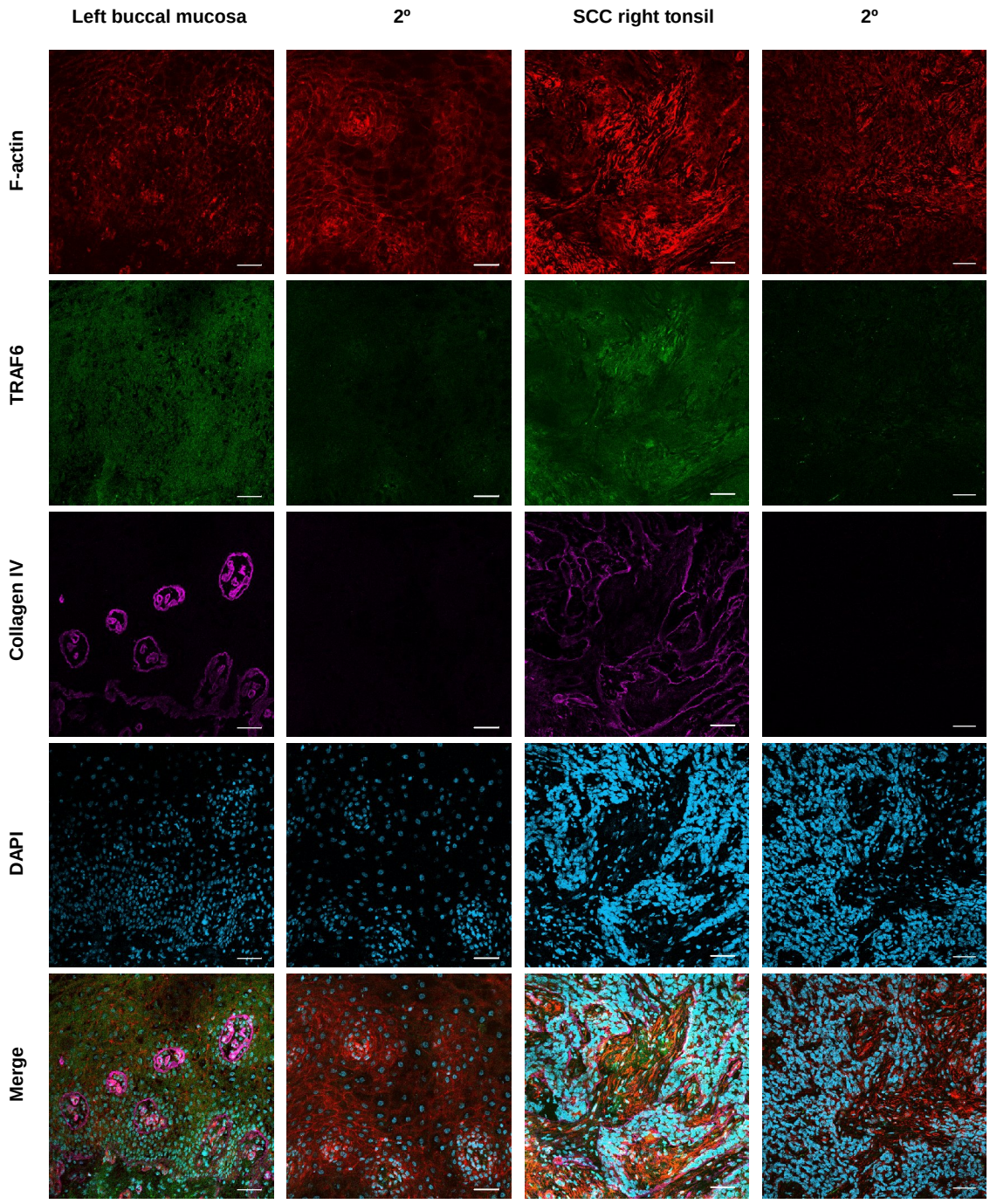

Figure 8.22 Confocal imaging: SCC of the right tonsil

Immunofluoresence staining of matched normal and tumour tissue from a 53 year old male with SCC of the right tonsil (T_2N_2): Case (**c**) of the SCCHN tissue bank samples illustrated in Figures 8.13-8.18. Sections stained with TRITC phalloidin (1:500), rabbit anti-TRAF6 (1:100), mouse anti-collagen IV (1:100) and DAPI (1:500). Scale bars represent 50µm.

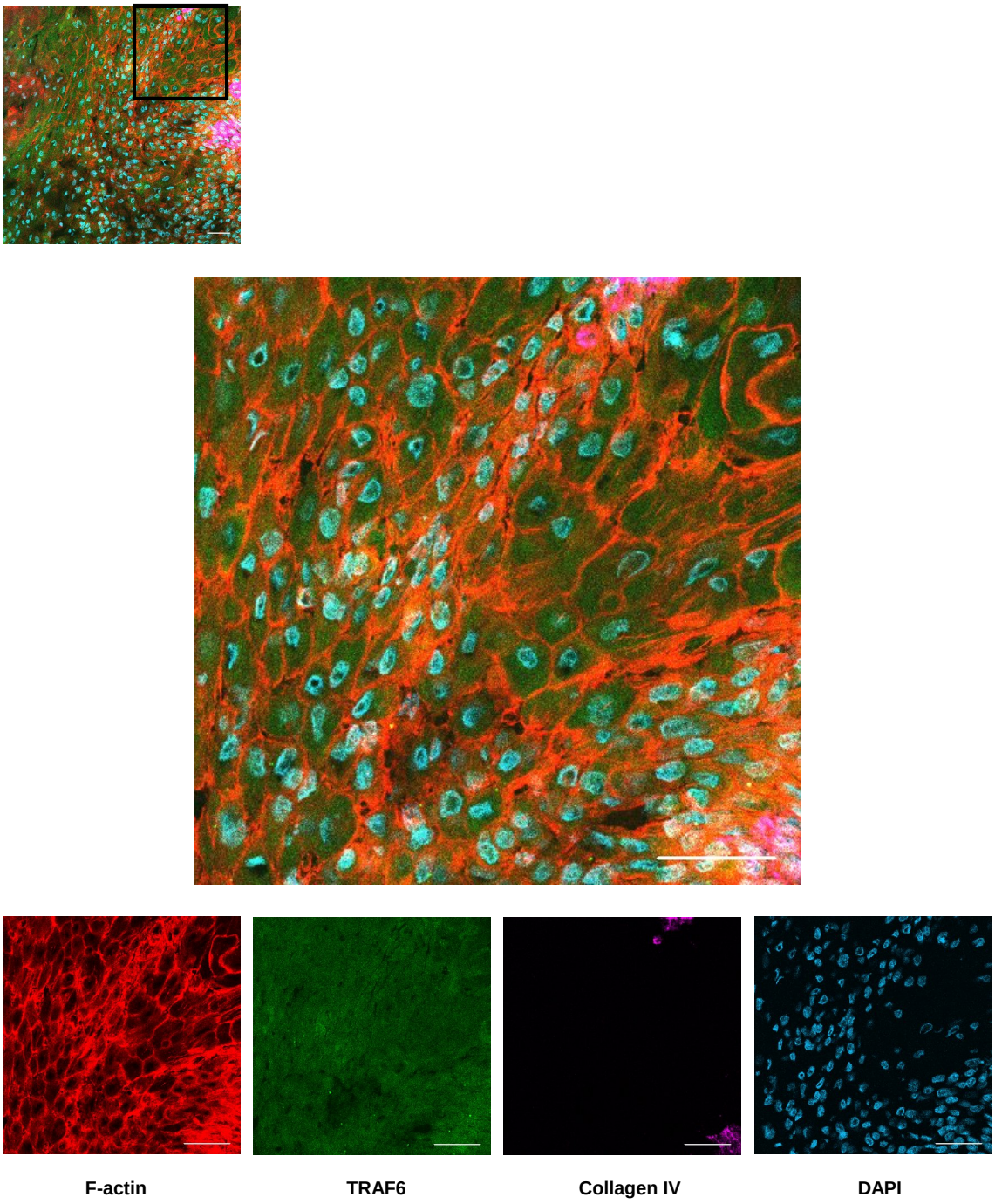

Figure 8.23 High power confocal imaging of SCC of the right FOM

Immunofluoresence staining of tumour tissue from a 70 year old male with SCC of the right floor of the mouth (T_2N_2): Case (**b**) of the SCCHN tissue bank samples illustrated in Figures 8.13-8.18. Sections stained with TRITC phalloidin (1:500), rabbit anti-TRAF6 (1:100), mouse anti-collagen IV (1:100) and DAPI (1:500). Scale bars represent 50μm.

8.6 Summary

- Ethical and R&D approval for the establishment of a human tissue bank was obtained and SCCHN tumour samples with patient matched control tissue is now being accrued.

- TRAF6 immunohistochemistry was optimised by assessing endogenous and exogenous protein expression in A431 cells 72 hours following siRNA gene depletion or transfection with the pUNO-hTRAF6-HA construct.

- Immunostaining of commercial tissue microarrays demonstrated that the normalised mean intensity of TRAF6 positive regions was equal to or greater than that expressed in A431 cells in a subset of SCC: SCCHN (33%), OSCC (80%), CSCC (56%) and vulval SCC (70%).

- Confocal microscopy in association with immunofluoresence staining allowed detailed imaging of tumour tissue, including the visualisation of cytoskeletal structures.

Chapter 9

Discussion

9.1 Introduction

Squamous cell carcinoma (SCC) is an epithelial derived cancer of variable clinical presentation. Important tumour-related factors which govern patient prognosis include the tumour type, size and grade, the depth of carcinoma invasion, and the presence or absence of metastases [3, 4].

Tumourigenesis is complex and is dependent on contextual signals between cancer cells and their associated stroma within the setting of a 'tumour micro-environment' [32]. Cancer cell invasion is accompanied by dramatic changes of cell phenotype and this requires remodelling of a cell's actin cytoskeleton as well as dynamic interactions with the surrounding ECM [108]. Understanding the regulatory pathways that govern cancer cell morphology, motility and invasion are therefore essential to gaining new insights into the clinical behaviour of tumours and their pattern of spread.

Three dimensional (3D) invasion assays and intra-vital imaging indicate that the HECT domain E3 ubiquitin ligase, Smurf1, regulates tumour cell plasticity by targeting Rho A for degradation at the leading edge of motile cells [142]. Given the integral role ubiquitination has in cell biology, knowledge of the temporal and spatial dynamics of ubiquitin-dependent processes is fundamental to understanding the pathological consequences of ubiquitin signalling in cancer.

The work described in this thesis was based upon the premise that ubiquitin-linked pathways are central to the process of cancer cell invasion. The results presented in Chapters 3-8 and their clinical implications are discussed here. Future investigations are also suggested.

9.2 Morphological siRNA screening

To test the hypothesis that ubiquitin-linked pathways are key regulators of the actin cytoskeleton, a series of morphological screens using siRNA targeting 289 E3 ubiquitin ligases and 137 DUBs were performed as detailed in Chapter 3. Cells were plated on collagen-Matrigel® matrix since this was considered to more closely resemble an *in vivo* environment compared to conventional two-dimensional (2D) cell culture. In a 3D matrix cells have distinct patterns of morphology and migration compared with those on a 2D planar surface [311, 312]. This is due to the deformable nature of the substrate which allows the contractile forces exerted by the cell to remodel the matrix and thus influence cell morphology. On rigid surfaces cells frequently appear flat with the underlying changes in contractility affecting cell phenotype being masked.

Morphological screening was initially carried out using A431 vulval carcinoma cells. Gene silencing was accompanied by a variety of cell phenotypes compared to control cells. These included cell rounding, cell elongation, actin-rich spikes, membrane blebs and a disrupted actin cell cortex (Figures 3.2-3.4). Cell morphology was assessed qualitatively and scored descriptively by at least two independent observers (Tables 3.1-3.6). Each screen was blind and performed twice. Prior to commencing this project, experience within our group had validated this screening process and, although labour intensive, the technique proved to be appropriate for the overall size of the screen (426 genes). Developing a high throughput automated system (as described by Bakal *et al.*) with the specificity and sensitivity to distinguish the cell phenotypes observed following gene depletion was beyond the scope of this work [313]. However such a system would be useful for future siRNA morphometric screens.

Forty-five '1st Round' gene hits were identified (Tables 3.7 and 3.8). Subsequent de-convolution of the respective SMARTpools to exclude 'off-target' phenomena reduced this number to 29 '2nd Round' hits (Table 3.9). Several of these genes: USP2, BAP1, RNF12 and RNF14 are up-regulated in a variety of cancers including breast, prostate and renal cell carcinoma [314]. Mdm4 regulates the activity of the tumour suppressor protein p53 and is frequently overexpressed in SCCHN [315, 316]. p53 is mutated in more than 50% of human tumours and has been studied principally for its functions in cell cycle arrest and apoptosis. There is growing evidence, however, for a role of p53 in cell motility [317, 318, 319] . Moreover, Mdm4 translocates to the cytoplasm of tumour cells which suggests that it may function independently of p53. Testing co-operation and

redundancy of Mdm4 with its regulatory partner Mdm2 in relation to p53, the actin cytoskeleton and cell movement may therefore be of future interest.

Tumours are not only composed of carcinoma cells, but of several other cell types capable of interacting with each other within a highly ordered ECM. Both stromal and epithelial phenotypes co-evolve during tumourigenesis and it is now clear that these stromal cells are not merely innocent bystanders [36]. Given this, an additional siRNA screen was performed to further test my 29 '2nd Round' gene hits as regulators of the actin cytoskeleton and to investigate their potential role in CAF function.

The morphology and behaviour of a fibroblast in a 3D collagen gel is dependent on the matrix organization and the overall physical environment of the cell [320]. In the floating matrix model (a low tension system) actin stress fibres are not seen in fibroblasts, few focal adhesion phenotypes are observed and matrix biosynthesis is limited [305]. Conversely, in attached or restrained matrices (as used here), a high tension state exists and fibroblasts become bipolar following massive cytoskeletal reorganization (Figure 3.8). This is characterised by the formation of stress fibres (Figure 3.13b) and focal adhesions [321]. Fibroblasts associate with collagen fibrils, are under isometric tension and develop reciprocal mechanical interactions with the collagen matrix. Consequently, fibroblast tractional forces are transmitted to the surrounding matrix inducing local and global matrix remodelling (contraction and compaction) [322]. This process is analogous to that seen in normal tissue, wound healing, tissue fibrosis and, importantly in the context of this work, cancer stromagenesis [305].

Eight genes (MKRN2, RKHD2, TRAF6, Mdm4, HERC4, SAE1, ZA20d1 and USP6) when individually depleted in HNCAF, resulted in markedly abnormal cell phenotypes (Figures 3.8-3.12). Of interest was the observation that the cell bodies in the majority of these cases had fewer stress fibres and an increased spread area. This appearance is more typical of a fibroblast in a floating matrix model where cells are not under isometric tension and tissue remodelling occurs primarily as a result of the motile activity of cells rather than force-mediated contraction [323]. Furthermore, these morphological traits resemble those of fibroblasts in 'quiescent' tissue *in vivo* [324]. Thus, these genes are likely to be important to the matrix remodelling activities of stromal fibroblasts in the context of the tumour micro-enviroment.

9.3 Functional siRNA screening

9.3.1 Organotypic modelling

Traditionally, cancer cell behaviour has been studied *in vitro* using 2D monolayer culture on plastic or glass with or without matrix. Although useful for investigating many aspects of cell biology, 2D systems are of limited value when studying dynamic processes such as tumour invasion. A defining feature of malignancy is the infiltration of cancer cells into the surrounding stroma. In turn, expansion of the stroma occurs to support tumour growth and is fundamental to further progression of the carcinoma. Tumour invasion occurs in three dimensions and thus the development of 3D model systems which recapitulate the tumour micro-environment *in vitro* continues to be of interest.

The organotypic culture (Figure 4.1) is one such system and was first used to study SCC invasion by Fusenig and colleagues [325]. By varying the cellular and matrix components, organotypic modelling has subsequently proven to be a resourceful technique to investigate many aspects of carcinoma invasion. It is particularly useful with regards to interrogating epithelial-stromal interactions [326]. Moreover, an objective and quantitative method for the analysis of SCC invasion in organotypic culture has been developed. The 'Invasion Index' combines depth and pattern of invasion in a single value and is a robust, accurate and reproducible method for the assessment of cancer cell invasion *in vitro* [302].

To investigate the role of my 29 '2nd Round' gene hits (Table 3.9) on SCC invasion, a functional siRNA screen was performed using an established organotypic model incorporating carcinoma cells (SCC12) with stromal fibroblasts (HNCAF) in a collagen-Matrigel® matrix [77]. Cdc42 is a key regulator of carcinoma invasion in this system and was included as the positive control to assess the effect of gene depletions on SCC12 behaviour [77]. Serial assays were undertaken and three genes, RKHD2 (Figure 4.3), TRAF6 (Figure 4.4) and ZA20d1 (Figure 4.8), emerged as regulators of cancer cell invasion. In addition, these three genes (along with MKRN2 and USP6) when individually knocked down in HNCAF impaired the ability of the stroma to support carcinoma invasion (Figures 4.10-4.12).

These results highlight the benefit of 3D 'physiological' systems in cancer cell biology. Twenty-one of the 29 genes identified as cytoskeletal regulators in A431 cells had no obvious effect on carcinoma invasion when depleted in SCC12 cells (data not shown). Bearing in mind potential intrinsic differences between the two cell lines, this observation emphasises that morphological changes (even if assessed in a 3D environment) do not necessarily translate to functional significance. The ease with which the system was adapted to examine the ability of gene depleted HNCAF to promote cancer cell invasion also demonstrates its versatile nature. Molecular and dynamic interactions between cells and their surrounding ECM can now be studied in detail, either together or in isolation, in an *in vitro* environment that mimics many aspects of biological tissue [305].

Obvious limitations of the organotypic culture system in its current form are the absence of a vasculature network and the lack of a tumour associated inflammatory response. The inclusion of endothelial cells, either within or beneath the matrix, would potentially allow modelling of angiogenesis alongside existing epithelial-stromal interactions [326]. Incorporating immune cells in to the system is another area for improvement since several studies have demonstrated the invasive promoting role of TAM [71].

A novel organotypic model based on human uterine leiomyoma tissue has recently been described [327]. In this system several oral, breast and melanoma cell lines were shown to invade with highly distinct patterns which were less discernible in collagen-based gels. The authors concluded that myoma-based cultures, compared to traditional organotypic models, more closely resembled the tumour micro-environment and that this was attributable to the natural nature of the stromal scaffold. Given these findings, the pattern of carcinoma invasion observed in our system may actually reflect the relative capacity of the stroma to support invasion rather than the intrinsic behaviour of the carcinoma cells themselves.

Large scale functional RNAi screens using organotypic cultures may be possible in the future. Such screens being more biologically representative are likely to yield results which are readily translated into clinically relevant findings [326].

9.3.2 Fibroblast-dependent collagen-Matrigel® matrix remodelling

Matrix remodelling by fibroblasts is integral to tumourigenesis and critical to cancer cell invasion [304]. In recent years significant progress has been made in understanding the adaptive and reciprocal interactions that occur between fibroblasts, their neighbouring cells and the ECM in tissues. Studies of fibroblasts in 3D collagen matrices have demonstrated the importance of both biomechanical conditions and molecular cues for co-ordinated cell signalling and movement [305]. Fibroblasts have the ability to contract collagen gels; a phenomenon that can be observed at the macroscopic level [303, 306]. Furthermore, a good correlation between the degree of macroscopic gel contraction and the extent of microscopic matrix remodelling exists [77].

Figure 4.17 presents scatterplots of mean carcinoma invasion and mean gel contraction for the organotypic assay assessing the functional significance of HNCAF interference (Section 4.2.2). Consistent with previous findings, the ability of ROCK depleted fibroblasts to contract their ECM was noticeably impaired (Figure 4.15) and was associated with reduced carcinoma invasion [77]. Five genes (MKRN2, RKHD2, TRAF6, ZA20d1 and USP6) when individually silenced in HNCAF resulted in a statistically significant decrease in SCC invasion. The relationship of the Contraction Index to the Invasion Index for each of these gels, however, was inconsistent. There are several potential explanations for this. Firstly, the Contraction Index is exactly that - it measures the degree of gel contraction but gives no indication of the other architectural changes that have occurred in the matrix. Gel contraction is therefore not a perfect marker of the extent of matrix remodelling and the latter by itself does not necessarily translate to increased cancer cell invasion. Secondly, protease-mediated matrix remodelling has been shown to be important for carcinoma invasion in this system and its contribution, relative to force-mediated remodelling, is possibly under represented by the Contraction Index [77]. Finally, as matrix remodelling progresses the gels contract and spontaneously detach from the underlying plate. In doing so, the system probably shifts from a high tension to a low tension state at which point fibroblast traction and force-mediated remodelling is likely to be restricted. Current evidence suggests that matrix remodelling in this setting primarily reflects the motile activity of fibroblasts, a situation which would still favour the collective invasion of cancer cells [323].

9.4 Validation of gene hits and candidate genes

A summary of the results of the morphological and functional screens described in Chapters 3 and 4 is presented in Figure 4.18. From the original 426 gene library, three E3 ubiquitin ligases (MKRN2, RKHD2 and TRAF6) and 2 de-ubiquitinating enzymes (ZA20d1 and USP6) emerged as potential candidate genes.

9.4.1 TRAF6 and ZA20d1

Following further validation using Qiagen® siRNA, qPCR and IMF (Chapter 5, Section 5.2) and after reviewing the scientific literature, TRAF6 and ZA20d1 were selected for in depth study. Data at this time suggested that ZA20d1 was the complementary DUB to TRAF6 and that both proteins participated in canonical NF-κB signalling following TNFR and IL-1R activation [163, 307, 308].

Having selected TRAF6 and ZA20d1 as candidate genes, I sought to confirm their function as regulators of carcinoma invasion. To this end, SCC12 organotypic assays using six targeting siRNA duplexes for each gene were performed. The results of these experiments were particularly convincing (Figures 5.14-5.18). Moreover, double gene depletion when compared to single gene depletion of either TRAF6 or ZA20d1 did not lead to greater inhibition of carcinoma invasion (Figures 5.19-5.21). This finding was not unexpected given the supposition of both proteins converging on the same NF-κB regulatory checkpoint.

Next, the functional significance of TRAF6 and ZA20d1 in A431 cells was assessed. Compared to SCC12 cells, A431 cells were intrinsically less invasive in organotypic culture and therefore the duration of the assays was lengthened to 2 weeks (Chapter 2, Section 2.2.8.5). Individual gene depletion of either TRAF6 or ZA20d1 in A431 cells resulted in a statistically significant reduction in cancer cell invasion (Figures 5.22-5.24).

A431 carcinoma invasion was characterised by a thick ‘epithelial’ layer and a broad based cohesive invasive front. These histological features, along with the inherently less invasive nature of A431 cells and their inability to metastasise *in vivo*, tentatively suggest that the cell line may have been derived from a verrucous vulval carcinoma.

Unfortunately, information in the literature pertaining to the nature of the original tumour is sparse.

9.4.2 RKHD2

To date, there is no experimental data regarding the function of RKHD2 other than a single study which speculatively links its E3 ligase activity to the pathogenesis of essential hypertension [309]. Knocking down RKHD2 in both SCC cells and HNCAF resulted in phenotypic changes similar to those observed with Rho A gene depletion (Chapter 3). Functionally, silencing RKHD2 in stromal fibroblasts impaired their ability to promote carcinoma invasion (Chapter 4, Section 4.2.2). These findings are consistent with previous work which has demonstrated that the activation of Rho is necessary for fibroblast-led collective invasion of cancer cells [77]. Examining a possible interaction of RKHD2 with the Rho-ROCK pathway would therefore be a natural starting point to investigate this gene further. Given that the Rho-ROCK pathway is an established regulator of smooth muscle contraction and hypertension [328], an interaction with RKHD2 would provide a potential explanation for the latter's association with essential hypertension.

9.4.3 MKRN2

MKRN2 is a well conserved member of the makorin RING zinc-finger gene family and possibly functions as a co-regulator of the Raf-1 proto-oncogene [329]. Raf occurs downstream of Ras in the MEK-ERK (ERK) pathway, a kinase signalling cascade that is constitutively active in several human cancers [330]. Activated ERKs are pleiotropic effectors of many aspects of cell physiology and have been linked to tumour growth, angiogenesis, invasion and metastasis. As Raf is integral to the ERK pathway several novel agents targeting it are currently being developed for clinical use [330, 331]. Given that somatic mutations of B-Raf are common in papillary thyroid cancer, it is particularly interesting to note that MKRN2 was recently included in a 19 gene molecular classifier capable of discriminating the latter from normal thyroid tissue [332]. If MKRN2 is in fact a co-regulator of Raf-1, it could be a valuable therapeutic target and as such would merit further investigation.

9.4.4 USP6

USP6 (TRE2 or TRE17) was originally identified in multiple transfection-based screens for novel oncogenes by its ability to transform MEFs [333]. It was subsequently shown to function as a ubiquitin-specific protease and is derived from the chimeric fusion of two genes (USP32 and TBC1D3) as a result of genomic rearrangement during evolution [334].

Translocation of USP6 occurs in over 60% of aneurysmal bone cysts (ABCs) [335]. ABCs were previously regarded as reactive inflammatory lesions but are now considered to be neoplastic in nature, accounting for 1-2% of all primary bone tumours [336]. They usually occur in the first two decades of life and may result in extensive local bone destruction leading to pathological fracture [337]. Histologically, ABCs are complex lesions consisting of blood-filled spaces separated by connective tissue septa composed of fibroblasts and reactive woven bone with osteoclast-like giant cells.

The mechanisms by which USP6 overexpression contributes to the pathogenesis of ABCs are poorly understood. Ye *et al.*, however, have recently shown that USP6 induces the production of MMP9 in a USP-dependent manner via Rho A - ROCK mediated NF-κB activation [335]. Prior to this, previous IHC studies of ABCs have consistently shown that MMP9 is expressed in the fibrous stroma. The authors therefore suggest that MMP9 is an effector of USP6 *in vivo* and is fundamental to the pathogenesis of ABCs [335]. They go on to comment that USP-specific inhibitors or NF-κB antagonists may represent novel therapies for ABCs in the future.

Due to the conserved nature of USP6 with respect to USP32, I was unable to generate a functional set of DNA primers necessary to validate the knockdown efficiency of the USP6 siRNA duplexes using qPCR (Chapter 5, Section 5.2.2). Consequently, USP6 was 'dropped' at that stage. The finding that USP6 was functionally significant in HNCAF is interesting, however, particularly in light of the data regarding its oncogenic role in ABCs. The signalling pathway of USP6 > Rho A - ROCK > NF-κB > MMP9 proposed by Ye *et al.* may be equally applicable to the stromal compartment of SCC.

9.5 NF-κB signalling in SCC invasion

Chapters 3, 4 and 5 describe the identification and selection of TRAF6 and ZA20d1 as candidate genes, as well as confirmation of their regulatory roles in carcinoma invasion. As mentioned previously, current literature suggested that both proteins were central to canonical NF-κB signalling in epithelial cells [163, 307]. In view of the latter's importance in the pathogenesis of SCC (Chapter 1, Section 1.5), it was conceivable that TRAF6 and ZA20d1 were influencing cancer cell invasion in a NF-κB dependent manner.

9.5.1 Carcinoma invasion is NF-κB dependent

The significance of NF-κB pathways in cancer cell invasion in our organotypic system was investigated using TNFα, IL-1α, several IKK inhibitors and infliximab (Chapter 6). These experiments demonstrated that carcinoma invasion could be driven by stimulation with both TNFα and IL-1α. The results also indicated that TNFα promoted SCC12 carcinoma invasion in a dose responsive manner by a duel influence on both the epithelial and stromal compartments of the system. Moreover, TNFα stimulation was associated with a dose responsive increase in fibroblast-dependent gel contraction which correlated positively with the Invasion Index. In contrast to this, IL-1α exerted a dose responsive effect on SCC12 invasion without potentiating the invasive promoting and matrix remodelling functions of HNCAF. The difference with respect to CAF activity was a reflection of the underlying NF-κB response, the latter failing to be elicited by IL-1α.

Molecular profiling studies show that NF-κB regulates a large array of genes which are functionally relevant to many aspects of tumourigenesis such as cell proliferation, cell survival, cell migration, angiogenesis and inflammation [219]. This work supports previous findings that NF-κB signalling is pertinent to the local invasion of SCC and, by inference, metastasis.

During tumourigenesis, the stroma facilitates disease progression through its interaction with carcinoma cells and the significance of this relationship with respect to carcinoma invasion was further demonstrated here. The importance of TNFα and IL-1α in the pathogenesis of several cancers is well established and has been previously discussed in

Chapter 1, Sections 1.6 and 1.7. Both cytokines have also been shown to sustain canonical NF-κB signalling [192, 310].

The results presented in Chapter 6 corroborate the above and provide additional evidence for the role of TNFα and IL-1α in the regulation of SCC invasion. Subsequent work performed by our group (data not shown) has confirmed that SCC12 cells constitutively express 10 times as much TNFα than either A431 cells or HNCAF. Comparative expression of TNFR1 across the three cell lines was also examined and shown to be 1.4, 1 and 1.8 respectively. Further delineating the intracrine, autocrine and paracrine activities of TNFα and IL-1α within the tumour micro-environment may therefore lead to novel advances in cancer therapy.

Recently, a short-term *ex vivo* organotypic culture method that utilises freshly procured tumour tissue has been described [338]. In this system, tissue architecture, cell viability, epithelial and stromal signalling activity as well as global gene expression profiles were preserved for up to 5 days. The authors were also able to demonstrate the value of this technique in predicting tumour sensitivity to small molecular inhibitors in a patient-specific manner.

Overall, the assortment of cytokines, their relative concentrations and the expression patterns of their receptors effectively mediate the interactions a cancer cell has with its neighbouring stromal and host immune cells [257]. It is the summation of these cellular interactions which ultimately determines the biological nature and behaviour of a tumour.

9.5.2 NF-κB as a therapeutic target in SCC

The role of NF-κB signalling in tissue homeostasis, acute and chronic inflammation as well as autoimmune disease is well documented [187]. There is also considerable evidence that NF-κB is constitutively active in SCC and is of broad importance to cancer in general [239, 240]. Consequently, NF-κB and the signalling pathways that regulate its activity have become a focal point for intense drug development [339].

To date, over 750 inhibitors of NF-κB have been identified but for the majority of these compounds the molecular basis of their action is poorly understood [340]. Broadly

speaking however, inhibition of NF-κB signalling can occur at the following points within the molecular cascade: (a) the receptor or adaptor level (b) the IKK complex, (c) the proteasome and (d) transcription in the nucleus.

The IKK complex has been an obvious target for the development of small molecular inhibitors given its central role in canonical NF-κB signalling. Approximately 150 compounds exist and these may be classified on the basis of their mode of action into: (a) IKKβ Cys-179 reagents, (b) allosteric inhibitors and (c) ATP analogs [340]. Four IKK inhibitors were used in this work to investigate whether carcinoma invasion was NF-κB dependent (Chapter 6, Section 6.4). IKKI-II (Wedelolactone) is the active ingredient of the herbal medicine *Eclipta alba* and interacts with Cys-179 in the activation loop of IKKβ. IKKI-III is an allosteric inhibitor of IKKβ. Both IKKI-2 and IKKI-X are synthetic ATP analogs. Presently, IKK inhibitors are not in clinical use but given their effectiveness at blocking SCC invasion *in vitro* they may have the potential to be anti-motility drugs in the future.

Bortezomib (Velcade® or PS-341) was the first selective 26S proteasomal inhibitor to be used clinically and has since been approved for the treatment of refractory multiple myeloma [341]. It has also been shown to have radiosensitizing effects in SCC cell lines and murine models which exhibit constitutively activated NF-κB [342]. At present, data regarding the influence of bortezomib on cancer cell invasion is lacking. It would thus be interesting to test it in our organotypic system in view of the NF-κB dependent nature of carcinoma invasion. Clinical trials involving bortezomib in the management of SCC are in progress.

In addition to small molecular NF-κB inhibitors, several commonly used compounds have been reported to have off-target anti-NF-κB activity. These include: non-steroidal anti-inflammatory drugs [343], anti-oxidants [344], thalidomide [345], and natural products such as curcumin and capsaicin [346]. Some of the above are already in use or are being investigated within the field of cancer chemotherapeutics. In time a greater knowledge of their target specificity, efficacy, and potential toxicity will allow a more rational use of these agents in the clinical setting.

Currently, the main factor limiting the clinical use of NF-κB inhibitors is the lack of target specificity which drastically reduces their therapeutic efficacy. This relates to the

varied biological functions of NF-κB signalling and the fact that a number of key intermediaries overlap with other molecular pathways. The challenge to identify compounds that only block NF-κB activation therefore remains. Alternatively, low dose combination therapy using several inhibitors that target multiple steps in NF-κB signalling may be an effective strategy which limits unwarranted side effects [340].

9.5.3 Targeting TNFα for cancer therapy

TNFα is not present in the plasma of healthy individuals but may be detected in cancer patients in picogram concentrations [252]. It is a pivotal chemical mediator within the tumour micro-environment and is highly expressed by both cancer and stromal cells in a variety of malignancies [191].

General and cell specific deletion of TNFα reduces the incidence of cancer in experimental animal models [252]. For example, TNFα KO and TNFR1 KO mice are resistant to chemically-induced carcinogenesis of the skin [347]. Moreover, in a mouse model of hepatocellular carcinoma TNFα from parenchymal cells was shown to cause paracrine activation of NF-κB in neighbouring hepatocytes and be instrumental to tumour development [348].

Other studies suggest that TNFα may confer metastatic properties to tumour cells [191, 245]. In a colon adenocarcinoma-lung metastasis model, metastatic lesions were demonstrated to be TNFα dependent [349]. Similar observations were also found in an experimental fibrosarcoma system in which the number of lung metastases was increased in mice pre-treated with TNFα and decreased in mice administered an anti-TNFα antibody [350].

Infliximab (Remicade® or cA2) is a chimeric monoclonal antibody composed of 75% human-derived and 25% mouse-derived amino acids. It was the first biological to be tested in the management of rheumatoid arthritis and is now used for the treatment of several chronic inflammatory conditions such as psoriasis and Crohn's disease [245]. Infliximab blocks circulating and membrane bound TNFα which in turn limits the production of other inflammatory cytokines including IL-1, IL-6, IL-8 and IFNγ. It has also been shown to down-regulate cell adhesion proteins and matrix metalloproteinases as well as inhibit angiogenesis and leucocyte trafficking to sites of inflammation [245].

These findings suggest that infliximab and other TNFα antagonists could have potential as cancer chemotherapeutic agents.

To date, less than ten Phase I and Phase II cancer trials using anti-TNFα therapy have been reported [191]. Brown *et al.* assessed the tolerability and biological effects of infliximab in 41 patients with a histologically confirmed diagnosis of advanced or metastatic non-haematological malignancy [351]. Tumour type was as follows: colorectal (12), ovarian (8), renal (4), melanoma (3) and other (14). Thirty-eight individuals were refractory to previous chemotherapy but all had an estimated life expectancy of at least 3 months. Participants received infliximab infusions at 0, 2 weeks and every 4 weeks thereafter at either 5 or 10mg/kg. Median serum infliximab concentrations one hour post administration were 107μg/ml and 252μg/ml respectively. Treatment was well tolerated with no dose-limiting side effects and in all cases neutralisation of serum TNFα was observed. Seven patients experienced disease stabilisation (range 10-50 weeks) and the authors concluded that further trials of infliximab and similar anti-TNFα agents may be warranted. Other trials involving etanercept (Enbrel®), a human recombinant TNFR-Fc fusion protein, have also reported disease stabilisation in cases of breast, ovarian and haematological cancers [352, 353, 354].

Having established carcinoma invasion in our organotypic system to be TNFα driven and NF-κB dependent, I corroborated these findings by investigating the effects of infliximab on cancer cell invasion (Chapter 6, Section 6.5). Infliximab was shown to block NF-κB signalling in both A431 cells (Figures 6.87-6.89) and HNCAF (Figures 6.90-6.92). Furthermore, it inhibited fibroblast-dependent collagen-Matrigel® matrix contraction and reduced SCC12 carcinoma invasion in a dose responsive manner (Figures 6.81-6.86).

To my knowledge, there is currently no published literature that specifically reports the inhibitory action of TNFα antagonists on SCC invasion. This data is exciting in that it suggests that infliximab could potentially be exploited as an anti-invasive cancer drug. This would be of considerable benefit to patients with SCCHN in which metastatic spread along the cervical chain of lymph nodes is associated with a markedly worse clinical prognosis. Given the opportunity, it would be interesting to validate these findings with other SCC cell lines, as well as *in vivo* using either intra-vital imaging techniques or experimental models of metastasis. The influence of other TNFα

antagonists such as adalimumab (Humira® or D2E7) on carcinoma invasion and tumour development as a whole would also be worthy of further investigation.

Patients receiving biological therapy require close monitoring throughout treatment. Reported side-effects of infliximab and related drugs include: blood dyscrasias such as thrombocytopaenia and aplastic anaemia, hypersensitivity reactions, heart failure, opportunistic infections including the re-activation of tuberculosis, septicaemia and increased malignancy risk. Prolonged concurrent use of TNFα inhibitors with other immunosuppressant agents such as azathioprine, ciclosporin and methotrexate is not recommended [245]. This dogma would most likely apply to their use in cancer chemotherapy.

The future role of TNFα antagonists in cancer treatment will depend on a number of factors. Firstly, a greater understanding of the nature of TNFα-associated epithelial-stromal interactions in early and late-stage malignancy is required. Secondly, criteria for identifying the patients and tumours most likely to respond to anti-TNFα therapy are needed. A low or absent plasma TNFα level has been suggested as a possible biomarker of response but is as yet unsubstantiated [351]. Thirdly, the biological efficacy and safety of these drugs in the context of the medically compromised cancer patient must be evaluated further. Finally, the economic and financial implications of the use of anti-TNFα drugs in the provision of cancer related healthcare would also need to be assessed.

In conclusion, TNFα continues to confound investigators. Conflicting observations regarding the actions of TNFα highlight the complexity of its biological roles, many of which are still not understood. Recent research has focused on the tumour promoting nature of TNFα. From this, however, is the realisation that TNFα may in fact be the Achilles heal of cancer in general, and if suitably exploited provide new exciting opportunities for targeted cancer therapies [191].

9.6 Regulation of the IKK complex by ubiquitination

Under normal circumstances, NF-κB activation is tightly controlled by several post-translational modifications, including phosphorylation and ubiquitination [355].

Ubiquitin is a 76 amino acid (8kDa) polypeptide which when covalently bound to target proteins may alter their half-life, localisation and function [146]. Ubiquitination requires the sequential action of three proteins: ubiquitin-activating enzyme (E1), ubiquitin-conjugating enzyme (E2) and ubiquitin ligase (E3) (Figure 1.9). Moreover, it can be reversed by proteases termed de-ubiquitinating enzymes (DUBs). This form of regulation is known as ubiquitin editing and is integral to NF-κB signalling, particularly at the level of the IKK complex.

9.6.1 TNF receptor-associated factors (TRAFs)

TNF receptor-associated factors (TRAFs) are involved in signal transduction of several receptor families. These include: TNFRs, IL-1Rs, TLRs, T-cell receptors (TCRs) and B-cell receptors (BCRs) [356, 357]. The TRAF family consists of seven members and all have a C-terminal TRAF domain and a series of zinc finger domains. TRAF2-7 also contain a well conserved N-terminal RING domain and function as E3 ubiquitin ligases [358, 359]. TRAF2 and TRAF5 signal only within the TNFR superfamily, where as TRAF6 is pleiotropic and important to the downstream events of many receptor systems [360].

9.6.1.1 TRAF6

TRAF6 is a RING domain E3 ligase which mediates signalling in the IL-1R and TLR pathways [361]. It also regulates downstream events following TNFR1 activation at several levels, but our understanding of these interactions is relatively limited at present.

Current knowledge surrounding the mechanism of IKK and NF-κB activation by TRAF6 is derived from biochemical investigations using a cell-free system [362]. From this work, two TRAF6-regulated IKK activators (TRIKAs) were identified [362]. TRIKA1 is a dimeric ubiquitin-conjugating enzyme (E2) complex that consists of UBC13 and the UBC-like protein, UEV1A [362]. TRIKA2 is a trimeric complex composed of TAK1 and two TAK1-binding proteins (TAB1 and TAB2/3) [363, 364].

Upon ligand binding to IL-1Rs or TLRs, TRAF6 is indirectly recruited to receptor complexes and forms oligomers [161]. TRAF6 oligomerization stimulates its ligase activity and requires dimerization of its N-terminal RING domain via its RING domain and linker helix [161]. This leads to K63 polyubiquitination of target proteins and TRAF6 autoubiquitination via the E2-TRAF6 complex described above. Ubiquitinated TRAF6 then associates with TRIKA2, resulting in TAK1-dependent IKKβ phosphorylation and IKK activation (Figure 9.1) [163]. Ubiquitinated TAK1 also phosphorylates MKK kinases which in turn activate the JNK and p38 kinase pathway [363].

Genetic and biochemical studies indicate that ubiquitinated TAK1 is essential for signalling through IKK and JNK [365]. Firstly, TAK1 activates both IKKβ and MKK6 [363]. Secondly, siRNA silencing or molecular inhibition of TAK1 reduces IKK activation and blocks JNK activation by TNFα and IL-1 [364, 366]. Thirdly, IKK and JNK activity is impaired in *Drosophilia melanogaster* TAK1 mutants [367]. Similar investigations focusing on the relative contributions of TAB1, TAB2 and TAB3 to TRIKA2 have demonstrated partial redundancy of these proteins with respect to NF-κB pathways [163].

Residual IKK activity following TAK1, TAB2 and TAB3 gene depletion may be explained by the presence of alternative pathways of IKK activation [163]. One such pathway involves p62. This is a ubiquitin-associated (UBA) domain protein that binds to TRAF6 and RIP, as well as atypical protein kinase C (PKCζ) [368]. On IL-1 stimulation, TRAF6 forms a complex with p62 and PKCζ which functions in a similar way to TRIKA2 and activates IKK. Evidence supporting this 'minor' pathway comes from experiments using dominant negative mutants of PKCζ which block IKK activation and NF-κB signalling [369, 370]. Furthermore, the activation of IKK by TNFα, IL-1 and lipopolysaccharide (LPS) is markedly reduced in PKCζ-deficient lung cells [371]. TRAF6 has also been shown to be crucial for thymosin α1 (Tα1) triggered PKCζ-dependent IKK activation in mouse embryonic fibroblasts (MEFs) [372]. Finally, it is possible that residual IKK activation does not require an upstream signal at all. TRAF6 mediated K63 polyubiquitination of NEMO or IKKαβ may promote IKK oligomerization, phosphorylation and autoactivation [163].

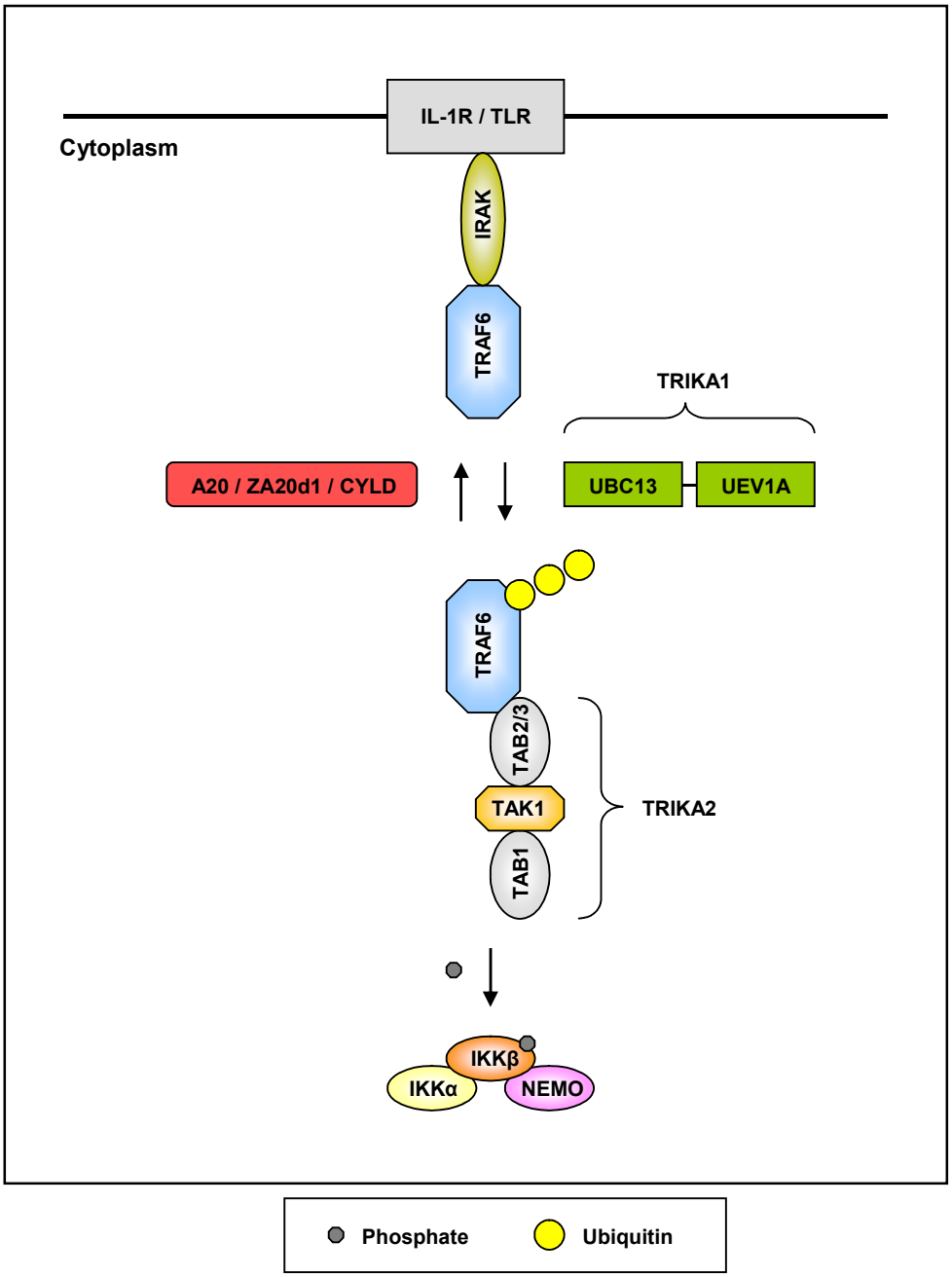

Figure 9.1 Regulation of the IKK complex by TRAF6 ubiquitination

Following IL-1R or TLR stimulation, TRAF6 is indirectly recruited to the receptor complexes. TRAF6 oligomerization leads to autoubiquitination via TRIKA1. Ubiquitinated TRAF6 then associates with TRIKA2 resulting in TAK1-dependent IKKβ phosphorylation and IKK activation. Conversely, TRAF6 can be de-ubiquitinated by the action of A20, ZA20d1 and CLYD there by inhibiting IKK activity.

Figure adapted from Chen ZJ. Ubiquitin signalling in the NF-κB pathway. *Nat Cell Biol* 2005; **7**: 758-765.

9.6.1.2 TRAF2 and TRAF5

Like TRAF6, TRAF2 is a RING-domain E3 ubiquitin ligase which activates canonical NF-κB signalling by promoting K63 polyubiquitination of UBC13 [373]. TRAF2 ubiquitination is also important for the activation of JNK [374]. MEFs deficient in TRAF2 can still activate NF-κB following stimulation with TNFα, but not JNK [375]. The functional redundancy of TRAF2 with respect to NF-κB activation relates to TRAF5 since TRAF2-TRAF5 double knockout cells are defective in both NF-κB and JNK signalling [373].

TRAF2 and TRAF5 have been implicated in the ubiquitination of RIP1 [364]. This leads to the recruitment of the TRIKA2 complex which phosphorylates and activates IKK [376]. Additionally, TRAF6 may also mediate ubiquitin editing of RIP1, performing a similar role to the co-operative activity of TRAF2 and TRAF5 [377]. These aspects of TRAF protein function in signal transduction require further investigation.

9.7 Regulation of the IKK complex by de-ubiquitination

9.7.1 A20

The zinc finger molecule A20, also known as TNFAIP3 or OTUD7C is an NF-κB induced protein and an established negative regulator of NF-κB signalling [378, 379]. It's N-terminal OTU-type DUB domain catalyses removal of K63-linked polyubiquitin chains from RIP1 and TRAF6, there by inhibiting IKK activation (Figure 1.10) [163, 380]. The mixing of A20 with ubiquitinated TRAF6 results in free polyubiquitin chains but not monoubiquitin. This observation suggests that TRAF6 polyubiquitin chains are cleaved at their proximal end and implies a direct interaction between both molecules [381]. A20 also functions as a ubiquitin ligase through its C-terminal zinc finger domains which promote K48-polyubiquitination of RIP1. This leads to the degradation of RIP1 by the proteasome and illustrates how A20 regulates its signalling targets by ubiquitin editing.

A20-deficient mice are hypersensitive to stimulation with TNFα and exhibit prolonged activation of NF-κB. Consequently, they die at an early age from systemic inflammatory response syndrome (SIRS) [183]. Multiple polymorphisms of the gene

encoding A20, TNFAIP3, have also been linked to the autoimmune condition, systemic lupus erythematosus (SLE) [382]. These findings are in keeping with the role of A20 as a negative regulator of NF-κB activation and are consistent with the concept that an imbalance in NF-κB signalling leads to excessive inflammation.

9.7.2 ZA20d1

Zinc finger A20 domain containing 1 (ZA20d1), also known as Cezanne or OTUD7B, is a 100kDa cytoplasmic protein that belongs to the A20 family of de-ubiquitinating cysteine proteases [308, 383]. Literature regarding ZA20d1 is very sparse, but does indicate that it behaves in a similar way to A20 in epithelial and endothelial cells. It too can inhibit NF-κB signalling at the level of the IKK complex or upstream of it by switching polyubiquitin chains and destabilising TRAF6 and RIP1 [307]. ZA20d1, like A20, can be induced by TNFα and IL-1 in cultured cells and has been shown to be recruited to activated TNFRs [307].

9.7.3 CYLD

Ubiquitin carboxyl-terminal hydrolase (CYLD) was the first DUB to be identified as a regulator of the IKK complex [384]. Mutations in CYLD, which is now recognised to be a tumour suppressor, are associated with familial cylindromatosis and multiple hereditary trichoepithelioma [385]. Both conditions are characterised by numerous adnexal skin tumours and enhanced activation of NF-κB. CYLD has been shown to inhibit IKK activation by disassembly of K63-linked polyubiquitin chains on several proteins including NEMO, TRAF2, and TRAF6 [384, 386].

9.8 TRAF6, ZA20d1 and NF-κB signalling in SCC invasion

To test the hypothesis that both TRAF6 and ZA20d1 were influencing cancer cell invasion in our organotypic sytem via their regulatory functions on NF-κB signalling, I investigated the effect of TNFα stimulation on SCC12 cells depleted of either gene (Chapter 7). In both cases, TNFα at a concentration of 31ng/ml rescued invasion (Figures 7.4-7.9). Furthermore, knocking down TRAF6 in SCC12 and A431 cells was

associated with a reduction in the phosphorylation and reciprocal degradation of IκBα under basal conditions (Figure 7.10 and 7.13).

9.8.1 TRAF6

To date, papers concerning the role of TRAF6 in NF-κB activation indicate that it is a positive regulator of the canonical pathway following IL-1R or TLR engagement. These studies suggest that TRAF6 primarily acts alongside TRIKA2 upstream of the IKK complex [151, 161, 163, 377].

Literature regarding its specific role in TNFR signalling is sparse and contradictory in that TNFα induced activation of IKK and NF-κB has been shown to be enhanced in TRAF6-deficient MEFs. The authors attribute this negative regulatory role of TRAF6 to its ubiquitin ligase activity [387]. Given the significance of K63 polyubiquitination to protein processing in general, TRAF6 E3 function seems to be central to its role as a downstream adaptor molecule.

A signalling mechanism to explain the findings presented in Chapter 7 is suggested below and illustrated in Figure 9.2.

Under basal conditions, TRAF6-dependent cytokines drive IκBα degradation leading to NF-κB activation; a situation which favours carcinoma invasion as described in Chapter 6. Given the established role that TRAF6 has in IL-1 signal transduction, it is likely that this pathway dominates over TNFα induced NF-κB signalling in this circumstance. Hence, depleting TRAF6 is associated with a reduction in carcinoma invasion.

When TRAF6 gene depleted SCC12 cells were stimulated daily with TNFα (31ng/ml) carcinoma invasion was rescued (Figures 7.4-7.6), implying that TRAF6 is functionally redundant in this instance. Essentially, IκBα degradation is TRAF6-independent in an enriched TNFα environment with downstream NF-κB signalling events being mediated through other intermediaries, notably TRAF2, TRAF5 and RIP1. Consequently, cancer cell invasion is recovered.

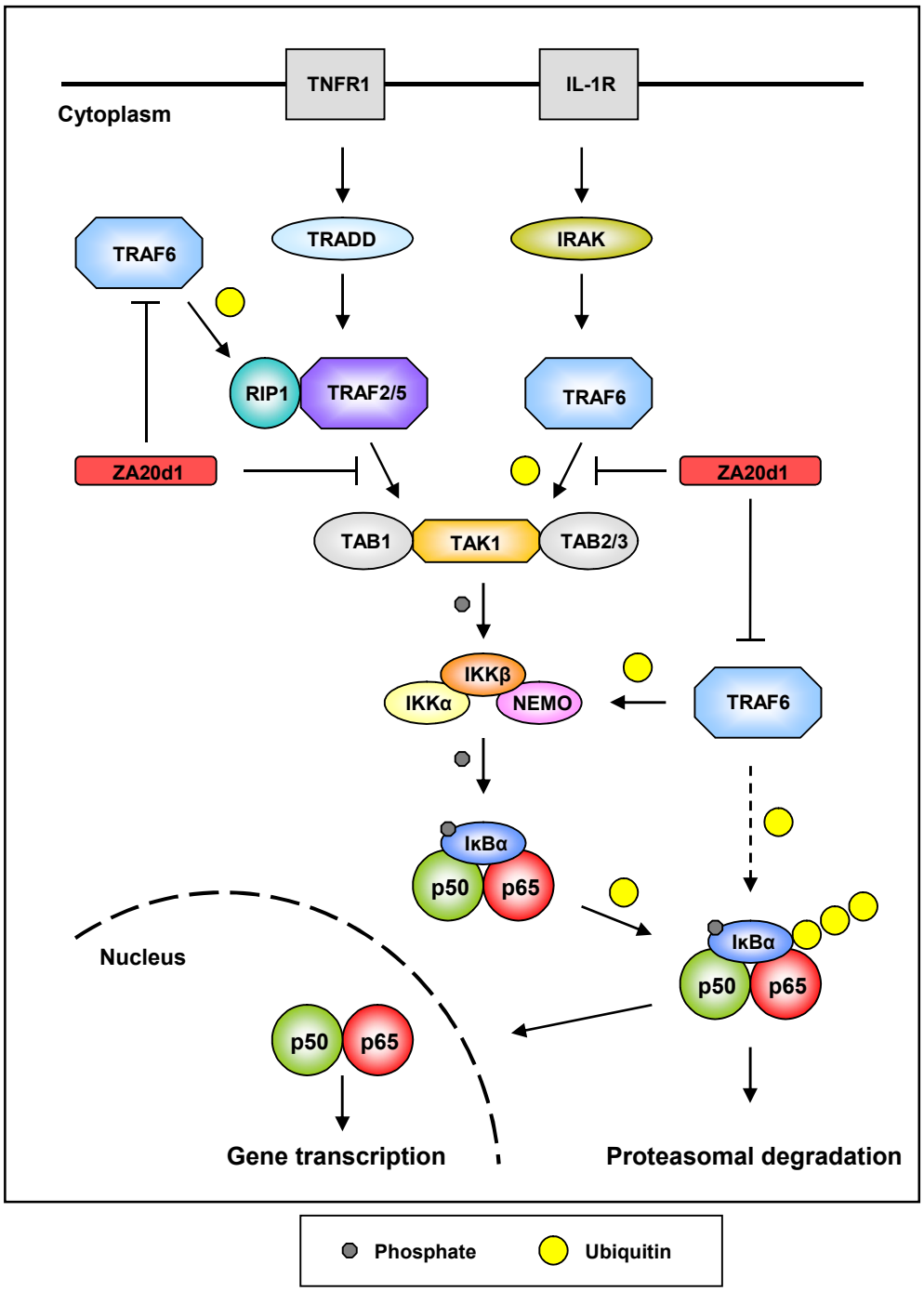

Figure 9.2 Regulation of TNFR1 and IL-1R mediated NF-κB activation by TRAF6 and ZA20d1

Ubiquitin editing is extensively involved in both TNFα and IL-1 induced NF-κB signalling pathways. TRAF6 and ZA20d1 are integral to this process but the nature of their interactions with each other is not fully understood at present.

Figure adapted from Chen ZJ. Ubiquitin signalling in the NF-κB pathway. *Nat Cell Biol* 2005; **7**: 758-765.

Further work is required to validate the above theory. It would be interesting, for example, to repeat the experiments detailed in Chapter 7 using IL-1α. Since IL-1α is known to transcriptionally regulate TNFα as well as potentiate its action, cancer cell invasion could again be rescued. Assessing cancer cell and stromal cell production of IL-1α along with the expression of the IL-1R would also be of value. Invasion assays in which carcinoma cells are depleted of TRAF2, TRAF5, and RIP1 either in isolation or together with TRAF6 would also be of interest.

Recent studies reveal that ubiquitination is extensively involved in TNFα induced NF-κB activation [355]. Although TRAF6 is considered to positively regulate NF-κB signalling upstream of IKK, it is also known to influence the ubiquitination of NEMO and IKKß directly. Figures 7.10 and 7.13 demonstrate that depletion of TRAF6 in both SCC12 and A431 cells was associated with a reduction in the phosphorylation and reciprocal degradation of IκBα. Whether this represents a further point within the NF-κB signalling cascade by which TRAF6 exerts a direct regulatory function remains to be determined.

The recognition that TRAF6 is itself a target for polyubiquitination suggests that an additional level of regulation exists within TNFα and IL-1 induced signalling pathways. The predominant autoubiquitination site in TRAF6 has been mapped to K124 [151, 161]. This is located on the linker helix between the first zinc finger domain and the N-terminal RING domain [388]. Dimerization of the latter promotes aggregation of ubiquitinated TRAF6. Both K124R and dimerization mutants of TRAF6 have impaired abilities to rescue IKK activation in TRAF6 deficient MEFs [388]. Comparison of TRAF6 distribution before and after cell stimulation has demonstrated coalescence and clustering of TRAF6 beneath the cell surface upon activation [161]. Collectively, these findings have led to the hypothesis that TRAF6 aggregation contributes to the formation of a protein scaffold which favours recruitment and ubiquitin editing of downstream signalling targets. TRAF6 may therefore indirectly influence the ubiquitin handling of a wider range of molecular intermediaries than previously thought.

The concept of an expanded lattice of protein processing and interactions would be particularly pertinent to IKK activation. It would also account for the pleiotropic nature of TRAF6 and provide a unifying connection for TNFR1, IL-1R, TLR, TCR, BCR and receptor tyrosine kinase (RTK) signalling [161, 377]. Considering the importance of these

pathways in cancer, it has been suggested that TRAF6 may be an uncharacterised oncogene and as such constitute a valuable therapeutic target [389].

9.8.2 ZA20d1

ZA20d1 and A20 are negative regulators of TNFα induced NF-κB signalling [307, 378]. Both proteins contain E3 ligase and de-ubiquitinase domains and act at the level of the IKK complex or upstream of it by ubiquitin editing TRAF6 and RIP1 [390]. Recently Shembade *et al.* have shown that A20 blocks IL-1 induced activation of NF-κB by binding to TRAF6, thus preventing the latter from associating with the E2 conjugating enzyme Ubc13 [378]. However, the nature of the ubiquitinating and de-ubiquitinating functions of A20 with respect to E2-E3 enzyme interactions remain unknown [391].

In light of the above, the finding that ZA20d1 gene depletion in both SCC12 and A431 cells reduced carcinoma invasion in organotypic culture was surprising. In fact, one might have expected that knocking down ZA20d1 would have resulted in an increase in NF-κB activation and thus greater carcinoma invasion. This result, however, is not so contradictory if the role of ZA20d1 with regards to the ubiquitin processing of TRAF6 and other key intermediaries is considered. In this context, the regulatory activities of ZA20d1 in NF-κB signalling take on a much broader significance.

One possible explanation for the regulatory activities of ZA20d1 on SCC invasion is that gene silencing may interfere with the ubiquitin editing of TRAF6 such that it is unable to autoubiquitinate, aggregate and activate IKK. Consequently, NF-κB signalling and carcinoma invasion is inhibited as previously described for TRAF6 depletion. Knocking down both genes compared to either TRAF6 or ZA20d1 alone did not lead to greater inhibition of cancer cell invasion (Section 9.4.1) and is supportive of this hypothesis. However, unlike TRAF6 depletion, silencing of ZA20d1 in SCC12 and A431 cells did not conclusively influence IκBα degradation (Figures 7.12 and 7.13); a result which is incongruous to the above findings.

An alternative explanation to the above theory is that ZA20d1 acts in an NF-κB independent manner with regards to SCC invasion (Section 9.9.2).

In summary, recent studies have provided additional insight into the role of ubiquitin in NF-κB activation and have revealed levels of complexity in ubiquitin-linked pathways not previously appreciated. Our knowledge of the biological functions of ZA20d1 is relatively sparse at present but this work supports previous literature in suggesting that the functional relationship of ZA20d1 with TRAF6 is worthy of further investigation.

9.9 Could TRAF6 and ZA20d1 be regulating SCC invasion independently of NF-κB signalling?

9.9.1 TRAF6

To date, the majority of literature regarding the functions of TRAF6 focuses on NF-κB activation. Given the overlapping nature of NF-κB pathways with other signalling cascades and the significance of ubiquitination to cell biology in general, it is likely that TRAF6 has a wider sphere of influence regarding signal transduction than previously thought.

TRAF6-deficient mice exhibit skin, hair and dental abnormalities similar to patients with X-linked hypohidrotic ectodermal dysplasia (HED) indicating it has a key role in epithelial embryogenesis and biology [392, 393]. These mice also develop osteopetrosis due to a defect in osteoclast function and ECM remodelling which leads to a progressive increase in bone density, the obliteration of marrow cavities and haematopoietic failure.

Bone resorption involves: (a) proliferation of osteoclast progenitor cells and differentiation to mononuclear prefusion osteoclasts (pOCs), (b) fusion and multinucleation of pOCs, (c) osteoclast pit formation and active bone resorption and (d) osteoclast apoptosis [394]. IL-1 is an important regulator of bone turnover *in vivo* and is associated with destructive bone disease in conditions such as rheumatoid arthritis and multiple myeloma [395]. It acts in a paracrine manner through osteoblasts and stromal cells by stimulating prostaglandin E_2 (PGE_2) synthesis [396]. Immunocytochemical analysis of osteoclast-like multinucleated cells (OCLs) has shown that IL-1 induces cytoskeletal reorganization and the redistribution of TRAF6 to F-actin structures at the cell's periphery, where it co-localizes with c-Src [397]. This TRAF6-cSrc complex is

considered to be necessary for osteoclast activation and the formation of a ruffled cell border characteristic of active bone resorption [397].

Another study using human embryonic kidney 293 (HEK293) cells has also confirmed the interaction of TRAF6 with Src and implicated it in PI3K dependent cytoskeletal changes [398].

Akt (protein kinase B) signalling is involved in many biological functions and its deregulation has been linked to many cancers [399]. Recently, Akt K63 ubiquitination was shown to be an important step for oncogenic Akt activation. TRAF6 was identified as the direct E3 ligase for Akt and was also responsible for its membrane recruitment and phosphorylation upon growth-factor stimulation [389]. Furthermore, in a xenograft tumour model using prostate cancer 3 (PC3) cells, two stable TRAF6 knockdowns had lower tumourigenic potential compared to control cells [389]. It is also important to note that many signalling cascades converge on IKK to promote NF-κB activation; Akt and PI3K pathways are amongst these.

Given more time it would have been interesting to investigate these signalling pathways in our organotypic system by overexpressing wild-type or mutant versions of TRAF6 in conjunction with the use of Src, PI3K and Akt inhibitors.

9.9.2 ZA20d1

As previously mentioned, literature regarding ZA20d1 is very limited. Currently it has only been reported to have a regulatory function in NF-κB signalling. Performing a screen to investigate the effect of depleting ZA20d1 on other pathways implicated in cancer cell motility and invasion would be useful in light of the reasons discussed in Section 9.8.2.

9.10 TRAF6 - a diagnostic tumour marker?

SCC constitutes a heterogeneous group of malignancies each of which has distinct pathophysiology, biological behaviour and varying degrees of response to therapeutic intervention [2]. This is particularly true for SCCHN for which patient mortality rates still exceed 50% in 5 years [1]. Identifying tumour markers and genetic signatures which correlate with metastatic risk is therefore of potential prognostic significance. Hence, human tissue banks have become a vital part of cancer research with the analysis of tumour samples leading to a greater understanding of cancer development and progression as well as advances in diagnosis and treatment.

Chapter 8 describes the establishment and management of a human tissue bank of SCCHN tumour specimens with patient matched control tissue. As discussed in Chapter 1, Section 1.8 the Human Tissue Authority (HTA) was established in 2005 under the Human Tissue Act (HT Act) of 2004 to protect the public from the covert collection of biological samples. Consequently, NREC and R&D applications for tissue collection were initially made in mid 2006 and final approval obtained in late 2008. Currently 40 pairs of matched tissue samples have been accrued. With the importance of bio-banking to medical research being increasingly recognised, legislation pertaining to the removal, storage and use of human tissue is under constant review. To this end, the Integrated Research Application System (IRAS) and the National Institute for Health Research Co-ordinated System for gaining NHS Permissions (NIHR CSP) were set up in 2008 to streamline the approval process for health care studies within the UK.

Chapter 8 Section 8.4 details the analysis of TRAF6 expression in several types of SCC using commercial tissue microarrays purchased from US Biomax Inc. TRAF6 immunostaining was cytosolic in nature and was assessed by measuring the normalised mean pixel intensity of 10 representative areas for each tumour (Chapter 2, Section 2.10.5). Paraffin embedded A431 cell pellets with and without TRAF6-HA expressing cells were stained alongside the tissue arrays and served as positive controls.

Figures 8.6, 8.8, 8.10 and 8.12 show the normalised mean pixel intensity of TRAF6 positive areas of each tumour included in the SCCHN, OSCC, CSCC and vulval SCC tissue microarrays respectively. The most significant result was that of the OSCC array in which 40 of the 50 cases had TRAF6 positive regions which stained with equal or

greater intensity than that observed in the A431 cell pellet. Furthermore, the values recorded for the tumour samples grouped together at a higher mean pixel intensity compared to those of the 9 cases of normal tissue included in the array (Figure 8.8).

The above results suggest that TRAF6 may have potential as a histological tumour marker in a subset of SCC but should be interpreted in light of the following: (a) absolute or total TRAF6 expression was not calculated since core sampling was not standardised and a like to like analysis of a comparative tumour region between cases could not be made. Neither the relative proportion of TRAF6 positive cells nor their distribution within each sample was recorded. (b) Normal tissue relative to tumour tissue was under represented in each array and was not patient matched. (c) The histological grade of each tumour included in the arrays was provided but information regarding the clinical stage was lacking. As a result, TRAF6 expression could not be related to patient outcome.

Representative photomicrographs of H&E and TRAF6 immunostained sections of tumour tissue from three SCCHN tissue bank cases are shown in Figure 8.13. Case (c) - a 53 year old male with SCC of the right tonsil (T_2N_2) was particularly interesting in that TRAF6 expression was similar to that of TRAF6-HA positive A431 cells (Figure 8.14). Moreover, stromal fibroblasts were TRAF6 positive - an observation supportive of the earlier finding that TRAF6 was functionally important in HNCAF (Chapter 4). Loss of pan-cytokeratin markers and strong vimentin immunostaining was also noted in this tumour (Figure 8.19). Given these results, an obvious but perhaps controversial question to ask is has this tumour undergone an EMT and if so, is it related to the increased expression of TRAF6?

In the last few years, SCCHN tumours and cell lines have been investigated using array-based comparative genomic hybridization and gene expression microarrays. Such analyses have resulted in the identification of copy number and gene expression alterations of potential importance in tumourigenesis [400]. In one such study, 18 OSCC cell lines were characterised and 9 high level amplification regions were identified [401]. Amongst these was 11p12-p13 - the region encoding TRAF6.

Figures 8.20-8.22 show matched normal and tumour tissue imaged by confocal microscopy. Tissue architecture was well preserved and detailed imaging of cytoskeletal structures was possible (Figure 8.23). If developed further this technique would be a useful adjunct to IHC to assess protein expression in clinical tumour samples. It could also be used to assess the nature of the interface between the invasive edge of a tumour and its surrounding stroma [402].

9.11 Targeting the ubiquitin-proteasome system

The recognition of the importance of ubiquitin-linked pathways in oncogenesis has generated exciting opportunities for the development of new anti-cancer strategies [403]. Current efforts are focusing on the discovery of specific inhibitors that target E3 ligases, DUBs, the sites of interaction of E3 ligases with their cognate E2s and inhibitors of E1. Table 9.1 lists examples of current inhibitors of the ubiquitin-proteasome system [404, 405].

Since ubiquitin-linked pathways have emerged as promising drug targets, the development of an effective agent capable of inhibiting carcinoma invasion remains a possible end result of this work. The 5 genes identified here: MKRN2, RKHD2, TRAF6, ZA20d1 and USP6 all have the potential to be the focus of future drug development programs.

Understanding the role of ubiquitin editing is fundamental to appreciating the pathological consequences of ubiquitin-linked pathways in cancer. As our knowledge of ubiquitin signalling improves, it is likely that new regulatory mechanisms will be uncovered and this in turn will hopefully lead to novel therapeutic approaches in the future.

Target	Inhibitor	Mode of Action
E3 ligase	Sempervirine	Inhibits the E3 activity of Mdm2
E2-E3 interaction	Nutlins	Block the recognition of p53 by Mdm2
E1	PYR-41	Blocks the initiation of ubiquitination
DUBs	Cyclopentenone PGs	Block proteasomal degradation of ubiquitinated proteins
Proteasome recognition	Ubistatins	Block proteasomal degradation of ubiquitinated proteins
Proteasome degradation	Bortezomib	Block proteasomal degradation of ubiquitinated proteins

Table 9.1 Examples of inhibitors of the ubiquitin-proteasome system

Table adapted from Yang Y, Kitagaki J, Wang H, Hou D, Peranton AO. Targeting the ubiquitin-proteasome system for cancer therapy. *Cancer Sci.* 2009; **100**: 24-28.

9.12 Conclusion

The work described in this thesis investigated the importance of ubiquitin-linked pathways in the process of cancer cell invasion. From a series of cytoskeletal and *in vitro* invasion screens 3 of 289 E3 ubiquitin ligases (MKRN2, RKHD2, and TRAF6) and 2 of 137 DUBs (ZA20d1 and USP6) emerged as hits (Chapters 3 and 4). Following further validation, TRAF6 and its complementary DUB ZA20d1 were selected as candidate genes for in depth study (Chapter 5).

Current literature suggested that both TRAF6 and ZA20d1 were critical to canonical NF-κB signalling events following TNFR and IL-1R engagement. Consequently, the importance of NF-κB activation in our organotypic invasion system was investigated in detail using TNFα, IL-1α, several IKK inhibitors and infliximab (Chapter 6). Carcinoma invasion was shown to be NF-κB dependent and could be driven by stimulation with TNFα in a dose responsive manner by a dual influence on both the epithelial and stromal compartments of the system. In contrast, IL-1α exerted a dose responsive effect on SCC12 invasion without potentiating the invasive promoting and matrix remodelling functions of HNCAF. The difference with respect to CAF activity was a reflection of the underlying NF-κB response, the latter failing to be elicited by IL-1α. Of particular interest, infliximab inhibited cancer cell invasion at a therapeutic dose raising the possibility that TNFα antagonists could be potentially exploited as anti-invasive agents in cancer chemotherapy.

To test the hypothesis that both TRAF6 and ZA20d1 were influencing carcinoma invasion via their regulatory functions on NF-κB signalling, the effect of TNFα stimulation on SCC12 cells depleted of either gene was investigated (Chapter 7). TRAF6 was shown to influence NF-κB activation in carcinoma cells by modulating the levels of IκBα. The mechanism by which ZA20d1 regulated cancer cell invasion was less clear but recent studies have revealed levels of complexity within ubiquitin-linked pathways and NF-κB activation not previously appreciated. The functional relationship of ZA20d1 with TRAF6 requires further investigation.

Ethical and R&D approval for the establishment of a human tissue bank of SCCHN tumour samples, with patient matched control tissue was obtained in accordance with the 2004 HT Act (Chapter 8). Analysis of these specimens and commercial tissue

microarrays indicated that TRAF6 was overexpressed in a subset of SCC. With further work, TRAF6 may have potential as both a histological tumour marker and therapeutic target.

Although this work was performed using cancer cell lines and an *in vitro* model of carcinoma invasion it does generate several interesting findings which, if validated *in vivo*, could eventually be translated into the clinical setting. TNFα antagonists, IKK inhibitors and drugs targeting the ubiquitin-proteasome system offer exciting new strategies in cancer chemotherapy.

Appendix I: SCCHN tissue bank poster

THE THOMAS TATUM HEAD AND NECK UNIT St George's Healthcare NHS
NHS Trust

Mr S M H Mady, FRCS
Mr P A Williamson, FRCS Ed
Mr T Odutoye, FRCS (ORL-HNS)
Mr M S Lee FRCS Ed, FRCS (ORL-HNS) Eng
Mr N Hyde, FDS FRCS (OMFS) MS
Mr BMW Bailey, FDS FRCS Ed
Mr G I Smith FRCS Eng, FRCS (OMFS)
Mr M Vesely, MD, FRCS (Plast)
Dr K Harrington, MRCP FRCR
Dr C Nutting, MD MRCP FRCR
Dr K Newbold MRCP FRCR

Secretary: 0208 725 2052
Fax No: 0208 725 3306
Appointments: 0208 725 2497/1747

Your help is needed in the fight against cancer

Tissue Donation for Head & Neck Tumour Bank

Analysis of Cell Signalling in Squamous Cell Carcinoma (SCC)

Scientists in the Tumour Cell Biology Laboratory at the Cancer Research UK London Research Institute are currently studying how cancer cells spread throughout the body. Understanding cancer cell behaviour offers exciting new opportunities for the development of anti-cancer drugs capable of blocking cancer cell invasion.

You are invited to take part in this research project which involves the donation of small tissue samples at the time of your surgery whilst under a general anaesthetic. For further information please speak to your Consultant Head & Neck Surgeon.

Together we will beat cancer

Principal Investigators

Mr Peter Williamson
Consultant ENT / Head & Neck Surgeon
St George's Hospital
Blackshaw Road, Tooting
London. SW17 0QT

Dr Kevin Harrington
Consultant in Clinical Oncology
The Royal Marsden Hospital
203 Fulham Road
London. SW3 6JJ

Dr Erik Sahai
Tumour Cell Biology Laboratory
CR-UK London Research Institute
44 Lincoln's Inn Fields
London. WC2A 3PX.

St George's University of London · The Institute of Cancer Research · The Royal Marsden NHS Foundation Trust · CANCER RESEARCH UK

Appendix II: Patient information sheet

THE THOMAS TATUM HEAD AND NECK UNIT

Mr S M H Mady, FRCS
Mr P A Williamson, FRCS Ed
Mr T Odutoye, FRCS (ORL-HNS)
Mr M S Lee FRCS Ed, FRCS (ORL-HNS) Eng
Mr N Hyde, FDS FRCS (OMFS) MS
Mr BMW Bailey, FDS FRCS Ed
Mr G I Smith FRCS Eng, FRCS (OMFS)
Mr M Vesely, MD, FRCS (Plast)
Dr K Harrington, MRCP FRCR
Dr C Nutting, MD MRCP FRCR
Dr K Newbold MRCP FRCR

Secretary: 0208 725 2052
Fax No: 0208 725 3306
Appointments: 0208 725 2497/1747

REC Ref: 06/Q0403/125 Protocol Version: Final Submission Date: 21st August 2006

PATIENT INFORMATION SHEET

1. Study Title.

Analysis of cell signalling and the cytoskeleton in squamous cell carcinoma (SCC).

Short Title: Analysis of cell signalling in squamous cell carcinoma (SCC).

2. Invitation to take part in this research project.

You are invited to take part in this research project. Before you decide to join, it is important you understand why the research is being done and what it involves. Please take time to read the following information carefully and discuss it with friends, relatives and your GP if you wish. Ask if there is anything that is unclear or if you would like more information.

Consumers for Ethics in Research (CERES) publish a leaflet entitled 'Medical Research and You'. This leaflet gives more information about medical research and looks at some questions you may want to ask. A copy may be obtained from CERES, PO Box 1365, London N16 0BW.

Thank you for taking the time to read this.

3. What is the purpose of the study?

Approximately 8000 new cases of squamous cell cancer (SCC) of the head and neck are diagnosed each year in the UK. Spread of the disease both locally (in the head and neck region) and distantly (to the rest of the body) are significant clinical problems.

Although there have been enormous advances in our understanding of how cancer cells spread in recent years, many aspects of their behaviour remain poorly understood. Our research aims to study how SCC cells change as they gain the ability to spread and to understand the factors that control this process.

Appendix II: Patient information sheet

4. Why have you been chosen?

You have been chosen because you have been diagnosed with SCC of the head and neck.

5. Do I have to take part?

Taking part in this research study is voluntary. It is up to you to decide whether or not to take part. If you do decide to join the study, you will be given this information sheet to keep and be asked to sign a consent form. A decision to withdraw, or a decision not to take part, will not affect the standard of care you receive in our unit.

6. What will happen to me if I take part?

If you decide to join this study, you will be asked to donate a small sample of cancerous tissue (approximately 7 x 7 mm in size) from your tumour once it has been removed. You will also be asked to donate a similar amount of 'healthy' tissue (a biopsy specimen) from the area adjacent to the site from which your tumour was removed.

By donating 'healthy' tissue you will potentially enable us to identify the changes that occur in the cancer cells more easily.

All procedures will be performed under general anaesthesia by the Head & Neck Surgeon responsible for your care.

7. What do I have to do?

If you decide to take part in this study, you will be asked to sign a form consenting to the donation of your tissue samples for research purposes.

8. What are the side effects of taking part?

This study involves the collection of tissue samples at the time of your head and neck surgery whilst under a general anaesthetic. It is not anticipated that your participation will lead to any additional pain, discomfort, distress or inconvenience than you would otherwise experience as a consequence of your routine clinical care. Pain, bruising, swelling, bleeding, infection, scarring and nerve damage are potential complications of a biopsy.

9. What are the possible disadvantages and risks of taking part?

As mentioned above it is not anticipated that your participation will lead to any additional pain, discomfort, distress or inconvenience than you would otherwise experience as a consequence of your routine clinical care.

Appendix II: Patient information sheet

10. What are the possible benefits of taking part?

There are no likely benefits for you if you take part in the study, although it may benefit future patients by leading to an increase in understanding of how cancer cells behave and the factors controlling the spread of cancer.

11. What if new information becomes available?

Sometimes during the course of a research project, new information becomes available that can have a benefit to patients. This study involves your participation at a single time point and it is unlikely that this research will lead to any developments which will impact on your care. Should this be the case however, then you will be fully informed of any such findings by your Head & Neck Surgeon.

12. What will happen to any samples I give?

All tissue samples donated by patients will be held in a secure Tissue Bank at the Cancer Research UK London Research Institute. Samples will be identified by a unique research number which will be known to only the Tissue Bank Manager. Only Cancer Research UK scientists will have access to the samples. Genetic analysis will not be performed on the samples. You will retain the right to withdraw consent to the use of your tissue samples at anytime. Should you decide to withdraw your consent, your tissue samples will be removed from the tissue bank and destroyed.

13. What happens when the research study stops?

It is anticipated that this research study will stop in October 2009. Tissue samples will be stored for up to 15 years and may be used for future cancer research by scientists at Cancer Research UK.

14. What if there is a problem?

If you are harmed by taking part in this research project, there are no special compensation arrangements. If you are harmed due to an individual's negligence, then you may have grounds for a legal action but you have to pursue this. Regardless of this, if you wish to complain about any aspect of the way you have been approached or treated during this study, the National Health Service complaints mechanisms are available.

15. Will my taking part in the study be kept confidential?

All information which is collected about you during the course of the research will be kept strictly confidential. Any information about you which leaves the hospital will have your name and address removed so that you cannot be recognised from it. All donated tissue samples will be identified by a unique research number and stored in a secure Tissue Bank at the Cancer Research UK London Research Institute. Research findings will not be directly traceable to any particular participant.

Appendix II: Patient information sheet

Your GP will be notified unless you express a wish that they should not be informed.

16. What will happen to the results of the research study?

The results of this study may be published in scientific journals and presented at scientific meetings. If you wish, we will keep you informed about any results that arise from this work - a summary of the research findings will be made available for participants on request. However, because research findings will not be directly traceable to any particular participant it will not be possible to give you specific information about your cancer.

17. Who is organising and funding the research?

The study is being organised across several acute teaching NHS hospitals in London (The Royal Marsden Hospital, St George's Hospital, and Charing Cross Hospital). It is being funded by Cancer Research UK.

18. Who has reviewed the study?

The study has been reviewed by Cancer Research UK and the NHS Research Ethics Committee. This committee consists of medical staff and members whose expertise is outside medicine.

Contact for further information

Any questions about this study should be directed to Mr Peter Williamson (Consultant ENT / Head & Neck Surgeon) or by telephone to 0208 725 2052.

In an emergency the leading investigator, Dr Kevin Harrington (Honorary Consultant in Clinical Oncology, The Royal Marsden Hospital, London), can be contacted on 0207 808 2732.

You will be given a copy of this information leaflet and your signed consent form to keep.

Thank you for taking the time to read this leaflet.

Appendix III: Patient consent form

THE THOMAS TATUM HEAD AND NECK UNIT

Mr S M H Mady, FRCS
Mr P A Williamson, FRCS Ed
Mr T Odutoye, FRCS (ORL-HNS)
Mr M S Lee FRCS Ed, FRCS (ORL-HNS) Eng
Mr N Hyde, FDS FRCS (OMFS) MS
Mr BMW Bailey, FDS FRCS Ed
Mr G I Smith FRCS Eng, FRCS (OMFS)
Mr M Vesely, MD, FRCS (Plast)
Dr K Harrington, MRCP FRCR
Dr C Nutting, MD MRCP FRCR
Dr K Newbold MRCP FRCR

Secretary: 0208 725 2052
Fax No: 0208 725 3306
Appointments: 0208 725 2497/1747

REC Ref: 06/Q0403/125 Protocol Version: Final Submission Date: 21st August 2006

CONSENT FORM

Title of Project: Analysis of cell signalling and the cytoskeleton in squamous cell carcinoma (SCC).

Name of Researcher: Mr Peter Williamson, St George's Hospital, London.

Name of Chief Investigator: Dr Kevin Harrington, The Royal Marsden Hospital, London.

Please initial box

1. I confirm that I have read and understand the information sheet dated 21st August 2006 for the above study and have had the opportunity to ask questions. ☐
2. I understand that my participation is voluntary and that I am free to withdraw at any time, without giving any reason, without my medical care or legal rights being affected. ☐
3. I understand that anonymous tissue and data concerning my person may be stored and used for the purpose of scientific investigation. ☐
4. I agree to my GP being informed of my participation in the study. ☐
5. I agree to take part in the above study ☐
6.

To be signed and personally dated by the patient*.

Name of Patient	Date	Signature
Name of Person taking consent (if different from researcher)	Date	Signature
Researcher	Date	Signature

*If patient is unable to read or unable to sign an impartial witness should be present during the entire informed consent discussion and should sign below

*** Witness Declaration of Patient's Informed Consent**
By signing the consent form I attest that the information was accurately explained to and apparently understood by the patient and that informed consent was freely given by the patient.

Name of Witness	Date	Signature

Comments:_____

Appendix IV: General practitioner information sheet

THE THOMAS TATUM HEAD AND NECK UNIT

Mr S M H Mady, FRCS
Mr P A Williamson, FRCS Ed
Mr T Odutoye, FRCS (ORL-HNS)
Mr M S Lee FRCS Ed, FRCS (ORL-HNS) Eng
Mr N Hyde, FDS FRCS (OMFS) MS
Mr BMW Bailey, FDS FRCS Ed
Mr G I Smith FRCS Eng, FRCS (OMFS)
Mr M Vesely, MD, FRCS (Plast)
Dr K Harrington, MRCP FRCR
Dr C Nutting, MD MRCP FRCR
Dr K Newbold MRCP FRCR

Secretary: 0208 725 2052
Fax No: 0208 725 3306
Appointments: 0208 725 2497/1747

REC Ref: 06/Q0403/125 Protocol Version: Final Submission Date: 21st August 2006

GENERAL PRACTITIONER INFORMATION SHEET

Study Title: Analysis of cell signalling and the cytoskeleton in squamous cell carcinoma (SCC).

GP Name: _____

Address: _____

_____

_____

Patient Name: _____

Date of birth: ____/____/_____

Dear Dr _____,

The above patient, who is registered at your practice, has agreed to donate a sample of tissue from their tumour for the creation of a Tissue Bank at the Cancer Research UK London Research Institute. He / She has also agreed to undergo a biopsy of 'healthy' tissue from the area adjacent to the site of their tumour at the time of his / hers' head and neck surgery. Tissue samples will be used by scientists at Cancer Research UK to study the process of squamous cell carcinoma invasion.

Ethical committee approval and appropriate signed informed consent have been obtained.

You will be informed of any relevant adverse events that the patient may experience, together with any other appropriate information about which you should be aware.

If you require further information regarding this please contact:

Mr Peter Williamson (Consultant ENT / Head & Neck Surgeon) on telephone 0208 725 2052.

Thank you for your co-operation.

Yours sincerely,

Signature: _____

References

1. Parkin DM, Bray F, Ferlay J, Pisani P. Global cancer statistics 2002. *CA Cancer J Clin* 2005; **55**: 74-108.

2. Gil Z, Fliss DM. Contemporary management of head and neck cancers. *Isr Med Assoc J* 2009; **11**: 296-300.

3. Yao M, Epstein JB, Modi BJ, Pytynia KB, Mundt AJ, Feldman LE. Current surgical treatment of squamous cell carcinoma of the head and neck. *Oral Oncol* 2007; **43**: 213-23.

4. Shah JP, Gil Z. Current concepts in management of oral cancer surgery. *Oral Oncol* 2009; **45**: 394-401.

5. Shingaki S, Takada M, Sasai K, Bibi R, Kobayashi T, Nomura T, Saito C. Impact of lymph node metastasis on the pattern of failure and survival in oral carcinomas. *Am J Surg* 2003; **185**: 278-84.

6. Schiff BA, Roberts DB, El-Naggar A, Garden AS, Myers JN. Selective vs modified radical neck dissection and postoperative radiotherapy vs observation in the treatment of squamous cell carcinoma of the oral tongue. *Arch Otolaryngol Head Neck Surg* 2005; **131**: 874-8.

7. Bernier J, Domenge C, Ozsahin M, Matuszewska K, Lefebvre JL, Greiner RH, Giralt J, Maingon P, Rolland F, Bolla M, Cognetti F, Bourhis J, Kirkpatrick A, van Glabbeke M. Postoperative irradiation with or without concomitant chemotherapy for locally advanced head and neck cancer. *N Engl J Med* 2004; **350**: 1945-52.

8. Haddad R, Wirth L, Posner M. Emerging drugs for head and neck cancer. *Expert Opin Emerg Drugs* 2006; **11**: 461-7.

9. Haddad R. Current and future directions in the treatment of squamous cell carcinoma of the head and neck: multidisciplinary symposium on head and neck cancer. *Expert Opin Ther Targets* 2006; **10**: 333-6.

10. Mourouzis C, Boynton A, Grant J, Umar T, Wilson A, Macpheson D, Pratt C. Cutaneous head and neck SCCs and risk of nodal metastasis - UK experience. *J Craniomaxillofac Surg* 2009; **37**: 443-7.

11. Alam M, Ratner D. Cutaneous squamous-cell carcinoma. *N Engl J Med* 2001; **344**: 975-83.

12. Johnson TM, Rowe DE, Nelson BR, Swanson NA. Squamous cell carcinoma of the skin (excluding lip and oral mucosa). *J Am Acad Dermatol* 1992; **26**: 467-84.

13. Veness MJ, Morgan GJ, Palme CE, Gebski V. Surgery and adjuvant radiotherapy in patients with cutaneous head and neck squamous cell carcinoma metastatic to lymph nodes: combined treatment should be considered best practice. *Laryngoscope* 2005; **115**: 870-5.

14. Ross AS, Schmults CD. Sentinel lymph node biopsy in cutaneous squamous cell carcinoma: a systematic review of the English literature. *Dermatol Surg* 2006; **32**: 1309-21.

15. Kwa RE, Campana K, Moy RL. Biology of cutaneous squamous cell carcinoma. *J Am Acad Dermatol* 1992; **26**: 1-26.

16. Jambusaria-Pahlajani A, Miller CJ, Quon H, Smith N, Klein RQ, Schmults CD. Surgical monotherapy versus surgery plus adjuvant radiotherapy in high-risk cutaneous squamous cell carcinoma: a systematic review of outcomes. *Dermatol Surg* 2009; **35**: 574-85.

17. Wollina U, Hansel G, Koch A, Kostler E. Oral capecitabine plus subcutaneous interferon alpha in advanced squamous cell carcinoma of the skin. *J Cancer Res Clin Oncol* 2005; **131**: 300-4.

18. Smith KJ, Hamza S, Skelton H. Topical imidazoquinoline therapy of cutaneous squamous cell carcinoma polarizes lymphoid and monocyte/macrophage populations to a Th1 and M1 cytokine pattern. *Clin Exp Dermatol* 2004; **29**: 505-12.

19. Maclean AB, Jones RW, Scurry J, Neill S. Vulvar cancer and the need for awareness of precursor lesions. *J Low Genit Tract Dis* 2009; **13**: 115-7.

20. Sideri M, Jones RW, Wilkinson EJ, Preti M, Heller DS, Scurry J, Haefner H, Neill S. Squamous vulvar intraepithelial neoplasia: 2004 modified terminology, ISSVD Vulvar Oncology Subcommittee. *J Reprod Med* 2005; **50**: 807-10.

21. Scurry J, Wilkinson EJ. Review of terminology of precursors of vulvar squamous cell carcinoma. *J Low Genit Tract Dis* 2006; **10**: 161-9.

22. de Hullu JA, van der Avoort IA, Oonk MH, van der Zee AG. Management of vulvar cancers. *Eur J Surg Oncol* 2006; **32**: 825-31.

23. Quinn MA, Benedet JL, Odicino F, Maisonneuve P, Beller U, Creasman WT, Heintz AP, Ngan HY, Pecorelli S. Carcinoma of the cervix uteri. FIGO 6th Annual Report on the Results of Treatment in Gynecological Cancer. *Int J Gynaecol Obstet* 2006; **95 Suppl 1**: S43-103.

24. Ackerman W. Verrucous carcinoma of the oral cavity. *Surgery* 1948; **23**: 670-8.

25. Kraus F, Perez-Mesa C. Verrucous carcinoma: clinical and pathological study of 105 cases involving the oral cavity, larynx and genitalia. *Cancer* 1966; **19**: 26-38.

26. Vandeweyer E, Sales F, Deraemaecker R. Cutaneous verrucous carcinoma. *Br J Plast Surg* 2001; **54**: 168-70.

27. Brandsma JL, Steinberg BM, Abramson AL, Winkler B. Presence of human papillomavirus type 16 related sequences in verrucous carcinoma of the larynx. *Cancer Res* 1986; **46**: 2185-8.

28. Ferlito A, Devaney KO, Rinaldo A, Putzi MJ. Papillary squamous cell carcinoma versus verrucous squamous cell carcinoma of the head and neck. *Ann Otol Rhinol Laryngol* 1999; **108**: 318-22.

29. Arduino PG, Carrozzo M, Pagano M, Gandolfo S, Broccoletti R. Verrucous oral carcinoma: clinical findings and treatment outcomes in 74 patients in Northwest Italy. *Minerva Stomatol* 2008; **57**: 335-9, 9-41.

30. Ferlito A, Rinaldo A, Mannara GM. Is primary radiotherapy an appropriate option for the treatment of verrucous carcinoma of the head and neck? *J Laryngol Otol* 1998; **112**: 132-9.

31. Hanahan D, Weinberg RA. The hallmarks of cancer. *Cell* 2000; **100**: 57-70.

32. Pietras K, Ostman A. Hallmarks of cancer: Interactions with the tumor stroma. *Exp Cell Res* 2010.

33. Albini A, Sporn MB. The tumour microenvironment as a target for chemoprevention. *Nat Rev Cancer* 2007; **7**: 139-47.

34. Polyak K, Haviv I, Campbell IG. Co-evolution of tumor cells and their microenvironment. *Trends Genet* 2009; **25**: 30-8.

35. Kolf CM, Cho E, Tuan RS. Mesenchymal stromal cells. Biology of adult mesenchymal stem cells: regulation of niche, self-renewal and differentiation. *Arthritis Res Ther* 2007; **9**: 204.

36. Franco OE, Shaw AK, Strand DW, Hayward SW. Cancer associated fibroblasts in cancer pathogenesis. *Semin Cell Dev Biol* 2010; **21**: 33-9.

37. Comoglio PM, Trusolino L. Cancer: the matrix is now in control. *Nat Med* 2005; **11**: 1156-9.

38. Wiseman BS, Werb Z. Stromal effects on mammary gland development and breast cancer. *Science* 2002; **296**: 1046-9.

39. Weber F, Shen L, Fukino K, Patocs A, Mutter GL, Caldes T, Eng C. Total-genome analysis of BRCA1/2-related invasive carcinomas of the breast identifies tumor stroma as potential landscaper for neoplastic initiation. *Am J Hum Genet* 2006; **78**: 961-72.

40. Weber F, Xu Y, Zhang L, Patocs A, Shen L, Platzer P, Eng C. Microenvironmental genomic alterations and clinicopathological behavior in head and neck squamous cell carcinoma. *JAMA* 2007; **297**: 187-95.

41. Bindra RS, Glazer PM. Genetic instability and the tumor microenvironment: towards the concept of microenvironment-induced mutagenesis. *Mutat Res* 2005; **569**: 75-85.

42. Kalluri R, Zeisberg M. Fibroblasts in cancer. *Nat Rev Cancer* 2006; **6**: 392-401.

43. Brown LF, Guidi AJ, Schnitt SJ, Van De Water L, Iruela-Arispe ML, Yeo TK, Tognazzi K, Dvorak HF. Vascular stroma formation in carcinoma in situ, invasive carcinoma, and metastatic carcinoma of the breast. *Clin Cancer Res* 1999; **5**: 1041-56.

44. Fukumura D, Xavier R, Sugiura T, Chen Y, Park EC, Lu N, Selig M, Nielsen G, Taksir T, Jain RK, Seed B. Tumor induction of VEGF promoter activity in stromal cells. *Cell* 1998; **94**: 715-25.

45. Nagy JA, Dvorak AM, Dvorak HF. VEGF-A and the induction of pathological angiogenesis. *Annu Rev Pathol* 2007; **2**: 251-75.

46. Shekhar MP, Pauley R, Heppner G. Host microenvironment in breast cancer development: extracellular matrix-stromal cell contribution to neoplastic phenotype of epithelial cells in the breast. *Breast Cancer Res* 2003; **5**: 130-5.

47. Ronnov-Jessen L, Petersen OW, Bissell MJ. Cellular changes involved in conversion of normal to malignant breast: importance of the stromal reaction. *Physiol Rev* 1996; **76**: 69-125.

48. Ishihara A, Yoshida T, Tamaki H, Sakakura T. Tenascin expression in cancer cells and stroma of human breast cancer and its prognostic significance. *Clin Cancer Res* 1995; **1**: 1035-41.

49. Brunner A, Mayerl C, Tzankov A, Verdorfer I, Tschorner I, Rogatsch H, Mikuz G. Prognostic significance of tenascin-C expression in superficial and invasive bladder cancer. *J Clin Pathol* 2004; **57**: 927-31.

50. Shimoda M, Mellody KT, Orimo A. Carcinoma-associated fibroblasts are a rate-limiting determinant for tumour progression. *Semin Cell Dev Biol* 2009; **21**: 19-25.

51. Strutz F, Okada H, Lo CW, Danoff T, Carone RL, Tomaszewski JE, Neilson EG. Identification and characterization of a fibroblast marker: FSP1. *J Cell Biol* 1995; **130**: 393-405.

52. Kunz-Schughart LA, Knuechel R. Tumor-associated fibroblasts (part I): Active stromal participants in tumor development and progression? *Histol Histopathol* 2002; **17**: 599-621.

53. Desmouliere A, Chaponnier C, Gabbiani G. Tissue repair, contraction, and the myofibroblast. *Wound Repair Regen* 2005; **13**: 7-12.

54. Hinz B. Formation and function of the myofibroblast during tissue repair. *J Invest Dermatol* 2007; **127**: 526-37.

55. Rodemann HP, Muller GA. Characterization of human renal fibroblasts in health and disease: II. In vitro growth, differentiation, and collagen synthesis of fibroblasts from kidneys with interstitial fibrosis. *Am J Kidney Dis* 1991; **17**: 684-6.

56. Bhowmick NA, Neilson EG, Moses HL. Stromal fibroblasts in cancer initiation and progression. *Nature* 2004; **432**: 332-7.

57. Strieter RM, Wiggins R, Phan SH, Wharram BL, Showell HJ, Remick DG, Chensue SW, Kunkel SL. Monocyte chemotactic protein gene expression by cytokine-treated human fibroblasts and endothelial cells. *Biochem Biophys Res Commun* 1989; **162**: 694-700.

58. Kim KK, Wei Y, Szekeres C, Kugler MC, Wolters PJ, Hill ML, Frank JA, Brumwell AN, Wheeler SE, Kreidberg JA, Chapman HA. Epithelial cell alpha3beta1 integrin links beta-catenin and Smad signaling to promote myofibroblast formation and pulmonary fibrosis. *J Clin Invest* 2009; **119**: 213-24.

59. Olumi AF, Grossfeld GD, Hayward SW, Carroll PR, Tlsty TD, Cunha GR. Carcinoma-associated fibroblasts direct tumor progression of initiated human prostatic epithelium. *Cancer Res* 1999; **59**: 5002-11.

60. Schafer M, Werner S. Cancer as an overhealing wound: an old hypothesis revisited. *Nat Rev Mol Cell Biol* 2008; **9**: 628-38.

61. Sugimoto H, Mundel TM, Kieran MW, Kalluri R. Identification of fibroblast heterogeneity in the tumor microenvironment. *Cancer Biol Ther* 2006; **5**: 1640-6.

62. Orimo A, Weinberg RA. Heterogeneity of stromal fibroblasts in tumors. *Cancer Biol Ther* 2007; **6**: 618-9.

63. Thiery JP. Epithelial-mesenchymal transitions in tumour progression. *Nat Rev Cancer* 2002; **2**: 442-54.

64. Thiery JP, Acloque H, Huang RY, Nieto MA. Epithelial-mesenchymal transitions in development and disease. *Cell* 2009; **139**: 871-90.

65. Xouri G, Christian S. Origin and function of tumor stroma fibroblasts. *Semin Cell Dev Biol* 2010; **21**: 40-6.

66. Orimo A, Weinberg RA. Stromal fibroblasts in cancer: a novel tumor-promoting cell type. *Cell Cycle* 2006; **5**: 1597-601.

67. Paunescu V, Bojin FM, Tatu CA, Gavriliuc OI, Rosca A, Gruia AT, Tanasie G, Bunu C, Crisnic D, Gherghiceanu M, Tatu FR, Tatu CS, Vermesan S. Tumor-associated fibroblasts and mesenchymal stem cells: more similarities than differences. *J Cell Mol Med* 2010.

68. Bar J, Moskovits N, Oren M. Involvement of stromal p53 in tumor-stroma interactions. *Semin Cell Dev Biol* 2010; **21**: 47-54.

69. Giampieri S, Manning C, Hooper S, Jones L, Hill CS, Sahai E. Localized and reversible TGFbeta signalling switches breast cancer cells from cohesive to single cell motility. *Nat Cell Biol* 2009; **11**: 1287-96.

70. Sahai E. Mechanisms of cancer cell invasion. *Curr Opin Genet Dev* 2005; **15**: 87-96.

71. Pollard JW. Tumour-educated macrophages promote tumour progression and metastasis. *Nat Rev Cancer* 2004; **4**: 71-8.

72. Sameni M, Dosescu J, Moin K, Sloane BF. Functional imaging of proteolysis: stromal and inflammatory cells increase tumor proteolysis. *Mol Imaging* 2003; **2**: 159-75.

73. Orimo A, Gupta PB, Sgroi DC, Arenzana-Seisdedos F, Delaunay T, Naeem R, Carey VJ, Richardson AL, Weinberg RA. Stromal fibroblasts present in invasive human breast carcinomas promote tumor growth and angiogenesis through elevated SDF-1/CXCL12 secretion. *Cell* 2005; **121**: 335-48.

74. Ao M, Franco OE, Park D, Raman D, Williams K, Hayward SW. Cross-talk between paracrine-acting cytokine and chemokine pathways promotes malignancy in benign human prostatic epithelium. *Cancer Res* 2007; **67**: 4244-53.

75. Rosenthal E, McCrory A, Talbert M, Young G, Murphy-Ullrich J, Gladson C. Elevated expression of TGF-beta1 in head and neck cancer-associated fibroblasts. *Mol Carcinog* 2004; **40**: 116-21.

76. San Francisco IF, DeWolf WC, Peehl DM, Olumi AF. Expression of transforming growth factor-beta 1 and growth in soft agar differentiate prostate carcinoma-associated fibroblasts from normal prostate fibroblasts. *Int J Cancer* 2004; **112**: 213-8.

77. Gaggioli C, Hooper S, Hidalgo-Carcedo C, Grosse R, Marshall JF, Harrington K, Sahai E. Fibroblast-led collective invasion of carcinoma cells with differing roles for RhoGTPases in leading and following cells. *Nat Cell Biol* 2007; **9**: 1392-400.

78. van 't Veer LJ, Dai H, van de Vijver MJ, He YD, Hart AA, Mao M, Peterse HL, van der Kooy K, Marton MJ, Witteveen AT, Schreiber GJ, Kerkhoven RM, Roberts C, Linsley PS, Bernards R, Friend SH. Gene expression profiling predicts clinical outcome of breast cancer. *Nature* 2002; **415**: 530-6.

79. Cardone A, Tolino A, Zarcone R, Borruto Caracciolo G, Tartaglia E. Prognostic value of desmoplastic reaction and lymphocytic infiltration in the management of breast cancer. *Panminerva Med* 1997; **39**: 174-7.

80. Kellermann MG, Sobral LM, da Silva SD, Zecchin KG, Graner E, Lopes MA, Nishimoto I, Kowalski LP, Coletta RD. Myofibroblasts in the stroma of oral squamous cell carcinoma are associated with poor prognosis. *Histopathology* 2007; **51**: 849-53.

81. Kellermann MG, Sobral LM, da Silva SD, Zecchin KG, Graner E, Lopes MA, Kowalski LP, Coletta RD. Mutual paracrine effects of oral squamous cell carcinoma cells and normal oral fibroblasts: induction of fibroblast to myofibroblast transdifferentiation and modulation of tumor cell proliferation. *Oral Oncol* 2008; **44**: 509-17.

82. Yang F, Tuxhorn JA, Ressler SJ, McAlhany SJ, Dang TD, Rowley DR. Stromal expression of connective tissue growth factor promotes angiogenesis and prostate cancer tumorigenesis. *Cancer Res* 2005; **65**: 8887-95.

83. Olson MF, Sahai E. The actin cytoskeleton in cancer cell motility. *Clin Exp Metastasis* 2009; **26**: 273-87.

84. Yamazaki D, Kurisu S, Takenawa T. Regulation of cancer cell motility through actin reorganization. *Cancer Sci* 2005; **96**: 379-86.

85. Pantaloni D, Le Clainche C, Carlier MF. Mechanism of actin-based motility. *Science* 2001; **292**: 1502-6.

86. Miki H, Takenawa T. Regulation of actin dynamics by WASP family proteins. *J Biochem* 2003; **134**: 309-13.

87. Takenawa T, Suetsugu S. The WASP-WAVE protein network: connecting the membrane to the cytoskeleton. *Nat Rev Mol Cell Biol* 2007; **8**: 37-48.

88. Stradal TE, Rottner K, Disanza A, Confalonieri S, Innocenti M, Scita G. Regulation of actin dynamics by WASP and WAVE family proteins. *Trends Cell Biol* 2004; **14**: 303-11.

89. Verma S, Shewan AM, Scott JA, Helwani FM, den Elzen NR, Miki H, Takenawa T, Yap AS. Arp2/3 activity is necessary for efficient formation of E-cadherin adhesive contacts. *J Biol Chem* 2004; **279**: 34062-70.

90. Carlier MF, Le Clainche C, Wiesner S, Pantaloni D. Actin-based motility: from molecules to movement. *Bioessays* 2003; **25**: 336-45.

91. Schirenbeck A, Arasada R, Bretschneider T, Schleicher M, Faix J. Formins and VASPs may co-operate in the formation of filopodia. *Biochem Soc Trans* 2005; **33**: 1256-9.

92. Mellor H. The role of formins in filopodia formation. *Biochim Biophys Acta* 2010; **1803**: 191-200.

93. Ridley AJ, Paterson HF, Johnston CL, Diekmann D, Hall A. The small GTP-binding protein rac regulates growth factor-induced membrane ruffling. *Cell* 1992; **70**: 401-10.

94. Yamaguchi H, Lorenz M, Kempiak S, Sarmiento C, Coniglio S, Symons M, Segall J, Eddy R, Miki H, Takenawa T, Condeelis J. Molecular mechanisms of invadopodium formation: the role of the N-WASP-Arp2/3 complex pathway and cofilin. *J Cell Biol* 2005; **168**: 441-52.

95. Yamaguchi H, Pixley F, Condeelis J. Invadopodia and podosomes in tumor invasion. *Eur J Cell Biol* 2006; **85**: 213-8.

96. Albiges-Rizo C, Destaing O, Fourcade B, Planus E, Block MR. Actin machinery and mechanosensitivity in invadopodia, podosomes and focal adhesions. *J Cell Sci* 2009; **122**: 3037-49.

97. Berdeaux RL, Diaz B, Kim L, Martin GS. Active Rho is localized to podosomes induced by oncogenic Src and is required for their assembly and function. *J Cell Biol* 2004; **166**: 317-23.

98. Spinardi L, Marchisio PC. Podosomes as smart regulators of cellular adhesion. *Eur J Cell Biol* 2006; **85**: 191-4.

99. Charras GT, Yarrow JC, Horton MA, Mahadevan L, Mitchison TJ. Non-equilibration of hydrostatic pressure in blebbing cells. *Nature* 2005; **435**: 365-9.

100. Sahai E, Marshall CJ. Differing modes of tumour cell invasion have distinct requirements for Rho/ROCK signalling and extracellular proteolysis. *Nat Cell Biol* 2003; **5**: 711-9.

101. Wyckoff JB, Pinner SE, Gschmeissner S, Condeelis JS, Sahai E. ROCK- and myosin-dependent matrix deformation enables protease-independent tumor-cell invasion in vivo. *Curr Biol* 2006; **16**: 1515-23.

102. Pinner S, Sahai E. Imaging amoeboid cancer cell motility in vivo. *J Microsc* 2008; **231**: 441-5.

103. Lele TP, Thodeti CK, Ingber DE. Force meets chemistry: analysis of mechanochemical conversion in focal adhesions using fluorescence recovery after photobleaching. *J Cell Biochem* 2006; **97**: 1175-83.

104. Cukierman E, Pankov R, Stevens DR, Yamada KM. Taking cell-matrix adhesions to the third dimension. *Science* 2001; **294**: 1708-12.

105. Cukierman E, Pankov R, Yamada KM. Cell interactions with three-dimensional matrices. *Curr Opin Cell Biol* 2002; **14**: 633-9.

106. Zamir E, Geiger B. Molecular complexity and dynamics of cell-matrix adhesions. *J Cell Sci* 2001; **114**: 3583-90.

107. Howell GM, Grandis JR. Molecular mediators of metastasis in head and neck squamous cell carcinoma. *Head Neck* 2005; **27**: 710-7.

108. Friedl P, Wolf K. Tumour-cell invasion and migration: diversity and escape mechanisms. *Nat Rev Cancer* 2003; **3**: 362-74.

109. Zhou H, Kramer RH. Integrin engagement differentially modulates epithelial cell motility by RhoA/ROCK and PAK1. *J Biol Chem* 2005; **280**: 10624-35.

110. Kramer RH, Shen X, Zhou H. Tumor cell invasion and survival in head and neck cancer. *Cancer Metastasis Rev* 2005; **24**: 35-45.

111. Kelley LC, Shahab S, Weed SA. Actin cytoskeletal mediators of motility and invasion amplified and overexpressed in head and neck cancer. *Clin Exp Metastasis* 2008; **25**: 289-304.

112. Mitra SK, Schlaepfer DD. Integrin-regulated FAK-Src signaling in normal and cancer cells. *Curr Opin Cell Biol* 2006; **18**: 516-23.

113. Gabarra-Niecko V, Schaller MD, Dunty JM. FAK regulates biological processes important for the pathogenesis of cancer. *Cancer Metastasis Rev* 2003; **22**: 359-74.

114. Schlaepfer DD, Mitra SK. Multiple connections link FAK to cell motility and invasion. *Curr Opin Genet Dev* 2004; **14**: 92-101.

115. Wolf K, Friedl P. Molecular mechanisms of cancer cell invasion and plasticity. *Br J Dermatol* 2006; **154 Suppl 1**: 11-5.

116. Friedl P, Wolf K. Tube travel: the role of proteases in individual and collective cancer cell invasion. *Cancer Res* 2008; **68**: 7247-9.

117. Friedl P, Wolf K. Proteolytic interstitial cell migration: a five-step process. *Cancer Metastasis Rev* 2009; **28**: 129-35.

118. Curran S, Murray GI. Matrix metalloproteinases: molecular aspects of their roles in tumour invasion and metastasis. *Eur J Cancer* 2000; **36**: 1621-30.

119. Kawata R, Shimada T, Maruyama S, Hisa Y, Takenaka H, Murakami Y. Enhanced production of matrix metalloproteinase-2 in human head and neck carcinomas is correlated with lymph node metastasis. *Acta Otolaryngol* 2002; **122**: 101-6.

120. O-Charoenrat P, Rhys-Evans PH, Eccles SA. Expression of matrix metalloproteinases and their inhibitors correlates with invasion and metastasis in squamous cell carcinoma of the head and neck. *Arch Otolaryngol Head Neck Surg* 2001; **127**: 813-20.

121. Hynes RO. The extracellular matrix: not just pretty fibrils. *Science* 2009; **326**: 1216-9.

122. Fukata Y, Amano M, Kaibuchi K. Rho-Rho-kinase pathway in smooth muscle contraction and cytoskeletal reorganization of non-muscle cells. *Trends Pharmacol Sci* 2001; **22**: 32-9.

123. Murata-Hori M, Fukuta Y, Ueda K, Iwasaki T, Hosoya H. HeLa ZIP kinase induces diphosphorylation of myosin II regulatory light chain and reorganization of actin filaments in nonmuscle cells. *Oncogene* 2001; **20**: 8175-83.

124. Pellegrin S, Mellor H. Actin stress fibres. *J Cell Sci* 2007; **120**: 3491-9.

125. Watanabe N, Kato T, Fujita A, Ishizaki T, Narumiya S. Cooperation between mDia1 and ROCK in Rho-induced actin reorganization. *Nat Cell Biol* 1999; **1**: 136-43.

126. Narumiya S, Tanji M, Ishizaki T. Rho signaling, ROCK and mDia1, in transformation, metastasis and invasion. *Cancer Metastasis Rev* 2009; **28**: 65-76.

127. Wolf K, Mazo I, Leung H, Engelke K, von Andrian UH, Deryugina EI, Strongin AY, Brocker EB, Friedl P. Compensation mechanism in tumor cell migration: mesenchymal-amoeboid transition after blocking of pericellular proteolysis. *J Cell Biol* 2003; **160**: 267-77.

128. Guarino M, Rubino B, Ballabio G. The role of epithelial-mesenchymal transition in cancer pathology. *Pathology* 2007; **39**: 305-18.

129. Friedl P, Zanker KS, Brocker EB. Cell migration strategies in 3-D extracellular matrix: differences in morphology, cell matrix interactions, and integrin function. *Microsc Res Tech* 1998; **43**: 369-78.

130. Friedl P. Prespecification and plasticity: shifting mechanisms of cell migration. *Curr Opin Cell Biol* 2004; **16**: 14-23.

131. Friedl P, Wolf K. Proteolytic and non-proteolytic migration of tumour cells and leucocytes. *Biochem Soc Symp* 2003: 277-85.

132. Friedl P, Gilmour D. Collective cell migration in morphogenesis, regeneration and cancer. *Nat Rev Mol Cell Biol* 2009; **10**: 445-57.

133. Ahmed F, Wyckoff J, Lin EY, Wang W, Wang Y, Hennighausen L, Miyazaki J, Jones J, Pollard JW, Condeelis JS, Segall JE. GFP expression in the mammary gland for imaging of mammary tumor cells in transgenic mice. *Cancer Res* 2002; **62**: 7166-9.

134. Sahai E, Wyckoff J, Philippar U, Segall JE, Gertler F, Condeelis J. Simultaneous imaging of GFP, CFP and collagen in tumors in vivo using multiphoton microscopy. *BMC Biotechnol* 2005; **5**: 14.

135. Wang W, Goswami S, Sahai E, Wyckoff JB, Segall JE, Condeelis JS. Tumor cells caught in the act of invading: their strategy for enhanced cell motility. *Trends Cell Biol* 2005; **15**: 138-45.

136. Buttery RC, Rintoul RC, Sethi T. Small cell lung cancer: the importance of the extracellular matrix. *Int J Biochem Cell Biol* 2004; **36**: 1154-60.

137. Hartmann TN, Burger M, Burger JA. The role of adhesion molecules and chemokine receptor CXCR4 (CD184) in small cell lung cancer. *J Biol Regul Homeost Agents* 2004; **18**: 126-30.

138. Wang HR, Zhang Y, Ozdamar B, Ogunjimi AA, Alexandrova E, Thomsen GH, Wrana JL. Regulation of cell polarity and protrusion formation by targeting RhoA for degradation. *Science* 2003; **302**: 1775-9.

139. Zhang Y, Wang HR, Wrana JL. Smurf1: a link between cell polarity and ubiquitination. *Cell Cycle* 2004; **3**: 391-2.

140. Wang HR, Ogunjimi AA, Zhang Y, Ozdamar B, Bose R, Wrana JL. Degradation of RhoA by Smurf1 ubiquitin ligase. *Methods Enzymol* 2006; **406**: 437-47.

141. Jaffe AB, Hall A. Cell biology. Smurfing at the leading edge. *Science* 2003; **302**: 1690-1.

142. Sahai E, Garcia-Medina R, Pouyssegur J, Vial E. Smurf1 regulates tumor cell plasticity and motility through degradation of RhoA leading to localized inhibition of contractility. *J Cell Biol* 2007; **176**: 35-42.

143. Hershko A. Ubiquitin: roles in protein modification and breakdown. *Cell* 1983; **34**: 11-2.

144. Jesenberger V, Jentsch S. Deadly encounter: ubiquitin meets apoptosis. *Nat Rev Mol Cell Biol* 2002; **3**: 112-21.

145. Pickart CM, Eddins MJ. Ubiquitin: structures, functions, mechanisms. *Biochim Biophys Acta* 2004; **1695**: 55-72.

146. Hoeller D, Hecker CM, Dikic I. Ubiquitin and ubiquitin-like proteins in cancer pathogenesis. *Nat Rev Cancer* 2006; **6**: 776-88.

147. Haglund K, Dikic I. Ubiquitylation and cell signaling. *EMBO J* 2005; **24**: 3353-9.

148. Petroski MD, Deshaies RJ. Function and regulation of cullin-RING ubiquitin ligases. *Nat Rev Mol Cell Biol* 2005; **6**: 9-20.

149. Pickart CM. Mechanisms underlying ubiquitination. *Annu Rev Biochem* 2001; **70**: 503-33.

150. Bernassola F, Karin M, Ciechanover A, Melino G. The HECT family of E3 ubiquitin ligases: multiple players in cancer development. *Cancer Cell* 2008; **14**: 10-21.

151. Skaug B, Jiang X, Chen ZJ. The role of ubiquitin in NF-kappaB regulatory pathways. *Annu Rev Biochem* 2009; **78**: 769-96.

152. Elsasser S, Finley D. Delivery of ubiquitinated substrates to protein-unfolding machines. *Nat Cell Biol* 2005; **7**: 742-9.

153. Wang J, Maldonado MA. The ubiquitin-proteasome system and its role in inflammatory and autoimmune diseases. *Cell Mol Immunol* 2006; **3**: 255-61.

154. Smith DM, Chang SC, Park S, Finley D, Cheng Y, Goldberg AL. Docking of the proteasomal ATPases' carboxyl termini in the 20S proteasome's alpha ring opens the gate for substrate entry. *Mol Cell* 2007; **27**: 731-44.

155. Liu CW, Li X, Thompson D, Wooding K, Chang TL, Tang Z, Yu H, Thomas PJ, DeMartino GN. ATP binding and ATP hydrolysis play distinct roles in the function of 26S proteasome. *Mol Cell* 2006; **24**: 39-50.

156. Sorokin AV, Kim ER, Ovchinnikov LP. Proteasome system of protein degradation and processing. *Biochemistry (Mosc)* 2009; **74**: 1411-42.

157. Nijman SM, Luna-Vargas MP, Velds A, Brummelkamp TR, Dirac AM, Sixma TK, Bernards R. A genomic and functional inventory of deubiquitinating enzymes. *Cell* 2005; **123**: 773-86.

158. Amerik AY, Hochstrasser M. Mechanism and function of deubiquitinating enzymes. *Biochim Biophys Acta* 2004; **1695**: 189-207.

159. Kim JH, Park KC, Chung SS, Bang O, Chung CH. Deubiquitinating enzymes as cellular regulators. *J Biochem* 2003; **134**: 9-18.

160. Reyes-Turcu FE, Ventii KH, Wilkinson KD. Regulation and cellular roles of ubiquitin-specific deubiquitinating enzymes. *Annu Rev Biochem* 2009; **78**: 363-97.

161. Yin Q, Lin SC, Lamothe B, Lu M, Lo YC, Hura G, Zheng L, Rich RL, Campos AD, Myszka DG, Lenardo MJ, Darnay BG, Wu H. E2 interaction and dimerization in the crystal structure of TRAF6. *Nat Struct Mol Biol* 2009; **16**: 658-66.

162. Li M, Brooks CL, Wu-Baer F, Chen D, Baer R, Gu W. Mono- versus polyubiquitination: differential control of p53 fate by Mdm2. *Science* 2003; **302**: 1972-5.

163. Chen ZJ. Ubiquitin signalling in the NF-kappaB pathway. *Nat Cell Biol* 2005; **7**: 758-65.

164. Sen R, Baltimore D. Multiple nuclear factors interact with the immunoglobulin enhancer sequences. *Cell* 1986; **46**: 705-16.

165. Gilmore TD. Multiple mutations contribute to the oncogenicity of the retroviral oncoprotein v-Rel. *Oncogene* 1999; **18**: 6925-37.

166. Pahl HL. Activators and target genes of Rel/NF-kappaB transcription factors. *Oncogene* 1999; **18**: 6853-66.

167. Li Q, Verma IM. NF-kappaB regulation in the immune system. *Nat Rev Immunol* 2002; **2**: 725-34.

168. Vallabhapurapu S, Karin M. Regulation and function of NF-kappaB transcription factors in the immune system. *Annu Rev Immunol* 2009; **27**: 693-733.

169. Pasparakis M. Regulation of tissue homeostasis by NF-kappaB signalling: implications for inflammatory diseases. *Nat Rev Immunol* 2009; **9**: 778-88.

170. Allen CT, Ricker JL, Chen Z, Van Waes C. Role of activated nuclear factor-kappaB in the pathogenesis and therapy of squamous cell carcinoma of the head and neck. *Head Neck* 2007; **29**: 959-71.

171. Sizemore N, Lerner N, Dombrowski N, Sakurai H, Stark GR. Distinct roles of the Ikappa B kinase alpha and beta subunits in liberating nuclear factor kappa B (NF-kappa B) from Ikappa B and in phosphorylating the p65 subunit of NF-kappa B. *J Biol Chem* 2002; **277**: 3863-9.

172. Hoffmann A, Baltimore D. Circuitry of nuclear factor kappaB signaling. *Immunol Rev* 2006; **210**: 171-86.

173. Senftleben U, Cao Y, Xiao G, Greten FR, Krahn G, Bonizzi G, Chen Y, Hu Y, Fong A, Sun SC, Karin M. Activation by IKKalpha of a second, evolutionary conserved, NF-kappa B signaling pathway. *Science* 2001; **293**: 1495-9.

174. Xiao G, Harhaj EW, Sun SC. NF-kappaB-inducing kinase regulates the processing of NF-kappaB2 p100. *Mol Cell* 2001; **7**: 401-9.

175. Tsukahara T, Kannagi M, Ohashi T, Kato H, Arai M, Nunez G, Iwanaga Y, Yamamoto N, Ohtani K, Nakamura M, Fujii M. Induction of Bcl-x(L) expression by human T-cell leukemia virus type 1 Tax through NF-kappaB in apoptosis-resistant T-cell transfectants with Tax. *J Virol* 1999; **73**: 7981-7.

176. Micheau O, Lens S, Gaide O, Alevizopoulos K, Tschopp J. NF-kappaB signals induce the expression of c-FLIP. *Mol Cell Biol* 2001; **21**: 5299-305.

177. Wang CY, Mayo MW, Korneluk RG, Goeddel DV, Baldwin AS, Jr. NF-kappaB antiapoptosis: induction of TRAF1 and TRAF2 and c-IAP1 and c-IAP2 to suppress caspase-8 activation. *Science* 1998; **281**: 1680-3.

178. Pasparakis M, Luedde T, Schmidt-Supprian M. Dissection of the NF-kappaB signalling cascade in transgenic and knockout mice. *Cell Death Differ* 2006; **13**: 861-72.

179. Gerondakis S, Grumont R, Gugasyan R, Wong L, Isomura I, Ho W, Banerjee A. Unravelling the complexities of the NF-kappaB signalling pathway using mouse knockout and transgenic models. *Oncogene* 2006; **25**: 6781-99.

180. Tanaka M, Fuentes ME, Yamaguchi K, Durnin MH, Dalrymple SA, Hardy KL, Goeddel DV. Embryonic lethality, liver degeneration, and impaired NF-kappa B activation in IKK-beta-deficient mice. *Immunity* 1999; **10**: 421-9.

181. Beg AA, Sha WC, Bronson RT, Ghosh S, Baltimore D. Embryonic lethality and liver degeneration in mice lacking the RelA component of NF-kappa B. *Nature* 1995; **376**: 167-70.

182. Beg AA, Sha WC, Bronson RT, Baltimore D. Constitutive NF-kappa B activation, enhanced granulopoiesis, and neonatal lethality in I kappa B alpha-deficient mice. *Genes Dev* 1995; **9**: 2736-46.

183. Lee EG, Boone DL, Chai S, Libby SL, Chien M, Lodolce JP, Ma A. Failure to regulate TNF-induced NF-kappaB and cell death responses in A20-deficient mice. *Science* 2000; **289**: 2350-4.

184. Rebholz B, Haase I, Eckelt B, Paxian S, Flaig MJ, Ghoreschi K, Nedospasov SA, Mailhammer R, Debey-Pascher S, Schultze JL, Weindl G, Forster I, Huss R, Stratis A, Ruzicka T, Rocken M, Pfeffer K, Schmid RM, Rupec RA. Crosstalk between keratinocytes and adaptive immune cells in an IkappaBalpha protein-mediated inflammatory disease of the skin. *Immunity* 2007; **27**: 296-307.

185. Greten FR, Eckmann L, Greten TF, Park JM, Li ZW, Egan LJ, Kagnoff MF, Karin M. IKKbeta links inflammation and tumorigenesis in a mouse model of colitis-associated cancer. *Cell* 2004; **118**: 285-96.

186. Arkan MC, Hevener AL, Greten FR, Maeda S, Li ZW, Long JM, Wynshaw-Boris A, Poli G, Olefsky J, Karin M. IKK-beta links inflammation to obesity-induced insulin resistance. *Nat Med* 2005; **11**: 191-8.

187. Karin M, Greten FR. NF-kappaB: linking inflammation and immunity to cancer development and progression. *Nat Rev Immunol* 2005; **5**: 749-59.

188. Krishnamoorthy S, Honn KV. Inflammation and disease progression. *Cancer Metastasis Rev* 2006; **25**: 481-91.

189. Lu H, Ouyang W, Huang C. Inflammation, a key event in cancer development. *Mol Cancer Res* 2006; **4**: 221-33.

190. Kundu JK, Surh YJ. Inflammation: gearing the journey to cancer. *Mutat Res* 2008; **659**: 15-30.

191. Balkwill F. Tumour necrosis factor and cancer. *Nat Rev Cancer* 2009; **9**: 361-71.

192. Apte RN, Dotan S, Elkabets M, White MR, Reich E, Carmi Y, Song X, Dvozkin T, Krelin Y, Voronov E. The involvement of IL-1 in tumorigenesis, tumor invasiveness, metastasis and tumor-host interactions. *Cancer Metastasis Rev* 2006; **25**: 387-408.

193. Ehrenreich M, Tarlow MM, Godlewska-Janusz E, Schwartz RA. Incontinentia pigmenti (Bloch-Sulzberger syndrome): a systemic disorder. *Cutis* 2007; **79**: 355-62.

194. Smahi A, Courtois G, Vabres P, Yamaoka S, Heuertz S, Munnich A, Israel A, Heiss NS, Klauck SM, Kioschis P, Wiemann S, Poustka A, Esposito T, Bardaro T, Gianfrancesco F, Ciccodicola A, D'Urso M, Woffendin H, Jakins T, Donnai D, Stewart H, Kenwrick SJ, Aradhya S, Yamagata T, Levy M, Lewis RA, Nelson DL. Genomic rearrangement in NEMO impairs NF-kappaB activation and is a cause of incontinentia pigmenti. The International Incontinentia Pigmenti (IP) Consortium. *Nature* 2000; **405**: 466-72.

195. Schmidt-Supprian M, Bloch W, Courtois G, Addicks K, Israel A, Rajewsky K, Pasparakis M. NEMO/IKK gamma-deficient mice model incontinentia pigmenti. *Mol Cell* 2000; **5**: 981-92.

196. Makris C, Godfrey VL, Krahn-Senftleben G, Takahashi T, Roberts JL, Schwarz T, Feng L, Johnson RS, Karin M. Female mice heterozygous for IKK gamma/NEMO deficiencies develop a dermatopathy similar to the human X-linked disorder incontinentia pigmenti. *Mol Cell* 2000; **5**: 969-79.

197. Omori E, Matsumoto K, Sanjo H, Sato S, Akira S, Smart RC, Ninomiya-Tsuji J. TAK1 is a master regulator of epidermal homeostasis involving skin inflammation and apoptosis. *J Biol Chem* 2006; **281**: 19610-7.

198. Pasparakis M, Courtois G, Hafner M, Schmidt-Supprian M, Nenci A, Toksoy A, Krampert M, Goebeler M, Gillitzer R, Israel A, Krieg T, Rajewsky K, Haase I. TNF-mediated inflammatory skin disease in mice with epidermis-specific deletion of IKK2. *Nature* 2002; **417**: 861-6.

199. van Hogerlinden M, Rozell BL, Ahrlund-Richter L, Toftgard R. Squamous cell carcinomas and increased apoptosis in skin with inhibited Rel/nuclear factor-kappaB signaling. *Cancer Res* 1999; **59**: 3299-303.

200. Lind MH, Rozell B, Wallin RP, van Hogerlinden M, Ljunggren HG, Toftgard R, Sur I. Tumor necrosis factor receptor 1-mediated signaling is required for skin cancer development induced by NF-kappaB inhibition. *Proc Natl Acad Sci U S A* 2004; **101**: 4972-7.

201. Griffiths CE, Barker JN. Pathogenesis and clinical features of psoriasis. *Lancet* 2007; **370**: 263-71.

202. Capon F, Trembath RC, Barker JN. An update on the genetics of psoriasis. *Dermatol Clin* 2004; **22**: 339-47, vii.

203. Krueger JG, Bowcock A. Psoriasis pathophysiology: current concepts of pathogenesis. *Ann Rheum Dis* 2005; **64 Suppl 2**: ii30-6.

204. Griffiths CE, Voorhees JJ, Nickoloff BJ. Characterization of intercellular adhesion molecule-1 and HLA-DR expression in normal and inflamed skin: modulation by recombinant gamma interferon and tumor necrosis factor. *J Am Acad Dermatol* 1989; **20**: 617-29.

205. Chua RA, Arbiser JL. The role of angiogenesis in the pathogenesis of psoriasis. *Autoimmunity* 2009; **42**: 574-9.

206. Lowes MA, Bowcock AM, Krueger JG. Pathogenesis and therapy of psoriasis. *Nature* 2007; **445**: 866-73.

207. Naldi L. Malignancy concerns with psoriasis treatments using phototherapy, methotrexate, cyclosporin, and biologics: facts and controversies. *Clin Dermatol* 2010; **28**: 88-92.

208. Bashir MM, Sharma MR, Werth VP. TNF-alpha production in the skin. *Arch Dermatol Res* 2009; **301**: 87-91.

209. Bashir MM, Sharma MR, Werth VP. UVB and proinflammatory cytokines synergistically activate TNF-alpha production in keratinocytes through enhanced gene transcription. *J Invest Dermatol* 2009; **129**: 994-1001.

210. Scully C, Chaudhry SI. Aspects of human disease. *Dent Update* 2007; **34**: 317.

211. Atreya R, Neurath MF. New therapeutic strategies for treatment of inflammatory bowel disease. *Mucosal Immunol* 2008; **1**: 175-82.

212. Schreiber S, Nikolaus S, Hampe J. Activation of nuclear factor kappa B inflammatory bowel disease. *Gut* 1998; **42**: 477-84.

213. Neurath MF, Pettersson S, Meyer zum Buschenfelde KH, Strober W. Local administration of antisense phosphorothioate oligonucleotides to the p65 subunit of NF-kappa B abrogates established experimental colitis in mice. *Nat Med* 1996; **2**: 998-1004.

214. Shibata W, Maeda S, Hikiba Y, Yanai A, Ohmae T, Sakamoto K, Nakagawa H, Ogura K, Omata M. Cutting edge: The IkappaB kinase (IKK) inhibitor, NEMO-binding domain peptide, blocks inflammatory injury in murine colitis. *J Immunol* 2007; **179**: 2681-5.

215. Nenci A, Becker C, Wullaert A, Gareus R, van Loo G, Danese S, Huth M, Nikolaev A, Neufert C, Madison B, Gumucio D, Neurath MF, Pasparakis M. Epithelial NEMO links innate immunity to chronic intestinal inflammation. *Nature* 2007; **446**: 557-61.

216. Biancone L, Petruzziello C, Calabrese E, Zorzi F, Naccarato P, Onali S, Pallone F. Long-term safety of Infliximab for the treatment of inflammatory bowel disease: does blocking TNFalpha reduce colitis-associated colorectal carcinogenesis? *Gut* 2009; **58**: 1703.

217. Clapper ML, Cooper HS, Chang WC. Dextran sulfate sodium-induced colitis-associated neoplasia: a promising model for the development of chemopreventive interventions. *Acta Pharmacol Sin* 2007; **28**: 1450-9.

218. Popivanova BK, Kitamura K, Wu Y, Kondo T, Kagaya T, Kaneko S, Oshima M, Fujii C, Mukaida N. Blocking TNF-alpha in mice reduces colorectal carcinogenesis associated with chronic colitis. *J Clin Invest* 2008; **118**: 560-70.

219. Loercher A, Lee TL, Ricker JL, Howard A, Geoghegen J, Chen Z, Sunwoo JB, Sitcheran R, Chuang EY, Mitchell JB, Baldwin AS, Jr., Van Waes C. Nuclear factor-kappaB is an important modulator of the altered gene expression profile and malignant phenotype in squamous cell carcinoma. *Cancer Res* 2004; **64**: 6511-23.

220. Duffey DC, Chen Z, Dong G, Ondrey FG, Wolf JS, Brown K, Siebenlist U, Van Waes C. Expression of a dominant-negative mutant inhibitor-kappaBalpha of nuclear factor-kappaB in human head and neck squamous cell carcinoma inhibits survival, proinflammatory cytokine expression, and tumor growth in vivo. *Cancer Res* 1999; **59**: 3468-74.

221. Ondrey FG, Dong G, Sunwoo J, Chen Z, Wolf JS, Crowl-Bancroft CV, Mukaida N, Van Waes C. Constitutive activation of transcription factors NF-(kappa)B, AP-1, and NF-IL6 in human head and neck squamous cell carcinoma cell lines that express pro-inflammatory and pro-angiogenic cytokines. *Mol Carcinog* 1999; **26**: 119-29.

222. Zhang PL, Pellitteri PK, Law A, Gilroy PA, Wood GC, Kennedy TL, Blasick TM, Lun M, Schuerch C, 3rd, Brown RE. Overexpression of phosphorylated nuclear factor-kappa B in tonsillar squamous cell carcinoma and high-grade dysplasia is associated with poor prognosis. *Mod Pathol* 2005; **18**: 924-32.

223. Nakayama H, Ikebe T, Beppu M, Shirasuna K. High expression levels of nuclear factor kappaB, IkappaB kinase alpha and Akt kinase in squamous cell carcinoma of the oral cavity. *Cancer* 2001; **92**: 3037-44.

224. Capaccio P, Pruneri G, Carboni N, Pagliari AV, Quatela M, Cesana BM, Pignataro L. Cyclin D1 expression is predictive of occult metastases in head and neck cancer patients with clinically negative cervical lymph nodes. *Head Neck* 2000; **22**: 234-40.

225. Tergaonkar V, Pando M, Vafa O, Wahl G, Verma I. p53 stabilization is decreased upon NFkappaB activation: a role for NFkappaB in acquisition of resistance to chemotherapy. *Cancer Cell* 2002; **1**: 493-503.

226. Kondo T, Higashiyama Y, Goto S, Iida T, Cho S, Iwanaga M, Mori K, Tani M, Urata Y. Regulation of gamma-glutamylcysteine synthetase expression in response to oxidative stress. *Free Radic Res* 1999; **31**: 325-34.

227. Nishimura T, Newkirk K, Sessions RB, Andrews PA, Trock BJ, Rasmussen AA, Montgomery EA, Bischoff EK, Cullen KJ. Immunohistochemical staining for glutathione S-transferase predicts response to platinum-based chemotherapy in head and neck cancer. *Clin Cancer Res* 1996; **2**: 1859-65.

228. Nishimura T, Newkirk K, Sessions RB, Andrews PA, Trock BJ, Rusmussen AA, Montogomery EA, Bischoff EK, Hanigan MH, Cullen KJ. Association between expression of glutathione-associated enzymes and response to platinum-based chemotherapy in head and neck cancer. *Chem Biol Interact* 1998; **111-112**: 187-98.

229. Chang AA, Van Waes C. Nuclear factor-KappaB as a common target and activator of oncogenes in head and neck squamous cell carcinoma. *Adv Otorhinolaryngol* 2005; **62**: 92-102.

230. Shintani S, Ishikawa T, Nonaka T, Li C, Nakashiro K, Wong DT, Hamakawa H. Growth-regulated oncogene-1 expression is associated with angiogenesis and lymph node metastasis in human oral cancer. *Oncology* 2004; **66**: 316-22.

231. Bancroft CC, Chen Z, Dong G, Sunwoo JB, Yeh N, Park C, Van Waes C. Coexpression of proangiogenic factors IL-8 and VEGF by human head and neck squamous cell carcinoma involves coactivation by MEK-MAPK and IKK-NF-kappaB signal pathways. *Clin Cancer Res* 2001; **7**: 435-42.

232. Andela VB, Schwarz EM, Puzas JE, O'Keefe RJ, Rosier RN. Tumor metastasis and the reciprocal regulation of prometastatic and antimetastatic factors by nuclear factor kappaB. *Cancer Res* 2000; **60**: 6557-62.

233. Wolf JS, Chen Z, Dong G, Sunwoo JB, Bancroft CC, Capo DE, Yeh NT, Mukaida N, Van Waes C. IL (interleukin)-1alpha promotes nuclear factor-kappaB and AP-1-induced IL-8 expression, cell survival, and proliferation in head and neck squamous cell carcinomas. *Clin Cancer Res* 2001; **7**: 1812-20.

234. von Biberstein SE, Spiro JD, Lindquist R, Kreutzer DL. Enhanced tumor cell expression of tumor necrosis factor receptors in head and neck squamous cell carcinoma. *Am J Surg* 1995; **170**: 416-22.

235. Zimmermann M, Zouhair A, Azria D, Ozsahin M. The epidermal growth factor receptor (EGFR) in head and neck cancer: its role and treatment implications. *Radiat Oncol* 2006; **1**: 11.

236. Pedrero JM, Carracedo DG, Pinto CM, Zapatero AH, Rodrigo JP, Nieto CS, Gonzalez MV. Frequent genetic and biochemical alterations of the PI3K/AKT/PTEN pathway in head and neck squamous cell carcinoma. *Int J Cancer* 2005; **114**: 242-8.

237. Hiscott J, Kwon H, Genin P. Hostile takeovers: viral appropriation of the NF-kappaB pathway. *J Clin Invest* 2001; **107**: 143-51.

238. Cummins EP, Comerford KM, Scholz C, Bruning U, Taylor CT. Hypoxic regulation of NF-kappaB signaling. *Methods Enzymol* 2007; **435**: 479-92.

239. Karin M, Cao Y, Greten FR, Li ZW. NF-kappaB in cancer: from innocent bystander to major culprit. *Nat Rev Cancer* 2002; **2**: 301-10.

240. Karin M. Nuclear factor-kappaB in cancer development and progression. *Nature* 2006; **441**: 431-6.

241. Old LJ. Tumor necrosis factor (TNF). *Science* 1985; **230**: 630-2.

242. Nedwin GE, Naylor SL, Sakaguchi AY, Smith D, Jarrett-Nedwin J, Pennica D, Goeddel DV, Gray PW. Human lymphotoxin and tumor necrosis factor genes: structure, homology and chromosomal localization. *Nucleic Acids Res* 1985; **13**: 6361-73.

243. Tang P, Hung MC, Klostergaard J. Human pro-tumor necrosis factor is a homotrimer. *Biochemistry* 1996; **35**: 8216-25.

244. Black RA, Rauch CT, Kozlosky CJ, Peschon JJ, Slack JL, Wolfson MF, Castner BJ, Stocking KL, Reddy P, Srinivasan S, Nelson N, Boiani N, Schooley KA, Gerhart M, Davis R, Fitzner JN, Johnson RS, Paxton RJ, March CJ, Cerretti DP. A metalloproteinase disintegrin that releases tumour-necrosis factor-alpha from cells. *Nature* 1997; **385**: 729-33.

245. Zidi I, Mestiri S, Bartegi A, Amor NB. TNF-alpha and its inhibitors in cancer. *Med Oncol* 2009.

246. Bazzoni F, Beutler B. The tumor necrosis factor ligand and receptor families. *N Engl J Med* 1996; **334**: 1717-25.

247. Aggarwal BB. Signalling pathways of the TNF superfamily: a double-edged sword. *Nat Rev Immunol* 2003; **3**: 745-56.

248. Varfolomeev EE, Ashkenazi A. Tumor necrosis factor: an apoptosis JuNKie? *Cell* 2004; **116**: 491-7.

249. Chen G, Goeddel DV. TNF-R1 signaling: a beautiful pathway. *Science* 2002; **296**: 1634-5.

250. Gaur U, Aggarwal BB. Regulation of proliferation, survival and apoptosis by members of the TNF superfamily. *Biochem Pharmacol* 2003; **66**: 1403-8.

251. Anderson GM, Nakada MT, DeWitte M. Tumor necrosis factor-alpha in the pathogenesis and treatment of cancer. *Curr Opin Pharmacol* 2004; **4**: 314-20.

252. Balkwill F. TNF-alpha in promotion and progression of cancer. *Cancer Metastasis Rev* 2006; **25**: 409-16.

253. Locksley RM, Killeen N, Lenardo MJ. The TNF and TNF receptor superfamilies: integrating mammalian biology. *Cell* 2001; **104**: 487-501.

254. Kontoyiannis D, Pasparakis M, Pizarro TT, Cominelli F, Kollias G. Impaired on/off regulation of TNF biosynthesis in mice lacking TNF AU-rich elements: implications for joint and gut-associated immunopathologies. *Immunity* 1999; **10**: 387-98.

255. McDermott MF. TNF and TNFR biology in health and disease. *Cell Mol Biol (Noisy-le-grand)* 2001; **47**: 619-35.

256. Quillinan N, Mohammad A, Mannion G, O'Keeffe D, Bergin D, Coughlan R, McDermott MF, McGonagle D. Imaging evidence for persistent subclinical fasciitis and arthritis in tumour necrosis factor receptor-associated periodic syndrome (TRAPS) between febrile attacks. *Ann Rheum Dis*.

257. Dinarello CA. The paradox of pro-inflammatory cytokines in cancer. *Cancer Metastasis Rev* 2006; **25**: 307-13.

258. Pfitzenmaier J, Vessella R, Higano CS, Noteboom JL, Wallace D, Jr., Corey E. Elevation of cytokine levels in cachectic patients with prostate carcinoma. *Cancer* 2003; **97**: 1211-6.

259. Bozcuk H, Uslu G, Samur M, Yildiz M, Ozben T, Ozdogan M, Artac M, Altunbas H, Akan I, Savas B. Tumour necrosis factor-alpha, interleukin-6, and fasting serum insulin correlate with clinical outcome in metastatic breast cancer patients treated with chemotherapy. *Cytokine* 2004; **27**: 58-65.

260. Karayiannakis AJ, Syrigos KN, Polychronidis A, Pitiakoudis M, Bounovas A, Simopoulos K. Serum levels of tumor necrosis factor-alpha and nutritional status in pancreatic cancer patients. *Anticancer Res* 2001; **21**: 1355-8.

261. Yoshida N, Ikemoto S, Narita K, Sugimura K, Wada S, Yasumoto R, Kishimoto T, Nakatani T. Interleukin-6, tumour necrosis factor alpha and interleukin-1beta in patients with renal cell carcinoma. *Br J Cancer* 2002; **86**: 1396-400.

262. Ferrajoli A, Keating MJ, Manshouri T, Giles FJ, Dey A, Estrov Z, Koller CA, Kurzrock R, Thomas DA, Faderl S, Lerner S, O'Brien S, Albitar M. The clinical significance of tumor necrosis factor-alpha plasma level in patients having chronic lymphocytic leukemia. *Blood* 2002; **100**: 1215-9.

263. Szlosarek PW, Balkwill FR. Tumour necrosis factor alpha: a potential target for the therapy of solid tumours. *Lancet Oncol* 2003; **4**: 565-73.

264. Lu T, Stark GR. Cytokine overexpression and constitutive NFkappaB in cancer. *Cell Cycle* 2004; **3**: 1114-7.

265. Fajardo LF, Kwan HH, Kowalski J, Prionas SD, Allison AC. Dual role of tumor necrosis factor-alpha in angiogenesis. *Am J Pathol* 1992; **140**: 539-44.

266. Grunhagen DJ, Brunstein F, ten Hagen TL, van Geel AN, de Wilt JH, Eggermont AM. TNF-based isolated limb perfusion: a decade of experience with antivascular therapy in the management of locally advanced extremity soft tissue sarcomas. *Cancer Treat Res* 2004; **120**: 65-79.

267. Dunn E, Sims JE, Nicklin MJ, O'Neill LA. Annotating genes with potential roles in the immune system: six new members of the IL-1 family. *Trends Immunol* 2001; **22**: 533-6.

268. Auron PE. The interleukin 1 receptor: ligand interactions and signal transduction. *Cytokine Growth Factor Rev* 1998; **9**: 221-37.

269. Dinarello CA. Interleukin-1, interleukin-1 receptors and interleukin-1 receptor antagonist. *Int Rev Immunol* 1998; **16**: 457-99.

270. O'Neill LA. Interleukin-1 signal transduction. *Int J Clin Lab Res* 1995; **25**: 169-77.

271. Sonnex C. Toll-like receptors and genital tract infection. *Int J STD AIDS* 2010; **21**: 153-7.

272. Song X, Voronov E, Dvorkin T, Fima E, Cagnano E, Benharroch D, Shendler Y, Bjorkdahl O, Segal S, Dinarello CA, Apte RN. Differential effects of IL-1 alpha and IL-1 beta on tumorigenicity patterns and invasiveness. *J Immunol* 2003; **171**: 6448-56.

273. Dinarello CA. Biologic basis for interleukin-1 in disease. *Blood* 1996; **87**: 2095-147.

274. Dinarello CA. Blocking IL-1 in systemic inflammation. *J Exp Med* 2005; **201**: 1355-9.

275. O'Neill LA. How Toll-like receptors signal: what we know and what we don't know. *Curr Opin Immunol* 2006; **18**: 3-9.

276. Aksentijevich I, Masters SL, Ferguson PJ, Dancey P, Frenkel J, van Royen-Kerkhoff A, Laxer R, Tedgard U, Cowen EW, Pham TH, Booty M, Estes JD, Sandler NG, Plass N, Stone DL, Turner ML, Hill S, Butman JA, Schneider R, Babyn P, El-Shanti HI, Pope E, Barron K, Bing X, Laurence A, Lee CC, Chapelle D, Clarke GI, Ohson K, Nicholson M, Gadina M, Yang B, Korman BD, Gregersen PK, van Hagen PM, Hak AE, Huizing M, Rahman P, Douek DC, Remmers EF, Kastner DL, Goldbach-Mansky R. An autoinflammatory disease with deficiency of the interleukin-1-receptor antagonist. *N Engl J Med* 2009; **360**: 2426-37.

277. Wessendorf JH, Garfinkel S, Zhan X, Brown S, Maciag T. Identification of a nuclear localization sequence within the structure of the human interleukin-1 alpha precursor. *J Biol Chem* 1993; **268**: 22100-4.

278. Werman A, Werman-Venkert R, White R, Lee JK, Werman B, Krelin Y, Voronov E, Dinarello CA, Apte RN. The precursor form of IL-1alpha is an intracrine proinflammatory activator of transcription. *Proc Natl Acad Sci U S A* 2004; **101**: 2434-9.

279. Kumar S, Millis AJ, Baglioni C. Expression of interleukin 1-inducible genes and production of interleukin 1 by aging human fibroblasts. *Proc Natl Acad Sci U S A* 1992; **89**: 4683-7.

280. Maier JA, Statuto M, Ragnotti G. Endogenous interleukin 1 alpha must be transported to the nucleus to exert its activity in human endothelial cells. *Mol Cell Biol* 1994; **14**: 1845-51.

281. Apte RN, Krelin Y, Song X, Dotan S, Recih E, Elkabets M, Carmi Y, Dvorkin T, White RM, Gayvoronsky L, Segal S, Voronov E. Effects of micro-environment- and malignant cell-derived interleukin-1 in carcinogenesis, tumour invasiveness and tumour-host interactions. *Eur J Cancer* 2006; **42**: 751-9.

282. Apte RN, Voronov E. Is interleukin-1 a good or bad 'guy' in tumor immunobiology and immunotherapy? *Immunol Rev* 2008; **222**: 222-41.

283. Oberyszyn TM, Sabourin CL, Bijur GN, Oberyszyn AS, Boros LG, Robertson FM. Interleukin-1 alpha gene expression and localization of interleukin-1 alpha protein during tumor promotion. *Mol Carcinog* 1993; **7**: 238-48.

284. La E, Muga SJ, Locniskar MF, Fischer SM. Altered expression of interleukin-1 receptor antagonist in different stages of mouse skin carcinogenesis. *Mol Carcinog* 1999; **24**: 276-86.

285. Scott KA, Arnott CH, Robinson SC, Moore RJ, Thompson RG, Marshall JF, Balkwill FR. TNF-alpha regulates epithelial expression of MMP-9 and integrin alphavbeta6 during tumour promotion. A role for TNF-alpha in keratinocyte migration? *Oncogene* 2004; **23**: 6954-66.

286. Suganuma M, Okabe S, Marino MW, Sakai A, Sueoka E, Fujiki H. Essential role of tumor necrosis factor alpha (TNF-alpha) in tumor promotion as revealed by TNF-alpha-deficient mice. *Cancer Res* 1999; **59**: 4516-8.

287. Li X, Eckard J, Shah R, Malluck C, Frenkel K. Interleukin-1alpha up-regulation in vivo by a potent carcinogen 7,12-dimethylbenz(a)anthracene (DMBA) and control of DMBA-induced inflammatory responses. *Cancer Res* 2002; **62**: 417-23.

288. Vanhamme L, Marshall GM, Schuh AC, Breitman ML, Vogt PK. Tumor necrosis factor alpha and interleukin 1 alpha induce anchorage independence in v-jun transgenic murine cells. *Cancer Res* 1993; **53**: 615-21.

289. Vale T, Ngo TT, White MA, Lipsky PE. Raf-induced transformation requires an interleukin 1 autocrine loop. *Cancer Res* 2001; **61**: 602-7.

290. Beaupre DM, Talpaz M, Marini FC, 3rd, Cristiano RJ, Roth JA, Estrov Z, Albitar M, Freedman MH, Kurzrock R. Autocrine interleukin-1beta production in leukemia: evidence for the involvement of mutated RAS. *Cancer Res* 1999; **59**: 2971-80.

291. Chen Z, Colon I, Ortiz N, Callister M, Dong G, Pegram MY, Arosarena O, Strome S, Nicholson JC, Van Waes C. Effects of interleukin-1alpha, interleukin-1 receptor antagonist, and neutralizing antibody on proinflammatory cytokine expression by human squamous cell carcinoma lines. *Cancer Res* 1998; **58**: 3668-76.

292. Lazar-Molnar E, Hegyesi H, Toth S, Falus A. Autocrine and paracrine regulation by cytokines and growth factors in melanoma. *Cytokine* 2000; **12**: 547-54.

293. Torisu H, Ono M, Kiryu H, Furue M, Ohmoto Y, Nakayama J, Nishioka Y, Sone S, Kuwano M. Macrophage infiltration correlates with tumor stage and

angiogenesis in human malignant melanoma: possible involvement of TNFalpha and IL-1alpha. *Int J Cancer* 2000; **85**: 182-8.

294. Tomimatsu S, Ichikura T, Mochizuki H. Significant correlation between expression of interleukin-1alpha and liver metastasis in gastric carcinoma. *Cancer* 2001; **91**: 1272-6.

295. The Human Tissue Authority (HTA). http://www.hta.gov.uk/

296. The Human Tissue Act (HT Act) 2004. http://opsi.gov.uk/acts/acts2004/ukpga_20040030_en_1

297. The National Research Ethics Service (NRES). http://www.nres.npsa.nhs.uk/

298. The National Institute for Health Research Co-ordinated System for gaining NHS Permissions (NIHR CSP). http://www.ukcrn.org.uk/index/clinical/csp.html

299. Shevde LA, Riker AI. Current concepts in biobanking: development and implementation of a tissue repository. *Front Biosci (Schol Ed)* 2009; **1**: 188-93.

300. Barnes DW. Epidermal growth factor inhibits growth of A431 human epidermoid carcinoma in serum-free cell culture. *J Cell Biol* 1982; **93**: 1-4.

301. Rheinwald JG, Beckett MA. Tumorigenic keratinocyte lines requiring anchorage and fibroblast support cultures from human squamous cell carcinomas. *Cancer Res* 1981; **41**: 1657-63.

302. Nystrom ML, Thomas GJ, Stone M, Mackenzie IC, Hart IR, Marshall JF. Development of a quantitative method to analyse tumour cell invasion in organotypic culture. *J Pathol* 2005; **205**: 468-75.

303. Hooper S, Gaggioli C, Sahai E. A chemical biology screen reveals a role for Rab21-mediated control of actomyosin contractility in fibroblast-driven cancer invasion. *Br J Cancer* 2009; **102**: 392-402.

304. Grinnell F. Fibroblast biology in three-dimensional collagen matrices. *Trends Cell Biol* 2003; **13**: 264-9.

305. Rhee S. Fibroblasts in three dimensional matrices: cell migration and matrix remodeling. *Exp Mol Med* 2009; **41**: 858-65.

306. Ngo P, Ramalingam P, Phillips JA, Furuta GT. Collagen gel contraction assay. *Methods Mol Biol* 2006; **341**: 103-9.

307. Enesa K, Zakkar M, Chaudhury H, Luong le A, Rawlinson L, Mason JC, Haskard DO, Dean JL, Evans PC. NF-kappaB suppression by the deubiquitinating enzyme Cezanne: a novel negative feedback loop in pro-inflammatory signaling. *J Biol Chem* 2008; **283**: 7036-45.

308. Evans PC, Taylor ER, Coadwell J, Heyninck K, Beyaert R, Kilshaw PJ. Isolation and characterization of two novel A20-like proteins. *Biochem J* 2001; **357**: 617-23.

309. Guzman B, Cormand B, Ribases M, Gonzalez-Nunez D, Botey A, Poch E. Implication of chromosome 18 in hypertension by sibling pair and association analyses: putative involvement of the RKHD2 gene. *Hypertension* 2006; **48**: 883-91.

310. Szlosarek P, Charles KA, Balkwill FR. Tumour necrosis factor-alpha as a tumour promoter. *Eur J Cancer* 2006; **42**: 745-50.

311. Friedl P, Brocker EB. The biology of cell locomotion within three-dimensional extracellular matrix. *Cell Mol Life Sci* 2000; **57**: 41-64.

312. Zaman MH, Trapani LM, Sieminski AL, Mackellar D, Gong H, Kamm RD, Wells A, Lauffenburger DA, Matsudaira P. Migration of tumor cells in 3D matrices is governed by matrix stiffness along with cell-matrix adhesion and proteolysis. *Proc Natl Acad Sci U S A* 2006; **103**: 10889-94.

313. Bakal C, Aach J, Church G, Perrimon N. Quantitative morphological signatures define local signaling networks regulating cell morphology. *Science* 2007; **316**: 1753-6.

314. Oncomine. https://www.oncomine.org/resource/login.html

315. Toledo F, Wahl GM. MDM2 and MDM4: p53 regulators as targets in anticancer therapy. *Int J Biochem Cell Biol* 2007; **39**: 1476-82.

316. Valentin-Vega YA, Barboza JA, Chau GP, El-Naggar AK, Lozano G. High levels of the p53 inhibitor MDM4 in head and neck squamous carcinomas. *Hum Pathol* 2007; **38**: 1553-62.

317. Roger L, Gadea G, Roux P. Control of cell migration: a tumour suppressor function for p53? *Biol Cell* 2006; **98**: 141-52.

318. Muller PA, Caswell PT, Doyle B, Iwanicki MP, Tan EH, Karim S, Lukashchuk N, Gillespie DA, Ludwig RL, Gosselin P, Cromer A, Brugge JS, Sansom OJ, Norman JC, Vousden KH. Mutant p53 drives invasion by promoting integrin recycling. *Cell* 2009; **139**: 1327-41.

319. Coutts AS, Weston L, La Thangue NB. Actin nucleation by a transcription co-factor that links cytoskeletal events with the p53 response. *Cell Cycle* 2010; **9**.

320. Miron-Mendoza M, Seemann J, Grinnell F. Collagen fibril flow and tissue translocation coupled to fibroblast migration in 3D collagen matrices. *Mol Biol Cell* 2008; **19**: 2051-8.

321. Petroll WM, Ma L. Direct, dynamic assessment of cell-matrix interactions inside fibrillar collagen lattices. *Cell Motil Cytoskeleton* 2003; **55**: 254-64.

322. Jiang H, Grinnell F. Cell-matrix entanglement and mechanical anchorage of fibroblasts in three-dimensional collagen matrices. *Mol Biol Cell* 2005; **16**: 5070-6.

323. Jiang H, Rhee S, Ho CH, Grinnell F. Distinguishing fibroblast promigratory and procontractile growth factor environments in 3-D collagen matrices. *FASEB J* 2008; **22**: 2151-60.

324. Tamariz E, Grinnell F. Modulation of fibroblast morphology and adhesion during collagen matrix remodeling. *Mol Biol Cell* 2002; **13**: 3915-29.

325. Borchers AH, Steinbauer H, Schafer BS, Kramer M, Bowden GT, Fusenig NE. Fibroblast-directed expression and localization of 92-kDa type IV collagenase along the tumor-stroma interface in an in vitro three-dimensional model of human squamous cell carcinoma. *Mol Carcinog* 1997; **19**: 258-66.

326. Chioni AM, Grose R. Organotypic modelling as a means of investigating epithelial-stromal interactions during tumourigenesis. *Fibrogenesis Tissue Repair* 2008; **1**: 8.

327. Nurmenniemi S, Sinikumpu T, Alahuhta I, Salo S, Sutinen M, Santala M, Risteli J, Nyberg P, Salo T. A novel organotypic model mimics the tumor microenvironment. *Am J Pathol* 2009; **175**: 1281-91.

328. Shimokawa H, Rashid M. Development of Rho-kinase inhibitors for cardiovascular medicine. *Trends Pharmacol Sci* 2007; **28**: 296-302.

329. Gray TA, Azama K, Whitmore K, Min A, Abe S, Nicholls RD. Phylogenetic conservation of the makorin-2 gene, encoding a multiple zinc-finger protein, antisense to the RAF1 proto-oncogene. *Genomics* 2001; **77**: 119-26.

330. Sridhar SS, Hedley D, Siu LL. Raf kinase as a target for anticancer therapeutics. *Mol Cancer Ther* 2005; **4**: 677-85.

331. Shepherd C, Puzanov I, Sosman JA. B-RAF inhibitors: an evolving role in the therapy of malignant melanoma. *Curr Oncol Rep* 2010; **12**: 146-52.

332. Jarzab B, Wiench M, Fujarewicz K, Simek K, Jarzab M, Oczko-Wojciechowska M, Wloch J, Czarniecka A, Chmielik E, Lange D, Pawlaczek A, Szpak S, Gubala E, Swierniak A. Gene expression profile of papillary thyroid cancer: sources of variability and diagnostic implications. *Cancer Res* 2005; **65**: 1587-97.

333. Nakamura T, Hillova J, Mariage-Samson R, Onno M, Huebner K, Cannizzaro LA, Boghosian-Sell L, Croce CM, Hill M. A novel transcriptional unit of the tre oncogene widely expressed in human cancer cells. *Oncogene* 1992; **7**: 733-41.

334. Paulding CA, Ruvolo M, Haber DA. The Tre2 (USP6) oncogene is a hominoid-specific gene. *Proc Natl Acad Sci U S A* 2003; **100**: 2507-11.

335. Ye Y, Pringle LM, Lau AW, Riquelme DN, Wang H, Jiang T, Lev D, Welman A, Blobel GA, Oliveira AM, Chou MM. TRE17/USP6 oncogene translocated in aneurysmal bone cyst induces matrix metalloproteinase production via activation of NF-kappaB. *Oncogene* 2010.

336. Mendenhall WM, Zlotecki RA, Gibbs CP, Reith JD, Scarborough MT, Mendenhall NP. Aneurysmal bone cyst. *Am J Clin Oncol* 2006; **29**: 311-5.

337. van de Luijtgaarden AC, Veth RP, Slootweg PJ, Wijers-Koster PM, Schultze Kool LJ, Bovee JV, van der Graaf WT. Metastatic potential of an aneurysmal bone cyst. *Virchows Arch* 2009; **455**: 455-9.

338. Vaira V, Fedele G, Pyne S, Fasoli E, Zadra G, Bailey D, Snyder E, Faversani A, Coggi G, Flavin R, Bosari S, Loda M. Preclinical model of organotypic culture for pharmacodynamic profiling of human tumors. *Proc Natl Acad Sci U S A* 2010; **107**: 8352-6.

339. Karin M, Yamamoto Y, Wang QM. The IKK NF-kappa B system: a treasure trove for drug development. *Nat Rev Drug Discov* 2004; **3**: 17-26.

340. Gilmore TD, Herscovitch M. Inhibitors of NF-kappaB signaling: 785 and counting. *Oncogene* 2006; **25**: 6887-99.

341. Saunders G. Overview of drug therapy for multiple myeloma. *J Oncol Pharm Pract* 2005; **11**: 83-100.

342. Chen Z, Ricker JL, Malhotra PS, Nottingham L, Bagain L, Lee TL, Yeh NT, Van Waes C. Differential bortezomib sensitivity in head and neck cancer lines corresponds to proteasome, nuclear factor-kappaB and activator protein-1 related mechanisms. *Mol Cancer Ther* 2008; **7**: 1949-60.

343. Kopp E, Ghosh S. Inhibition of NF-kappa B by sodium salicylate and aspirin. *Science* 1994; **265**: 956-9.

344. Carcamo JM, Pedraza A, Borquez-Ojeda O, Golde DW. Vitamin C suppresses TNF alpha-induced NF kappa B activation by inhibiting I kappa B alpha phosphorylation. *Biochemistry* 2002; **41**: 12995-3002.

345. Keifer JA, Guttridge DC, Ashburner BP, Baldwin AS, Jr. Inhibition of NF-kappa B activity by thalidomide through suppression of IkappaB kinase activity. *J Biol Chem* 2001; **276**: 22382-7.

346. Epinat JC, Gilmore TD. Diverse agents act at multiple levels to inhibit the Rel/NF-kappaB signal transduction pathway. *Oncogene* 1999; **18**: 6896-909.

347. Moore RJ, Owens DM, Stamp G, Arnott C, Burke F, East N, Holdsworth H, Turner L, Rollins B, Pasparakis M, Kollias G, Balkwill F. Mice deficient in tumor necrosis factor-alpha are resistant to skin carcinogenesis. *Nat Med* 1999; **5**: 828-31.

348. Pikarsky E, Porat RM, Stein I, Abramovitch R, Amit S, Kasem S, Gutkovich-Pyest E, Urieli-Shoval S, Galun E, Ben-Neriah Y. NF-kappaB functions as a tumour promoter in inflammation-associated cancer. *Nature* 2004; **431**: 461-6.

349. Luo JL, Maeda S, Hsu LC, Yagita H, Karin M. Inhibition of NF-kappaB in cancer cells converts inflammation-induced tumor growth mediated by TNFalpha to TRAIL-mediated tumor regression. *Cancer Cell* 2004; **6**: 297-305.

350. Malik ST, Naylor MS, East N, Oliff A, Balkwill FR. Cells secreting tumour necrosis factor show enhanced metastasis in nude mice. *Eur J Cancer* 1990; **26**: 1031-4.

351. Brown ER, Charles KA, Hoare SA, Rye RL, Jodrell DI, Aird RE, Vora R, Prabhakar U, Nakada M, Corringham RE, DeWitte M, Sturgeon C, Propper D, Balkwill FR, Smyth JF. A clinical study assessing the tolerability and biological effects of infliximab, a TNF-alpha inhibitor, in patients with advanced cancer. *Ann Oncol* 2008; **19**: 1340-6.

352. Madhusudan S, Foster M, Muthuramalingam SR, Braybrooke JP, Wilner S, Kaur K, Han C, Hoare S, Balkwill F, Talbot DC, Ganesan TS, Harris AL. A phase II study of etanercept (Enbrel), a tumor necrosis factor alpha inhibitor in patients with metastatic breast cancer. *Clin Cancer Res* 2004; **10**: 6528-34.

353. Madhusudan S, Muthuramalingam SR, Braybrooke JP, Wilner S, Kaur K, Han C, Hoare S, Balkwill F, Ganesan TS. Study of etanercept, a tumor necrosis factor-alpha inhibitor, in recurrent ovarian cancer. *J Clin Oncol* 2005; **23**: 5950-9.

354. Tsimberidou AM, Thomas D, O'Brien S, Andreeff M, Kurzrock R, Keating M, Albitar M, Kantarjian H, Giles F. Recombinant human soluble tumor necrosis factor (TNF) receptor (p75) fusion protein Enbrel in patients with refractory hematologic malignancies. *Cancer Chemother Pharmacol* 2002; **50**: 237-42.

355. Wertz IE, Dixit VM. Signaling to NF-kappaB: regulation by ubiquitination. *Cold Spring Harb Perspect Biol* 2010; **2**: a003350.

356. Wu H. Assembly of post-receptor signaling complexes for the tumor necrosis factor receptor superfamily. *Adv Protein Chem* 2004; **68**: 225-79.

357. Pineda G, Ea CK, Chen ZJ. Ubiquitination and TRAF signaling. *Adv Exp Med Biol* 2007; **597**: 80-92.

358. Bradley JR, Pober JS. Tumor necrosis factor receptor-associated factors (TRAFs). *Oncogene* 2001; **20**: 6482-91.

359. Chung JY, Park YC, Ye H, Wu H. All TRAFs are not created equal: common and distinct molecular mechanisms of TRAF-mediated signal transduction. *J Cell Sci* 2002; **115**: 679-88.

360. Ye H, Arron JR, Lamothe B, Cirilli M, Kobayashi T, Shevde NK, Segal D, Dzivenu OK, Vologodskaia M, Yim M, Du K, Singh S, Pike JW, Darnay BG, Choi Y, Wu H. Distinct molecular mechanism for initiating TRAF6 signalling. *Nature* 2002; **418**: 443-7.

361. Cao Z, Xiong J, Takeuchi M, Kurama T, Goeddel DV. TRAF6 is a signal transducer for interleukin-1. *Nature* 1996; **383**: 443-6.

362. Deng L, Wang C, Spencer E, Yang L, Braun A, You J, Slaughter C, Pickart C, Chen ZJ. Activation of the IkappaB kinase complex by TRAF6 requires a dimeric ubiquitin-conjugating enzyme complex and a unique polyubiquitin chain. *Cell* 2000; **103**: 351-61.

363. Wang C, Deng L, Hong M, Akkaraju GR, Inoue J, Chen ZJ. TAK1 is a ubiquitin-dependent kinase of MKK and IKK. *Nature* 2001; **412**: 346-51.

364. Kanayama A, Seth RB, Sun L, Ea CK, Hong M, Shaito A, Chiu YH, Deng L, Chen ZJ. TAB2 and TAB3 activate the NF-kappaB pathway through binding to polyubiquitin chains. *Mol Cell* 2004; **15**: 535-48.

365. Hayden MS, Ghosh S. Signaling to NF-kappaB. *Genes Dev* 2004; **18**: 2195-224.

366. Takaesu G, Surabhi RM, Park KJ, Ninomiya-Tsuji J, Matsumoto K, Gaynor RB. TAK1 is critical for IkappaB kinase-mediated activation of the NF-kappaB pathway. *J Mol Biol* 2003; **326**: 105-15.

367. Silverman N, Zhou R, Erlich RL, Hunter M, Bernstein E, Schneider D, Maniatis T. Immune activation of NF-kappaB and JNK requires Drosophila TAK1. *J Biol Chem* 2003; **278**: 48928-34.

368. Sanz L, Sanchez P, Lallena MJ, Diaz-Meco MT, Moscat J. The interaction of p62 with RIP links the atypical PKCs to NF-kappaB activation. *EMBO J* 1999; **18**: 3044-53.

369. Sanz L, Diaz-Meco MT, Nakano H, Moscat J. The atypical PKC-interacting protein p62 channels NF-kappaB activation by the IL-1-TRAF6 pathway. *EMBO J* 2000; **19**: 1576-86.

370. Leitges M, Sanz L, Martin P, Duran A, Braun U, Garcia JF, Camacho F, Diaz-Meco MT, Rennert PD, Moscat J. Targeted disruption of the zetaPKC gene results in the impairment of the NF-kappaB pathway. *Mol Cell* 2001; **8**: 771-80.

371. Lallena MJ, Diaz-Meco MT, Bren G, Paya CV, Moscat J. Activation of IkappaB kinase beta by protein kinase C isoforms. *Mol Cell Biol* 1999; **19**: 2180-8.

372. Zhang P, Chan J, Dragoi AM, Gong X, Ivanov S, Li ZW, Chuang TH, Tuthill C, Wan Y, Karin M, Chu WM. Activation of IKK by thymosin alpha1 requires the TRAF6 signalling pathway. *EMBO Rep* 2005; **6**: 531-7.

373. Tada K, Okazaki T, Sakon S, Kobarai T, Kurosawa K, Yamaoka S, Hashimoto H, Mak TW, Yagita H, Okumura K, Yeh WC, Nakano H. Critical roles of TRAF2 and TRAF5 in tumor necrosis factor-induced NF-kappa B activation and protection from cell death. *J Biol Chem* 2001; **276**: 36530-4.

374. Habelhah H, Takahashi S, Cho SG, Kadoya T, Watanabe T, Ronai Z. Ubiquitination and translocation of TRAF2 is required for activation of JNK but not of p38 or NF-kappaB. *EMBO J* 2004; **23**: 322-32.

375. Yeh WC, Shahinian A, Speiser D, Kraunus J, Billia F, Wakeham A, de la Pompa JL, Ferrick D, Hum B, Iscove N, Ohashi P, Rothe M, Goeddel DV, Mak TW. Early lethality, functional NF-kappaB activation, and increased sensitivity to TNF-induced cell death in TRAF2-deficient mice. *Immunity* 1997; **7**: 715-25.

376. Ea CK, Deng L, Xia ZP, Pineda G, Chen ZJ. Activation of IKK by TNFalpha requires site-specific ubiquitination of RIP1 and polyubiquitin binding by NEMO. *Mol Cell* 2006; **22**: 245-57.

377. Hacker H, Karin M. Regulation and function of IKK and IKK-related kinases. *Sci STKE* 2006; **2006**: re13.

378. Shembade N, Ma A, Harhaj EW. Inhibition of NF-kappaB signaling by A20 through disruption of ubiquitin enzyme complexes. *Science* 2010; **327**: 1135-9.

379. Evans PC, Ovaa H, Hamon M, Kilshaw PJ, Hamm S, Bauer S, Ploegh HL, Smith TS. Zinc-finger protein A20, a regulator of inflammation and cell survival, has de-ubiquitinating activity. *Biochem J* 2004; **378**: 727-34.

380. Wertz IE, O'Rourke KM, Zhou H, Eby M, Aravind L, Seshagiri S, Wu P, Wiesmann C, Baker R, Boone DL, Ma A, Koonin EV, Dixit VM. De-ubiquitination and ubiquitin ligase domains of A20 downregulate NF-kappaB signalling. *Nature* 2004; **430**: 694-9.

381. Lin SC, Chung JY, Lamothe B, Rajashankar K, Lu M, Lo YC, Lam AY, Darnay BG, Wu H. Molecular basis for the unique deubiquitinating activity of the NF-kappaB inhibitor A20. *J Mol Biol* 2008; **376**: 526-40.

382. Musone SL, Taylor KE, Lu TT, Nititham J, Ferreira RC, Ortmann W, Shifrin N, Petri MA, Ilyas Kamboh M, Manzi S, Seldin MF, Gregersen PK, Behrens TW, Ma A, Kwok PY, Criswell LA. Multiple polymorphisms in the TNFAIP3 region are independently associated with systemic lupus erythematosus. *Nat Genet* 2008; **40**: 1062-4.

383. Evans PC, Smith TS, Lai MJ, Williams MG, Burke DF, Heyninck K, Kreike MM, Beyaert R, Blundell TL, Kilshaw PJ. A novel type of deubiquitinating enzyme. *J Biol Chem* 2003; **278**: 23180-6.

384. Kovalenko A, Chable-Bessia C, Cantarella G, Israel A, Wallach D, Courtois G. The tumour suppressor CYLD negatively regulates NF-kappaB signalling by deubiquitination. *Nature* 2003; **424**: 801-5.

385. Bignell GR, Warren W, Seal S, Takahashi M, Rapley E, Barfoot R, Green H, Brown C, Biggs PJ, Lakhani SR, Jones C, Hansen J, Blair E, Hofmann B, Siebert R, Turner G, Evans DG, Schrander-Stumpel C, Beemer FA, van Den Ouweland A, Halley D, Delpech B, Cleveland MG, Leigh I, Leisti J, Rasmussen S. Identification of the familial cylindromatosis tumour-suppressor gene. *Nat Genet* 2000; **25**: 160-5.

386. Trompouki E, Hatzivassiliou E, Tsichritzis T, Farmer H, Ashworth A, Mosialos G. CYLD is a deubiquitinating enzyme that negatively regulates NF-kappaB activation by TNFR family members. *Nature* 2003; **424**: 793-6.

387. Funakoshi-Tago M, Kamada N, Shimizu T, Hashiguchi Y, Tago K, Sonoda Y, Kasahara T. TRAF6 negatively regulates TNFalpha-induced NF-kappaB activation. *Cytokine* 2009; **45**: 72-9.

388. Lamothe B, Besse A, Campos AD, Webster WK, Wu H, Darnay BG. Site-specific Lys-63-linked tumor necrosis factor receptor-associated factor 6 auto-ubiquitination is a critical determinant of I kappa B kinase activation. *J Biol Chem* 2007; **282**: 4102-12.

389. Yang WL, Wang J, Chan CH, Lee SW, Campos AD, Lamothe B, Hur L, Grabiner BC, Lin X, Darnay BG, Lin HK. The E3 ligase TRAF6 regulates Akt ubiquitination and activation. *Science* 2009; **325**: 1134-8.

390. Heyninck K, Beyaert R. A20 inhibits NF-kappaB activation by dual ubiquitin-editing functions. *Trends Biochem Sci* 2005; **30**: 1-4.

391. Sriskantharajah S, Ley SC. Cell biology. Turning off inflammation signaling. *Science* 2010; **327**: 1093-4.

392. Ohazama A, Courtney JM, Tucker AS, Naito A, Tanaka S, Inoue J, Sharpe PT. Traf6 is essential for murine tooth cusp morphogenesis. *Dev Dyn* 2004; **229**: 131-5.

393. Lomaga MA, Yeh WC, Sarosi I, Duncan GS, Furlonger C, Ho A, Morony S, Capparelli C, Van G, Kaufman S, van der Heiden A, Itie A, Wakeham A, Khoo W, Sasaki T, Cao Z, Penninger JM, Paige CJ, Lacey DL, Dunstan CR, Boyle WJ, Goeddel DV, Mak TW. TRAF6 deficiency results in osteopetrosis and defective interleukin-1, CD40, and LPS signaling. *Genes Dev* 1999; **13**: 1015-24.

394. Boyce BF, Aufdemorte TB, Garrett IR, Yates AJ, Mundy GR. Effects of interleukin-1 on bone turnover in normal mice. *Endocrinology* 1989; **125**: 1142-50.

395. Dinarello CA. The interleukin-1 family: 10 years of discovery. *FASEB J* 1994; **8**: 1314-25.

396. Akatsu T, Takahashi N, Udagawa N, Imamura K, Yamaguchi A, Sato K, Nagata N, Suda T. Role of prostaglandins in interleukin-1-induced bone resorption in mice in vitro. *J Bone Miner Res* 1991; **6**: 183-9.

397. Nakamura I, Kadono Y, Takayanagi H, Jimi E, Miyazaki T, Oda H, Nakamura K, Tanaka S, Rodan GA, Duong le T. IL-1 regulates cytoskeletal organization in osteoclasts via TNF receptor-associated factor 6/c-Src complex. *J Immunol* 2002; **168**: 5103-9.

398. Wang KZ, Wara-Aswapati N, Boch JA, Yoshida Y, Hu CD, Galson DL, Auron PE. TRAF6 activation of PI 3-kinase-dependent cytoskeletal changes is cooperative with Ras and is mediated by an interaction with cytoplasmic Src. *J Cell Sci* 2006; **119**: 1579-91.

399. Blanco-Aparicio C, Renner O, Leal JF, Carnero A. PTEN, more than the AKT pathway. *Carcinogenesis* 2007; **28**: 1379-86.

400. Sparano A, Quesnelle KM, Kumar MS, Wang Y, Sylvester AJ, Feldman M, Sewell DA, Weinstein GS, Brose MS. Genome-wide profiling of oral squamous cell carcinoma by array-based comparative genomic hybridization. *Laryngoscope* 2006; **116**: 735-41.

401. Jarvinen AK, Autio R, Kilpinen S, Saarela M, Leivo I, Grenman R, Makitie AA, Monni O. High-resolution copy number and gene expression microarray analyses of head and neck squamous cell carcinoma cell lines of tongue and larynx. *Genes Chromosomes Cancer* 2008; **47**: 500-9.

402. Einenkel J, Braumann UD, Horn LC, Kuska JP, Hockel M. 3-D analysis of the invasion front in squamous cell carcinoma of the uterine cervix: histopathologic evidence for collective invasion per continuitatem. *Anal Quant Cytol Histol* 2007; **29**: 279-90.

403. Hoeller D, Dikic I. Targeting the ubiquitin system in cancer therapy. *Nature* 2009; **458**: 438-44.

404. Petroski MD. The ubiquitin system, disease, and drug discovery. *BMC Biochem* 2008; **9 Suppl 1**: S7.

405. Yang Y, Kitagaki J, Wang H, Hou DX, Perantoni AO. Targeting the ubiquitin-proteasome system for cancer therapy. *Cancer Sci* 2009; **100**: 24-8.